ECC-SMART PROJECT

Joint European Canadian Chinese development of Small Modular Reactor Technology

Grant Agreement Number: 945234
H2020 – NFRP-2019-2020

Start Date of the Project: 1/09/2020
Duration: 54 Months

Deliverable Title:	**D3.5 Report on CFD modelling and simulations in corroded environment under supercritical conditions**
Lead party:	16-KIT
Author(s):	Ivan Otic (KIT), Attila Kiss (BME), László Adorján (BME), Zénó Bertesina (BME), Balázs Kiss (BME), Vladislav Filonov (IPP), Yuliia Filonova (IPP), Haipeng Li (KTH), Henryk Anglart (KTH), Andrea Pucciarelli (UNIPI), Sara Kassem (UNIPI), Walter Ambrosini (UNIPI), Yuhao Xu (UoN), Jie Zhu (UoN)
Participant(s):	KIT, UNIPI, BME, IPP, KTH, UoN
Due Date:	31/08/2024

Version Number: 0.2

Approved by: Coordinator

Date: 15.11. 2024

Dissemination level		
PU	Public	**X**
CO	Confidential: only for ECC-SMART Partners (including the Commission Services)	
EU-RES	Classified Information: RESTREINT UE*	
EU-CON	Classified Information: CONFIDENTIEL UE*	
EU-SEC	Classified Information: SECRET UE*	

**Commission Decision 2005/444/EC*

Document History – Version Control

Version	Issue Date	Stage	Description of Changes	Contributor
0.1	September 25. 2024	Draft Version	First integrated version	KIT, UNIPI, BME, IPP, KTH, UoN
0.2	November 13. 2024	Final version	Final version with all changes integrated	KIT, UNIPI, BME, IPP, KTH, UoN

Project information

Project acronym:	ECC-SMART
Project title:	Joint European Canadian Chinese development of Small Modular Reactor Technology
Grant Agreement n°	945234
Start date:	1.9.2020
Duration	54 months
Programme:	Framework Programme for Research and Innovation (2019-2020) under the call NFRP-2019-2020
Coordinator:	Centrum Výzkumu Řež, s.r.o. (Czech Republic)

Document information

Work package:	WP3 - Thermal Hydraulics and Safety of the SCW-SMR
Contractual Date of Delivery:	31.08.2024
Actual Date of Delivery to the EC:	15.11.2024
Document type:	Report
Dissemination level:	Public (PU)
Number of pages:	296

Abstract:
This deliverable reports on developing and validating Computational Fluid Dynamics (CFD) modelling for supercritical water small modular reactors (SCW-SMR), particularly focusing on corrosive environment conditions. The work was conducted under Task 3.3 of Work Package 3 (WP3).
Key contributions include:

- Development and implementation of heat transfer correlations and CFD models by UNIPI, CNL, BME, IPP, and UoN, with validation against experimental data;
- Enhancement of engineering models for turbulent heat transfer under supercritical conditions by IPP;
- CFD modelling of heat transfer along corroded rough surfaces by KTH and UNIPI, with validation using CO2 and R134a experimental data;
- Advanced RANS modelling of turbulent heat and mass transfer by UoN and UNIPI, particularly focusing on surface roughness effects.

The research demonstrates significant progress in predicting heat transfer behaviour in supercritical water conditions. However, some models require further refinement for improved accuracy, particularly in cases involving surface roughness and heat transfer deterioration.

Copyright / Disclaimer

The document is property of the ECC-SMART consortium members. This document reflects only the author's view. It does not represent the view of the European Commission, and the European Commission is not responsible for any use that may be made of the information it contains. This deliverable contains original unpublished work except where clearly indicated otherwise. Acknowledgement of previously published material and of the work of others has been made through appropriate citation, quotation or both. Reproduction is authorized provided the source is acknowledged. (OR) No copying or distributing, in any form or by any means, is allowed without the prior written agreement of the owner of the property rights

The ECC-SMART project has received funding from the Euratom research and training programme 2019-2020 under grant agreement No 945234.

Executive Summary

Within WP3, Task 3.3 “Development and improvement of system-, subchannel- and CFD-codes for SCW-SMR" aims to validate and demonstrate the applicability and limitations of system-, subchannel- and Computational Fluid Dynamics- codes, which will be applied to design, safety and licensing.

This deliverable presents the results in Computational Fluid Dynamics (CFD) modelling and simulation applied for corrosive environments under supercritical conditions as well as for the operating conditions of the proposed SCW-SMR design. The results for the development and improvement of system-, subchannel- are reported in other deliverables of the WP3.

The Task 3.3. includes the following sub-tasks which are completely or partially dedicated to CFD analysis and modelling:

3.3.1. Contribution to establishing heat transfer correlations and CFD models appropriate for postulated operating conditions (Contributors: UNIPI, BME, IPP, UoN)

The University of Pisa (UNIPI) engaged in subtask 3.3.1 by conducting various activities to enhance understanding of the key phenomena involved in predicting fluid dynamics and heat transfer at supercritical pressures. This involved using a CFD RANS model established in prior activities (Pucciarelli et al., 2016) that turned out to be useful as a basis for discussion of observed phenomena and to reveal and explain trends which are also observed in experimental data. In addition to this activity, UNIPI performed a comprehensive study of existing heat transfer correlations, assessing their effectiveness in predicting two sets of experimental data taken as reference, the CO2 ones by Kline (2017) and the water ones by Watts (1980).

The research group at the Budapest University of Technology and Economics (BME) conducted comprehensive CFD analyses using ANSYS CFX to study supercritical water flow in nuclear fuel assemblies. The methodology progressed from simple geometries with smooth tubes, to complex configurations (2×2 rod bundles and horizontal SCW-SMR fuel assemblies). Model validation is utilized within the IBSCTH international benchmark activity. IBSCTH was organized by the National Power Institute of China (NPIC) and Xian Jiao-Tong University, China and was also part of the ECC-SMART project cooperation. The study finally resulted in coupled CFX-Serpent Monte Carlo simulations of horizontal SCW flow in fuel assemblies, including variants with wrapped wire spacers.

IPP's contribution to Subtask 3.3.1 is focused on enhancing the predictive capabilities of CFD methods for modelling supercritical fluid behaviour. The work progressed through several stages: first analysing existing experimental studies, then testing various turbulence models with wall functions and low-Reynolds effects. Based on these findings, the research advanced to adapting temperature wall functions and modifying the eddy viscosity turbulence model to account for non-linear heat transfer effects. These developments were validated using a novel non-linear differential method, developed as part of the ECC-SMART project at IPP.

University of Nottingham (UoN) performed a numerical investigation to validate computational fluid dynamics (CFD) capabilities for supercritical water applications. The study first reproduced the experimental results by Huang et al. (2022) using ANSYS FLUENT to show the capability of commercial CFD code to predict the flow and heat transfer of supercritical water. Building on this validation, the research extended to CFD analysis of heat transfer characteristics of supercritical water flowing through a horizontal

rod bundle with heated fuel rods, providing insights into nuclear reactor thermal-hydraulic performance.

3.3.3. Investigation and implementation of heat transfer correlations (Contributor: CNL)

The friction correction factors have been implemented in an interim version of the subchannel code ASSERT-PV to assess their impact on pressure drop prediction. The results showed that a correction factor reduces the uncertainty of the ASSERT-PV SC predictions for pressure drop. This is more pronounced for cases close to the critical or pseudo-critical point. For further improvement an oxide layer growth model for the proposed cladding materials by Guzonas et al. 2018 is implemented and validated.

3.3.4. Improvement, implementation and validation of engineering models for turbulent heat transfer under supercritical conditions (Contributor: IPP)

This work summarizes research on enhancing engineering models for turbulent heat transfer under supercritical conditions, conducted at IPP within the ECC-SMART project. The study focuses on two main approaches: adapting universal wall functions (UWFs) for heat transfer deterioration (HTD) prediction and developing a modified eddy viscosity turbulence model incorporating Popov's theory and density pulsation corrections. The resulting non-linear algebraic turbulence model, which accounts for gravity force and turbulent effects, was implemented in a 2D differential procedure (Narrow Channel model) due to its recursive nature making standard CFD implementation challenging. Validation against CO2 experimental data demonstrated accurate prediction of wall temperature peaks in both location and magnitude, outperforming standard RANS turbulence models.

3.3.5. CFD modelling and validation of supercritical water heat transfer along corroded rough surfaces (Contributors: KTH, UNIPI)

University of Pisa (UNIPI) focused on the development and validation of a CFD model to predict heat transfer along rough surfaces under supercritical pressure conditions. The model was validated against two distinct experimental datasets: one utilizing CO2 flow in a vertically heated tube (Kassem et al., 2023) and another employing Freon R134a under similar conditions (Kassem et al., 2025). Results demonstrated the model's capability to effectively capture wall roughness effects on heat transfer, particularly at higher roughness values, though some discrepancies were observed at lower roughness levels. These discrepancies could potentially be addressed through finer calibration when a broader range of experimental conditions becomes available. As part of the ECC-SMART project, the University of Pisa's model was recently applied to analyse experimental data collected by KIT using R134a as a working fluid at supercritical pressure.
Royal Institute of Technology (KTH) developed numerical models to predict supercritical heat transfer along rough corroded surfaces using RANS CFD with specialized wall treatments. Two low-Re turbulence models are formulated with modified source terms and boundary conditions for turbulent kinetic energy and dissipation. These models, based on low-Re k-ω SST modelling approach, are validated against experimental data using supercritical CO2 and R134a, showing good agreement in predicting both heat transfer deterioration and enhancement due to surface roughness. While promising for thermal-hydraulic design of SCW-SMRs, further refinement is needed to improve prediction capabilities.

3.3.6. Two and more equation RANS modelling of turbulent heat and mass transfer along corroded surfaces (Contributors: UoN, UNIPI)

At the University of Nottingham (UoN) CFD simulations using the k-ω SST turbulence model were performed and validated against experimental data for supercritical water flow in tubes. The model accurately predicted flow behaviour at 23 and 25 MPa. Results demonstrated the impact of the roughness constant (Cs) on heat transfer predictions. While non-uniform rough tubes exhibited higher friction factors than uniform ones, the SST k-ω model outperformed both standard and buoyant k-ε models in capturing roughness effects and overall flow characteristics, particularly due to its superior handling of surface roughness impacts.

The work performed at UNIPI presents a CFD modelling approach developed for analysing oxygen, hydrogen, and corrosion product transport in supercritical water conditions. Building on previous heat transfer studies, the AHFM model developed at UNIPI employs passive scalar transport in STAR-CCM+ to simulate mass transfer phenomena. The preliminary results suggest the potential of the developed model for predicting complex mass transport behaviour in SCWR cores, particularly considering material diversity and turbulence effects from structural components.

Table of contents

List of acronyms and abbreviations 10
List of tables 11
List of figures 12
1 Introduction 22
Related documents 25
2 Subtask 3.3.1 Contribution to establish heat transfer correlations and CFD models appropriate for postulated operating conditions 26
2.1 CONTRIBUTION BY UNIPI 26
2.1.1 Introductory remarks 26
2.1.2 General considerations on heat transfer at supercritical pressure 27
2.1.3 Usefulness of a fluid-to-fluid similarity theory for heat transfer to SC fluids 31
2.1.4 Adopted fluid-to-fluid similarity theory and its relevant applications 32
2.1.5 Literature survey and discussion of selected heat transfer correlations 48
2.1.6 Analysis of two different heat transfer deterioration modes 98
2.1.7 Considerations on the role of CFD in the work made by UNIPI 112
2.2 CONTRIBUTION BY BME 113
2.2.1 Ansys CFX model validation to upward SCW flow in tubes 113
2.2.2 Ansys CFX model validation to upward and horizontal SCW flow in tubes 117
2.2.3 Ansys CFX model validation for upward SCW flow in 2×2 rod bundles 128
2.2.4 CFD modelling of horizontal SCW flow in SCW-SMR FA with/without WWS 137
2.2.5 Coupled calculations with Ansys CFX-Serpent on the horizontal SCW flow in the FA of SCW-SMR 149
2.3 CONTRIBUTION BY CNL 154
2.3.1 Fouling—Cladding corrosion 155
2.4 CONTRIBUTION BY IPP 158
2.4.1 Introductory remarks 158
2.4.2 Selection of experimental studies most applicable for testing existing CFD models and validating their possible modifications 159
2.4.3 Application of existed CFD methods for modelling the regimes with HTD 163
2.4.4 Concluding remarks 170
2.5 CONTRIBUTION BY UoN 171
2.5.1 Introduction 171
2.5.2 Theory 172
2.5.3 Description of test rig 173

2.5.4 Experiment and simulation settings 174
2.5.5 Results and discussion 176
2.5.6 Rod bundle CFD simulation 178
2.5.7 Summary 194
2.6 CONTRIBUTION BY NPIC 195
3 Subtask 3.3.3 Investigation and implementation of heat transfer correlations (CNL) 196
4 Subtask 3.3.4 Improvement, implementation and validation of engineering models for turbulent heat transfer under supercritical conditions (IPP) 196
4.1 Introductory remarks 196
4.2 Universal wall functions adaptation for calculation the heat transfer at supercritical conditions 197
4.2.1 Adaptation of "classical" temperature wall functions 198
4.2.2 Peculiarities of implementation and application of the modified wall function (SWF) 200
4.2.3 SWF application examples 202
4.3 Modification of Eddy viscosity turbulence model to take into account non-linear effects of heat transfer 204
4.3.1 Description of the proposed modifications for obtaining the closing turbulent characteristics 205
4.3.2 Validation 208
4.4 Concluding remarks 213
5 Subtask 3.3.5 CFD modelling and validation of supercritical water heat transfer along corroded rough surfaces (KTH, UNIPI) 214
5.1 CONTRIBUTION BY UNIPI 214
5.1.1 Model description 214
5.1.2 Assessing Heat Transfer Dynamics Through Parametric Analysis of Various Fluids 216
5.1.3 Assessing Wall Roughness Effects on Carbon Dioxide: Data Comparison 221
5.1.4 Assessing Wall Roughness Effects on R134a: A Recent Data Comparison 222
5.2 CONTRIBUTION BY KTH 227
5.2.1 Introduction 228
5.2.2 Model description 229
5.2.3 Results and discussion 231
5.2.4 Conclusions 238
6 Subtask 3.3.6 Two and more equation RANS modelling of turbulent heat and mass transfer along corroded surfaces (UoN, UNIPI) 238
6.1 CONTRIBUTION BY UoN 238

6.1.1 Introduction 238
6.1.2 Governing equations and turbulent models 239
6.1.3 Vertical flow in a pipe with rough surface 241
6.1.4 Horizontal flow in a rough tube with different roughness constants 248
6.1.5 Horizontal flow in a rough tube with different roughness heights 255
6.2 CONTRIBUTION BY UNIPI 261
6.2.1 Modelling of turbulent mass transfer 262
6.2.2 Selected calculation case 264
6.2.3 Concluding Remarks 268
7 REFERENCES 269
APPENDIX – Table of correlations from the survey by UNIPI 280

List of acronyms and abbreviations

Nomenclature

Cs	Roughness constant
D_{in}	Tube inner diameter [m]
G	Mass flux [kg/m^2/s]
L_1	Entrance length of test sections [mm]
L_2	Heat length of test sections [mm]
L_3	Full length of test sections [mm]
m	Mass flow rate [kg/s]
n	Number of numerical cells in a numerical mesh [pcs]
$n_{n,i}$	Number of nodes in “i” direction [pcs]
p	Absolute pressure [bar or MPa]
R_a	Average or arithmetic average of profile height deviations from the mean line [µm]
T	Temperature [°C]
T_{pc}	Pseudo-critical temperarture [°C]
$T_w(h_b)$	Wall temperature versus the bulk fluid enthalpy [°C]
Δh_{total}	Total specific enthalpy rise along the full length of CD
Δp_{total}	Total pressure drop along the full length of CD
q_w	Heat flux [kW/m^2]
y_1^+	Dimensionless distance between the wall and the first node in the numerical grid close to the wall [-]
Δy	Height of the first numerical layer next to the solid wall [µm]
ΔZ_j	Axial size of the numerical elements in the “j” mesh [mm]

Abbreviations

AXM	Axial (numerical) mesh
BC	Boundary conditions
BLM	Boundary Layer Mesh (numerical, near the solid wall)
BME	Budapest University of Technology and Economics
BS	Boundary surface
BSL-RSM	BSL-Reynolds Stress Model (RANS turbulence model)
CD	Computational domain
CFD	Computational Fluid Dynamics
CHT	Conjugate Heat Transfer
CIRM	Circumferential (numerical) mesh
DC	Direct current
DHT	Deteriorated heat transfer
ECC-SMART	(Joint) European Canadian Chinese development of Small Modular Reactor Technology
FA	Fuel assembly (of e.g. SCW-SMR)
FABW	Fuel assembly box wall
GIF	Generation IV International Forum
HTD	Heat transfer deteoriation

IAEA	International Atomic Energy Agency
LWR	Light water reactor
MBW	Moderator box wall
MSS	Mesh Sensitivity Study
NHT	Normal heat transfer
NPIC	Nuclear Power Institute of China
PPCD	Pre-pre conceptual design (of the SCW-SMR)
SC	Subchannel
SCW	Supercritical (pressure) water
SCW-SMR	Supercritical water-cooled small modular reactor
SCWR	Supercritical-Water-Cooled Reactor
SST	Shear Stress Transport (RANS turbulence model)
WP	Work package
WRSS	Wall Roughness Sensitivity Study
WWS	Wrapped wire spacer
XJTU	Xi'an Jiaotong University

List of tables

Table 1. values of the constants and coefficients used in the analysis..... 66
Table 2. List of the selected heat transfer correlations..... 68
Table 3. Assessement for heat transfer correlations for supercritical carbon dioxide data by Kline. 70
.Table 4. Coefficient and exponents for the correlation in Eq. (31) in “correlation mode” 78
Table 5. Coefficient and exponents for the correlation in Eq. (31) in both modes 81
Table 6. Coefficient and exponents for the correlation in Eq. (32) in both modes 84
Table 7. Coefficient and exponents for the correlation in Eq. (33) in both modes 86
Table 8. Coefficient and exponents for the correlation in Eq. (36) in “prediction” mode 90
Table 9. Coefficient and exponents for the correlation in Eq. (37) in “prediction” mode 92
Table 10. Coefficient and exponents for the correlation in Eq. (39) in “prediction” mode..... 94
Table 11. Examined experimental conditions and geometry for the deteriorated heat transfer case of Shitsman 1963 114
Table 12. Dimensionless wall distance (y1+) and total number of cells 115
Table 13. The BCs and uncertainties of temperature measurements. 116
Table 14. The applied boundary conditions of the eight experimental cases (Yamagata et al. 1972) 120
Table 15: Details of the three different boundary layer numerical meshes. 121
Table 16: Details of the three different circumferential numerical meshes 121
Table 17: Details of the three different axial numerical meshes 122
Table 18: The used average sand grain height values 122
Table 19: Required CIRM resolution needed based on the two key parameters..... 125
Table 20 Thermal conductivity measurements for the proposed cladding materials. 157
Table 21. NTUU test matrix 162
Table 22. Chosen calculation regimes description..... 164
Table 23. Integral pressure losses comparison 167
Table 24. Chosen calculation regimes description..... 168

Table 25. Boundary conditions 174
Table 26. Mesh analysis 174
Table 27. Mesh settings 175
Table 28. Mesh settings 179
Table 29. Boundary conditions 180
Table 30. Mesh information 180
Table 31. Errors 180
Table 32. Mesh evaluation 181

List of figures

Figure 1. Trends of relevant properties of water and CO_2 at two relevant pressures for the data considered in the present report 28
Figure 2. Pseudo-Nukiyama curve proposed to display deteriorated heat transfer phenomena in Sharabi and Ambrosini (2009) 29
Figure 3: Description of the main steps in the similarity rationale 33
Figure 4. Results from DNS and RANS calculations in dimensionless form (Pucciarelli et al., 2020) 35
Figure 5. Prediction of Kline's CO_2 data at q"= 18 kW/m^2 and trends obtained by the application of the similarity theory for water, NH3 and R23 (ID = 4.6 mm) 36
Figure 6. Trends of the relevant dimensionless numbers along the channel showing similarity for the case of Kline's data with q" =18 kW/m2 and Tin= 24 °C 38
Figure 7. Trends of dimensionless parameters for the data by Kline with q"=20 kW/m^2 and T_{in} = 33 °C 39
Figure 8. Data by Watts: Water 25 MPa, 25.4 mm ID, (nominal) T_{in}=200 °C, q"=400 kW/m^2, upward flow, G expressed in kg/m^{2}s 40
Figure 9. Data by Watts: Water 25 MPa, 25.4 mm ID, (nominal) T_{in}=250 °C, q"=400 kW/m^2, upward flow, G expressed in kg/m^{2}s 40
Figure 10. Trends of dimensionless parameters for the data by Watts with nominal Tin = 200 °C, G = 318 kg/m^{2}s 40
Figure 11. Relation between dimensionless density and dimensionless enthalpy for four fluids 42
Figure 12. Presence of envelopments of deteriorated heat transfer trends in Kline's data (G=300 kg/(m^{2}s)) 45
Figure 13. Predictions obtained in Pucciarelli and Ambrosini (2017) of the data by Pis'menny et al. (2005, 2005a) with water at 23.5 MPa, 6.28 mm ID, T_{in} = 300 °C, G = 508 kg/(m^{2}s), q" = 390 kW/m^2 46
Figure 14. Comparison of predictions of Kline's data with extrapolated Pis'menny et al. Data .. 47
Figure 15. Procedure for iterating on wall temperature 64
Figure 16. Comparison of the calculated Nu values Vs. the experimental one, using the correlation by Bae et al. (2009) to find the Nu values in the correlation mode with the use of original form (left) and the optimized coefficients (right). 67
Figure 17. Wall temperature trends predicted using Bae et al. (2009) correlation in original form (left) and in optimized coefficients (right) for the case by Kline CO_2 data at p=8.35 MPa, Tin=16°C, G=300 kg/m^{2}s and q=20 KW/m^2. 67

Figure 18. Wall temperature trends predicted using Bae et al. (2009) correlation in original form (left) and in optimized coefficients (right) for the case by Watts H2O data at p=25 MPa, Tin=200°C, G=375 kg/m^{2}s and q=340 KW/m^2. 69
Figure 19. Comparison of the calculated Nu values Vs. the experimental one, using the correlation by Chen and Fang (2014) to find the Nu values in the correlation mode with the use of original form (left) and the optimized coefficients(right). 69
Figure 20. Wall temperature trends predicted using Chen and Fang (2014)correlation in original form (left) and in optimized coefficients (right) for the case by Kline CO_2 data at p=8.35 MPa, Tin=16°C, G=300 kg/m^{2}s and q=20 KW/m^2. 69
Figure 21. Wall temperature trends predicted using Chen and Fang (2014) correlation in original form (left) and in optimized coefficients (right) for the case by Watts H2O data at p=25 MPa, Tin=200°C, G=375 kg/m^{2}s and q=340 KW/m .^{2} 70
Figure 22.Wall temperature trends obtained in the prediction mode by different heat transfer correlation and compared to the case of CO_2 Kline's Data at p = 8.35 MPa, Tin = 16 °C, G=300 kg/(m^{2}s) and q"=20 kW/m^2..... 72
Figure 23 Wall temperature trends for CO_2 Kline's Data at p = 8.35 MPa, Tin = 16 °C, G=300 kg/(m^{2}s) and q"=20 kW/m^{2}obtained by applying Bruch et al. (2009) correlation. 72
Figure 24. Wall temperature trends for CO_2 Kline's Data at p = 8.35 MPa, Tin = 16 °C, G=300 kg/(m^{2}s) and q"=20 kW/m^{2}obtained by applying Gupta et al (2010) correlation. 73
Figure 25. Wall temperature trends for CO_2 Kline's Data at p = 8.35 MPa, Tin = 16 °C, G=300 kg/(m^{2}s) and q"=20 kW/m^{2}obtained by applying Kuang et al. (2008) correlation. 73
Figure 26. Wall temperature trends for CO_2 Kline's Data at p = 8.35 MPa, Tin = 16 °C, G=300 kg/(m^{2}s) and q"=20 kW/m^{2}obtained by applying Watts and Chou (1982) correlation. 73
Figure 27. Wall temperature trends obtained in the prediction mode by different heat transfer correlations and compared to the case of H2O Watts' Data at p = 25 MPa, Tin = 200 °C, G=375 kg/(m^{2}s) and q"=340 kW/m^2..... 74
Figure 28. Wall temperature trends for H_2O Watts' Data at p = 25 MPa, Tin = 200 °C, G=375 kg/(m^{2}s) and q"=340 kW/m^{2}obtained by applying Bruch et al (2009) correlation. 74
Figure 29. Wall temperature trends for H_2O Watts' Data at p = 25 MPa, T_{in} = 200 °C, G=375 kg/(m^{2}s) and q"=340 kW/m^2 obtained by applying Zhu B. et al. (2020) correlation. 75
Figure 30. Global fitting of the simple Re^x Pr^y correlation with density and viscosity ratio corrections in "correlation mode" 79
Figure 31. Wall temperature trend for the 1st sample case of the data by Kline in "correlation mode" 79
Figure 32. Wall temperature trend for the 2nd sample case of the data by Kline in "correlation mode" 80
Figure 33. Wall temperature trend for the 1st sample case of the data by Watts in "correlation mode" 80
Figure 34. Wall temperature trend for the 2nd sample case of the data by Watts in "correlation mode" 80
Figure 35. Global fitting of the simple Re^x Pr^y correlation with density and viscosity ratio corrections in "prediction mode" (i.e., up to convergence on wall temperature) 81
Figure 36. Wall temperature trend for the 1st sample case of the data by Kline in "prediction mode" 82
Figure 37. Wall temperature trend for the 2nd sample case of the data by Kline in "prediction mode" 82

Figure 38. Wall temperature trend for the 1st sample case of the data by Watts in "prediction mode" 82
Figure 39. Wall temperature trend for the 2nd sample case of the data by Watts in "prediction mode" 83
Figure 40. Global fitting of the simple Re^x Pr^y correlation with density, viscosity and heat conduction ratio corrections in "correlation" (left) and "prediction" (right) modes 84
Figure 41. Wall temperature trend for the 1st sample case of the data by Kline in "correlation" (left) and "prediction" (right) modes 84
Figure 42. Wall temperature trend for the 2nd sample case of the data by Kline in "correlation" (left) and "prediction" (right) modes 85
Figure 43. Wall temperature trend for the 1st sample case of the data by Watts in "correlation" (left) and "prediction" (right) modes 85
Figure 44. Wall temperature trend for the 2nd sample case of the data by Watts in "correlation" (left) and "prediction" (right) modes 85
Figure 45. Global fitting of Eq. (33) in "correlation" (left) and "prediction" (right) modes 87
Figure 46. Wall temperature trend for the 1st sample case of the data by Kline in "correlation" mode 87
Figure 47. Wall temperature trend for the 2nd sample case of the data by Kline in "correlation" mode 87
Figure 48. Wall temperature trend for the 1st sample case of the data by Watts in "correlation" mode 88
Figure 49. Wall temperature trend for the 2nd sample case of the data by Watts in "correlation" mode 88
Figure 50. Wall temperature trend for the 1st sample case of the data by Kline in "prediction" mode 88
Figure 51. Wall temperature trend for the 2nd sample case of the data by Kline in "prediction" mode 89
Figure 52. Wall temperature trend for the 1st sample case of the data by Watts in "prediction" mode 89
Figure 53. Wall temperature trend for the 2nd sample case of the data by Watts in "prediction" mode 89
Figure 54. Global fitting of Eq. (36) in "prediction" mode 90
Figure 55. Wall temperature trend for the 1st and 2nd sample case of the data by Kline in "prediction" mode 91
Figure 56. Wall temperature trend for the 1st and 2nd sample case of the data by Watts in "prediction" mode 91
Figure 57. Global fitting of Eq. (37) in "prediction" mode 92
Figure 58. Wall temperature trend for the 1st and 2nd sample case of the data by Kline in "prediction" mode 92
Figure 59. Wall temperature trend for the 1st and 2nd sample case of the data by Watts in "prediction" mode 92
Figure 60.Trend of the Richardson number for the 1st sample case of the data by Kline and the 1st sample case of the data by Watts in "prediction" mode 93
Figure 61. Global fitting of Eq. (39) in "prediction" mode 94
Figure 62. Wall temperature trend for the 1st and 2nd sample case of the data by Kline in "prediction" mode 94

Figure 63. Wall temperature trend for the 1st and 2nd sample case of the data by Watts in "prediction" mode 94
Figure 64. Wall temperature trends for the 1st sample cases of the data by Kline and Eq. (33) during iterations 96
Figure 65. Wall temperature trends for the 1st sample cases of the data by Watts and Eq. (33) during iterations 97
Figure 66. Comparison between the experimental Nusselt number and the value predicted by the Dittus-Boelter correlation for the addressed data base 98
Figure 67. Trends of dimensionless parameters for the data by Kline with q"=20 kW/m^2 and T_{in} = 33 °C 99
Figure 68. Wall temperature trends predicted by CFD for two cases by Watts 100
Figure 69. Considered Kline case: G = 300 kg/m^{2}s, q''=15 kW/m^2 100
Figure 70 Richardson number: local distribution and its integral 101
Figure 71. Watts data: analysis of the $NuExp - Nu0Nu0$ distribution as a function of $RiINT$ .. 102
Figure 72. Watts data: analysis of the $NuExp - Nu0Nu0$ distribution as a function of $RiINT$ .. 103
Figure 73 Considered Shape Functions 103
Figure 74. Watts Data series for Tin = 150°C: Comparison of experimental al calculated trends 104
Figure 75. Watts Data series for Tin = 200°C: Comparison of experimental al calculated trends 105
Figure 76. Watts Data series for Tin = 250°C: Comparison of experimental al calculated trends 105
Figure 77. Watts Data series for Tin = 310°C: comparison of experimental and calculated trends 106
Figure 78. Evolution of the predicted wall temperature distribution as a function of the number of iterations for a selected case 106
Figure 79. Scaling Attempts with CO_2 at 8.35 MPa 107
Figure 80. Experimental trends and CFD model predictions obtained for Kline's data with CO_2 in upward flow at 8.35 MPa at q"=20 kW/m^2, G=300 kg/(m2s) with an ID = 4.6 mm 107
Figure 81. Experimental trends obtained for Kline's data with CO_2 in upward flow at 8.35 MPa at q"=20 kW/m2, G=300 kg/(m^{2}s) with an ID of 4.6 mm 108
Figure 82. Classical examples of Nukiyama curves for pool boiling with indication of heat transfer regimes 109
Figure 83. Experimental and predicted trends of wall temperature for Kline's data with CO_2 for upward flow at 8.35 MPa, ID=4.6 mm and G = 300 kg/(m^{2}s) and corresponding pseudo-Nukiyama curve 110
Figure 84. Pseudo-Nukiyama curves obtained by the CFD model for Kline's experimental apparatus with CO_2 for upward flow at 8.35 MPa, ID=4.6 mm and different values of G, expressed in kg/(m^{2}s) 111
Figure 85. Classical 3D description of boiling heat transfer phenomena at subcritical pressure as a function of quality, wall temperature and heat flux (see Collier and Thome, 1999) 111
Figure 86. 3D representation of supercritical pressure heat transfer deterioration phenomena obtained processing results obtained for Kline's experimental apparatus with CO_2 at 8.35 MPa for G = 300 kg/(m^{2}s) and Tin= 0 °C: continuous surface form 112
Figure 87. The geometry of the test section with the applied BCs of the CFD model 114
Figure 88. The schema of the CFD model 115

Figure 89. The result of the parametric study – the wall temperature along the modelled length for the reference case (R_a = 0 μm) and the rough wall cases (R_a = 1, 5, 10, 50, 100 μm)..... 117
Figure 90. The geometry model of the validation cases in the Ansys ICEM CFD..... 119
Figure 91. The process of the sensitivity studies 120
Figure 92. Comparison of $T_w(h_b)$ for the BLM sensitivity study (a., H233, b., H698 case) 123
Figure 93. Comparison of $T_w(h_b)$ for the CIRM sensitivity study (U930 case)..... 124
Figure 94. Comparison of $T_w(h_b)$ for the CIRM sensitivity study (H930 case)..... 125
Figure 95. Comparison of $T_w(h_b)$ for the AXM sensitivity study (H465 case) 126
Figure 96. Comparison of $T_w(h_b)$ for the WR sensitivity study (H930) 126
Figure 97. Comparison of $T_w(h_b)$ for the WR sensitivity study (U698) 127
Figure 98. IBSCTH Part 1/1.1: a., the details of the cross section of the experimental test section, b., the CFD model of BME for Case 1 & 2 in the Ansys CFX pre-processor program 129
Figure 99. IBSCTH Part 1/1.2: a., the details of the cross section of the experimental test section, b., the details of the fuel rod with local wire wraps, c., the axial positions of the local wire wraps, d., the CFD model of BME for Case 3 in the Ansys CFX pre-processor program 129
Figure 100. IBSCTH Part 1/1.3: a., the details of the cross section of the experimental test section, b., the CFD model of BME for Case 4 & 5 in the Ansys CFX pre-processor program 130
Figure 101. Comparison of experimental and CFD results for Case 1 of IBSCTH Part 1/1.1 Bare Rod Bundle Channel subtask (inner wall temperatures at mp-5 position for Rod #1)..... 130
Figure 102. Comparison of experimental and CFD results for Case 1 of IBSCTH Part 1/1.1 Bare Rod Bundle Channel subtask (inner wall temperatures at mp-5 position for Rod #2)..... 131
Figure 103. Comparison of experimental and CFD results for Case 2 of IBSCTH Part 1/1.1 Bare Rod Bundle Channel subtask (inner wall temperatures at mp-5 position for Rod #1)..... 131
Figure 104. Comparison of experimental and CFD results for Case 2 of IBSCTH Part 1/1.1 Bare Rod Bundle Channel subtask (inner wall temperatures at mp-5 position for Rod #2)..... 132
Figure 105. Comparison of experimental and CFD results for Case 3 of IBSCTH Part 1/1.2 Local wire-wrapped rod bundle channel subtask (inner wall temperatures at mp-1/2/3/4 positions of Rod #1)..... 132
Figure 106. Comparison of experimental and CFD results for Case 3 of IBSCTH Part 1/1.2 Local wire-wrapped rod bundle channel subtask (inner wall temperatures at mp-1/2/3/4 positions of Rod #2)..... 133
Figure 107. Comparison of experimental and CFD results for Case 3 of IBSCTH Part 1/1.2 Local wire-wrapped rod bundle channel subtask (inner wall temperatures at mp-1/2/3/4 positions of Rod #3)..... 133
Figure 108. Comparison of experimental and CFD results for Case 3 of IBSCTH Part 1/1.2 Local wire-wrapped rod bundle channel subtask (inner wall temperatures at mp-1/2/3/4 positions of Rod #4)..... 134
Figure 109. Comparison of experimental and CFD results for Case 4 of IBSCTH Part 1/1.3 Full-length wire-wrapped rod bundle channel subtask (inner wall temperatures at mp-5 position for Rod #2) 135
Figure 110. Comparison of experimental and CFD results for Case 4 of IBSCTH Part 1/1.3 Full-length wire-wrapped rod bundle channel subtask (inner wall temperatures at mp-5 position for Rod #4) 135
Figure 111. Comparison of experimental and CFD results for Case 5 of IBSCTH Part 1/1.3 Full-length wire-wrapped rod bundle channel subtask (inner wall temperatures at mp-5 position for Rod #2) 136

Figure 112. Comparison of experimental and CFD results for Case 5 of IBSCTH Part 1/1.3 Full-length wire-wrapped rod bundle channel subtask (inner wall temperatures at mp-5 position for Rod #4) 136
Figure 113. a., The rod bundle (WWS removed) of the SCW-SMR concept (Adorján 2022), b., The geometry of the FA without WWS (Adorján 2022) 138
Figure 114. The block structure of the SCW flow in the FA without WWS (cross-sectional view): a., the entire block structure of the FA, b., the block structure of a fuel rod, c., enlarged details (Adorján 2022) 139
Figure 115. The mesh of the SCW flow in FA without WWS (cross-sectional view): a., global mesh at the corner, b., zoomed global mesh at the corner, c., zoomed details of the boundary layer mesh (Adorján 2022) 139
Figure 116. Meshing details of the solid domains (FABW, MBW, fuel rod cladding and fuel) and for the SCW flow in MB (isometric view on the left and cross-sectional view on the right) (Adorján 2022) 140
Figure 117. Meshing details of the solid domains (FABW, MBW, fuel rod cladding and fuel) and for the SCW flow in MB (isometric view on the left and cross-sectional view on the right) (Adorján 2022) 141
Figure 118. The isometric view of the CHT CFD models of the FA with the main BCs (Adorján 2022) 142
Figure 119. Linear regression on SST models for the target variable Δh_{total}, R^2=0.99 (very good) (Adorján 2022) 143
Figure 120. Linear regression on SST models for the target variable Δp_{total}, R^2=0.97 (very good) (Adorján 2022) 144
Figure 121. The distributions of: a., the cross section averaged velocity, b., the total pressure drop of the SCW flow in the FA without and with WWS (Adorján 2022) 144
Figure 122. The distributions of the maximum temperatures along the length (Z [m]) for the fuel, the cladding solid and the SCW flow in FA fluid domains without/with WWS (Adorján 2022) .. 145
Figure 123. The flow pattern in the SCW flow in FA fluid domains with WWS: **a.,** the stream lines in the FA and **b.,** the so-called sweeping flow in the cross section of the FA (Kiss 2018, Adorján 2022, Kiss and Mervai 2016, Kiss et al. 2011) 146
Figure 124. The velocity distributions on the BSs of different types of SC pairs for: **a.,** the SCW flow in the FA without WWS and **b.,** the SCW flow in the FA with WWS (Kiss 2018, Adorján 2022, Kiss and Mervai 2016, Kiss et al. 2011) 146
Figure 125. Abolute pressure distribution along the seven stages for Ansys CFX models M02, M04 and M05 of BME 147
Figure 126. SCW coolant temperature distribution along the seven stages for Ansys CFX models M02, M04 and M05 of BME 148
Figure 127. The CFD model of 1.3 full-length wire-wrapped rod bundle channel (Case 4 & 5) 150
Figure 128: a., The Serpent 2 core (left) and b., the fuel assembly (right) models 150
Figure 129**:** a., Improved core model enrichment map (left) and b., the hot channel MLHR profiles (right) 151
Figure 130: The SCW-SMR assembly model developed in Serpent 2 for coupled CFD and Serpent 2 calculations 151
Figure 131: the geometry and boundary conditions of the ANSYS CFX model 153
Figure 132: Volumetric heat source density along the fuel assembly for the 1st iteration series 154

Figure 133: Volumetric heat source density along the fuel assembly for the 2nd iteration series 154
Figure 134 Representation of a fuel element thermal layers 156
Figure 135 Cross-sectional view of a corroded coupon showing the oxide layer thickness. 157
Figure 136. Experimental profiles during the heat transfer deterioration for the upward and downward flow of a supercritical medium 161
Figure 137. Annular channel (1R) and rod bundles (3R, 7R) geometry 161
Figure 138. Axial wall temperature distribution (NTUU experimental results) 163
Figure 139. The general view of the calculation models geometry 164
Figure 140. Axial distribution of the averaged wall temperature in the annular channel (1-rod assembly) obtained with RNG (k-ε family) and SST (k-ω) turbulence models 165
Figure 141. Distribution of the annular channel heating surface temperature for the regime 1R#3 without/with low-Re correction 166
Figure 142. Axial distribution of average wall temperature in the 3-rod assembly 166
Figure 143. Distribution of heating surface temperature in the 3-rod assembly 167
Figure 144. General view of the 3-rod and 7-rod assemblies calculation models with details of their discretisation and applied boundary conditions 168
Figure 145. Comparison of the obtained temperature distributions on the external surface with the visualized experimental ones 169
Figure 146. Axial temperature distributions obtained for 3-rod bundle and 7-rod bundle (shown for central rod #1 and peripheral rod #7) and compared with corresponding experimental data .. 170
Figure 147. Full test rig schematic (Huang et al., 2022) 173
Figure 148. Horizontal test section (Huang et al., 2022) 174
Figure 149. Full length view of geometry and mesh 175
Figure 150. Meshes of pipe outlet 175
Figure 151. Wall temperature comparison 176
Figure 152. Results at 523 K 177
Figure 153. Results at 623 K 177
Figure 154. Results at 653 K 178
Figure 155. Results at 661 K 178
Figure 156. Rod bundle diagram 179
Figure 157. Mesh diagram 179
Figure 158. Section view of model 181
Figure 159. Results of temperature (Shang et al., 2010) 182
Figure 160. Temperature at point 1 182
Figure 161. Temperature at point 2 183
Figure 162. Temperature at point 3 184
Figure 163. Orientation diagram 184
Figure 164. Results of wall temperature (Shang et al., 2010) 184
Figure 165. Results of rod 1 185
Figure 166. Results of rod 3 186
Figure 167. Results of rod 4 186
Figure 168. Results of rod 6 187
Figure 169. Rresult of wall temperature (Shang et al., 2010) 187
Figure 170. Results of rod 1 188
Figure 171. Results of rod 3 188
Figure 172. Results of rod 4 189

Figure 173. Results of rod 6 189
Figure 174. Results of wall temperature (Shang et al., 2010) 190
Figure 175. Results of rod 1 190
Figure 176. Results of rod 3 191
Figure 177. Results of rod 4 191
Figure 178. Reults of rod 6 192
Figure 179. Heat transfer coefficients (Shang et al., 2010) 192
Figure 180. Heat transfer coefficients of rod 1 193
Figure 181. Heat transfer coefficients of rod 3 193
Figure 182. Heat transfer coefficients of rod 4 194
Figure 183. Heat transfer coefficients of rod 6 194
Figure 184. Demonstration of the problem of applying the UWF in the calculation of the heat transfer regime at supercritical parameters near the pseudo-phase transition point 197
Figure 185. Experimental UWF (NORM - normal, DHT - deteriorated heat transfer) 198
Figure 186. Adapted UWF(SWF) (ST - standard, ALL - adaptation (Eq. (62)), TR - thermal resistance adaptation $B(Pr, Pr_t)$) 199
Figure 187. Adapted UWF (SWF) in the range of y+ from 30 to 300 (ST - standard, ALL - adaptation (Eq. (62)), TR - thermal resistance adaptation $B(Pr, Pr_t)$) 200
Figure 188. SWF application results (a – reference temperature at the wall for T^+ and u_τ with different methods of determining tangential stresses; б - reference temperature at the wall for T^+ and u_τ for different average values of the proportionality ratio K; в - reference wall temperature for T^+ and u_τ, implicit formulation) 202
Figure 189. SWF application results (a – reference temperature at the wall for T^+ and u_τ; б - reference wall temperature for T^+ and u_τ, implicit formulation) 203
Figure 190. The results of applying the SWF for the HTD regime (a – 1-rod bundle; б – 3-rods bundle) 204
Figure 191. Schematization of the test section (calculation region) 209
Figure 192. General view of the applied computational mesh 209
Figure 193. Calculated values of turbulent viscosity obtained by different models for upward (a) and downward (b) flows 210
Figure 194. Comparison of axial wall temperature distribution with experimental values for upward and downward flow (a – for different applied turbulence models, b - for different correlations of Pr_t, applying them in the "V" model) 211
Figure 195. Comparison of the velocity and temperature radial profiles in cross section x/d = 62.5 (see subsection 2.4.2.1) (a - upward, b - downward) 211
Figure 196. Enthalpy flow growth fields comparison 212
Figure 197. Nikuradse curves and the wall friction factor prediction provided by the model by Ambrosini et al. (2015) (left); and preliminary predictions of wall-roughness impact on heat transfer phenomena (right). 215
Figure 198. Wall temperature trends for Kline's CO_2 case at inlet temperature of 24 °C, mass flux of 300 kg/(m^{2}s), and heat flux of 20 kW/m^2. Adapted from Kassem et al., 2023 217
Figure 199 Wall temperature trends at different roughness heights adopting the results from the similarity theory for Kline's CO_2 case at Tin of 24 °C, mass flux of 300 kg/(m^{2}s), and heat flux of 20 kW/m^2. Adapted from Kassem et al., 2023 217

Figure 200. Universal velocity trends for CO_2 at 8.35 MPa, inlet temperature 24°C, mass flux of 300 kg/(m^{2}s), and heat flux of 20 kW/m^2 and with roughness 1 μm. Adapted from Kassem et al., 2023 218
Figure 201. Axial velocity distribution across the pipe diameter for CO_2 at 8.35 MPa, inlet temperature 24°C, mass flux of 300 kg/(m^{2}s), and heat flux of 20 kW/m^2 and with roughness 1 μm. Adapted from Kassem et al., 2023 219
Figure 202. Dimensionless velocity trends for CO_2 at different axial positions. Adapted from Kassem et al., 2023 220
Figure 203. Dimensionless velocity trends for water at different axial positions. Adapted from Kassem et al., (2023) 220
Figure 204. Wall temperature trends with different roughness heights for CO_2 at 9 MPa, inlet temperature 25°C, heat flux of 50 kW/m^2. Adapted from Kassem et al., 2023 222
Figure 205. Inner wall temperature trends for the heated tube section at 4.35 MPa operating pressure, mass flux of 500 kg/m^{2}s, heat flux at 40 kW/m^2 and inlet temperature of 50°C 224
Figure 206. Inner wall temperature trends for the heated tube section at 4.35 MPa operating pressure, mass flux of 500 kg/m^{2}s, heat flux at 25 kW/m^2 and inlet temperature of 80°C 224
Figure 207. Inner wall temperature trends for the heated tube section at 4.35 MPa operating pressure, mass flux of 750 kg/m^{2}s, heat flux at 75 kW/m^2 and inlet temperature of 50°C 224
Figure 208. Inner wall temperature trends for the heated tube section at 4.35 MPa operating pressure, mass flux of 1000 kg/m^{2}s, heat flux at 130 kW/m^2 and inlet temperature of 50°C ... 224
Figure 209. Inner wall temperature trends for the heated tube section at 4.35 MPa operating pressure, mass flux of 1250 kg/m^{2}s, heat flux at 90 kW/m^2 and inlet temperature of 60°C 224
Figure 210. Inner wall temperature trends for the heated tube section at 4.35 MPa operating pressure, mass flux of 1500 kg/m^{2}s, heat flux at 140 kW/m^2 and inlet temperature of 60°C ... 224
Figure 211. Inner wall temperature trends for the heated tube section at 4.35 Mpa operating pressure, mass flux of 1750 kg/m^{2}s, heat flux at 120 kW/m^2 and inlet temperature of 70°C ... 225
Figure 212. Inner wall temperature trends for the heated tube section at 4.35 Mpa operating pressure, mass flux of 2000 kg/m^{2}s, heat flux at 130 kW/m^2 and inlet temperature of 70°C ... 225
Figure 213. Inner wall temperature trends for the heated tube section at 4.6 MPa operating pressure, mass flux of 500 kg/m^{2}s, heat flux at 40 kW/m^2 and inlet temperature of 50°C 225
Figure 214. Inner wall temperature trends for the heated tube section at 4.6 MPa operating pressure, mass flux of 500 kg/m^{2}s, heat flux at 35 kW/m^2 and inlet temperature of 70°C 225
Figure 215. Inner wall temperature trends for the heated tube section at 4.6 MPa operating pressure, mass flux of 750 kg/m^{2}s, heat flux at 55 kW/m^2 and inlet temperature of 60°C 225
Figure 216. Inner wall temperature trends for the heated tube section at 4.6 MPa operating pressure, mass flux of 750 kg/m^{2}s, heat flux at 75 kW/m^2 and inlet temperature of 70°C 225
Figure 217.Inner wall temperature trends for the heated tube section at 4.6 MPa operating pressure, mass flux of 1000 kg/m^{2}s, heat flux at 90 kW/m^2 and inlet temperature of 50°C 226
Figure 218. Inner wall temperature trends for the heated tube section at 4.6 MPa operating pressure, mass flux of 1000 kg/m^{2}s, heat flux at 130 kW/m^2 and inlet temperature of 50°C ... 226
Figure 219. Inner wall temperature trends for the heated tube section at 4.6 MPa operating pressure, mass flux of 1250 kg/m^{2}s, heat flux at 60 kW/m^2 and inlet temperature of 60°C 226
Figure 220. Inner wall temperature trends for the heated tube section at 4.6 MPa operating pressure, mass flux of 1250 kg/m^{2}s, heat flux at 120 kW/m^2 and inlet temperature of 70°C ... 226
Figure 221. Inner wall temperature trends for the heated tube section at 4.6 MPa operating pressure, mass flux of 1500 kg/m^{2}s, heat flux at 170 kW/m^2 and inlet temperature of 80°C ... 226

Figure 222. Inner wall temperature trends for the heated tube section at 4.35 MPa operating pressure, mass flux of 1500 kg/m^{2}s, heat flux at 140 kW/m^2 and inlet temperature of 60°C using different values of C_{rough} 226
Figure 223. Friction factors calculated and the comparison to Moody diagram (Haaland correlation) and Nikuradse curves. 232
Figure 224. Velocity profiles calculated from the rough wall model compared to experimental data. 232
Figure 225. Wall temperature results for smooth walls. 233
Figure 226. Wall temperature results for G=350 kg/m^{2}s at various wall roughnesses. 234
Figure 227. Wall temperature results for G=500 kg/m^{2}s at various wall roughnesses. 234
Figure 228. Wall temperature results for smooth walls, G=750 kg/m^{2}s, and at various wall heat fluxes. 235
Figure 229. Wall temperature results for smooth walls, G=1500 kg/m^{2}s, and at various wall heat fluxes. 236
Figure 230. Wall temperature results for rough walls, G=750 kg/m^{2}s, and at low wall heat flux. 236
Figure 231. Wall temperature results for rough walls, G=750 kg/m^{2}s, and at high wall heat flux. 236
Figure 232. Wall temperature results for rough walls, G=1500 kg/m^{2}s, and at low wall heat flux. 237
Figure 233. Wall temperature results for rough walls, G=1500 kg/m^{2}s, and at high wall heat flux. 237
Figure 234. Pipe and its geometric model 242
Figure 235. Pipe cross section 242
Figure 236. Mesh model 243
Figure 237. Element sizes of solid bodies 243
Figure 238. Pipe element size 244
Figure 239. Roughness property (Belyadi et al., 2017) 244
Figure 240. Pipe material 245
Figure 241. Rod wall condition 245
Figure 242. Main steps 246
Figure 243. Temperature variations with pipe length (k-ε model) 247
Figure 244. Temperature variations with pipe length (SST k-ω model) 247
Figure 245. Pressure drop variations with pipe length (SST k-ω model) 248
Figure 246. Structure of the test section (Yu et al., 2011) 249
Figure 247. Tube mesh design 249
Figure 248. Non-dimensional length y+ 250
Figure 249. Wall temperature distributions at 23 MPa under smooth surface condition 251
Figure 250. Wall temperature distributions at 25 MPa under smooth surface condition 252
Figure 251. Wall temperatures in rough tube with P=23MPa 253
Figure 252. Wall temperatures in rough tube with P=25MPa 254
Figure 253. Friction factor variations with inlet Reynolds number 255
Figure 254. Schematic of test facility (Bazargan et al., 2005) 256
Figure 255. Meshes of tube inlet 256
Figure 256. Model verification under smooth condition: P=24.4 MPa, G=340 kg/m^{2}s, q=300 kW/m^2 258

Figure 257. Wall temperature variations with bulk enthalpy by standard k-ε turbulent model: P=24.4 MPa, G=340 kg/m^{2}s, q=300 kW/m^2 259
Figure 258. Wall temperature variations with bulk enthalpy by buoyant k-ε turbulent model: P=24.4 MPa, G=340 kg/m^{2}s, q=300 kW/m^2 260
Figure 259. Wall temperature variations with bulk enthalpy by SST k-ω turbulent model: P=24.4 MPa, G=340 kg/m^{2}s, q=300 kW/m^2 261
Figure 260. An example of the use of passive scalars in STAR-CCM+..... 262
Figure 261. Passive scalar balance equations afopted in the STAR-CCM+ code (Simcenter STAR-CCM+®, 2018)..... 263
Figure 262. Weight gain due to corrosion for differet materials (from Penttilä, 2020) 263
Figure 263. Predictions obtained of the data by Pis'menny et al. (2005, 2005a) with water at 23.5 MPa, 6.28 mm ID, Tin = 300 °C, G = 508 kg/(m^{2}s), q" = 390 kW/m^2 for the selected roughness heigths 264
Figure 264. Values of the normalised Oxygen source along the radial direction of the pipe close to the surface (in the region of the roughness crests) at different axial locations in the pipe assumed for the selected calculation case for ε_{rough} = 15 μm 266
Figure 265 Values of the normalised Oxygen source along the radial direction of the pipe close to the surface (in the region of the roughness crests) at different axial locations in the pipe assumed for the selected calculation case for ε_{rough} = 30 μm 266
Figure 266. Normalised Oxygen concentration along the radial direction the pipe at different axial locations for εrough = 15 μm 266
Figure 267 Normalised Oxygen concentration along the radial direction the pipe at different axial locations for εrough = 30 μm 266
Figure 268. Values of the normalised corroded material source along the radial direction of the pipe close to the surface (in the region of the roughness crests) at different axial locations in the pipe assumed for the selected calculation case for ε_{rough} = 15 μm 267
Figure 269 Values of the normalised corroded material source along the radial direction of the pipe close to the surface (in the region of the roughness crests) at different axial locations in the pipe assumed for the selected calculation case for ε_{rough} = 30 μm 267
Figure 270. Normalised corroded matarial source along the pipe, as affected by the temperature distribution..... 267
Figure 271. Normalised corroded material concentration along the radial direction of the pipe at different axial locations for ε_{rough} = 15 μm..... 268
Figure 272 Normalised corroded material concentration along the radial direction of the pipe at different axial locations for ε_{rough} = 30 μm..... 268

1 Introduction

The ECC-SMART project seeks to establish the design requirements for Small Modular Reactors (SMRs) utilizing Supercritical Water Reactor (SCWR) technology. The SCWR reactor concept, was primarily focused on large-scale reactors over the past few decades. Reviews of these SCWR concepts have been documented in literature (see Pioro and Duffey, 2007; Oka et al., 2010; Schulenberg and Starflinger, 2012) and in IAEA technical documents resulting from Coordinated Research Projects (IAEA 2014; IAEA 2019a; IAEA 2020a). Recently, SMRs have gained significant attention within the nuclear community due to their potential advantages (IAEA 2020b). Their lower power levels could reduce the consequences and likelihood of severe

accidents. Additionally, the modularity of SMRs, allowing partial construction in workshops and on-site assembly, could reduce economic risks and offer greater flexibility in adapting to future electrical grids dominated by renewable energy sources. These benefits align well with the inherent advantages of SCWR technology, such as higher core outlet temperatures compared to current Light Water Reactors (LWRs), leading to increased energy conversion efficiencies (see Pioro and Duffey, 2007; Schulenberg and Starflinger, 2012). Moreover, the more compact design, enabled by a direct cycle, promises to reduce overall plant costs.

Work package three (WP3) is focused on thermal-hydraulic investigations related to the design and safety of the SCW-SMR. The knowledge and experience gained from these developments will support the design specifications and optimization of the SCW-SMR proposed in this project.

Main Objectives of WP3:

- Building on the existing results and experience, the first objective of this work package is to conduct further system design analysis and develop a joint design requirement document which will serve as the foundation for future conceptual design efforts.
- Surface-Coolant Interaction and Corrosion Prediction: The second objective is to analyse and model the interaction between the surface and coolant to predict corrosion under supercritical water conditions. Corrosion is a critical challenge identified within the Generation IV Supercritical Water-Cooled Reactor (SCWR) framework. Accurately predicting corrosion rates under both nominal operating and upset conditions is essential. This work package will generate new experimental data and direct numerical simulations (DNS) of turbulent heat and mass transfer along corroded surfaces. This will include leveraging proven methods for predicting rough surface behavior using accurate RANS turbulence models. The resulting extended database will be used to analyze, develop, and validate models for turbulent heat and mass transfer in both corroded and non-corroded environments. This objective is closely linked with WP2.
- Thermal-Hydraulic Phenomena Investigation: The third objective is to conduct numerical and experimental investigations of thermal-hydraulic phenomena relevant to the safety and feasibility of the SCW-SMR. This includes developing and refining numerical tools used in engineering environments. Specifically, the focus will be on fast transients (such as those occurring in Loss of Coolant Accident (LOCA) conditions), improving heat transfer correlations for system codes, and enhancing and validating turbulence heat transfer models for Computational Fluid Dynamics (CFD) codes.

  The overarching goal of this work package is to enhance and provide the scientific foundation necessary for the design and safety demonstration of the SCW-SMR concept.

Within WP3, the Task 3.3 “Development and improvement of system-, subchannel- and CFD-codes for SCW-SMR" aims to validate and demonstrate the applicability and limitations of system-, subchannel- and Computational Fluid Dynamics- codes, which will be applied for design, safety and licensing. This deliverable presents the results in Computational Fluid Dynamics (CFD) modelling and simulation applied for a corrosive environment under supercritical conditions. The results for development and improvement of system-, subchannel- are reported in other deliverables of the WP3. The Task 3.3. includes the following sub-tasks which are completely or partially dedicated to CFD analysis and modelling:

3.3.1. Contribution to establish heat transfer correlations and CFD models appropriate for postulated operating conditions UNIPI, BME, CNL, IPP, UoN, NPIC

3.3.3. Investigation and implementation of heat transfer correlations (CNL)

3.3.4. Improvement, implementation and validation of engineering models for turbulent heat transfer under supercritical conditions (IPP)

3.3.5. CFD modelling and validation of supercritical water heat transfer along corroded rough surfaces (KTH, UNIPI)

3.3.6. Two and more equation RANS modelling of turbulent heat and mass transfer along corroded surfaces (UoN, UNIPI)

This report summarizes the activities within Task 3.3 on CFD modelling and simulations in the corrosive environment under supercritical conditions.

Related documents

2 Subtask 3.3.1 Contribution to establish heat transfer correlations and CFD models appropriate for postulated operating conditions

2.1 CONTRIBUTION BY UNIPI

2.1.1 Introductory remarks

The University of Pisa contributed to subtask 3.3.1 by different activities that were aimed at improving the understanding of the main phenomena involved in the prediction of the fluid-dynamic and heat transfer behaviour of fluids at supercritical pressures. This heavily involved the use of a CFD RANS model set up in previous activities (Pucciarelli et al., 2016) that turned out to be useful as a basis for discussion of observed phenomena and to reveal and explain trends also observed in experimental data. A parallel activity developed in this frame is related to the study of existing heat transfer correlations, assessing their effectiveness in predicting two sets of experimental data taken as reference, the CO_2 ones by Kline (2017) and the water ones by Watts (1980).

In order to introduce the work done in this frame in its rational and chronological development, a list of the main steps performed is reported hereafter, with reference to the main journal, internal report and conference publications which resulted from it.

- A starting point was the work on a similarity theory, which had been set up and validated before the start of the ECC-SMART project (Pucciarelli and Ambrosini, 2016; Pucciarelli et al., 2020; Pucciarelli and Ambrosini, 2020; Kassem et al. 2021). The theory was anyway used and better assessed in different steps during the ECC-SMART project (Kassem et al., 2021a; De Angelis et al. 2021; De Angelis, 2021; Pucciarelli et al., 2021; Pucciarelli et al., 2021a; Pucciarelli et al., 2021b). This work suggested the most important dimensionless parameters to be used for imposing “similar” boundary conditions in experiments made with different fluids to obtain “similar” heat transfer phenomena. As such, its development was aimed to understand which dimensionless numbers were best suited to represent the relevant phenomena, for instance in engineering correlations, thus paving the way to further considerations on correlation adequacy. The methodology heavily relies on the use of RANS models to obtain its conclusions, so that many of the achieved results require a reasonable prediction of reference experimental data.
- In the wake of developing the mentioned fluid-to-fluid similarity theory, a line of research was started for the first time at the University of Pisa, in the frame of both the ECC-SMART project and the doctoral work of Dr. Sara Kassem (Kassem, 2024). In particular, an internal University of Pisa report (Kassem et al., 2022) identified more than 60 existing correlations and adopted specifically developed computational tools to test the validity of their classical forms in front of a database of more than 33,000 data extracted from the ones by Kline (2017) and Watts (1980). In this frame, in the aim to establish a better methodology of correlation assessment, two different ways of correlation assessment were identified, named “correlation mode” and “prediction mode”; the former relies on the experimental values of the wall temperature, adopted whenever needed in the right hand side dimensionless groups of a correlation, while the latter instead adopts an iterative procedure to obtain a more correct assessment by identifying values of wall temperature coherent with the correlation itself. To support these analyses, a technique for evaluating the residual of the difference between the experimental Nusselt number and the one identified by a correlation as a function of wall temperature helped in identifying possible branches of the zero locus, which can give rise to multiple

solutions, a problem already identified by some previous literature works. In addition to the mentioned University of Pisa internal report, this work resulted in a publication at an international conference (Kassem et al., 2022a) and in a joint archival publication co-authored with BME (Hungary) and IPP (Ukraine) highlighting the need for a better methodology for assessing heat transfer correlations (Varju et al., 2024), capable to highlight what the colleagues by IPP named the degree of "correlation robustness".

- CFD analyses had also an important role in the work that the University of Pisa performed in the frame of the ECC-SMART project to identify different modes of heat transfer deterioration (HTD). In particular, the analysis of experimental data, e.g., those by Watts (1980) and Kline (2017), reveals at least two modes of deterioration:
    - a local deterioration, often occurring close to the inlet of a heated section, to be ascribed to the deformation of the velocity profiles owing to the effect of mixed convection that leads to laminarisation, then finding a heat transfer recovery owing to the formation of an M-shaped profile restoring turbulence production;
    - a more stable deterioration pattern that, after the onset of the wall temperature excursion due to laminarization, gives rise to the transition to a higher wall temperature manifold at which the system stabilizes after oscillations up to the point in which heat transfer restoration may get in, owing to the transition of the bulk fluid to gas-like conditions and a more reduced effect of buoyancy.

  The two phenomena, once identified, were dealt with by two different techniques. The former was treated by the use of shape functions, to be trained over specific target heat transfer conditions, which simulate the different levels of the observed peaking trends on the basis of a shape function blending algorithm (Pucciarelli and Ambrosini, 2022). The latter mode of HTD suggested to dust off a treatment already proposed at the University of Pisa in previous work (Sharabi and Ambrosini, 2009) to suggest the use of pseudo-Nukiyama curves that, in similarity with the well-known counterpart at subcritical pressure, may allow to describe these deterioration phenomena in both heat flux and wall temperature controlled heat transfer cases.
- In addition to the above developments, the University of Pisa was also involved in the CFD benchmarking activity proposed by NPIC in the frame of the IBSCTH exercise and already reported in deliverable D3.2 of the ECC-SMART Project.

The above described developments will be summarised in the following subsections, highlighting the original aspects and the advancements in knowledge experienced in the frame of the ECC-SMART project, aming to improve the state-of-the-art in the field. The already issued internal University of Pisa report by Kassem et al. (2022) will be the source of a large part of the material reported herein.

2.1.2 General considerations on heat transfer at supercritical pressure

Heat transfer to supercritical pressure fluids presents a known complex behaviour stemming from the changes in fluid properties experienced at supercritical pressure, which have no counterpart in single-phase fluid conditions at subcritical pressures. Reviews of the available related experimental information and correlations is provided in several past references, including a well-known textbook by Pioro and Duffey (2007) and a document by Cheng and Schulenberg (2001) issued in the frame of a previous European project. More recent reviews (see e.g., Li et al., 2019) though other ones are available) have been also produced providing interesting suggestions

about the present status of correlation accuracy from the quantitative and also the phenomenological points of view.

The occurrence of phenomena like heat transfer “enhancement” and “deterioration” strongly complicates the behaviour of fluids at supercritical pressures, especially when they approach the pseudo-critical temperature, being the condition at a given pressure at which the specific heat shows a maximum which is larger the closer the operating pressure is at the critical value. The trends of properties of water and CO_2 at two relevant pressures for the experimental data considered in this report are shown in Figure 1. As it can be easily understood, the change from “liquid-like” to “gas-like” densities may introduce in heated ducts phenomena as buoyancy and acceleration, which have a strong effect on turbulence production and heat transfer.

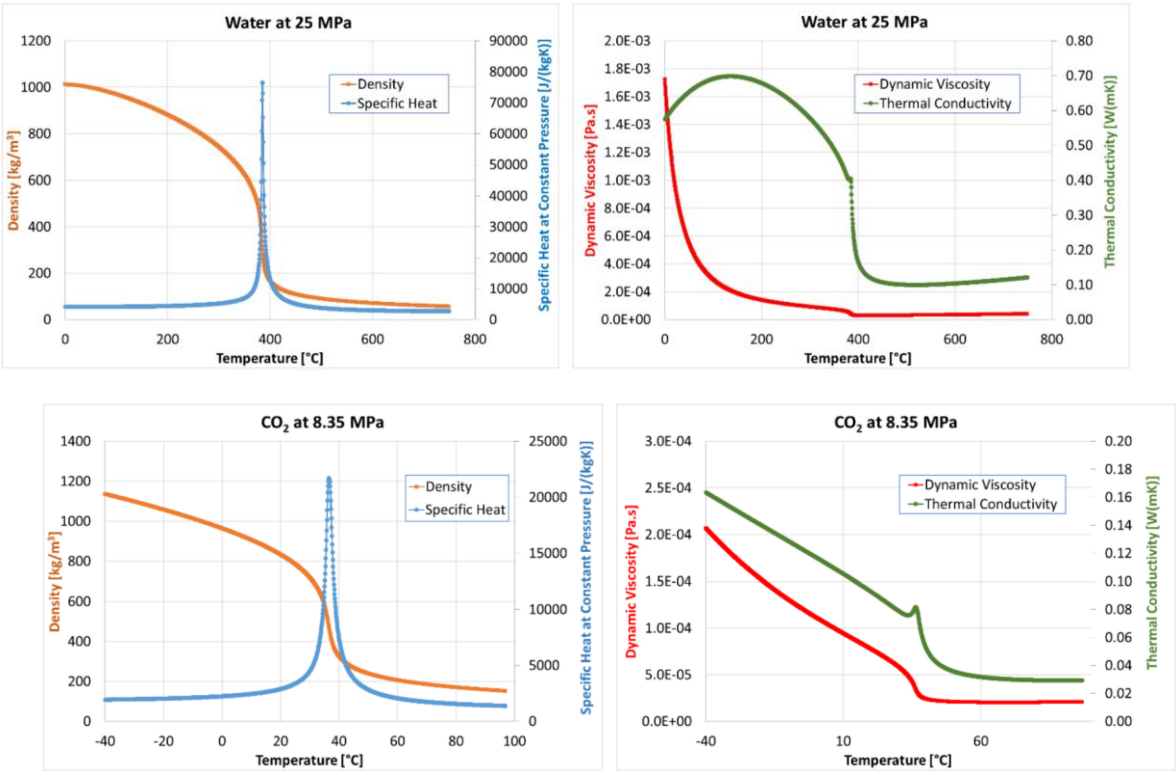

Figure 1. Trends of relevant properties of water and CO_2 at two relevant pressures for the data considered in the present report

The two above considered pressures have been selected and will be mainly referred to herein because they are of relevance for experimental data by Watts’(1980) and Kline (2017) taken as reference for correlation development and assessment. In addition, 25 MPa represents for water the targeted pressure for many design concepts of Supercritical Water Reactors (SCWRs, in short), a Generation IV concept (see the website of the Generation IV International Forum) making use of water at supercritical pressure as a coolant and moderator. These reactors are based on conventional Light Water Reactor (LWR) technology and aim at achieving higher energy conversion efficiencies and lower costs, owing to higher operating temperatures and a rather compact design. Information on such plant concepts can be found in classical textbooks (see e.g., Pioro and Duffey, 2007; Schulenberg and Starflinger, 2012); additional information on plant concepts, together with the collection of relevant recent data on phenomena involved in reactor design are reported in the TECDOCs issued in the frame of two Coordinated Research Projects of IAEA which paved the way for present studies (IAEA 2014, 2019, 2020). The ECC-SMART Project, aiming to lay down the basis of the pre-conceptual licensing of a Small Modular Reactor

based on this technology, is inheriting prior work on the subject and aiming to further develop it in its specific aims.

As anticipated, the reason for the mentioned complexity of heat transfer behaviour exhibited by supercritical pressure fluids is definitely to be attributed to the huge changes in fluid thermodynamic and thermo-physical properties whose examples were shown in Figure 1. Especially when the wall temperature is larger than the pseudocritical threshold and the bulk one keeps below it, the conditions of the fluid at the wall may be strongly different from the ones in bulk, causing the flow at supercritical pressure to closely resemble the one that can be obtained at subcritical pressures in some two-phase flow conditions. In fact, except for the absence of any interface between the heavy and the light phases, there is a strong similarity in behaviour with some regimes occurring in two-phase flow and the ones at supercritical pressure when a low density fluid is wetting the wall. Indeed, similarities between supercritical pressure flow phenomena and two-phase flow ones do exist at the level of both flow instabilities (Ambrosini, 2007) and heat transfer. For the latter aspect, an interesting presentation of early considerations, including “pseudo-two-phase models”, is proposed in Chapter 15 of Hsu and Graham (1976) though the presence of deteriorated heat transfer is there attributed also to buoyancy and acceleration effects, in agreement with what proposed by Jackson and Hall at the University of Manchester in several works (see, e.g., Jackson and Hall, 1979).

A phenomenological similarity between heat transfer deterioration and the critical heat flux phenomena at subcritical pressure was pointed out also in (Sharabi and Ambrosini, 2009) displaying computed heat transfer deterioration data in the form of a pseudo-Nukyiama curve (see Figure 2). Even in that case it was clear, on the basis of computed data, that the phenomenon at the root of the decrease in heat flux at the crossing of the pseudo-critical temperature at the wall was mainly the effect of flow laminarisation due to turbulence generation decrease, as suggested by Jackson and Hall (1979) This aspect is being presently reconsidered as a way to interpret the sharp transitions in wall temperature occurring when deterioration occurs, in view of the repeated damped oscillations observed in this parameter in many experimental trends.

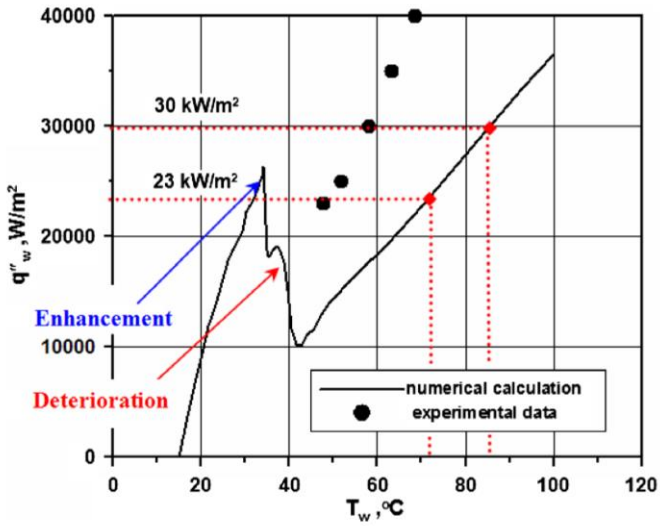

Figure 2. Pseudo-Nukiyama curve proposed to display deteriorated heat transfer phenomena in Sharabi and Ambrosini (2009)

The particular attention devoted to the data by Watts (1980) and Kline (2017) in this report is a consequence of their richness in terms of description of phenomena, covering two complementary operating regions:

- Watts' data, obtained with water as a working fluid, are per se interesting since they were collected at the supercritical pressure of 25 MPa; most of them refer to operating conditions in the liquid-like region, though deterioration beyond the pseudo-critical pressure is also observed;
- Kline's data, instead, thanks to the lower thermal loading needed for carbon dioxide to exceed pseudocritical conditions, explore a region embracing both liquid-like and gas-like conditions, up to the transition to gas-like fluid in bulk; therefore, the resulting information on phenomena is more complete and the mechanisms of deterioration can be studied up to the point in which a final restoration in heat transfer is observed, when the fluid at the wall and in bulk have sufficiently similar density to reduce the effect of buoyancy and allow for the restart of a considerable turbulence production by shearing (see the discussion in Buzzi et al., 2019).

These two data sets and selected others have been the basis for studies related to the development and the validation of an original fluid-to-fluid similarity theory, supported at the moment only by numerical analyses performed by CFD RANS, DNS and LES calculations, which seems to have solved most of previous uncertainties in defining "similar" boundary conditions for achieving comparable heat transfer phenomena with different fluids over a wide range of conditions (see Pucciarelli, 2017; Pucciarelli and Ambrosini, 2016; Pucciarelli et al., 2020; Pucciarelli and Ambrosini, 2020; Kassem et al., 2021). This similarity theory represents the starting point of our studies in the frame of ECC-SMART on heat transfer, providing hope that a better understanding of the dimensionless numbers which make successful the comparison of computed heat transfer conditions with different fluids may also suggest the best dimensionless groups to be used in setting up correlations. Moreover, the similarity theory, if further proven successful on the basis of experimental data, will allow to enlarge the base of data to be considered for engineering heat transfer correlation assessment, hopefully eliminating the need to tailor formulations for each specific fluid.

With these aims, while addressing the issue of correlation assessment and improvement for Task 3.3.1 of ECC-SMART, work was performed during 2021 in order to dig into the characteristics of the similarity theory, aiming at a deeper understanding of its significance and implications. In particular, during the first year of the work within ECC-SMART, the following aspects of the similarity theory were further considered:

- a general reflection on some of the obtained results of the theory not reported in previous publications helped in achieving greater confidence in its capabilities (Kassem et al., 2021)
- an extension of the theory to non-uniform axial power distributions helped in preparing higher fidelity representations of reactor core conditions, in pile and in scaled experiments (Pucciarelli et al., 2021);
- a closer analysis of the results already obtained for Watts data (1980) highlighted problems in scaling from water as reference fluid to fluids with higher values of the Prandtl number (De Angelis et al., 2021);
- considering the interest for the R134a fluid within the ECC-SMART project, it was ascertained that, though the characteristics of this fluid deviate considerably from those of fluids adopted in previous applications of the similarity theory, reasonable results could be anyway obtained in scaling (Kassem et al., 2021a);

- a clearer overview of the features of the similarity theory was published in a gold open access paper to make openly available the characteristics of the proposed rationale to researchers worldwide (Pucciarelli et al., 2021a);
- a reflection on a non-trivial aspect of the procedure adopted for the similarity theory (i.e., the selection of corresponding pressures for the different fluids) was presented at a relevant conference and was better clarified to potential external users of the theory (Pucciarelli et al., 2021b);
- a somehow easy but needed extension of the similarity theory to a more interesting water pressure value (i.e., 25 MPa) than the one considered in proposing similarity with the data by Kline in previous work (i.e., 24.5 MPa) (Kassem et al., 2022b);
- a first overview of the work presented herein on the analysis of existing correlations, to be better described in the next sections (Kassem et al., 2022c).

In the present document, the early work performed in the analysis of existing correlations is reported focusing on the following aspects:

- firstly, the features of the fluid-to-fluid similarity theory will be shortly summarised, aiming to illustrate to the reader its significance, not only as a general methodology for preparing counterpart experimental tests with different fluids, but also as a workbench to test the suitability of dimensionless group as candidate ingredients of engineering correlations;
- furthermore, a literature survey about existing correlations and a detailed discussion of some of them in their effectiveness in really predicting the observed phenomena will be presented;
- then, a systematic analysis of some of the most commonly proposed correlation forms in view of their capability to predict qualitatively and quantitatively heat transfer data by Watts and Kline will be reported;
- an alternative approach trying to introduce shape functions aiming at suggesting a possible development path for heat transfer correlations for supercritical fluids is presented;
- relevant conclusions and the lesson learned up to now in view of the aims of the ECC-SMART project will be finally proposed.

2.1.3 Usefulness of a fluid-to-fluid similarity theory for heat transfer to SC fluids

Experimental data for heat transfer to supercritical (SC) fluids have been collected with a variety of fluids whose critical conditions may ease designing and running experimental campaigns. Even when water is the target fluid for a specific application, as it is in the case of Supercritical Water Reactors, surrogate fluids may be used to avoid reaching too high temperatures and pressures during the operation of experimental apparatuses. The use of CO_2 in place of water, for instance, grants a reduction of the critical temperature to 304.13 K (i.e., 30.98 °C) and of the critical pressure to 7.3773 MPa (according to NIST REFPROP10) with respect to the values for water (647.1 K or 373.95 °C and 22.064 MPa), with corresponding advantages in terms of safety and lower thermal and stress loads on materials. However, data obtained with surrogate fluids need to be translated to corresponding water conditions to be considered meaningful for assessing the design of apparatuses conceived to operate with water.

Similarity theories have been proposed in the past mainly on the basis of the values of reduced pressure and temperature, referring to concepts of corresponding state theory (see e.g., the works referred to by Pioro and Duffey (2007) as the one by Jackson and Hall (1979). Recent reviews of the published theories provided counterfeiting information about their applicability (see e.g., Azih and Yaras, 2017; Mouslim and Tavoularis, 2020). Of course, the search for a sufficiently

validated theory for fluid-to-fluid similarity in this field, as in many others, is well justified at least by the following purposes:

- defining sound criteria for designing experiments with surrogate fluids that can be considered meaningful for an intended reference fluid application;
- making use of the large body of data obtained with different fluids for drawing conclusions about a specific application;
- assessing the usefulness of the different dimensionless groups highlighted by the similarity theory in view of setting up engineering correlations.

The latter of the above advantages brought about by a sound fluid-to-fluid similarity theory is the most relevant one in the present context.

2.1.4 Adopted fluid-to-fluid similarity theory and its relevant applications

General descritpion of the theory

Dimensionless groups for defining flow stability conditions in heated ducts containing fluids at supercritical pressure were identified at the University of Pisa in an early work on the subject (Ambrosini and Sharabi, 2006) and provided a useful basis for comparing the flow stability behaviour of different fluids in close similarity. This early work had the little merit to highlight the possibility that Ledinegg instabilities might occur also in the case of fluids at supercritical pressure, something better confirmed by analyses shown in a subsequent work (Ambrosini, 2007) and confirmed by other researchers.

It must be remarked that the most important aspect that made the similarity theory for stability successful enough was recognising that the use of specific dimensionless definitions for density and specific enthalpy can make the trend of the former as a function of the latter almost unique for four different fluids, being water, carbon dioxide, ammonia and R23, though it has been found somehow different for other fluids to which the similarity theory could be anyway applied (namely R134a, see Kassem et al., 2021a). This unique trend, reported in many referenced works, is at the very basis of the similarity, owing to the great importance that the relation between density and specific enthalpy has in view of fluid thermal expansion: since the latter governs both stability and heat transfer phenomena, via buoyancy forces and acceleration, this represents a basic ingredient to assure similarity in both conditions.

The definition of dimensionless density and of the dimensionless specific enthalpy are as follows:

$$\rho^* = \frac{\rho}{\rho_{pc}} \qquad h^* = \left(h - h_{pc}\right)\frac{\beta_{pc}}{C_{p,pc}} \tag{1}$$

In this context, two additional dimensionless numbers play an important role, being the trans-pseudocritical and the sub-pseudocritical numbers:

$$N_{TPC} = \frac{\dot{Q}\beta_{pc}}{WC_{p,pc}} \qquad N_{SPC} = -h_{in}^* \tag{2}$$

As shown in Figure 3, for the description of STEP 2 of the methodology, the inlet value of the dimensionless enthalpy (represented by the opposite of N_{SPC}) and the dimensionless power-to-flow ratio (N_{TPC}) determine the evolution of the bulk fluid density all along the channel, something very important for both stability and heat transfer.

After early attempts to extend the successful theory developed for flow stability to the case of heat transfer (Ambrosini, 2011) more in depth developments took place leading to an improved formulation of the similarity theory (Pucciarelli, 2017; Pucciarelli and Ambrosini, 2016), validated on the basis of RANS and LES calculations, that were later confirmed also by DNS data (He et al., 2018). This finding provided renewed confidence in the principle at its basis, suggesting deeper assessments and analyses.

While a more complete overview of the theory and of its latest developments is presented in a mentioned golden open access paper (Pucciarelli et al, 2021a) published during the first year of the ECC-SMART project, its main characteristics and results are shortly summarised herein.

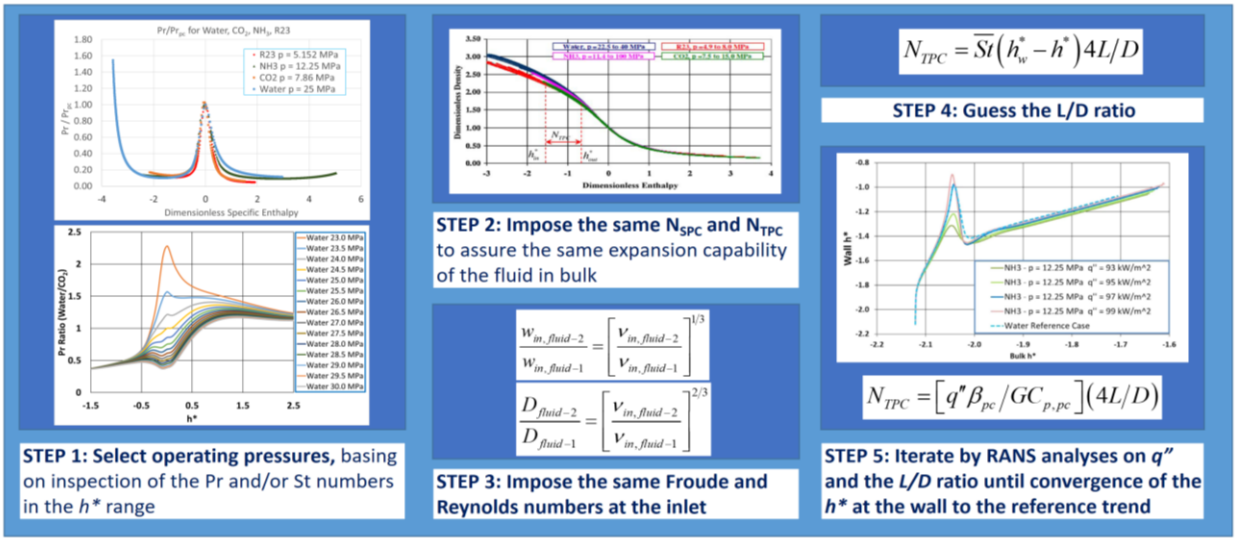

Figure 3: Description of the main steps in the similarity rationale

With reference to Figure 3, it can be noted that a first step in the application of the procedure (STEP 1) concerns the definition of corresponding pressures for the two different fluids; the rationale for defining this step has been the subject of a recent study (Pucciarelli et al., 2021b) and resulted slightly different in the case of operating conditions mostly in the liquid-like region and when the dimensionless enthalpy window also embraces a consistent part of the gas-like region. A good starting guess is anyway the use of equal reduced pressures. Actually, the selection of the operating pressures (STEP 1) aims at taking profit of the variability of the Prandtl number in the pseudocritical region in order to achieve sufficiently uniform ratios of its values for the two fluids in the region were the fluid evolution is expected in terms of dimensionless specific enthalpy.

It must be then clarified that, on the basis of the above reported definitions, *two flow conditions are considered similar if they involve similar distributions of the dimensionless enthalpy and then of the dimensionless density along and across the channel.* This definition is proposed in recognition of the considerable importance that the differences in the density of the considered fluids have in determining the flow regimes, as already mentioned via the effects of buoyancy and acceleration. As it will be shown in the following, the success in applying the theory to specific cases via RANS analyses is ultimately depending on this key aspect. As a consequence, STEP 2, involving to impose the same inlet pseudo-subcooling and the same dimensionless power-to-flow ratio represents an obvious requirement for establishing similarity.

The Froude and the Reynolds numbers, defined as

$$Fr = \frac{w^2}{gD} \qquad Re = \frac{\rho w D}{\mu} = \frac{GD}{\mu} \qquad (^1) \qquad (3)$$

and evaluated on the basis of bulk and cross section averaged variables, are imposed at the inlet. Imposing these two requirements has different purposes:

- to assign the same inertia to gravity ratio at channel inlet (through the Froude number);
- to assign the same level of turbulence at the inlet (through the Reynolds number).

It can be shown that owing to the use of equal values of N_{SPC} and N_{TPC}, assigning the same Froude number at the channel inlet implies the equality of this parameter for the different fluids along the channel; more importantly, it also assures everywhere the equality of the Richardson number, defined as $Ri = Gr_\rho / Re^2 = \left[\left(\rho - \rho_w\right) gD\right] / \rho w^2$ since it can be shown that $Ri = \left(\rho - \rho_w\right) / \left(\rho Fr\right) = \left(\rho^* - \rho_w^*\right) / \left(\rho^* Fr\right)$. This represents a relevant result in view of keeping the same ratio of buoyancy to inertia forces all along the duct for the two fluids. Viceversa, the evolution of the Reynolds number along the channel is different for different fluids, owing to the trends of the dynamic viscosity: this suggests that the levels of turbulence, though equal at the inlet section, will be unavoidably somehow different for the two fluids along the channel, suggesting a slight imperfection in the similarity. As shown in Figure 3, assigning the inlet values of both the Froude and the Reynolds numbers results in the need to specify different values of the inlet velocity and of the diameter of the pipe in consideration of the inlet values of the kinematic viscosity of both fluids.

STEP 4 consists in defining the length-over-diameter ratio to be used for the two fluids. In fact, it happens that the values of the Stanton numbers may be different for different fluids (e.g., owing to the differences in the Prandtl numbers). The equality

$$N_{TPC} = \overline{St}\left(h_w^* - h^*\right) 4L/D \qquad (4)$$

can be easily obtained from the Newton's law of convection, considering the definitions $\overline{St} = Nu / Re\overline{Pr}$, $\overline{Pr} = \overline{C}_p \mu / k$ and $\overline{C}_p = \left(h_w - h\right) / \left(T_w - T\right)$. On this basis, assuming that the trends of dimensionless specific enthalpy at the wall and in bulk are the same by virtue of the similarity, the product $\overline{St} \times 4L/D$ must be the same for the different fluids. This step must be accomplished together with the following STEP 5, since it can be also demonstrated that $N_{TPC} = \left[q'' \beta_{pc} / GC_{p,pc}\right]\left(4L/D\right)$: therefore, exact preservation of the trans-pseudocritical number, N_{TPC}, must be accomplished by varying the heat flux and the L/D ratio at the same time, considering the obtained distribution of the wall dimensionless enthalpy. This is needed owing to the approximate nature of the similarity theory and also because of the <u>great sensitivity</u> of the phenomena to be predicted, in order to adjust the boundary conditions of the surrogate fluid up to the point in which the trends observed for the dimensionless enthalpy at the wall in the reference fluid are reproduced for the surrogate one. In this regard, it must be noted that:

- though the above methodology may look vague for the need of iterating on the heat flux and also in the selection of the operating pressure, it can be assured that its application is not too cumbersome and it is routinely made with no great difficulty by the researchers using it at the

(1) Note that thermodynamic and thermo-physical properties without subscript are assumed to be evaluated in the bulk fluid, while those with subscript "w" refer to the wall.

University of Pisa through spreadsheets that allow to visualise computed data an adjust boundary condition up to convergence;

- the purely numerical application of the methodology presently adopted may be replaced by an experimental one; it is not difficult, in fact, to envisage a procedure of tuning the heat flux supplied to a test section while adapting its useful length (e.g., introducing sufficient allowance for a longer pipe than theoretically needed) in accordance with the heat flux, to obtain some reference behaviour achieved with a different fluid.

Tutorials for the application of the methodology by both numerical and experimental means can be provided and will help in getting the requested experimental verification of the proposed theory.

Applications of the similarity theory

In the aim to show the applicability of the similarity theory to some data of interest, a few examples from recently published papers are reported herein.

Figure 4 presents the comparison of the dimensionless specific enthalpy trends at the wall for a DNS calculation performed at the University of Sheffield (He et al., 2018)) for a sample problem evaluated by DNS and run with different fluid properties. In Figure 4a, the results of the original calculations by DNS obtained applying the boundary conditions suggested in the similarity theory are reported, while Figure 4b presents the results of RANS calculations performed with the same geometry and boundary conditions for the same fluids. As it can be noted, though the trends obtained by DNS and RANS slightly differ for the two different calculation methodologies, in both cases there is a striking similarity between the trends obtained for the different fluids, suggesting that the specified boundary conditions correspond closely to each other, somehow independently on the numerical tool used.

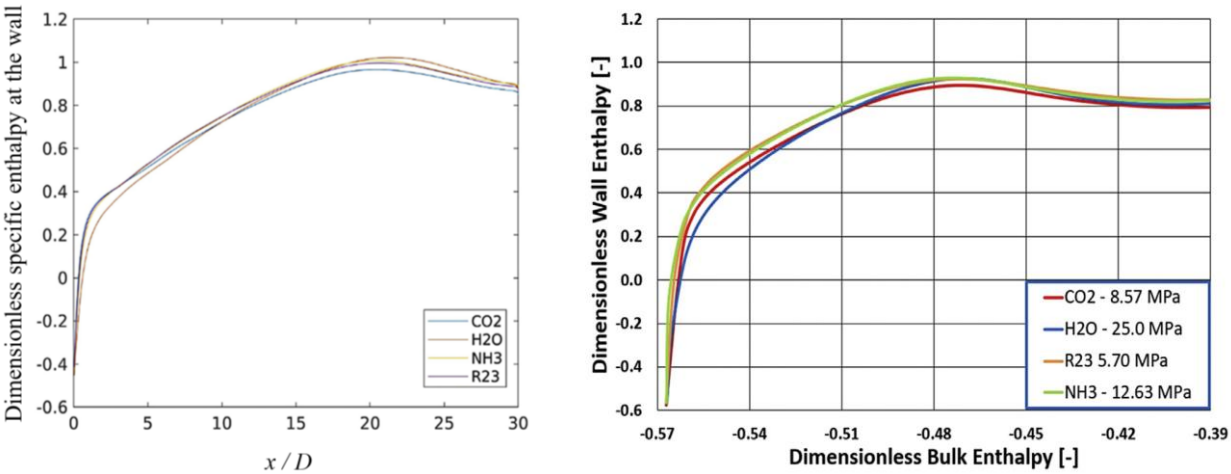

a) DNS calculations by Sheffield University b) RANS calculations

Figure 4. Results from DNS and RANS calculations in dimensionless form (Pucciarelli et al., 2020)

It must be acknowledged that the results obtained by the University of Sheffield on the basis of the early proposal of the similarity theory presented in (Ambrosini, 2011) triggered a new interest for the more extended theory already presented in previous publications, suggesting to revisit it in the aim to present its features in a more systematic way. This led to new publications in which the similarity theory was applied to data by Watts (1980) and Kline (2017) having the already mentioned characteristics of systematic investigations of heat transfer deterioration mainly in the

liquid-like region with water and in both the liquid-like and the gas-like region with carbon dioxide, respectively.

In particular, the data by Watts (1980) considered here were obtained in upward flow conditions in an experimental facility having a 2 m long test section with an inner diameter of 25.4 mm and operated with water at 25 MPa. On the other hand, the data by Kline (2017) were obtained with carbon dioxide at 8.35 MPa flowing in upward flow in a vertical test section with inner diameters of 4.6, 8.0 and 22.0 mm and heated lengths of 1200, 1940, and 2000 mm. A common aspect of the two sets of data, which triggered our interest, was the systematic coverage of entire ranges of boundary conditions that allowed identifying clear effects of relevant parameters, as inlet temperature, heat flux and mass flux. In the case of Kline's data, owing to the lower operating temperature allowed by the use of carbon dioxide, it was possible to show complete ranges of phenomena, from normal heat transfer, through deterioration up to heat transfer to gas-like conditions.

Among the several predictions of Kline's data obtained by the use of the STAR-CCM+ code (Simcenter 2018) making use of the Lien et al. (1996) k-ε model available in it, integrated with an Algebraic Heat Flux Model (AHFM) developed by A. Pucciarelli during his PhD thesis work (Pucciarelli, 2017) and also collected in a subsequent MSc thesis work (Buzzi et al., 2019) Figure 5 reports a subset of interesting cases. As it can be seen from Figure 5a, the predictions of experimental data obtained by the CFD RANS calculations were reasonably accurate, suggesting that the overall trends and phenomena were grasped by the code.

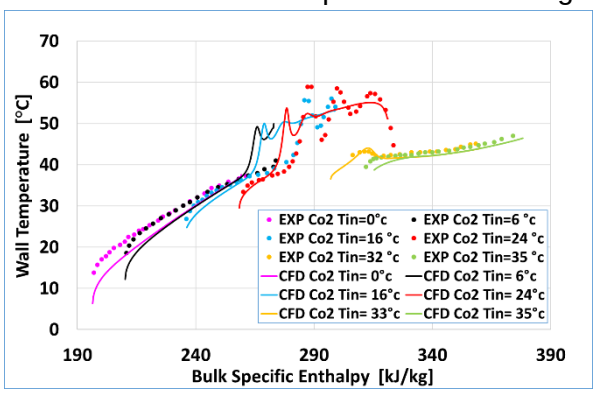

a) CO_2 data and their prediction

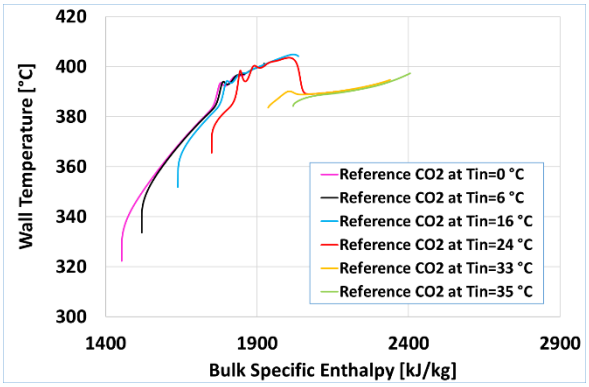

b) similar trends for water at 24.5 MPa

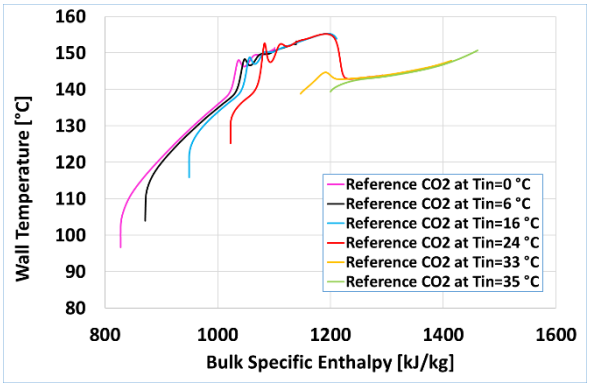

c) similar trends for NH3 at 12.5 MPa

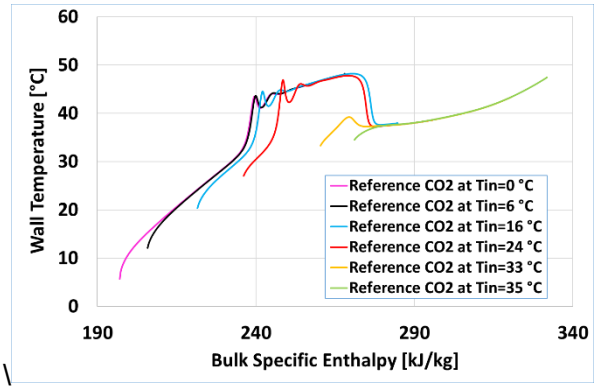

d) similar trends for R23 at 5.56 MPa

Figure 5. Prediction of Kline's CO_2 data at q"= 18 kW/m^2 and trends obtained by the application of the similarity theory for water, NH3 and R23 (ID = 4.6 mm)

Among the phenomena predicted by the model, normal and deteriorated heat transfer, together with the final restoration of heat transfer at the transition to gas-like conditions can be identified. This observation stimulated the application of the similarity theory for investigating if the model could forecast similar behaviours for other fluids, by just changing the fluid properties and applying the similarity theory for achieving corresponding trends of the dimensionless specific enthalpy at the wall.

Figure 5b, c and d present the obtained results. As it can be noted, the predictions obtained for CO_2, were reproduced in very good phenomenological agreement with water at 24.5 MPa, with NH3 at 12.5 MPa and with R23 at 5.56 MPa. It is implied that for each one of the different inlet temperatures it was necessary to apply the similarity theory with the iterative procedure for the heat flux and the length over diameter ratio described above, resulting in a relatively large number of calculations aiming at converging at similar dimensionless trends of wall dimensionless specific enthalpy.

In order to better clarify the already described procedure, attention is drawn to Figure 6a, where these wall dimensionless specific enthalpy trends are shown in comparison with each other. The figure describes the level of similarity obtained in the distribution of dimensionless enthalpy both along and across the channel, considering that the dimensionless bulk specific enthalpy trend is imposed to be the same. The different ranges of bulk specific enthalpy for the different fluids appearing in the plots are due to the fact that the computational domain adopted in the analyses corresponded to different heated lengths, so that data beyond the nominal N_{TPC} defined for each case have been obtained.

Indeed, Figure 5 demonstrates that it is possible to apply to different fluids corresponding boundary conditions that provide similar phenomenological trends. In particular, cases with only incipient or no deterioration can be observed at the lowest inlet temperatures, while deterioration further progresses at higher inlet temperatures, up to the point at which a renewed production of turbulence is observed causing a final restoration of heat transfer or deterioration does not occur at all. In this regard, the richness of the data by Kline must be recognised for highlighting a variety of trends whose interpretation is straightforward on the basis of arguments related to laminarisation and heat transfer restoration due to buoyancy effects.

Figure 6, in addition to showing the trends of dimensionless wall enthalpy (Figure 6a), provides further information on the behaviour of the relevant dimensionless numbers along the channel for the different fluids. In particular:

- Figure 6b shows very similar trends of the Richardson number, predicted by the theory to be nearly the same for the different fluids; it can be noted that the increase of *Ri* causes (or it is at the same time an effect of) deterioration, coherently with the relevance that buoyancy has in determining laminarisation;
- Figure 6c confirms the prediction that the Froude number, imposed to be the same at the channel inlet, deviates only slightly from a common trend for the different fluids, as a consequence of the approximate nature of any similarity theory;

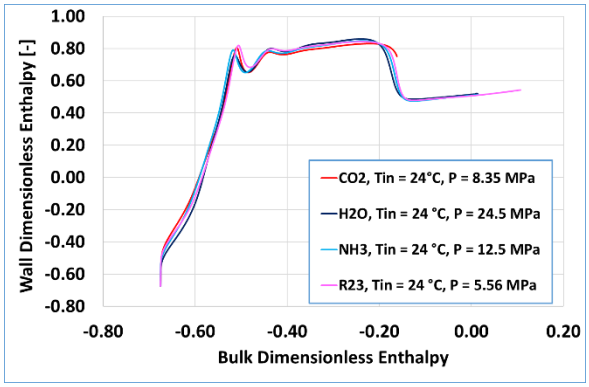

a) wall dimensionless enthalpy

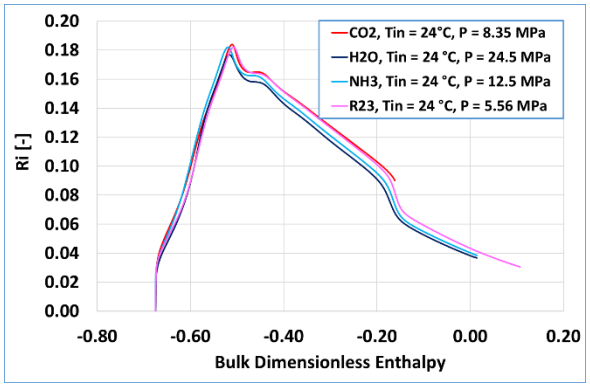

b) Richardson number

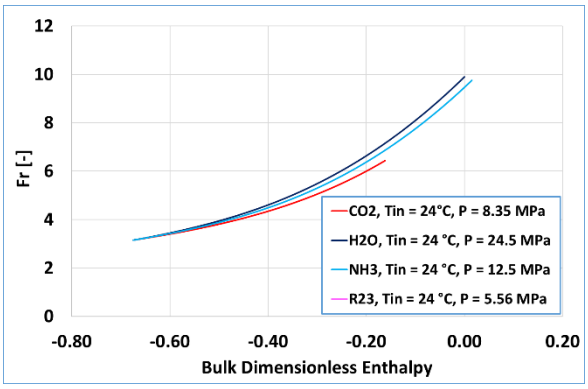

c) Froude number

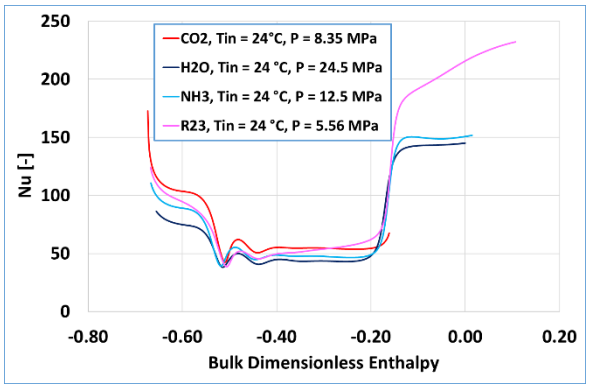

d) Nusselt number

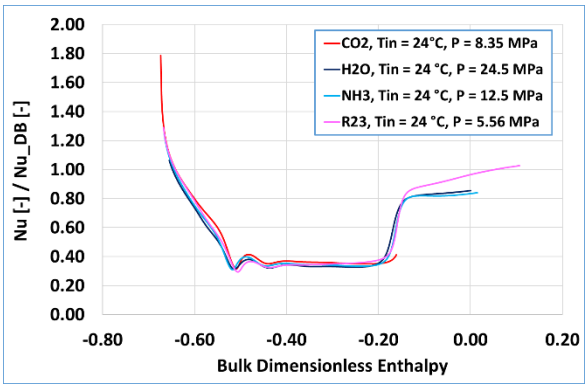

e) Nusselt number ratio

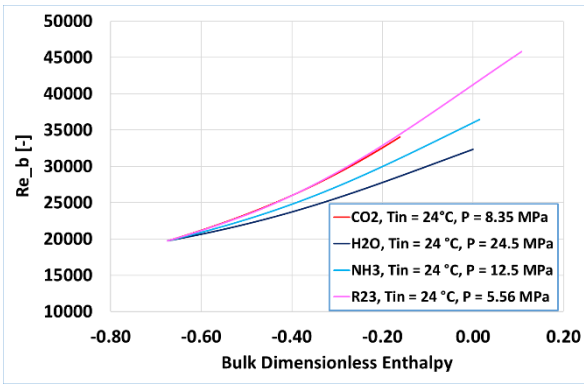

f) Reynolds number

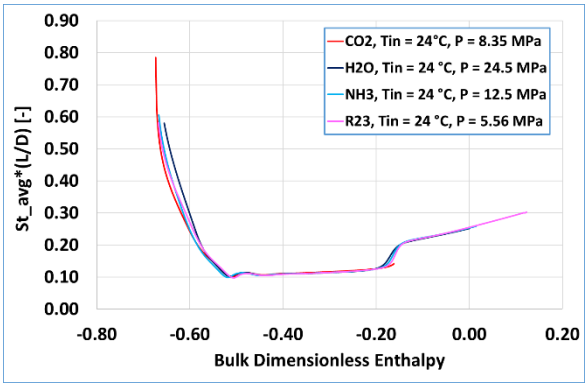

g) $\overline{St}\,L/D$

Figure 6. Trends of the relevant dimensionless numbers along the channel showing similarity for the case of Kline's data with q" =18 kW/m2 and Tin= 24 °C

- Figure 6d and Figure 6e suggest that while the Nusselt number is different for the different fluids, the ratio of the computed Nusselt number to the one predicted by the Dittus-Boelter correlation has a very similar trend for all the fluids;
- Figure 6f simply shows that the Reynolds number, imposed to be the same at channel inlet cannot be preserved all along the heated length;
- Figure 6g, finally, shows that the product of the average Stanton number by L/D is instead very well preserved.

Figure 7, collecting similar plots for another calculation case from the database by Kline, confirms the generality of the above conclusions in relation to the trends of the dimensionless numbers.

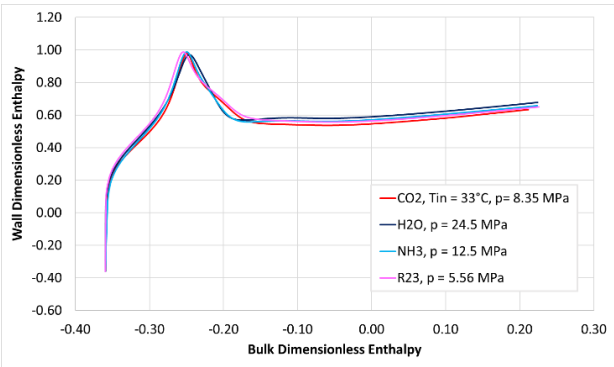

a) wall dimensionless enthalpy

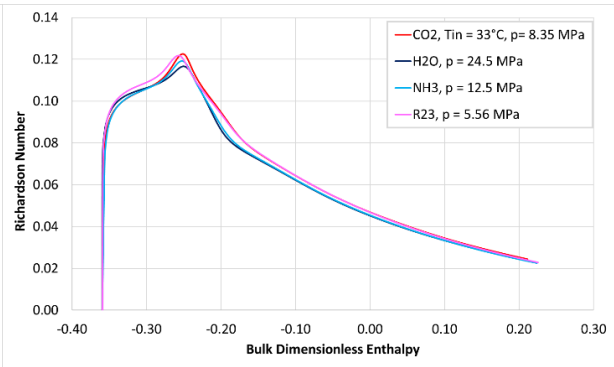

b) Richardson number

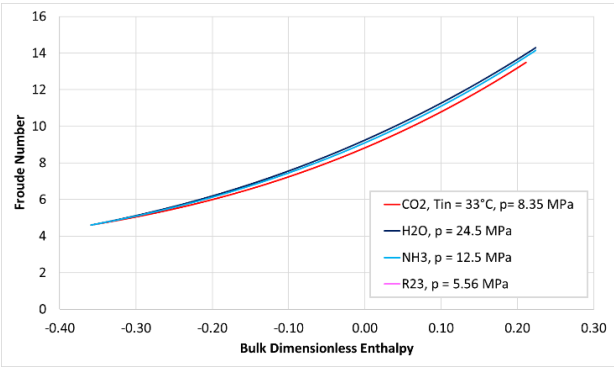

c) Froude number

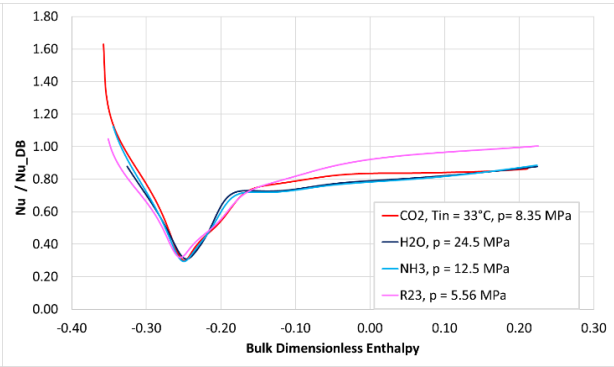

d) ratio of Nu / NuDB

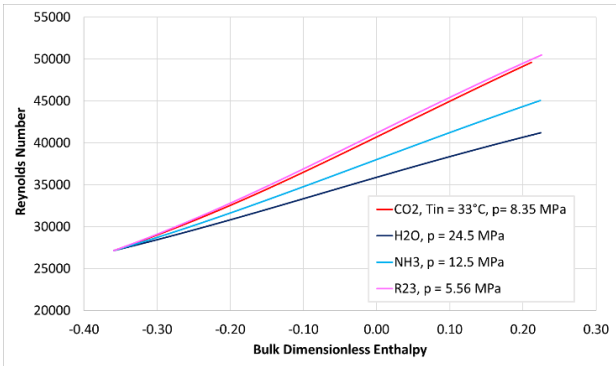

e) Reynolds number

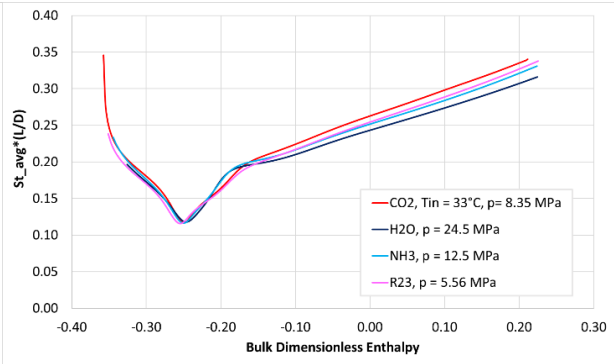

f) $\overline{St}(L/D)$

Figure 7. Trends of dimensionless parameters for the data by Kline with q"=20 kW/m^2 and T_{in} = 33 °C

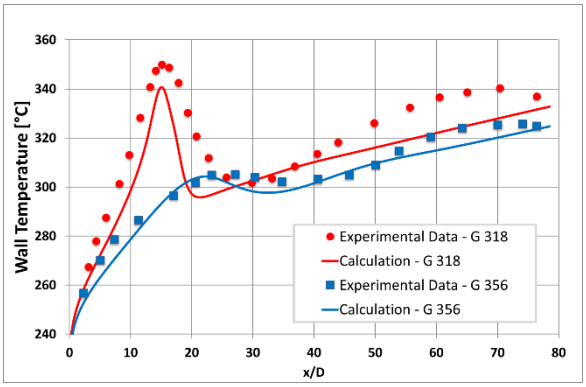

Figure 8. Data by Watts: Water 25 MPa, 25.4 mm ID, (nominal) T_{in}=200 °C, q"=400 kW/m^2, upward flow, G expressed in kg/m^{2}s

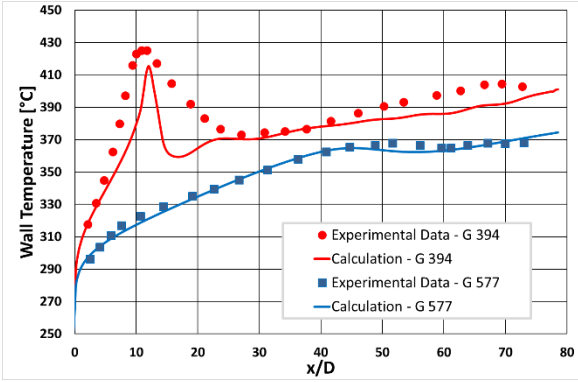

Figure 9. Data by Watts: Water 25 MPa, 25.4 mm ID, (nominal) T_{in}=250 °C, q"=400 kW/m^2, upward flow, G expressed in kg/m^{2}s

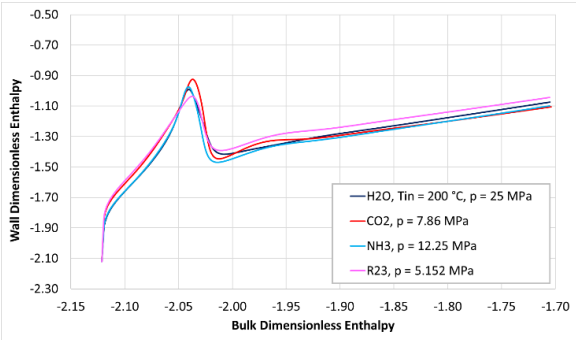

a) wall dimensionless enthalpy

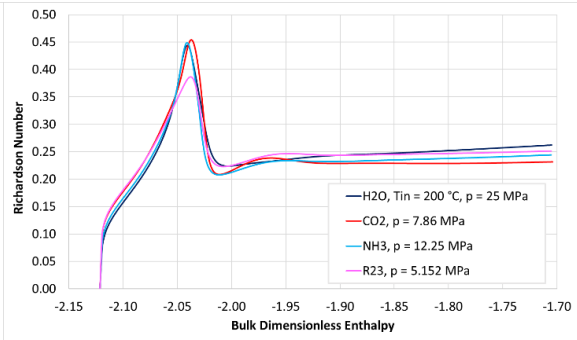

b) Richardson number

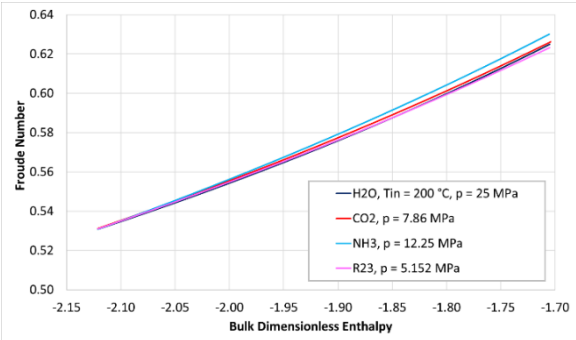

c) Froude number

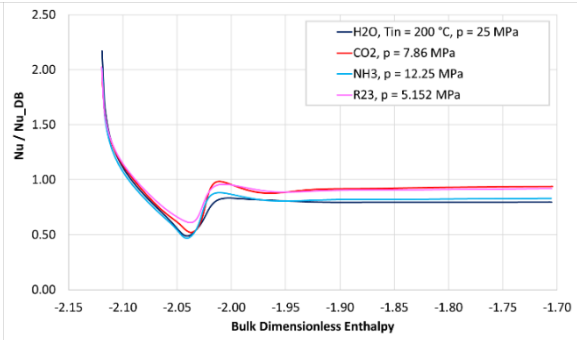

d) ratio of Nu / NuDB

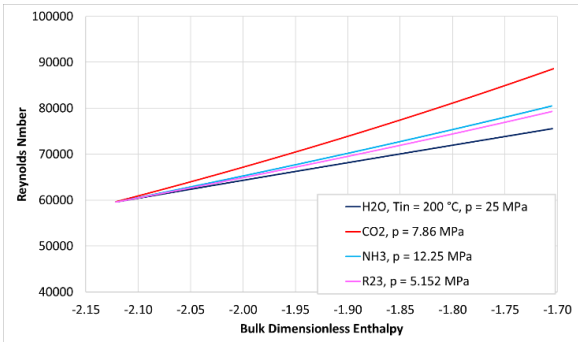

e) Reynolds number

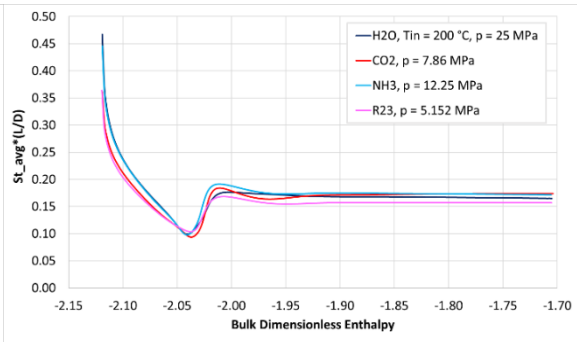

f) $\overline{St}(L/D)$

Figure 10. Trends of dimensionless parameters for the data by Watts with nominal Tin = 200 °C, G = 318 kg/m^{2}s

Shifting to Watts' data, Figure 8 and Figure 9 show the level of accuracy obtained in predicting water experimental data at different values of inlet temperature and flow rates, giving rise to different levels of deterioration at temperatures below the pseudocritical one. Figure 10 represents the corresponding dimensionless trends obtained for one of the considered cases, allowing for drawing similar conclusions as in the case of Kline's data in relation to the trends of dimensionless numbers.
In summary, the similarity theory proved to be successful in the application via RANS calculations to some relevant experimental data showing interesting behaviour for the analysis of deterioration phenomena.

Worth of the similarity theory in view of engineering correlations
As mentioned in the previous sections, the fluid-to-fluid similarity theory, in addition to be per se of interest to envisage the boundary conditions to be applied to obtain similar phenomena with different fluids, should provide greater insight on the dimensionless numbers that must be taken into account for setting up engineering correlations. In this respect, the following considerations apply.

- **Sub-pseudocritical number and trans-pseudocritical number**
  The two numbers N_{SPC} and N_{TPC} play a major role in locating the dimensionless enthalpy window along the horizontal axis of the ρ^* vs. h^* curve (see Figure 3), thus determining the capability of the fluid to expand and then to generate buoyancy and acceleration. In this respect, it seems clear that heat transfer efficiency cannot be the same, ceteris paribus, all along the curve, both in bulk and at the wall.
- **Local "N_{TPC}"**
  In the analytical developments leading to the similarity theory, it was recognised that

$$N_{TPC} = \frac{q''\beta_{pc}}{GC_{p,pc}} \frac{4L}{D} \tag{5}$$

It is interesting also to consider the quantity

$$N_{TPC,loc} = \frac{q''\beta_{pc}}{GC_{p,pc}} \tag{6}$$

as a dimensionless heat flux to mass flux ratio that can possibly substitute classical "dimensional" relationships proposed, e.g., for identifying the onset of deterioration. In this regard, it is also interesting to note that a slightly different form of this formulation may appear equally interesting:

$$N_{TPC,loc-x} = \frac{q''\beta}{GC_p} \tag{7}$$

This dimensionless group differs from the previous one just by the use of the local ratio of the thermal expansion coefficient and of the specific heat in place of the corresponding value at the pseudocritical threshold. In this regard, it must be noted that

$$\frac{\beta}{C_p} = -\frac{1}{\rho}\frac{\partial\rho}{\partial T}\bigg|_p \frac{\partial T}{\partial h}\bigg|_p = -\frac{1}{\rho}\frac{\partial\rho}{\partial h}\bigg|_p \tag{8}$$

represents the fluid expansion coefficient per unit specific enthalpy and that

$$-\frac{1}{\rho^*}\frac{\partial \rho^*}{\partial h^*}\bigg|_p = -\frac{1}{\rho}\frac{\partial \rho}{\partial h^*}\bigg|_p = \underbrace{-\frac{1}{\rho}\frac{\partial \rho}{\partial T}\bigg|_p}_{\beta}\ \underbrace{\frac{\partial T}{\partial h}\bigg|_p}_{1/C_p}\ \underbrace{\frac{\partial h}{\partial h^*}\bigg|_p}_{C_{p,pc}/\beta_{pc}} = \frac{\beta}{C_p}\frac{C_{p,pc}}{\beta_{pc}} \tag{9}$$

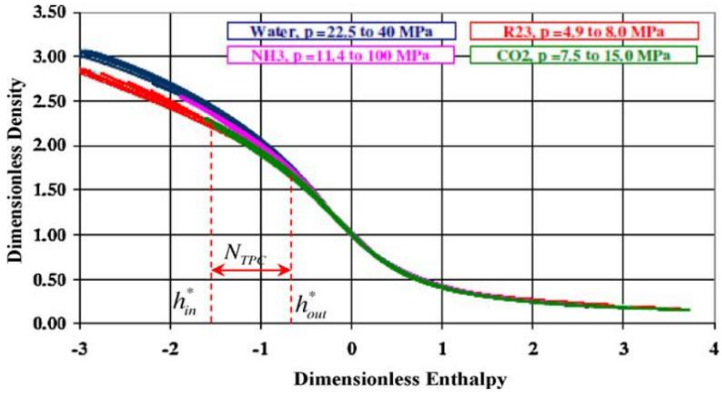

Figure 11. Relation between dimensionless density and dimensionless enthalpy for four fluids

Therefore, it can be recognised that in view of Figure 11 the dimensionless group in Eq. (9) also represents a unique function of h^*, having approximately the same value for all the fluids (the exception of R134a must be anyway dealt with). Its physical meaning is clearly related to the expansion of the fluid expressed in dimensionless form: indeed, it may be considered useful in estimating the causes of both buoyancy and acceleration. It is expected that such expansion coefficient will attain a maximum close to the pseudocritical point. In summary, both the quantities $N_{TPC,loc}$ and $N_{TPC,loc-x}$ may be good candidates to express the capability of the fluid to expand under the action of heating, being a precious information for determining heat transfer regimes at supercritical pressure.

- **Dimensionless specific enthalpy and dimensionless density**

  The numerical value of the dimensionless specific enthalpy, h^*, being negative for liquid-like conditions and positive for gas-like ones, may take the role of indicators previously introduced in literature to estimate the distance to the pseudo-critical conditions. In particular, h^* (i.e., h^*_b) and h^*_w may be directly used as quantitative estimates of the status of the fluid in bulk and at the wall, for instance translating the observation that frequently deterioration occurs when $h^* < 0$ (bulk in liquid-like conditions) and $h^*_w > 0$ (wall in gas-like conditions). Likewise, the dimensionless density can be used in the same purpose, considering that $h^* < 0 \Leftrightarrow \rho^* < 1$ and $h^* > 0 \Leftrightarrow \rho^* > 1$. It must be also considered that the ratio ρ^*_w / ρ^*_b is simply equal to ρ_w / ρ_b; so, the values of ρ^*_w and ρ^*_b can be introduced separately as factors in variants of the classical equations where ρ_w / ρ_b appears, giving additional degrees of freedom in correlating data.

- **Nusselt number from the Dittus-Boelter correlation and average Stanton number**

  A very intriguing feature of the results obtained by the application of the similarity theory is that the ratio of the Nusselt number to the one evaluated by the Dittus-Boelter correlation appears to be nearly the same for all the fluids in “similar” conditions as defined according to

the theory (see, e.g., Figure 6e and Figure 7d). On the other hand, the Nusselt Number may be different for different fluids in similar conditions (owing to differences in the Prandtl number) and the product $\overline{St}\left(L/D\right)$ is the same "by definition of similarity" (i.e., equal values of the dimensionless enthalpy), as it follows from the equality of the N_{TPC} and from the mentioned relation $N_{TPC} = \overline{St}\left(h_w^* - h^*\right)4L/D$. In this view, it is very tempting to draw one of the following conclusions:

- correlations should be expressed in terms of the Dittus-Boelter correlation (though it may be assumed that Gnielinski's or Petukhov's ones may be suitable as well or even more accurate) introducing corrections for evaluating abnormal heat transfer behaviour; this is not a novelty in this field, of course, though in this case the suggestion could be to choose correction factors in terms of dimensionless parameters that proved to be useful in the fluid-to-fluid similarity theory;
- correlations could be expressed directly in terms of the average Stanton number, also considering the relation $q''\beta_{pc}/GC_{p,pc} = \overline{St}\left(h_w^* - h^*\right)$, being evidently another form of the Newton's law of convection, which highlights the Stanton number as the parameter to focus on.

These two conclusions could be obviously validated in correlating data.

- **Froude Number and Richardson number**
  The similarity theory gives to these two dimensionless numbers a central role. Indeed, the fact that dimensionless density has nearly the same distribution for the different fluids in "similar"([2]) conditions is a key aspect, determining the equality of the values of Froude and Richardson numbers all along the channel. This means, for instance, that deterioration starts at the same value of the Richardson number, coherently with the basic understanding of the role of the competition of buoyancy vs. inertia in determining laminarisation. These observations are an incentive to ascertain if the simple formulation of Richardson number as Gr_ρ / Re^2 can be used in correlations in place of the several times introduced buoyancy number having a similar meaning but with different exponents, e.g., $Gr_\rho / Re^{2.7}$.
- **Reynolds number**
  The role of this dimensionless number in determining the turbulence level in the fluid is well known and needs really no special comment. It must be anyway mentioned that in an early form of the similarity theory, imposing the equality of the Reynolds number at the inlet of the channel was not considered strictly necessary, also in view of the fact that its value unavoidably changes anyway owing to heating and the subsequent change in dynamic viscosity, which is different for different fluids. It was a suggestion from the University of Sheffield (Prof. S. He) that led to the inclusion of this constraint as an additional boundary condition in the similarity theory, definitely improving its formal coherence with known similarity principles in fluid-dynamics. Indeed, the previous observation about the striking equality predicted by RANS calculations of the ratio between the Nusselt number and the one by the Dittus-Boelter correlation for different fluids supports the classical role of the Reynolds number in determining heat transfer with an exponent in the range of 0.8 – 1.

([2]) The word "similar" is repeatedly put in quotes in the text to remark that the definition of similarity in the present theory means "*equal distribution of dimensionless enthalpy and, then, of dimensionless density all along and across the channel*". This specific definition is different from previous ones introduced in literature and, as shown, does not imply the equality of Nusselt numbers.

Role of the CFD models in understanding experimentally observed phenomena

Indeed, the adopted CFD model has a role in making possible the establishment of the similarity theory. It must be observed that its development has been at the basis of the capability to support the similarity theory in the present form by RANS analyses, thanks to a good comparison with experimental trends in a reasonable range of operating conditions. While there are cases in which the comparison is still unacceptable, asking for possible improvements, the development of the model was a key step in achieving understanding of the involved phenomena.

The 2D axisymmetric computations performed by the k-ε AHFM modified turbulence model have, in fact, the merit to interpret in a sufficiently correct way the experimental trends, hopefully for good reasons, leading to very similar trends of wall temperature with respect to the observed ones. Movies of computed results were set up in order to diagnose the reason for the occurrence of the experimentally observed phenomena, as deterioration, recovery and final heat transfer restoration. The purpose of this work was to stimulate ideas about the best way in which correlations may reproduce the observed behaviour; indeed, experimental data cannot easily provide information on the radial distributions of relevant quantities, which are at the basis of heat transfer phenomena. This information can be instead obtained by RANS calculations, provided they are considered sufficiently validated by the comparison with experimental data, normally in the simple form of measured wall temperature trends.

In the aim to show the considerations that can be drawn from inspection of calculated data, analyses of some relevant cases were shown hereafter in the form of videos obtained by MATLAB elaborating calculations performed by the RANS model. Observation of the animations shown in Kassem et al., 2022, not reported in the present document, is very instructive. It must be remarked that the corresponding analyses were found in reasonably good agreement with experimental data, as far as it was possible to compare results in terms of wall temperature. It must be clarified that the radial profiles shown in the animations were obtained at cross sections moving along the axial coordinate in agreement with the motion of the marker shown in the first of the displayed plot.

It can be here summarised that all the reported animations suggest that in the considered cases deteriorated heat transfer is due to laminarisation, coherently with the early interpretation by Jackson and Hall (1979) of their experimental data. In particular, the following considerations can be made.

- In the considered cases, deterioration may start above or below the pseudocritical temperature (this results by the comparison of the cases by Kline with the ones by Watts) owing to changes in dimensionless specific enthalpy in the radial direction that have the result to flatten the velocity profile, thus decreasing the velocity gradients that are at the root of the production of turbulence by shearing.
- Heat transfer recovery is obtained with a mildly “M-shaped” profile that partly restores turbulence production.
- Considering turbulence kinetic energy (TKE), a striking aspect is the complete disappearance of the peak close to the wall characterising turbulent velocity profile distributions, with a complete phenomenological change in the profile of TKE occurring when deterioration sets in.
- Kline’s data exhibit the presence of wall temperature oscillations that are even more marked and protracted along the axis in the experimental data than in the predictions. The computations suggest that this phenomenon is involved in the dynamics of deterioration and can be interpreted as a sort of overshooting in the redistribution of fluid velocity occurring at

the onset of deterioration. It is very suggestive to interpret this overshooting on the basis of some pseudo-Nukiyama curve similar to the one reported in Figure 2, as a dynamic effect occurring when the heat flux cannot be anymore exchanged in normal conditions and a quick transition to the right branch of deteriorated conditions occurs. In view of such phenomenon, two considerations can be proposed:

- it seems doubtful to assume that simple scalar correlations can be successful in representing such oscillations, in the lack of a dynamic representation of what is occurring along the channel axis; in fact, it must be reminded that the RANS CFD model predicts this phenomenon at the price of the solution of steady-state equations in two-dimensions that represent an evolution along the axial coordinate: such a representation might not be achievable by the simple evaluation of locally defined dimensionless groups;
- the jump from normal to deteriorated heat transfer conditions should be hopefully represented by correlations, but it can be argued if this jump can be evaluated by a single branch of the correlation; again in view of Figure 2, the presence of multiple solutions for engineering correlations giving rise to observed difficulty in convergence of some of the proposed formulations (see e.g., Zahlan et al. 2018) might be a needed feature of a correlation grasping deterioration. A further striking feature of the interesting data series by Kline is the presence of "envelopments" of curves representing the deteriorated branch of possible correlation solution.

- Figure 5a, again reported in Figure 12 for convenience in this discussion together with similar data at 20 kW/m^2, shows that both computed data and experimental ones tend to predict the presence of conditions at which normal heat transfer cannot be anymore sustained (something occurring close to the pseudocritical conditions) and jumps to deteriorated heat transfer conditions occur, more or less delayed by the increasing values of inlet temperature. Finally, when bulk conditions approach the transition to the gas-like conditions, the difference in fluid density in bulk and at the wall seems not to be sufficient to give rise to such intense buoyancy forces causing deterioration, and the level of wall temperature drops again, notwithstanding the lower value of fluid conductivity of the gas-like region.

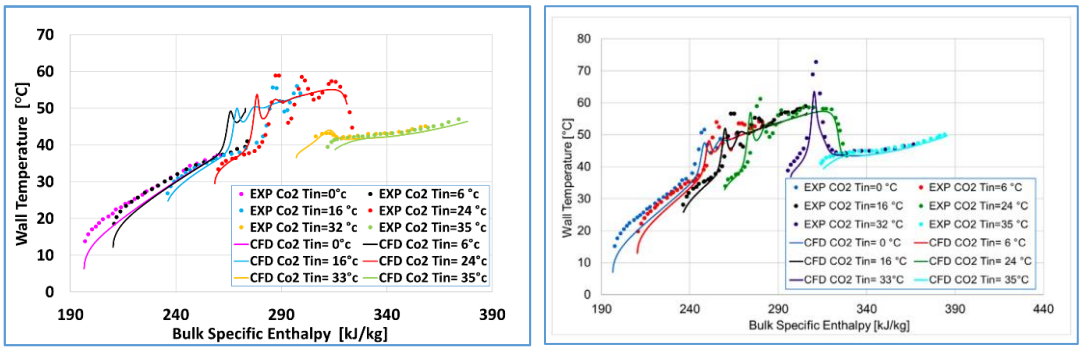

a) q"=18 kW/m^2 b) q"=20 kW/m^2

Figure 12. Presence of envelopments of deteriorated heat transfer trends in Kline's data (G=300 kg/(m^{2}s))

In summary, Kline's data seem to identify two different levels of wall temperatures for normal heat transfer and deteriorated heat transfer, the latter identified by an envelopment of curves and experimental data whose presence is confirmed at different levels of heating. Indeed, a consequence of what shown in Figure 12 is that wall temperature depends not only from the local conditions in terms of heating and on bulk properties, but also on the upstream conditions

in terms of inlet temperature and allowance for establishing the radial profiles of velocity and density determining the occurrence of deterioration. If this conjecture is confirmed, it is clear that correlating data with such a dependence from upstream conditions may be quite challenging if not impossible for classical semi-empirical correlations.

- In view of the above, a statement of the problem we are facing can be the following: *how is it possible to correlate experimental data that exhibit different values of the wall temperature with the same local boundary and bulk fluid conditions, just taking into account the upstream history?* This problem reminds of similar ones occurring at sub-critical pressure, e.g., in the dependence of DNB and dry-out on upstream history, accounted for by the "Tong Factor" or by critical quality vs. critical length approaches. A possible interpretation is to consider heat transfer at supercritical pressures strongly affected by "entrance effects", which persist all along the pipe, because of the continuous evolution of the fluid owing to expansion. It is clear that such observations strongly challenge our capability to correlate heat transfer phenomena with supercritical fluids by usual means, suggesting a possible reason why, notwithstanding the several tens of correlations proposed in the past, it was not yet possible to establish a single completely successful one.
- Unfortunately, further difficulties in interpreting experimental data related to deteriorated heat transfer can be observed by contrasting the complete trends shown by the data by Kline with trends often offered by experiments with water that cannot be carried out with too much high temperatures for problems related to material resistance and safety in running experiments. Figure 13 shows predictions of challenging data obtained by Pis'menny et al. (2005, 2005a) that were successfully reproduced by A. Pucciarelli with different versions of the AHFM model. These experimental data were obtained with a 1 m long test section, whose first 40 cm were left unheated for achieving fully developed conditions, as it is customary to do for avoiding biasing the data by not easily quantifiable entrance effects. After having the opportunity to consider Kline's data, thus observing the final restoration of heat transfer exhibited when bulk conditions approach the pseudocritical threshold, it was tried to understand by RANS analyses if a similar behaviour could be forecasted for the addressed Pis'menny's data by considering a longer test section. Figure 14 shows the results of the related analyses, in comparison with the observed and calculated trends for the data by Kline. As it can be noted, the RANS model predicts that the deterioration plus recovery phase observed in the addressed experimental data by Pis'menny et al. (2005, 2005a) could be nothing but an oscillatory part of a more complex deteriorated behaviour, which would then terminate with a final restoration.

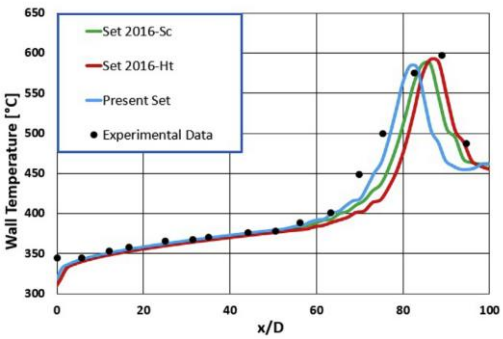

Figure 13. Predictions obtained in Pucciarelli and Ambrosini (2017) of the data by Pis'menny et al. (2005, 2005a) with water at 23.5 MPa, 6.28 mm ID, T_{in} = 300 °C, G = 508 kg/(m^{2}s), q" = 390 kW/m^2

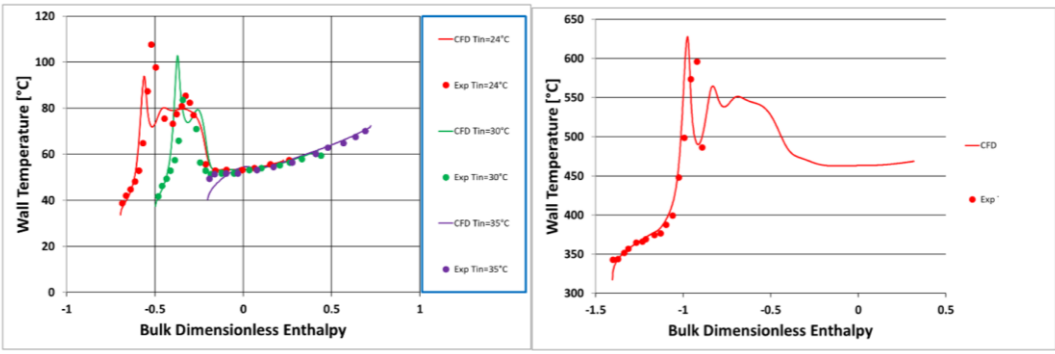

a) Kline's CO_2 data b) Pis'menny et al. water data

Figure 14. Comparison of predictions of Kline's data with extrapolated Pis'menny et al. Data

Whether this can be confirmed, it is clear that many of the classical experimental data available in literature should be reconsidered under a different perspective. In this regard, systematic series of data as the ones by Kline (2017) are really precious to stimulate understanding of the body of experiments now available. It is in fact necessary to remark that two of the above conclusions should be clearly borne in mind while addressing the use of experimental data by setting up engineering correlations on the basis of local data:

- observed evolutions of wall temperature may be strongly dependent on upstream conditions and, possibly, there is only hope to predict the mentioned envelopment of deteriorated data, with no pretence to be too accurate in predicting the inlet oscillatory evolution strongly affected by entrance conditions;
- some of the available experimental data trends may represent only a part of the full trend that could be obtained by longer test sections; so, the nature of the observed evolutions may be wrongly interpreted as mostly determined by local conditions, while they belong to trends quite sensitive to upstream conditions and that may not represent adequately the envelopments of deteriorated behaviours whose prediction could be a possible target in setting up engineering correlations.

Concluding remarks on the use of the similarity theory

The adoption of the fluid-to-fluid similarity theory allows identifying boundary conditions that, if properly imposed to different fluids, may produce similar heat transfer behaviour no matter the fluid properties. The theory is presently proven only by numerical means, but the variety of tools used (DNS, LES and mostly RANS) provides coherent support to its conclusions. In addition, the rationale at its basis provides a set of reasonable guidelines that can be adopted in future experiments to try reproducing the complex behaviour observed with some reference fluid also with different ones.

The dimensionless numbers, whose role has been identified to specify "similar" boundary conditions, may be considered as good candidates to appear in engineering correlations, besides or in place of commonly adopted ones. However, intrinsic difficulties have been highlighted by the application of CFD models in view of setting up engineering correlations. In particular, it appears evident that many of the phenomena exhibited by available experimental data have to be considered as determined by the deformation along the channel axis of radial variable profiles that need detailed dynamic models to be properly accounted for as a function of the inlet conditions and of their subsequent evolution along the channel.

Though a sort of desperate conclusion from these considerations would be that it is hopeless to try achieving engineering correlations based on local values, suggesting to concentrate efforts on the development of more complex and still uncertain CFD models, it seems wise to assess the capabilities of presently available correlation forms, coping with known difficulties in their application. This is the purpose of the work described in the next sections.

2.1.5 Literature survey and discussion of selected heat transfer correlations

2.1.5.1 Survey of the studies of heat transfer at supercritical pressures

Extensive reviews were presented on heat transfer to fluids at supercritical pressures by Cheng and Schulenberg (2001), Pioro et al. (2004) and Pioro and Duffey (2007). A large number of research studies on heat transfer of SC water (SCW) were reported within the last decade. Moreover, Rahman et al. (2007) provides a literature survey on heat transfer at supercritical pressures for nuclear applications, covering both experimental studies and numerical simulations, which enhances the understanding of basic heat transfer phenomena of SCW and is valuable to SCWR developers.

As known, phase change of water is eliminated with increasing temperature at supercritical pressures. Therefore, current safety criteria for nuclear reactor operation, based on the departure from nucleate boiling (DNB) or dry-out, are no longer applicable. Instead, developers of the SCWR concepts have adopted the peak cladding and fuel centreline temperatures as the criteria. This would require improved understanding of the heat transfer phenomena at supercritical pressures and accurate prediction methods for heat transfer coefficients.

Water at supercritical pressures is considered as a single-phase fluid with associated single-phase heat transfer characteristics in a heated channel, due to the lack of phase change. These characteristics can be represented with a single-phase heat transfer correlation, such as the well-known Dittus and Boelter (see Dittus, 1930) correlation, however, the sharp variations in the thermophysical properties at the vicinity of the pseudo-critical point challenge the application of this heat transfer correlation. In addition, the complex buoyancy and acceleration effects at the near wall region lead to significant changes to the single-phase heat transfer characteristics.

A vast number of past works have provided experimental data, correlations and look up tables for calculating the heat transfer coefficient. Other studies proposed correlations for the prediction of the heat flux causing the onset of the deterioration of heat transfer. Also there exists a large number of theoretical and numerical studies to explain the unique heat transfer behaviour.

In general, the existing heat transfer correlations could be divided into three categories as proposed by Liao (2014). The first type of heat transfer correlation for supercritical water was built on the basis of the Dittus-Boelter correlation; however, the thermophysical properties of the SCW experience dramatic change in the vicinity of pseudocritical point which might have great impact on the heat transfer behaviour. In view of this fact, a few correction terms consisting of the fluid thermophysical properties, such as ρ_w/ρ_b, μ_w/μ_b and λ_w/λ_b among the others, were introduced to the first type correlations, resulting in the emergence of a second type heat transfer correlations for SCW. With the deepening research on heat transfer phenomena of SCW, buoyancy effect and thermal acceleration were considered to be the main reasons for deteriorated heat transfer of SCW and then two special correction terms were proposed in terms of Grashof number to represent the buoyancy correction and q^+ to represent the thermal acceleration correlation. Such terms were added to the second type correlations, yielding the third type heat transfer correlations for SCW.

The work done in the past by many authors like Pioro and Duffey (2007) and Cheng and Schulenberg (2001) draw a conclusion that, after reviewing the existing heat transfer correlations for SCW, none of the existing correlations could predict the heat transfer (DHT) of SCW accurately under all heat transfer regimes. Therefore, a new and accurate correlation for heat transfer of SCW is expected to be effectively accurate under all heat regimes of SCW, and special emphasis should be directed onto the DHT phenomena, which is the most dangerous situation to not only thermal power plants but also to the Gen-IV SCWRs.

In this section, experimental studies on heat transfer of supercritical water and other fluids like carbon dioxide, helium and freons are briefly recalled including both the enhanced heat transfer (EHT) and the DHT regimes. In addition, the available existing heat transfer correlations for supercritical fluids are reviewed. More over detailed assessments of prediction accuracy of some of the existing correlations are also conducted against the collected experimental data by Kline and Watts. On the basis of the evaluation of the prediction behaviour of the existing heat transfer correlations, some new forms are proposed and the prediction capability of the new correlation is also assessed against the collected experimental data. Appendix A reports a table of most of the here mentioned correlations.

McAdams et al. 1950 (see Pioro and Duffey, 2007)

McAdams et al. conducted experiments with an upward flow of water in a vertical annulus with internal heating. The objective was to estimate local HTCs for turbulent flow inside an annulus. Four thermocouples, spaced at *76.2 mm* intervals, were installed inside a heated rod. These measured temperatures were used to calculate local HTCs along the heated rod. The experiments showed that, for given Reynolds and Prandtl numbers, a value of the local Nusselt number always decreased as a value of L/D_{hy} increased, regardless of the temperature at which the physical properties were evaluated. The experimental data obtained by McAdams were generalized into a correlation where maximum error was evaluated by *17%.*

Bringer and Smith 1957 (see Pioro and Duffey, 2007)

Bringer and Smith conducted experiments with supercritical CO_2 flowing inside a thin walled Inconel tube ($d = 6.35\,mm, \delta w = 0.89\,mm, and\ L = 610\,mm$). Bringer and Smith used thermocouples installed inside mixing chambers to measure bulk fluid temperatures at the inlet and outlet of the test section. The authors reasoned the use of the Inconel made it possible to use a thin wall tube due to the high tensile strength. Also, the Inconel temperature coefficient of electrical resistivity was sufficiently low not to have an appreciable effect on its electrical resistance. Therefore, a heat flux profile was uniform over the heated length in spite of the non-uniform temperature profile. In the early studies by Bringer and Smith in1957, the peak in thermal conductivity was not taken into account. However, thermal conductivity was assumed a smoothly decreasing function with temperature near the critical and pseudocritical points.

Krasnoshchekov and Protopopov 1960 (see Pioro and Duffey, 2007)

Krasnoshchekov and Protopopov (1959, 1960) and, later on, together with Petukhov et al. 1961 proposed a general correlation for forced convective heat transfer in carbon dioxide and water at supercritical pressures. However, the correlation of Krasnoshchekov- Protopopov gave less accurate prediction according to Kirillov et al 1961. In their development, Krasnoshchekov and Protopopov used the Pr and C_p averaged over a ranges to account for the thermophysical properties variations. The majority of their data (85%) were generalized and showed discrepancies within ±15%.

Goldman (1961) (see Pioro and Duffey, 2007)

One of the earliest investigations with supercritical water was done by Goldmann in 1961. In his experiments, Goldmann was able to observe effects that indicate two-phase behaviour. In tube experiments, two different heat transfer behaviours determined as a function of the heat flux density. At low Heat flux densities, normal heat transfer could be measured, while at high heat flux densities, a whistle could be heard during heat transfer. In tests with a whistling sound, the wall temperature could drop and almost a constant value can be observed at the test outlet, at the same time there was an increase of the system pressure by 0.3 MPa. As a result, a kind of boiling mechanism comparable to that at subcritical conditions was postulated. The phenomenon that could only be observed at bulk temperatures below the pseudo-critical temperature. The occurrence of the whistling sound during heat transfer could be changed by varying the inlet temperature, mass flow density and heat flow density. By lowering the inlet temperature, the whistling sound occurred at a lower heat flux density, while at higher mass flux densities a whistling sound was only recorded at higher heat flux densities.

Goldmann was among the first investigators to develop models for supercritical heat transfer, he used an expression for eddy diffusivity derived originally for a constant property flow; the eddy diffusivity was calculated at different radial locations considering property variations at these locations.

Petukhov et al. 1961 (see Petukhov et al. 1961)

At the same time, Petukhov et al. studied heat transfer in supercritical carbon dioxide. By analysing their experiments with carbon dioxide (CO_2) and consideration of other authors' experiments with supercritical water, they developed a general correlation for both material systems. This correlation takes into account the influence of radial changes in the fluid properties at small temperature differences between wall and bulk.

In particular, the influence of variable fluid properties on heat transfer was investigated. This influence was evaluated by two different test procedures. First, the inlet temperature was varied while the wall temperature was kept constant at the point x=*50 D* in the pipe. On the other hand, the bulk temperature was at the same place kept almost constant and the wall temperature varies. So, it was, in both cases, possible to examine the influence on the heat transfer coefficient. With the increase of the temperature difference between wall and bulk increased the heat transfer coefficient and then dropped in accordance with the physical properties of the fluid close to the wall. If the wall temperature is still below the pseudo-critical temperature, the heat transfer coefficient increases with an increase in the bulk temperature. If the wall temperature lies within the pseudo-critical region, the heat transfer coefficient first increases but decreases later. Above the pseudo-critical temperature, the heat transfer coefficient only drops with higher bulk temperatures. A dependency on the pseudo-critical heat capacity was determined and considered as the ratio of the average specific heat capacity $\overline{C_p}$ to the heat capacity of the bulk C_{pb}. With the results obtained, a correlation for water and carbon dioxide was proposed.

Shitsman 1963 (see Pioro and Duffey, 2007, and Shitsman 1963)

Shitsman in (1959) analyzed the heat transfer experimental data of supercritical water flowing inside tubes, and generalized these data with the Dittus-Boelter type correlation where the *Pr* value was evaluated at the bulk fluid temperature or at the wall temperature, whichever is less. However, Shitsman, based on the knowledge at that time, assumed that thermal conductivity was a smoothly decreasing function of temperature near the critical and pseudocritical points.

Investigations by Shitsman in 1963 were mainly carried out with a stainless-steel tube with a length of *1500 mm* and an inner diameter of *8 mm.* The heat transfer was analysed with eleven welded thermocouples. Through preliminary investigations, the heat losses to the environment were considered small compared to the heat input to the fluid and accordingly neglected. In the low mass flow density range in vertical upward flow with water, the sudden occurrence of deterioration of heat transfer was analyzed in experiments. For Shitsman these deteriorations under supercritical conditions show analogies to film boiling in subcritical pressures.

At heat flux densities below $q=281\ kW/m^2$, no deterioration of heat transfer could be observed at mass flux densities of $G=430\ kg/m^2s$. After an increase to $q=299\ kW/m^2$, the wall temperature rose sharply to more than *500 °C*. These temperature peaks, sometimes just under *600°C*, were noticeable by a red glow of the tube. The test area in which temperature peaks occurred is characterized by strong fluctuations of the wall temperature. By increasing the mass flow density, the deterioration could be reduced or a normal heat transfer was measured, and the temperature peak can also be reduced by increasing the pressure. A further increase in the heat flow density did not lead to any stabilization of the flow.

A deteriorated heat transfer was found at $G=300\text{-}700\ kg/m^2s$ up to enthalpy of *2093 kJ/kg*. Occasionally, a pulsation of the system pressure and the wall temperature could be registered with a deteriorated heat transfer. At a period of *15s*, the pressure pulsations reached amplitudes of *2.5MPa*, which disappeared again by increasing the heat flow density. The pulsations were observed in areas where the fluid moves through the tube with significant changes in thermophysical properties. At a high mass flow density $G=1500\ kg/m^2s$, no deterioration of the heat transfer could be observed up to $q=1104\ kW/m^2$. However, between $q=872\text{-}1104\ kW/m^2$ fluctuations in the pressure at the test outlet were recorded.

Domin 1963 (see Pioro and Duffey, 2007)

Domin performed experiments with supercritical water flowing inside horizontal tubes ($d = 2\ mm\ and\ L = 1.075\ m, and\ d = 4\ mm\ and\ L = 1.233\ m$) and proposed a HT correlation obtained within the following range: $p = 233\ -\ 263\ MPa$ and $q =\ 0.58\ -\ 4.65\ MW/m^2$.

Swenson et al. 1965 (see Swenson et al., 1965)

According to Swenson et al., conventional correlations cannot predict heat transfer in fluids in the pseudo-critical range. To solve this problem, they conducted some experiments with forced flow of water in vertical pipes. A stainless-steel pipe (AISI Type 304) of length *l=2946 mm* was examined, divided into an unheated inlet section (*l=889 mm*), a heated length of *l=1828 mm* and an outlet section. Only data from the second half of the tube were considered to be fully developed for their empirical correlation to be applied, as there were significant thermal entry effects (up to *x/d =97*). A density ratio was used to better describe the material properties. At high heat flux densities, a decrease of the heat transfer coefficient could be observed which further decreases with increasing the pressure.

The correlation describes *94.9%* of the data with a standard deviation of *15%*. The physical properties in the pseudo-critical range were not sufficiently known at this time, so a smoothing of the physical properties in this range was applied. According to Swenson et al. thermal conductivity was a decreasing function of temperature near the critical and the pseudocritical points. Unlike other correlations, the thermophysical properties here are related to the wall temperature.

Bishop et al. 1965 (see Bishop et al. 1965)
With four different tube geometries, Bishop et al. conducted investigations in supercritical water. Pipes made of stainless steel (SS 316) in vertical upward flow were used within the following range of flow and operating parameters: pressure *22.8 − 27.6 MPa*, bulk fluid temperature *282°C − 527°C*, mass flux *651 − 3662 kg/m²s* and heat flux *0.31 − 3.46 MW/m²*.

During the tests, a whistling sound was occasionally recorded at high heat flux densities when the bulk temperature was near the pseudo-critical temperature (T_{pc}) and the wall temperature was above T_{pc}. A disturbance in the thermal boundary layer was suspected due to the strong density changes. The whistle was preceded by an increase in wall temperature. Only in the case of heat flux density that was *10-30%* greater than was necessary for initiating the whistle tones did the temperature increase by about *100°C*. The intensity of the whistle seemed to increase due to lower inlet temperatures. At higher mass flow densities, higher heat flow densities were needed to initiate the whistling sound. During the occurrence of a whistle, oscillations of the measured values were observed, but could not be recorded in more detail. It was assumed by Bishop et al. that despite the attenuation of heat transfer in experiments with whistle, obviously there is no change in the heat transfer mechanism. They developed a heat transfer correlation with which the wall temperature of the experiments could be calculated in a *95%* probability range with a standard deviation of *15%.*

Vikhrev et al. 1967 (see Vikhrev et al., 1967)
Vikhrev et al. investigated the heat transfer of supercritical water in a vertical upward flow. Two stainless steel tubes of different geometries were investigated. A short pipe (*d=7.85mm*) with a heated length of *1515 mm* and a long pipe (*d=20.4mm*) with a heated length of *6000 mm*, each taking into account an unheated inlet section.

Analyses with the short tube showed that, in various experiments, heat transfer was deteriorated in the heated area *x/d=40-60*. The position of the temperature peak, due to the deteriorated heat transfer, was dependent on the inlet enthalpy. It was assumed that this was in connection with the thermal development of the flow.

In experiments with different heat and mass flow densities at *p=26.5MPa*, the relationship between temperature peaks and inlet enthalpy was also observed in the long pipe with *d=20.4 mm*. Only from heat flux densities of *q=505 kW/m²* at *G=495 kg/m²s* heat transfer deteriorated *at x/d=50*. At lower heat flux densities, this deterioration was not pronounced. An increase in the heat flux density to *q=570 kW/m²* also led to a further steep rise in the wall temperature shortly before the test outlet. Compared to *q=505 kW/m²*, the first temperature peak shifted towards the test inlet section at *q=570 kW/m²*. A deterioration of the heat transfer near the pipe entrance section could already be achieved by lower heat flow densities at higher inlet temperatures. At mass flow densities above *G=1000 kg/m²s*, deterioration could not be observed in the first sections up to *q=1250 kW/m²*, while at *G=1400 kg/m²s* wall temperature peaks at the pipe end were only registered at heat flow densities of *q>930 kW/m²*.

Shitsman 1968 (see Shitsman 1968)
Following the 1963 studies, Shitsman carried out further studies in 1968 using supercritical water. The heat transfer in stainless steel pipes was analyzed for different flow directions with different diameters and lengths (*d=3-16 mm, l=700-3200 mm*). For the visual inspection of the pipe, gaps (*30-40 mm*) in the insulation were provided in order to detect temperature peaks while occurring. Investigations into the boiling behaviour at *10 MPa* have shown that the wall temperature peak is significantly higher at *24.5 MPa* at similar heat flow density. The temperature peak caused by

high heat flow densities was shifted to the pipe inlet by increasing the heat flow density. An extension of the inlet section, while reducing the heated section, did not change this behaviour. The wall temperature rises in the flow direction depending on the respective heat flow density. A higher heat flow density resulted in a higher wall temperature at the outlet in addition to the displacement of the temperature peak.

When the heat flux density was increased at about $G=380 kg/m^2s$ from $q=500\ kW/m^2$ to $q=700\ kW/m^2$, a degeneration of the temperature peaks was determined. In this case, the wall temperature no longer drops after a temperature peak. A downward flow did not produce a temperature peak with the same boundary conditions as the upward flow. It was concluded that the temperature peaks arise from an interaction of forced and free convection.

Shitsman assumed that there was a reduction in turbulence in upward flows with high heat input, so that the boundary layer became laminar and thus led to a temperature peak. It was also assumed that the temperature peak was related to a reorientation of the flow. Since this laminarization occurred only due to the changing of the fluid properties, it can only occur below the pseudo-critical temperature.

In principle, it was concluded from the investigation that in long straight pipes, with large enthalpy increases and low inlet enthalpies, two wall temperature peaks can occur as a result of a deterioration of the heat transfer. The first peak is directly related to the pipe entry, while the second peak occurs just before the pseudo-critical temperature. By increasing the inlet temperature, the first peak can be avoided. By increasing the pipe diameter, the temperature peaks could be shifted to the pipe inlet. A variation of the pressure $p=24.5\text{-}34.3\ MPa$ had no significant effect on the temperature peaks in the tests carried out. It was concluded that a laminarization of the flow occurs only if the wall temperature reaches a certain value and thus free convection is dominated.

Ackerman 1970 (see Ackerman 1970)

In 1970, Ackerman continued the series of experiments by Swenson et al. and deterioration in supercritical water was investigated on the same test experiment. Ackerman investigated heat transfer to water at supercritical pressures flowing in smooth vertical tubes and tubes with internal ribs over a wide range of pressures, mass fluxes, heat fluxes, and diameters. Ackerman referred to the deterioration in heat transfer, by analogy with film boiling in subcritical water, as pseudo-film boiling. The experiments with a ribbed tube showed that pseudo-film boiling was suppressed. This suppression permitted operation at higher heat fluxes compared to operation with smooth tubes as might be expected for a single-phase fluid when turbulence is enhanced.

At very low inlet enthalpies, still below the pseudo-critical enthalpy, no deteriorated heat transfer could be determined in a tube with $d=9.4\ mm$ at a mass flow density of $G=1220\ kg/m^2s$ up to $q=1260\ kW/m^2$. Tests carried out at higher enthalpy and inlet enthalpy just below the pseudo-critical value, instead showed significant temperature peaks from $q=787\ kW/m^2$. Increasing the heat flux increases the temperature peak, decreasing the mass flux increases the magnitude of the temperature peak, while increasing it tends to suppress the effect. At pressures close to the critical pressure, this temperature peak was the highest observed.

In experiments with a tube diameter of $d=18.5\ mm$, a second temperature peak was observed near the pseudocritical enthalpy. While the first temperature peak is much more pronounced and then the wall temperature again for a short time decreases, the second temperature peak is developed over a wide area of the tube. With a larger pipe diameter of $d=24.3mm$ and a mass flow density of $G=406.8\ kg/m^2s$, the sharp peak in temperature at the beginning of the pipe occurred at low enthalpies. An occurrence of the deteriorated heat transfer

could already be observed at lower values of the heat flux density than in tests with *d=18.5mm*. By reducing the diameter from *d=24.3mm* to *d=9.4mm*, the permissible heat flux could be increased by *40%*.

Grass et al. 1971 (see Grass et al. 1971)
By modifying Prandtl's boundary layer model, Grass et al. established a correlation for predicting heat transfer in supercritical water. The Prandtl model can be converted into a representation in which the thermal resistance of the entire system is considered as parts of the laminar boundary layer and the turbulent core.

A new heat transfer correlation was given with the basic consideration that the average temperature of the bulk is the basis for the turbulent part and the boundary layer temperature for the laminar part. The Prandtl number was referred to the effective boundary layer temperature. At $Pr_b<0.5Pr_w$, the fluid properties of the boundary layer temperature are related to the bulk temperature, while at $Pr_b>0.5Pr_w$ they are related to the wall temperature. Using the experimental results of Herkenrath et al. (see Grass et al. 1971) a mean deviation of less than 10% was achieved with this correlation.

Ornatsky et al. 1971 (see Ornatsky et al., 1971)
Ornatsky et al. investigated heat transfer in supercritical water especially in small pipes with vertical upward and downward flows. They used a stainless-steel tube of length *l=750 mm* and a diameter *d=3 mm* to investigate the appearance of deteriorated heat transfer in five parallel tubes with stable and pulsating flow. They found that the deteriorated heat transfer in the assembly at supercritical pressures depended on the heat flux to mass flux ratio and flow conditions.

At inlet enthalpies of $h_b \leq 1350$ *kJ/kg*, deterioration of heat transfer in upward flows at $q/G \geq 0.93\text{-}1.05$ *kJ/kg* was observed, while there was no deterioration at $q/G < 0.9$ *kJ/kg*, independent of the inlet enthalpy of heat transfer. A temperature peak due to deteriorated heat transfer could not also be measured at inlet enthalpies of $h_b > 1350\text{-}1500$ *kJ/kg*. For downward flows, the onset of the deterioration could already be reached at q/G=0.7-0.85 kJ/kg. This is in contrast to Shitsman (*see Shitsman 1968*), who found a deterioration in downward flows only at higher heat flux densities than in upward flows.

With an almost constant heat flow to mass flow density ratio $q/G = 0.765$ *kJ/kg* and almost constant inlet enthalpy $h_b=800$ *kJ/kg*, the mass flow density was reduced in a downward flow to $G=3000\text{-}800$ *kg/m²s*. Ornatsky et al. observed that the temperature drop after the temperature peak decreased as the mass flux was reduced. A temperature drop after a temperature peak progressively disappeared starting at $G=1200$ *kg/m²s*, so that at $G=800$ *kg/m²s* there was no temperature drop. It was then assumed by Ornatsky et al. that the deterioration in heat transfer and the associated temperature peaks are caused by an interaction between free and forced convection.

Yamagata et al. 1972 (see Yamagata et al., 1972)
Yamagata et al. studied the heat transfer in supercritical water with forced convection in horizontal and vertical flow. The experiments served to determine factors that affect the deteriorated heat transfer in pipes (*d=7.5,10 mm*). At low heat flux densities $q=233$ *kW/m²* ($G=1260$ *kg/m²s*), no dependence of the flow direction on the gravitational field could be observed, while at $q=698$*kW/m²* there were clear wall temperature differences. Yamagata et al. noticed that the upward flow has lower heat transfer coefficients than that of the downward flow. At high heat flux densities and at the same time low mass flux densities, the differences were more pronounced.

This phenomenon could not be clarified by the investigation. However, Yamagata et al. assumed that this was probably due to a behaviour similar to two-phase flows or to buoyancy effects.

In order to predict the wall temperatures, a heat transfer correlation was developed based on experimental data for normal heat transfer. The correlation had a discontinuity when the wall temperature reached the pseudocritical temperature. This discontinuity had already been recognized by the authors as a serious weak point. Yamagata et al. also proposed the following equation for detecting the onset of heat transfer deterioration: $q = 200\ G^{1.2}$, this equation was derived based on experimental data in a *10 mm* circular tube.

Jackson and Fewster 1975 (see Pioro and Duffey, 2007)

Jackson and Fewster (1975) modified the correlation of Krasnoshchekov et al. to employ a Dittus-Boelter type form for Nu_0. Finally, they obtained a correlation similar to that of Bishop et al. (1964) without the effect of geometric parameters and with different values of the constant and exponents. Hence, it can be expected that Jackson and Fewster correlation will follow closely a trend predicted by Bishop et al. correlation.

Yaskin et al 1977 (see Pioro and Duffey, 2007)

Yaskin et al. found that available data on heat transfer to supercritical helium in a purely forced convection flow regime can be correlated on the basis of an analogy with the heat-transfer process accompanying gas injection through a heated wall. They proposed a correlation in which Nu_0 was calculated according to the Dittus-Boelter correlation.

Dyadyakin and Popov 1977 (see Pioro and Duffey, 2007, and A. Nava-Dominguez 2020)

The correlation by Dyadyakin and Popov was the only identified friction factor correlation developed specifically for wire wrapped bundles at supercritical conditions. The correlation was obtained based on experiments of a tight lattice seven rod bundle with helical fins under supercritical conditions. They tested five bundles with different flow areas and hydraulic diameters. However, as stated, this correlation is expressed in terms of the inlet conditions and therefore is only valid for the specific experimental configuration. Moreover, it does not take into account the geometry involved (i.e., pitch to diameter ratio). This correlation fits the data (504 points) to within ±20%. The maximum deviation of the experimental data from the correlating curve corresponds to points with small temperature differences between the wall temperature and bulk temperature. Sixteen experimental points had deviations from the correlation within ±30%.

Jackson and Hall 1979 (see Pioro and Duffey, 2007)
In 1979, Jackson and Hall reviewed a number of previous works concerning forced-convection heat transfer to fluids at supercritical pressures. In their review the authors contributed to special features of heat transfer to fluids at supercritical pressures, they discussed the effects of acceleration due to heating on heat transfer deterioration as well as the effect of buoyancy.
Based on the correlation by Krasnoshekov and Protopopov (*see Pioro and Duffey, 2007)*, Jackson and Hall developed a simplified correlation form in 1979. The new correlation simplifies the part for constant material properties, which has been replaced by a Dittus-Boelter correlation. The exponent "n" of the heat capacity ratio depends on the relative magnitude of the wall and bulk temperatures in relation to the pseudo-critical temperature. With a much simpler structure, the correlation gave the same good prediction as the original.

Yeroshenko and Yaskin 1981 (see Pioro and Duffey, 2007)
Yeroshenko et al. analyzed the applicability of correlating equations for the Nusselt number of some of the existing correlations and proposed a new correlation by correcting the Dittus-Boelter correlation. The correction factor *F* accounts for possible heat transfer enhancement. The non-iteration prediction of the supercritical helium heat transfer from a given wall temperature can be performed for values of Ψ up to *32*. The new correlation predicts about *95%* of the experimental values of Nu within ±*20%*.

Watts and Chou 1982 (see Pioro and Duffey, 2007)
Watts and Chou focused their investigations on heat transfer in mixed convection. Experiments in tubes (*d=25.4, 32.2mm*) with different flow directions were carried out in which the test arrangement used enabled free convection to develop. Experiments were only performed for bulk enthalpy below the pseudo-critical one, while the wall temperature was partly above T_{pc}.
Due to the decrease of the mass flux density in a vertical upward flow, the formation of a temperature peak could be observed. With further decrease of the mass flux, the temperature peak was shifted to the pipe inlet. An engineering correlation was suggested for vertical upward flow in pipes, which takes buoyancy effects into account through a correction term.

Petukhov et al. 1983 (see Pioro and Duffey, 2007)
Petukhov et al. performed analyses that involved experimental data from a number of authors on heat transfer to water, carbon dioxide, and helium for the normal heat transfer regime. The authors obtained a correlation to calculate heat transfer coefficient.

Bogachev et al. 1983 (see Pioro and Duffey, 2007)
Bogachev et al. used a stainless-steel tube ($d = 1.8\,mm, L = 400\,mm, and\ \delta w = 0.1\,mm$) with *78 mm* unheated part just upstream of the heated length to study helium flowing in downward direction, the authors gave special attention to the conditions of heat transfer increase in turbulent flow of helium where free convection effect can be neglected. Bogachev et al. used Germanium Resistance Temperature Detectors (RTDs) installed at 15 cross sections along the heated length (pitch *25 mm*), which were pressed through a thin electrical insulating film ($\delta w = 10\,\mu m$) on the tube surface to measure the bulk temperature.

Razumovskiy et al. 1990 (see Pioro and Duffey, 2007)
Investigations on heat transfer and pressure drop in supercritical water were carried out in 1990 by Razumovskiy et al. The authors suggested that when $T_b<T_{pc}<T_w$, the heat transfer may

deteriorate depending on the heat flux which could become dangerous for the experimental apparatus either due to high maximum temperatures or the occurrence of strong fluctuations in pressure. Moreover, they stated that the fluid in contact with the element cladding would behave as a gas-like phase whereas the bulk temperature of the coolant might behave as a liquid-like phase. This local change in the near wall density affects the hydraulic resistance, similar to the film boiling phenomena observed in subcritical flows. With the experiments carried out, Razumovskiy et al. suggested a correction term for the coefficient of friction in isothermal flow which could be determined and the new correlation using this coefficient of friction has a standard deviation of *14.5%*.

Gorban' et al 1990 (see Pioro and Duffey, 2007)
Gorban' et al. investigated heat transfer to water and Freon-12 (R-12) flowing at subcritical and supercritical pressures inside a circular tube (d = 10 mm and l = 1 m). The range of investigated parameters was as follows: $P = 1.08$ and 4.46 MPa, $G = 500 – 2000$ kg/m^{2}s, $T_{in} = 20 – 140$ °C and $q = 6 – 290$ kW/m^2. Gorban' et al. developed a fluid-to-fluid modelling technique for supercritical pressures to scale water-equivalent conditions into Freon-12 equivalent conditions and vice versa. The authors generalized their experimental data to propose a heat transfer correlation of Freon-12 flowing inside a circular tube at temperatures higher than the critical temperature.

Griem 1996 (see Griem 1996)
In order to quantify the improvement of heat transfer in water with ribbed and dimpled tubes, measurements were carried out both on these tube geometries and on smooth tubes in the two-phase area and above the critical pressure. The experiments showed no improvement in heat transfer near the pseudo-critical point, which would have been expected due to the large heat capacity. Moreover, from p=22 MPa, no boiling could be observed before the departure from nucleate boiling (DNB). Thus, according to Griem, it can already be spoken of supercritical behaviour, if the heat flux density exceeds a critical value at a certain mass flux density a heat transfer deterioration occurs.

Based on heat transfer studies in near-critical and supercritical water, a new correlation with modified heat capacity was developed by Griem in 1996. The heat capacity is calculated using five interpolation points, in which the two highest values ($C_{p,max}$ and $C_{p,2max}$) and thus closest to the pseudo-critical state are discarded. The average of the three remaining values represents the characteristic heat capacity. In addition, the correlation takes into account a correction for low enthalpies.

Kitoh et al. 1999 (see Kitoh et al., 1999)
Kitoh et al. proposed a heat transfer coefficient for forced convection in supercritical water, within the range of bulk temperature from *20 to 550 °C* (bulk fluid enthalpy from *100 - 3300 kJ/kg*), mass flux from *100 - 1750* kg/m^{2}s, and heat flux from *0 - 1.8* MW/m^2.

Koshizuka and Oka 2000 (see Pioro and Duffey, 2007)
The correlation of Koshizuka and Oka is based on their earlier numerical study on forced convective SC flow of water in a *10 mm* diameter tube. The authors performed analysis of the heat transfer deterioration mechanism by numerical simulation using the $k–\varepsilon$ turbulence model. Transient and accident analysis code for fast reactors and calculation of the Oka-Koshizuka heat transfer correlation for the safety analysis at supercritical pressure were performed. The authors

used their correlation for safety analysis in which they concluded that it gives smaller heat transfer coefficients at low mass flux condition compared with experiments and other existing correlations, such as the Watts–Chou correlation and Bishop correlation. In addition, the correlation predicts higher cladding temperature than other correlations. Location of the hottest cladding temperature tended to be at the high temperature "gas-like" coolant region above 500 °C where the heat transfer coefficient should agree with the Dittus–Boelter correlation. The Oka–Koshizuka correlation agrees relatively well with the Dittus–Boelter correlation at this region compared with the other correlations.

Jackson 2002 (see Pioro and Duffey, 2007)
Jackson modified the original correlation of Krasnoshchekov et al. for forced convective heat transfer in water and carbon dioxide at supercritical pressures to employ the Dittus-Boelter type form for Nu_0. Hence, it can be expected that the Jackson correlation will follow closely a trend predicted by the Krasnoshchekov et al. correlation. Based on previous work of Jackson and Hall (1979) for reviewing and assessing several heat transfer correlations, based on the experimental data (2000 points) of water (75% of 2000 points) and carbon dioxide (25%). The authors found correlation of Krasnoshchekov et al. (1967) and its modified version of Jackson (2002) to be the most accurate ones, *97 %* of the experimental data were correlated with the accuracy of ***±25%***.

Kirillov et al. 2003 (see Pioro and Duffey, 2007)
Heat transfer in upward flows of supercritical water in *1 m* and *4 m* stainless-steel vertical tubes (*d=10 mm*) was investigated in 2003 by Kirillov et al. At low heat flux densities, a monotonic wall temperature gradient could be measured along the tube. At higher heat flux densities, the gradient depends on the mass flow density and the inlet temperature. If the inlet temperature is above the pseudocritical temperature, a monotonic gradient was observed even at higher heat flux densities. At lower inlet temperatures, a deterioration of the heat transfer was observed from $q/G > 0.6$ *kJ/kg*, which was evident from temperature peaks.

In 2005, Kirillov et al. continued the investigations started in 2003. The experiments with water were performed to determine scaling effects on other fluids. The difference between calculated and measured outlet temperature gave satisfactory results (about *1%*).
At a mass flux density G=200 kg/m^{2}s, an increase in the wall temperatures in the range ($x/d \leq 30$) from $q=227$ *kW/m*^{2} was observed in a pipe with a diameter *d=10 mm*. By increasing the heat flux density, the wall temperature rise became steeper. At higher mass flow densities $G=1500$ *kg/m*^{2}*s* the temperature peak at the pipe entrance was less pronounced. Analyses of the causes of the deteriorated heat transfer were not performed.

Kuang et al. 2008 (see H. Zahlan et al., 2015)
Kuang et al. used their databank of supercritical heat transfer to water for vertical upward flow in a tube to develop their correlation. They studied the enhanced and deteriorated heat transfer based on the normal heat transfer coefficient (HTC) predicted by Dittus–Boelter correlation. The correlation by Kuang et al. was developed for normal and deteriorated heat transfer. Kuang et al. used the modified Grashof number Gr^* to account for the buoyancy effect. In addition, they used the non-dimensional heat flux number q^+ to consider the thermal acceleration effect from heating on the HTC.

Cheng et al. 2009 (see Cheng et al., 2009)

Cheng et al. developed a new heat transfer correlation based on a selected data points by Herkenrath et al. (1967) experimental investigation on heat transfer in vertical circular tubes at high pressures up to 25 MPa. Cheng et al. proposed a correction factor (*F*) to the general form of the Dittus–Boelter equation. An extensive analysis was carried out for the effect of various parameters on the correction factor. It was found that the dependence on the acceleration parameter is strong and unique and whose relation can be divided into two regions. In the region of small values of the acceleration parameter, the correction factor increased with increasing acceleration parameter, whereas in the region of large acceleration parameter, a decrease in the correction factor was obtained. The relationship in the first region was well described with a single curve for different experimental conditions, whereas in the second region various curves were required for different parameter combinations, which can be characterized by the maximum value of the acceleration parameter. For each combination of pressure, mass flux and heat flux, the acceleration parameter depends on fluid temperature. The authors stated that for about *70%* of the data prediction the deviation between the measured and the calculated Nusselt numbers falls into an error band of *20%.*

Mokry et al. 2009 (see Mokry et al., 2009)

The Pioro-Mokry correlation was verified within the following operating conditions, only for NHT and EHT regimes, but not for the DHT regime, SCW, upward flow, vertical bare circular tubes with inside diameters of 3–38 mm, pressure of 22.8–29.4 MPa, mass flux of 200–3000 kg/m^{2}s, and heat flux of 70–1250 kW/m^2. All thermophysical properties of SCW were calculated according to NIST REFPROP software (2013). This correlation has accuracy of ±25% for HTCs and ±15 for wall temperatures. Eventually, this non-dimensional correlation can be also used for other SCFs. However, its accuracy can be less or even significantly less in these cases.

Yoon et al. 2009 (see Yoon et al., 2009)

Bae et al. carried out an experiment of heat transfer to CO_2, which flows upward and downward in a circular tube with an inner diameter of 6.32 mm, with mass flux of *285-1200 kg/m^{2}s* and heat flux of *30-170 kW/m^2* at pressures of *7.75* and *8.12* MPa, respectively. The tube inner diameter corresponds to the equivalent hydraulic diameter of the fuel assembly subchannel, which is being studied at Korea Atomic Energy Research Institute (KAERI).

The authors evaluated some of the existing heat transfer correlations, among the tested correlations, the Bishop correlation predicted the experimental data most accurately, but only *66.9%* of normal heat transfer data were predicted within ***±30%*** error range. The Watts and Chou correlation, which is claimed to be valid for both the normal and deteriorated heat transfer regime, showed unsatisfactory performance. A significant decrease in Nusselt number was observed in the range of $10^{-6} < Gr_b/Re_b^{2.7} < 2 \times 10^{-5}$ before entering a serious heat transfer deterioration regime. The heat transfer deteriorated when the value of the buoyancy parameter $\frac{Gr_b}{Re_b^{2.7}}$ exceeded 2×10^{-5} close to the Jackson and Hall's criterion. As soon as the heat transfer deteriorated, it entered a new regime and did not return to a normal heat transfer regime, although the value of buoyancy parameter $\frac{Gr_b}{Re_b^{2.7}}$ reduced below the deterioration criterion 2×10^{-5}.

The authors concluded that this may justify the requirement of developing separate correlations for the normal and deteriorated regimes. Hence, they proposed that since a single curve, representing the present experimental data for deteriorated heat transfer, cannot be formulated unless introducing a highly complicated function, it was decided to formulate functions applying

to each segment having consistent data. The functional dependence of $\frac{Nu_{\exp}}{Nu_b}$ to buoyancy parameter *Bu* was found in the segments divided arbitrarily for normal and deteriorated regimes.

Gupta et al. 2010 (see Gupta et al., 2010)
Gupta et al. modified the Swenson et al. (1965) correlation which evaluates the fluid properties in *Nu*, *Re* and average *Pr* at the wall temperature. Gupta et al. added a viscosity ratio term, to account for viscosity variations at the wall and at the bulk fluid. Also, it was decided to add an entrance effect to make this correlation even more accurate. This entrance effect was modelled by an exponentially decreasing term. The authors stated that the developed heat transfer correlation has an uncertainty of about ***±25%*** for HTC values and about ***±15%*** for calculated wall temperatures within the same ranges as Mokry's correlation (see S. Mokry et al. 2010). It should be noted that this heat transfer correlation is also intended only for NHT and EHT regimes.

Chen and Fang 2014 (see Chen and Fang 2014)
A new correlation for supercritical water flowing in vertical tubes is developed based on the database available in literature. Chen and Fang compiled 5366 data points from 13 sources. The data were for water flowing vertically upward in a round tube. They calculated the ratio of experimental to predicted HTC by Dittus–Boelter; based on the value of this ratio, Chen and Fang classified each experimental data point in 1 of 3 heat transfer modes: normal, enhanced, or deteriorated heat transfer. Then, the categorized data were used for assessing each of the 20 Nusselt number correlations. Chen and Fang also developed a new correlation: they reviewed functional dependence of known correlations and proposed a general form.
The authors compared the results of their developed correlation with some of the existing ones and stated that their correlation has a mean absolute deviation (MAD) of *5.4%* and predicts *95.7%* of the entire database within ***±15%***, while the best existing correlation only has an MAD of *13.6%* and predicts *64.4%* of the entire database within ***±15%***. Besides, the new correlation predicts the normal, improved, and deteriorated heat transfer regimes with an MAD of *5.5%*, *5.0%*, and *5.6%*, respectively, far better than any existing correlation for the given regime.

Zhao et al. 2014 (see Zhao M. et al., 2014)
Zhao et al. performed an experimental study on heat transfer of supercritical water flowing downward in circular tubes with *7.6 mm* inner diameter on the SWAMUP test facility. More than *3500* test data were obtained with the following test conditions: pressure from *23.0 MPa to 26.0 MPa*, mass flux from *450 kg/m^{2}s* to *1500 kg/m^{2}s*, heat flux from *0.17 MW/m^2* to *1.4 MW/m^2* and bulk temperature from *280 °C to 410 °C*. Effect of various parameters on heat transfer was investigated. Test data in the present study were also compared with those obtained in tubes with upward flow. In addition, comparison of the test data with available correlations indicates that none of the correlations give an accurate prediction. Based on the test data and sensitivity study of various dimensionless numbers, a new correlation was developed in which the authors introduced an additional dimensionless number π_B to correct the conventional Dittus–Boelter equation and give a satisfying agreement with the test data.

Wang and Li 2014 (see Wang and Li 2014)
Wang et al. carried out an evaluation of the heat transfer correlations for supercritical pressure water in vertical tubes the authors stated that there are still some uncertainties and deficiencies in the accurate prediction for supercritical fluid heat transfer coefficient due to the large and fast

variations of fluids properties in the so-called pseudo-critical region. In their evaluation, 15 correlations were selected from the literature and were compared with each other to verify their capability in predicting heat transfer coefficient of supercritical pressure water in vertical tubes. Based on the comparison between the calculation results of the existing heat transfer correlations and the experimental data obtained from the open literature, it was found that the Swenson et al. correlation and the Hu correlation can reasonably predict the heat transfer coefficient of supercritical water in the pseudo-critical region. After evaluating these correlations, the authors conducted polynomial fitting for the collected experimental data and got a new correlation for heat transfer coefficient of water at supercritical pressures. The authors claim their new correlation can fit well with the experimental data even in the neighbourhood of pseudo-critical temperature.

Wang et al. 2019 (see Wang et al., 2019)

Wang et al. developed a CFD model to study the turbulent heat transfer of sCO_2 flows in large horizontal tubes having diameters of 15.75 mm, 20 mm and 24.36 mm using RANS turbulence models. The numerical models were validated against experimental data published in literature to demonstrate the reliability of CFD simulations on the heat transfer coefficient prediction and buoyancy effect capture to turbulent SCO_2. Based on the validated model, several computations have been performed, involving a wide range of operating conditions, in the range of G = 200–800 kg/m^{2}s, p = 8–10 MPa, q = 5–36 kW/m^2. The authors concluded that the developed CFD model shows the best consistencies with the experimental measurements and was also able to well reproduce the heat transfer characteristics under various conditions and the pressure had a significant effect on the distribution of heat transfer coefficient, as well its peak drops sharply with rising pressure. J Wang et al. investigated 6 existing heat transfer correlations for in-tube cooling of turbulent sCO_2 in horizontal pipes and found considerable deviations with the existing heat transfer correlations compared to the experimental data which necessitated the development of a new correlation to predict the heat transfer coefficients. Based on the computational datasets from the developed CFD model, a Nusselt number equation based on the Gnielinski form with the ratio of density incorporated was suggested a new Nusselt number equation is formulated. The new heat transfer correlation showed a good accuracy with mean absolute relative deviation of 3.3%.

Huixiong Li et al. 2020 (see Li H. Et al., 2019)

Huixiong Li et al. reviewed 34 heat transfer correlations proposed for predicting the heat transfer characteristics of SCW in vertically upward tubes. Huixiong Li et al. based their studies on large experimental data set of approximately 12,704 data points and 250 experimental cases retrieved and collected from the published literatures. The experimental data used in their work covered the parameters of pressures from 22.5 to 31.03 MPa, mass fluxes from 200 kg/(m^{2}s) to 2500 kg/(m^{2}s), heat fluxes from 148 to 2000 kW/m^2, and the tube diameters from 3 to 38 mm. Among the 250 experimental cases collected, 134 cases are in the EHT regimes, while 116 cases of them are in the DHT regimes. Based on the evaluation of the 34 existing heat transfer correlations, Huixiong Li et al. found significant discrepancies among the results predicted by all the correlations, and there was no correlation which could give satisfactory prediction under different heat transfer (i.e. DHT\EHT) conditions and that most of the Nu number values predicted by the correlations are out of ±20% error band. Based on the findings, Huixiong Li et al. suggested a general form of heat transfer correlations for SCW and used multiple-variable linear regression model in their development. The authors adopted the full set of the experimental data including both the DHT regimes.

Pengcheng Guo et al. 2020 (see Pencheng G et al., 2020)

Pengcheng Guo et al. studied the heat transfer coefficient of SCO_2, especially under the heating conditions with high ratios of heat flux to mass flux (q/G). The authors investigated experimentally the heat transfer of SCO_2 in a mini tube (d = 2 mm) in the range of p = 7.6–8.4 MPa, q = 100–200 kW/m^2 and G = 400–700 kg/m^2 s, in which the ratio of q/G was within 250–500 J/kg. Pengcheng Guo et al. concluded that the heat transfer coefficient decreased with increasing heat flux and decreasing mass flux, in addition it was slightly affected by the pressure. The authors stated that under high q/G conditions, the buoyancy effect was significant, and heat transfer was deteriorated in the whole experimental setup.

The authors carried out a comparison of the heat transfer correlations for SCO_2 with the experimental data; however, the prediction errors of these correlations are relatively high, especially in pseudo-critical regions. Consequently, Pengcheng Guo et al. developed new heat transfer correlation for SCO_2 under high q/G conditions, in which buoyancy effect and variations in thermophysical properties are both considered. The proposed correlation can capture the trend of the experimental data and showed a very good prediction with respect to the experimental Nusselt number, and it was observed that the largest error is less than ±15% and the standard deviation is 4.63%. Pengcheng Guo et al. examined the applicability of the new correlation for other experimental data of SCO_2 available in literature, the new correlation can capture the overall trend of the experimental data in qualitative manner, however this time the standard deviation increased significantly to be in the range of 11-17.5%.

Zhu et al. 2020 (see Zhu B. et al.,2020)

The pseudo-boiling assumption is introduced to deal with supercritical heat transfer (SHT). Fluids at supercritical pressures are treated to have a heterogeneous structure consisting of vapour-like fluid and liquid-like fluid. Similarity analysis between subcritical boiling and SHT creates a new dimensionless parameter, the K number, representing evaporation induced momentum force relative to inertia force to govern the growth of wall attached vapour-like fluid layer thickness, which is key to dominate SHT. The authors used totally, 5560 data points, including newly obtained *2028* data points for supercritical CO_2 with pressures up to *21 MPa*, and other *3532* data points cited from *18* articles for carbon dioxide, water and R134a, are used to determine the coefficients and the exponents of their correlation by the use of regression method. The authors found that a negative exponent *-0.0313* for the K number is better explaining the improved heat transfer capabilities by increasing pressures. The new correlation was also compared with R22 data. Even though such data were not involved in the development of the correlation, but their predictions excellently matched the experimental data.

Wahl et al. 2021 (see Wahl et al.,2021)

Wahl et al. studied the heat transfer of carbon dioxide near the critical point in a horizontal tube with 2 mm inner diameter. Wahl et al. examined the effects of the CO_2 mass fluxes in the range of 400–1300 kg/m^{2}s, CO_2 inlet pressures between 77 and 85 bar, CO_2 bulk fluid temperatures between 10 and 85 °C and cooling water temperatures between 10 and 40 °C on the heat transfer. The experimental results were compared with existing correlations for SCO_2 heat transfer in small diameter tubes. The authors concluded that heat transfer coefficient increases with increasing mass flux. The influence of the mass flux on the HTC is significantly stronger near the pseudocritical temperature and the comparison of the experimental data and the available correlations showed that it is necessary to propose a new correlation for heat transfer of CO_2 near the critical point. Solving a multiple-variable linear regression model Wahl et al. developed a

modified Dittus-Boelter correlation to predict the heat transfer coefficients with an accuracy of 20%.

A table reporting the mathematical form of the mentioned correlations has been reported in APPENDIX – Table of correlations from the survey by UNIPI.

2.1.5.2 Assessment of some of the existing correlations

In this section, twenty of the existing heat transfer correlations were assessed against some of the experimental carbon dioxide data by Kline (2017) and water data by Watts (1980). The assessment takes into account the analysis in two different modes, named “Correlation“ and “Prediction” mode respectively.

In the correlation mode, the Nusselt number or the heat transfer coefficient (HTC) is calculated without iterations for wall temperature, i.e. the different dimensionless and thermo-physical parameters that appears in the original form of the correlation are calculated on the basis of the experimental wall temperature; on the other hand, in the prediction mode, the HTC is calculated using all the dimensionless numbers including wall temperature evaluated at the values of this parameter predicted from the Nusselt number provided by the correlation. The corresponding wall temperature is calculated based on the estimated HTC, heat flux and bulk fluid temperature. It is worth reporting that an iteration algorithm had to be developed for wall temperature, which resulted in convergence issues and produced more than single solutions in some cases. The challenge at this moment is to identify the most realistic solution and decrease the uncertainty.

In the correlation mode, the examined heat transfer correlations are firstly applied in their original form (i.e. the original constants and coefficients) and then their coefficients are customized for a specific data set by a linear regression analysis. In other words, the analysis includes trials to establish variants of the same empirical correlations obtained by optimizing their coefficients on the basis of the chosen data sets, which are composed by a number of local data in the order of 33,000, including the already mentioned Kline and Watts data. This analysis allows showing the capability of the proposed correlations to reproduce different phenomena as observed in the targeted experiments and then to ascertain at what extent these correlations could be better customized to fit the specific data set.

Based on the analysis of the existing correlations, a general form of heat transfer correlation for supercritical water heat transfer is proposed as follows;

$$Nu_b = c_0 X_1^{c_1} X_2^{c_2} \cdots X_k^{c_k} \tag{10}$$

where $X_1, X_2, \ldots, X_k$ are the selected dimensionless groups, and $c_0, c_1, c_2, \ldots, c_k$ are the constants needed to be determined. Taking the natural logarithm on the both sides of the above equation, it follows

$$\ln\ Nu_b = \ln c_0 + c_1 \ln\ X_1 + c_2 \ln\ X_2 + \cdots c_k \ln\ X_k \tag{11}$$

Equation (11) is a typical multivariate linear regression model, whose least square solution can be given as

$$C = (X^T X)^{-1} X^T Y \tag{12}$$

where $X, Y,$ and C are the matrices given by

$$X = \begin{bmatrix} 1 & \ln X_1(1) & \ln X_2(1) & \cdots & \ln X_k(1) \\ 1 & \ln X_1(2) & \ln X_2(2) & \cdots & \ln X_k(2) \\ \vdots & \vdots & \vdots & \vdots & \vdots \\ 1 & \ln X_1(n) & \ln X_2(n) & \cdots & \ln X_k(n) \end{bmatrix}_{n\times(k+1)} \quad Y = \begin{bmatrix} \ln Nu_b(1) \\ \ln Nu_b(2) \\ \vdots \\ \ln Nu_b(n) \end{bmatrix}_{n\times 1} \quad C = \begin{bmatrix} \ln c_0 \\ c_1 \\ \vdots \\ c_k \end{bmatrix}_{(k+1)\times 1} \tag{13}$$

where k and n are the number of the selected dimensionless groups and the sample data points, respectively. By the use of the previous method it was possible to optimize the coefficients of the selected correlations and investigate them on that basis.

A MATLAB code was developed in order to iterate on the wall temperature. The starting point in predicting the wall temperature is defining the inlet and boundary conditions, i.e. the operating pressure, the inlet temperature, the mass flux, the heat flux and the diameter of the selected data set of the examined case. Then, calculating the fluid bulk thermophysical properties using the tables of the National Institute of Standards and Technology (NIST), by assuming an initial guess for the wall temperature, such that the one calculated by the Dittus-Boelter correlation, the wall thermophysical properties can be calculated using the NIST data base. By selecting a certain form of a correlation, the values of the dimensionless parameters and accordingly the Nu number are defined based on the selected initial wall temperature. In order to update and iterate on the value of the wall temperature, the HTC is calculated from the Nu number equation and the new wall temperature value is obtained. The difference of the old and new wall temperatures is compared to a preselected tolerance value and the iteration is stopped once this tolerance is achieved (see Figure 15).

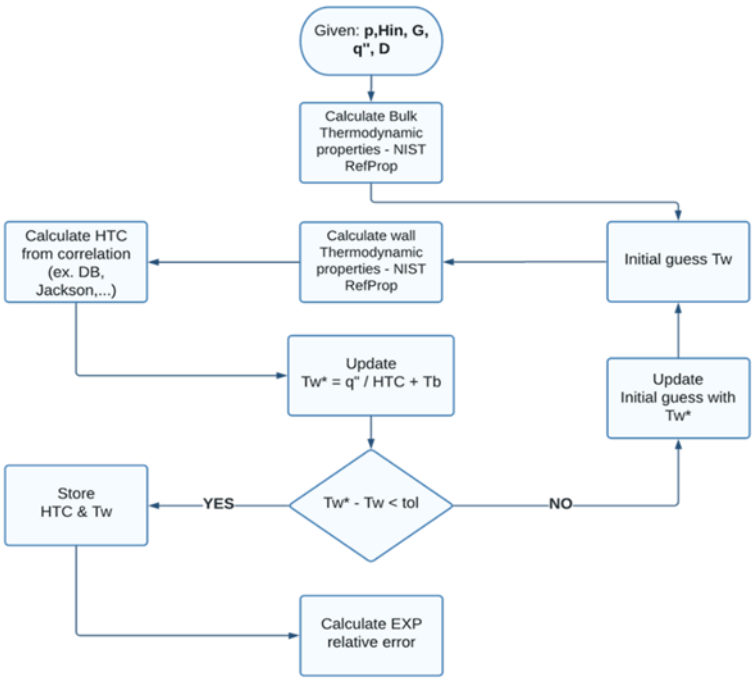

Figure 15. Procedure for iterating on wall temperature

In total, 20 heat transfer correlations were considered and applied to the entire database for different fluids including water and carbon dioxide.

Table 2 summarizes the list of selected correlations and their range of applicability. In addition, a statistical error analysis was performed in order to show the capability of the selected correlation to reproduce the different heat transfer phenomena as seen in experiments.

$$\mathrm{ME} = \frac{1}{n}\sum_{i=1}^{n} \frac{Nu_{\mathrm{cal}} - Nu_{\mathrm{exp}}}{Nu_{\mathrm{exp}}} \times 100\% \tag{14}$$

$$\mathrm{MAE} = \frac{1}{n}\sum_{i=1}^{n} \frac{\left|Nu_{cal} - Nu_{\mathrm{exp}}\right|}{Nu_{\mathrm{exp}}} \times 100\% \tag{15}$$

$$\mathrm{RMSE} = \sqrt{\frac{1}{n}\sum_{i=1}^{n} \left[\frac{Nu_{\mathrm{cal}} - Nu_{\mathrm{exp}}}{Nu_{\mathrm{exp}}}\right]^2} \times 100\% \tag{16}$$

It is necessary to perform a thorough comparison between predictions using the different correlations and experiments. The mean relative error (ME), mean absolute relative error (MAE) and root mean-square relative error (RMSE) characterize the assessment of predictions using the correlations in literature. The mean relative error, as formulated in Eq. (14), summarizes the overall tendency of a correlation to over-predict or under-predict the measured values. Because ME concerns the sign of the relative error, positive and negative deviations can offset each other, thus ME can indicate the error distribution. In addition, as in pre-design studies the maximum possible temperature is of interest and is rather over- then under- predicted, it becomes clear that heat transfer correlations with a negative and low ME are desirable. On the other hand, the mean absolute relative error, as formulated in Eq. (15), describes the arithmetic mean of the absolute errors, expressing the correlation accuracy. Finally, the root-mean-square relative error, as formulated in Eq. (16), emphasizes larger deviations. In general, large deviations in terms of the temperature prediction may result in system requirements (e.g. cladding material), which are unnecessarily high or insufficient.

Figure 16 to Figure 18 show the results obtained by the use of Bae et al. (2009) correlation, Eq. (17), in **"correlation" mode**. A comparison of the cumulative calculated values of the Nusselt number to the experimental ones is reported for both original and optimized coefficients case, the values of the constants and the coefficients are reported in Table 1 for Bae et al. and Chen and Fang correlations. Clearly, the values of the Nu numbers are a bit more accurate in the optimized case; it is even clearer from Figure 17 that the trends of the wall temperatures are better predicted for the case of Kline data.at p=8.35 MPa, Tin=16°C, G=300 kg/m^{2}s and q=20 KW/m^2. Another comparison is presented in Figure 18 for the case by Watts data at p=25 MPa, Tin=200°C, G=375 kg/m^{2}s and q=340 KW/m^2, as it is shown, the enhancement by the use of the optimized coefficients is less visible. This is possibly due to the fact that most of the chosen experimental data set are CO_2 data, about 31000 data point and only 2000 data point for water. So, basically the linear regression algorithm is trained on more many CO_2 data.

$$Nu_{\text{Bae}} = \text{Nu} * f(Bu)$$
$$f(Bu) = (1 + 1.0 \times 10^8 Bu)^{-0.032}, \text{ for } 5.0 \times 10^{-8} < Bu < 7.0 \times 10^{-7}$$
$$f(Bu) = 0.00185 \times Bu^{-0.43465}, \text{ for } 7.0 \times 10^{-7} < Bu < 1.0 \times 10^{-6}$$
$$f(Bu) = 0.75, \text{ for } 1.0 \times 10^{-6} < Bu < 1.0 \times 10^{-5}$$
$$f(Bu) = 0.0119 \times Bu^{-0.36}, \text{ for } 1.0 \times 10^{-5} < Bu < 3.0 \times 10^{-5}$$
$$f(Bu) = 32.4 \times Bu^{0.40}, \text{ for } 3.0 \times 10^{-5} < Bu < 1.0 \times 10^{-4} \tag{17}$$
$$\text{Nu} = 0.021\text{Re}_\text{b}^{0.82}\ \text{Pr}_\text{b}^{0.5}\left(\frac{\rho_w}{\rho_b}\right)^{0.3}\left(\frac{\overline{C_p}}{C_{\text{p},b}}\right)^{\text{n}}$$
$$n = 0.4 \text{ for } T_b < T_w < T_{pc}, 1.2T_{pc} < T_b < T_w$$
$$n = 0.4 + 0.2\left(T_w/T_{pc} - 1\right) \text{ for } T_b < T_{pc} < T_w$$
$$n = 0.4 + 0.2\left(T_w/T_{pc} - 1\right)\left[1 - 5\left(T_b/T_{pc} - 1\right)\right]$$
$$\text{for } T_{pc} < T_b < 1.2T_{pc} \text{ and } T_b < T_w$$
$$Nu_b = C1\text{Re}_b^{C2}\left(\frac{Pr_w}{Pr_b}\right)^{C3}\left(\frac{v_w}{v_b}\right)^{C4}\left(\frac{\overline{C_p}}{c_{p,b}}\right)^{C5}\left(\frac{Gr_b^*}{Gr_b}\right)^{C6} \tag{18}$$

Another similar set of results obtained using Chen and Fang (2014) correlation, see Eq. (18), are shown in Figure 19 to Figure 21. Though Chen and Fang correlation was originally developed for supercritical water the cumulative Nu number and the wall temperature trends are better represented than by the Bae et al. correlation. The proposed form accounted for 8 dimensionless groups and by the use of a regression analysis software, the number of dimensionless groups was further reduced. The numerical coefficients and exponents of the general form of the correlation were found and optimized based on the experimental data using the least squares method.

Table 1. values of the constants and coefficients used in the analysis.

Correlation	C1	C2	C3	C4	C5	C6
Chen and Fang (2014)	0.46	0.16	0.10	-0.55	0.88	0.81
Optimized Chen and Fang (2014)	1.47	-0.02	0.21	-0.17	1.03	0.95
Bae et al. (2009)	0.021	0.82	0.5	0.3	n	-
Optimized Bae et al. (2009)	0.0016	1.01	0.61	0.45	0.56	-

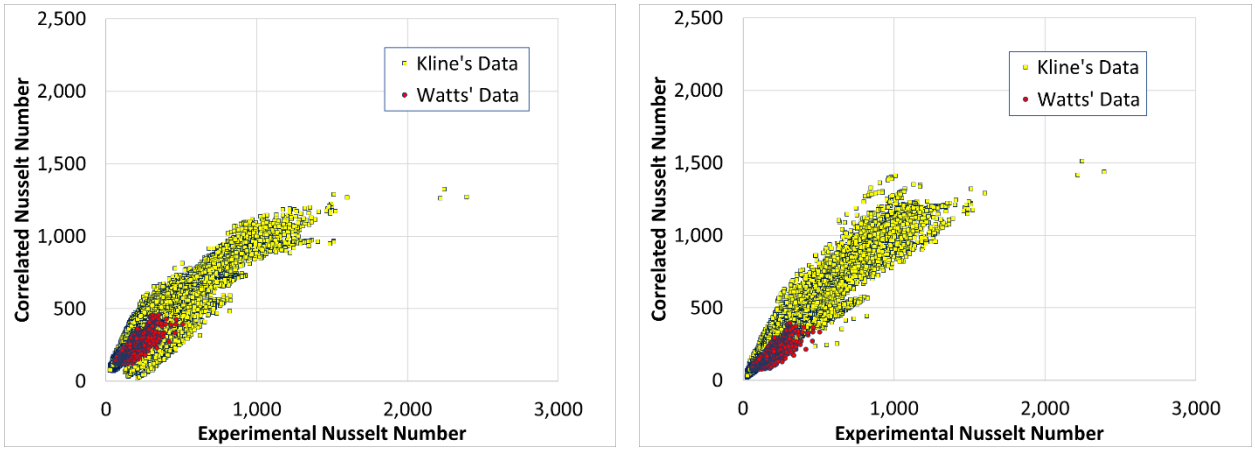

Figure 16. Comparison of the calculated Nu values Vs. the experimental one, using the correlation by Bae et al. (2009) to find the Nu values in the correlation mode with the use of original form (left) and the optimized coefficients (right).

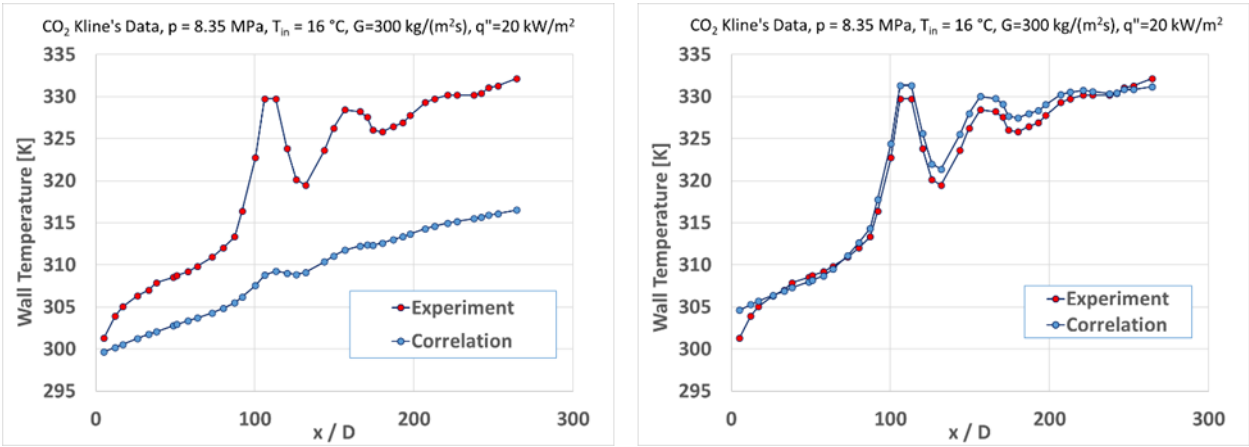

Figure 17. Wall temperature trends predicted using Bae et al. (2009) correlation in original form (left) and in optimized coefficients (right) for the case by Kline CO_2 data at p=8.35 MPa, Tin=16°C, G=300 kg/m^{2}s and q=20 KW/m^2.

Table 2. List of the selected heat transfer correlations.

Author	Range of Applicability	Remarks
Dittus Boelter (1930)	Subcritical pressures	
Bringer and Smith (1959	P: up to 34.5 [MPa]	H_2O, CO_2
Ornatsky et al. (1970)	P: 22.6/29.4 [MPa], G: 450–3000 [kg m^{-2} s^{-1}] d: 3 [mm]	H_2O
Yamagata et al., (1972)	P: 22.6/29.4 [MPa], G: 310–1830 [kg m^{-2} s^{-1}] q: 116–930 [kWm^{-2}], d: 7.5/10 [mm]	H_2O
Jackson and Fewster (1975)	Based on the experimental database	H_2O, CO_2
Watts-Chou et al., (1982)	P: 25 [MPa], G: 132–1060 [kg m^{-2} s^{-1}] q: 175–440 [kWm^{-2}], d: 25.4/32.2 [mm]	H_2O
Jackson (2002)	Based on the experimental database	CO_2
Kuang et al. (2008)	P: 22.75/31 [MPa], G: 380–2600 [kg m^{-2} s^{-1}] q: 233–3474 [kWm^{-2}], d: 7.5/26 [mm]	H_2O
Cheng et al. (2009)	P: 22.5/25 [MPa], G: < 3500 [kg m^{-2} s^{-1}] q: < 2000 [kWm^{-2}], d: 10.2 [mm]	H_2O
Yu et al. (2009)	Based on the experimental database	H_2O
Bruch et al. (2009)	P: 7.4/12 [MPa], G: 50 – 590 [kg m^{-2} s^{-1}] q: up to 150 [kWm^{-2}], d: 0.5 – 2.16 [mm]	CO_2, vertical channel
Bae et al. (2009)	P: 7.75, 8.12, 8.85 [MPa] G: 400, 500, 750, 1000, 1200 [kg m^{-2} s^{-1}] q: up to 150 [kWm^{-2}]	CO_2, vertical channel
Mokry et al. (2010)	P: 22.8/29.4 [MPa], G: 200–1500 [kg m^{-2} s^{-1}] q: 70–1250 [kWm^{-2}], d: 10 [mm]	H_2O
Gupta et al. (2012)	P: 7.4/8.8 [MPa], G: 900 – 3000 [kg m^{-2} s^{-1}] q: 15 – 615 [kWm^{-2}], d: 8 [mm]	CO_2, vertical channel
Wang et al. (2012)	Based on the experimental database	H_2O vertical tubes
Lee et al. (2013)	P: 8/10 [MPa], G: 1200–2000 [kg m^{-2} s^{-1}] d: 4.6 [mm]	CO_2, horizontal channel
Chen and Fang (2014)	Based on the experimental database	H_2O vertical tubes
Wang et al. (2014)	P: 24/24.5 [MPa], G: 500–1500 [kg m^{-2} s^{-1}] q: 240–883 [kWm^{-2}], d: 7.5/10 [mm]	H_2O vertical tubes
Zhao et al. (2014)	P: 23 - 26 [MPa], G: 450 -1500 [kg m^{-2} s^{-1}] q: 170 - 1400 [kWm^{-2}], d: 7.6 [mm]	H_2O vertical tubes, downward flow
Zhu et al. (2020)	Based on the experimental database	H_2O, CO_2, R134a
Li et al. (2020)	Based on the experimental database	H_2O vertical tubes

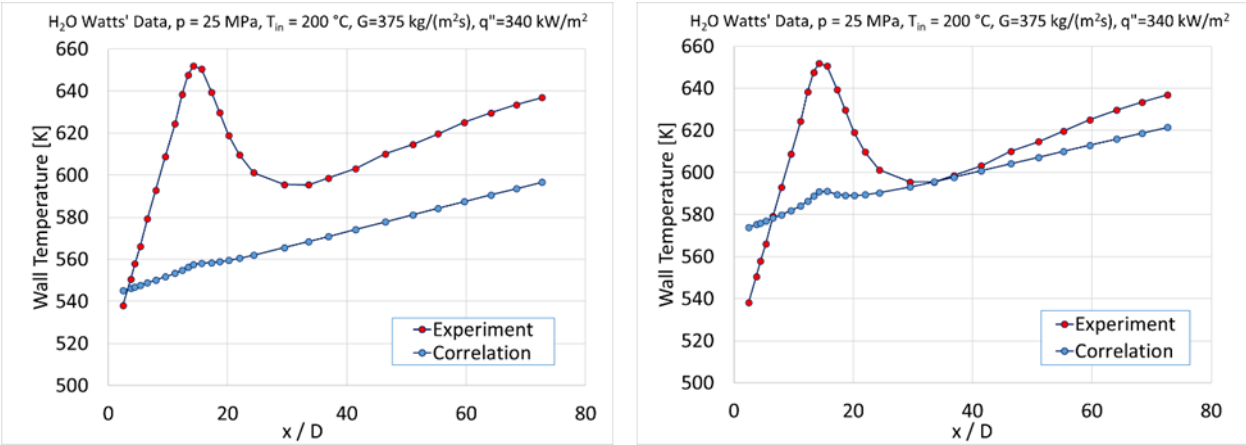

Figure 18. Wall temperature trends predicted using Bae et al. (2009) correlation in original form (left) and in optimized coefficients (right) for the case by Watts H2O data at p=25 MPa, Tin=200°C, G=375 kg/m^{2}s and q=340 KW/m^2.

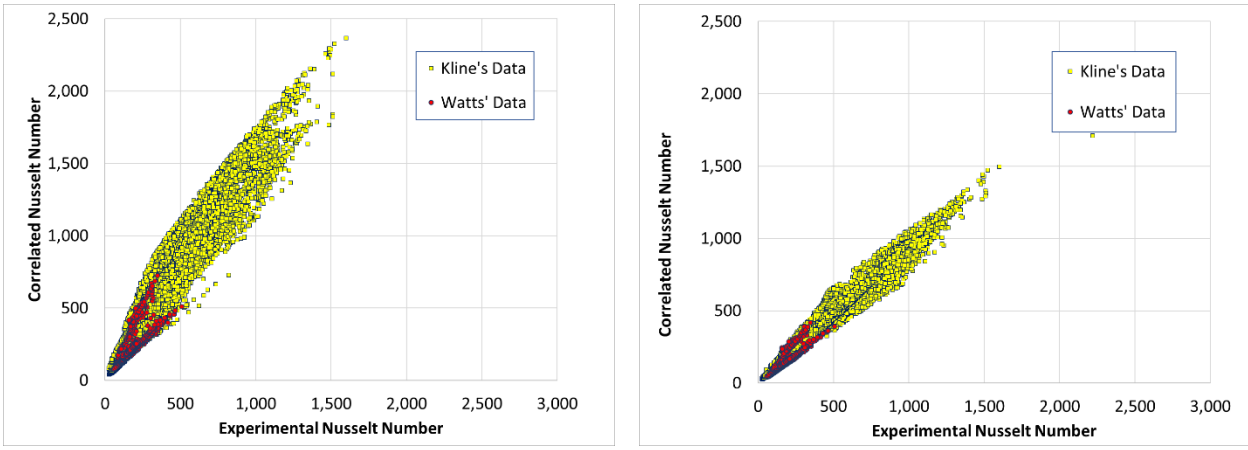

Figure 19. Comparison of the calculated Nu values Vs. the experimental one, using the correlation by Chen and Fang (2014) to find the Nu values in the correlation mode with the use of original form (left) and the optimized coefficients(right).

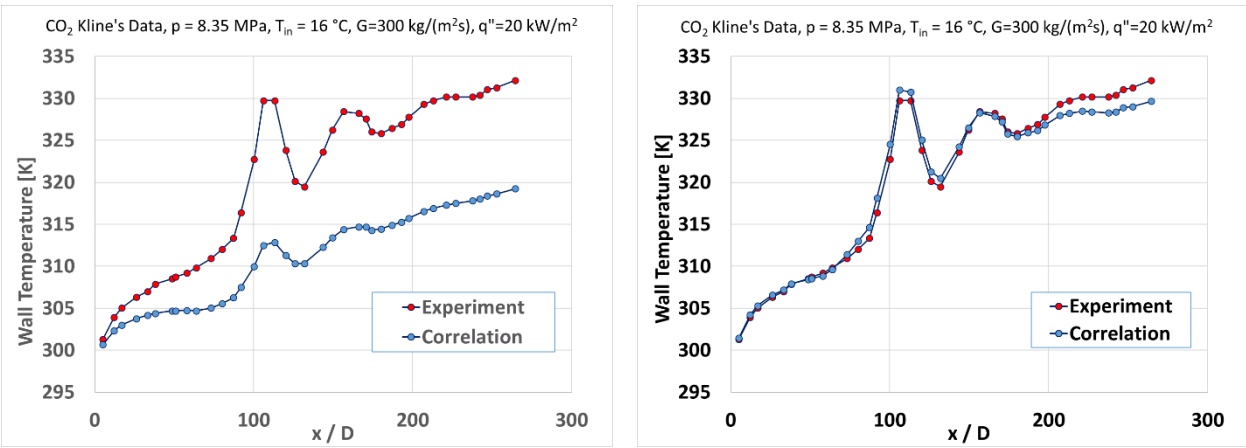

Figure 20. Wall temperature trends predicted using Chen and Fang (2014)correlation in original form (left) and in optimized coefficients (right) for the case by Kline CO_2 data at p=8.35 MPa, Tin=16°C, G=300 kg/m^{2}s and q=20 KW/m^2.

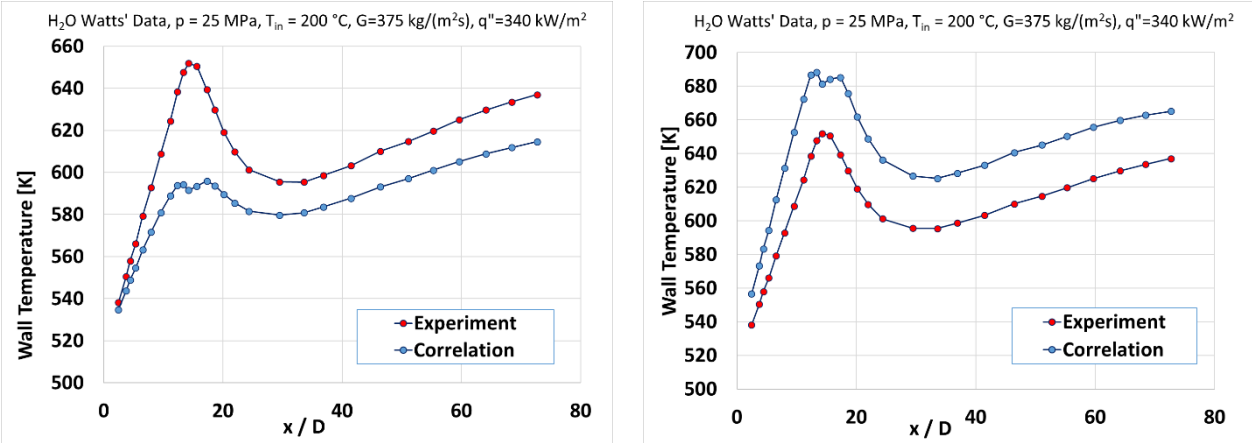

Figure 21. Wall temperature trends predicted using Chen and Fang (2014) correlation in original form (left) and in optimized coefficients (right) for the case by Watts H2O data at p=25 MPa, Tin=200°C, G=375 kg/m^{2}s and q=340 KW/m .^{2}

Table 3. Assessement for heat transfer correlations for supercritical carbon dioxide data by Kline.

Author	ME (%)	MAE (%)	RMSE (%)
Bae et al.	-26.12	26.12	27.52
Zhu B. et al. 2020	-13.74	21.63	23.28
Bringer and Smith 1977	-34.23	34.23	34.61
Bruch et al. 2009	19.41	19.77	26.43
Chen and Fang	-28.72	28.72	30.24
Cheng et al.	-15.61	16.18	19.26
Fewster and Jackson	-24.41	24.41	26.26
Gupta et al. 2012	-11.71	12.20	15.02
Jackson 2002	-23.62	23.62	25.48
Kuang et al. 2008	-18.00	18.00	18.66
Lee et al. 2014	-42.55	42.55	42.69
Li et al. 2020	-30.30	30.30	31.28
Mokry et al. 2010	-23.00	23.05	25.55
Ornatsky et al. 1970	-26.56	26.56	27.59
C.Wang et al. 2012	-25.12	25.13	27.46
Watts and Chou 1982	-15.87	15.91	18.31
Yamagata 1972	-28.74	28.74	30.18
Yu et al.2009	-38.75	38.75	38.97
Zhao et al. 2014	-11.9	15.64	17.72

As mentioned above, tailoring a correlation on the values of the experimental wall temperature usually gives good trends for the dynamic phenomenon such as heat transfer deterioration, though this success is biased and cannot be relied upon. On the other hand, iterating on the wall temperature poses difficulties while applying correlations containing dimensionless numbers depending on wall temperatures. This problem, unfortunately, is not well established in literature and it is only recently that some researchers have highlighted it.

The analysis in this report can be regarded as first steps in defining the problem and trying to find possible solutions to it. Applying what we previously called the **"prediction" mode** to the selected correlations resulted in the prediction of the wall temperature for two experimental data

cases by Kline and Watts shown in Figure 22 to Figure 27. Wall temperature trends obtained in the prediction mode by different heat transfer correlation are compared to the case of H_2O Watts' data at p = 25 MPa, T_{in} = 200 °C, G=375 kg/(m^{2}s) and q"=340 kW/m^2 respectively.

As it can be seen, the general trend of most of the correlations is very poor and is not representing the phenomena observed in the experiments. However, correlations by Kuang et al. (2008) and Bruch (2009) show some sort of jumps near the pseudocritical temperatures. These jumps are seen in CO_2 case when using the Kuang et al. correlation, see Figure 22, and in water case with Bruch et al correlation instead, see Figure 27. In order to understand why these jumps occur, one possible reason is that there exist multiple solutions for wall temperature at given bulk fluid conditions and heat flux values. To make sure this was the case, contour plots were made in order to check the difference between the actual value of the Nu number, calculated on the basis of the heat flux and a predefined range of wall temperatures, and the Nu number calculated on the basis of different correlations. A further discussion about this procedure can be found in later; however, it is sufficient here to say that the loci of the zero of the represented function in the contour plot are the loci of the wall temperature predicted by the correlation, showing possibly having multiple roots at some location.

Figure 23 -Figure 26 present thee contour maps for the case of of CO_2 Kline's Data at p = 8.35 MPa, Tin = 16 °C, G=300 kg/(m^{2}s) and q"=20 kW/m^2 using different correlations, more specifically as it is shown in Figure 25 there exists 3 solutions at about $\frac{x}{D} = 12 - 40$ and this can contribute to the jump observed in Figure 22 by Kuang et al correlation. Similar contour maps are plotted to investigate the jumps appeared in the case of H_2O Watts' data at p = 25 MPa, Tin = 200 °C, G=375 kg/(m^{2}s) and q"=340 kW/m^2 when applying the correlation by Bruch et al., see Figure 28, and by Zhu B. et al. (2020),see Figure 29. The jump in the case of Zhu B. et al. (2020) correlation (referred to Bingguo 2020 in the figure legend) is not corresponding to a multiple solution and may be due to iteration problems and convergence issues, needing further check.

The performance of selected correlations (see Table 3) is assessed against the Kline's data. In total, 20 correlations are applied, whose limitation in terms of range of flow conditions, applicable heat transfer mode, and type of fluid are not considered. Statistical error analysis is performed and shows that correlations by Gupta et al. (2012), Zhao et al. (2014) and Cheng et al. (2009) are among the leading ones.

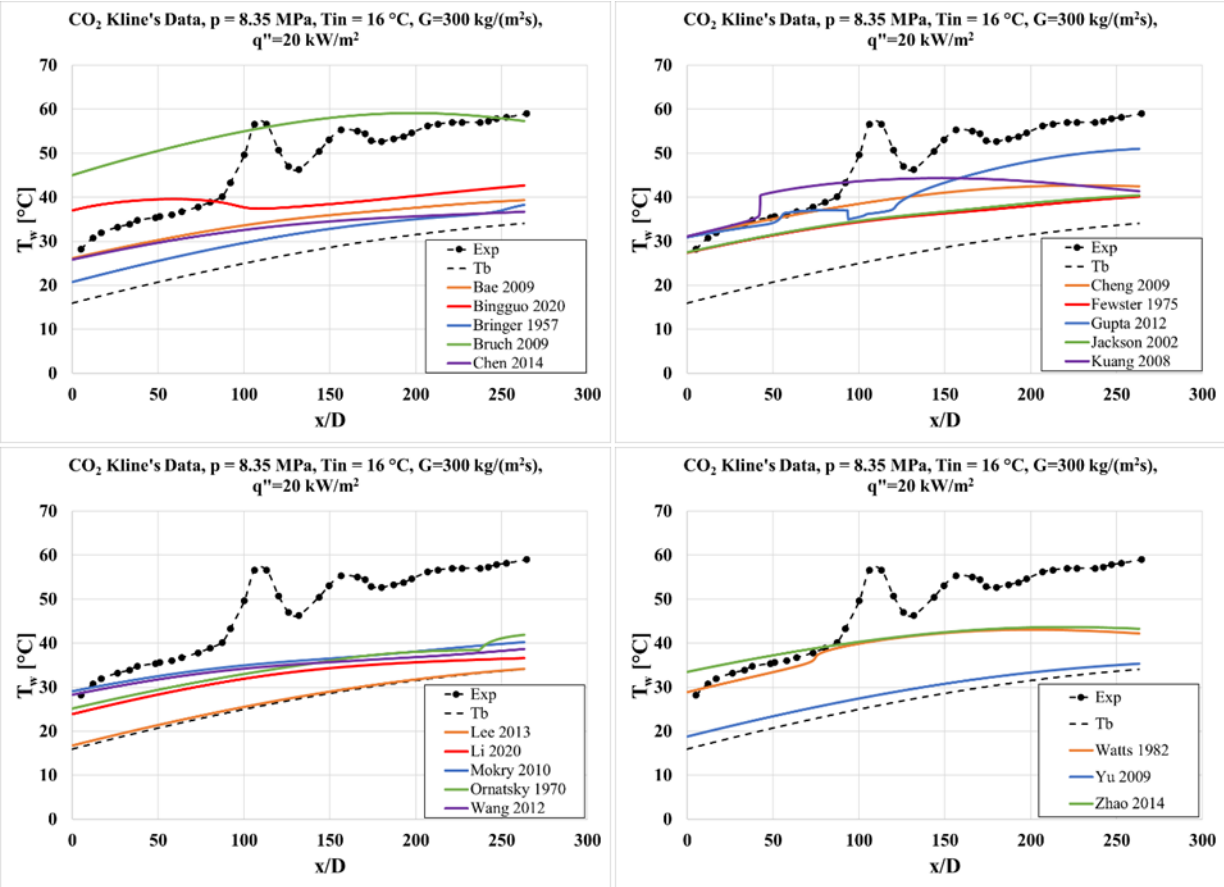

Figure 22.Wall temperature trends obtained in the prediction mode by different heat transfer correlation and compared to the case of CO_2 Kline's Data at p = 8.35 MPa, Tin = 16 °C, G=300 kg/(m^{2}s) and q"=20 kW/m^2.

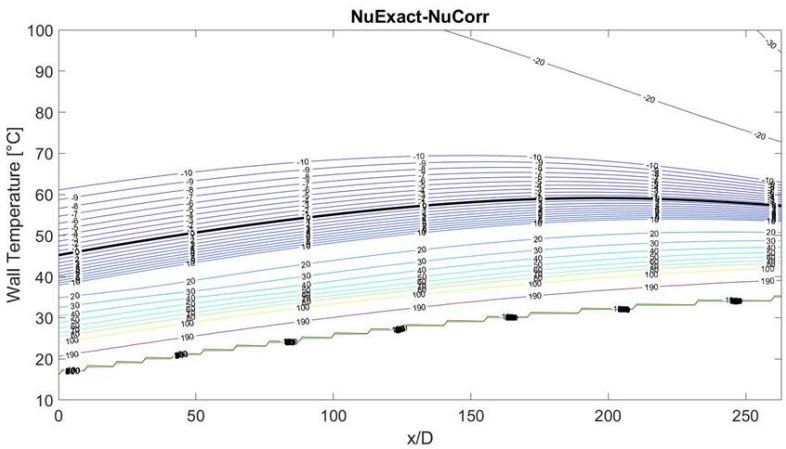

Figure 23 Wall temperature trends for CO_2 Kline's Data at p = 8.35 MPa, Tin = 16 °C, G=300 kg/(m^{2}s) and q"=20 kW/m^{2}obtained by applying Bruch et al. (2009) correlation.

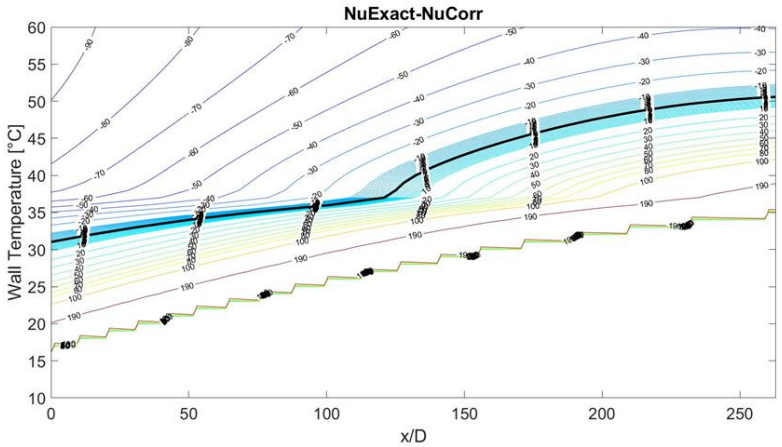

Figure 24. Wall temperature trends for CO_2 Kline's Data at p = 8.35 MPa, Tin = 16 °C, G=300 kg/(m^{2}s) and q"=20 kW/m^{2}obtained by applying Gupta et al (2010) correlation.

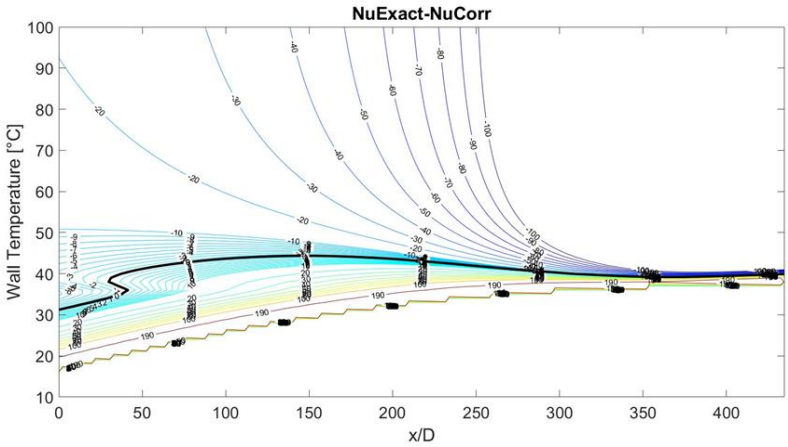

Figure 25. Wall temperature trends for CO_2 Kline's Data at p = 8.35 MPa, Tin = 16 °C, G=300 kg/(m^{2}s) and q"=20 kW/m^{2}obtained by applying Kuang et al. (2008) correlation.

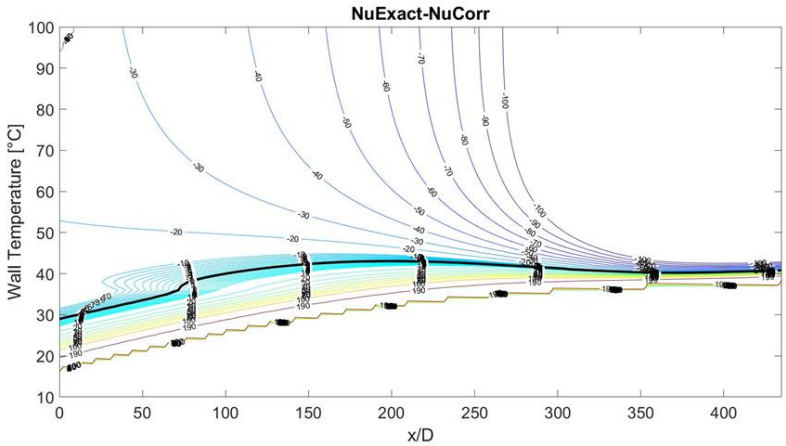

Figure 26. Wall temperature trends for CO_2 Kline's Data at p = 8.35 MPa, Tin = 16 °C, G=300 kg/(m^{2}s) and q"=20 kW/m^{2}obtained by applying Watts and Chou (1982) correlation.

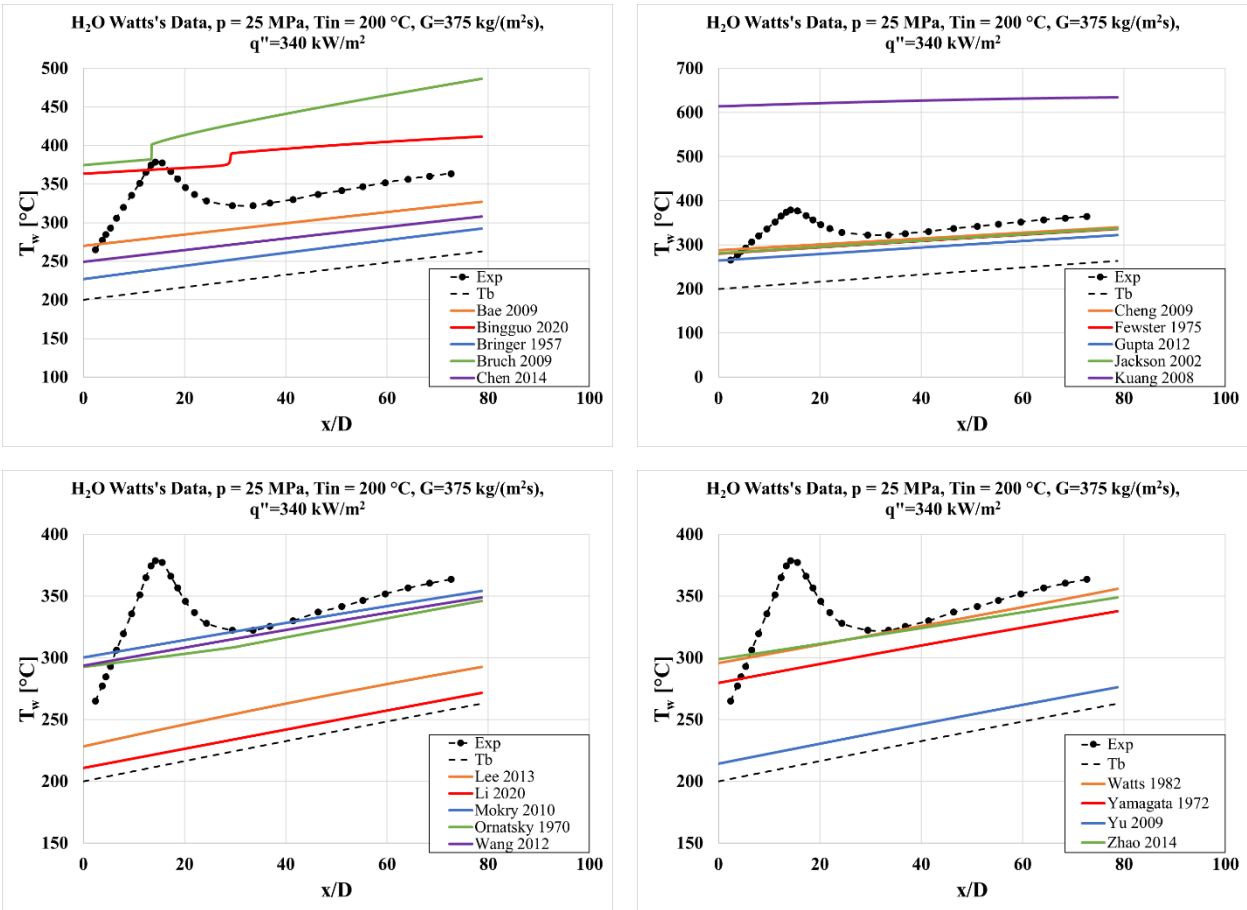

Figure 27. Wall temperature trends obtained in the prediction mode by different heat transfer correlations and compared to the case of H2O Watts' Data at p = 25 MPa, Tin = 200 °C, G=375 kg/(m^{2}s) and q"=340 kW/m^2.

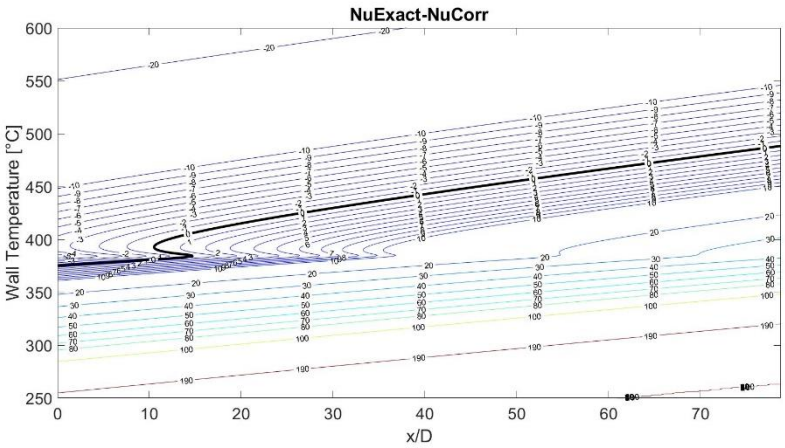

Figure 28. Wall temperature trends for H_2O Watts' Data at p = 25 MPa, Tin = 200 °C, G=375 kg/(m^{2}s) and q"=340 kW/m^{2}obtained by applying Bruch et al (2009) correlation.

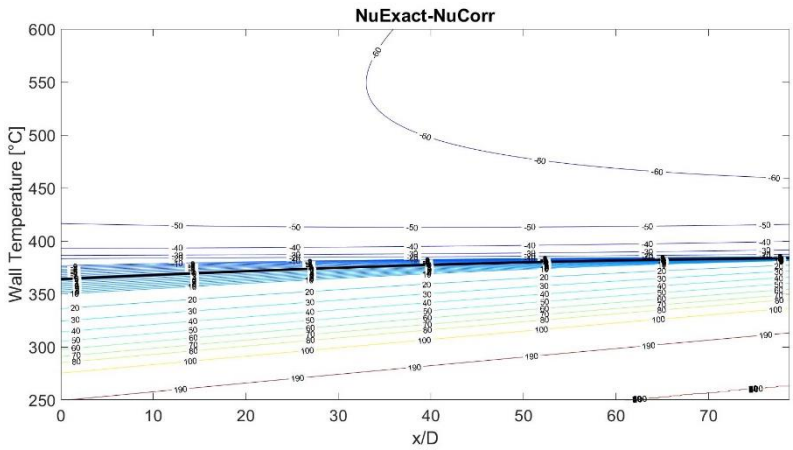

Figure 29. Wall temperature trends for H_2O Watts' Data at p = 25 MPa, T_{in} = 200 °C, G=375 kg/(m^2s) and q"=340 kW/m^2 obtained by applying Zhu B. et al. (2020) correlation.

In a nutshell, depending on the evaluation method, it remains to be seen whether these correlations provide a significant accuracy or not. Moreover, the more complex a correlation becomes, the more many stability problems may occur. In addition, the possible reason for the divergence in the results of both assessment methods, correlation and prediction, besides the aforementioned issues, might be found in the method used to derive nearly all investigated correlations, being a linear regression analysis of experimental data based on the least square method without considering the iterative solution of the exact Nu number.

As a result, applying the correlation mode leads to unpleasant results in terms of prediction accuracy and misinterpreted results in terms of the applicability to thermal-hydraulic system codes.

2.1.5.3 Analysis of generic correlation forms

Adopted methodology for the analysis

As mentioned in the previous Section, in the first analyses about correlations we firstly moved along the path of classical data regression techniques, in order to have a quick guess about the effectiveness of some dimensionless groups in correlating the considered experimental data. Though we are prepared to go further with a more complete non-linear regression technique for correlations in whatever generic form, at the moment we addressed the classical power-law formulations to be optimised after transformation to logarithmic form.

In similarity with what already described in the previous section, the type of correlation assumed is the following

$$Nu = C \prod_{k=2}^{N_p} p_k^{x_k} \tag{19}$$

where p_k are relevant dimensionless groups. Shifting to logarithmic form, we obtain:

$$\ln Nu = \ln C + \sum_{k=2}^{N_p} x_k \ln p_k \tag{20}$$

Or

$$\ln Nu = x_1 + \sum_{k=2}^{N_p} x_k \ln p_k \tag{21}$$

Considering N_{data} experimental values of the Nusselt number, we have:

$$x_1 + \sum_{k=2}^{N_p} x_k \ln p_{k,i} = \ln Nu_i \qquad \left(i = 1, \ldots, N_{data}\right) \tag{22}$$

being a linear system with more many equations than unknowns.
Defining:

$$a_{i,1} = 1,\ a_{i,k} = \ln p_{k,i}, \quad \left(k = 2, \ldots, N_p\right) \qquad b_i = \ln Nu_i \qquad \left(i = 1, \ldots, N_{data}\right) \tag{23}$$

the linear system having N_{data} equations in N_p unknowns is written as

$$\mathbf{Ax} = \mathbf{b} \tag{24}$$

and its least square solution is obtained by solving the $N_p \times N_p$ system

$$\mathbf{A}^T\mathbf{Ax} = \mathbf{A}^T\mathbf{b} \tag{25}$$

As said, in the case in which functional forms other than the power-law type will be considered, it will be necessary to shift towards a completely non-linear technique of optimisation based on the Newton-Raphson method, which is presently avoided for the additional complexity that it would introduce in this first guess approach. By the way, since most of the existing correlation are in power-law form this approach seems for the time being rather justified.

A simple programme in FORTRAN language has been developed for the purpose of optimising the coefficients of the power law formulation on the basis of the experimental data by Watts (1980) and Kline (2017). In total, the number of considered data points is 33314, representing the digitalisation of plots reported in the available references of 1580 axial trend of wall temperature, whose great majority belongs to the Kline's dataset. The program accomplishes with the following functions:

1. starting with the experimental values of the bulk and wall conditions, the above described N_p parameters $p_{k,i}$ are evaluated for each one of the N_{data} data series and the resulting $\mathbf{x}$ vector of the N_p coefficients are used to evaluate the correlated values of the Nusselt number, to be compared with the experimental values by evaluating the Root Mean Square of the deviations by the formulation:

$$RMS_{Nu} = \sqrt{\frac{1}{N_{data}} \sum_{i=1}^{N_{data}} \left[Nu_{exp,i} - Nu_{corr,i} \right]^2} \tag{26}$$

2. if requested by the user, the values of the wall temperature are updated on the basis of the obtained correlation and the process of coefficient optimisation can be restarted as in the above point 1, until a specified number of iterations or, usually, until convergence is reached, presently identified in terms of a tolerance in the relative error of the new value of the RMS_{Nu} with respect to the one at previous iteration; an under-relaxation procedure is applied in iterating on wall temperature.

The programme is therefore able to perform evaluations of the correlation coefficients in two different ways, according to the "correlation" and "prediction" modes envisaged in (Kassem et al., 2022). In fact:

- if the process of optimisation is stopped at the first iteration, the correlation coefficients in vector $\mathbf{x}$ are obtained using the values of wall temperature as provided by the database, i.e., obtained by experimental trends; this is what in Kassem et al. (2022a) and in the previous

section is called the "correlation mode", which does not assure that the correlation will actually predict the observed heat transfer efficiency while used in thermal-hydraulic codes;

- on the other hand, if the iterations are carried on up to convergence, the obtained correlation coefficients in vector $\mathbf{x}$ will be coherent with the predicted wall temperature values entering the dimensionless parameters and can be realistically used in codes to provide data in what in (Kassem et al., 2022) and the previous section is called the "prediction mode", possibly requiring iterations on T_w to be adopted.

The program finally prints out the following information:

- the values of $Nu_{exp,i}$ and $Nu_{corr,i}$ to be globally displayed in plots showing the global accuracy of the obtained correlation;
- detailed values of the bulk and wall fluid parameters along the channel for each series of data, in the purpose of showing the local trends of each series, thus suggesting the phenomenological correctness of the correlation; indeed, global $Nu_{corr,i}$ vs. $Nu_{exp,i}$ plots provide only an overall view of accuracy that can be quite misleading in suggesting the real correctness in the representation of physical phenomena;
- for a number (presently lower then 10) of data series, the values of the function

$$F_{Nu,i}\left(T_w\right)=\frac{q_i''}{T_w-T_{b,i}}\frac{D_i}{k_{b,i}}-\exp\left(x_1\right)\prod_{k=2}^{N_p}p_{k,i}^{x_k}\left(T_w\right) \tag{27}$$

dependent on a number of useful variables (e.g., x/D and T_w) are obtained, suitable to set up contour plots similar to the ones in the previous section; since this function is the one that must be zeroed in any iterative process trying to evaluate the wall temperature on the basis of the correlation represented by the second addendum at the RHS of (27), these contour plots are useful to highlight the presence of single, multiple or no solution in this process, as already shown above.

The latter feature is interesting not only to check the consistency of the wall temperature calculated during the iteration process but also for showing the presence of branches in the solutions of the equation that may result in instabilities in the process of convergence. Use of this feature will be largely made in the following to assess the conclusions obtained by the optimisation of engineering relationships in both the "correlation mode" and the "prediction mode", as defined in Kassem et al. (2022a).

Assessment of various correlation forms

In the following, some of the correlation forms proposed in literature will be discussed, considering their application to Watts' (1980) and Kline's (2017) data. The results obtained in both the "correlation mode" (stopped at the first iteration in the programme) and the "prediction mode" (with iterations performed up to convergence) are shown in the general comparison of $Nu_{corr,i}$ vs. $Nu_{exp,i}$ and also for selected series in the two considered databases. The use of the contour plot maps is also made to ascertain the presence of possible problems to be expected in convergence in "prediction mode".

Entrance effects

In order to assess entrance effects, an integral entrance effect multiplier formulation having the form

$$\frac{1}{x}\int_0^x f(x')\,dx' = 1 + C\left(\frac{D}{x}\right)^n \tag{28}$$

was assumed, resulting in the following form for the local heat transfer multiplier:

$$\begin{aligned} f(x) &= \frac{d}{dx}\left[x + Cx\left(\frac{D}{x}\right)^n\right] = 1 + C\left(\frac{D}{x}\right)^n - nC\,x\,D^n x^{-(n+1)} \\ &= 1 + C\left(\frac{D}{x}\right)^n - nC\left(\frac{D}{x}\right)^n = 1 + C(1-n)\left(\frac{D}{x}\right)^n \end{aligned} \tag{29}$$

So, assuming the values C = 1 and n=0.7 as suggested by McAdams (see the Todreas and Kazimi (1990) textbook, Chapter 10), we have:

$$f(x) = 1 + 0.3\left(\frac{D}{x}\right)^{0.7} \tag{30}$$

Needless to say, this represents a possibly controversial choice, taken in the absence of other possible evidence of different behaviour in front of other choices available in literature. It is anyway hoped that its effect is concentrated at the entrance of pipes, where an evidence of the need for such a multiplier is noted, not influencing too much the rest of the experimental trends.

Simple Re^x Pr^y correlation with density and viscosity ratio corrections

A first tried formulation has a classical form reported in literature in different variants, e.g., with or without the viscosity correction or also with a conductivity correction to be investigated later:

$$Nu = \left[1 + \frac{0.3}{(x/D)^{0.7}}\right]\exp(x_1)\,Re^{x_2}\,\overline{Pr}^{\,x_3}\left(\frac{\rho_w}{\rho_b}\right)^{x_4}\left(\frac{\mu_w}{\mu_b}\right)^{x_5} \quad ([3]) \tag{31}$$

The Prandtl number was introduced in the bulk-to-wall “averaged” version. The correlation has been firstly optimised in “correlation mode”, i.e., stopping the process of optimisation at the first iteration. The global result of the fitting is reported in Figure 30, where the data Kline and those by Watts are separately highlighted. As it can be noted, the fitting looks qualitatively reasonable and the RMS is equal to 87.36; the values of the obtained coefficients are as reported in Table 4.

.Table 4. Coefficient and exponents for the correlation in Eq. (31) in “correlation mode”

$\exp(x_1)$	x_2	x_3	x_4	x_5
0.001976	0.9986	0.6321	0.3276	0.1716

([3]) The dimensionless numbers without subscripts are assumed to be calculated with bulk properties.

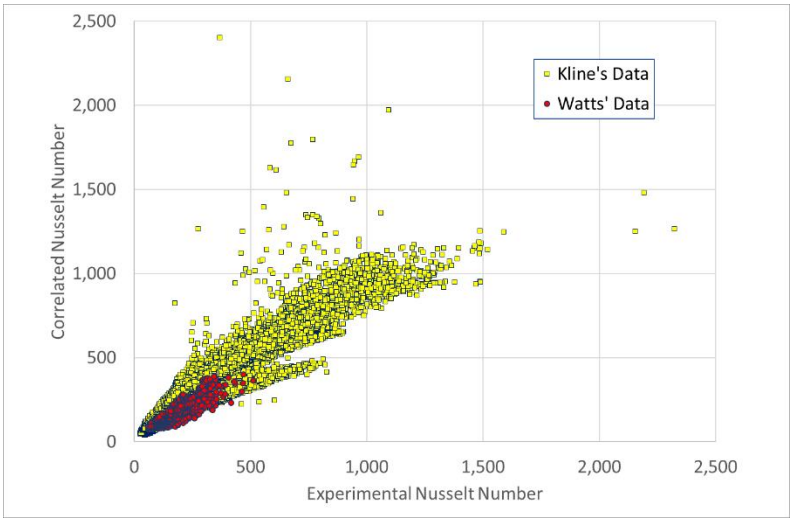

Figure 30. Global fitting of the simple Re^x Pr^y correlation with density and viscosity ratio corrections in "correlation mode"

In order to better consider the quality in the phenomenological prediction of the observed trends, the plots in Figure 31 to Figure 34 show the comparison of the experimental and the correlated trends of wall temperature (on the left in each figure) and the contours of $F_{Nu,i}(T_w)$ (on the right in each figure) for two sample cases in each one of the databases by Kline and by Watts. The cases are fully identified in each one of the XY plots and in the contour plots, so, their information is not repeated in the captions for the sake of brevity. The contour plots show the regions in the plane T_w vs. x/D in which the function takes positive and negative values, delimited by a yellow coloured line where $F_{Nu,i}(T_w) = 0$. This yellow line represents the locus of the actual value of the wall temperature in the "prediction mode", i.e., the values of wall temperature that would be really obtained by a computer code making use of the correlation with converged iterations. Similar figures will be presented in the following also for other correlations, allowing for a systematic presentation of data that, though limited to four of the total 1580 series, provides interesting information.

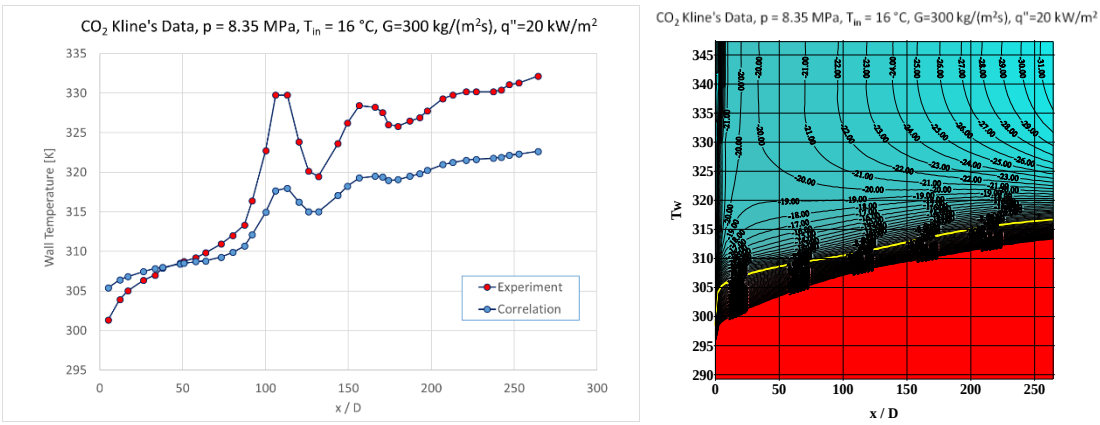

Figure 31. Wall temperature trend for the 1st sample case of the data by Kline in "correlation mode"

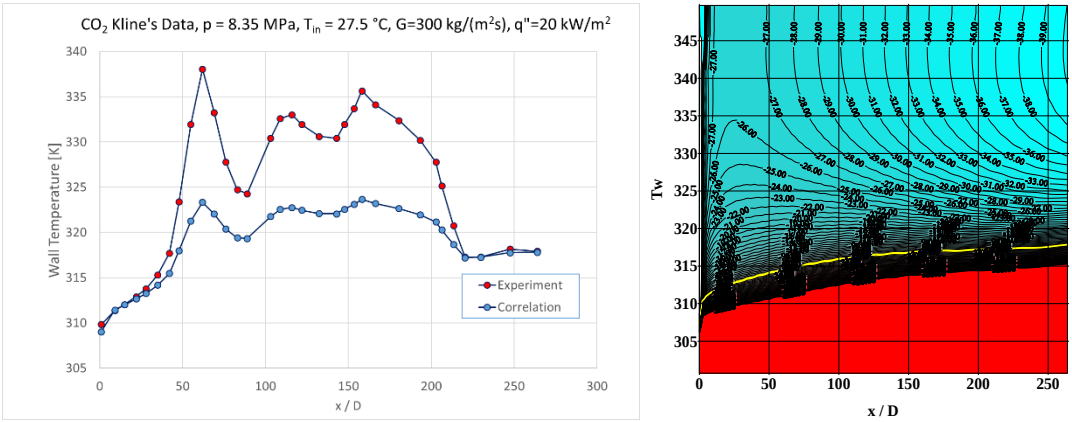

Figure 32. Wall temperature trend for the 2nd sample case of the data by Kline in "correlation mode"

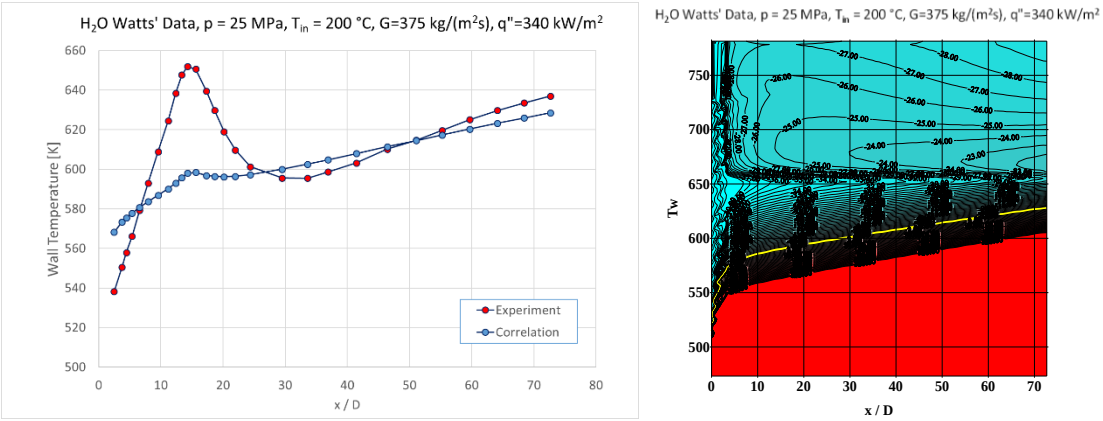

Figure 33. Wall temperature trend for the 1st sample case of the data by Watts in "correlation mode"

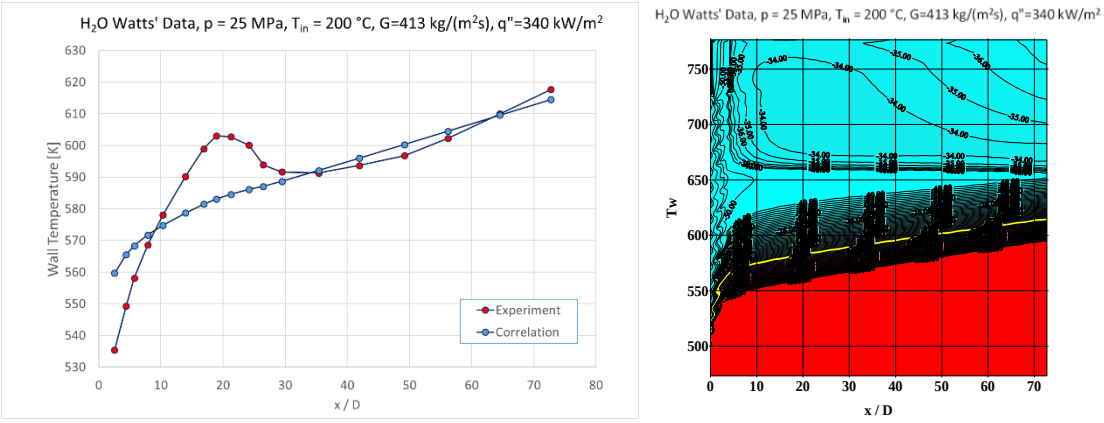

Figure 34. Wall temperature trend for the 2nd sample case of the data by Watts in "correlation mode"

The contour plots are obtained by processing with a graphical package a 101x101 matrix of values of $F_{Nu,i}(T_w)=0$ in terms of x/D and $T_w - T_b$, then represented in terms of x/D and T_w for the sake of better clarity in the comparison with the trends shown in the left part of each figure. Little distortions in the obtained contours appear.

As a comment to the obtained results, it can be noted that while the correlated values on the left side of the figure show a behaviour that is somehow mimicking the experimental trends, though being quite different from them, the yellow line is not exhibiting any such trend. This

represents the huge difference in the "correlation" and the "prediction" modes: though the coefficient and exponents in the correlation are optimised on the basis of the experimental data of wall temperature (in this cases entering the factor $\overline{Pr}^{x_3}\left(\frac{\rho_w}{\rho_b}\right)^{x_4}\left(\frac{\mu_w}{\mu_b}\right)^{x_5}$ and used for representing the "correlation" light blue markers appearing on the left of the figures), when used in the "prediction mode" (yellow line in the contour plots on the right) the correlation provides different values of the wall temperature. This difference is one of the main subjects discussed in Kassem et al. (2022a) as well as in the previous section and suggests that in showing the performance of a correlation attention must be paid not to make use of the values of the wall temperature as in the experimental data, computing T_w by the correlation itself.

In order to achieve trends of the "correlated" lines matching with each other in the left (light blue markers) and in the right part (yellow line in the contour plot), it is necessary to ask the FORTRAN programme to proceed to compete convergence on wall temperature by the iterations. The number of necessary iterations in this case on wall temperature was 20 and the reached coefficient and exponents are shown in Table 5.

Table 5. Coefficient and exponents for the correlation in Eq. (31) in both modes

Mode	$\exp(x_1)$	x_2	x_3	x_4	x_5	RMS
Correlation	0.001976	0.9986	0.6321	0.3276	0.1716	87.36
Prediction	0.004866	0.9124	0.4882	0.0540	0.1826	120.56

In the plots from Figure 35 to Figure 39 quantitative information on prediction mode results is reported.

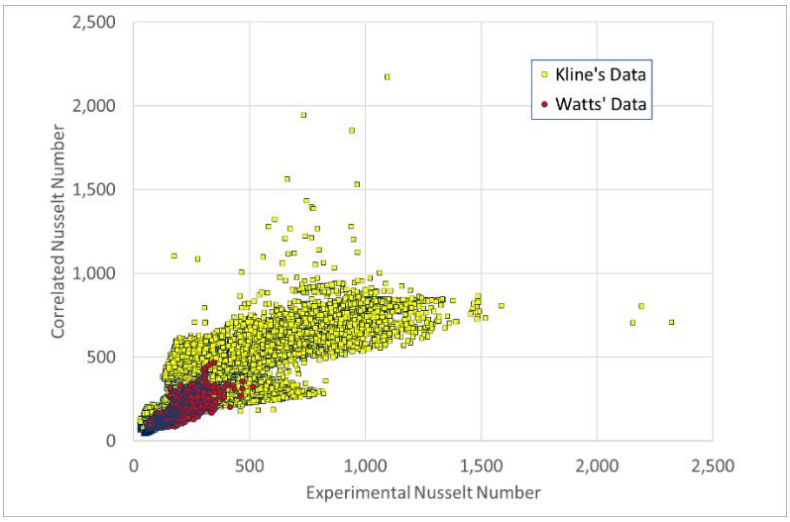

Figure 35. Global fitting of the simple Re^x Pr^y correlation with density and viscosity ratio corrections in "prediction mode" (i.e., up to convergence on wall temperature)

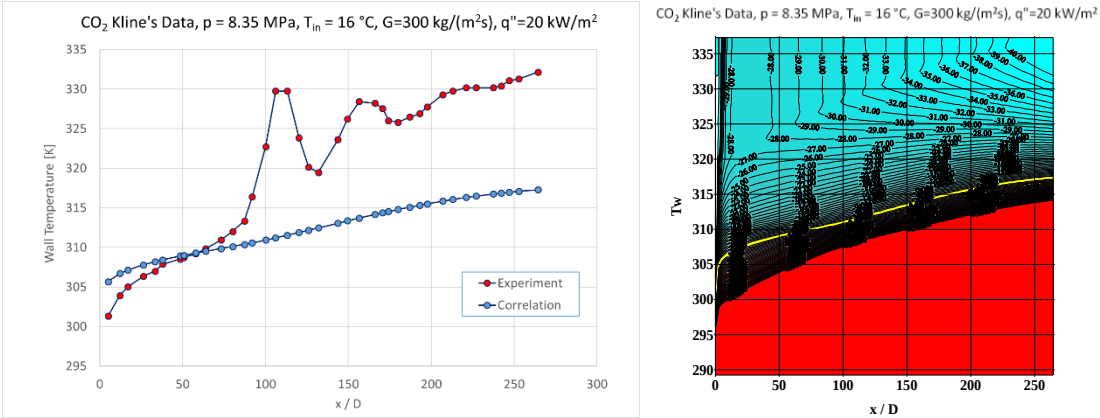

Figure 36. Wall temperature trend for the 1st sample case of the data by Kline in "prediction mode"

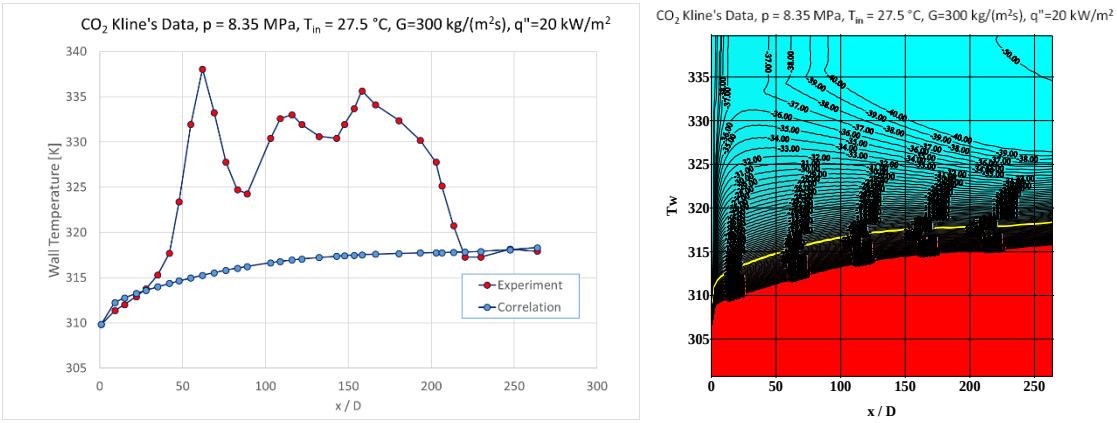

Figure 37. Wall temperature trend for the 2nd sample case of the data by Kline in "prediction mode"

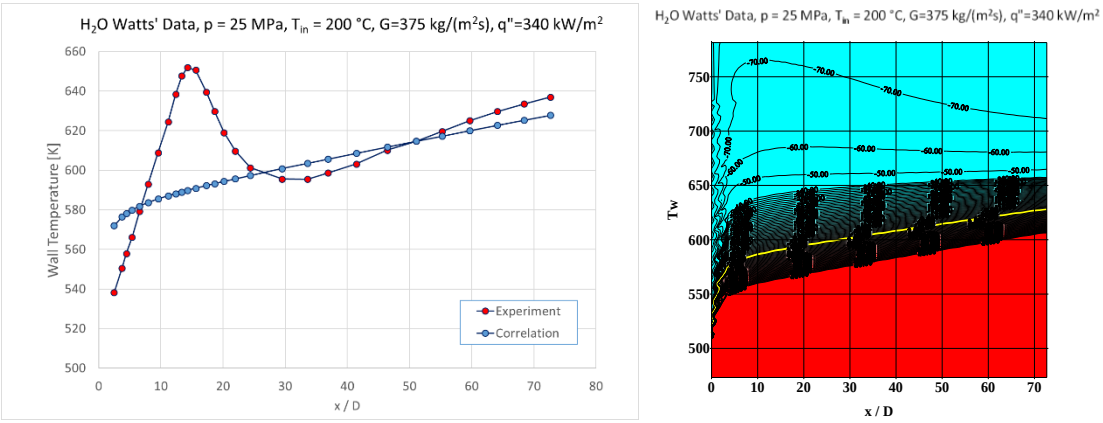

Figure 38. Wall temperature trend for the 1st sample case of the data by Watts in "prediction mode"

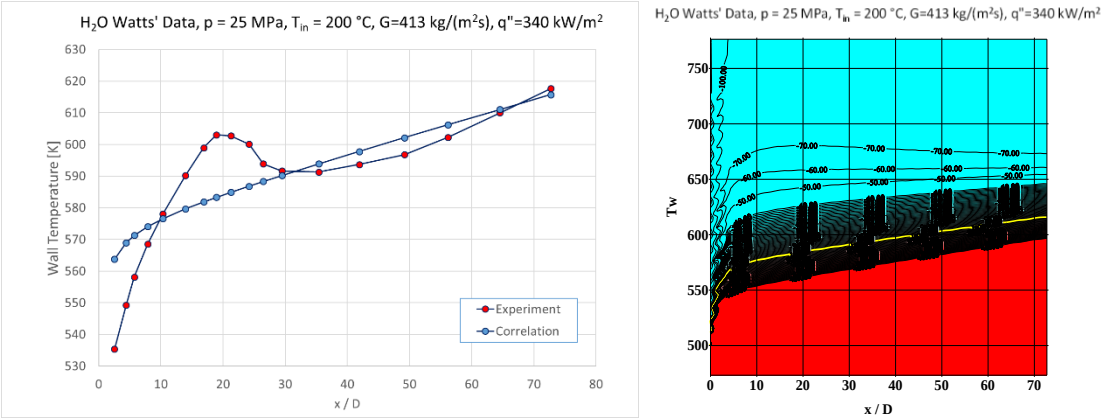

Figure 39. Wall temperature trend for the 2nd sample case of the data by Watts in "prediction mode"

The following considerations apply:

- the global accuracy in correlation is now strongly decreased, as shown in Figure 35, coherently with the fact that the RMS after the 20th iteration has now increased from 87.36 to 120.56; this is clearly due to the fact that in the dimensionless groups involving wall temperature the values obtained by the correlation itself have substituted the experimental ones: this is indeed the very difference between the "correlation" and the "prediction" mode;
- agreement is observed in the values of wall temperature presented in the left XY plots (the light blue markers) and in the contour plots at the right (the yellow line): now, in the limits of the accuracy achieved by the iteration process, the two curves appear identical;
- considering the coefficient and exponents presented in Table 5 it can be noted that the exponents of the Prandtl number and of the density ratio both decrease in the prediction mode; for the density ratio, the exponent is becoming low enough to make the related correction relatively irrelevant; the exponent of the Reynolds number keeps above 0.9 in both cases, suggesting an increase embedded in the addressed data with respect to the Dittus-Boelter correlation
- the oscillatory behaviour observed in the experimental trends has no counterpart in the predicted wall temperature: this seems to confirm the scepticism expressed in previous sections about the capability of simple correlations in representing such dynamic trends, mainly due to the progressive adjustment of the radial velocity and density profiles across the duct.

Simple Re^x Pr^y correlation with density, viscosity and conductivity ratio corrections

Proceeding to introduce further parameters in the correlation, the ratio of thermal conductivity at the wall and in bulk is added as a factor:

$$Nu = \left[1 + \frac{0.3}{(x/D)^{0.7}}\right] \exp(x_1)\, Re^{x_2}\, \overline{Pr}^{x_3} \left(\frac{\rho_w}{\rho_b}\right)^{x_4} \left(\frac{\mu_w}{\mu_b}\right)^{x_5} \left(\frac{k_w}{k_b}\right)^{x_6} \tag{32}$$

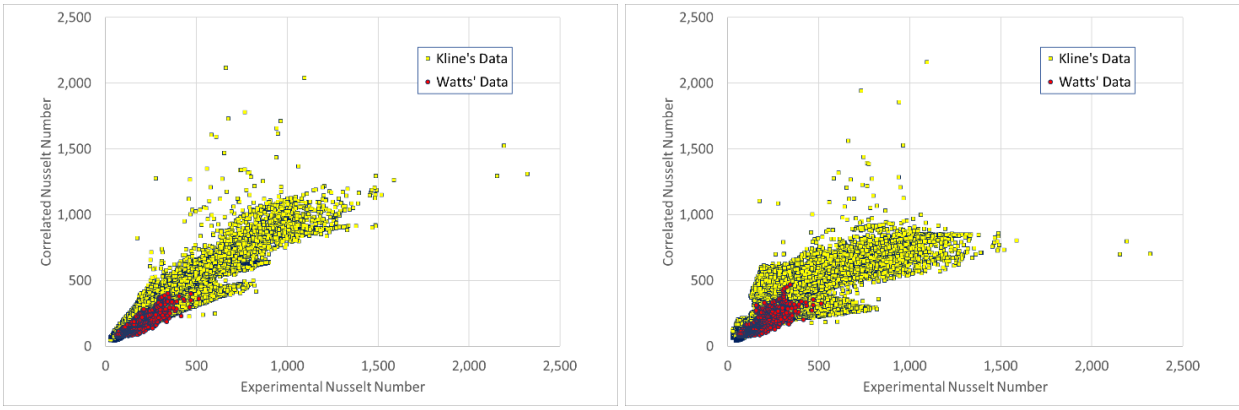

Figure 40. Global fitting of the simple Re^x Pr^y correlation with density, viscosity and heat conduction ratio corrections in "correlation" (left) and "prediction" (right) modes

Table 6. Coefficient and exponents for the correlation in Eq. (32) in both modes

Mode	$\exp(x_1)$	x_2	x_3	x_4	x_5	x_6	RMS
Correlation	0.00190	1.0021	0.6370	0.4078	0.1931	-0.1295	88.07
Prediction	0.00489	0.9120	0.4868	0.0430	0.1791	0.0179	120.43

Figure 40 and Table 6 report the global performance of the correlation and the fitting parameters in both the correlation and the prediction modes. Figure 41 to Figure 44 compare the results obtained in the two modes for the selected test cases. As in the case of the correction with the density and viscosity ratios only, the new formulation confirms a poor behaviour in predicting the deteriorated trends of heat transfer in the prediction mode. It can be noted that not only the oscillatory behaviour but also the different levels of heat transfer occurring owing to deterioration are practically ignored and that the slightly better performance obtained in the correlation mode is due mostly to the adoption of wall temperature values in the application of the correlation. Indeed, both forms of the correlation do not appear attractive for predicting deteriorated heat transfer conditions.

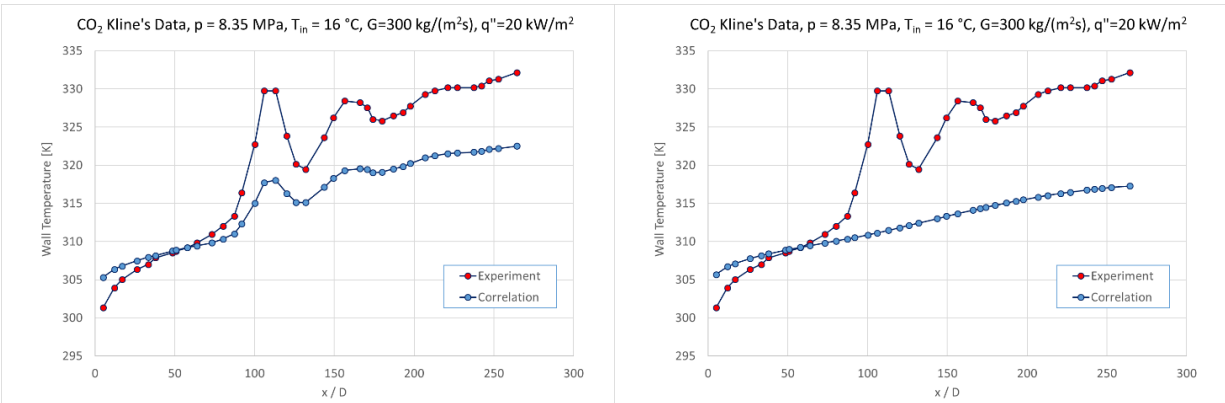

Figure 41. Wall temperature trend for the 1st sample case of the data by Kline in "correlation" (left) and "prediction" (right) modes

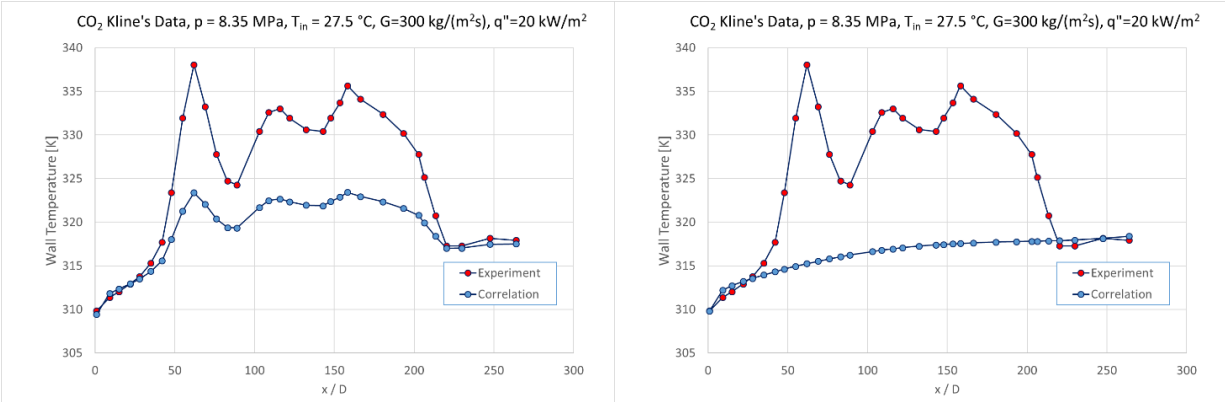

Figure 42. Wall temperature trend for the 2nd sample case of the data by Kline in "correlation" (left) and "prediction" (right) modes

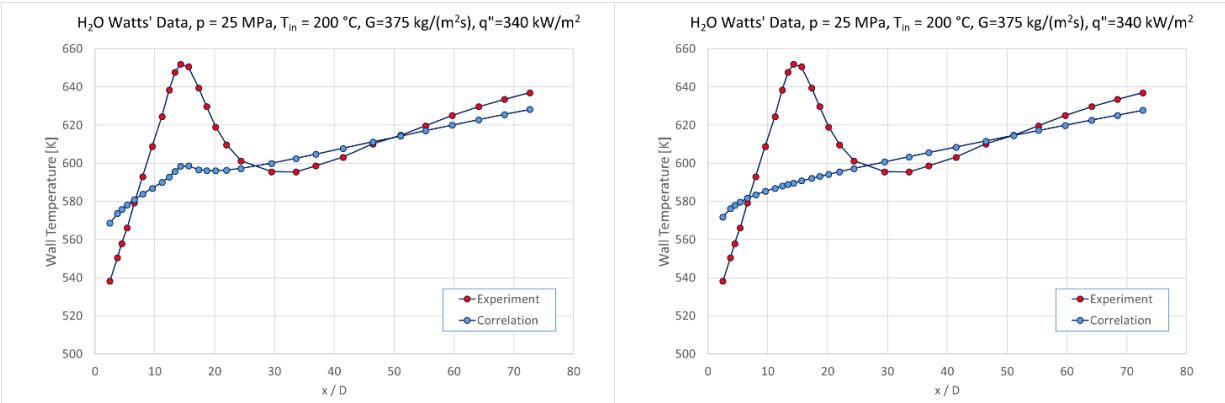

Figure 43. Wall temperature trend for the 1st sample case of the data by Watts in "correlation" (left) and "prediction" (right) modes

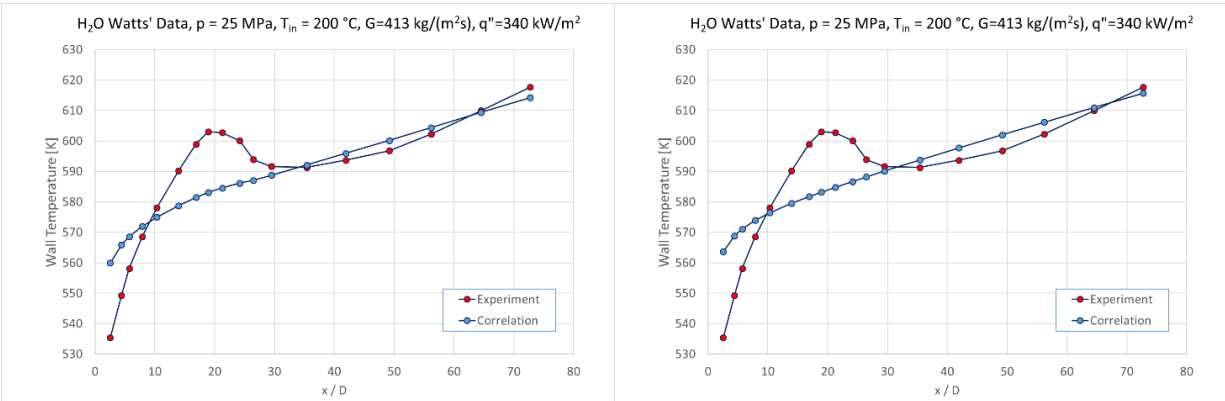

Figure 44. Wall temperature trend for the 2nd sample case of the data by Watts in "correlation" (left) and "prediction" (right) modes

It must be observed that in these applications, the effect of inlet temperature (Kline's cases) and flow rates (Watts' cases) are almost not affecting the converged trends of the correlation, something rather deluding in view of the application of correlations in codes. It is apparent that no more than a generic estimate of the heat transfer, mostly due to the Dittus-Boelter-like form of the correlation, can be achieved.

Trying over-fitting with additional dimensionless parameters

In view of the previous results, it was then tried to over-fit (meaning to fit with a too large number of parameters to pretend a real physical basis of the correlation), also trying to highlight the

possible dependence from new parameters suggested by the similarity theory. Actually, this trial has not the pretence to be a physically based one, having the main purpose to highlight possible dependencies in both the “correlation” and the “prediction” modes.

$$Nu = \left[1 + \frac{0.3}{\left(x/D\right)^{0.7}}\right] Nu_{DB} \exp\left(x_1\right) Re^{x_2} \overline{Pr}^{x_3} Fr^{x_4} \left(1 + Ri\right)^{x_5} Ri^{x_6} N_{TPC,loc}^{x_7} \rho_w^{*x_8} \rho_b^{*x_9} \left(\frac{\mu_w}{\mu}\right)^{x_{10}} \left(\frac{k_w}{k}\right)^{x_{11}} \quad (33)$$

In this formulation, the Dittus-Boelter correlation is introduced in the form:

$$Nu_{DB} = 0.023 Re^{0.8} \overline{Pr}^{0.4} \quad (34)$$

noting explicitly that the Prandtl number has been introduced in its averaged form given by

$$\overline{Pr} = \frac{h_w - h_b}{T_w - T_b} \frac{\mu_b}{k_b} \quad (35)$$

The introduction of the Richardson number has been made in two different forms trying to provide a greater degree of freedom in correlating buoyancy effects. The Froude number is also introduced, while in lieu of the density ratio it was preferred to introduce separately the wall and dimensionless densities. $N_{TPC,loc}$ is also introduced owing to the potential importance of this dimensionless parameters on the onset of deterioration as a dimensionless q''/G ratio. As said, it is not expected that the correlation has a real meaning from the physical point of view, but consideration of the effects of both the great number of adjustable exponents and of the variety in the choice of dimensionless parameter is the target of the present attempt.

reports the coefficient and exponents and the values of RMS for Eq. (33) in both correlation and prediction modes. The difference in the values of the RMS obtained in the two cases anticipates what can be confirmed by looking at the plots in Figure 45 to Figure 53. In particular, while in correlation mode the obtained fit is tight, in prediction mode a considerable spread in the data can be observed (Figure 45). The results in correlation mode in Figure 46 to Figure 49 can be observed to match also qualitatively with the trends of wall temperature, though the related contour plots do not confirm their trends.

Table 7. Coefficient and exponents for the correlation in Eq. (33) in both modes

Mode	$\exp\left(x_1\right)$	x_2	x_3	x_4	x_5	x_6
Correlation	3.7755	0.2017	0.7996	-0.4739	-0.3691	-0.4854
Prediction	0.0781	0.1717	0.1511	-0.1128	-0.5920	-0.1294
Mode	x_7	x_8	x_9	x_{10}	x_{11}	RMS
Correlation	0.6723	0.5050	-0.6254	0.3221	-0.4207	69.53
Prediction	-0.0175	0.1266	-0.1555	-0.0238	1.39×10^{-4}	125.37

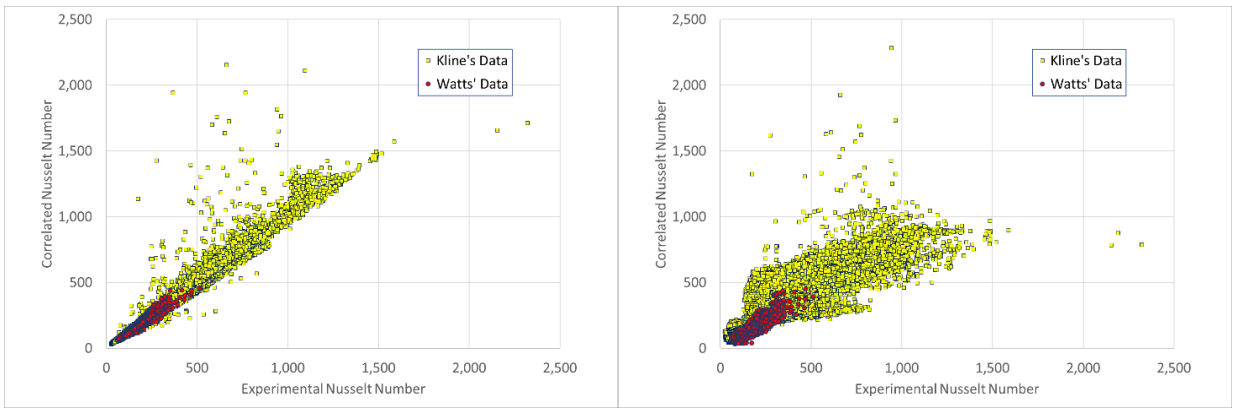

Figure 45. Global fitting of Eq. (33) in “correlation” (left) and “prediction” (right) modes

Moreover, the trends of the yellow line in the contour plots suggesting the real loci of the wall temperature show even the presence of branches suggesting the possibility to find multiple or no solutions. This is of course a problem for the iterative convergence on wall temperature when the correlation is included into a system code. So, it can be concluded that the very good match observed in the plots at the right in Figure 46 to Figure 49 is only an artefact of the use of the experimental values of T_w in the dimensionless groups containing it.

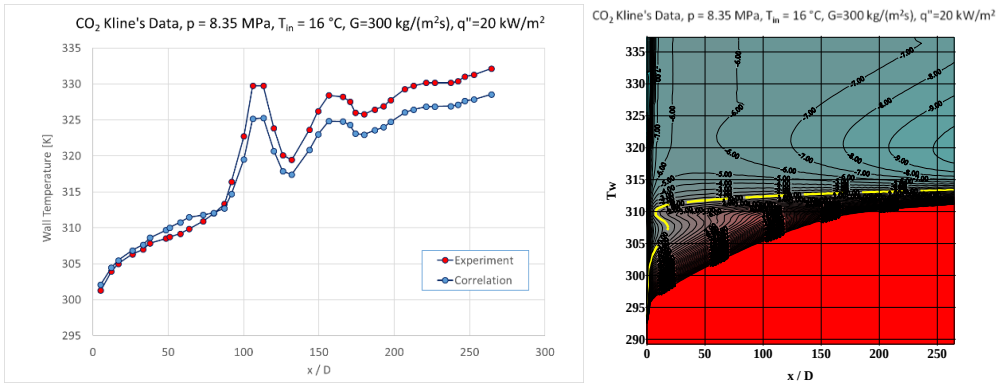

Figure 46. Wall temperature trend for the 1st sample case of the data by Kline in “correlation” mode

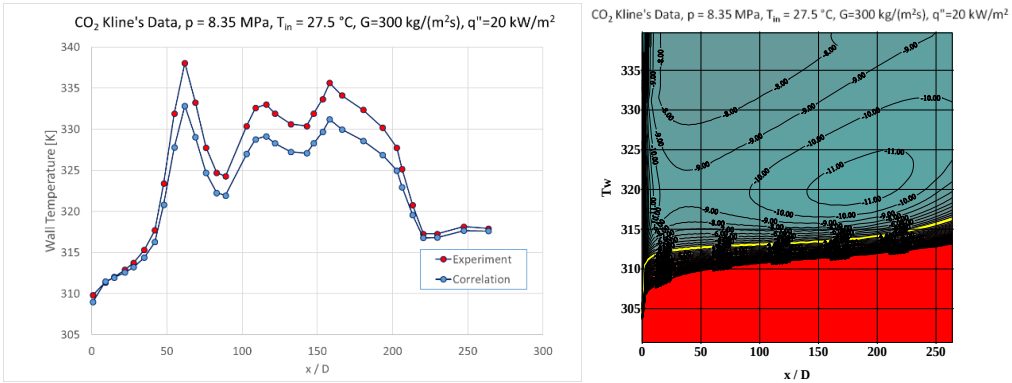

Figure 47. Wall temperature trend for the 2nd sample case of the data by Kline in “correlation” mode

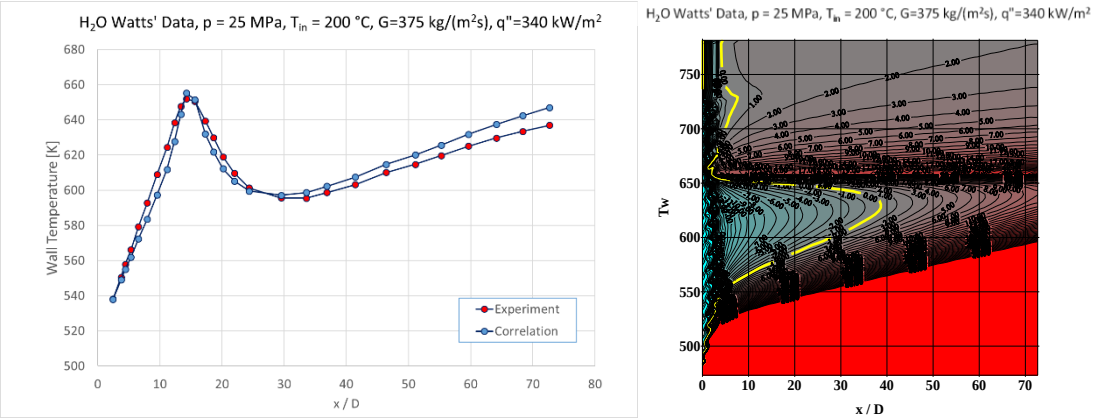

Figure 48. Wall temperature trend for the 1st sample case of the data by Watts in "correlation" mode

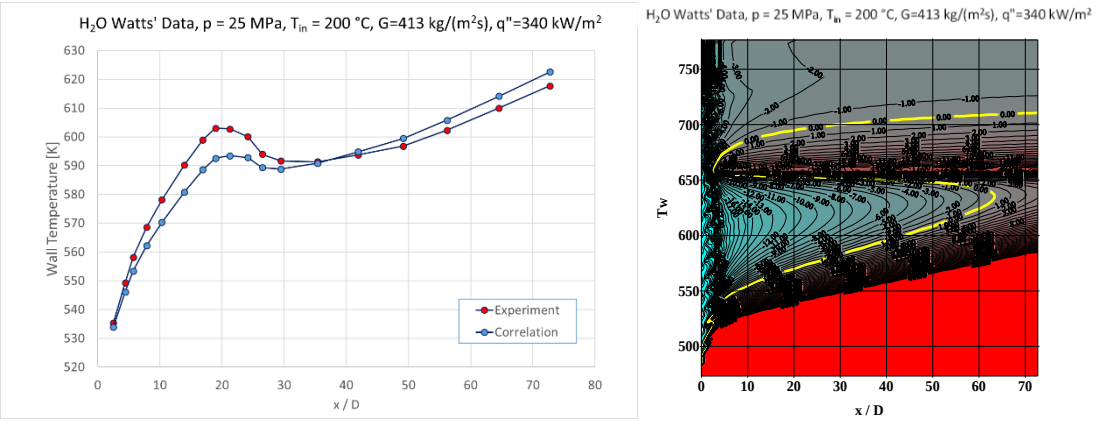

Figure 49. Wall temperature trend for the 2nd sample case of the data by Watts in "correlation" mode

Viceversa, Figure 50 to Figure 53 are better coherent in their right and left parts, showing that the correlation obtained by converging on the values of wall temperature is in disagreement with the observed wall temperature trends. This must be attributed to the completely different weight given to some of dimensionless groups by the values of their exponents.

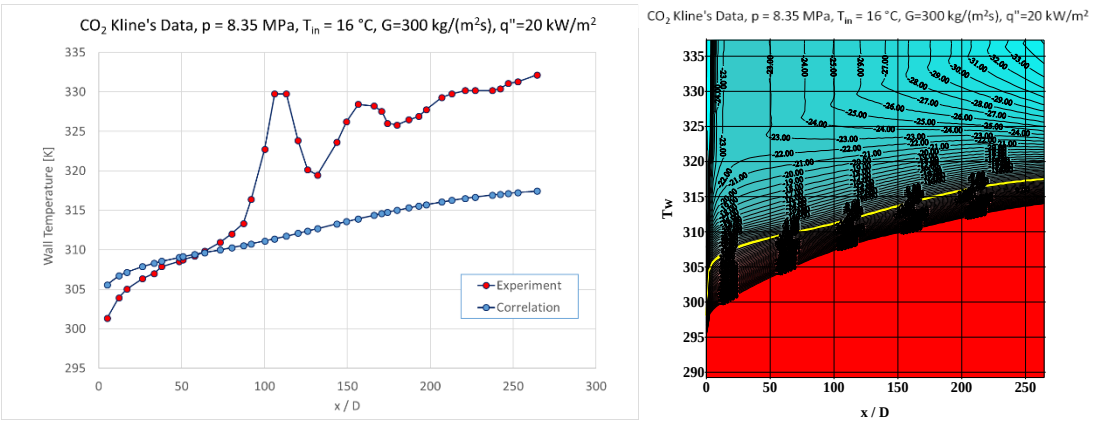

Figure 50. Wall temperature trend for the 1st sample case of the data by Kline in "prediction" mode

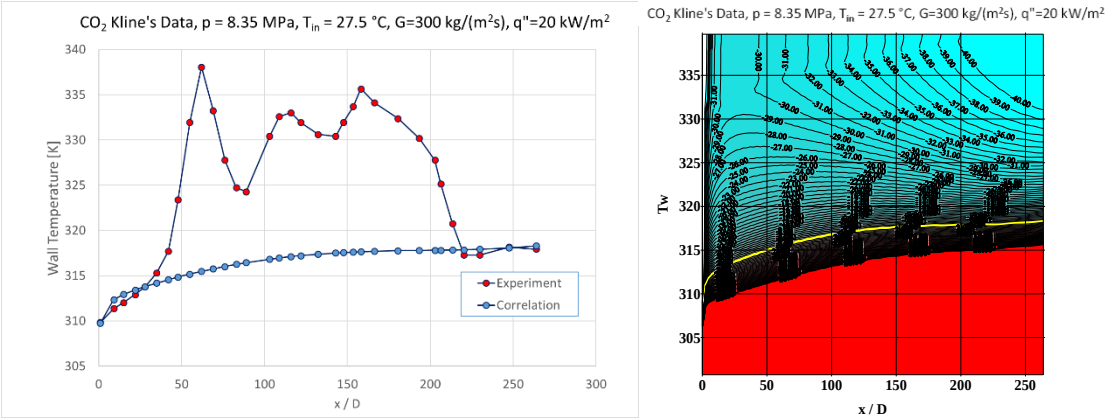

Figure 51. Wall temperature trend for the 2nd sample case of the data by Kline in "prediction" mode

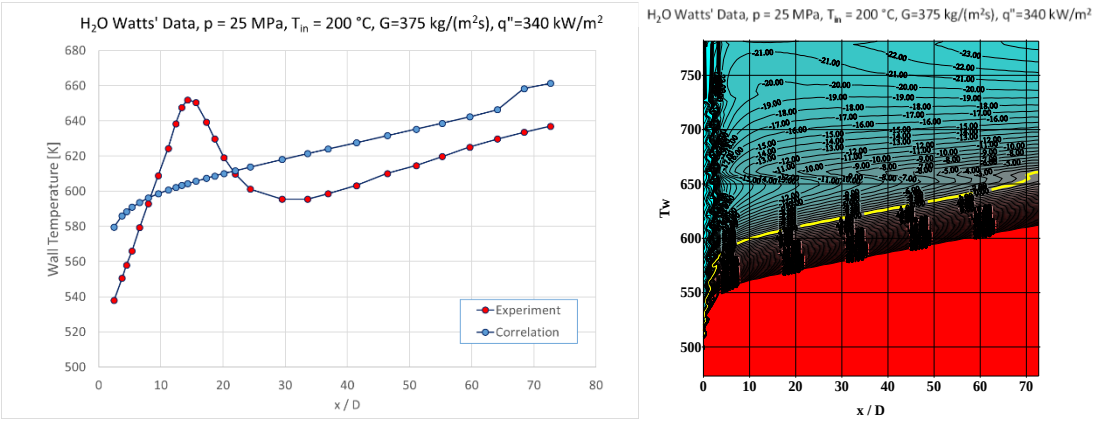

Figure 52. Wall temperature trend for the 1st sample case of the data by Watts in "prediction" mode

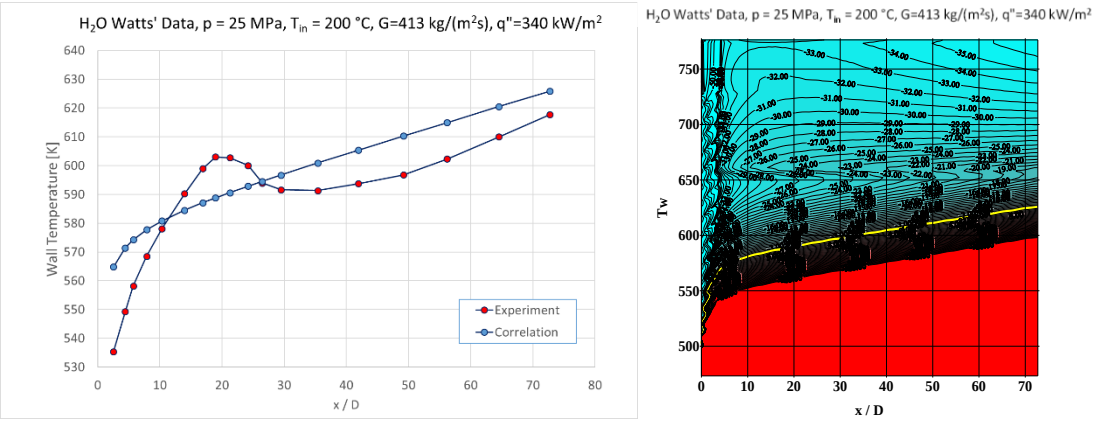

Figure 53. Wall temperature trend for the 2nd sample case of the data by Watts in "prediction" mode

In summary, even such a complex correlation with many dimensionless groups combined in a power law format seems to provide poor results in representing deterioration phenomena. It is remarkable to note the tendency for this correlation, as well as for the two previous ones, to represent the wall temperature trends mostly by smooth trends that do not reproduce the deteriorated behaviour observed in the experiments. Though allowance was given for the inclusion of additional factors in the correlation, their role appears weak and the trend is dominated by a factor in the order of $Re\ \overline{Pr}^{0.6} \big/ (1+Ri)^{0.6}$. In the present case, the presence of

the Richardson number does not introduce any of the expected effects due to buoyancy, showing that the pretended formalism is basically wrong in representing the target effect owing to deterioration.

As a lesson learned from this quick inquiry in the correlation forms, it seems that the simple adopted power law formulations in terms of some of the relevant dimensionless numbers is not sufficient to represent the addressed phenomena suggesting to change dimensionless groups and/or formalism.

Other considerer correlation forms

Though about 30 correlation forms have been tested in total during this work, only a few more are discussed hereafter, in order to highlight possible ideas to be further discussed with the Participants in the ECC-SMART project, aiming to possibly improve the state-of-the-art in the field.

- *Accounting for the expansion in bulk and at the wall*

The following correlation has been considered addressing only the "prediction" mode, i.e. carrying the iterations up to convergence:

$$Nu = \left[1 + \frac{0.3}{(x/D)^{0.7}}\right] Nu_{DB} \exp(x_1) Re^{x_2} \overline{Pr}^{x_3} \exp\left[x_4\left(\frac{\rho_w}{\rho_{in}}\right)\right] \exp\left[x_5\left(\frac{\rho_b}{\rho_{in}}\right)\right] \quad (36)$$

In this formulation, the Dittus-Boelter correlation is taken as a basis, accounting by exponential terms for the expansion of the fluid at the wall and in bulk from the inlet up to local position. Possible correction of the exponents for the Reynolds and the Prandtl numbers are also envisaged, explicitly accounted by the exponents x_2 and x_3. The plots in Figure 54 to Figure 56 and

Table *8* report the obtained results.

Figure 54. Global fitting of Eq. (36) in "prediction" mode

Table 8. Coefficient and exponents for the correlation in Eq. (36) in "prediction" mode

Mode	$\exp(x_1)$	x_2	x_3	x_4	x_5	RMS
Prediction	0.1939	0.1269	0.1061	0.4827	-0.5662	119.43

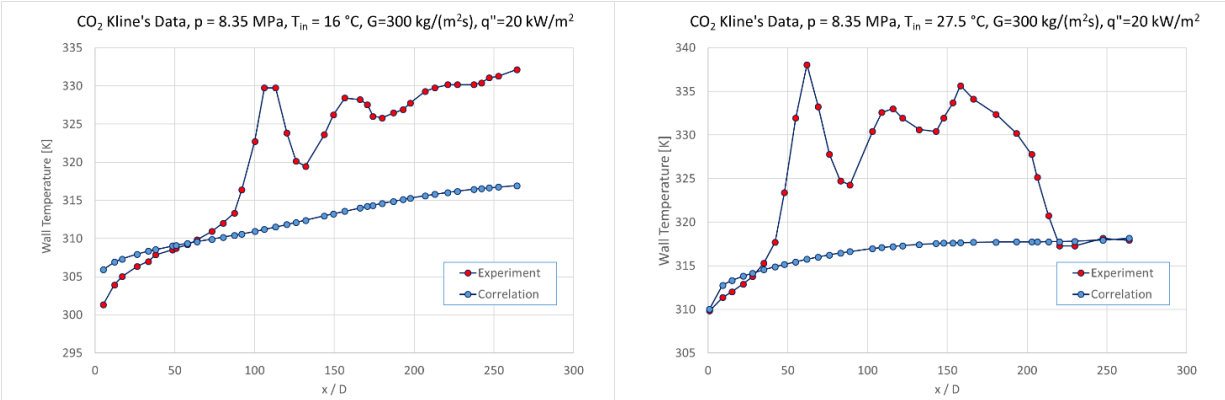

Figure 55. Wall temperature trend for the 1st and 2nd sample case of the data by Kline in "prediction" mode

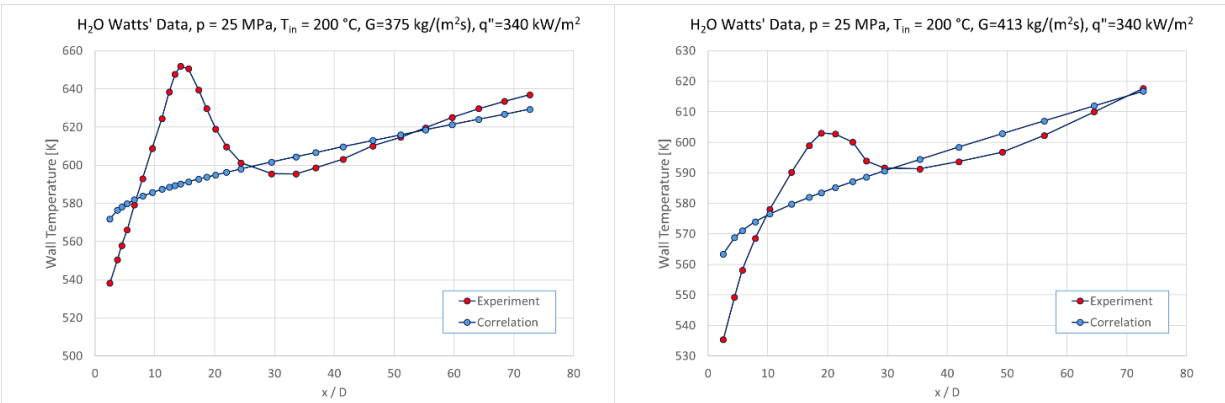

Figure 56. Wall temperature trend for the 1st and 2nd sample case of the data by Watts in "prediction" mode

As it can be noted, even this idea of linking the local prediction to the expansion of the fluid since the channel inlet is not providing any better result: the RMS keeps in the same range as in the previous cases of the "prediction" mode and the representation of local deterioration phenomena is quite poor.

- *Representing laminarisation by a decrease in the exponent of the Reynolds number*

A further tested idea is considering the effect of "laminarisation" as a decrease in the exponent of the Reynolds number, to be achieved in consideration of a relevant parameters indicating the effect of buoyancy, as the Richardson number. This was tried by a correlation having the form:

$$Nu = \left[1 + \frac{0.3}{(x/D)^{0.7}}\right] \exp(x_1)\, Re^{x_2}\, \overline{Pr}^{x_3}\, Re^{x_4 Ri} \tag{37}$$

which could be also expressed as

$$Nu = \left[1 + \frac{0.3}{(x/D)^{0.7}}\right] \exp(x_1)\, Re^{x_2 + x_4 Ri}\, \overline{Pr}^{x_3} \tag{38}$$

In a nutshell, provided the coefficient x_4 is negative, a high Richardson number would tend to decrease the exponent of the Reynolds number.

Figure 57. Global fitting of Eq. (37) in "prediction" mode

Mode	$\exp(x_1)$	x_2	x_3	x_4	RMS
Prediction	0.00447	0.9132	0.4278	-0.0316	122.37

Table 9. Coefficient and exponents for the correlation in Eq. (37) in "prediction" mode

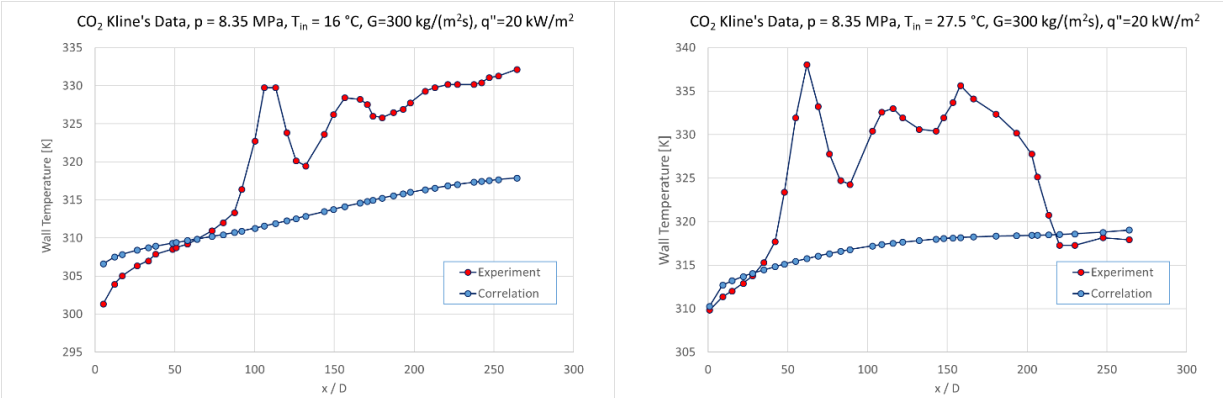

Figure 58. Wall temperature trend for the 1st and 2nd sample case of the data by Kline in "prediction" mode

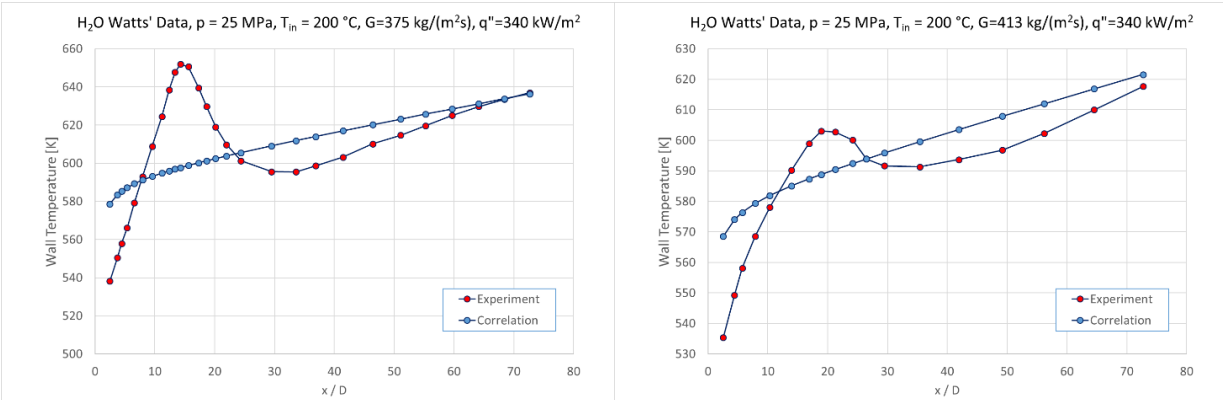

Figure 59. Wall temperature trend for the 1st and 2nd sample case of the data by Watts in "prediction" mode

As it can be noted, though the coefficient multiplying the Richardson number is negative, coherently with expectations, its effect in representing deterioration is not a remarkable one. This seems to be due to the final trend of temperature reached by iterations, which results in values of the Richardson number much lower than expected in the experiments. This is shown in Figure 60

for two of the sample cases by Kline and Watts; very evidently, while the Richardson number should exhibit the effect of the bumps observed in the experimental wall temperature, owing to their effect on wall density, the wall temperature trends to which the correlation is settling do not help at all in curbing the trend towards any deteriorated behaviour.

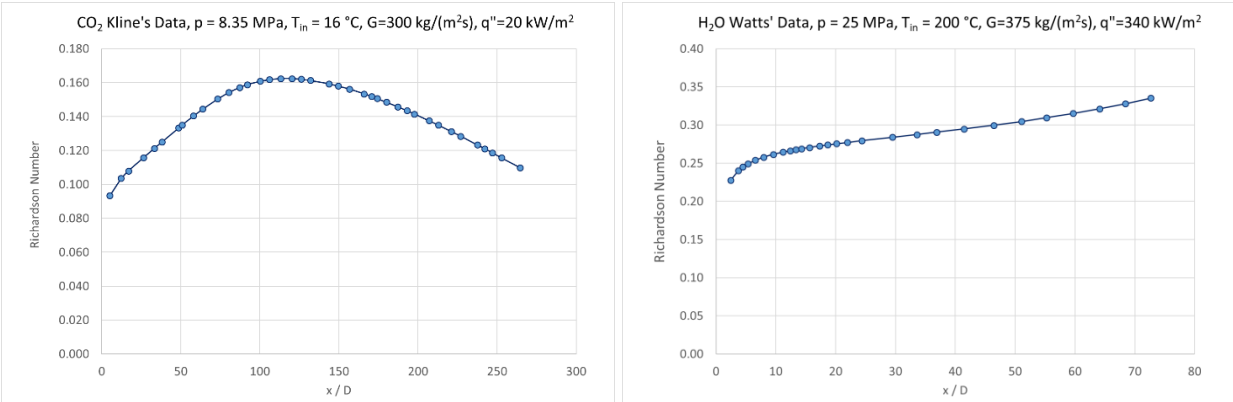

Figure 60.Trend of the Richardson number for the 1st sample case of the data by Kline and the 1st sample case of the data by Watts in "prediction" mode

In practice, the deterioration is not represented by the trends reached at convergence and this has a feedback on the dimensionless numbers that should translate its effects into the correlation: this is something needing further clarification.

- *Jacksons' type correlation*

As already mentioned in previous sections, Jackson's (2013) correlation is one of the most widespread adopted correlation and is accredited for good results. It is similar to the ones already considered above, though it deviates from them because of use of the bulk Prandtl number, then allowing a correction for the ratio of the averaged Prandtl number and the bulk one. The correlation has the form:

$$Nu = \left[1 + \frac{0.3}{(x/D)^{0.7}}\right] \exp(x_1)\, Re^{x_2} Pr^{x_3} \left(\frac{\rho_w}{\rho_b}\right)^{x_4} \left(\frac{\overline{C_p}}{C_{p,b}}\right)^{x_5} \tag{39}$$

with $\exp(x_1) = 0.0183$, $x_2 = 0.82$, $x_3 = 0.5$, $x_4 = 0.3$ and $x_5 = 0.4 \div 0.6$, the latter depending on bulk and wall temperatures. The plots in Figure 61 to Figure 63 and the
Table *10* show that also this correlation form, once optimised as in previous cases does not introduce significant variants in the predictions with respect to data obtained by other correlations. As it can be noted, the exponent of the Reynolds number is larger than suggested by Jackson (2013) hence the smaller leading coefficient, while the other exponents are not far from suggestions, except for the one of the density ratio that is nearly halved.

Figure 61. Global fitting of Eq. (39) in “prediction” mode

Table 10. Coefficient and exponents for the correlation in Eq. (39) in “prediction” mode

Mode	$\exp(x_1)$	x_2	x_3	x_4	x_5	RMS
Prediction	0.004438	0.9212	0.4489	0.1696	0.4196	122.53

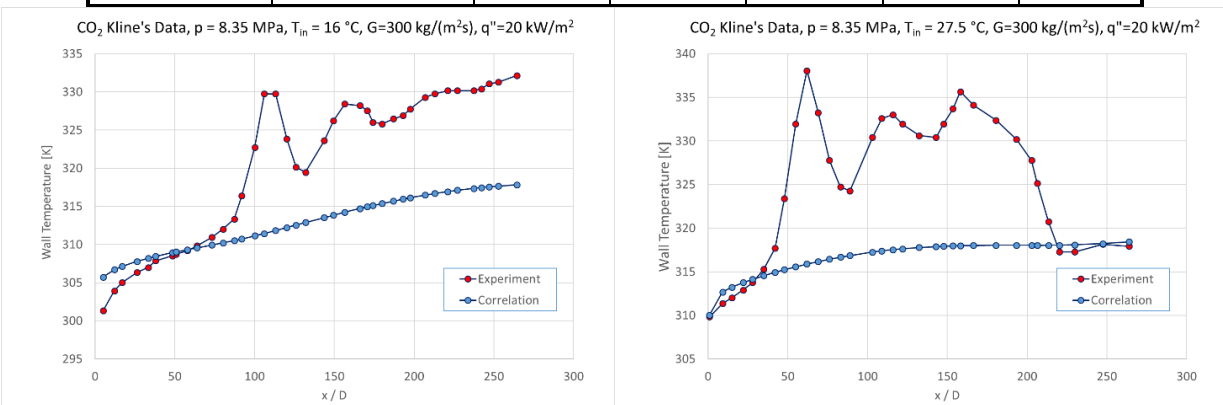

Figure 62. Wall temperature trend for the 1st and 2nd sample case of the data by Kline in “prediction” mode

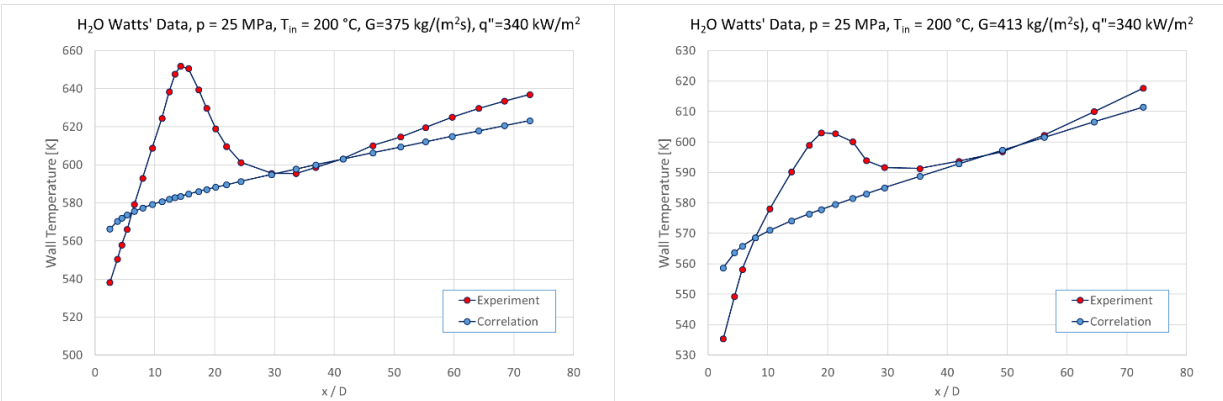

Figure 63. Wall temperature trend for the 1st and 2nd sample case of the data by Watts in “prediction” mode

Lesson learned so far

The previously presented analyses on correlations having classical form, or even provided with somehow innovative features, suggest the following considerations.

- In “correlation” mode it is easily possible to mimic the trends observed in the experiments about wall temperature, including local deterioration effects, but this apparent success, often reported in literature, does not correspond to a real quality of predictions when the dimensionless numbers containing wall temperature are calculated coherently with the fitted correlation, as it is in the case of code “predictions”.
- On the other hand, the procedure followed in this report for achieving correlation parameters fitting the experimental data, basing on the values of wall temperature predicted by the correlation itself, provides unacceptable quality in the representation of observed qualitative trends, though they do correspond to the actual values that would be obtained in code “predictions”. In other words, notwithstanding the variety of considered forms, the obtained wall temperature trends are desperately very similar in the various addressed cases and tend to settle to similar values of RMS, showing that at the moment it is not possible to obtain much more than a global prediction similar to the one that could be achieved by the Dittus-Boelter correlation.

A legitimate suspicion in relation to the adopted procedure is that the simple iteration process here developed forces to converge towards “stable” manifolds of the possible solutions of the fitting problem, while deterioration may be represented by branches of possibly existing multiple solutions (as shown in some of the cases considered in “correlation” mode) that may not always possess sufficient stability to be reached by an iterative procedure. This suspicion led to check different starting values of temperature in iteration (e.g., twice the experimental values), trying to assess if any different final set of data could be obtained; even these trials did not provide any better result.

In order to contribute in clarifying this issue, Figure 64 and Figure 65 show the progressive adjustment of wall temperature to the final values during selected iteration steps for the correlation conceived as an over-fitting of the experimental data (Eq. (33)). As it can be noted, even for this correlation, which at the first iteration (i.e., in “correlation” mode) is providing data very close to the experimental ones, there is a progressive deviation from the initial guess towards a rather smooth trend of wall temperature which does not represent the actually observed deteriorated trends. Iteration 35 represents the previously shown converged trends, achieved by successive under-relaxations, with an under-relaxation factor equal to 0.5.

It is interesting to observe in the deteriorated heat transfer case by Watts (Figure 65) the presence of a point that tends to deviate upwards during iterations, probably settling on a higher manifold of the possible solution. The last part of the curve at high values of the dimensionless coordinate also shows to be on a higher manifold persisting longer during iterations.

These observations suggest that the existence of multiple solution branches in correlations could be a feature to be considered possible, if not even desirable, in a coefficient optimisation procedure, to be attentively analysed in view of casting the final correlation into the best form for predicting deteriorated heat transfer. At the time of writing, this is just a reasonable conjecture that is stimulating to experiment further iteration procedures and formulations, whose characteristics should be better considered in view of establishing a functional form of the correlation that my serve as guidance in setting up more successful correlations for bare tubes and bundles.

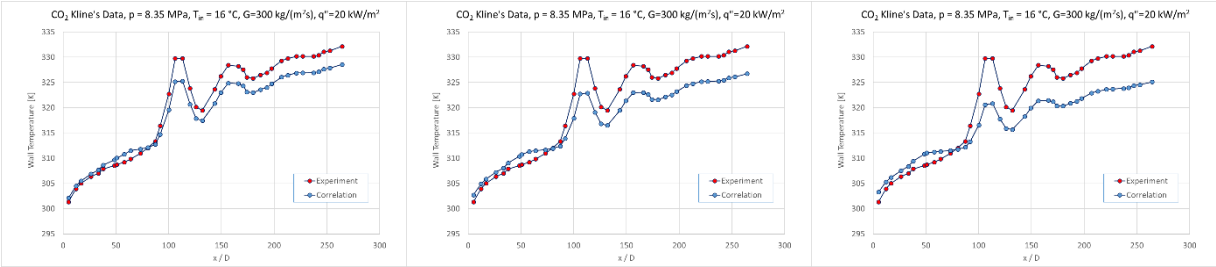

Iteration 1 Iteration 2 Iteration 3

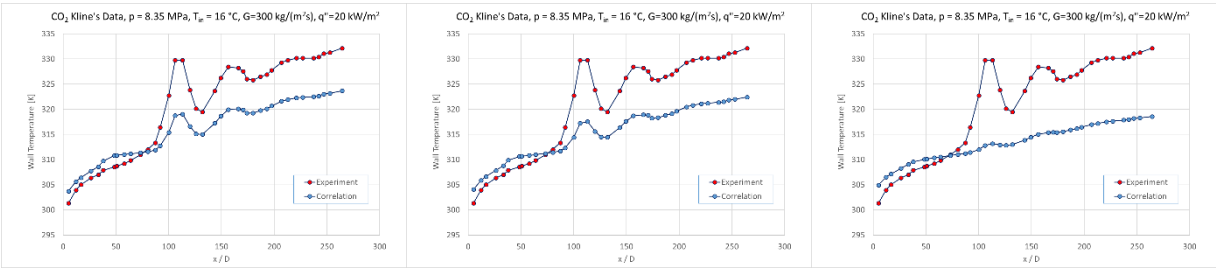

Iteration 4 Iteration 5 Iteration 10

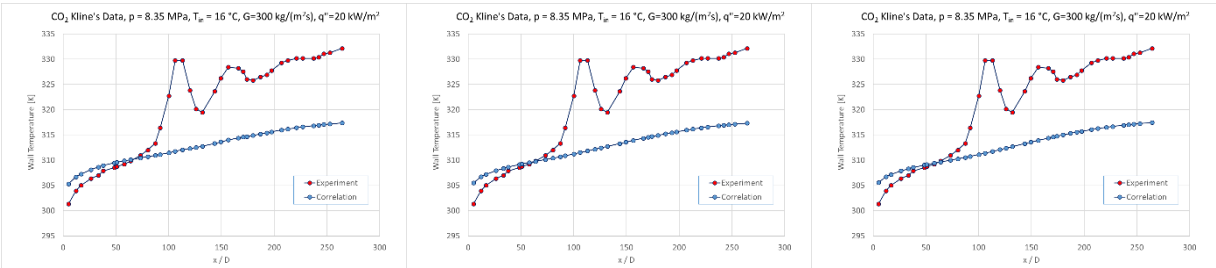

Iteration 15 Iteration 20 Iteration 35

Figure 64. Wall temperature trends for the 1st sample cases of the data by Kline and Eq. (33) during iterations

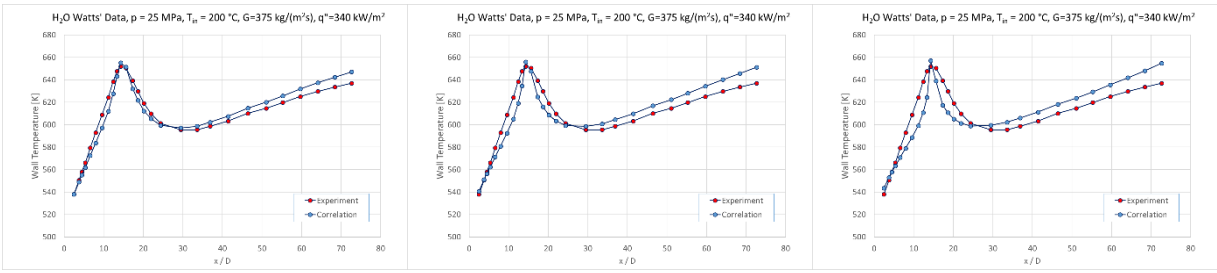

Iteration 1 Iteration 2 Iteration 3

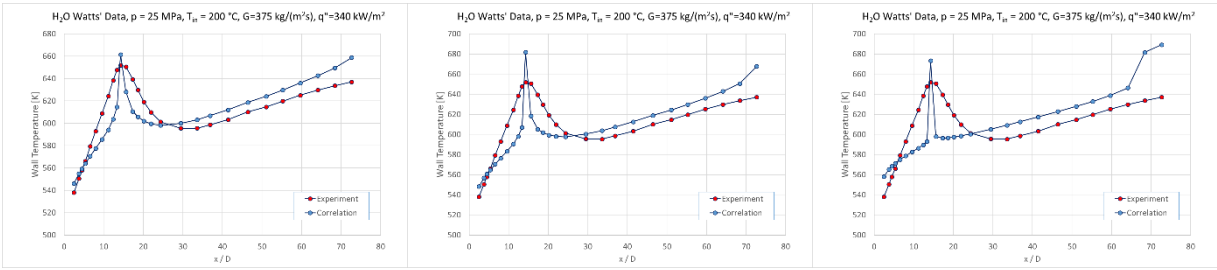

Iteration 4 Iteration 5 Iteration 10

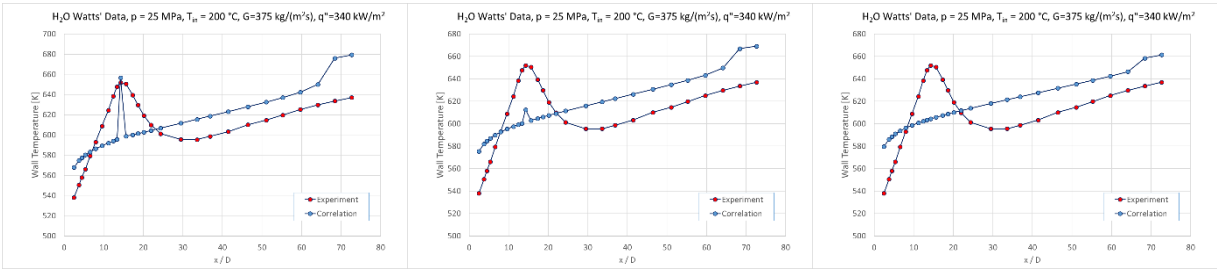

Iteration 15 Iteration 20 Iteration 35

Figure 65. Wall temperature trends for the 1st sample cases of the data by Watts and Eq. (33) during iterations

Indeed, except for the use of the Richardson and the Froude numbers and for the inclusion in one of the selected forms of the information about the inlet conditions, the similarity theory was not yet fully exploited in conceiving the investigated correlations. However, the scepticism about the capability of simple scalar equations in predicting the observed heat transfer efficiency in deteriorated heat transfer cases turns out to be reinforced by the results obtained so far, suggesting to experiment possible alternative techniques for heat transfer prediction.

A reasonable explanation of the mentioned convergence of any of the above considered correlation form towards smooth trends, which do not represent the actual phenomena observed in many data series affected by deterioration, can be obtained by considering Figure 66, representing the comparison of the experimental values of the Nusselt number vs. the ones predicted by the Dittus-Boelter correlation for the whole considered data set. As it can be noted, though a global tendency towards deterioration is observed, the spread below and above the bisector line is such that it cannot be really hoped that a global correlation approach as the one adopted herein may provide much more than a trend similar to the ones provided by the Dittus-Boelter correlation itself.

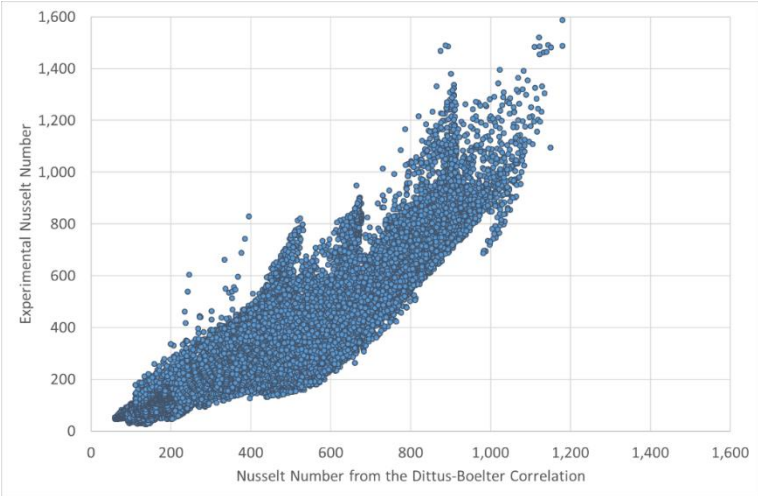

Figure 66. Comparison between the experimental Nusselt number and the value predicted by the Dittus-Boelter correlation for the addressed data base

This calls for a possible discrimination of data to be used for predicting specific phenomena, as already proposed in literature, though without too much success, in achieving general prediction capabilities for the phenomena observed in heat transfer with supercritical fluids.

2.1.6 Analysis of two different heat transfer deterioration modes

2.1.6.1 A "Shape Function" approach

As observed in the previous sections, it seems that the classical "power-law" type correlations can hardly reproduce the complicated phenomena occurring when addressing heat transfer to supercritical fluids. In addition, as already pointed out, discrepancies between the expected and real capabilities of the developed correlations may occur, owing to the strongly non-linear behaviour of the fluid properties. Attempts also involving "over-fitting" correlations seem providing limited results and none of the tested forms seems able to predict the occurrence of heat transfer deterioration. In the present section, an alternative approach trying to introduce "Shape Functions" is presented, aiming at suggesting a possible development path for heat transfer correlations for supercritical fluids.

The fluid-to-fluid scaling methodology reported in Section 2 is here considered as a starting point of the proposed methodology. As observed in the previous sections and reported again in Figure 67 in order to improve the readability of this description, once suitable operating conditions are imposed, it is possible to obtain similar trends of the relevant dimensionless numbers even when adopting different fluids. In particular, it is important to stress the attention on Figure 67b and Figure 67d, which clearly show that, once the similarity in terms of $h_w^* \; vs \; h_b^*$ trends is achieved, the same trends of Richardson number and Nu_{exp}/Nu_{DB} as a function of h_b^* are obtained as well. Two main lessons may be drawn from these figures:

- a correlation coherent with the adopted fluid-to-fluid scaling methodology should take into account the Richardson number distribution in order to predict buoyancy effects;
- as remarked in previous literature, a "base" correlation in a form like the one developed by Dittus-Boelter may be suitable in order to represent a "fundamental" behaviour, to be then refined adopting additional parameters and functions to fit the real Nusselt number trend.

The Richardson number, while being a relevant indicator of the local buoyancy conditions, may not be sufficient for providing a good estimation of the involved phenomena. As reported in Figure 67b, in fact, the same values of the Richardson number may refer to two completely different conditions: the temperature rise phase of the deterioration phenomenon and the descent phase at the heat transfer recovery. A correlation that takes only into account this parameter would not thus be able to recognize the different phases of the heat transfer phenomenon, since it lacks the capability to consider the upstream "history" of the phenomenon itself.

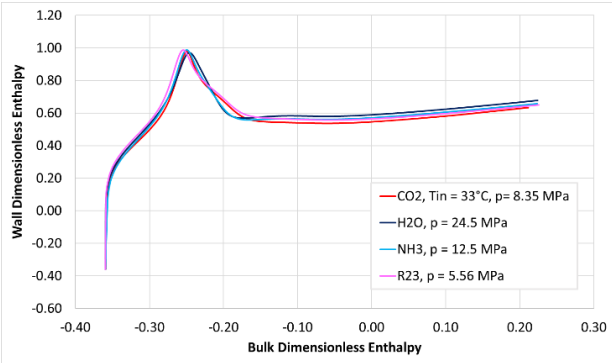

b) wall dimensionless enthalpy

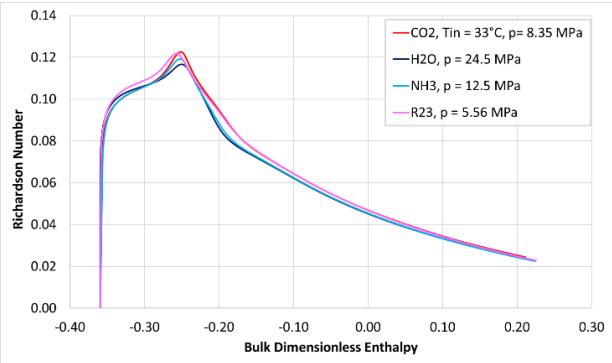

b) Richardson number

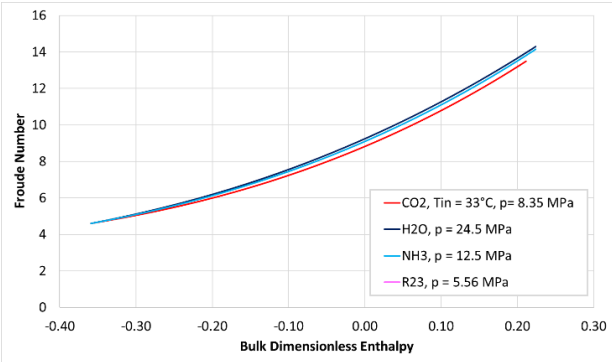

d) Froude number

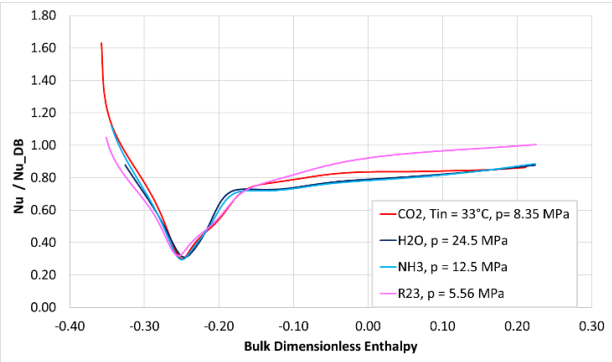

d) ratio of Nu / NuDB

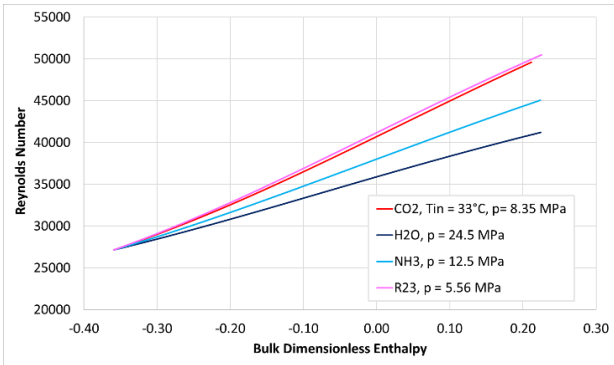

f) Reynolds number

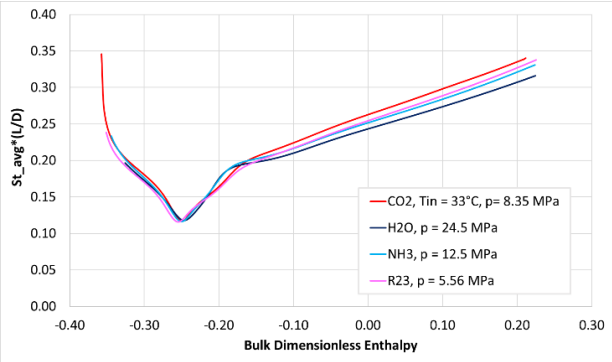

f) $\overline{St}(L/D)$

Figure 67. Trends of dimensionless parameters for the data by Kline with q"=20 kW/m^2 and T_{in} = 33 °C

The "history" of the flow is particularly relevant when heat transfer deterioration phenomena occur as a consequence of the redistribution of the velocity field due to entrance effects and developing flows. Figure 68 reports the results of two CFD calculations inspired to the Watts data series also discussed previous sections. As it can be observed, the deterioration phenomenon occurs

downstream the start of the heated section and it is not linked to local (bulk) phenomena only. Similar phenomena may also be identified in other data series, as the one by Kline in Figure 69. Again, it can be observed that, in these cases, deterioration mainly occurs as a consequence of the entrance effects, whereas normal-like heat transfer conditions are instead to be expected once the flow is sufficiently developed.

This class of phenomena thus cannot be predicted by power law correlations that are not able to account for this upstream "history" of the flow. An additional parameter depending on what occurred at previous locations along the test section is thus needed in order to predict heat transfer deterioration and restoration phenomena.

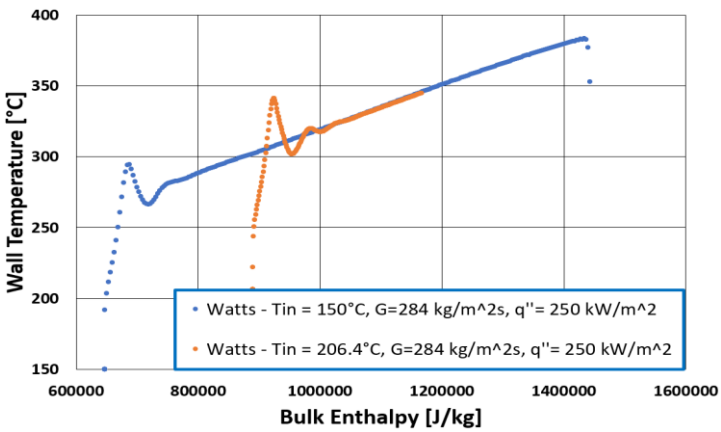

Figure 68. Wall temperature trends predicted by CFD for two cases by Watts

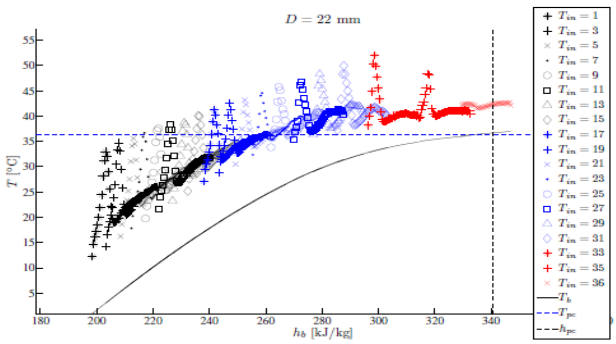

(a) All cases

Figure 69. Considered Kline case: G = 300 kg/m^{2}s, q''=15 kW/m^2

An eligible parameter in this purpose should thus be able to provide both local information about the buoyancy phenomena and also to take into account the upstream flow conditions; the parameter should also provide the capability to allow for scalability when adopting different fluids. Recalling the outcomes of the fluid-to-fluid similarity theory, it is clear that, once the similarity is achieved in terms of $h_w^* \; vs \; h_b^*$, similarity is also achieved in terms of $Ri \; vs \; h_b^*$ (Figure 70a). As a consequence, similar cases, will also share the same heat transfer capabilities at the same values of the integral of the Richardson number with respect to h_b^*, i.e. the area below the curve reported in Figure 70b.

By performing an integral along the heated section, this parameter should provide the capability to take into account the "history" of the flow, while also granting information about the

local buoyancy phenomena and allowing for fluid-to-fluid scalability. The present choice in this regard is:

$$Ri_{INT,0} = \int_0^x Ri_D \; dh_b^* = \int_0^x Ri_D \; NTPC_{loc} \frac{4\,dx}{D} \tag{40}$$

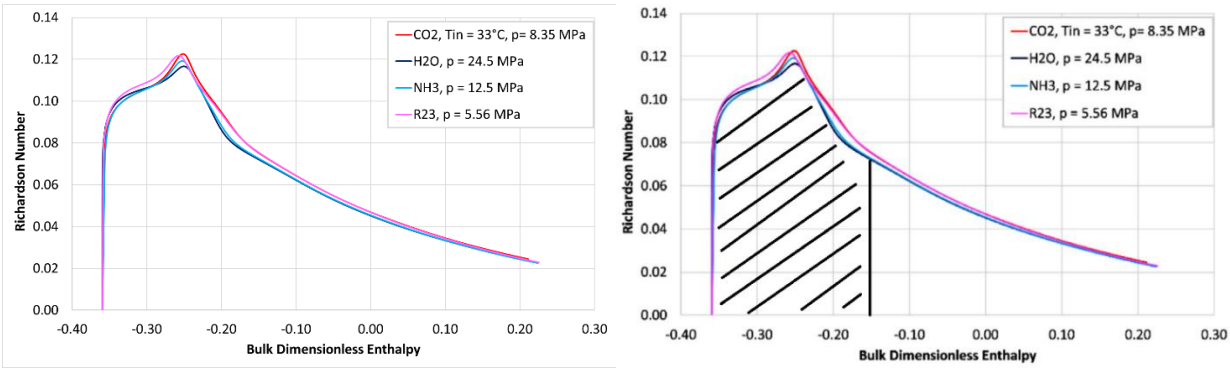

a) Richardson number b) Richardson number integral

Figure 70 Richardson number: local distribution and its integral

As anticipated (see e.g. Figure 67d), the local Nusselt value may be calculated taking into account two components: a base correlation calculating “normal-like” heat transfer conditions (similar to the Dittus-Boelter one) and a shape function that will provide the actual heat transfer conditions, being normal or deteriorated. The shape function may be a function of a series of parameters being, e.g., the diameter, $NTPC_{loc}$, h_b^* and the $Ri_{INT,0}$.

This approach is here applied to the “rather” simple operating conditions adopted in the data by Watts, in which the supercritical water exhibits normal and deteriorated heat transfer while being at a sufficiently large pseudo-subcooling conditions. Deterioration is thus mainly due to buoyancy effects and events related to other phenomena (i.e., exceeding of the pseudo-critical temperature at the wall) are not considered.

The base correlation is selected to be in the form:

$$Nu_0 = Entr * 0.021\, Re^{0.8} \overline{Pr}^{0.66} \tag{41}$$

where the function

$$Entr = 1 + 1.4 \frac{D}{x} \tag{42}$$

takes into account the better heat transfer capabilities usually observed at the beginning of the heated section during the flow development. The exponent of the Prandtl number was selected in similarity with the one observed to be a good candidate for obtaining good matchings in the fluid-to-fluid similarity theory in previous works of the authors of this report, thus slightly deviating from the classical Dittus-Boelter correlation.

The analysis of the Watts data is performed taking into account the normalized difference between the Nusselt number measured during the experiments and the one provided by the base correlation Nu_0 (i.e. $\frac{Nu_{Exp} - Nu_0}{Nu_0}$). The integral of the Richardson number is considered as a potential relevant parameter but, with respect to the previous definition, the following one is adopted instead after data observation:

$$Ri_{INT} = \int_0^x Ri_D \; NTPC_{loc} \left(\frac{\rho_w}{\rho_b}\right)^{0.5} \frac{4\,dx}{D} \tag{43}$$

The introduction of $\left(\frac{\rho_w}{\rho_b}\right)^{0.5}$ should not prevent or impair the scaling capabilities of the parameter owing to the similarities observed for the density distribution as a function of h^* also reported in Section 2. Nevertheless, it was observed that the introduction of the density ratio improves, at least in this case, the predicting capabilities of the considered shape function approach.

The trends obtained for $\frac{Nu_{Exp}-Nu_0}{Nu_0}$ as a function of Ri_{INT} for all the Watts data are reported in Figure 71. The plot clearly shows that all the experimental paths seem to be reproducible following a very limited number of "characteristic" trends, from here on named "shape-functions". The red dots refer to cases at T_{in} =310 °C, in which the wall temperature always exceeds the pseudo-critical temperature; as it can be observed, the trend is completely different from the ones reported for other inlet temperature values. While in general it can be accepted that the different inlet conditions will imply a different behaviour of the flow, in this very case it is possible to make this trend to better fit the other ones introducing a corrective coefficient taking into account the h_w^* distribution.

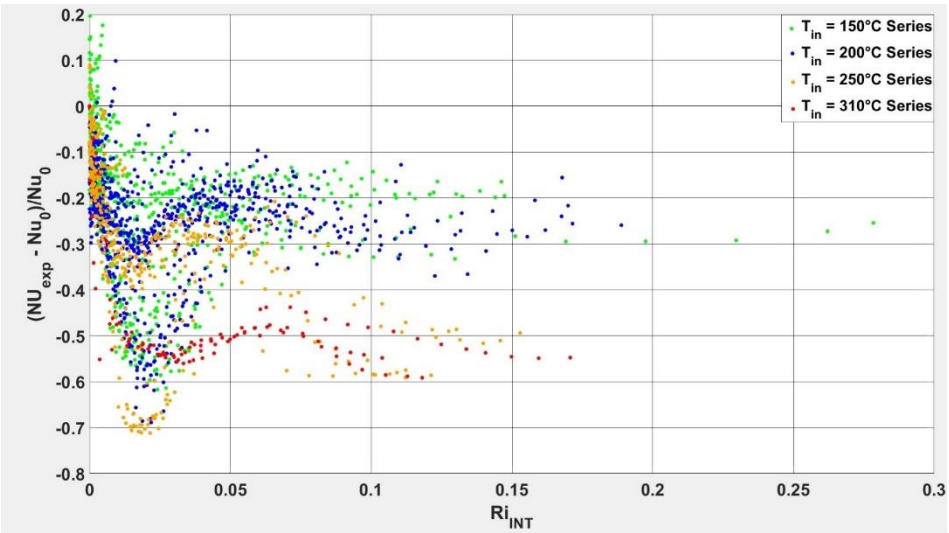

Figure 71. Watts data: analysis of the $\frac{Nu_{Exp}-Nu_0}{Nu_0}$ distribution as a function of Ri_{INT}

By introducing a corrective coefficient in the form:

$$f(h_w^*) = \begin{cases} 1 & h_w^* < -0.5 \\ 0.65 - 0.7\, h_w^* & -0.5 < h_w^* < 0 \\ 0.65 & h_w^* \geq 0 \end{cases} \tag{44}$$

the base correlation becomes

$$Nu_0 = Entr * f(h_w^*) * 0.021\, Re^{0.8} \overline{Pr}^{0.66} \tag{45}$$

With this choice, the trends obtained for $\frac{Nu_{Exp}-Nu_0}{Nu_0}$ as a function of Ri_{INT} become as shown in Figure 72.

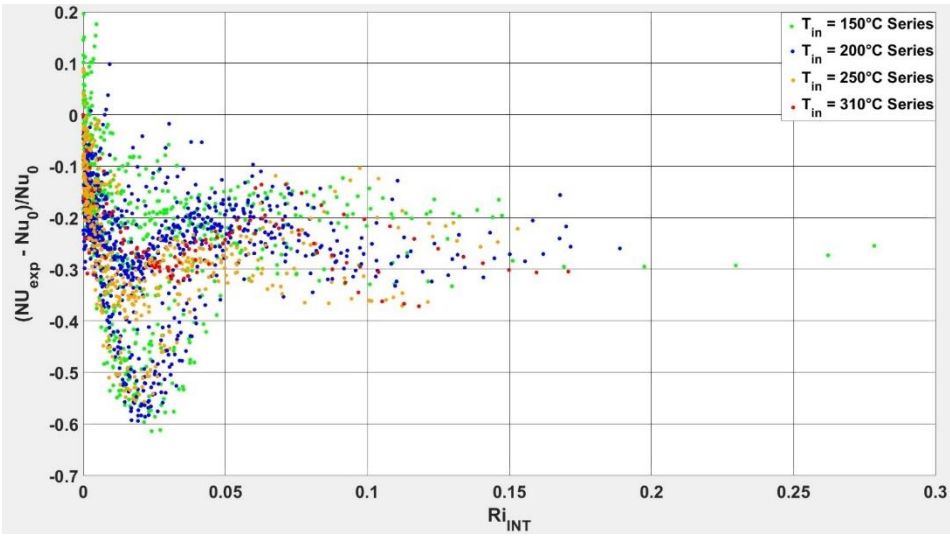

Figure 72. Watts data: analysis of the $\frac{Nu_{Exp}-Nu_0}{Nu_0}$ distribution as a function of Ri_{INT}

The distribution reported in Figure 72 may be reproduced with a reasonable accuracy introducing only 3 shape functions; the selected trends are reported in Figure 73: “Normal heat transfer”, “Mild Deterioration” and “Severe Deterioration” conditions may thus be recognized.

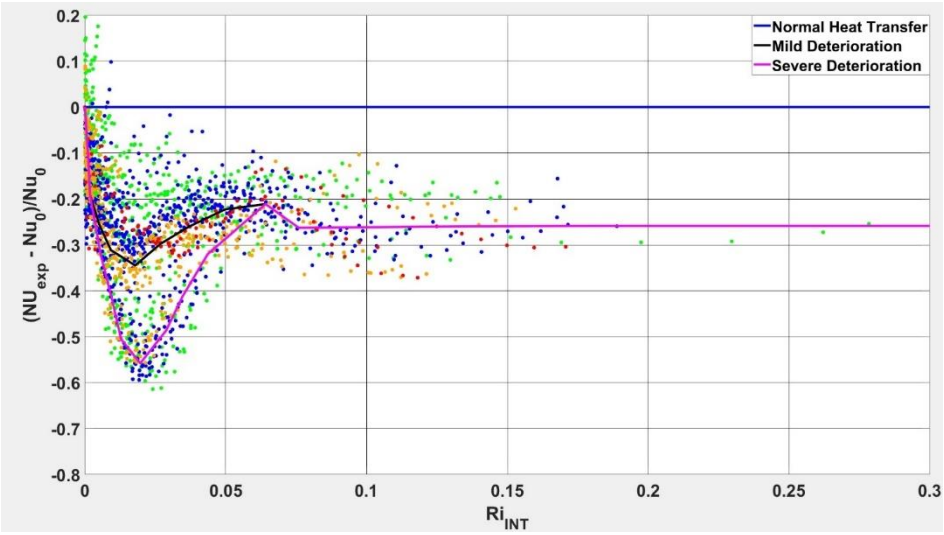

Figure 73 Considered Shape Functions

As a consequence, it is reasonable hoping that a correlation in the form

$$Nu_{calc} = Entr * f(h_w^*) * 0.021\, Re^{0.8}\overline{Pr}^{0.66} * (1 + Shape_{Function}) \quad (46)$$

is able to provide a good prediction of the whole Watts data set. A predicting tool can thus be created as described hereafter.

- The base function Nu_0 (i.e. normal heat transfer) will be considered as a first estimation of the heat transfer capabilities. The actual heat transfer capabilities will be later defined introducing the shape function. The tool must be able to understand autonomously which one of the shape functions must be considered for the prediction. Thresholds for the occurrence of mild and severe deterioration are thus required.

- These thresholds may be searched for in a form which is dependent on the Richardson number or on Ri_{INT}. Values which proved to be a good estimation at least for the Watts data are:
  - Ri > 0.07 in order to move from normal to mildly deteriorated conditions;
  - Ri > 0.125 and $Ri_{INT} < 0.0005$ to move from mildly to severely deteriorated conditions.

Different values are to be expected for other applications, to be tailored on the specific data.

At each iteration the code updates the predicted wall temperature; in particular, it calculates Ri and Ri_{INT} at each location and, consequently, defines the shape function to be considered in order to obtain the actual Nu profile and, consequently, the wall temperature trend. In the following (Figure 74 to Figure 76), the obtained results are reported.

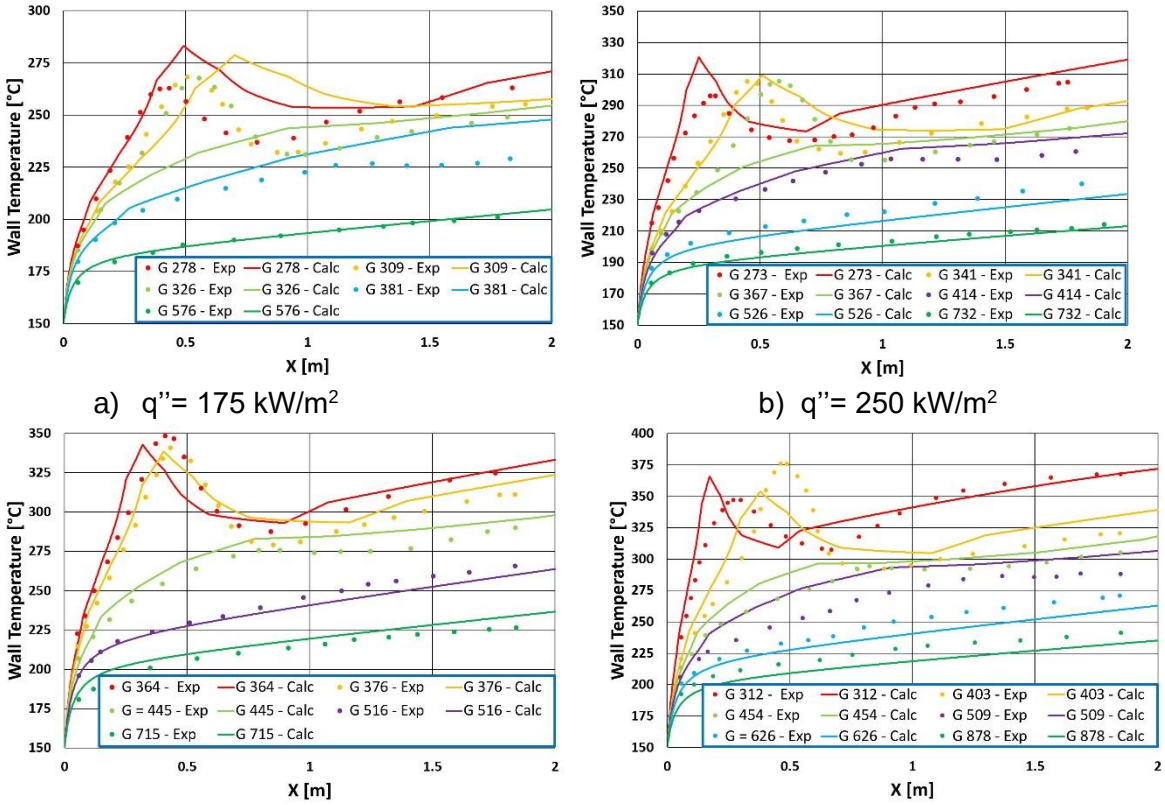

a) q''= 175 kW/m^2 b) q''= 250 kW/m^2

c) q''= 340 kW/m^2 d) q''= 400 kW/m^2

Figure 74. Watts Data series for Tin = 150°C: Comparison of experimental al calculated trends

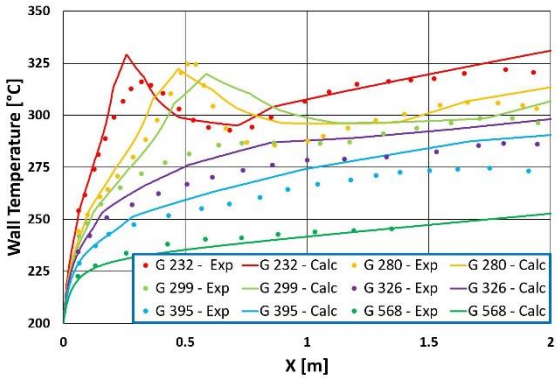

a) q''= 175 kW/m^2

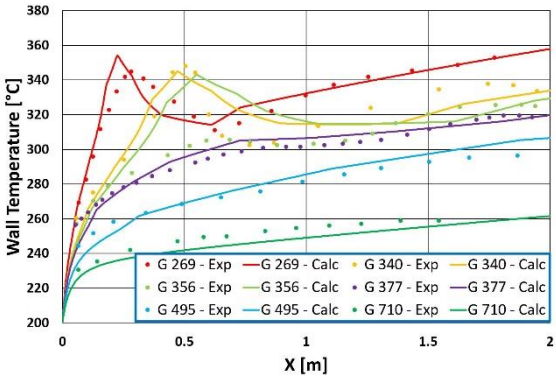

b) q''= 250 kW/m^2

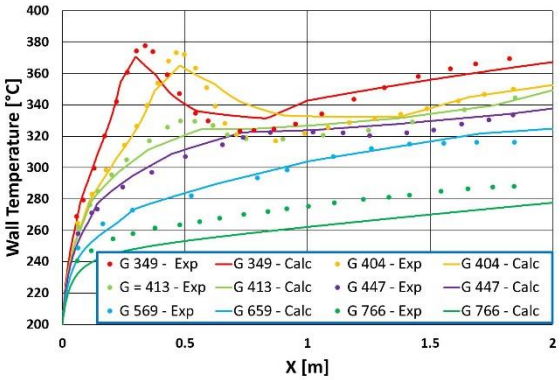

c) q''= 340 kW/m^2

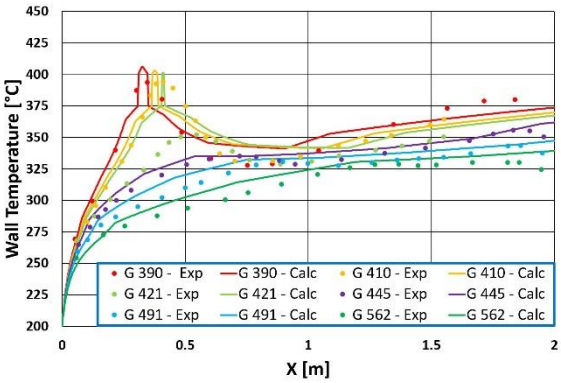

d) q''= 400 kW/m^2

Figure 75. Watts Data series for Tin = 200°C: Comparison of experimental al calculated trends

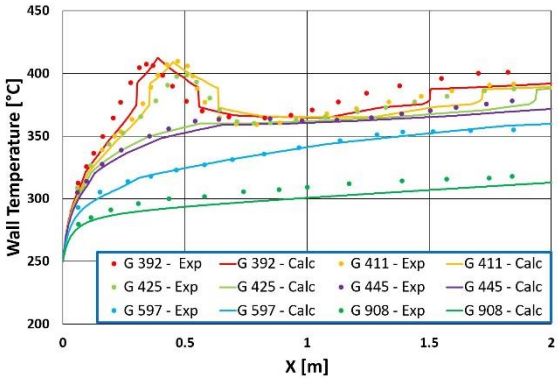

a) q''= 340 kW/m^2

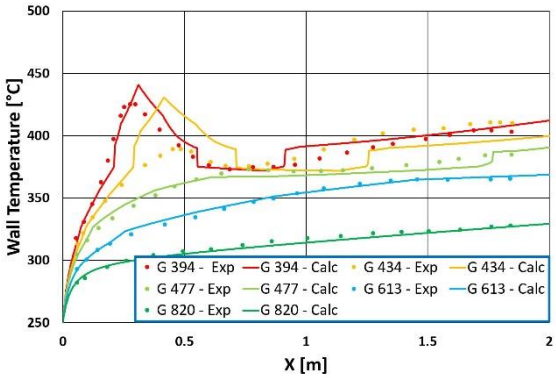

b) q''= 400 kW/m^2

Figure 76. Watts Data series for Tin = 250°C: Comparison of experimental al calculated trends

In addition, with a slightly different choice for the threshold, it is also possible to obtain a good estimation for the cases at Tin = 310 °C (Figure 77).

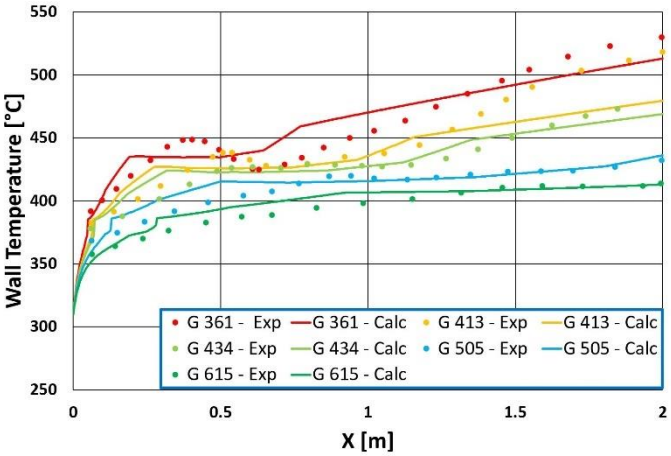

Figure 77. Watts Data series for Tin = 310°C: comparison of experimental and calculated trends

As it can be observed, very good predictions of the measured trends can be obtained adopting the considered strategy. Discrepancies can be of course observed, especially for conditions straddling across the threshold between mild and severe deterioration conditions; nevertheless, the quality of the obtained trends seems very promising. The numerical tool can predict both normal and deteriorated heat transfer conditions and, basing on the adopted thresholds, may also opt for a mild or severe deterioration form. Since the considered correlation mainly relies on the shape functions and not on properties ratios which may prevent convergence (see i.e., the problems discussed in the previous sections), the adopted numerical model seems able to easily find a solution and, also in the most complicated cases exceeding the pseudo-critical temperature, convergence is achieved in less than 200 iterations.

A sample of the evolution of the predicted solution as a function of iterations is reported in Figure 78 for the case G =392 kg/m^{2}s, q'' = 400 kW/m^2 and T_{in} = 250°C. As it can be observed, in the addressed case the first prediction returns a normal heat transfer conditions, while after a few iterations, instead, the severe deterioration appears and the solution is later refined till convergence is achieved.

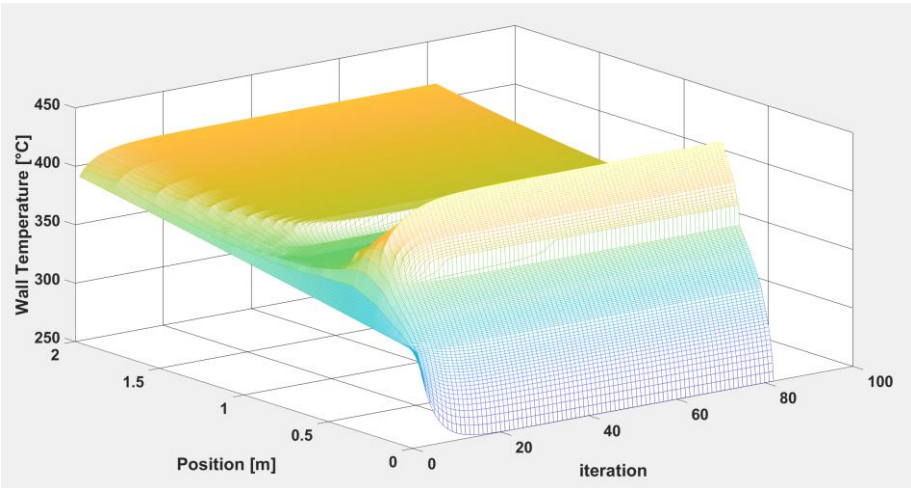

Figure 78. Evolution of the predicted wall temperature distribution as a function of the number of iterations for a selected case

The methodology was also developed in order to fulfil the requirements of scalability when adopting different fluids.

Figure 79 reports two attempts for the Watts series at T_{in} = 250 °C and q''= 400 kW/m^2 and a scaling attempt with CO_2 at 8.35 MPa. The operating conditions were set taking into account the similarity theory discussed in previous sections: the optimal heat flux should be found with a trial and error procedure. For the reference case at G = 394 kg/m^{2}s, similarity was obtained at the first attempt, with a heat flux of 86 kW/m^2, the one suggested as a first approximation by the similarity theory. For the second case, with G = 477 kg/m^{2}s for the water reference case, CO_2 reported a severe deterioration with a heat flux of 86 kW/m^2; a mild deterioration and a trend similar to the water reference case was obtained instead reducing the heat flux by 10%, at about 77 kW/m^2. Of course, no perfect matching may be expected, nevertheless the observed uncertainty ranges of 10% seems very promising.

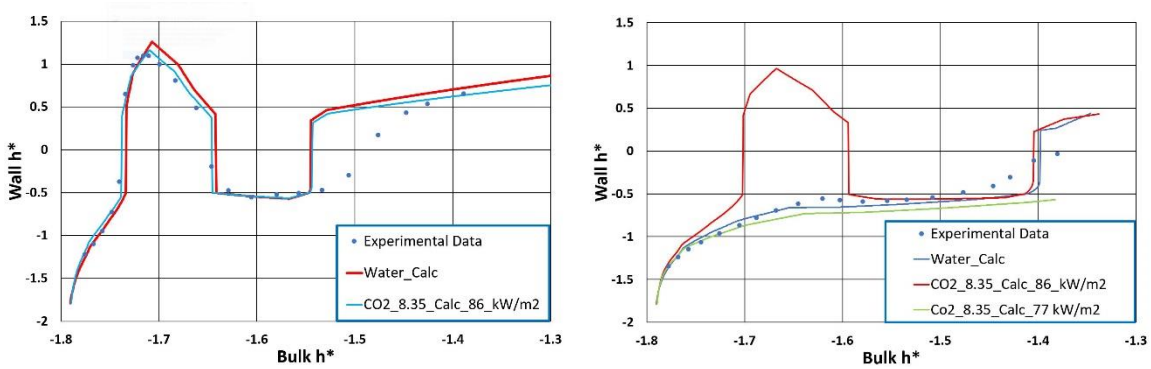

a) G = 392 kg/m^{2}s b) G = 477 kg/m^{2}s

Figure 79. Scaling Attempts with CO_2 at 8.35 MPa

2.1.6.2 Pseudo-Nukiyama curves

A further mode of heat transfer deterioration has been identified in the frame of the analyses performed for Kline's (2017) experimental data as those shown in Figure 80, where both experimental measurements and CFD modelling results have been reported.

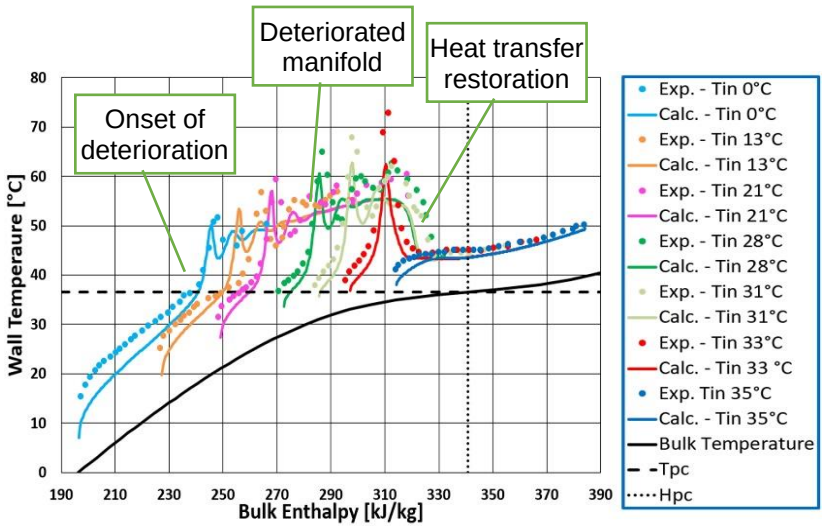

Figure 80. Experimental trends and CFD model predictions obtained for Kline's data with CO_2 in upward flow at 8.35 MPa at q"=20 kW/m^2, G=300 kg/(m2s) with an ID = 4.6 mm

As it can be noted, in difference from the deterioration mode identified for the Watts' (1980) experimental data at large inlet subcooling with respect to pseudocritical temperature, for which the shape function approach was developed, after the onset of deterioration the heat transfer mode keeps deteriorated, with the wall temperature shifting to a higher temperature manifold. This situation persists up to a point along the channel axis in which the bulk temperature becomes sufficiently close to the pseudocritical one that the wall-to-bulk density difference is no more sufficient to maintain a level of buoyancy causing laminarization because of mixed convection effects; this occurs close to the transition to gas-like fluid in bulk, showing that laminarization as a consequence of buoyancy effects is definitely more powerful in generating heat transfer deterioration than the shift to a lower thermal conductivity in bulk and at the wall.

This phenomenon is clearly visible in the plots of Figure 81, showing experimental data only from the dataset by Kline. As it can be noted, in this second mode of deterioration at increasing values of inlet temperature deteriorated heat transfer gets in at the channel inlet and, after usual wall temperature oscillations, the wall temperatures settle to a sort of envelop of higher values, highlighted by the black-dotted line that follows an increasing trend up to the mentioned heat transfer restoration. As it can be noted, this phenomenon occurs at different values of operating parameters, as tube diameter and heat flux, showing a characteristic repeatable trend.

These observations suggest the presence of a threshold phenomenon (i.e., the onset of deterioration) similar to what observed at subcritical pressure with the onset of critical heat flux (CHF). The essential features of this phenomenon are highlighted in Figure 82 showing in a sketchy way the classical Nukiyama curves and the well-known mechanism of departure from nucleate boiling occurring in boiling systems in which heat flux is imposed at the heating wall.

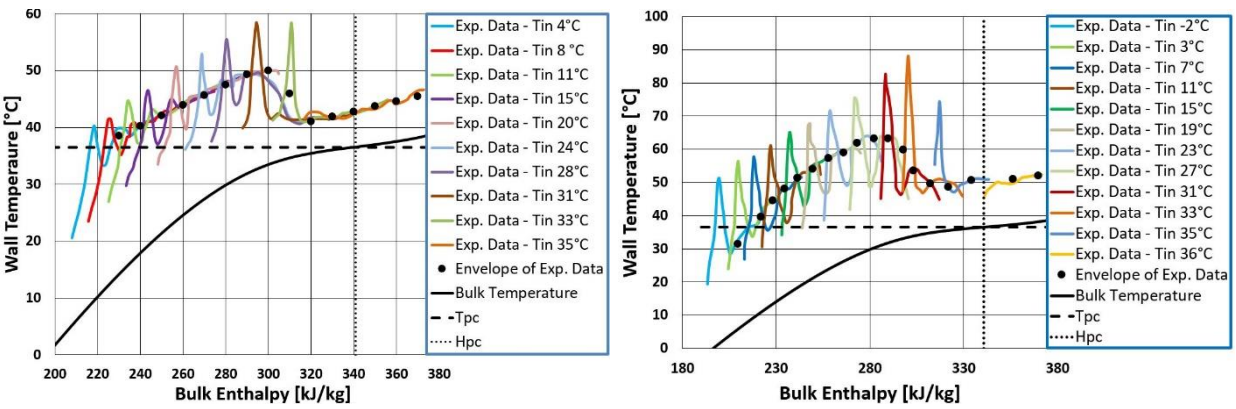

a) q"=18 kW/m^2, G=300 kg/(m^{2}s), ID = 8 mm b) q"=35 kW/m^2, G=400 kg/(m^{2}s), ID = 22 mm

Figure 81. Experimental trends obtained for Kline's data with CO_2 in upward flow at 8.35 MPa at q"=20 kW/m2, G=300 kg/(m^{2}s) with an ID of 4.6 mm

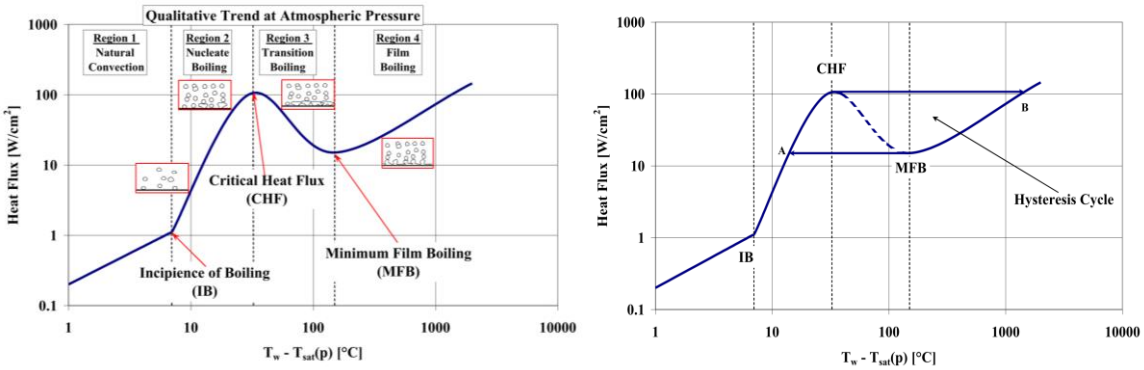

a) description of phenomena b) temperature excursions at imposed heat flux

Figure 82. Classical examples of Nukiyama curves for pool boiling with indication of heat transfer regimes

Following this suggestion, an already applied methodology for highlighting such a threshold behaviour from the computational point of view (Sharabi and Ambrosini, 2009) was retrieved in the frame of the studies conducted for ECC-SMART, leading to a new elaboration (Pucciarelli et al., 2022) that took profit of the greater accuracy assured by the presently adopted CFD tools in predicting heat transfer at supercritical pressure with respect to those available in former applications.

The methodology consists in applying to the heating wall a value of temperature progressively increasing along the pipe axis so that, instead of witnessing the onset of deterioration as a jump to a higher manifold, it could be observed instead as a decrease in the corresponding wall heat flux. Such a procedure had been already used to obtain the results shown in Figure 2 (from Sharabi and Ambrosini, 2009), though at the time, as above mentioned, the adopted CFD model did not allow for sufficient accuracy, providing only qualitative indications.

In the present case, instead, the application of this methodology to Kline's data, owing to the greater accuracy that was possible to obtain in the simulations, gave the possibility to reach better defined conclusions. This is shown, in particular, by the sequence of predictions obtained for three series of Kline's data at wall heat fluxes equal to 15, 18 and 20 kW/m^2 that were characterised by different degrees of heat transfer deterioration. As it can be noted in Figure 83 a, b and c, the predictions obtained by the RANS CFD model are particularly good in comparison with experimental data and follow in most conditions the behaviour of experiments in showing no deterioration at 15 kW/m^2 (there is a single deviation obviously due to the imperfection of the model in Figure 83a) and relatively high fidelity predictions of the level of deterioration at 18 and 20 kW/m^2 (see Figure 83b and Figure 83c).

This provided the opportunity to test the idea of applying a sufficiently steep increase in wall temperature at the wall obtaining the curve reported in Figure 83d, closely resembling the classical Nukiyama's trend. In this figure, the three mentioned values of heat flux have been highlighted to show why the three values of heat flux produced different levels of deterioration; indeed, the case at 15 kW/m^2 did not involve any heat transfer deterioration since the imposed heat flux is lower than the maximum allowable in those particular conditions, so that the corresponding horizontal line intersects the rising branch of the pseudo-Nukiyama curve (corresponding to nucleate boiling in the analogy with subcritical phenomena). On the other hand,

18 and 20 kW/m^2 are higher than the maximum of the first rising branch of the curve so that the only possible operating points fall into the second rising branch (corresponding to film boiling).

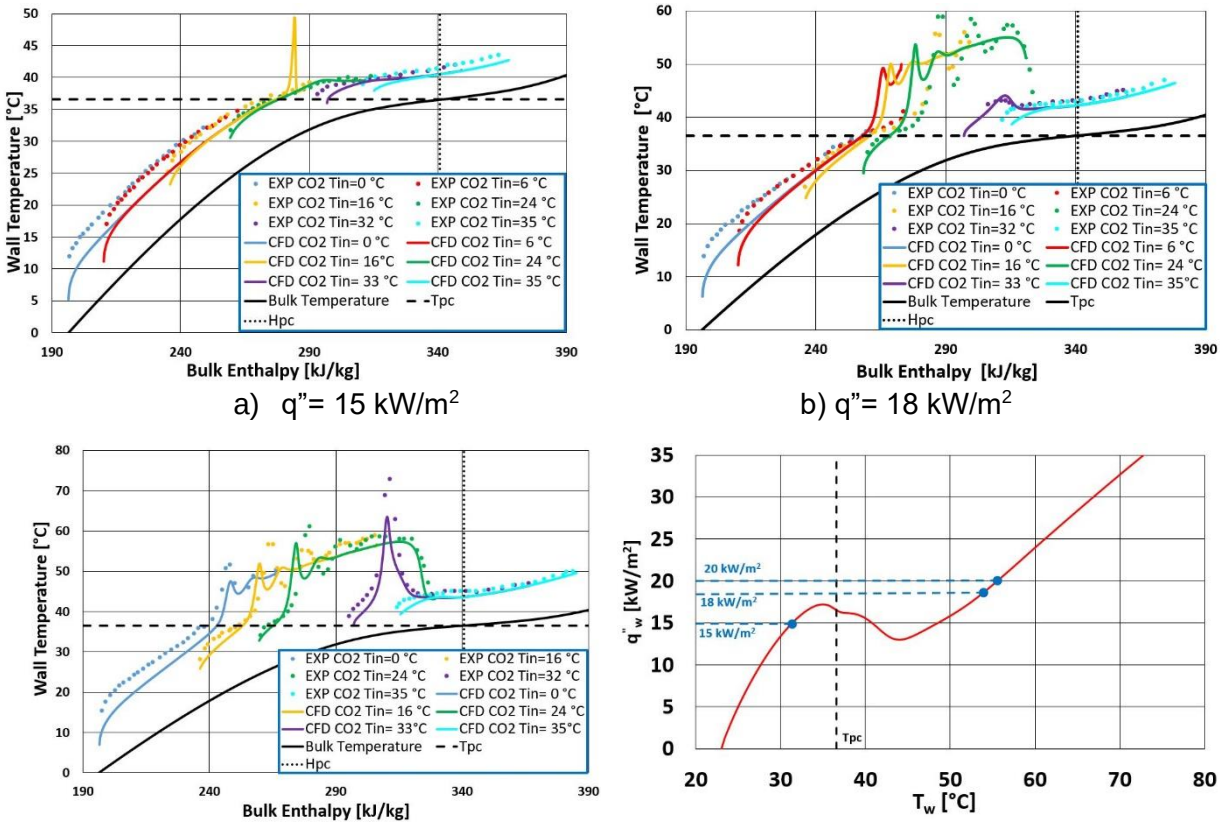

a) q"= 15 kW/m^2 b) q"= 18 kW/m^2

c) q"= 20 kW/m^2 d) pseudo-Nukiyama curve

Figure 83. Experimental and predicted trends of wall temperature for Kline's data with CO_2 for upward flow at 8.35 MPa, ID=4.6 mm and G = 300 kg/(m^{2}s) and corresponding pseudo-Nukiyama curve

Though the involved phenomena at subcritical and supercritical pressures are definitely very different, the analogy is really striking and suggests to make use of similar modelling tools for both conditions. In particular, while at subcritical pressure CHF is caused by hydrodynamic instabilities that cause the wall surface to be exposed to vapour, in the case of supercritical pressure fluids the main phenomenon causing the departure from an efficient cooling of the wall is mostly related to laminarisation. Nevertheless, the perspective to use similar boiling and pseudo-boiling curves in system codes to cope with heat transfer deterioration, in continuity with the phenomena occurring at lower pressures, represents an interesting perspective for future code development, calling for further efforts in refining the present capabilities to identify criteria for the onset of deterioration and for heat transfer restoration.

A sensitivity analysis was made in order to consider the effect of flow rate on the shape of the obtained pseudo-Nukiyama curves. The results are shown in Figure 84, highlighting an expected behaviour of lower and lower relevance of the negative slope branch of the curve with increasing flow rate, supporting the idea that the phenomenon depicted by the CFD code is a laminarisation effect, which tends to be cancelled by a sufficiently large flow rate as to make forced convection to prevail over mixed convection phenomena.

Having in mind the classical description of boiling heat transfer phenomena from the textbook by Collier and Thome (1999) (see Figure 85), an even more compelling similarity was

searched for and was found in a 3D representation of heat transfer deterioration as a function of relevant variables.

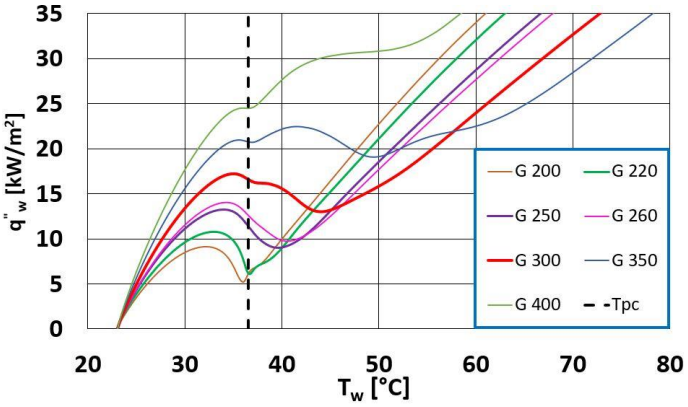

Figure 84. Pseudo-Nukiyama curves obtained by the CFD model for Kline's experimental apparatus with CO_2 for upward flow at 8.35 MPa, ID=4.6 mm and different values of G, expressed in kg/(m^{2}s)

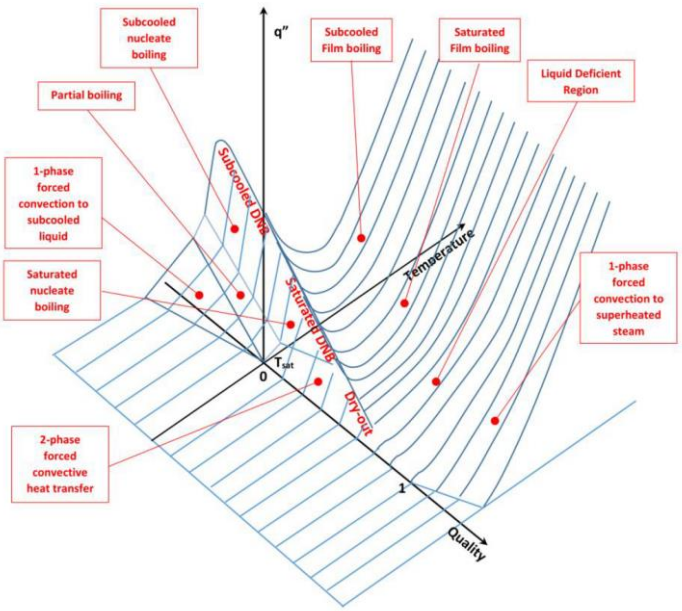

Figure 85. Classical 3D description of boiling heat transfer phenomena at subcritical pressure as a function of quality, wall temperature and heat flux (see Collier and Thome, 1999)

Figure 86 presents results obtained by running several analyses with constant wall temperatures at different levels, obtaining a 3D representation of the wall heat flux as a function of wall temperature and bulk dimensionless enthalpy. In the analogy with subcritical phenomena, dimensionless enthalpy replaces equilibrium quality, representing in a parametric way the bulk fluid conditions.

As it can be noted, the obtained surface presents interesting characteristics, including pseudo-Nukiyama curves at constant dimensionless bulk enthalpy, a ridge at the onset of deterioration and a ridge for heat transfer restoration, the latter occurring close to $h^*_{bulk} = 0$, i.e., where the bulk fluid approaches the pseudo-critical conditions.

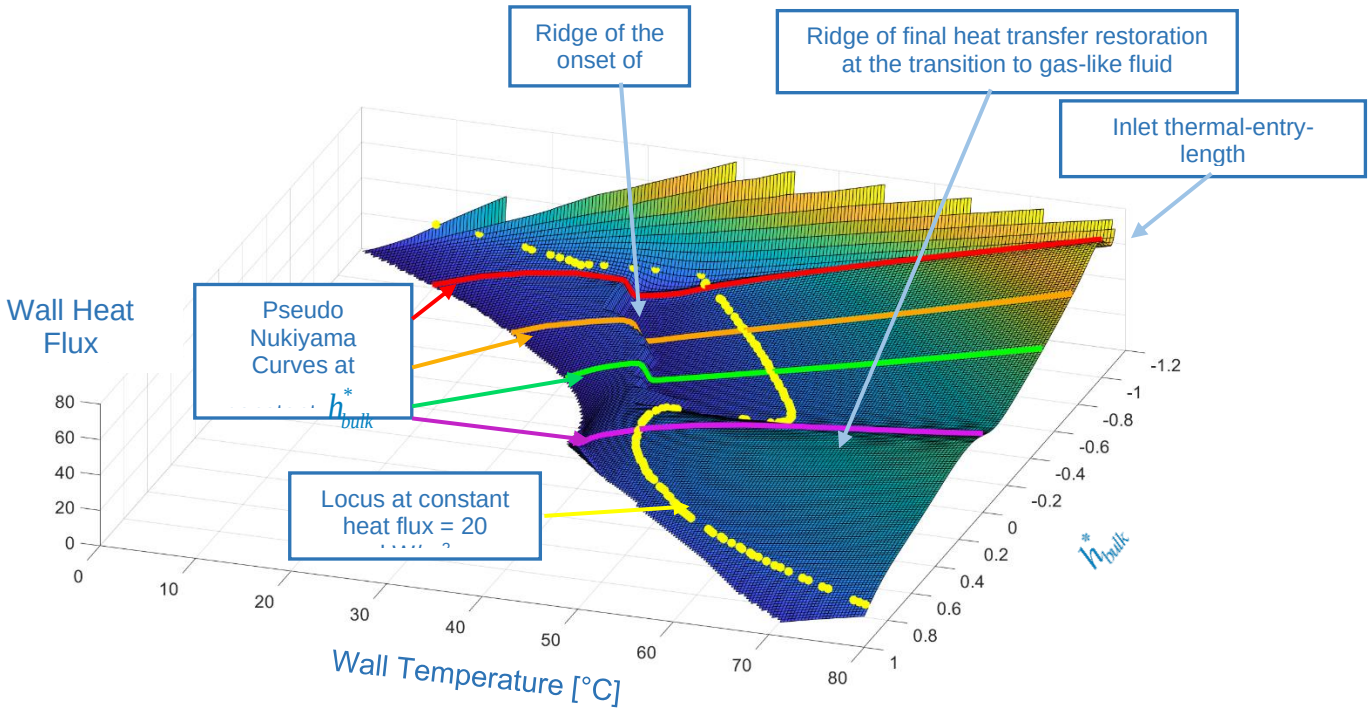

Figure 86. 3D representation of supercritical pressure heat transfer deterioration phenomena obtained processing results obtained for Kline's experimental apparatus with CO_2 at 8.35 MPa for G = 300 kg/(m^{2}s) and Tin= 0 °C: continuous surface form

These phenomena can be demonstrated to occur non only for CO_2 but also for water, something demonstrated via the application of the fluid-to-fluid similarity theory. Other details of relevance to draw conclusions about the possible universality of the observed phenomena are described in Pucciarelli et al. (2022).

It is here remarked that these developments are interesting for the ECC-SMART project since they pave the way for the establishment of a tighter and tighter analogy between subcritical pressure and supercritical pressure heat transfer phenomena that may provide a base for a theory of supercritical pressure fluids sufficiently complete as the one adopted for two-phase flow, making use of modelling tools to be implemented in system codes having similar features as the ones for two-phase flow conditions.

2.1.7 Considerations on the role of CFD in the work made by UNIPI

The work performed by the University of Pisa in the frame of the ECC-SMART project heaviliy relied on CFD modelling capabilities. The Algebraic Heat Flux Model (AHFM) developed by A. Pucciarelli in the frame of his PhD work (Pucciarlli, 2017) constituted the basis for assessing ideas for understanding and modelling deteriorated heat transfer. Without this essential tool that made possible a step forth in our modelling capabilities, it would have been nearly impossible to draw sound conclusions about a number of aspects, including the fluid-to-fluid similarity theory, the validation of the idea of pseudo-Nukiyama curves and the understanding of deteriorated heat

transfer mechanisms that guided the inquiry into the proper way of proposing heat transfer correlations that covered a considerable part of the University of Pisa contribution in this report.

CFD analyses were also provided by the University of Pisa for addressing the International Benchmark on SuperCritical Thermal Hydraulics (IBSCTH) proposed inter alia by the Nuclear Power Institute of China (NPIC), which was reported in D3.2. In that case, owing to the complexity of the involved problems, classical two equations turbul[i]4ent models were adopted, obtaining results that could be improved in case of a second phase of the Benchmark exercise.

It must be also mentioned that in the frame of the ECC-SMART project the University of Pisa for the first time coupled the AHFM model with the rough wall treatment developed in previous work (Ambrosini et al., 2015) that was adopted to deal with experimental data for assessing the effect of roughness on heat transfer at supercritical pressure. This is the subject of the further discussions reported in sections 5.1 and 6.2.

2.2 CONTRIBUTION BY BME

The BME research group performed many different complex CFD analyses using the commercial CFD software package "Ansys CFX" within the framework of ST3.3.1. The basic strategy applied was to start the CFD investigation with the simplest geometry (straight, smooth-bore tube), to continue with more complex geometry (2×2 rod bundle) and, based on the experience gained, to proceed step by step to the most complex geometry (the horizontally installed SCW-SMR fuel assembly):

1. Ansys CFX model validation for **upward SCW flow** in smooth bare, straight **tubes** heated by direct current through the tube wall (simplest geometry, used experiment: “Shitsman 1963” (Shitsman 1963));
2. Ansys CFX model validation to **upward and horizontal SCW flow** in smooth-bore, straight **tubes** heated by direct current (DC) through the tube wall (simplest geometry, used experiment: “Yamagata 1972” (Yamagata et al 1972));
3. Ansys CFX model validation to **upward SCW flow** in smooth-bore, straight **2×2 rod bundles** heated by DC through the rod wall in the framework of the IBSCTH international benchmark (more complex geometries, CFD modelling on three different geometries of 2×2 rod bundles, used experiments provided by the Nuclear Power Institute of China (NPIC) and Xi'an Jiaotong University (XJTU) (NPIC 2021));
4. CFD modelling of the **horizontal SCW flow** in the **SCW-SMR fuel assembly** (FA) by Ansys CFX with and without wrapped wire spacers (WWS) (most complex geometry based on the pre-pre conceptual design (PPCD, see Schulenberg and Otic 2021) of the SCW-SMR);
5. Coupled calculations with Ansys CFX-Serpent Monte-Carlo code on the **horizontal SCW flow** in the **FA of the SCW-SMR** (most complex geometry based on the PPCD of the SCW-SMR).

2.2.1 Ansys CFX model validation to upward SCW flow in tubes

According to the basic strategy of BME described above, the CFD analysis series was started with a CFD validation on the simplest geometry (straight, smooth-bore tube cooled by upward SCW flow) using the well-known results of the Shitsman experiment (Shitsman 1963).

4

2.2.1.1 Description of the Shitsman experiment

The results of the Shitsman experiment were used to validate the CFX code and for the parametric study of wall roughness. The test section was a straight, smooth-bored tube of a certain length. The forced convection of water flowing upward inside a vertically installed tube with an electrically heated center section was measured around the pseudo-critical temperature of the SCW. The test section (measured tube) consisted of three sections (see Figure 87): the unheated inlet section - where the hydraulic boundary layer grew (referred to as the "Unheated wall"), the heated middle section - where the measurements were performed (referred to as the "Heated wall"), and the outlet section - where the flow pattern and temperature field became more homogeneous (referred to as the "Discharge wall"). Measurements were made at pressures above the critical pressure and a deteriorated heat transfer (DHT) case was selected. Figure 87 shows not only the parts of the test section, but also the boundary conditions (BCs) applied to the CFD model.

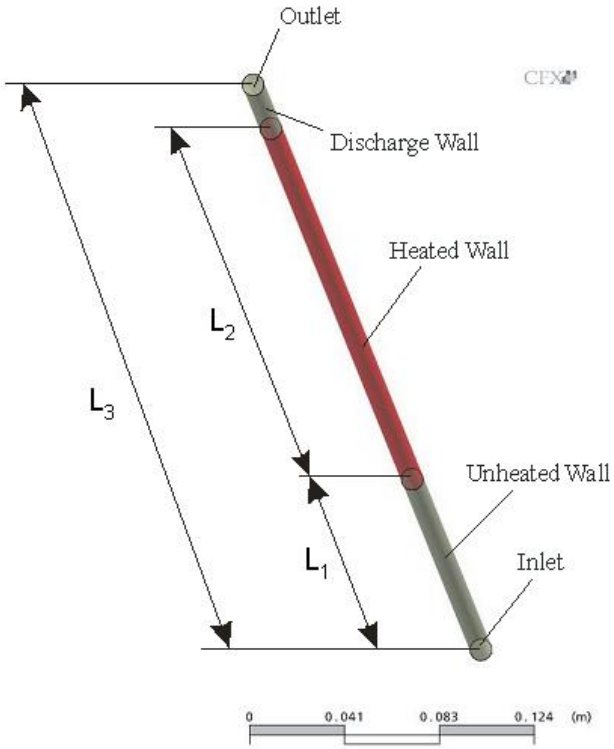

Figure 87. The geometry of the test section with the applied BCs of the CFD model

The used boundary conditions (defined by the published experimental conditions) and the geometry parameters are shown in Table 11.

Table 11. Examined experimental conditions and geometry for the deteriorated heat transfer case of Shitsman 1963

Parameters	p [bar]	T_{pc}[°C]	q_w [kW/m^2]	G [kg/m^2/s]	D_{in}[mm]	L_1[mm]	L_2[mm]	L_3[mm]	q_w/G
Shitsman 1963	233	379.1	319.9	430	8	783	1500	2495	0.74

2.2.1.2 The computational domain and boundary conditions

Since it is not necessary to discretize the full circumference of the circular test sections reported in recent studies (Kiss 2018) to model the thermal hydraulics of SCW in straight pipes, a 3 degree sector was modelled in this CFD analysis (see Figure 88).

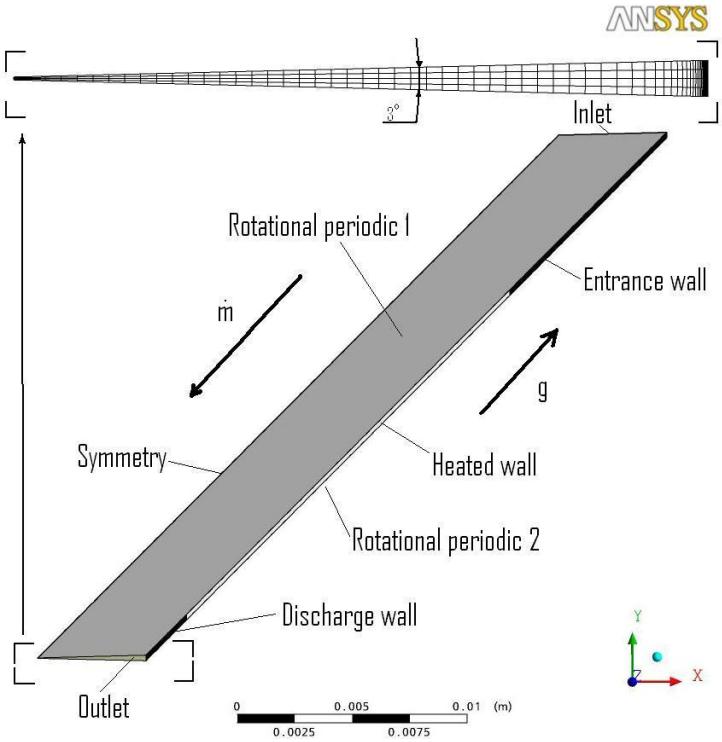

Figure 88. The schema of the CFD model

The fluid dynamics models represent single-phase, steady-state, turbulent, buoyant flow (the effect of buoyancy on the turbulence is not considered) with the following details. Due to the important role of all three tube sections, the CFD model also includes the entire tube length (see Figure 88) with the geometry parameters shown in Table 11. The thickness of the tube wall was modelled (so it is a conjugate heat transfer (CHT) CFD model) and the inner smooth bore (as a reference case with R_a = 0 µm) or rough wall (as rough cases of the parametric study with R_a = 1, 5, 10, 50, 100 µm) of the tube was modelled with a no-slip wall boundary condition. The wall of the tube was divided into three parts: the “Entrance” and the “Discharge wall” parts were adiabatic while the “Heated wall” was modelled with imposed constant heat flux. This simplification is appropriate because the thermal conductivity of the tube wall was relatively high and the heat capacity of the wall did not play an important role in the experiment. Due to the simple geometry block structured hexahedral 3D mesh was generated with fine boundary layer resolution (the dimensionless wall distance is $y_1^+ \approx 0.01$) near the wall for all cases (see Figure 88). The geometries were constructed and the meshes were generated using the Ansys ICEM 23 R1 program. The CFD modelling was performed in the CFD program Ansys CFX 23 R1.

An appropriate boundary layer mesh resolution and mesh parameters were selected based on the previously performed mesh sensitivity study (see Kiss 2018). The SST turbulence model was used for all cases. The area averaged y^+ on the walls of the heated sections for each case and the total number of nodes are shown in Table 12.

Table 12. Dimensionless wall distance (y1+) and total number of cells

Case	y^+ on Heated wall	Number of numerical cells

Shitsman 1963	0.01	778,500

The mass flow rate and inlet bulk fluid temperature (T_{in}[°C]) were specified at the "Inlet" BC (see Table 13). The "Entrance and Discharge walls" were modelled as smooth adiabatic walls. The heat flux (q_w [kW/m^2], see Table 11) was set at the smooth-bore or rough "Heated wall". The average static pressure at the "Outlet" boundary was set to -10,000 Pa. A small symmetry plane (modelled by Symmetry BC) at the tube axis was used for mesh generation purpose. The remaining two boundary surfaces were coupled with a rotational periodic interface (see Figure 88).

Table 13. The BCs and uncertainties of temperature measurements.

Case	T_{in}[°C]	T_{out}[°C]	Uncertainty of temperature measurement	m [kg/s]
Shitsman 1963	324.9	377.2	+/- 2-3 °C	0.000194

2.2.1.3 Results and discussion of the Shitsman validation

Figure 89 shows the result of this validation and parametric study by distributions of wall temperature along the modelled length for the reference case (R_a = 0 µm) and for the rough wall cases of the parametric study (R_a = 1, 5, 10, 50, 100 µm). As it can be seen, the two DHT peaks of wall temperature (see the measured wall temperature values (~660°C and ~552°C) at Z = 1.1 m and 1.6 m as two values of "Shitsman 63 Case 08 exp. result" in Figure 89) were predicted qualitatively well, quantitatively less accurately by the results of the Ansys CFX model of the reference case (see the red coloured distribution "Smooth wall (F2 grid size)" in Figure 89). The parametric study showed that the consideration of the wall roughness dramatically influences the distribution of the wall temperature: the higher the value of R_a the lower the peak value(s) of the wall temperature (see the R_a = 1, 5 and 10 µm). If the value of R_a increases up to 50 µm or higher, then the heat transfer can be classified as normal heat transfer (NHT) instead of DHT (see the R_a

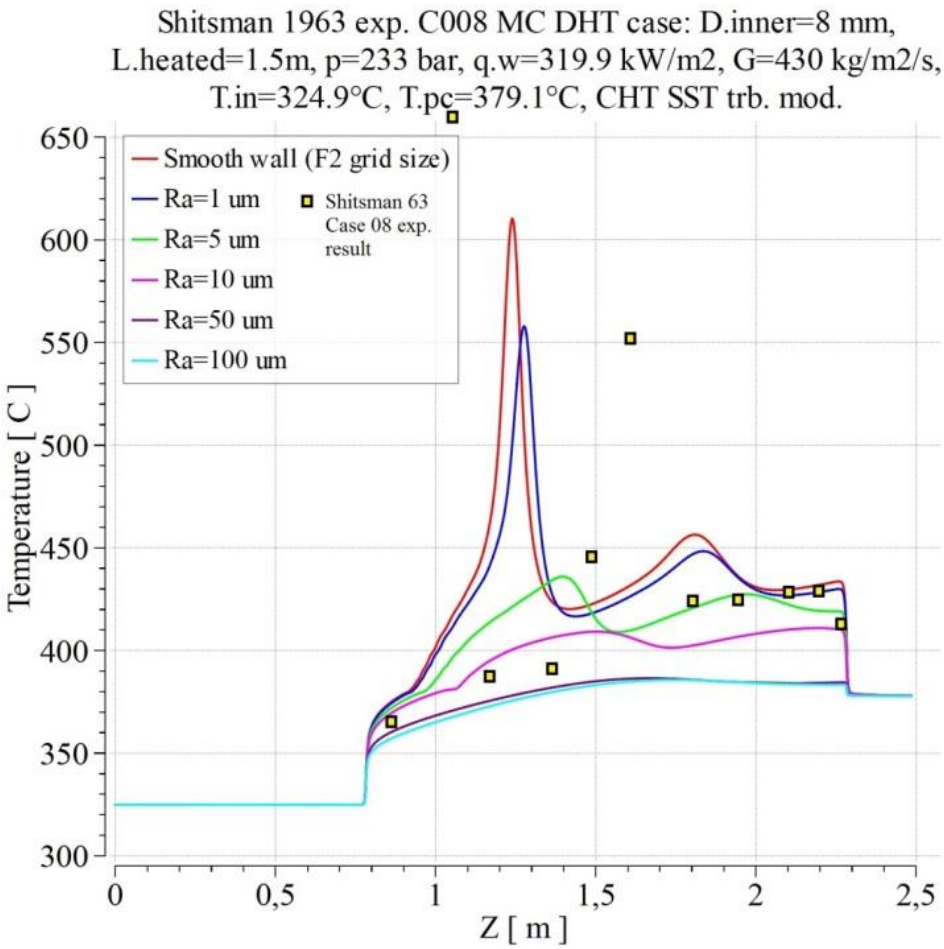

Figure 89. The result of the parametric study – the wall temperature along the modelled length for the reference case (R_a = 0 μm) and the rough wall cases (R_a = 1, 5, 10, 50, 100 μm)

2.2.2 Ansys CFX model validation to upward and horizontal SCW flow in tubes

The EU-funded H2020 Research and Innovation Action (RIA) Joint European Canadian Chinese Development of Small Modular Reactor Technology (ECC-SMART 2020) aims to assess the feasibility and identify the safety characteristics of an intrinsically and passively safe small modular reactor (SCW-SMR) cooled by supercritical water (SCW). The main objectives of the project are to define the design requirements for the future SCW-SMR technology, to develop the pre-licensing study together with the guidelines for the safety demonstration in further development stages of the SCW-SMR concept, including the methodologies and tools to be used, to identify the main obstacles for the future licensing of SMRs and to propose a strategy for this process. To achieve these objectives, specific technical knowledge gaps for the future smooth licensing and implementation of the SCW-SMR technology will be defined and assessed (in particular, the behaviour of materials in the SCW environment and under irradiation, the validation of codes and the design of the reactor core will be developed, evaluated by simulation and investigated experimentally). The consortium and the scope of the project have been defined according to the joint research activities under the umbrella of the International Atomic Energy Agency (IAEA), Generation-IV International Forum (GIF) (ECC-SMART 2020).

The active core of the original Supercritical-Water-Cooled Reactor (SCWR) is vertically oriented, while being moderated and cooled by downward and (mostly) upward SCW flows (GIF 2024), (Schulenberg and Starflinger 2012). For this reason, the thermal hydraulics of vertical SCW

flows has been extensively studied by experimental and numerical (mainly CFD analysis) methods (see e.g.: Schulenberg and Starflinger 2012, Pioro and Duffey 2007, Kiss 2018 and Rohde et al. 2016). The numerical analysis of horizontal SCW flows has been rare for the above described reason.

BME is involved in all scientific-technical work packages (WPs) of ECC-SMART project and has important tasks in the thermal-hydraulic work package (WP3) through computational fluid dynamics (CFD) and system code analysis (ECC-SMART 2020). Due to the orientation of the SCW-SMR active core, which is horizontal according to the available pre-pre-conceptual design (pre-PCD) (Schulenberg and Otic 2021), an essential need has arisen to assess how to correctly model the horizontal SCW flow using the Reynolds-averaged Navier-Stokes (RANS) method in CFD codes. This subtask is presented in this section.

The computer-aided design (CAD) geometry and numerical grids were created in Ansys ICEM CFD, while the CFD models were developed in the commercial Ansys CFX software package. In the first part of the CFD analysis, a systematic numerical grid sensitivity analysis was performed to select the most appropriate near-wall (boundary layer) numerical grid structure and the appropriate axial and circumferential grid resolutions. Furthermore, an additional sensitivity analysis on the effect of wall roughness on the numerical results was carried out, supported by the comparison between experimental values and simulation results obtained with different wall roughness settings (different equivalent sand grain roughness values). The CFD results with the most appropriate numerical grid and wall roughness settings were compared with the experimental results for both horizontal and vertical upward flow cases. The lessons learnt from this validation were used to gain the necessary insight to properly set up and fine-tune the CFD models of the fuel assemblies (FAs) of the SCW-SMR concept.

2.2.2.1 The Modelled Experimental Flow Cases

This CFD analysis, using the authentic SCW measured data from the well-known Yamagata experiment (Yamagata et al. 1972) (abbreviated as “Y1972” in the captions of most of the figures), was performed in order to enable the sufficiently accurate CFD modelling of the thermal hydraulics of SCW flowing horizontally through the FAs of the SCW-SMR.

2.2.2.1.1 The Yamagata experiment

The aim of the Yamagata experiment (Yamagata et al. 1972) was to promote the development of fossil-fired SCW boilers. The experiment is still considered to be one of the best sources of SCW data available in the field (Pioro and Duffey 2007, Kiss 2018). The experiment was conducted using a specially designed apparatus (Yamagata et al. 1972) in which the SCW, after numerous preparatory steps, mainly pre-heating, homogenisation and chemical treatments, was passed through the test section (vertically or horizontally installed straight pipe) where the SCW flow was heated by the pipe wall. The pipe wall of the test section was heated by the direct current of low voltage electric heater (Yamagata et al. 1972).

2.2.2.1.2 The test section of the Yamagata experiment

The test section is 1500 mm long with an inner tube diameter (Din) of 7.5 mm and the temperature is measured at every 100 mm. The only exception is at the inlet and outlet where there is a distance of 200 mm to the nearest thermocouple. The accuracy of the measured temperature values is within 1°C (not shown in the figures as it is too small), the power and mass flow rates have a maximum error of 1% (Yamagata et al. 1972). The experiment was conducted over a wide range of pressures, temperatures, mass flow rates, heat fluxes and flow directions. This particular test was chosen for the CFD model validation purposes due to the wide range of data sets available and their high accuracy.

2.2.2.2 The Developed CFD Models

The commercial CFD software Ansys CFX developed by Ansys® was used to build and simulate the CFD models for the validation cases. Due to the simplicity of the geometry, which is a simple heated tube, it was decided to use a structured mesh with an O-grid to properly simulate the boundary layer adjacent to the heated wall. The CFD calculation consisted of two steps for each validation case. In the first step, a CFD calculation was performed with the most robust k-ε turbulence model and its results were used as a reference state for the second step calculation (to improve and accelerate the convergence of the second CFD calculation). Then, in the second step, the final calculation was performed with the more advanced Shear Stress Transport (SST) turbulence model (often used for SCW tube flows Kiss 2018, Rohde et al. 2016) to obtain the highly accurate final result.

2.2.2.2.1 The geometry

As previously discussed, the test section geometry is a simple 1500 mm long, straight smooth bore heated tube. In order to obtain an undisturbed and homogeneous SCW flow, a 750 mm (100 Din) long so-called entrance tube part was applied and modelled upstream of the heated section, and a 300 mm (40 Din) long so-called discharge tube part downstream of the heated section (Figure 90).

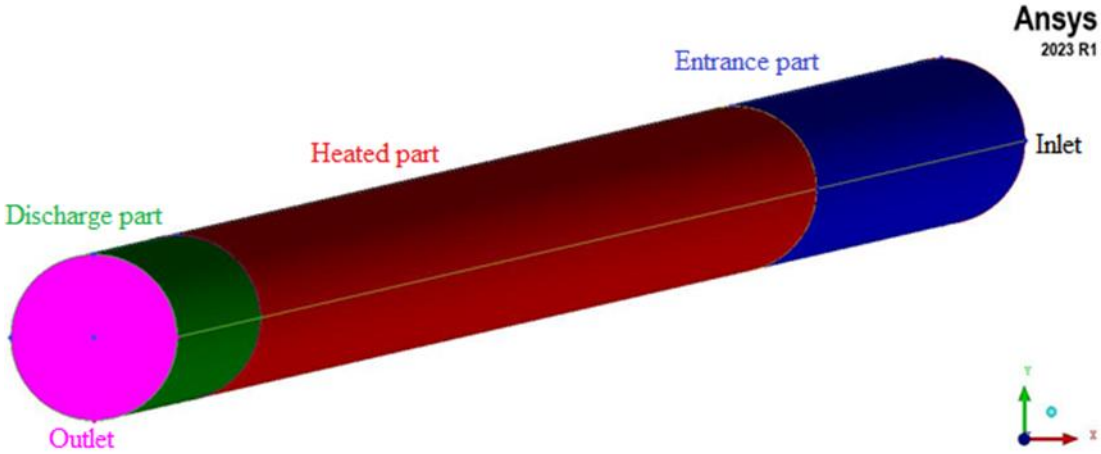

Figure 90. The geometry model of the validation cases in the Ansys ICEM CFD

These two additional sections have adiabatic walls with the same specifications as the heated section and are used to homogenise the entry and exit of the SCW flow and to prevent any perturbations that would be caused by the too close positions of the inlet and outlet boundary conditions to the investigated heated tube part. The geometry model of the CFD models developed in the Ansys ICEM CFD software is shown in Figure 90.

2.2.2.2.2 The applied boundary conditions

A total of eight experimental cases were simulated in this CFD analysis (see in Table 1). Four of them were horizontal and four of them were vertical upward SCW flows. Four different heat flux scenarios (e.g.: “q233”) were investigated for both flow directions. Due to the constant heat flux values of the heated section were published for the experiment, it was decided not to model the wall (so these are not conjugate heat transfer (CHT) models with specified volumetric heat source in the wall), instead a simple wall heat flux boundary condition (BC) was used at the inner surface of the tube wall (Table 1). The reference pressure and mass flux were identical for all cases: it is 24.5 MPa and 1260 kg/m2/s respectively (Table 14). The mass flux was specified after conversion to the mass flow rate value (0.0556651 kg/s), and this BC implies a constant average flow velocity of 1.885 m/s at the inlet surface. The flow field can develop along the

unheated entrance part, so this constant inlet velocity BC does not affect the thermal hydraulics of the studied heated central part of the computational domain. The inlet temperatures (Table 1) were also specified at the inlet BCs for all CFD models as well. In terms of inlet turbulence, 5% inlet turbulence intensity was specified for all CFD models. Regarding the wall roughness, a smooth wall condition (Ra = 0 μm) was applied for all solid walls except for the models used in the sensitivity study of the wall roughness effect.

Table 14. The applied boundary conditions of the eight experimental cases (Yamagata et al. 1972)

BC parameter\ Exp. case:	H233	H465	H698	H930	U233	U465	U698	U930
Flow direction	Horizontal				Vertical upward			
Heat Flux [kW/m^2]	233	465	698	930	233	465	698	930
Reference pressure [MPa]	24.5							
Mass flux/mass flow rate:	1260 kg/m^2/s / 0.0556651 kg/s							
Inlet temperature [°C]	330.5	291.9	293.9	293.9	330.5	334.4	334.4	334.4

2.2.2.2.3 Sensitivity studies

During the Mesh Sensitivity Study (MSS), three mesh settings and parameters were investigated as shown in Figure 91.

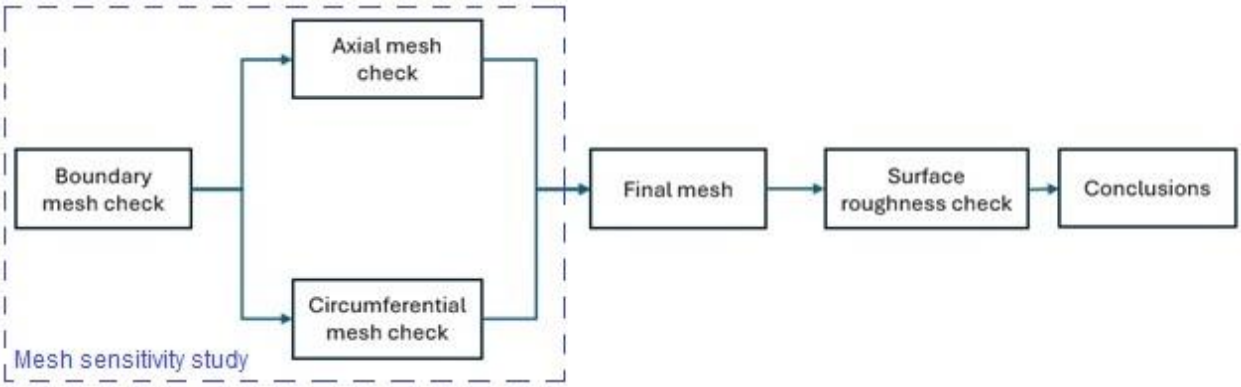

Figure 91. The process of the sensitivity studies

These parameters are the boundary layer mesh settings, the size/number of the circumferential-, and the axial elements/nodes. A further parameter investigated in the sensitivity studies was the effect of wall roughness (with different artificial wall roughness values that modelled the assessed R_a values). This was the value of the equivalent sand grain roughness size. The sensitivity studies were carried out in the order shown below (see Figure 91), and only one settings or parameter was changed at a time, leaving all other BCs and mesh/CFD model settings unchanged. The results of the boundary layer study were used for the circumferential and axial studies, but these studies were carried out in parallel to determine which mesh discretisation was more important, the component which is parallel or normal compared to the direction of SCW flow.

2.2.2.2.4 Sensitivity study of the boundary layer mesh

For the sensitivity analysis of the effect of the boundary layer mesh (BLM), three numerical meshes with three different resolutions were created. These meshes were named as: BLM01, BLM02 and BLM03. The number in their names refers to their resolution quality (the lower the number the finer the near wall BLM). The detailed parameters of these meshes are given in Table 15 below.

Table 15: Details of the three different boundary layer numerical meshes.

Name	Resolution	Δy_1 [μm][5]	Growth ratio [-][6]	Aspect-ratio [-][7]	# of radial nodes [pcs]
BLM01	High	0.15	1.2	3196	50
BLM02	Mid	0.3	1.2	1598	40
BLM03	Low	0.6	1.2	799	35

As a starting point, the axial resolution was chosen to be one node every half millimetre, giving a total of 6103 nodes (601 for the entrance, 4001 for the heated and 1501 for the discharge part) and the number of the circumferential nodes was chosen to be 21×21 nodes.

2.2.2.2.5 Sensitivity study of the circumferential resolution

For the sensitivity analysis of the effect of the circumferential mesh (CIRM), three numerical meshes with three different resolutions were created. These meshes were named as: CIRM01, CIRM02 and CIRM03 (Table 16).

Table 16: Details of the three different circumferential numerical meshes

Name	Resolution	Number of nodes ($n_{n,i}$) along ¼/full circumference [pcs]
CIRM01	High	41/161
CIRM02	Mid	21/81
CIRM03	Low	11/41

The number in their names refers to their resolution quality (the lower the number the finer the CIRM). It is important to note that unlike the BLM study, where the initial mesh was generated without any prior input, the CIRM study had the selected BLM mesh available. It was decided that this pre-existing mesh would be used as the reference mesh for the study. Therefore, a dual direction method was followed where the resolution of the circumferential parameter compared to the reference mesh was increased and decreased. In this way the three meshes were created, where CIRM02 would be the reference mesh, which would also be the same mesh as BLM01 based on the conclusions of the BLM study (details will be discussed later). The details of these meshes are given in the table below (see Table 16).

2.2.2.2.6 Sensitivity study of the axial resolution

For the sensitivity analysis of the effect of the axial mesh resolution (AXM), three numerical meshes with three different, but equidistant (constant axial size of the elements, ΔZ_i [mm]) resolutions were created. These meshes were named as: AXM01 (ΔZ_{AXM01} = 0.25 mm), AXM02 (ΔZ_{AXM02} = 0.5 mm) and AXM03 (ΔZ_{AXM03} = 1 mm). The number in their names refers to their resolution quality (the lower the number the finer the AXM). Identically, as it was discussed in the CIRM study, AXM02 is the reference mesh for this study (this mesh is also the same as BLM01 and therefore CIRM02), while AXM01 and AXM03 represent an increased and decreased axial

[5] This is the height of the first numerical grid layer adjacent to the solid wall.
[6] This is the growth ratio of the height of the layers in the BLM (e.g.: ratio of the heights of the nth and n-1th layers).
[7] This is the maximum ratio of the longest and shortest edges of all numerical cells (from the whole mesh). These are the worst values for all meshes used, so further aspect ratios are not shown in the paper.

mesh resolution respectively. The details of these meshes are given in the table below (see Table 17).

Table 17: Details of the three different axial numerical meshes

Name	Resolution/ΔZ_j [mm]	Number of axial nodes [pcs]
AXM01	High/0.25	10,201
AXM02	Mid/0.5	5101
AXM03	Low/1	2551

2.2.2.2.7 Sensitivity study of the wall roughness

On completion of the mesh sensitivity study, the 'final mesh' was created based on the findings of the mesh sensitivity study. This 'final mesh' (details will be discussed later) was used for the wall roughness study. Five different wall roughness cases were analysed, excluding the smooth wall case which was the default option in the mesh sensitivity studies (the results of the smooth wall case were also compared). The arithmetic mean of the profile height deviations from the mean line (R_a) was modelled by an artificial wall roughness specified by average sand grain height values. The five new rough wall cases were named Ra-X, where Ra- is the average sand grain height and X- is this height in µm. Details of these cases are given in the table below (see Table 18).

Table 18: The used average sand grain height values

Name	Average grain height [µm]
Ra-0.5	0.5
Ra-1.0	1.0
Ra-2.0	2.0
Ra-5.0	5.0
Ra-10.0	10.0

2.2.2.3 Results and discussion

The results, which are a good representation of the findings of each sensitivity study, are presented in the order of their mention in the previous chapter. The distributions of wall temperature versus bulk fluid enthalpy ($T_w(h_b)$) have been compared for each study in a figure showing the numerical and the experimental results mostly for the SCW-SMR relevant horizontal cases.

2.2.2.3.1 Results of the boundary layer mesh sensitivity study

The results show that the boundary layer mesh (BLM) has only a small quantitative effect on the CFD results and does not affect the qualitative nature of the calculated $T_w(h_b)$ (see Figure 92). The quantitative effect becomes stronger in the horizontal cases with higher heat flux (e.g.: H698 (Figure 92./b) and H930), but even there the effect is still very moderate. For the low heat flux cases (H/U233, H/U465) the CFX models underestimate the $T_w(h_b)$ (see Figure 92./a), while for the high heat flux cases (H/U698 and H/U930) they tend to overestimate it (see Figure 92./b). In all cases the BLM01 mesh results are quantitatively the closest to the experimental data (Figure 92), and quantitatively, the most accurate simulated results (just barely below/above the measured $T_w(h_b)$) have been calculated for the H698 case (Figure 92./b).

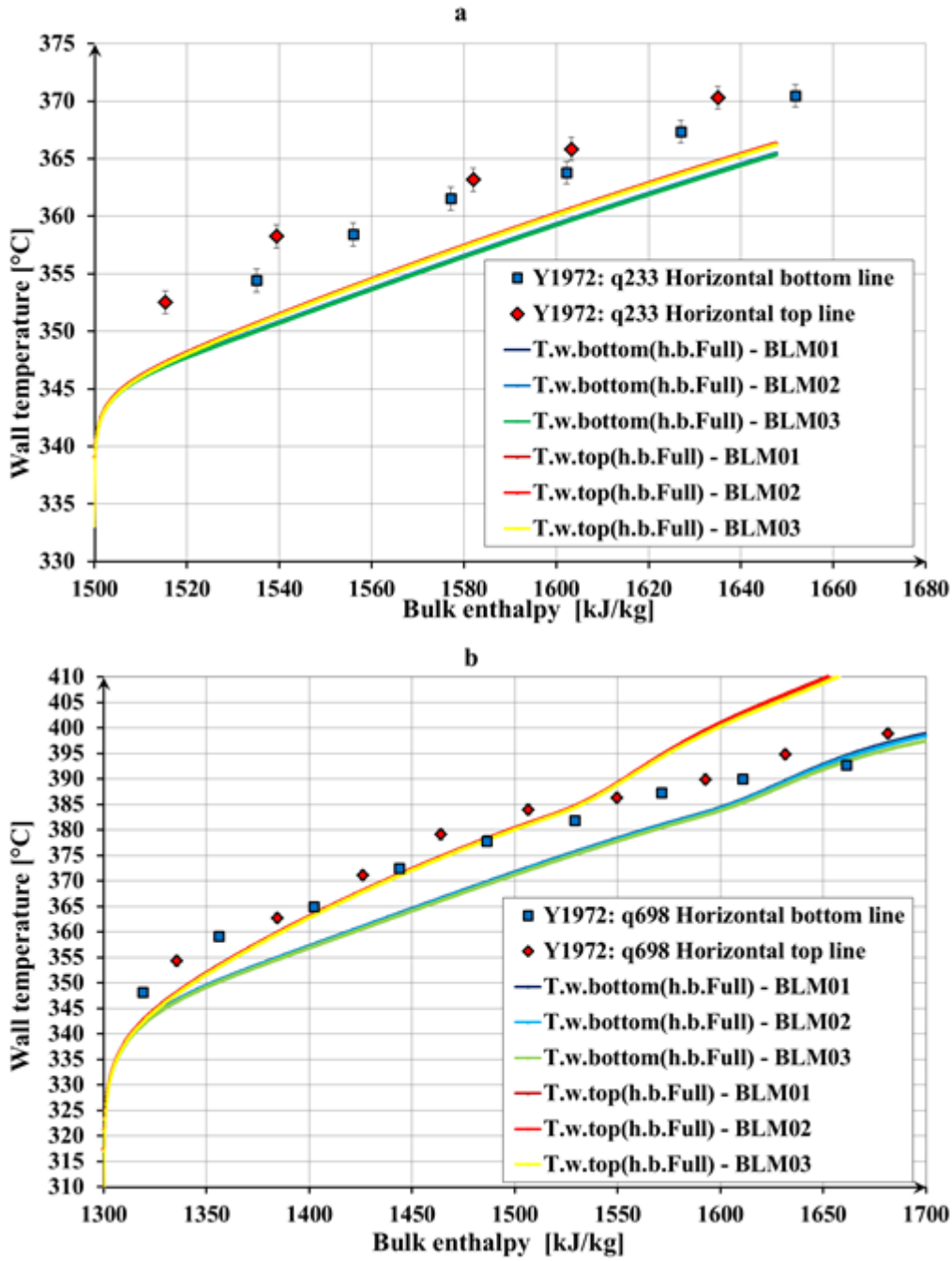

Figure 92. Comparison of $T_w(h_b)$ for the BLM sensitivity study (a., H233, b., H698 case)

Qualitatively, the CFD results give back the higher $T_w(h_b)$ along the top line (caused by the known strong buoyancy effect perpendicular to the main flow direction in horizontal flows Pioro and Duffey 2007, Yamagata et al. 1972) compared to the bottom line distributions. Based on the results, the highest quality mesh (BLM01) was conservatively selected for further CFD modelling. Although the investigated parameters of the boundary layer mesh have only a small influence on the numerical results, increasing the resolution of this local part of the mesh requires only a small amount of additional computational resources and is therefore recommended.

2.2.2.3.2 Results of the circumferential resolution sensitivity study

For the sensitivity study of the CIRM resolution, a base mesh (CIRM02 with $n_{n,CIRM02}$=81, identical to BLM01) was used alongside a finer (CIRM01, $n_{n,CIRM01}$=161) and a coarser (CIRM03

with $n_{n,CIRM03}$=41) circumferential resolution. It was concluded, that the CIRM has a significant effect on the accuracy of the results, both qualitatively and quantitatively. This effect is so significant that if the CIRM resolution is too low, the simulation results will be completely unusable as they will predict a fake deterioration of the heat transfer (DHT) (see Figure 93 and Figure 94).

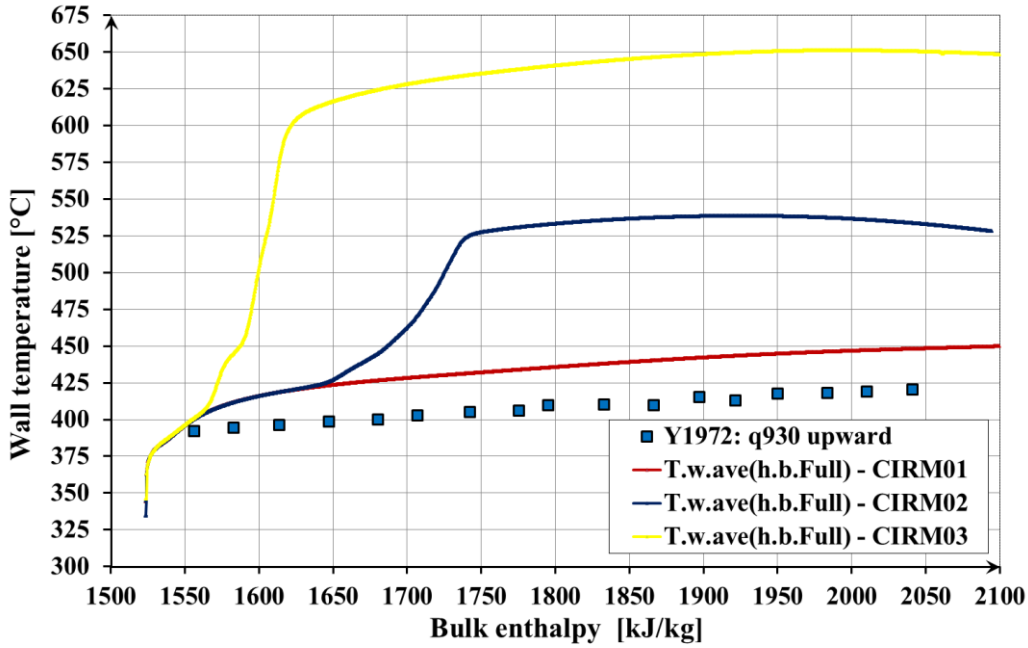

Figure 93. Comparison of $T_w(h_b)$ for the CIRM sensitivity study (U930 case)

The CFD models with low CIRM resolution (CIRM03) give completely nonsensical results, immediately deviating from the upward experimental data (Figure 93) or predicting fake DHT in the first half of the tube in the horizontal case (Figure 94), while the CFD models with medium CIRM resolution (CIRM02) are somewhat able to describe the real $T_w(h_b)$ for both upward and horizontal cases, but still fail because they predict a fake DHT event (see Figure 93 and Figure 94) as well.

Only the CFD models with high CIRM resolution (CIRM01) were able to predict results that were sufficiently similar to the experimental data (see Figure 93 and Figure 94). Quantitatively, the higher CIRM resolution reduces the temperature underestimation at lower heat fluxes and reduces the overestimation at higher heat fluxes, resulting in more realistic CFD results. Based on this, it was concluded that the CIRM resolution is a critical parameter for SCW modelling and that there are two key parameters that determine how much CIRM resolution is needed. These two parameters are the direction of the SCW flow and the heat flux. Horizontal flow modelling requires higher CIRM resolution than vertical, and higher heat flux cases require higher CIRM resolution than lower heat flux cases. This relationship is best illustrated by a 2×2 matrix in Table 19.

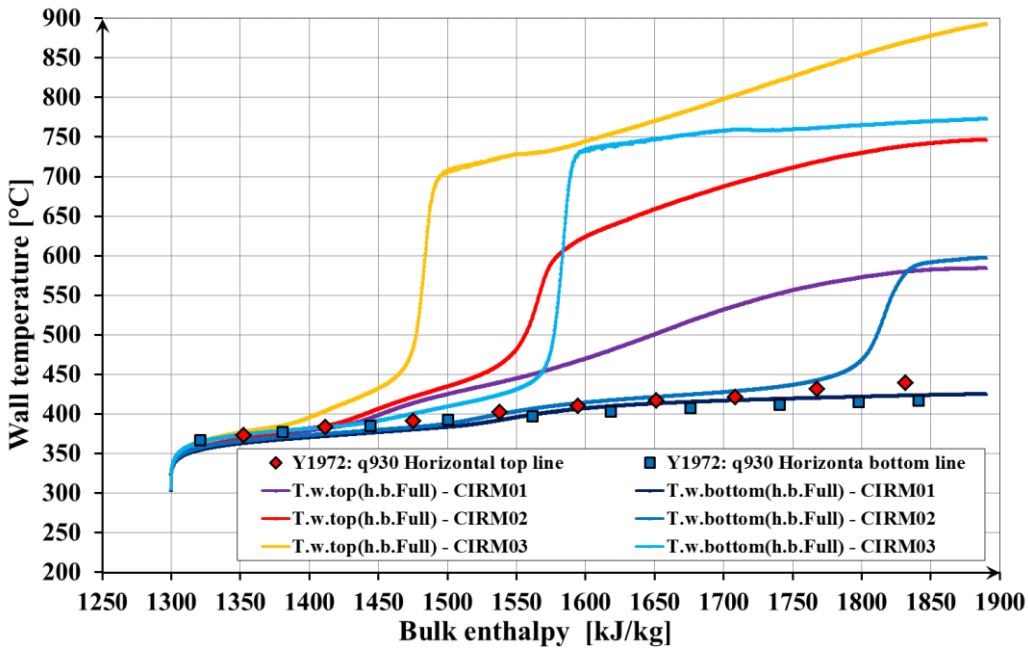

Figure 94. Comparison of $T_w(h_b)$ for the CIRM sensitivity study (H930 case)

Table 19: Required CIRM resolution needed based on the two key parameters

Flow direction → Heat flux ↓	Vertical (Upward)	Horizontal
High	High	Extra-High
Low	Medium	High

Based on the results, the CFD model with the CIRM01 mesh was selected as the most suitable for SCW modelling and this was used to construct the final mesh. This is an unfortunate result considering that increasing the circumferential resolution also significantly increases the computational cost of handling these CFD models.

2.2.2.3.3 Results of the axial resolution sensitivity study

For the sensitivity study of the axial mesh (AXM) resolution, two further meshes were created: a higher resolution one (AXM01) and a lower resolution one (AXM03) in addition to the already existing base mesh (AXM02, identical to BLM01), similar to the CIRM study. The results of the calculations showed that the axial resolution has only a negligible effect on the accuracy of the simulation results. This effect is even smaller than that of the BLM (compare Figure 95 & Figure 92).

Furthermore, increasing the axial resolution also significantly increases the computational cost. Based on this, it was concluded that the effects of the increased axial resolution so negligible, that it is simply not worth the effort to use a higher axial mesh resolution. For this reason, the AXM03 (ΔZ_{AXM03} = 1 mm) was selected for further use.

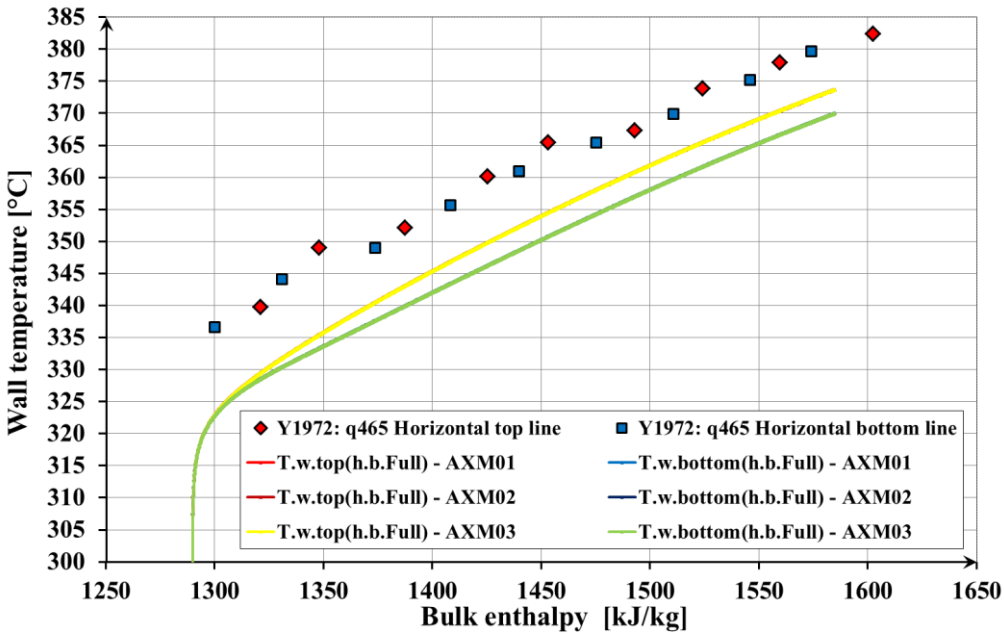

Figure 95. Comparison of $T_w(h_b)$ for the AXM sensitivity study (H465 case)

2.2.2.3.4 Results of the wall roughness sensitivity study

The final mesh (called B1C1A3, which means BLM01 with CIRM01 circumferential and AXM03 axial resolutions) was generated for the Wall Roughness Sensitivity Study (WRSS) based on the conclusions of the mesh sensitivity studies. This B1C1A3 mesh was used in this study with the exception of the CFD model with smooth wall condition (until this study all the CFD models used smooth wall BC): the CFD model with smooth wall BC was represented with the result of CIRM01 used with finer AXM resolution (due to the axial resolution effect is negligible). The results showed, that as the wall roughness increases then the turbulence, the turbulent mixing and thus the turbulent heat transfer enhances and this trend leads to lower $T_w(h_b)$ (see Figure 96 and Figure 97).

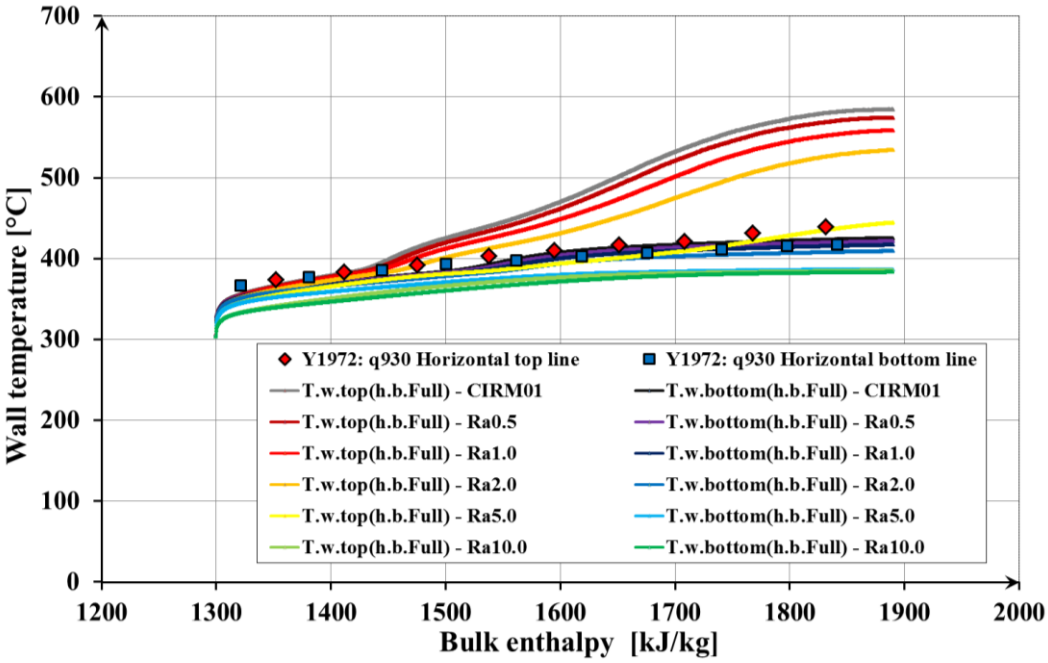

Figure 96. Comparison of $T_w(h_b)$ for the WR sensitivity study (H930)

It is important to note that, the wall roughness in Ansys CFX-Pre has been increased as a parameter of the wall BC, which means that this wall roughness is artificial and represents the original material surface roughness caused by the finishing used during the manufacturing process. In reality the surface roughness in reactors also increases due to the formation of an oxide layer on the outer surfaces of the fuel pins. This oxide layer usually has a detrimental effect on the thermal conductivity of the outer (coolant-connected) layer of cladding material, resulting in higher wall temperatures due to reduced heat transfer. Therefore, the temperature reducing effects of the increased mixing and the temperature increasing effects of the reduced thermal conductivity counteract each other. This will be of particular importance for SCWR-s due to the highly corrosive nature of the SCW, which will result in increased oxide layer formation compared to currently operating light water reactors (LWRs). Unfortunately, the necessary thermal conductivity and corrosion data are not currently available for the oxidised structural materials proposed for SCW-SMRs. Nevertheless, surface roughness will certainly play an important role in the cooling process of SCWRs, but further research is needed to properly describe the effects of oxide layer formation.

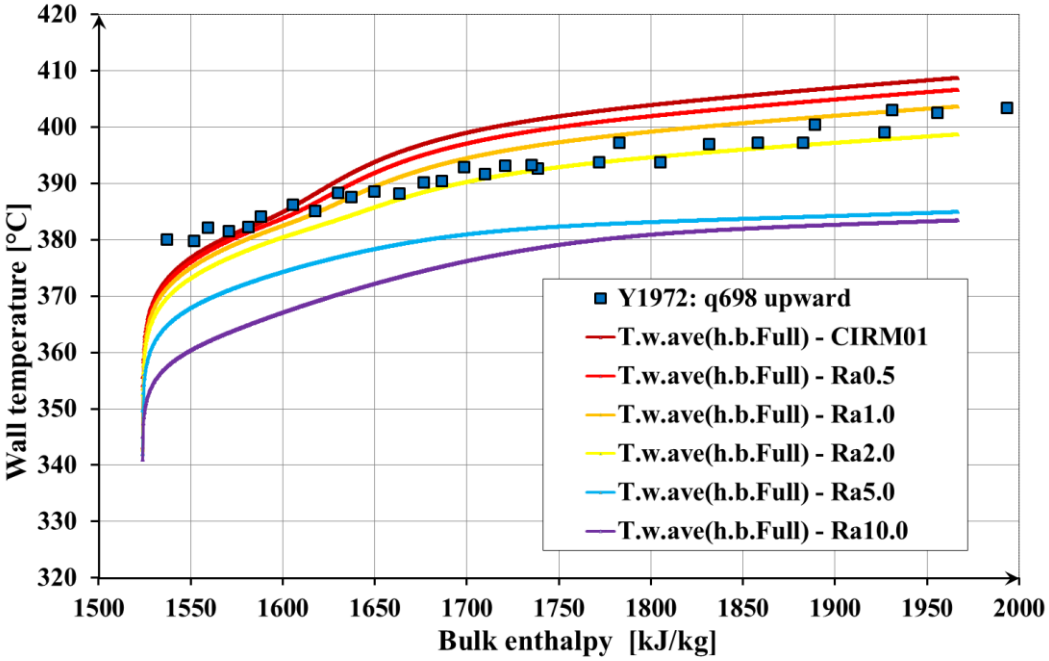

Figure 97. Comparison of $T_w(h_b)$ for the WR sensitivity study (U698)

2.2.2.4 Conclusions on Section 2.2.2

This Section 2.2.2 presents a complex CFD analysis, using the measured data of supercritical water flowing in horizontal (four cases) and vertical upward (another four cases) directions in straight tubes of the well-known Yamagata experiment. The analysis was performed in order to assist the sufficiently accurate CFD modelling of the thermal hydraulics of supercritical water flowing horizontally through the fuel assemblies of the European SCW-SMR concept.

Three types of mesh settings were investigated during the Mesh Sensitivity Study: the boundary layer mesh settings, the size/number of the circumferential-, and the axial elements/nodes. A further parameter was investigated in the sensitivity studies as well: this was the effect of wall roughness with different artificial wall roughness values. During the sensitivity studies only one settings or parameter was changed at a time, leaving all other boundary conditions, the numerical mesh and the settings of CFD model unchanged. The results of the

boundary layer study were used for the circumferential and axial studies, but these studies were carried out in parallel to determine which mesh discretisation was more important. The main conclusion of the **boundary layer mesh** ("BLM") sensitivity study is that the boundary layer mesh has only a small quantitative effect on the CFD results and does not affect the qualitative nature of the calculated distribution of wall temperature. The quantitative effect becomes stronger in the horizontal cases with higher heat flux, but even there the effect is still very moderate. For the low heat flux cases the CFX models underestimate the distributions of wall temperature, while for the high heat flux cases they tend to overestimate it. Qualitatively, the CFD results give back the higher distribution of wall temperature along the top line compared to the bottom line distributions. Regarding the sensitivity study of the **circumferential mesh resolution** ("CIRM"), it was concluded, that the circumferential resolution has a significant effect on the accuracy of the CFD results, both qualitatively and quantitatively. This effect is so significant that if the circumferential resolution is too low, the simulation results will be completely unphysical as they will predict a fake deterioration of the heat transfer. Only the CFD models with high circumferential resolution were able to predict results that were sufficiently similar to the experimental data. Quantitatively, the higher circumferential resolution reduces the temperature underestimation at lower heat fluxes and reduces the overestimation at higher heat fluxes, resulting in more realistic CFD results. It was concluded that the circumferential resolution is a critical parameter for supercritical water CFD modelling and that there are two key parameters that determine how much circumferential resolution is needed. These two parameters are: the direction of the flow and the heat flux. Horizontal flow modelling requires higher circumferential resolution than vertical, and higher heat flux cases require higher circumferential resolution than lower heat flux cases. The results of the calculations for the sensitivity study of the **axial mesh resolution** ("AXM") showed that the axial resolution has only a negligible effect on the accuracy of the simulation results. For the eight investigated cases 1 mm high elements in axial direction was found sufficient.

The results of the sensitivity study of the **wall roughness** ("WR") showed that as the wall roughness increases then the turbulence, the turbulent mixing and thus the turbulent heat transfer enhances and this trend leads to lower distribution of wall temperature. It is important to note that, the specified wall roughness is artificial and represents the original material surface roughness caused by the finishing of the manufacturing not taking into account the effect of oxide layer formation caused by the corrosion. Unfortunately, the necessary thermal conductivity and corrosion data are not currently available for the oxidised structural materials proposed for SCW-SMRs. Nevertheless, surface roughness will certainly play an important role in the cooling process of SCWRs, but further research is needed to properly describe the effects of oxide layer formation.

2.2.3 Ansys CFX model validation for upward SCW flow in 2×2 rod bundles

- Based on the experiment conducted by Nuclear Power Institute of China (NPIC) and Xi'an Jiaotong University (XJTU), the International Benchmark on SuperCritical Thermal Hydraulics (IBSCTH) has been established, including two parts with many experimental cases to be investigated (NPIC 2021):

1. part: Heat Transfer Characteristics of Supercritical Water in 2×2 Rod Bundle Channel;
2. part: Flowing Instability of Supercritical Water in Parallel Channels.

BME participated in the CFD benchmarking activity proposed in the frame of the IBSCTH exercise and already reported in deliverable D3.2 of the ECC-SMART project.

2.2.3.1 The CFD models of BME for the IBSCTH benchmark

All the five cases of part 1 of the IBSCTH benchmark (NPIC 2021) have been modelled by the BME research group using the commercial CFD software package Ansys CFX version 19.5. Thus, a total of five CFD models were developed in the framework of the first part of the benchmark (Heat Transfer Characteristics of SCW in 2×2 Rod Bundle Channel) with the following details:

- Two CFD models were created for Case 1 and 2 of the part 1/1.1 Bare Rod Bundle Channel subtask (Figure 98);
- One CFD model was created for Case 3 of the part 1/1.2 Local wire-wrapped rod bundle channel subtask (Figure 99);
- Two CFD models were created for Case 4 and 5 of the part 1/1.3 Full-length wire-wrapped rod bundle channel subtask (Figure 100).

Mesh sensitivity studies were performed for Case 1 and Case 3 (not shown here), and the lessons learned were incorporated into the models for the final computations as well as for the CFD analysis of the fuel assembly of the SCW-SMR concept.

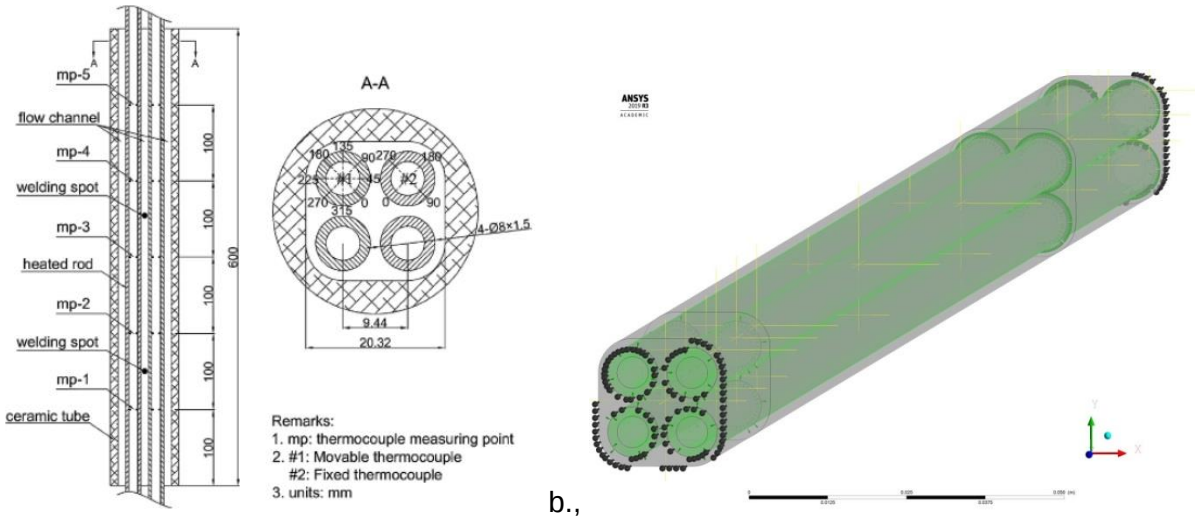

Figure 98. IBSCTH Part 1/1.1: a., the details of the cross section of the experimental test section, b., the CFD model of BME for Case 1 & 2 in the Ansys CFX pre-processor program

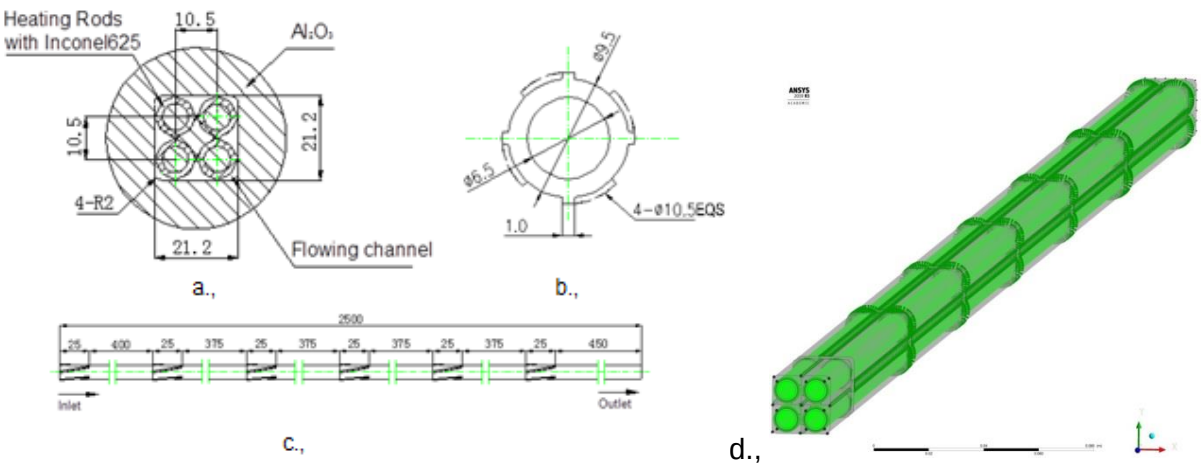

Figure 99. IBSCTH Part 1/1.2: a., the details of the cross section of the experimental test section, b., the details of the fuel rod with local wire wraps, c., the axial positions of the local wire wraps, d., the CFD model of BME for Case 3 in the Ansys CFX pre-processor program

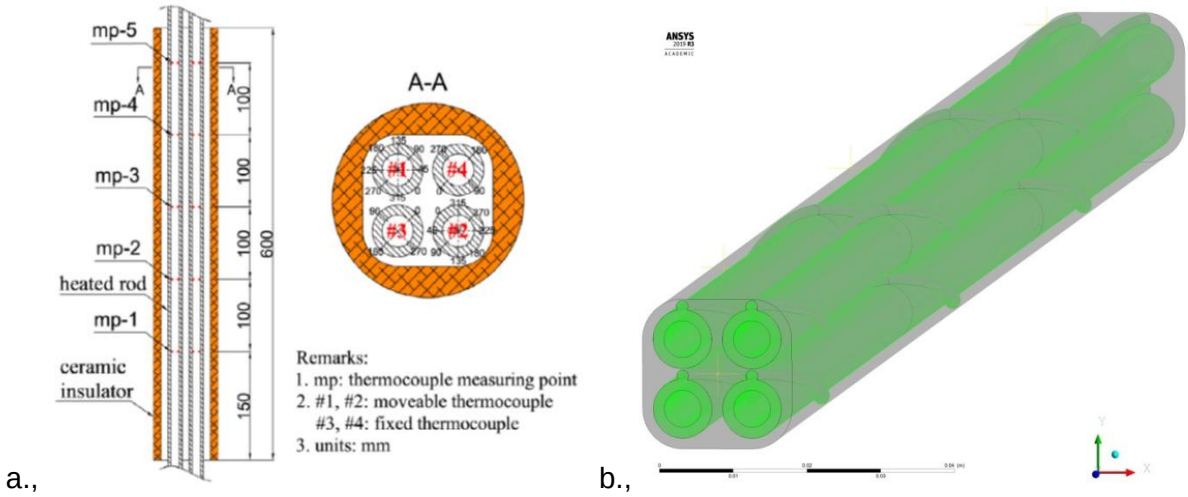

a., b.,

Figure 100. IBSCTH Part 1/1.3: a., the details of the cross section of the experimental test section, b., the CFD model of BME for Case 4 & 5 in the Ansys CFX pre-processor program

2.2.3.2 The CFD results of BME compared to the experimental results

Since the detailed comparison between the experimental results and the CFD results submitted by the participants of the international benchmark has been published in Deliverable 3.2 of the ECC-SMART project, only the main CFD results of BME are presented here with a compact discussion.

The experimental and CFD results are in good agreement at Rod #1 and #2 of Case 1 within a temperature mismatch of 1°C (Figure 101) and 1,5°C (Figure 102) respectively.

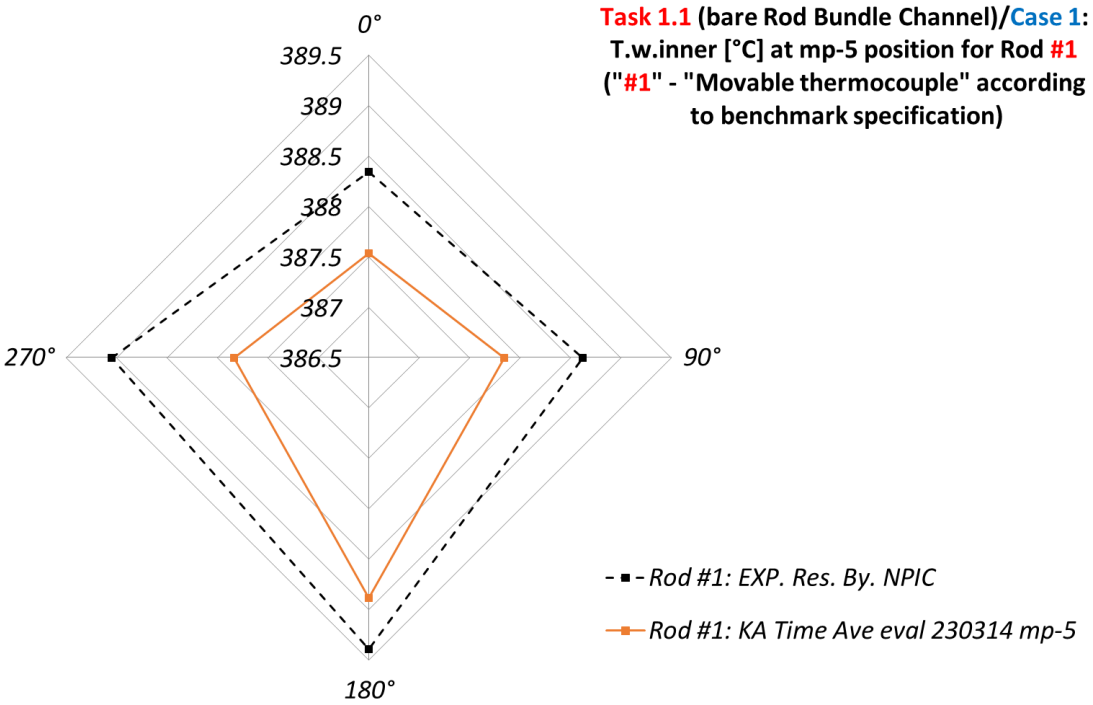

Figure 101. Comparison of experimental and CFD results for Case 1 of IBSCTH Part 1/1.1 Bare Rod Bundle Channel subtask (inner wall temperatures at mp-5 position for Rod #1)

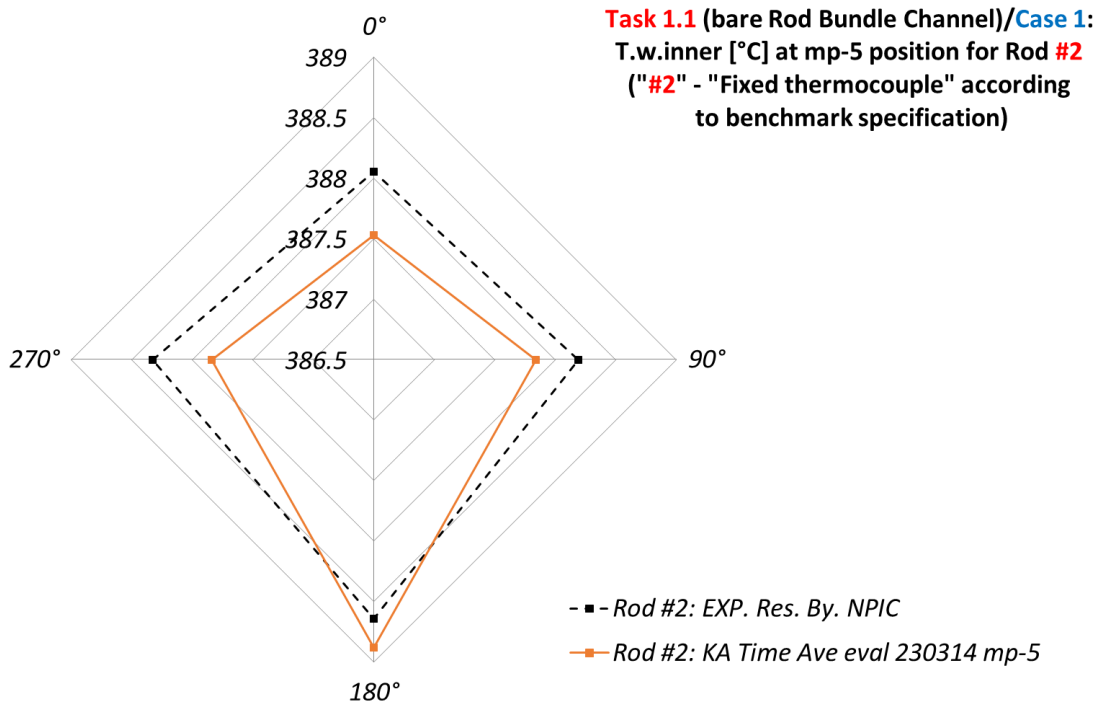

Figure 102. Comparison of experimental and CFD results for Case 1 of IBSCTH Part 1/1.1 Bare Rod Bundle Channel subtask (inner wall temperatures at mp-5 position for Rod #2)

The experimental and CFD results for Rod #1 and #2 of Case 2 are also in good agreement within a temperature discrepancy of 6°C (Figure 103) and 7°C (Figure 104) respectively.

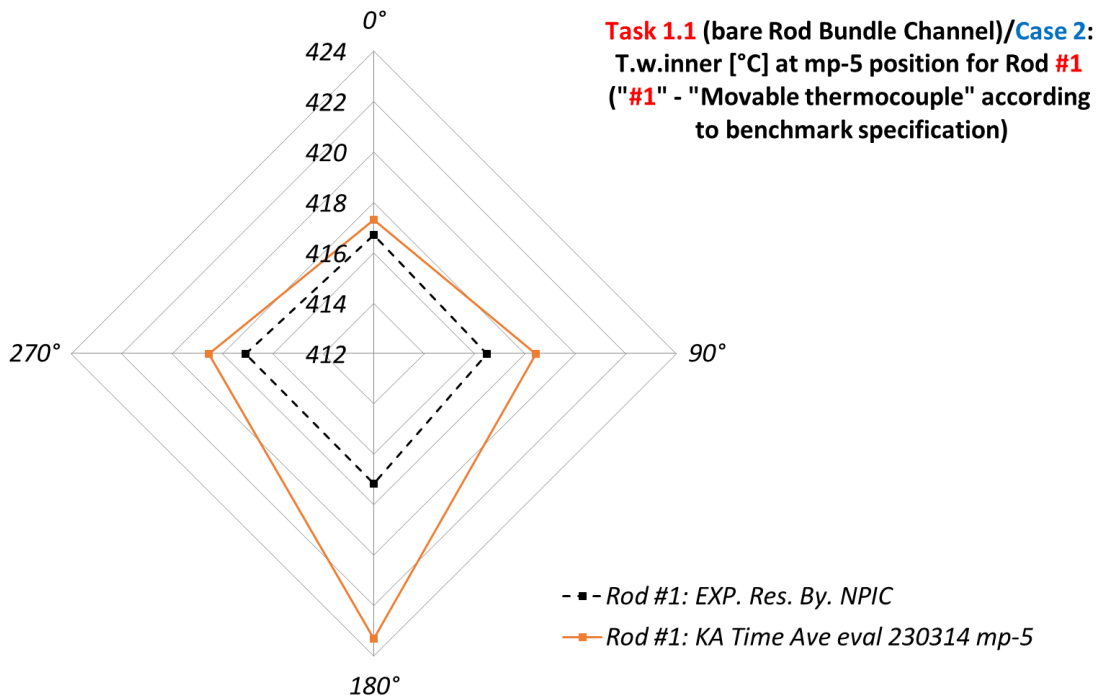

Figure 103. Comparison of experimental and CFD results for Case 2 of IBSCTH Part 1/1.1 Bare Rod Bundle Channel subtask (inner wall temperatures at mp-5 position for Rod #1)

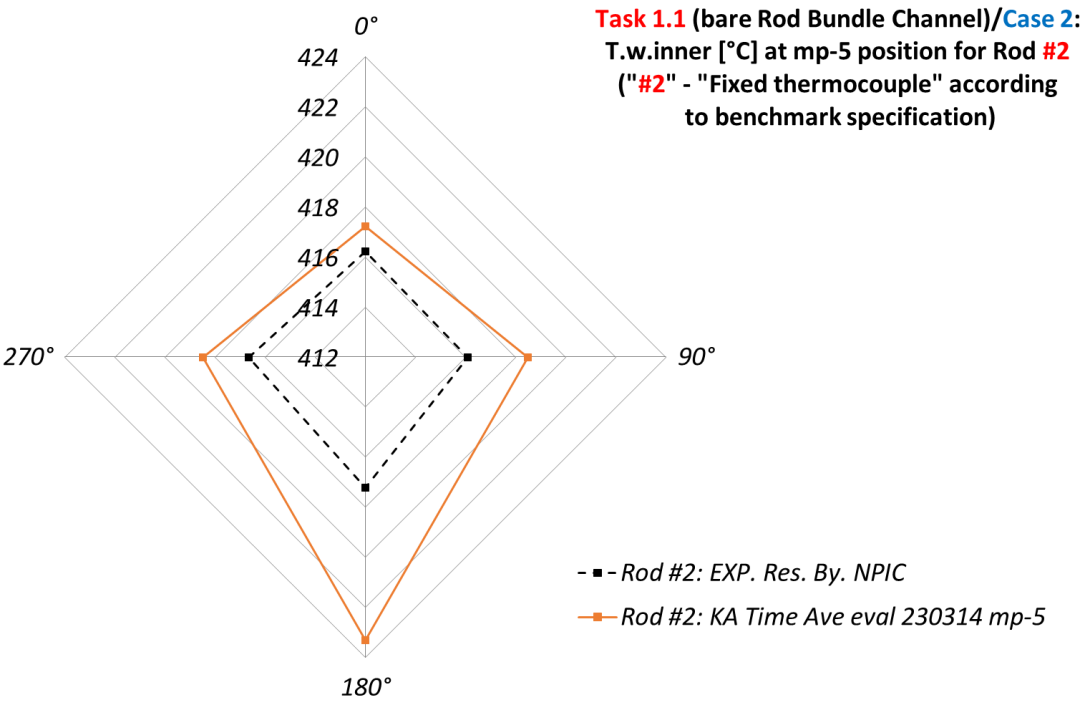

Figure 104. Comparison of experimental and CFD results for Case 2 of IBSCTH Part 1/1.1 Bare Rod Bundle Channel subtask (inner wall temperatures at mp-5 position for Rod #2)

The experimental and CFD results for Rod #1, #2, #3 and #4 of Case 3 are in moderate agreement in both qualitatively and quantitatively (see Figure 105 – Figure 108).

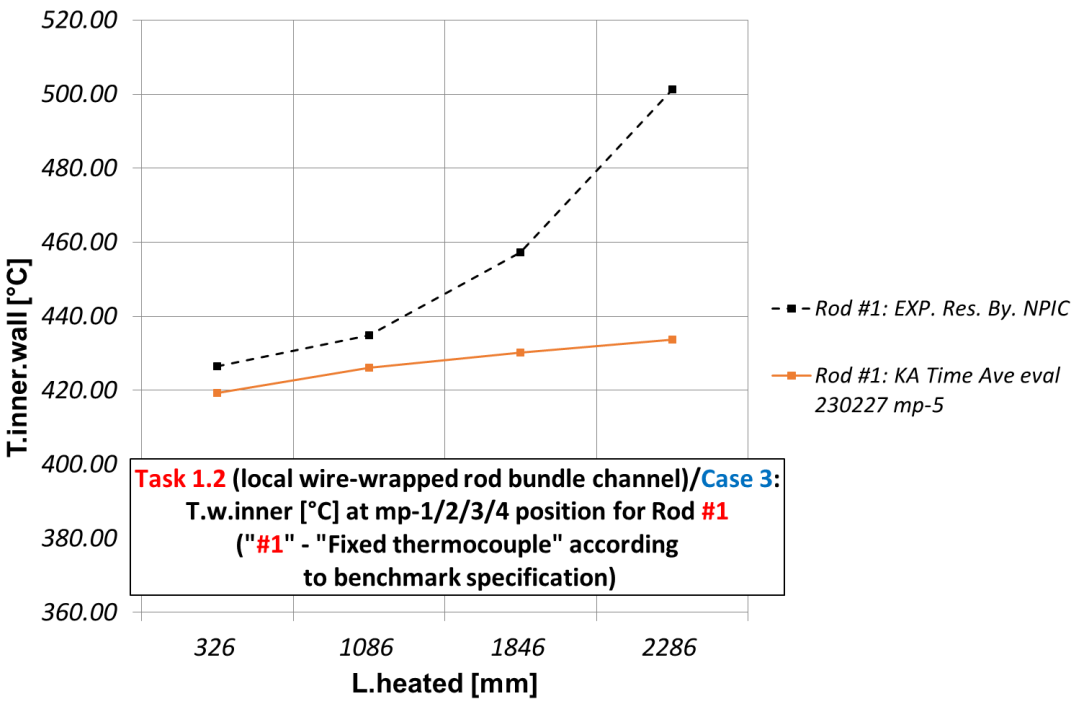

Figure 105. Comparison of experimental and CFD results for Case 3 of IBSCTH Part 1/1.2 Local wire-wrapped rod bundle channel subtask (inner wall temperatures at mp-1/2/3/4 positions of Rod #1)

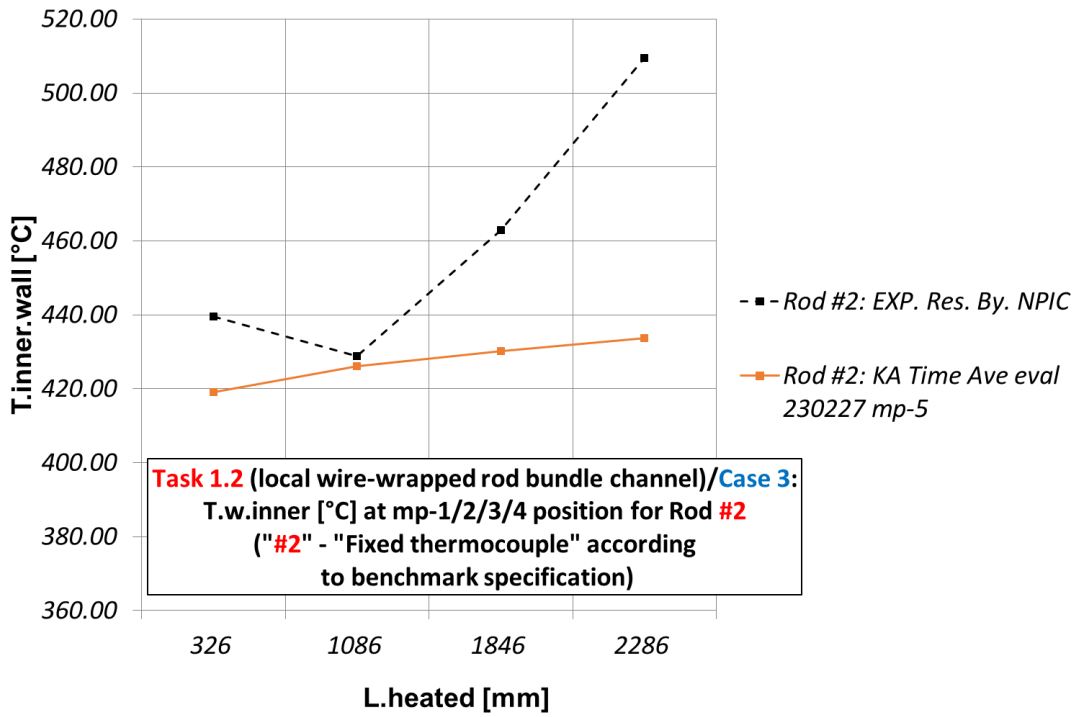

Figure 106. Comparison of experimental and CFD results for Case 3 of IBSCTH Part 1/1.2 Local wire-wrapped rod bundle channel subtask (inner wall temperatures at mp-1/2/3/4 positions of Rod #2)

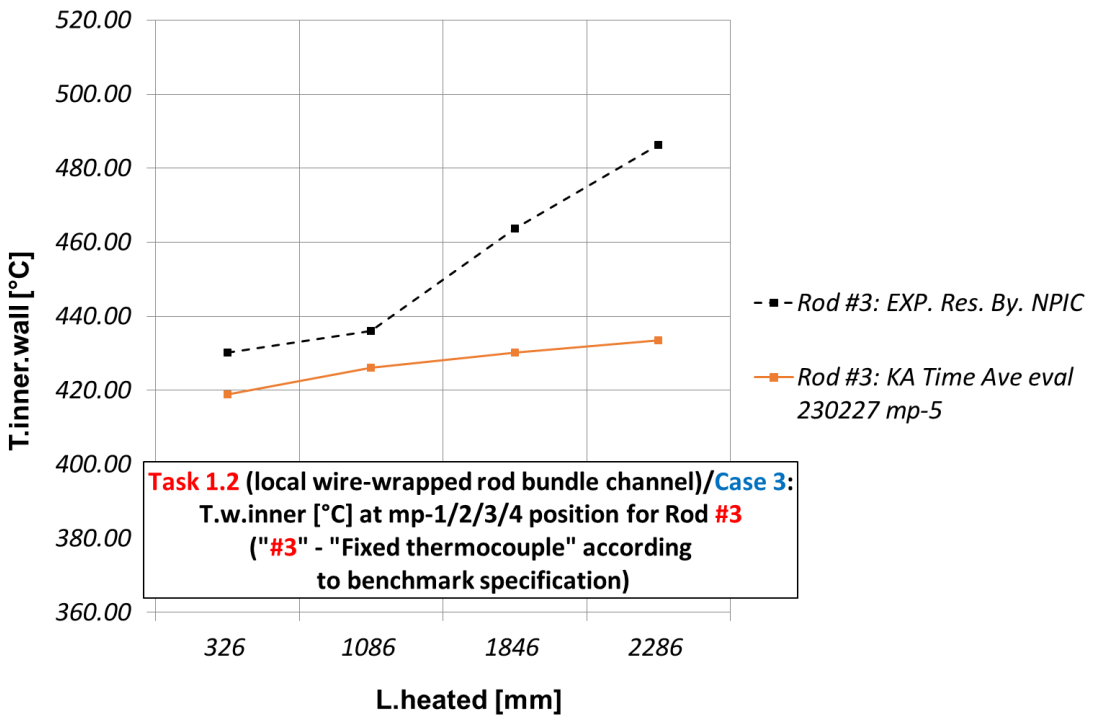

Figure 107. Comparison of experimental and CFD results for Case 3 of IBSCTH Part 1/1.2 Local wire-wrapped rod bundle channel subtask (inner wall temperatures at mp-1/2/3/4 positions of Rod #3)

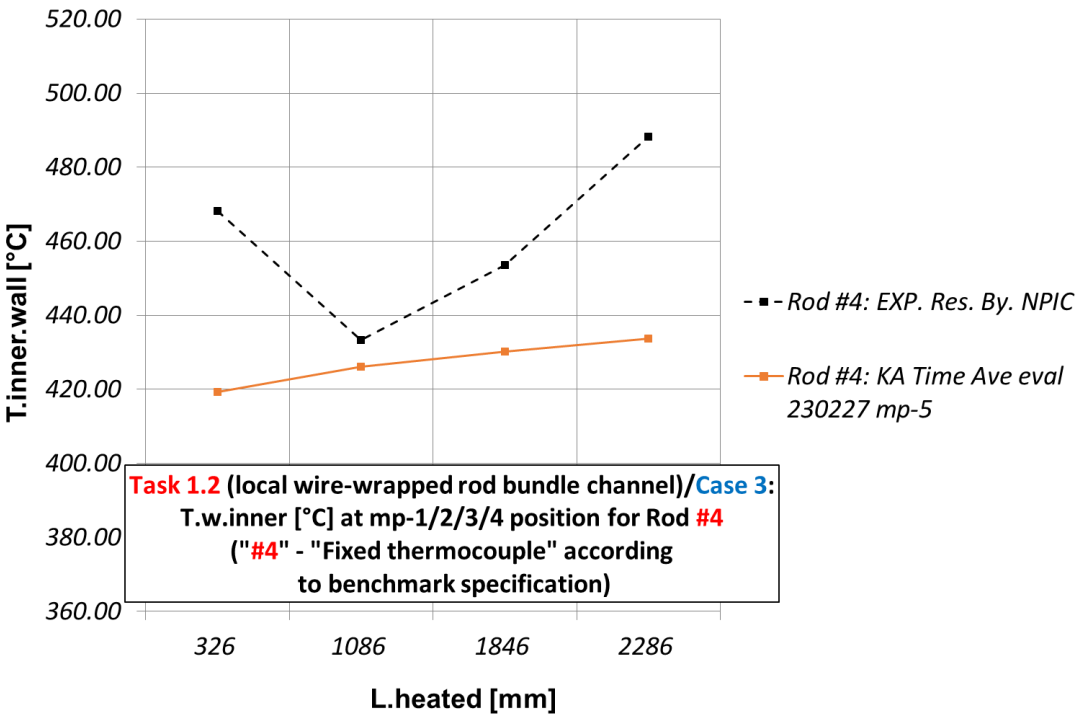

Figure 108. Comparison of experimental and CFD results for Case 3 of IBSCTH Part 1/1.2 Local wire-wrapped rod bundle channel subtask (inner wall temperatures at mp-1/2/3/4 positions of Rod #4)

The experimental and CFD results for Rod #2 and #4 of Case 4 are also in moderate agreement within a temperature discrepancy of 30°C (see Figure 109) and 25°C (see Figure 110), respectively.

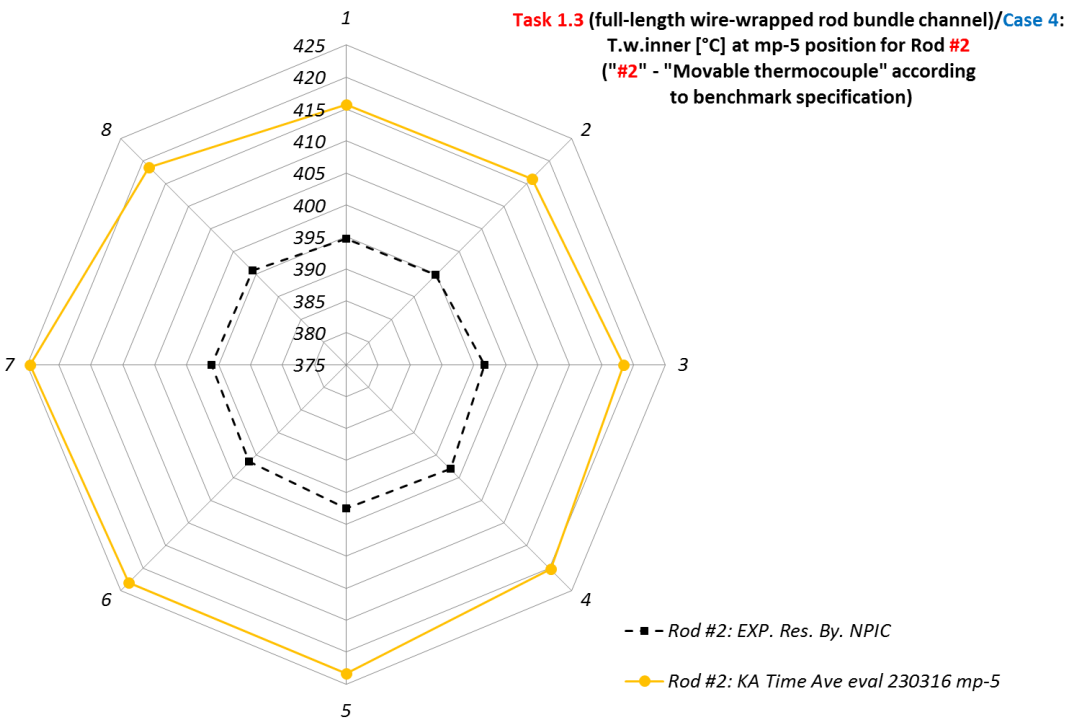

Figure 109. Comparison of experimental and CFD results for Case 4 of IBSCTH Part 1/1.3 Full-length wire-wrapped rod bundle channel subtask (inner wall temperatures at mp-5 position for Rod #2)

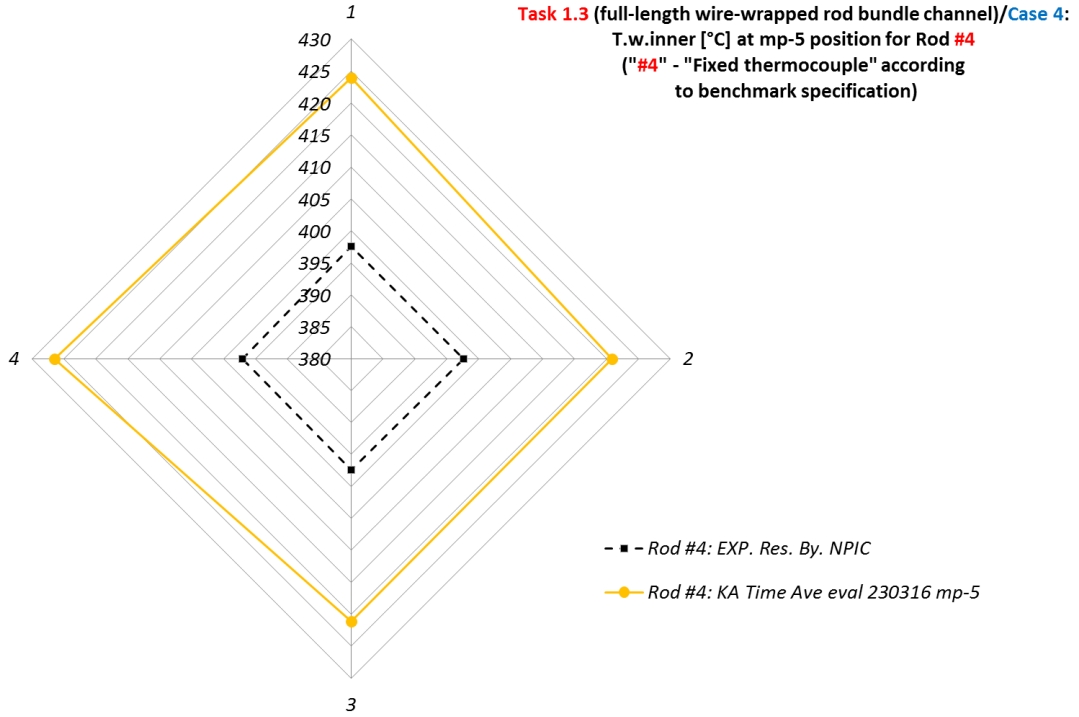

Figure 110. Comparison of experimental and CFD results for Case 4 of IBSCTH Part 1/1.3 Full-length wire-wrapped rod bundle channel subtask (inner wall temperatures at mp-5 position for Rod #4)

The experimental and CFD results for Rod #2 and #4 of Case 5 are also in moderate agreement within a temperature discrepancy of 20-25°C (see Figure 111) and 18-25°C (see Figure 112), respectively.

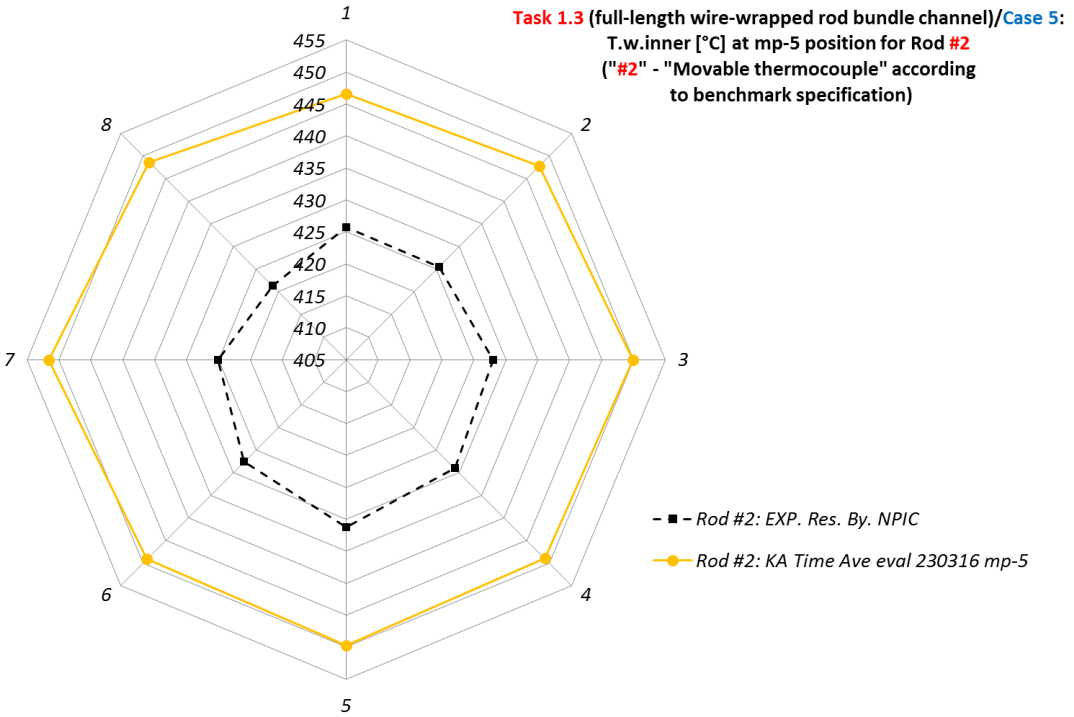

Figure 111. Comparison of experimental and CFD results for Case 5 of IBSCTH Part 1/1.3 Full-length wire-wrapped rod bundle channel subtask (inner wall temperatures at mp-5 position for Rod #2)

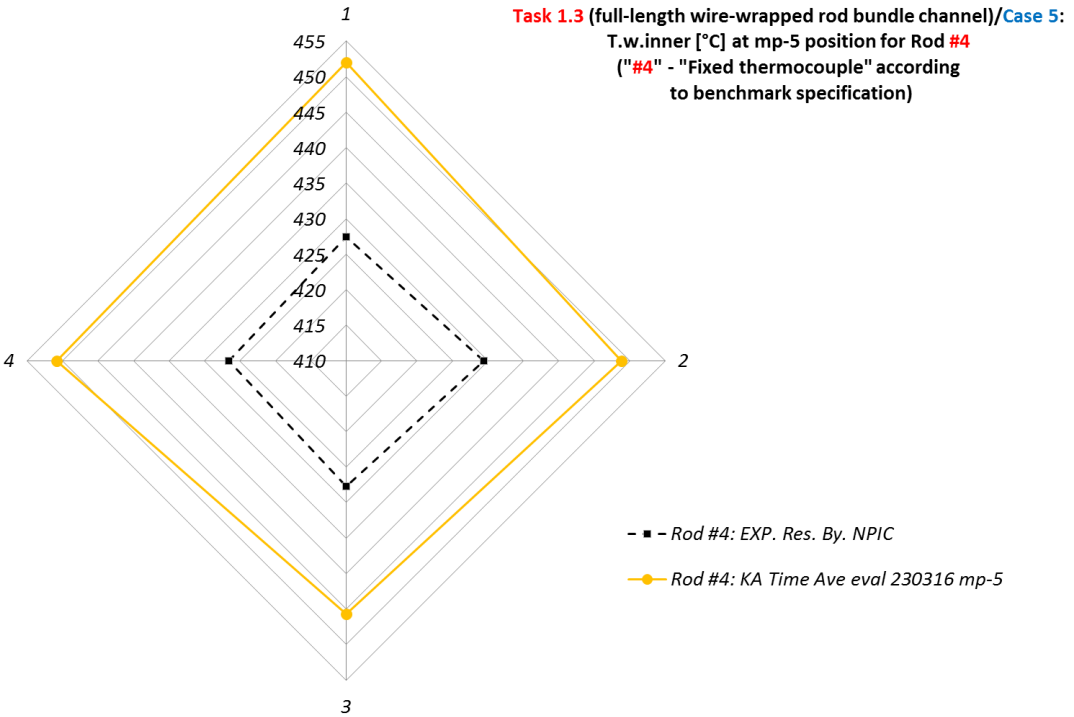

Figure 112. Comparison of experimental and CFD results for Case 5 of IBSCTH Part 1/1.3 Full-length wire-wrapped rod bundle channel subtask (inner wall temperatures at mp-5 position for Rod #4)

2.2.3.3 Summary

All the five cases of part 1 of the IBSCTH benchmark (NPIC 2021) have been modelled by the BME research group with relatively good agreement using the commercial CFD software

package Ansys CFX version 19.5. Mesh sensitivity studies were performed for Case 1 and Case 3 (not shown here), and the lessons learned were incorporated into the models for the final computations as well as for the CFD analysis of the fuel assembly of the SCW-SMR concept.

2.2.4 CFD modelling of horizontal SCW flow in SCW-SMR FA with/without WWS

The thermal hydraulics of SCW has been studied since the mid-1950s, while the SCWRs have been developed for more than fifty years (Kiss 2018). Based on this experience, the ECC-SMART project (ECC-SMART 2020) aims to assess the feasibility and identify the safety characteristics of an intrinsically and passively safe small modular reactor (SCW-SMR) cooled by supercritical water. The main objectives of the project are to define the design requirements for the future SCW-SMR technology, to develop the pre-licensing study together with the guidelines for the safety demonstration in further development stages of the SCW-SMR concept (including the methodologies and tools to be used), to identify the main obstacles for the future licensing of SMRs and to propose a strategy for this process. To achieve these objectives, specific technical knowledge gaps for the future smooth licensing and implementation of the SCW-SMR technology will be defined and assessed: in particular, the behaviour of materials in the SCW environment and under irradiation, the validation of different codes used in different fields and the design of the reactor core will be developed, evaluated by simulation and investigated experimentally. The consortium and the scope of the project have been defined according to the joint research activities under the umbrella of the International Atomic Energy Agency (IAEA), Generation-IV International Forum (GIF) (ECC-SMART 2020).

The active zone of the original SCWR is vertically oriented, while being moderated and cooled by downward and (mostly) upward SCW flows (GIF 2024, Schulenberg and Starflinger 2012). For this reason, the thermal hydraulics of vertical SCW flows has been extensively studied by experimental and numerical (mainly computational fluid dynamics (CFD) analysis) methods (see e.g.: Kiss 2018, Pioro and Duffey 2007, Rohde et al. 2016, Schulenberg and Otic 2021). The numerical analysis of horizontal SCW flows has been rare for the reason described above. Due to the orientation of the SCW-SMR active core, which is horizontal according to the available pre-pre-conceptual design (PPCD) (Adorján 2022), an essential need has arisen to assess the horizontal SCW flow in the FAs using the Reynolds-averaged Navier-Stokes (RANS) CFD method.

Two main CFD model types were developed for the investigated FA geometry: without and with the WWS. In the first part of the CFD analysis, a systematic numerical mesh sensitivity analysis was performed to select the most appropriate near-wall (boundary layer) mesh structure and the appropriate axial and circumferential mesh resolutions for the simpler geometry without WWS. Here, the simpler geometry of the SCW flow in FA allowed the application of the so-called block-structured numerical mesh in the case of all fluid and solid domains, more advanced turbulence models (the Shear Stress Transport (SST) and the BSL-Reynolds Stress Model (BSL-RSM)) with rough wall modelling (Ra = 1.5 μm). In the second part of the analysis, the more complex geometry of the SCW flow in FA (with WWS) was constructed, discretised by an unstructured numerical mesh (without fine local near-wall mesh, but all other domains had the same block-structured numerical meshes) and studied by a CFD model with the standard k-ε turbulence model and rough wall modelling (Ra = 1.5 μm). In the third part, the effect of the WWS was investigated by comparing the results of two main types of CFD models of the FA with and without WWS. The lessons learned are summarised and will be used in the ongoing more

advanced CFD analysis of the FA of the SCW-SMR concept. These CFD analyses are presented in this section.

2.2.4.1 The Developed CFD Models

The computer-aided design (CAD) geometry of the SCW-SMR FA and its numerical meshes were created in Ansys ICEM CFD version “2022 R1”, while the CFD models were developed in the commercial Ansys CFX version “2022 R1” software package. The two main types of CFD models are presented in this chapter: the FA geometry without and with the WWS, the numerical meshes generated, the boundary conditions applied and the results of the sensitivity analysis carried out.

2.2.4.1.1 The investigated geometry

The investigated geometry without and with the WWS represents one FA in each of the seven horizontal stages located in the horizontally oriented SCW-SMR active zone. The stages have a different number of rows of twenty horizontally oriented FAs (the distance between the FA box wall (FABW) outer surfaces of two FAs is 15 mm): stages 1-3 have 2, stages 4 and 5 have 3, while stages 6 and 7 have 4 rows. This gives a total of 20 rows, e.g. 400 FAs (20 rows × 20 FAs/row) in the active zone (Adorján 2022). Each FA has 40 fuel rods in a 7×7 array, with a 3×3 bundle removed from the centre (Figure 113/a) to make room for a so-called moderator box (MB) in the centre of the horizontal FA (Figure 113). The heated (or active) length of the fuel rods is 1680 mm, the outer diameter of each fuel rod is 8 mm, while the pitch is 9.44 mm (Figure 113/b). The thickness of the cladding is 0.5 mm, thus the outer diameter of the fuel is 7 mm (Figure 113/b).

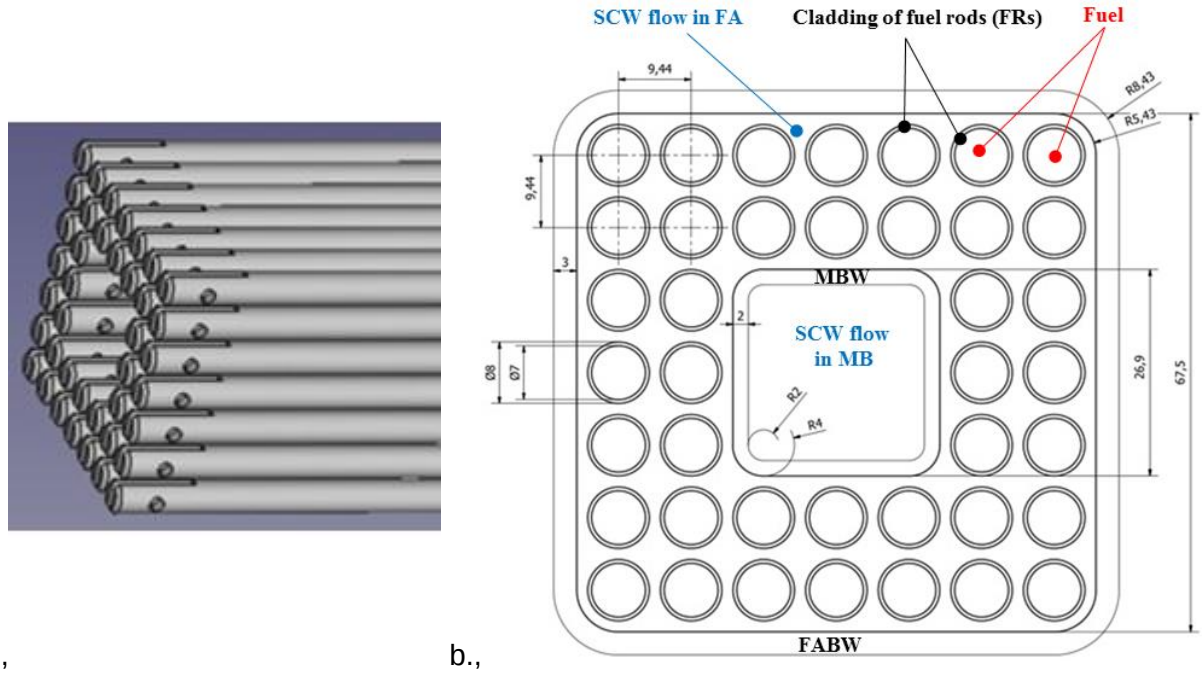

a., b.,

Figure 113. a., The rod bundle (WWS removed) of the SCW-SMR concept (Adorján 2022), b., The geometry of the FA without WWS (Adorján 2022)

The FABW has a rounded square shape with an internal width of 67.5 mm and a wall thickness of 3 mm (Figure 113/b). The MB wall (MBW) also has a rounded square shape with an external width of 26.9 mm and a wall thickness of 2 mm (Figure 113/b). Later, the homogeneous (1-1 layer) designs of the FABW and MBW were modified into improved designs with 3-3 layers of different materials, but here 1-1 homogeneous layer was used.

The total lengths of the CFD models without and with WWS are 1786 mm and 1800 mm respectively: 1680 mm heated (active) length followed by a 106 and 120 mm long unheated discharge sections to minimize the effect of the Outlet type boundary condition (BC) at the end of the studied heated part of the computational domain (CD) (Adorján 2022).

2.2.4.1.2 The generated numerical meshes

As it was shown previously, the CFD model without WWS has a simpler geometry, which allowed the application of the so-called block-structured numerical mesh, resulting in a dense local (so-called boundary layer) mesh near the bounding solid walls. This block-structured numerical mesh contains hexahedral (brick-shaped) 3D elements in the volume of the CD and quadratic (rectangle-shaped) 2D elements on the boundary surfaces (BS). Figure 114 shows the so-called block structures for the FA geometry without WWS (Adorján 2022).

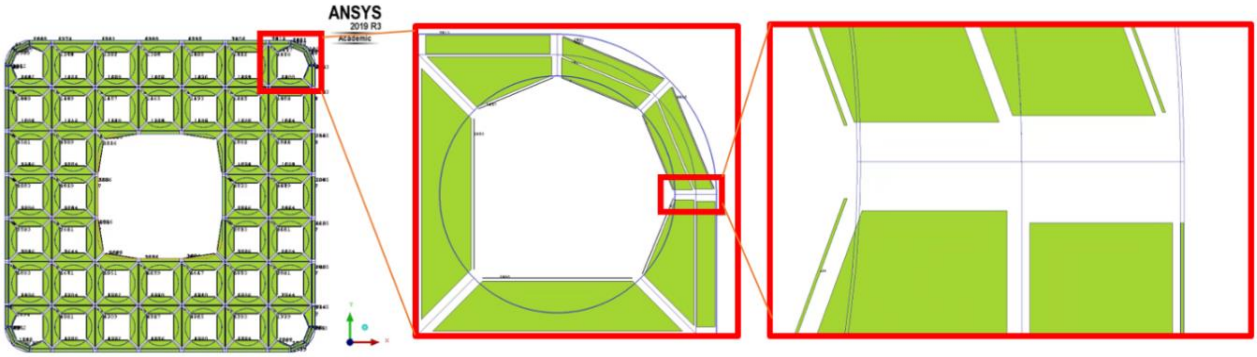

a., b., c.,

Figure 114. The block structure of the SCW flow in the FA without WWS (cross-sectional view): a., the entire block structure of the FA, b., the block structure of a fuel rod, c., enlarged details (Adorján 2022)

The base parameter set of the boundary layer mesh is: height of the first layer adjacent to the solid wall Δy = 0.6 μm, growth ratio 1.2 and number of layers 9. Figure 115 shows the details of the block-structured numerical mesh generated using the basic parameter set of both the boundary layer and global meshes (Adorján 2022).

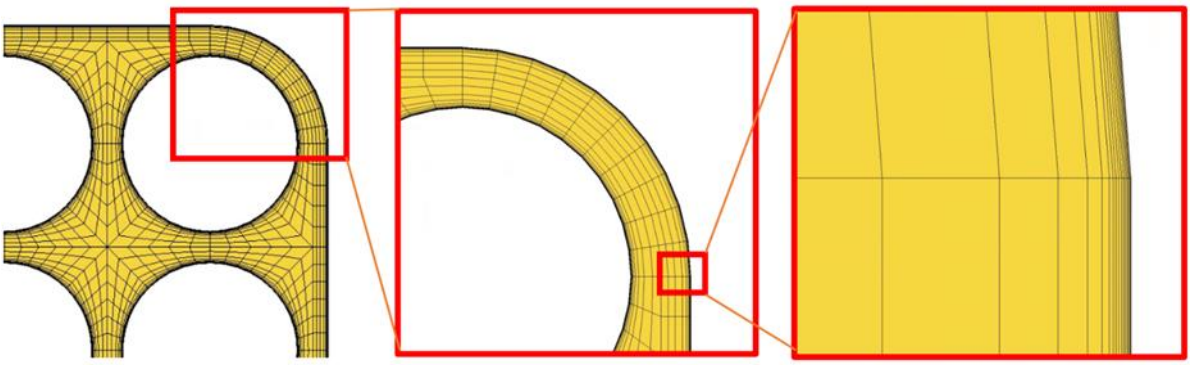

a., b., c.,

Figure 115. The mesh of the SCW flow in FA without WWS (cross-sectional view): a., global mesh at the corner, b., zoomed global mesh at the corner, c., zoomed details of the boundary layer mesh (Adorján 2022)

The solid domains of FABW, MBW, fuel rod cladding and fuels were also discretized as this CFD model is a CHT model as mentioned above. Figure 116 shows the details of the meshes of the above-mentioned solid domains and the mesh of the SCW flow in the MB.

The CFD model with WWS has a more complex geometry of the SCW flow in the FA, so only this fluid domain was discretized with an unstructured numerical mesh (without dense local near-wall mesh, but all other domains had the same block-structured numerical meshes). This unstructured numerical mesh contains tetrahedral (bounded by four triangular faces) 3D elements in the volume of the CD and tri (triangular shape) 2D elements on the BSs. Figure 117 shows the CD with all solid and fluid domains of the CFD model of the FA with WWS. As it can be seen there are two fluid domains (SCW flow in FA and MB) and four types of solid domains (FABW, MBW, fuel rod cladding & WWSs and fuels) in this CHT CFD model. Two major differences can be identified by comparing Figure 116 and Figure 117. The first is the type of the mesh of the SCW flow in the FA fluid domain: it is block-structured in the case of the FA model without WWS, while it is an unstructured mesh in the case of the FA model with WWS. The second difference is the presence of the WWS in Figure 117: the geometry and the mesh of the WWS have been added to the solid domain of fuel rod cladding, so that this solid domain got a new name: “fuel rod cladding & WWS”.

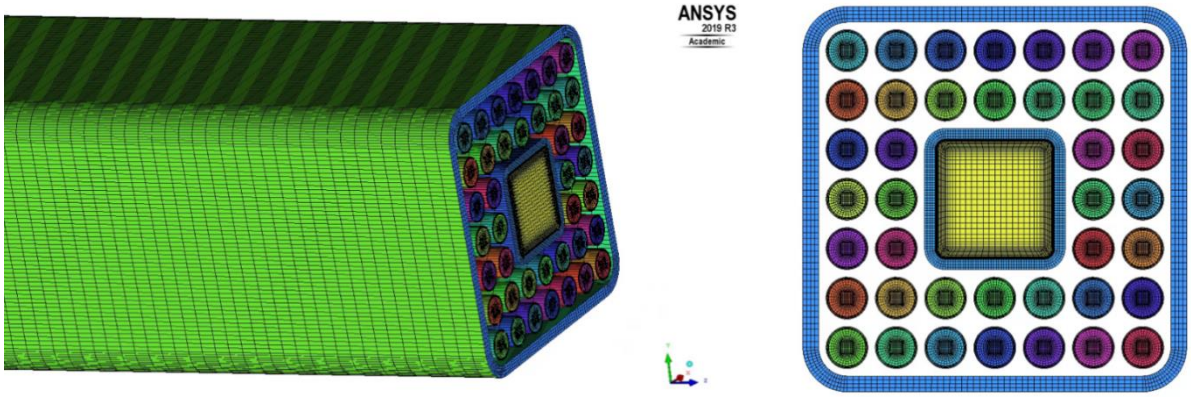

Figure 116. Meshing details of the solid domains (FABW, MBW, fuel rod cladding and fuel) and for the SCW flow in MB (isometric view on the left and cross-sectional view on the right) (Adorján 2022)

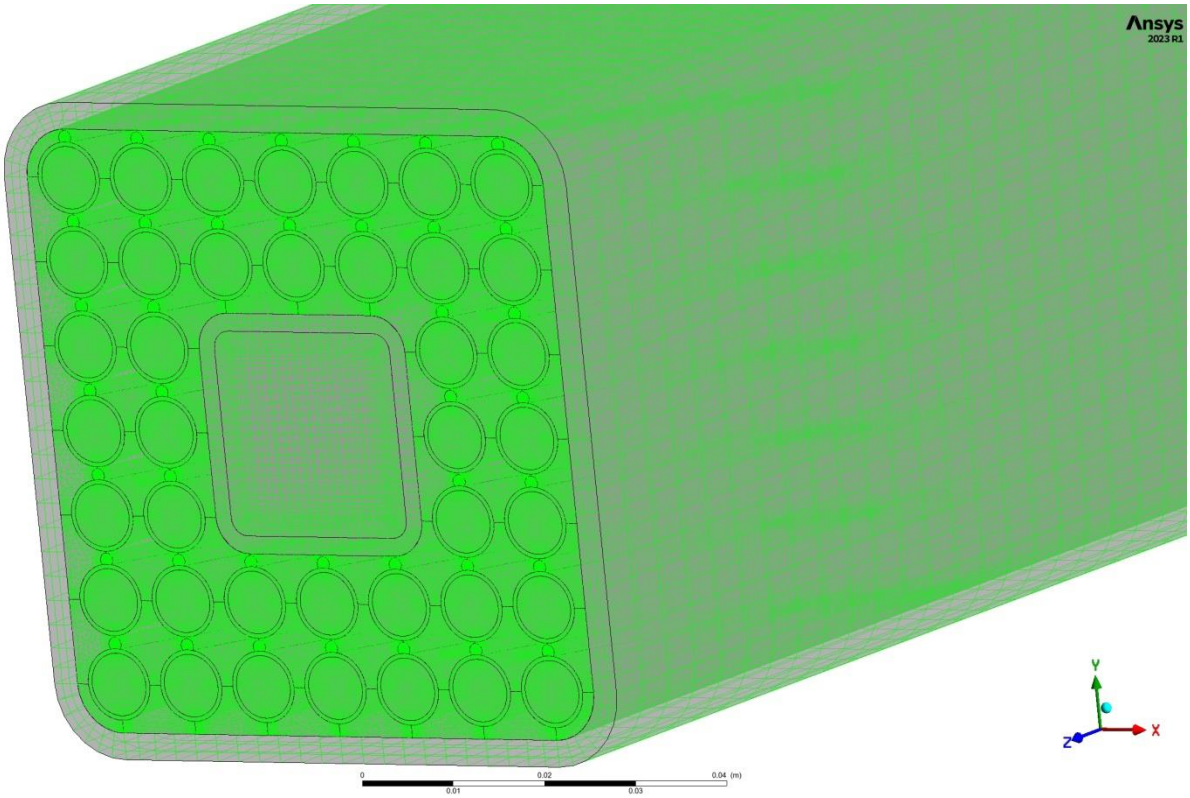

Figure 117. Meshing details of the solid domains (FABW, MBW, fuel rod cladding and fuel) and for the SCW flow in MB (isometric view on the left and cross-sectional view on the right) (Adorján 2022)

2.2.4.2 The applied boundary conditions

The applied boundary conditions correspond to an average heated FA in each of the seven so-called stages of the SCW-SMR (Adorján 2022). Figure 118 shows the main boundary conditions for both types of CHT CFD models. As can be seen, the SCW flows in the MB and FA have opposite flow directions in these models (these directions were later changed to be identical with the development of the PPCD).

In general, adiabatic no slip rough wall (Ra = 1.5 μm) BCs were defined at the BSs (parallel to the XY plane) of the solid domains at the start (Z = 0 mm) and end (Z = 1786/1800 mm) of the CD (Adorján 2022). In the solid fuel domain, a cosine profile of the volumetric heat source density (calculated by the Serpent reactor physical code (Adorján 2022)) was set in the heated section (Z = 0 ÷ 1680 mm) according to a user-defined function called AxialVolHeatSource1(Z). A constant temperature BC (309.45°C) was defined at the outer surface of the FABW. All other BSs of the solid domains were defined as the solid side of solid-solid (connecting the outer/inner BSs of the fuel/cladding) or solid-fluid (connecting the BSs of the solid domains to the BSs of the fluid domains) general connection type interfaces.

The two fluid domains are defined by inlet type BCs with constant temperature (SCW flow in FA/MB: 308/280°C) and mass flow rate (SCW flow in FA/MB: 3.625/0.16 kg/s) and outlet type BCs with constant (SCW flow in FA/MB:-25,000/-20,000 Pa) relative pressure. All other BSs of the SCW flow in FA and MB fluid domains have been defined as the fluid side of general connection type solid-fluid interfaces. These BCs represent the first stage of the seven stages in the active zone.

In these coupled thermal hydraulic CHT CFD simulations, the heat exchange between the different material regions was allowed and provided by the above mentioned interfaces. All of the CFD calculations were performed in a steady-state mode.

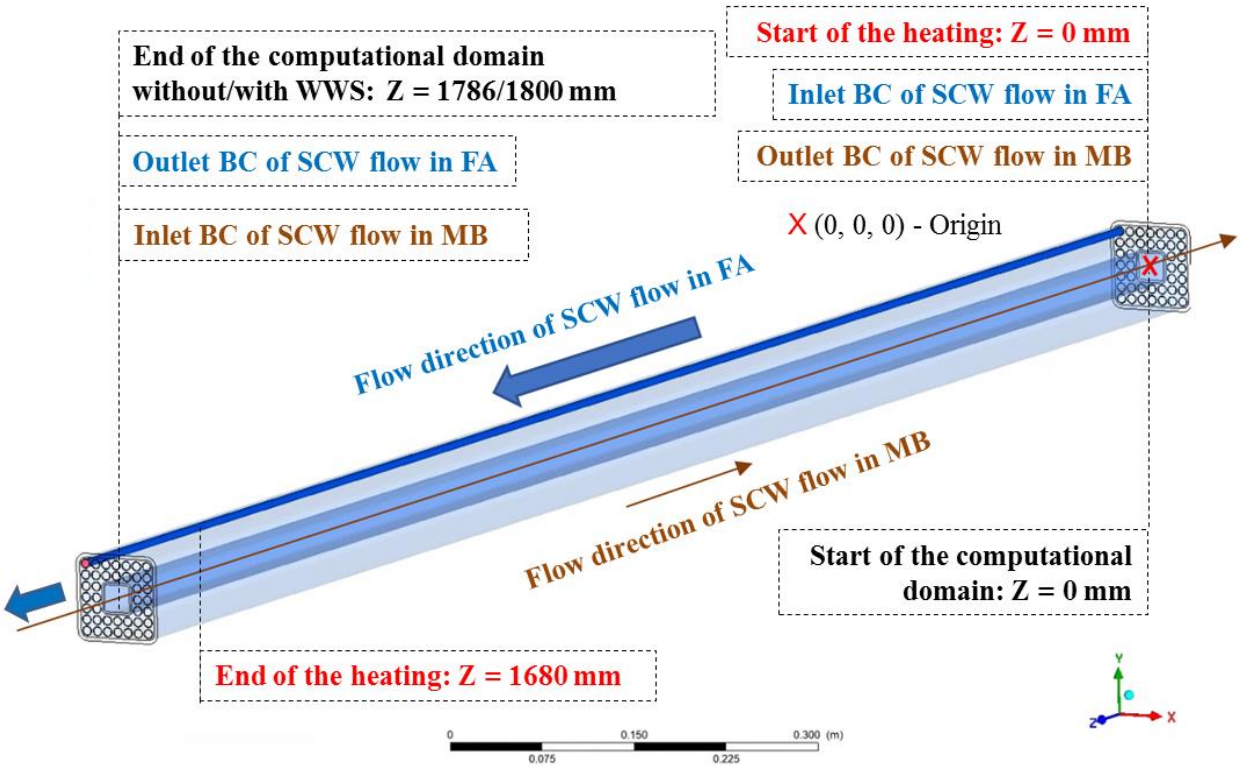

Figure 118. The isometric view of the CHT CFD models of the FA with the main BCs (Adorján 2022)

For the CFD model of the FA without WWS, three turbulence models were used in the calculations. For the final calculations with the most advanced turbulence model (BSL-RSM), the initial conditions were provided by the moderately advanced vorticity viscosity model SST. For the calculation with the SST model, the initial conditions were taken from the preliminary calculation with the least advanced but most robust k-ε model. The wall roughness was modelled with R_a = 1.5 μm equivalent sand grain size.

In the second part of the analysis, the more complex geometry with WWS was constructed, discretized and investigated by the CHT CFD model with the standard k-ε turbulence model and rough wall modelling (Ra = 1.5 μm). The k-ε turbulence model was used because the fine local near-wall mesh in the numerical mesh of the SCW flow in the FA could not be developed adjacent to the solid walls (due to computational/mesh size limitations), and more advanced turbulence models showed divergence in solving this CFD model.

2.2.4.3 Sensitivity studies

In CFD calculations, the results can be significantly affected by the model settings used and the mesh size, as it was demonstrated in previous CFD investigations on the vertically installed FA of the European HPLWR concept (Kiss and Mervai 2016, Kiss et al. 2011). The result (the appropriate meshing strategy of the SCW flow domain in the FA and the CFD model settings) of these sensitivity studies was directly applied to the current CFD model with WWS, as the FA geometry of the HPLWR and the SCW-SMR concept are identical, the only difference being the orientation of the FA (vertical for the HPLWR and horizontal for the SCW-SMR concept).

In the first part of this CFD analysis, a systematic numerical mesh sensitivity analysis was performed to select the most appropriate local or near-wall (boundary layer) mesh structure and the appropriate global (radial, axial and circumferential) mesh resolution for the simpler geometry without WWS. Three different mesh sizes (F1: 13.6 M, F2: 27 M and F4: 52.5 M cells) were used in the sensitivity analysis of the global mesh resolution. The number of layers (5, 9 and 15), the inflation ratio (1.1, 1.2, 1.3 and 1.4) and the Δy value (0.3, 0.6, 1.2 and 2.4 μm) were investigated in the near wall (boundary layer) mesh resolution sensitivity analysis. As illustrative examples of the results, the two figures below show the application of the Richardson extrapolation (Kiss 2018, Adorján 2022) for the total specific enthalpy increase – Δh_{total} (Figure 119) and the total pressure drop – Δp_{total} (Figure 120) along the full length of the CD versus the reciprocal of the square of the number of cells ($1/n^2$).

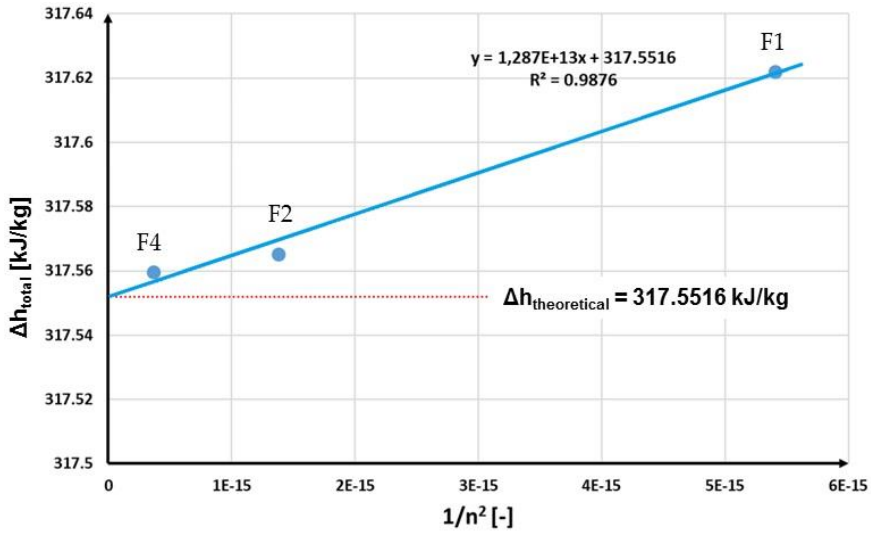

Figure 119. Linear regression on SST models for the target variable Δh_{total}, R^2=0.99 (very good) (Adorján 2022)

The main results of the local and global mesh sensitivity studies showed that the optimal (considering the two contractionary standpoints of numerical cost and accuracy) global mesh is the F2 while the best near-wall mesh parameter set consists of 9 layers with Δy = 0.6 μm and an inflation ratio of 1.2. This selected final mesh had 27 M numerical cells. The SST turbulence model was chosen for the final calculations and the results obtained with the k-ε turbulence model were used as reference states to make the convergence of the SST model calculations more robust.

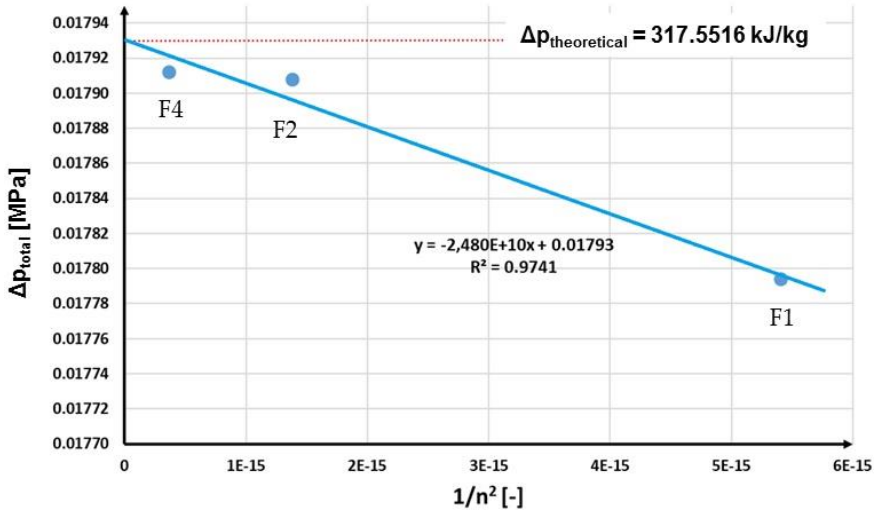

Figure 120. Linear regression on SST models for the target variable Δp_{total}, R^2=0.97 (very good) (Adorján 2022)

2.2.4.4 Results and discussion

In this chapter some exemplary results and their discussion are presented to illustrate the effect of the wrapped wire spacers by comparing the results of the two types of CFD models (without and with WWS).

The function of the WWS is twofold: to support the fuel rods and to provide more efficient heat transfer by increasing the level of turbulence around the fuel rods and mixing the flow. As a result, lower fuel rod temperatures and more favourable outlet (or "fresh steam") parameters are expected in advance. However, the presence of a WWS reduces the flow cross-section, resulting in higher flow velocities and hence higher pressure losses. These phenomena are well reproduced by the simulations, as shown in Figure 121.

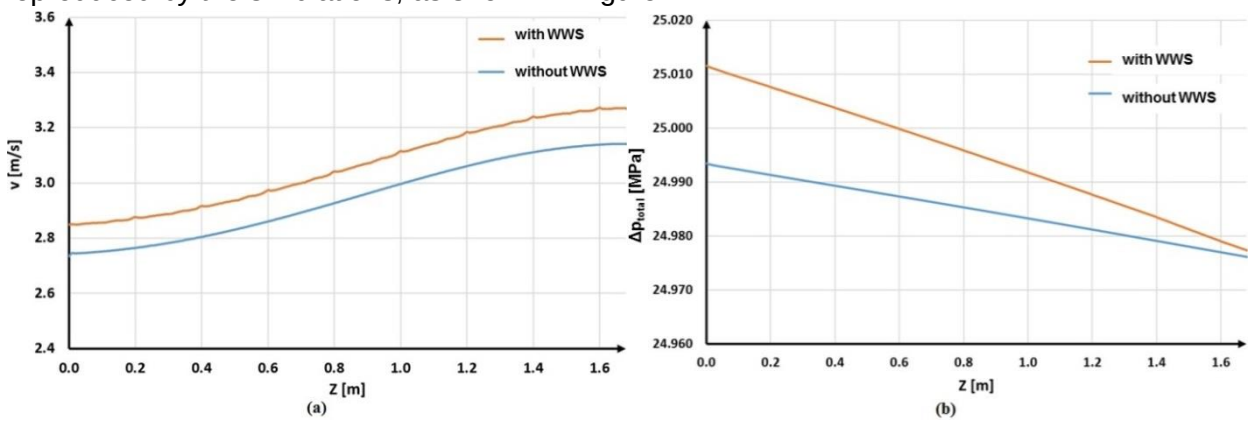

Figure 121. The distributions of: a., the cross section averaged velocity, b., the total pressure drop of the SCW flow in the FA without and with WWS (Adorján 2022)

The specific enthalpy of the SCW flow in the FA leaving the heated section (at Z = 1680 mm) is 1597 kJ/kg and 1602 kJ/kg for the case without and with WWS respectively. The core temperature without and with WWS is 346°C and 347°C respectively. Thus, the preliminary expectation of more favourable outlet (or "fresh steam") parameters cannot be clearly said to have been unfulfilled.

Figure 122 shows the distributions of the maximum temperatures along the length (Z [m]) of the CD for the fuel-, the cladding solid and the SCW flow in FA fluid domains without and with

WWS (Yamagata et al. 1972) to illustrate that the WWS generally reduce the temperature values throughout the CD. These temperature values are not taken from a single fuel or fuel rod, but as a conservative approach, are the highest temperature values that always occur in the cross section at a given axial height for a studied solid or fluid domain. The simulations confirm the beneficial effect of the WWS (Figure 123): the maximum fuel temperatures are reduced by about 19°C (compare the two fuel lines without and with WWS in Figure 122) and the maximum cladding temperatures are reduced about 16°C (compare the two cladding lines without and with WWS in Figure 122). The maximum coolant temperature of the SCW flow in the FA is higher in the case without WWS (compare the two lines of SCW flow in the FA without and with WWS in Figure 122), because a thicker laminar boundary layer can be formed on the heated surface of the fuel rods due to the reduced turbulence. However, the outlet core temperature and the specific enthalpy of the coolant are higher in the CFD case with WWS. Overall, therefore, the WWS improves the heat transfer in the FA.

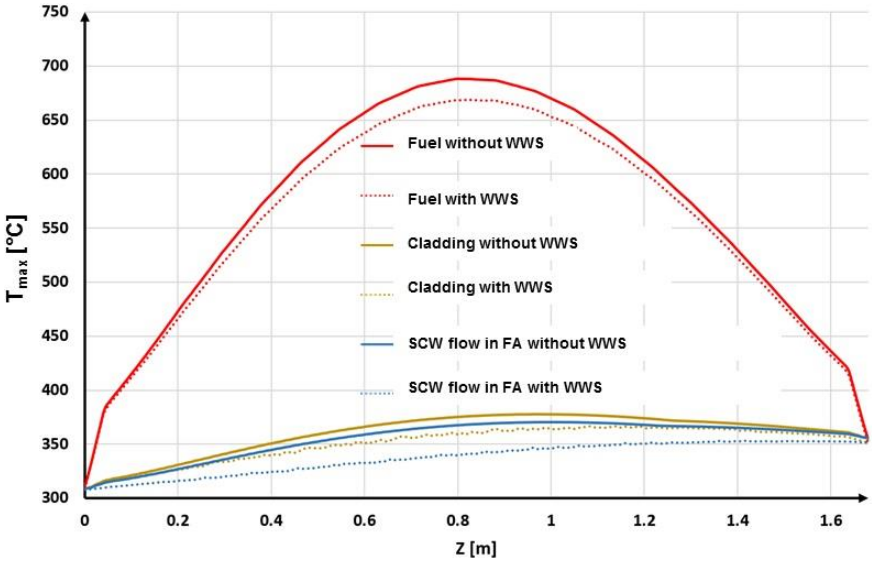

Figure 122. The distributions of the maximum temperatures along the length (Z [m]) for the fuel, the cladding solid and the SCW flow in FA fluid domains without/with WWS (Adorján 2022)

The flow field is simpler without WWS: the SCW flow in the FA has weak secondary flow pattern perpendicular to the main flow direction (Figure 124/a) (Kiss 2018, Adorján 2022). The flow field is more complex with WWS because the WWS cause significant mixing within subchannels (SC) and in the same time between neighbouring SCs (there are five different types of SCs: external corner, external wall, central, internal wall, internal corner) (Kiss 2018, Adorján 2022, Kiss and Mervai 2016, Kiss et al. 2011). The flow pattern and velocity field are mainly determined by the presence of WWS. They twist the flow lines (Figure 123), resulting in a rotating pressure and temperature field in the FA in the axial direction. The boundary surfaces between two SCs adjacent to the FABW and MBW (outer corner - outer wall, outer wall - outer wall, inner wall - inner corner, inner wall - inner wall) are always crossed only by the WWS of the adjacent fuel rod, which always directs the SCW flow in the same direction (Figure 124/b). This results in a so-called sweep flow along the walls. Viewed from the positive direction of the Z-axis, the sweep is counter-clockwise for the FABW and clockwise for the MBW. This can be seen in Figure 123/b and Figure 124/b. The sweep direction of the WWS is also plotted here, which is the direction of twist as Z is continuously increased.

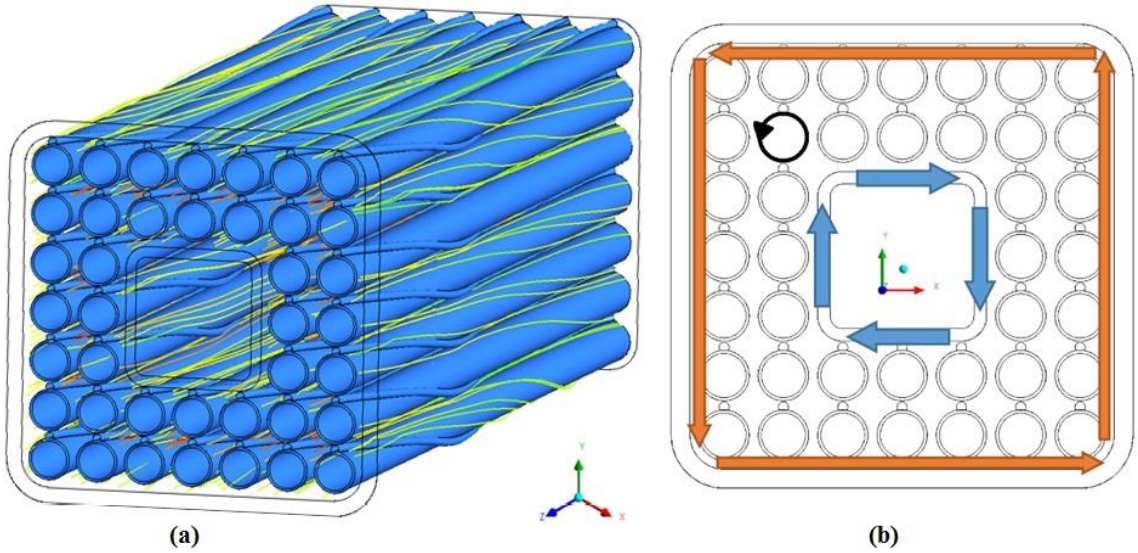

Figure 123. The flow pattern in the SCW flow in FA fluid domains with WWS: **a.,** the stream lines in the FA and **b.,** the so-called sweeping flow in the cross section of the FA (Kiss 2018, Adorján 2022, Kiss and Mervai 2016, Kiss et al. 2011)

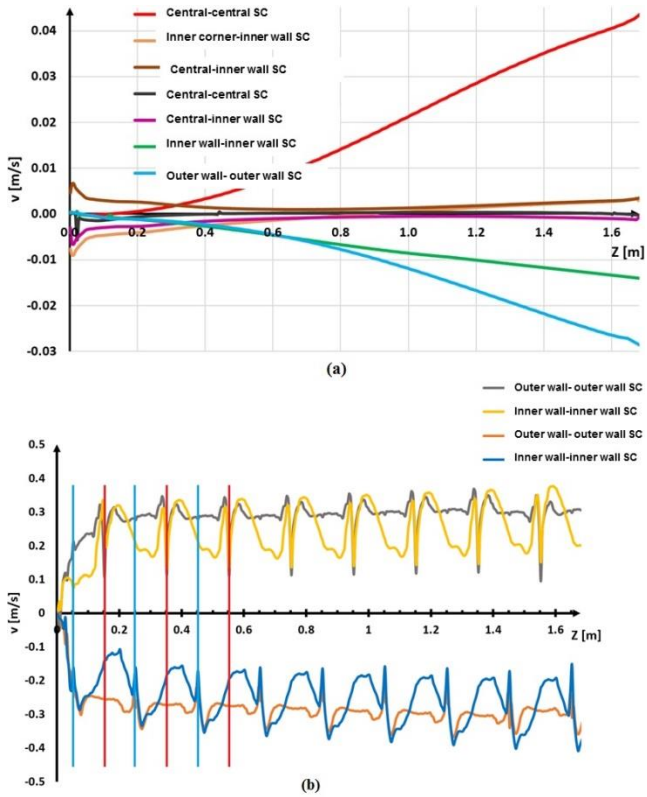

Figure 124. The velocity distributions on the BSs of different types of SC pairs for: **a.,** the SCW flow in the FA without WWS and **b.,** the SCW flow in the FA with WWS (Kiss 2018, Adorján 2022, Kiss and Mervai 2016, Kiss et al. 2011)

2.2.4.5 Further development of the SCW-SMR FA model

The flow directions of the SCW flows in the FA and MB were opposite in the original SCW-SMR FA model of BME (see Figure 118). Later, the flow directions were changed to identical in the system code analysis, so it was modified and made identical in the Ansys CFX model of BME as well.

The reference pressure and the volumetric heat source density were improved from M02 to M04 models. These improvements resulted in higher outlet pressure (equal approximately to 25 MPa in M04 and M05, see Figure 125) and outlet temperature (Figure 126). The flow directions are opposite in M02 and M04, while they are identical in M05 for the SCW flow in the FA and MB as well. As it can be seen, the change in flow direction has only a very moderate effect on the heating and pressure drop along the seven stages (see Figure 125 and Figure 126). The relatively large differences between the outlet pressure or temperature of some stages and the values of the neighbouring stages are due to the applied BCs (there is an un-modelled flow path in between two neighbouring stages, whose effect on the pressure and temperature fields was taken into account by the BCs).

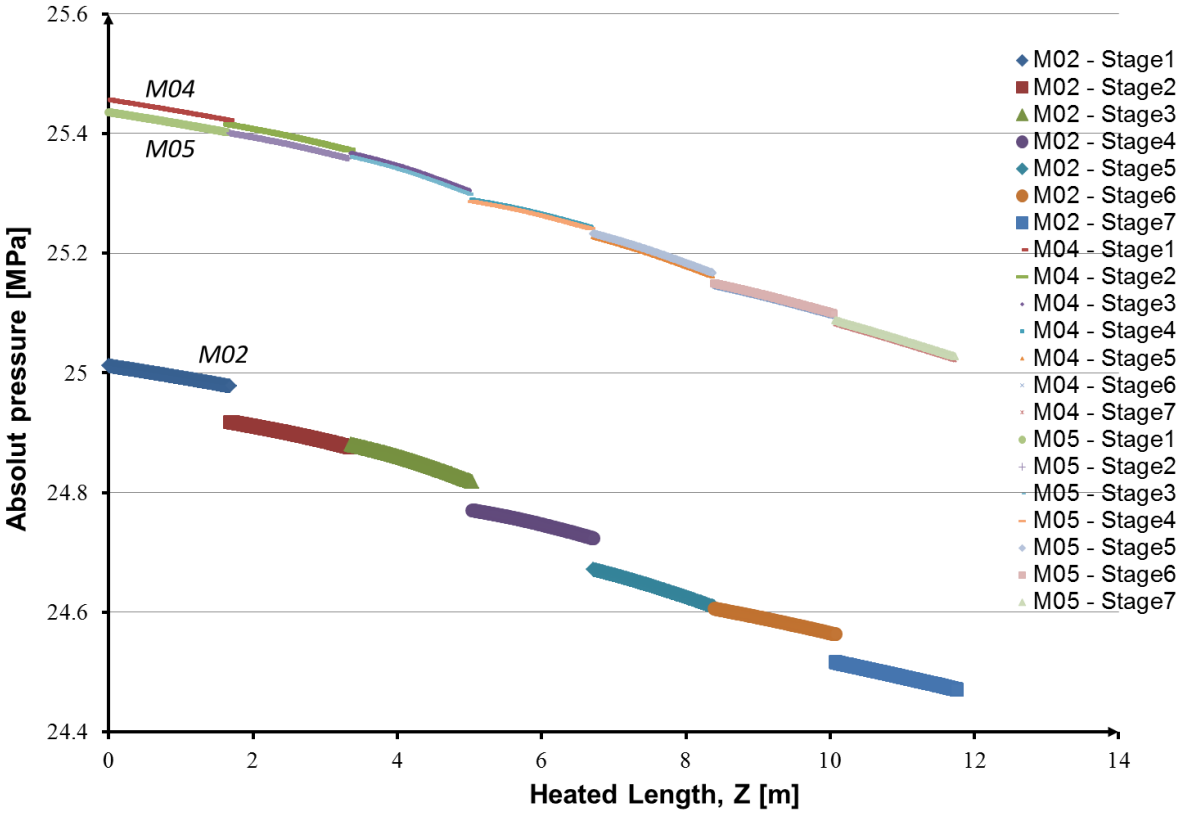

Figure 125. Abolute pressure distribution along the seven stages for Ansys CFX models M02, M04 and M05 of BME

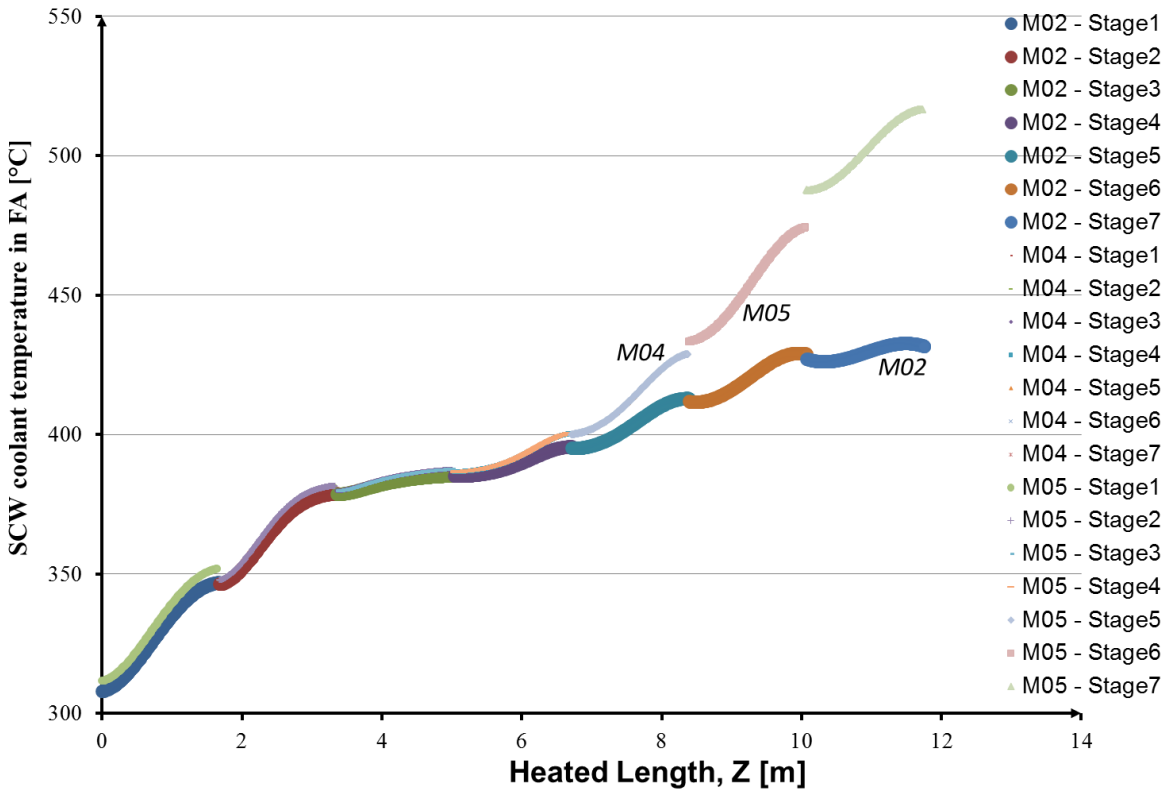

Figure 126. SCW coolant temperature distribution along the seven stages for Ansys CFX models M02, M04 and M05 of BME

2.2.4.6 Conclusions on Section 2.2.4

This Section 2.2.4 presents the CFD analysis of two main model types for the investigated FA geometry: without and with the wrapped wire spacer (WWS). In the first part of the CFD analysis, a systematic numerical mesh sensitivity analysis was performed to select the most appropriate near-wall (boundary layer) mesh structure and the appropriate axial and circumferential mesh resolutions for the simpler geometry without WWS. Here, the simpler geometry of the SCW flow in the fuel assembly (FA) allowed the application of the so-called block-structured numerical mesh in the case of all fluid and solid domains, more advanced turbulence models (the Shear Stress Transport (SST) and the BSL Reynolds Stress Model (BSL-RSM)) with rough wall modelling (Ra = 1.5 μm). In the second part of the analysis, the more complex geometry of the SCW flow in FA with WWS was constructed, discretised by an unstructured numerical mesh (without fine local near-wall mesh, but all other domains had the same block-structured numerical meshes) and studied by a CFD model with the standard k-ε turbulence model and rough wall modelling (Ra = 1.5 μm). In the third part, the effect of the WWS was investigated by comparing the results of two main types of CFD models of the FA with and without WWS.

The CFD models of the FA with and without WWS are slightly different, but the conservatism of the WWS model allows the results to be compared. The simulation results are accurate and show the beneficial effect of the WWS as the maximum temperatures are significantly reduced. It is also found that the outlet parameters of the SCW flow in the FA fluid domain (the "fresh steam parameters") are not significantly improved by the presence of the WWS. However, the disadvantage of the WWS is the higher pressure drop, since the presence of the WWS accelerates the SCW flow by reducing the cross-section and thus increasing the

hydraulic resistance. The clockwise and counterclockwise sweeping flows are identified and shown adjacent the moderator box wall (MBW) and fuel assembly box wall (FABW) respectively.

Changing the direction of the SCW flow in the FA and MB has only a very moderate effect on the heating and pressure drop along the seven stages.

2.2.5 Coupled calculations with Ansys CFX-Serpent on the horizontal SCW flow in the FA of SCW-SMR

Prior to the project, BME had already performed numerous CFD analyses in the past to investigate the suitability of available CFD models (e.g. sensitivity studies to define the appropriate numerical grid resolution or the most suitable turbulence model for the almost identical fuel assembly CFD model of the HPLWR concept) and had thus gained considerable experience (which was applied to the present CFD analysis) in the detailed thermal hydraulics analysis of heat transfer processes in SCWRs (Kiss 2018). In addition, a new benchmark exercise was also carried out in the frame of the ECC-SMART project. All the five cases of Experiment series 1 of the IBSCTH benchmark (NPIC 2021) have been modelled using the commercial CFD software package Ansys CFX version 19.5. Thus, a total of five CFD models have been developed in the framework of the first part of the benchmark (Heat Transfer Characteristics of SCW in 2×2 Rod Bundle Channel) with the following details: two models for 1.1 bare Rod Bundle Channel (Case 1 & 2); one for 1.2 local wire-wrapped rod bundle channel (Case 3) and two more for 1.3 full-length wire-wrapped rod bundle channel (Case 4 & 5). Mesh sensitivity studies have been performed for Case 1 and Case 3, and the lessons learnt have been incorporated into the models of the final calculations as well as for the present CFD analysis of the fuel assembly of the SCW-SMR concept.

The SCW flowing in the fluid domains was modelled as a turbulent, compressible, supercritical pressure (with case- dependent reference pressure around 23 and 25 MPa), dissipative (frictional and heat transfer) fluid using the Reynolds averaged Navier-Stokes equations (using the RANS CFD method). The supercritical water was modelled using the IAPWS-IF97 material property functions available in Ansys CFX over case-dependent temperature and pressure ranges. The modelling of solid domains (rod walls, spacers, shroud walls, etc.), the boundary conditions and other CFD settings (e.g. solver settings) were specified in case-dependent manner as well. Figure 127 depicts the CFD model of Case 4 and 5.

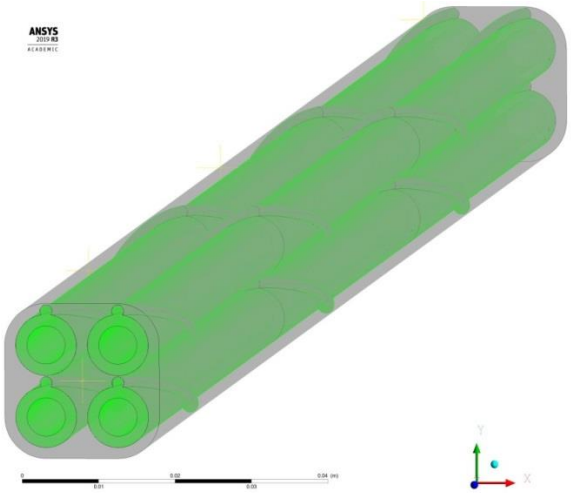

Figure 127. The CFD model of 1.3 full-length wire-wrapped rod bundle channel (Case 4 & 5)

Based on the CFD results and the comparison between CFD and experimental data it can be stated that relatively good agreement was achieved in the benchmark exercise.

2.2.5.1 The Serpent 2 models

The main objective of the investigations carried out with the Serpent 2 particle transport code was to develop a full-core model with an improved core design that can serve as a basis for further examinations. The initial core model was based on the pre-conceptual design of (Schulenberg and Otic 2021 and 2022) and is presented in Figure 128. The core model consists of the fuel assembly lattice, the outer moderator which fills the space in between the assemblies, the inner reflector, and the steel plates surrounding the assembly lattice and the inner reflector. The fuel assemblies consist of the outer assembly walls, the fuel pin lattice, the coolant that fills the space between the fuel pins and the moderator box in the center of the assembly which is filled by the inner moderator. The initial core model contained UO_2 fuel assemblies with 5% enrichment.

a., 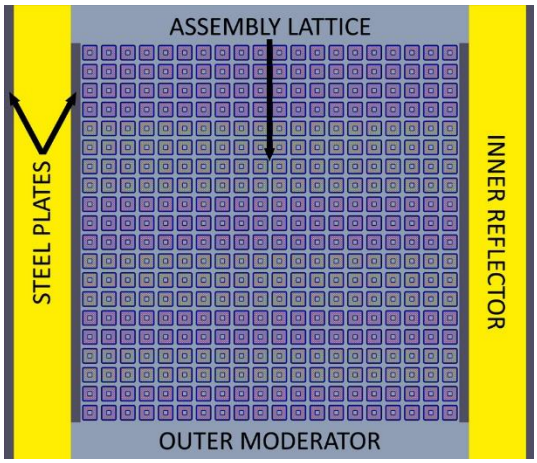

b., 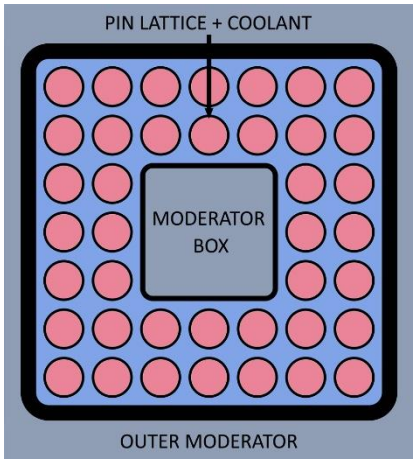

Figure 128: a., The Serpent 2 core (left) and b., the fuel assembly (right) models

Based on the initial examinations and the preliminary single channel analysis of (Schulenberg and Otic 2021), the core improvement process targeted two key parameters: the burnup cycle length and the core power distribution. For a longer burnup cycle length, the reserve reactivity could be increased by simple modifications in the model. The preliminary studies did not consider fuel shuffling, nor the usage of reactivity control rods or burnable absorbers. Therefore, these modifications included a new assembly structure with lower neutron absorption, reduced moderator temperature and increased assembly gaps for better moderation, and finally, an improved enrichment map with the application of MOX besides the UO_2 fuel assemblies. As a result of the various modifications, the burnup cycle length could be increased from a few months to more than 2 years (without shuffling).

The core power distribution was mainly improved through the modification of the enrichment map. The preliminary single channel analysis determined a target maximum linear heat rate (MLHR) profile considering the fuel centerline and cladding temperatures (Schulenberg and Otic 2021). Therefore, the enrichment map of the improved core was determined in such a way that the resulting MLHR profile, calculated from the hottest assemblies at each heat-up stage, could follow it as closely as possible. The enrichment map of the final core model and the MLHR profiles are presented in Figure 129. Considering the need for a sufficiently high reactivity reserve, the average enrichment of the core had to be kept relatively high. As a consequence and due to the preliminary nature of these calculations, a suitable but not perfect MLHR profile was obtained with the chosen enrichment map.

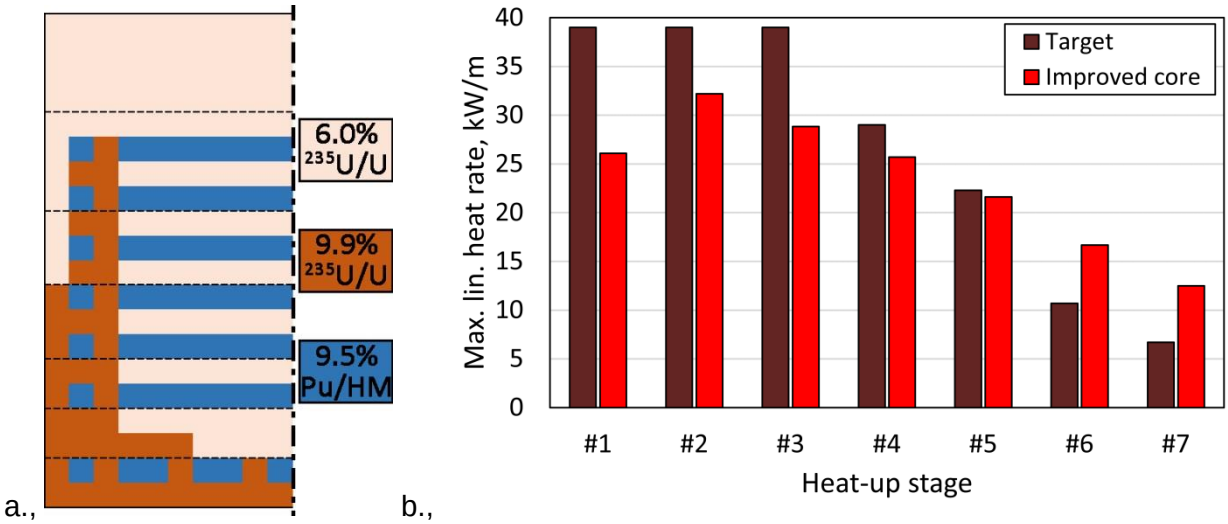

Figure 129**:** a., Improved core model enrichment map (left) and b., the hot channel MLHR profiles (right)

The improved full-core Serpent 2 model is primarily coupled to the APROS system code, the implementation of which is semi-automatic. By this we mean that the codes do not communicate and exchange data directly with each other as in SPNDYN (see Section 3.3), but write their results to a file, which is then processed using MATLAB scripts to generate the input dataset in the desired format needed to run the next iteration of the other code (Mészáros et al. 2023). The dataset exchanged between the codes is practically identical for Serpent 2 and SPNDYN (density and temperature profiles in one direction and power distribution in the other), only the method of communication and the input data format required by the two reactor physics codes differ.

In addition to the entire core reactor model, BME developed a detailed SCW-SMR assembly model in Serpent 2 as part of an MSc thesis for later coupled CFD and Serpent 2 calculations (see Figure 130) [24].

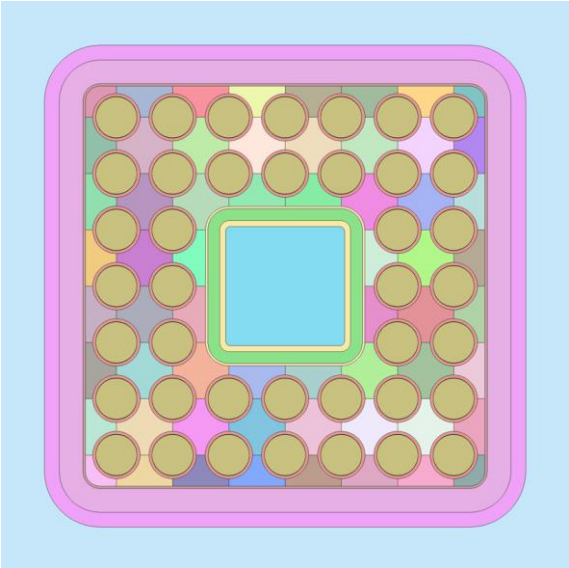

Figure 130: The SCW-SMR assembly model developed in Serpent 2 for coupled CFD and Serpent 2 calculations

The aim was to characterize an average assembly, so a radially reflective, axially vacuum boundary condition was applied. The model is unique due to the large number of different material

domains. The assembly is divided axially into 32 nodes (5.25 cm each), and each of the 60 subchannels corresponding to each fuel pin represents a separate material region to account for the axially varying coolant and moderator temperatures and densities. The fuel and other structural elements are assumed to have constant axial temperature and density profiles. The large number of material regions with different temperatures and densities lead to high memory consumption; therefore, the fractional reconstruction tolerance of the unionized energy grid was increased to 0.005 in Serpent 2 (set egrid 0.005). The helical wire wrap was not modelled, and the ENDF/B-VII.1 nuclear data library was used for the coupled computations. For energy deposition calculations, the default option was used (edepmode set to 0).

2.2.5.2 The Ansys CFX model

The CFD model for the horizontal fuel assembly (FA) of the SCW-SMR was developed in the 19R3 version of the commercial Ansys CFX software package. The objective of the model was to calculate the thermal hydraulics fields of the SCW flowing as both coolant and moderator inside the FA in sufficient detail through a series of iterations by weak coupling with the Serpent 2 reactor physics model. The ultimate goal of the CFD model was to compare its results with those of the APROS and RELAP5 (from UNIPI) system code models after further development, and thus to verify the model.

The model geometries (see Figure 131) and numerical grids were created in Ansys ICEM CFD 19R3 for two fluid domains: the coolant flowing inside the FA (discretized with a numerical grid of tetragonal elements) and the moderator flowing inside the moderator channel (discretized with a numerical grid of block-structured hexagonal elements).

The coolant flows in the opposite direction to the moderator in this model. The effect of the moderator flowing from bottom to top in the so-called gaps between the FAs was taken into account by a constant temperature boundary condition (309.45°C), which was specified as a boundary condition on the outer surface of the FA wall (transparent grey area in Figure 131). In addition to the liquid domains, the CFD model also includes 82 solid domains, which are: 40 solid domains of fuel rods (red area in Figure 131) with an outer diameter of 7 mm and an active length of 1.68 m; 40 joint cladding and wrapped wire spacer solid domains surrounding the fuels (blue in Figure 131) with an outer diameter of 8 mm and a length of 1.8 m (the pitch of the wrapped wires is 0.2 m); 1 FA wall solid domain (transparent grey in Figure 131) and 1 moderator box wall solid domain (transparent green in Figure 131).

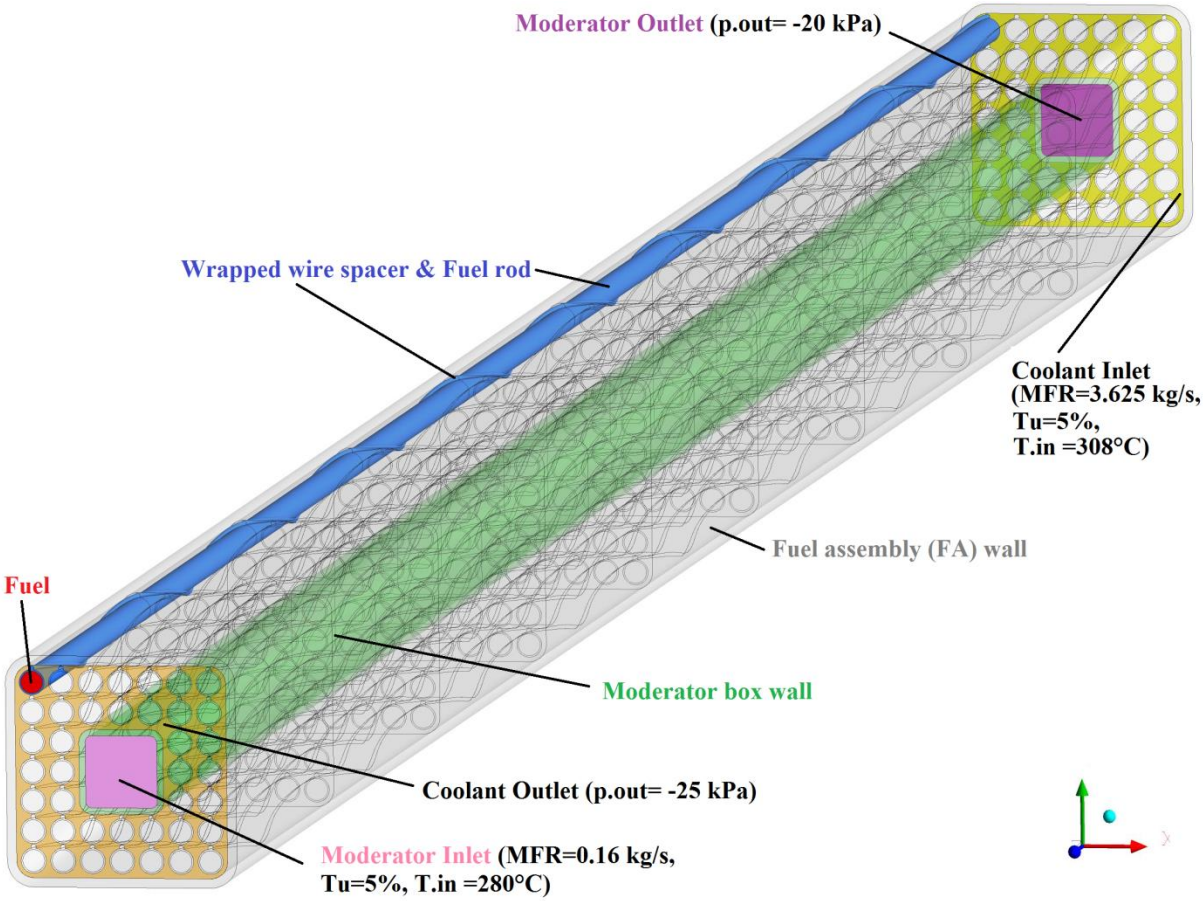

Figure 131: the geometry and boundary conditions of the ANSYS CFX model

The standard k-ε turbulence model was used in the preliminary CFD calculations (when the so-called "pre-pre conceptual design" was changing) and the more advanced SSG Reynolds Stress Model is currently used in the final CFD calculations (to model the complex thermal hydraulics that occur in the FA in a more physically realistic way than the standard k-ε) for the SCW fluid domains, while 1.5 μm wall roughness was specified for each solid wall.

2.2.5.3 SCW-SMR calculation results by Serpent 2 – Ansys CFX coupling

A weak coupling method was also used for the coupled calculations performed with Ansys CFX and Serpent 2. The pin-by-pin axial power distribution was determined by Serpent 2 and used as input for the Ansys CFX calculations. The CFD calculations determined the temperature and density values, which were used as inputs in the subsequent calculation step performed with Serpent 2. To make the weakly coupled calculations less susceptible to potential human error, the Serpent 2 input model modifications were performed using dedicated MATLAB scripts.

Two iteration series were performed with the coupled code system described above. Figure 132 and Figure 133 show the volumetric heat source density along the FA for the 1st and 2nd iteration series.

Regarding both sets of calculations, the results varied only slightly between the subsequent iteration steps. At the end of the iteration, the vast majority of the observed deviations were within the calculated one sigma uncertainty of Serpent 2. The results of the two sets of calculations converged to approximately the same distribution. This is due to the fact that the same Serpent 2 model was used for the iterations and that the Ansys CFX models also showed a high degree of similarity.

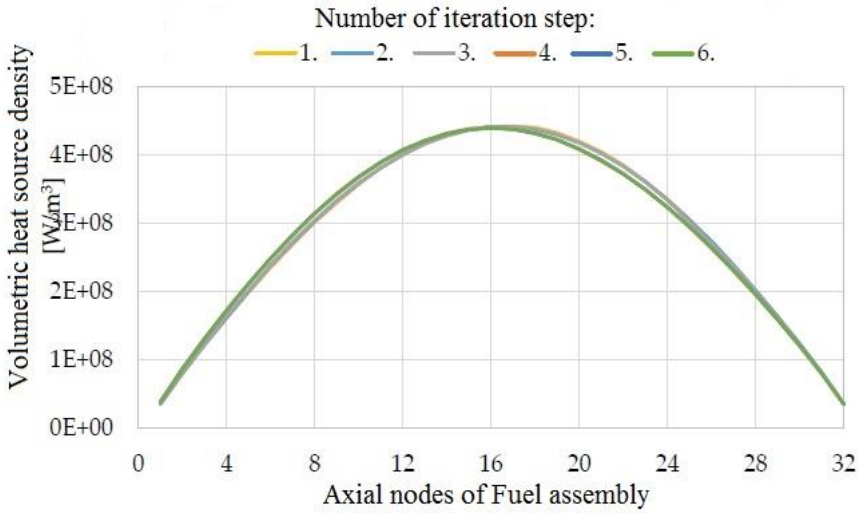

Figure 132: Volumetric heat source density along the fuel assembly for the 1st iteration series

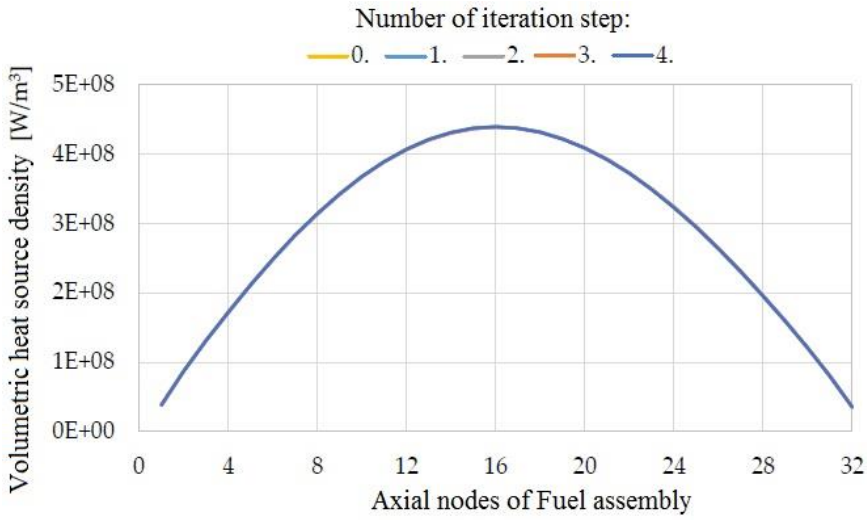

Figure 133: Volumetric heat source density along the fuel assembly for the 2nd iteration series

2.2.5.4 Conclusion on Section 2.2.5

The work presented in this Section 2.2.5 was carried out in the frame of the ECC-SMART project, and included both comprehensive benchmarking exercises and various analyses related to the pre-conceptual design of the SCW-SMR. For these purposes, a number of models have been developed using APROS, Ansys CFX, Serpent 2 and SPNDYN. Furthermore, various coupling methods have been established using these codes. The code systems obtained have proved to be suitable for carrying out a wide range of analyses of the new concept with. The results obtained are consistent with each other and show the consistency of the design with its main objectives so far. Now, both the analysis tools and the proposed design concept can be further improved, and optimized, taking into account a wide spectrum of relevant phenomena.

2.3 CONTRIBUTION BY CNL

It is known that the surface finishing, such as roughnes,s is an important varaible in hydraulic resiance and heat transfer. For example, for internal flows, such as a fuel assembly, the cladding's roughness increases the turbulence of the flow, thus enhancing the heat transfer, but with the

trade off of an increased pressure drop. Norris (Norris, used several experimental datasets to approximate empirically the interplay between roughness and roughness. Norris (Norris, 1970) proposes the following relation:

$$\frac{\mathrm{Nu}}{\mathrm{Nu}_s} = \left(\frac{f}{f_s}\right)^n, \tag{47}$$

Where,

$$n = 0.68(\mathrm{Pr})^{0.215}. \tag{48}$$

$$\text{for } 1 < \mathrm{Pr} < 6.$$

In these equations, f is the fanning friction factor, Nu is the Nusselt number, and the subscript s stands for smooth.

This relationship has also been used to develop friction correction factors. Pioro reported three friction correction factors for diabatic supercritical flows. These are:

The Kirillov correlation (Kirillov P.L., 2000):

$$f_{non-iso} = f_{iso}\left(\frac{\rho_w}{\rho_b}\right)^{0.4}, \tag{49}$$

$$\text{for } 8\times10^4 < \mathrm{Re} < 1.5\times10^6.$$

The Razumovskiy et al. Correlation (Razumovskiy et al., 2016):

$$f_{non-iso} = f_{iso}\left(\frac{\rho_w}{\rho_b}\frac{\mu_w}{\mu_b}\right)^{0.15}, \tag{50}$$

for $H_b \leq 1500$ kJ/kg and $H_b \geq 2250$ kJ/kg, $0.8 < q''/G < 1.0$ kJ/kg.

and the Yamashita et al. Correlation (Yamashita et al., 2003)

$$f_{non-iso} = f_{iso}\left(\frac{\mu_w}{\mu_b}\right)^{0.72}. \tag{51}$$

These friction correction factors have been implemented in an interim version of the subchannel code ASSERT-PV to assess their impact on pressure drop prediction. The results showed that a correction factor reduces the uncertainty of the ASSERT-PV SC predictions for pressure drop. This is more pronounced for cases close to the critical or pseudo-critical point.

A limited analysis was published by A. Nava Dominguez (Nava Dominguez, 2020). These friction correction factors will be formally evaluated in the upcoming validation exercise of ASSERT-PV SC.

2.3.1 Fouling—Cladding corrosion

During the reactor operation, the surface of the cladding reacts with the water (coolant) to form a layer of oxide film at the surface. This oxide film and its properties are time-dependent and usually grow with time. For current LWRs using Zircaloy, a total oxidation of 17% of the cladding thickness and a maximum cladding temperature of 1204°C are current regulatory-imposed limits (Todreas and Kazimi, 2021).

Multiple models have been developed to take into account the effect of corrosion on the heat transfer of a nuclear fuel cladding material (Bison, Reyman Ed. 1978, Todreas and Kazimi, 2021).

The nuclear codes BISON and MATPRO models are based on the heat conduction equation for a long cylinder. For example, Todreas and Kazimi (Todreas and Kazimi, 2021) proposes a model based on the overal thermal resistance.

$$T_{max} - T_m = \frac{q'}{2\pi}\left[\frac{1}{2k_f} + \frac{1}{R_g h_g} + \frac{1}{k_c}\ \ln\left(\frac{R_{co}}{R_{ci}}\right) + \frac{1}{R_{oo}\, k_{ox}/\delta_{ox}} + \frac{1}{R_{oo} h}\right] \quad (52)$$

$$T_{co} = T_{oo} + \frac{q''}{k_{ox}/\delta_{ox}} \quad (53)$$

$$T_{oo} - T_m = \frac{q'}{2\pi R_{oo} h} \quad (54)$$

$$q' = 2\pi R_{oo} h (T_{oo} - T_m) \quad (55)$$

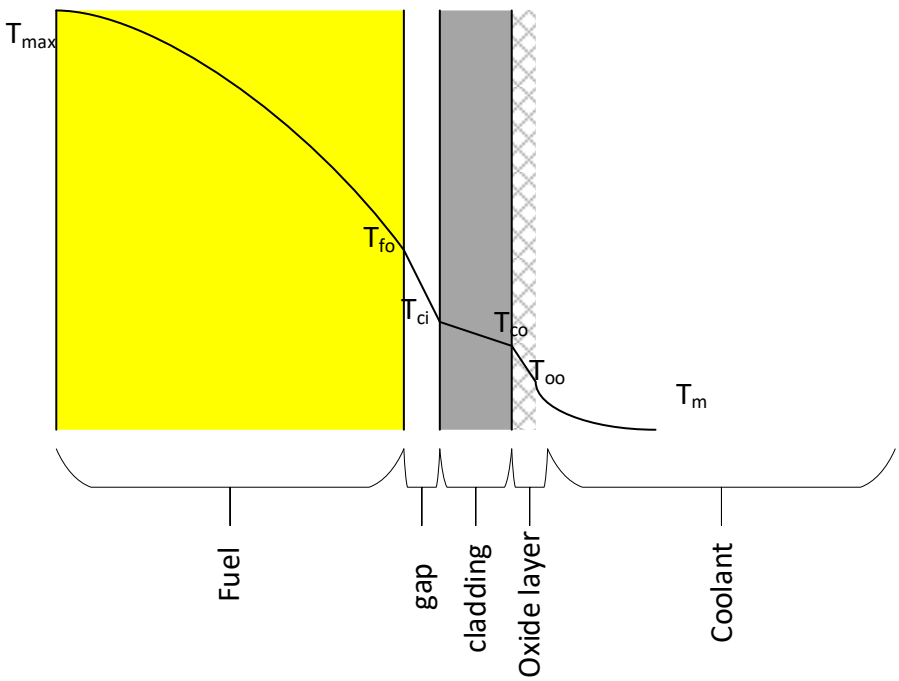

Figure 134 Representation of a fuel element thermal layers

Where T_{co} is the temperature at the interface between the oxide layer and the cladding, T_{oo} is the temperature of the outer surface of the oxide layer, q'' is the heat flux, S is the oxide layer thickness, and k_{ox} is the thermal conductivity of the oxide layer.

However, a key variable needed to complete the model is the thermal conductivity of the oxide layer and the oxide layer thickness. To complete this model, one of the objectives of the ECC-SMART project is to develop a oxide layer growth model for the proposed cladding materials. These materials are SS-310 and Alloy 800H. Multiple participants of this project conducted corrosion experiments and several coupons were exposed to supercritical conditions. CNL carried out experiments to estima the thermal conductivity of several coupons. The results are listed in Table *20*. Figure *135* shows a cross-sectional view of an exposed coupon showing the oxide layer.

Table 20 Thermal conductivity measurements for the proposed cladding materials.

Material	Sample Treatment	Average Oxide Thickness [µm]	Thermal Conductivity @ 140°C [W/(m K)]	Thermal Conductivity @ 250°C [W/(m K)]	Thermal Conductivity @ 420°C [W/(m K)]
800H	As-received	-	13.5	15.7	18.2
310S	As-received	-	14.4	16.5	18.6
800H	3000-h at 380°C and 23 MPa	0.8	10.3	10.9	14.4
310S	3000-h at 380°C and 23 MPa	1.3	11.6	14.1	13.6
800H	3000-h at 500°C and 23 MPa	7.3	6.1	6.3	8.7
310S	3000-h at 500°C and 23 MPa	1.4	11.0	11.7	7.0
800H	7000-h at 380°C and 23 MPa		5.5	5.6	10.1
310S	7000-h at 380°C and 23 MPa		5.0	7.1	12.0

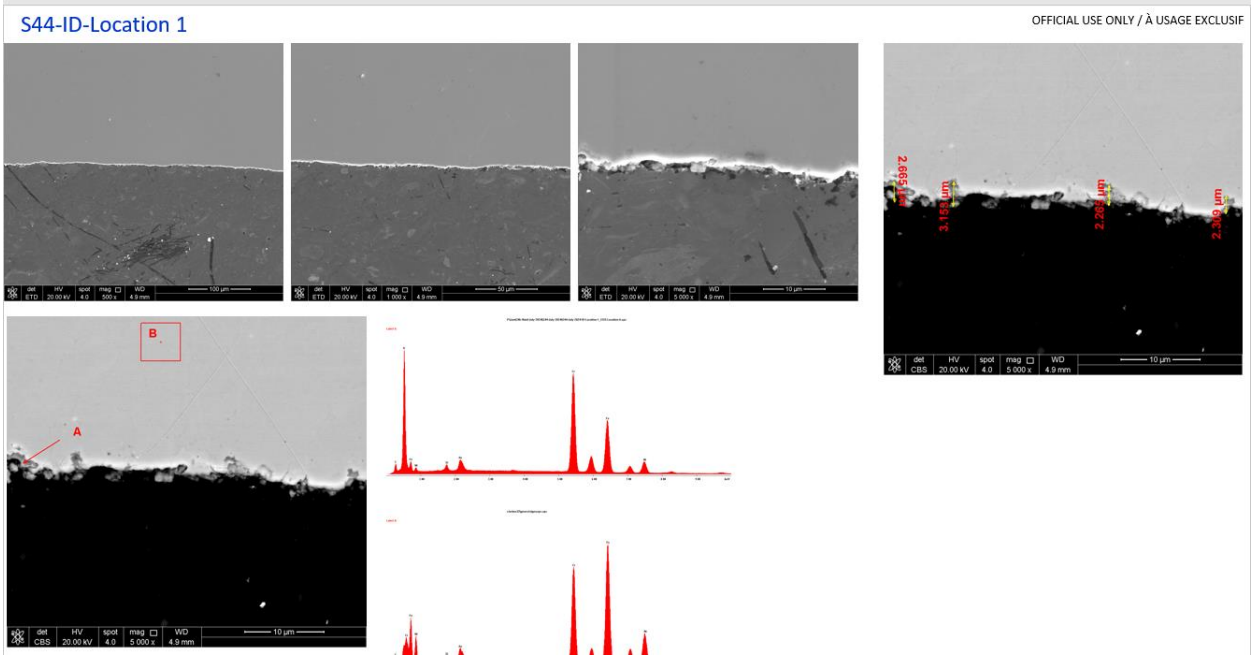

Figure 135 Cross-sectional view of a corroded coupon showing the oxide layer thickness.

Furthermore, these coupons were analyzed to gain knowledge of their oxide structure and formation.

Unfortunately, the oxide groth model is still under development. However, Guzonas et at. (Guzonas et al., 2018) proposes the following model of weight gain for Alloy 800H exposed to supercritical water conditions:

$$\Delta W = (0.6T - 302) + 17 \exp\left(\frac{51000}{RT}\right) t \quad (56)$$

Where R is the gas constant, T is the temperature, and t is the exposure time. Similar models were proposed for 310 SS. Note that, the results of Equation(*56*) need to be transformed to thickness.

The proposed model to take into account the effect of the surface finishing on heat transfer and hydraulic resistance is based on the model proposed by Todreas and Kazimi (Todreas and Kazimi, 2021). To close the model, it is possible to use Equation (*52*)alongside a friction correction factor (Equations (49), (50), or (51)). The oxide layer thickness can be estiamted using Equation (*56*) and the thermal conductivity of the oxide deposits from Table *20*.

Due to time limitation, the complete assessment of the proposed model has not been completed. For that reason, it is recommended that the validity of the assumptions used in the model be verified using the data generated in this project from Deliverable 3.1 "Reference Database" of this project.

The CATHENA and ASSERT-PV SC results on the effect of surface finishing will be presented in Deliverable 3.4 "Report on the improved system codes describing how they improved". The rationale for presenting the results in Deliverable 3.4 is to quantify the improvement by using the models presented in this section for roughness and heat transfer fouling, against simulation results from previous studies.

2.4 CONTRIBUTION BY IPP

2.4.1 Introductory remarks

The problem of using existing calculation methods for heat transfer processes at supercritical parameters becomes much more relevant in the context of designing promising nuclear reactors with SC water parameters.

The IPP contribution to Subtask 3.3.1 is aimed primarily at improving the understanding of the predictive capabilities of existing computational fluid dynamics methods in modeling the hydrodynamic and heat transfer behavior of fluids under supercritical conditions.

So, the first IPP actions included the following stages:

- The initial step was the analysis of existing experimental studies and the selection of those that are primarily referent for testing and validating the applied CFD models;
- Testing the applicability of different turbulence models in CFD using wall functions or taking into account the so-called low-Reynolds effects (low-Re), which began to be carried out even before the start of the ECC-SMART project (Filonov et al., 2018), and further developed within the framework of ECC-SMART (Dubyk et al., 2021). This work was aimed at clarifying the predictive capabilities of standard CFD methods with the involvement of various turbulence models and formulating conclusions regarding necessity of their further developments/adaptations.

Based on the formulated conclusions, the further stages of the work were as follows:

- Adaptation of temperature wall function for calculation of the heat transfer at supercritical conditions with the aim of improving the predictive capabilities of the applied CFD methods, which is described further in section 4.2.
- Modification of Eddy viscosity turbulence model to take into account non-linear effects of heat transfer, the description of which could be found in section 4.3. The applicability and effect of the proposed modifications due to the complexity of implementation in commercial CFD packages were primarily tested using a Non-linear differential method for predicting the intensity of heat transfer and energy dissipation at supercritical parameters. This method was proposed and developed by IPP as part of the work on "Improvement of system analysis methods" performed and documented in deliverable D3.4, where the key idea is to replace the HTC correlations using the proposed differential procedure based on the Narrow channel model (Filonov et al., 2024).

The last described works are a logical continuation of those carried out in current Subtask 3.3.1 and were developed simultaneously within the framework of the ECC-SMART project and doctoral work of Vladislav Filonov (Filonov, 2023). The description and results of application of the proposed modifications are included in Chapter 4 dedicated to Subtask 3.3.4 – “Improvement, implementation and validation of engineering models for turbulent heat transfer under supercritical conditions (IPP)”.

It is also worth noting that some other works related to establish HTC correlations and CFD models appropriate for SCW conditions were carried out at IPP in parallel:

- On testing the predictive capabilities of HTC correlations, where more then 60 existing correlations identified and described by UNIPI (Kassem et al., 2022) were implemented. However, it was conducted using IPP’s internal 1D code – TMM (Varju et al., 2024; Filonov et al., 2024), so the corresponding description and conclusions can be found in deliverable D3.4 dedicated to the system codes improvements.
- And on the implementation of the pseudo-boiling concept to describe the supercritical state of the coolant with the possibility of transition to a two-phase region (Filonov et al., 2024; Filonov et al., 2025). Such generalization was implemented in ANSYS CFX to provide the possibility to assess the LOCA initial dynamics behavior. This part of the IPP work was described in the framework of the Safety and design analysis of the SCW SMR concept in deliverable D3.3.

2.4.2 Selection of experimental studies most applicable for testing existing CFD models and validating their possible modifications

Deteriorated heat transfer in supercritical region is a multifactorial problem, which is determined not only by the extreme nonlinearity of thermophysical properties, but also by non-linear turbulent transfer. The relationship between turbulent momentum and energy transfer in this case has a more complex dependence than in the Reynolds analogy and is largely affected by the balance of buoyancy, inertia, and thermal acceleration forces (Kurganov et.al., 2018). This is an important feature of this type of non-isothermal flow. Therefore, the phenomenon of heat transfer deterioration should be investigated in-depth, including the structure of the turbulent flow.

Today there is a very limited number of comprehensive experimental studies, despite the fact that the HTD phenomenon was discovered by Styrykovych and Shytsman (Strykovich et.al., 1955) in the middle of the last century. This is due to the complexity of organizing the experiments, as well as achieving repeatability of the results, and even ensuring the required level of instrumental accuracy, which is still a problem for this type of experiment.

The existing experimental studies can be classified into four main categories:

- «Comprehensive» experimental studies that include measurements of the characteristics of velocity and temperature profile in the radial direction (Wood and Smith, 1964; Bourke and Puiling, 1971; Bourke et.al., 1968), as well as hydraulic resistance (and friction resistance) and axial temperature profile (unique studies). In this case, both the thermal-hydraulic state of the flow under a wide variation of operating parameters and the effect of the flow orientation relative to gravity are studied (Kurganov and Kaptil'ny, 1993; Kurganov and Kaptil'ny, 1992).
- «Experimental» studies that allow to evaluate the temperature profile, as well as hydraulic resistance, including friction resistance (complete experimental studies).
- «Temperature» experiments, which include the vast majority of modern studies (IAEA-TECDOC-1746, 2014; IAEA-TECDOC-1900, 2020), characterized by the analysis of the temperature field not only in the axial direction, but also in the azimuthal direction (Wang et.al., 2016). Most of the new studies concern rod assemblies (Razumovskiy et.al., 2016; Eter et.al., 2016), which simulate the non-uniformity of energy release (University of Wisconsin, 2017), or different configurations of ribs – the heat transfer intensifiers (Razumovskiy et.al., 2016; Eter et.al., 2016; University of Wisconsin, 2017; Yaras, 2015).
- «Indicator» experiments, the main purpose of which is to identify the HTD establishing for a different set of operating parameters by visually changing the color of the heating surface (Razumovskiy, 1984). Such experimental studies are relevant in the case of creating a criterion for the beginning of the heat transfer transition from normal to deteriorated.

Thus, within the analysis of available and accessible for IPP experimental data sets obtained by different research groups, an experimental database was formed. That was subsequently distributed within the framework of the ECC-SMART project and used by its participants in activities related to internal benchmarking of system codes (deliverable D3.2) and testing the predictive capabilities of various HTC correlations for supercritical coolant parameters.

Some of the research results collected in the experimental database are of particular interest from the point of view of testing the capabilities of existing CFD methods and validating their possible modifications. Below is a brief description of the datasets selected by IPP for these purposes.

2.4.2.1 Kurganov Probe Data

The first data set is Kurganov Data, which belongs to the first conditional type of comprehensive experimental studies. This dataset is quite unique, since it makes it possible to study the structure of the turbulent flow, which define the temperature and hydraulic regime of a non-isothermal flow.

Comprehensive studies of heat transfer, hydraulic resistance, velocity and temperature fields during the heating of carbon dioxide in a vertical pipe for the upward and downward coolant flow were carried out. A more detailed description of the experimental facility is given in deliverable D3.2.

In addition to the classical axial temperature profile, the authors provide a radial profile of velocity and temperature, as well as the enthalpy field (Kurganov et.al., 2018; Kurganov and Kaptil'ny, 1993; Kurganov and Kaptil'ny 1992). These data can be used as calibration data for new models, as well as for analyzing the influence of a specific component (term) in the equations of motion (e.g., gravity). Figure 136 shows the results of measurements for one of the regimes with HTD, which was conducted both during the upward and downward movement of the coolant.

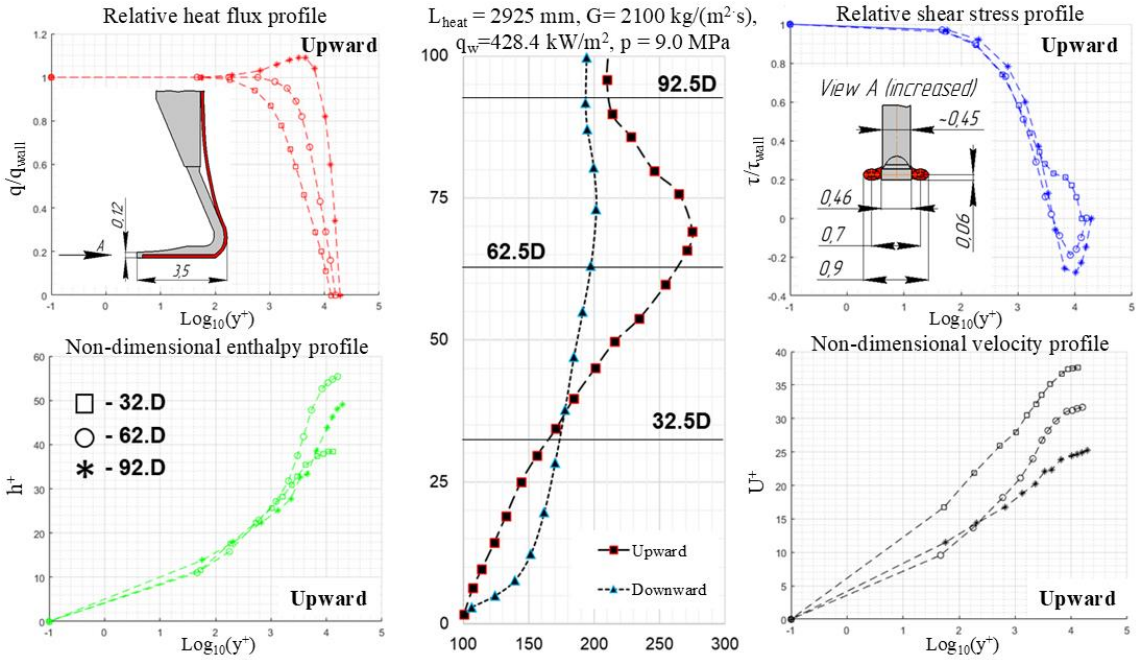

Figure 136. Experimental profiles during the heat transfer deterioration for the upward and downward flow of a supercritical medium

These fundamental experimental studies were used by IPP as the basis for validating the proposed modifications (see section 4).

2.4.2.2 NTUU Rod Bundles data

In terms of predicting the temperature field of the heated wall, the HTD regimes obtained at NTUU for the rod bundles are indicative, since they allow to assess the capabilities of turbulence models when using them for geometries close to the real fuel assemblies. Many experimental studies were conducted at Igor Sikorsky Kyiv Polytechnic Institute on various test sections. The detailed description of the NTUU experimental facility and assemblies geometry is given in deliverable D3.2.

The most illustrative regimes were obtained on the test sections of the 1R, 3R, and 7R fuel rod simulator assemblies, the general view of which is shown in Figure 137. For the rods positioning in the assemblies, the special ribs were used, which also provided the flow swirling that facilitated its turbulization.

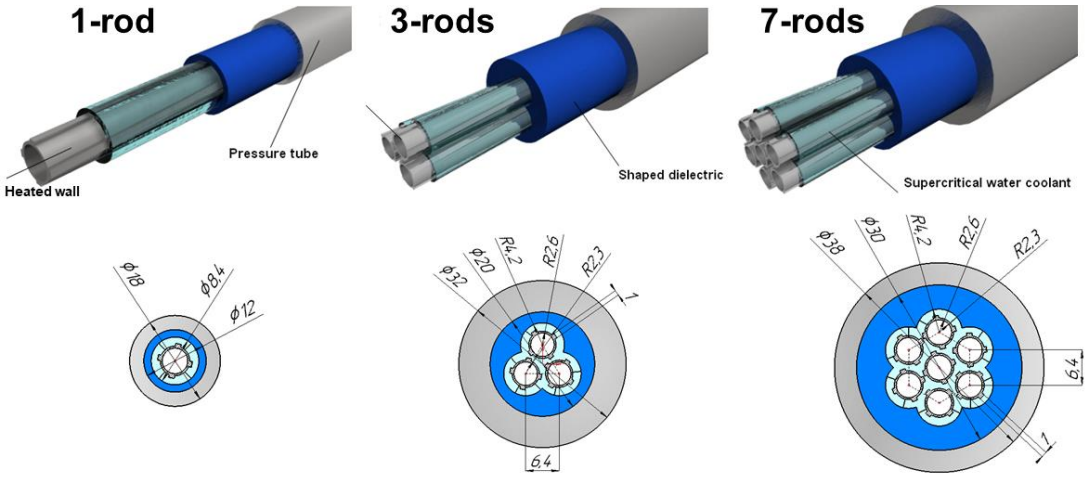

Figure 137. Annular channel (1R) and rod bundles (3R, 7R) geometry

The obtained experimental data is quite valuable in the context of small modular supercritical pressure reactors. Firstly, because of the geometric features (the heating part is up to 600 mm) and the set of operating parameters (see Table 21). Secondly, it is the unique data on the heat transfer deterioration obtained on assemblies of 1R, 3R, and 7R, taking into account the presence of ribs (turbulizers). It is believed that this shifts the region of HTD occurrence towards higher thermal loads at a fixed mass velocity.

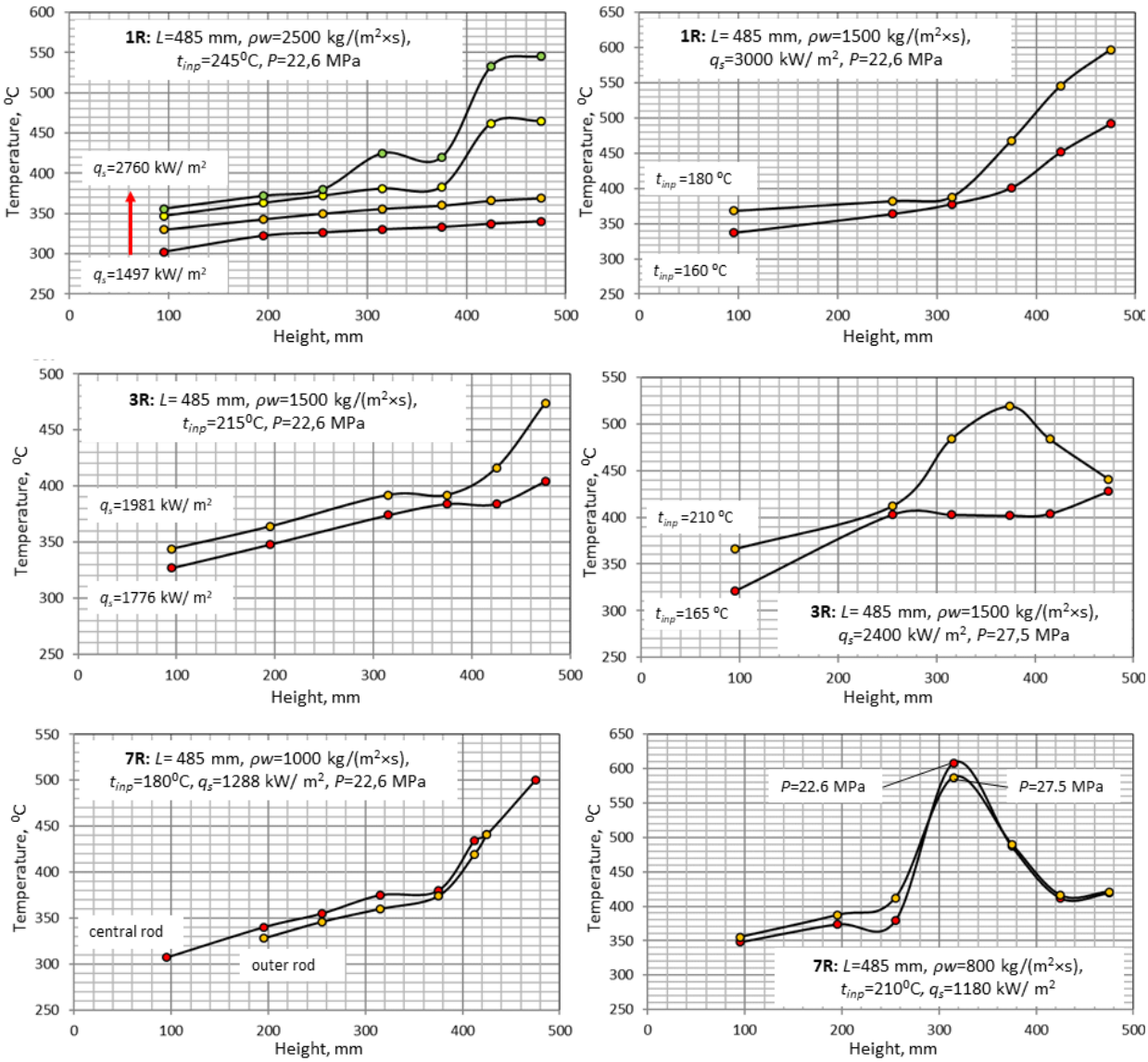

Figure 138 shows examples of axial temperature distributions obtained on assemblies that demonstrate the presence of the HTD phenomenon.

Table 21. NTUU test matrix

P, MPa	t_{in}, ºC	t_{out}, ºC	G, kg/(m²s)	q, MW/m²	q/G, kJ/kg
		1-rod bundle (annular channel)			
22.6, 24.5	125–352	206–366	800–3000	1.03–3.45	<2.4
		3-rod bundle			
22.6, 24.5, 27.5	125–337	216–372	1000–2700	1.25–4.58	<2.5
		7-rod bundle			
22.6, 24.5, 27.5	125–337	216–372	800-1000	0.71-1.29	<2.5

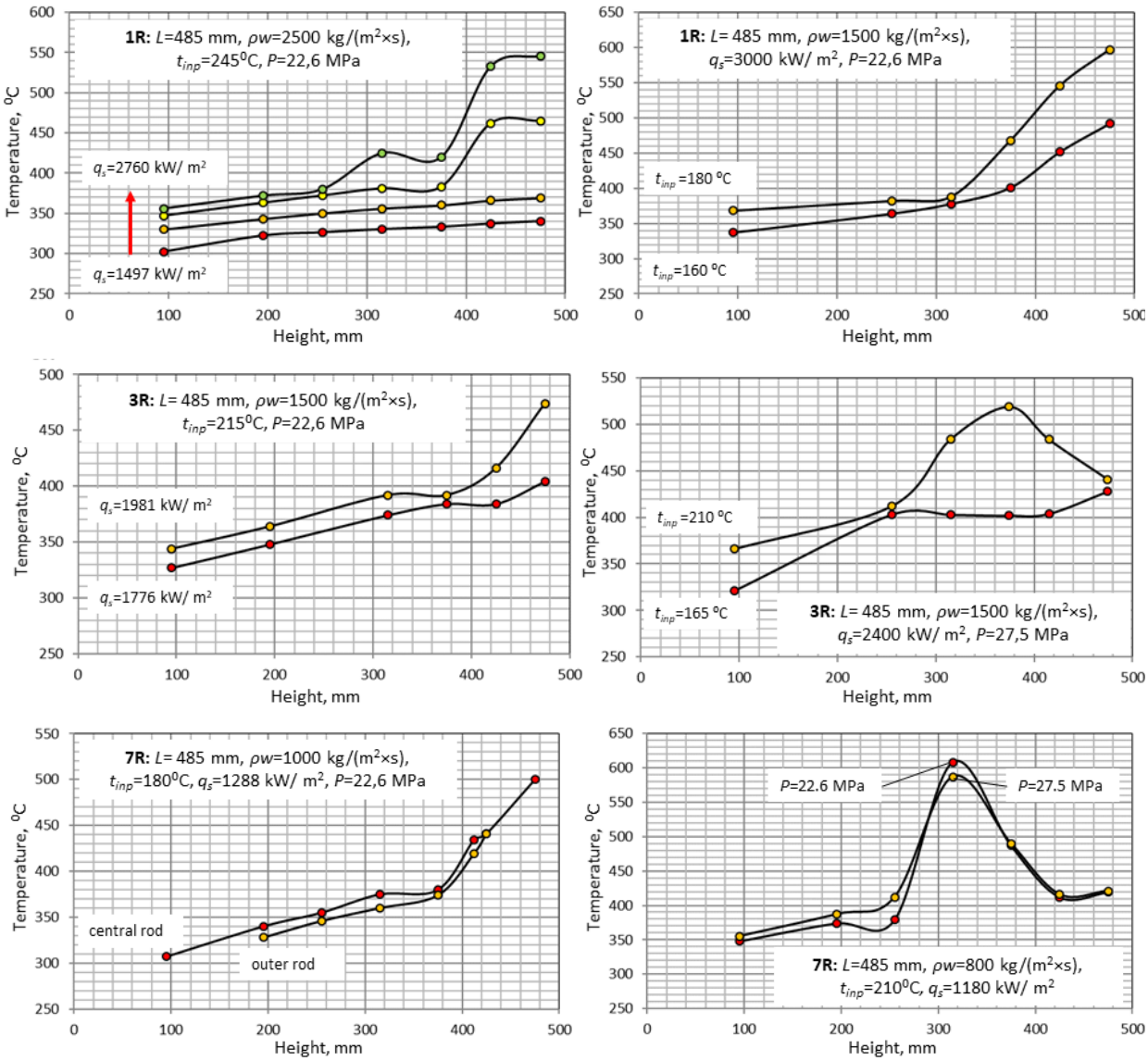

Figure 138. Axial wall temperature distribution (NTUU experimental results)

In the IPP's work, the described NTUU experimental data is used to test the applicability of both the existing CFD methods (see section 2.4.3) and the further proposed modifications (see description of Subtask 3.3.4 in Section 4).

2.4.3 Application of existed CFD methods for modelling the regimes with HTD

2.4.3.1 Application of CFD with SST and RNG turbulence models to simulate HTD regimes

First attempts to perform CFD simulations on the rod-assemblies were conducted on NTUU data for the 1 and 3-rods geometries (Filonov et al., 2018). The evaluation of the thermohydraulic properties was carried out for the chosen experimental regimes, described in Table 22.

Table 22. Chosen calculation regimes description

Regime (Upflow)	Description			
1R#1	P_{ref}=22.6 MPa;	T_{in}=200°C;	q_s=1758 kW/m^2;	ρw=2000 kg/(m^{2}s)
1R#2	P_{ref}=22.6 MPa;	T_{in}=200°C;	q_s=2547 kW/m^2;	ρw=2000 kg/(m^{2}s)
1R#3	P_{ref}=22.6 MPa;	T_{in}=246°C;	q_s=2760 kW/m^2;	ρw=2500 kg/(m^{2}s)
3R#1	P_{ref}=24.5 MPa;	T_{in}=168°C;	q_s=2427 kW/m^2;	ρw=1500 kg/(m^{2}s)
3R#2	P_{ref}=24.5 MPa;	T_{in}=260°C;	q_s=3200 kW/m^2;	ρw=2700 kg/(m^{2}s)

In simulations the solid domains were replaced by equivalent boundary conditions, and only the coolant domains were considered. The geometric model was limited in the axial direction by the heated section of the channel(s). The initial and final sections of the stabilization were neglected and the preliminary degree of swirl was taken into account by a 10% degree of turbulence at the inlet. The boundary conditions were formed as those of Dirichlet. On the heating surface, the non-zero density of the heat flux was set, and on the isolation side the adiabatic wall was applied. For the 3-rod assembly, the curvature of the screw end was fictitiously added to ensure the correct topology in the places of their contact. Such changes added an uncertainty of 0.5-1% in the cross-section area, as well as in the heating surface. The general view of the calculation geometry is shown in Figure 139.

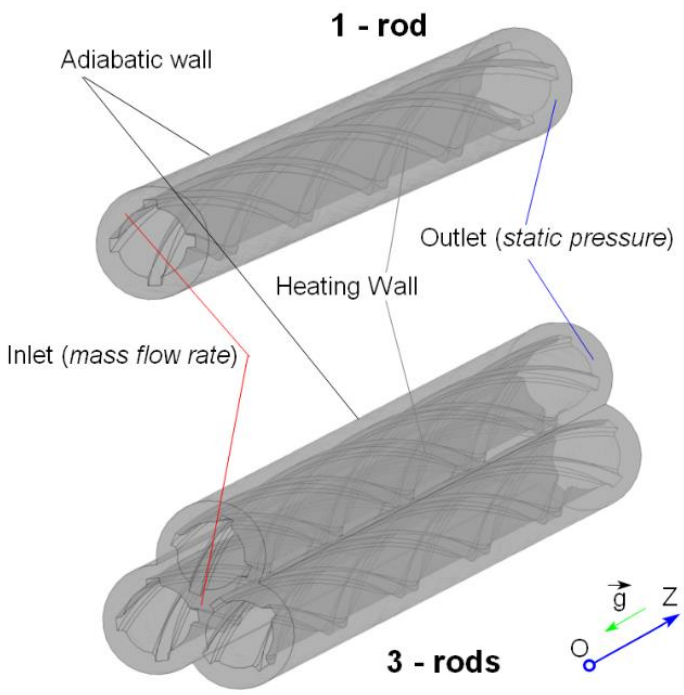

Figure 139. The general view of the calculation models geometry

The processes of energy dissipation and heat transfer intensity are determined in the boundary layer, so special attention was paid to its discretization. To estimate the discretization, the semi-empirical dependencies were used, neglecting the edge effects in the channels.

As the basic models two main two-parameter turbulence models of the k-ε family (RNG) and SST (k-ω) were used. The RNG model, despite the ambiguous success of its applicability for heat transfer calculations with supercritical parameters (Filonov et al., 2018), has an increased ability to adequately predict the velocity field of swirling flows. The control of the boundary layer density was implemented in ANSYS CFX, which provides an automatic transition from scalable

wall function (SWF) to direct flow resolution taking into account low-Re effects. For this purpose, SST (k-ω) turbulence model was considered, which is more stable than the k-ε family models with allowance of low-Re. In addition, in this region the k-ω family models are less demanding for y+ (<2) in comparison with k-ε (y+ <0.2).

In the case of 1-rod assembly, the computational domain discretization was considered to allow including of low-Re effects. In this case, instead of RNG, k-ε (1E) low-Re model was used. For this purpose, the 1-rod (low-Re) computational mesh was constructed in such a way that y+<0.2.

The specific density of the heat flux was assumed constant on the heating surface. The boundary condition at the outlet was assumed equal to zero static pressure with respect to P_{ref}. To take into account the buoyancy force, the value averaged over the surface of the boundary condition "Inlet" was chosen as the reference density. To calculate thermophysical coolant properties, the IAPWS-IF97 library built into the ANSYS CFX was applied.

The resulting heating surface perimeter-averaged values of wall temperature axial distribution in the annular channel cross-section is shown in Figure 140.

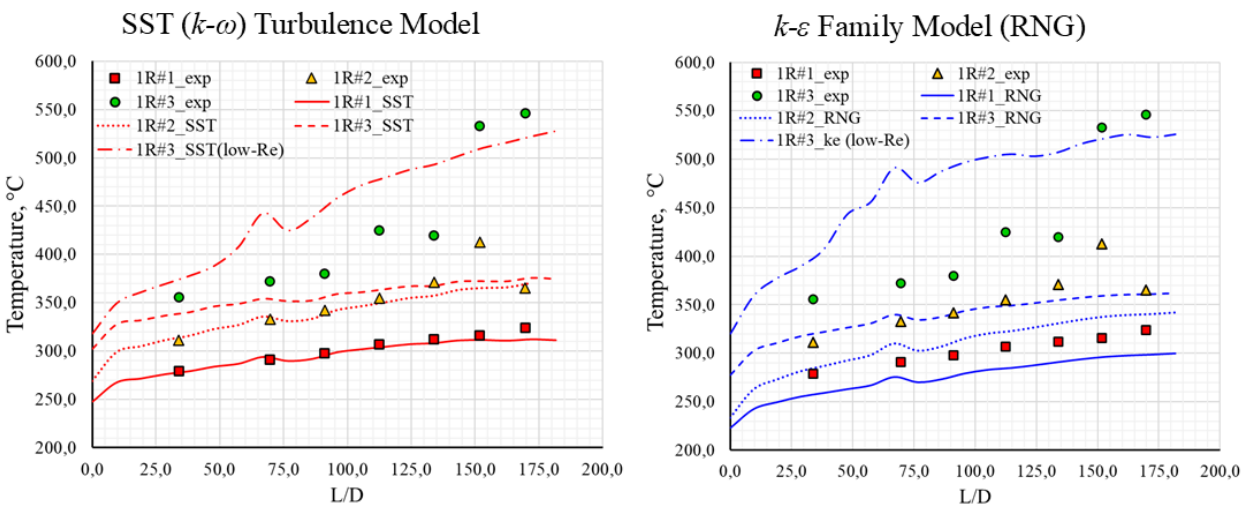

Figure 140. Axial distribution of the averaged wall temperature in the annular channel (1-rod assembly) obtained with RNG (k-ε family) and SST (k-ω) turbulence models

Results, obtained by using RNG with a scalable wall function, indicate a prediction with an underestimation of the temperature regime. Such conclusions do not contradict with yet obtained experience of RNG application without specific modifications of the wall functions (Yu, 2010; IAEA-TECDOC-1746, 2014). The SST (k-ω) provided a more reliable prediction of the wall temperature field in absence of HTD. The average value of y+ for "1-rod" mesh did not exceed 3.4.

An attempt to improve the estimation of the temperature field by taking into account the low-Re formulation at HTD as a whole made the prediction more plausible. The average temperature of the heating surface has increased in comparison with the calculations neglected low-Re correction (Figure 141).

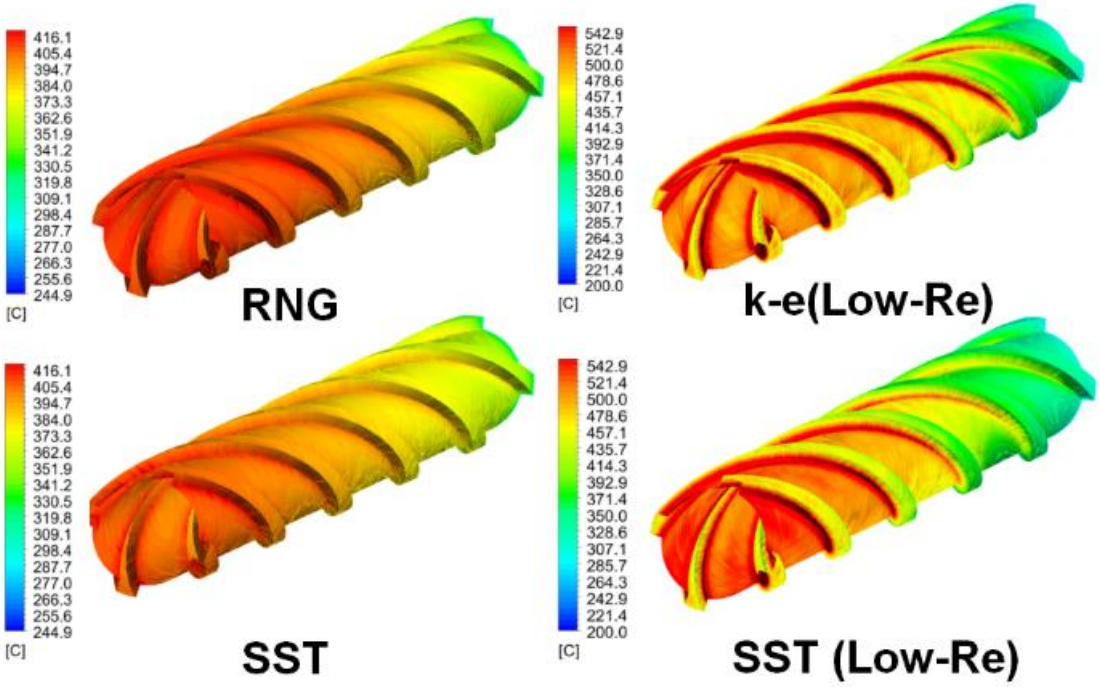

Figure 141. Distribution of the annular channel heating surface temperature for the regime 1R#3 without/with low-Re correction

Nevertheless, the obtained results indicate the low sensitivity of the model to HTD using standard parameters of CFD tools. The average value of y+ for "1-rod (low-Re)" mesh was 0.08. It should be noted that the k-ε (1E) low-Re and SST (k-ω) models provided almost identical results.

The heating surface perimeter-averaged value of wall temperature axial distribution in 3-rod assembly cross-section is shown in Figure 142. Figure 143 represents the corresponding surface distributions of the temperature field.

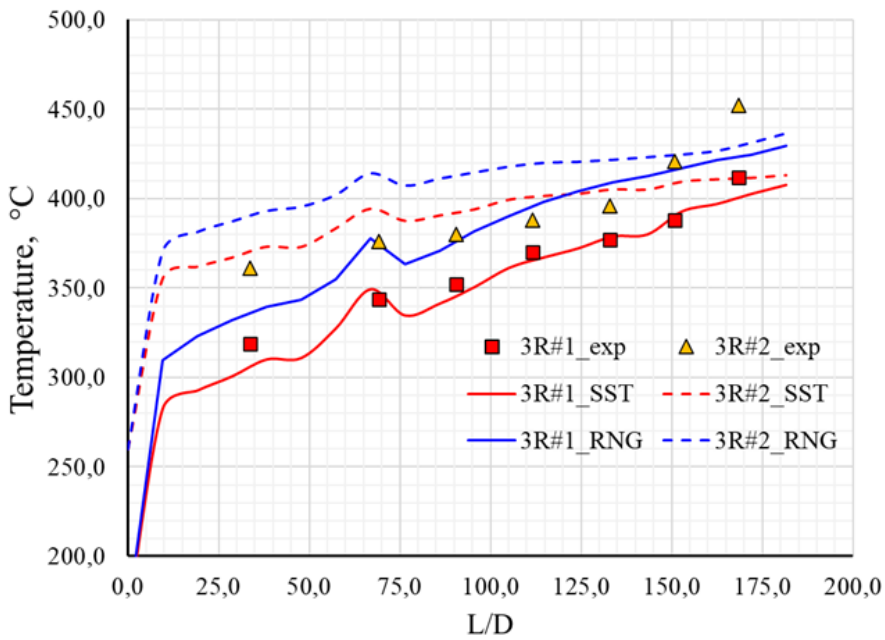

Figure 142. Axial distribution of average wall temperature in the 3-rod assembly

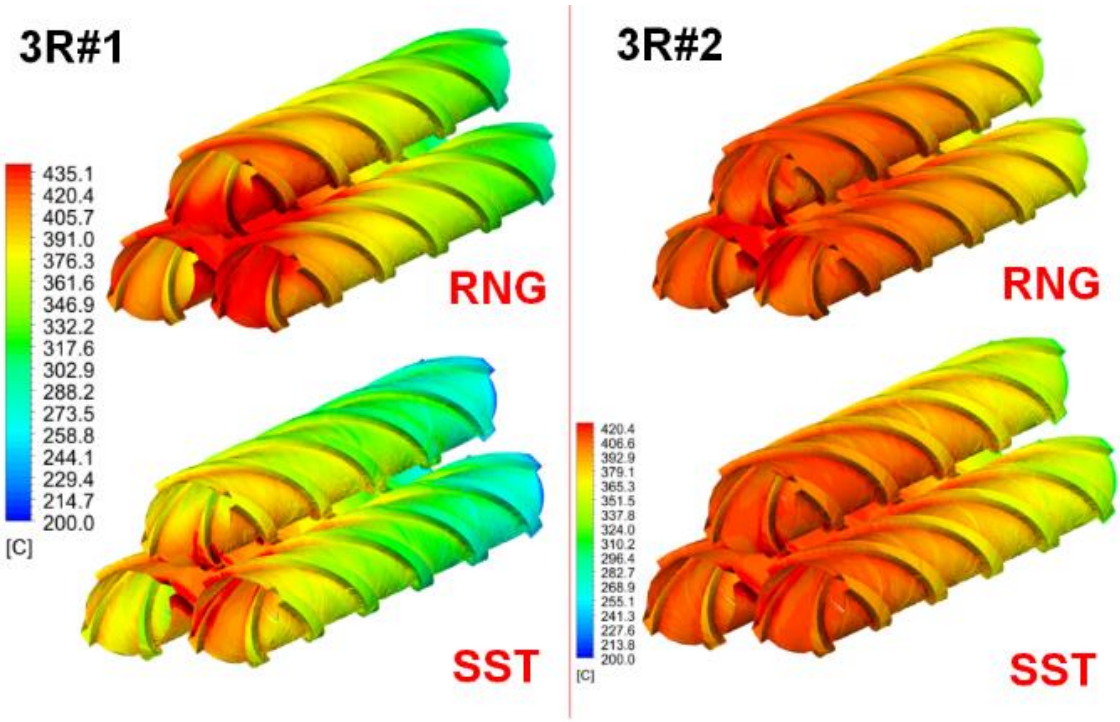

Figure 143. Distribution of heating surface temperature in the 3-rod assembly

Application of turbulence models with the wall functions, similar to the annular channel case, provided an acceptable prediction of the temperature field only for regimes without HTD. Comparison of the integral pressure loss results, obtained in CFD, with the results of empirical assessment is presented in Table 23.

Table 23. Integral pressure losses comparison

Regime (Upflow)	**ΔP, kPa CFD**		**Empirical ΔP, kPa**
	RNG	**SST**	
1R#1	8.49	9.65	9.10
1R#2	8.58	9.62	9.55
1R#3	13.44	15.04	14.82
3R#1	5.69	6.36	5.65
3R#2	17.61	18.8	20.84

So, from first obtained results it could be seen that RNG model results indicate an underestimation of the temperature regime. Nevertheless, the temperature profile qualitatively agrees with the experimental data. In the region of the quasilinear distribution of the wall temperature, which corresponds to the regime without HTD, SST (k-ω) within 10% deviation in the temperature is consistent with the experimental data.

In the presence of heat transfer deterioration the results are unsatisfactory. Even accounting of low-Re correction does not allow adequately predicting the temperature field. Nevertheless, the integral pressure loss, obtained by the CFD model, agrees equally well with the experimental data. This tendency persists regardless of the heat transfer regime and low-Re effects accounting. This indicates that the temperature wall function can be directly adapted and modified.

2.4.3.2 Application of CFD with low-Re EVT turbulence models to simulate HTD regimes

After the first obtained results and conclusions, attempts were made to conduct CFD modelling using another turbulence model. As before, from an engineering point of view, the RANS approach remains predominant, since in most practical problems it is a compromise between accuracy and speed of obtaining a result. That is why there is interest in the adaptation of RANS turbulence models for heat transfer problems with SCW (Yu, 2011). An important feature of the RANS application is that it is necessary to apply low-Re turbulence models, which leads to increased requirements for discretization of the near-wall region.

The calculations were carried out using ANSYS CFX 18 for the selected 3-rod and 7-rod bundles NTUU data. The description of chosen cases is presented in Table 24.

Table 24. Chosen calculation regimes description

Regime (Upflow)	Description
3R#1	P_{ref}=24.5 MPa; T_{in}=260°C; q_s=3200 kW/m^2; G=2700 kg/(m^2 s)
3R#2	P_{ref}=27.5 MPa; T_{in}=212°C; q_s=2400 kW/m^2; G=1500 kg/(m^2 s)
7R#1	P_{ref}=22.6 MPa; T_{in}=178°C; q_s=1288 kW/m^2; G=1000 kg/(m^2 s)
7R#2	P_{ref}=27.5 MPa; T_{in}=210°C; q_s=1188 kW/m^2; G=800 kg/(m^2 s)

The low-Re Eddy-Viscosity Transport (EVT) model was used as the closing turbulence model, which is based on k-ε and is called (k-ε)1E. Low-Re effects are accounted for by near wall damping functions provided y+<1.0. Taking into account the low-Re effects essentially means a detailed solution of the medium transport equations near the wall, as well as the consideration of special damping terms in the turbulence model. This approach requires detailed discretization of the near-wall geometry, which entails an increase in required numerical resources. The general view of the computational model is shown in Figure 144.

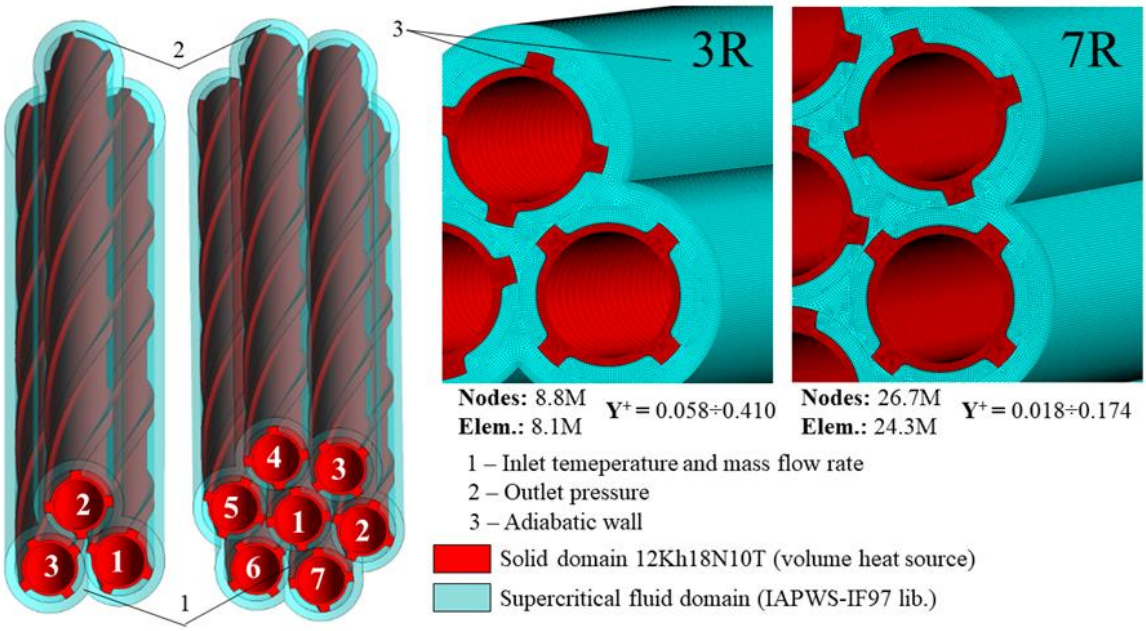

Figure 144. General view of the 3-rod and 7-rod assemblies calculation models with details of their discretisation and applied boundary conditions

To perform the analysis of these regimes the widespread in engineering practice SST turbulence model was also used. The choice of these models is due to the fact that they are the most promising in terms of future modifications for HTD regimes modelling.

The obtained results of the temperature field distribution on the heating surface are shown in Figure 145. To clarify the difference between the calculated and real picture, the experimental results were visualized on the calculated geometry. It should be noted that the calculations were carried out in a coupled formulation between solid and fluid. The heat source was specified in the form of volumetric heat release, which leads to a lower value of the maximum wall temperature (Ikryannikov et.al., 1973).

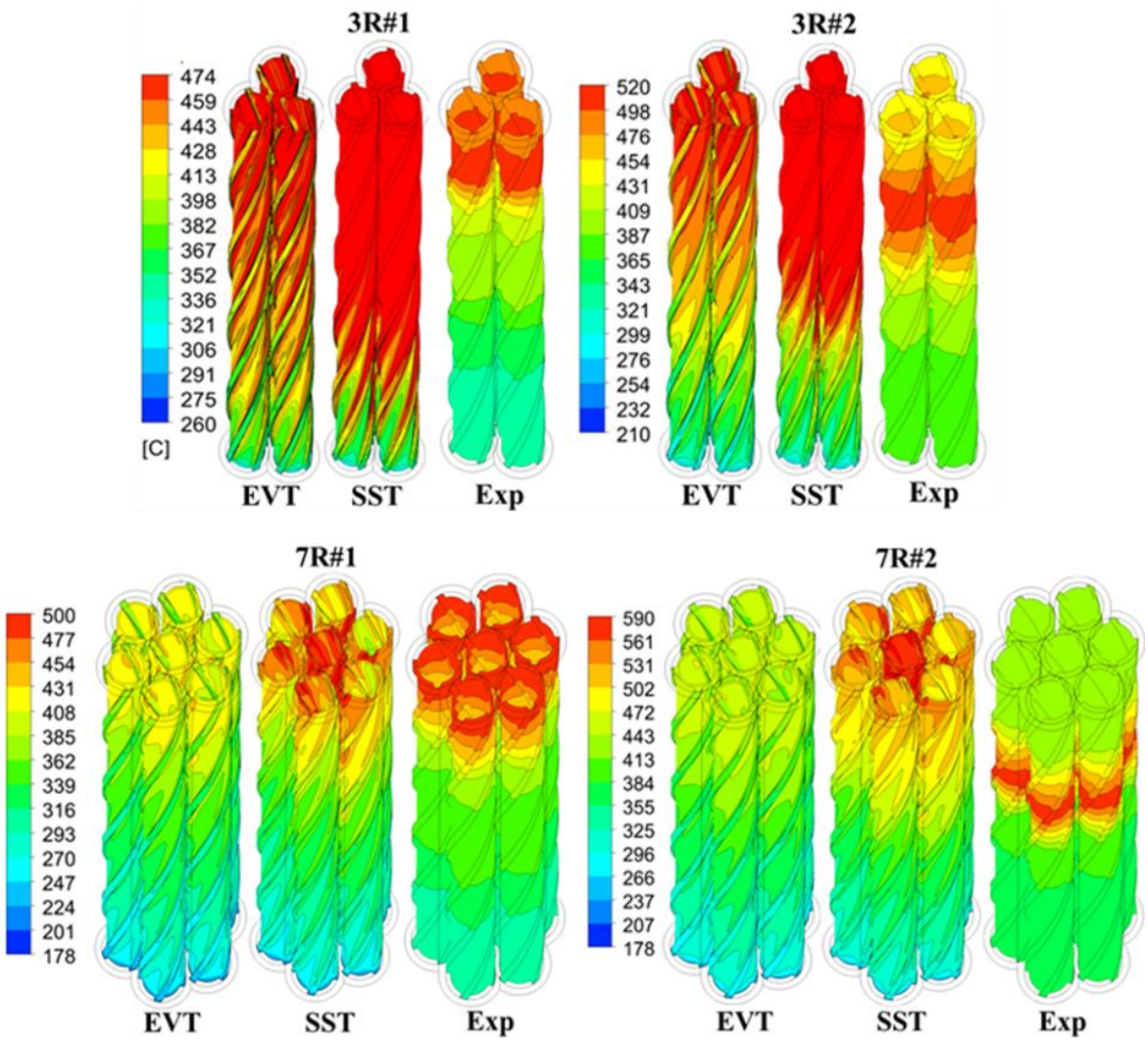

Figure 145. Comparison of the obtained temperature distributions on the external surface with the visualized experimental ones

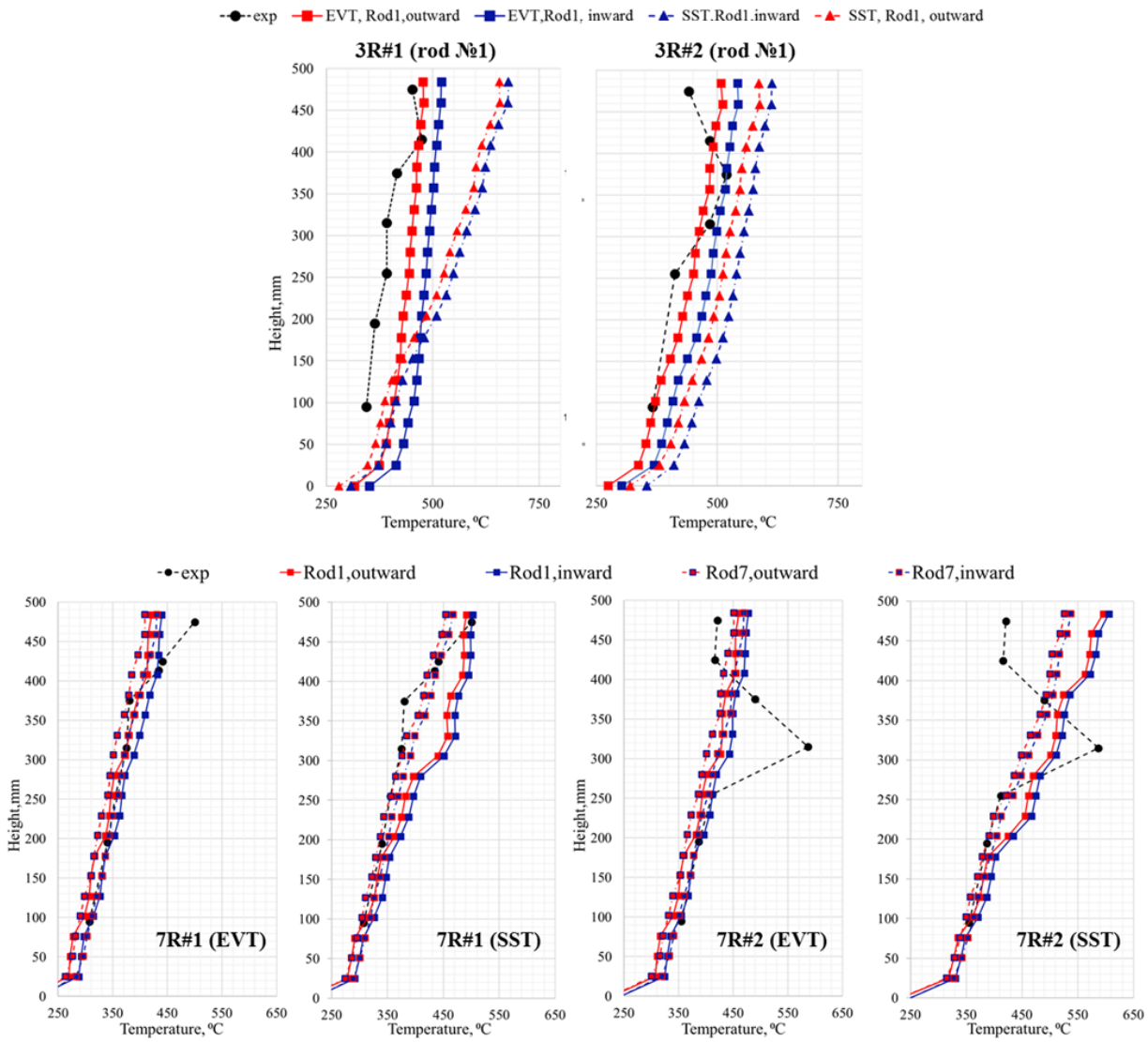

Figure 146. Axial temperature distributions obtained for 3-rod bundle and 7-rod bundle (shown for central rod #1 and peripheral rod #7) and compared with corresponding experimental data

For Regimes 3R#1 and 3R#2, the axial temperature profile is qualitatively different from the experimental one (see Figure 145 and Figure 146). At the same time, the maximum temperature is close to the experimental value. For Regimes 7R#1 and 7R#2, both the quantitative and qualitative picture differs from the experimental one.

As a result, both of the applied turbulence models qualitatively indicate the presence of DHT effect, but do not restore the local characteristics of the axial temperature distribution, especially in regime 7R#2 where the temperature peak was clearly captured in the experiment. Obtained results can qualify for quantitative prediction of DHT phenomena, and it still need further improvements for better coincidence with experimental data.

2.4.4 Concluding remarks

In the conducted and presented IPP tests of applicability and, first of all, predictive capabilities of RNG, SST (with/without low-Re effects consideration) and Low-Re EVT turbulence models, the following can be summarized. Even if the considered standard models give good quantitative

agreement (maximum values of wall temperature with the exception of RNG with the scalable wall functions, which provided a strong underestimation), then the results still indicate the low sensitivity of applied models to HTD (especially in temperature peaks, which couldn't be captured in CFD).

Based on the obtained results, IPP made conclusions about the need to develop additional methods and modifications of the existing models. For engineering practice, those methods are promising, which would not complicate the formulation of the problem and thus would not increase the requirements for calculation models. In the above context, it is possible to distinguish the next approaches, which consist in the adaptation of existing methods by introducing additional terms:

1) Adaptation of temperature wall functions, which based on the results obtained in section 2.4.3.1 can have an effect. Since, despite the fairly significant deviations of the axial temperature profile, the error in determining the pressure drop did not exceed 10%, both with and without the application of wall functions. This gives the right to consider only the modification of the temperature wall function in the first approximation. Consideration of the problems when using universal wall functions (UWF) and attempts of IPP to create special wall functions (SWF) are carried out and described further in section 4.2.

2) Adding the calculation of the turbulent Prandtl number, which is also discussed and implemented within the framework of section 4.3.1.

3) Creation of special turbulence models, which are based on the peculiarities of heat transfer at supercritical parameters (Valueva, 2012; Valueva, 2015; Valueva, 2014; Pucciarelli et.al., 2015). In this direction, IPP attempted to modify the Eddy Viscosity Turbulence model to take into account non-linear heat transfer effects and described it below in section 4.3.

Therefore, despite the obtained results, IPP concludes that the RANS approach has not exhausted itself in the field of non-linear heat transfer prediction and can be adapted/supplemented with new ratios in order to make it appropriate for modeling the regimes with supercritical coolant conditions.

2.5 CONTRIBUTION BY UoN

2.5.1 Introduction

Although the majority of nuclear reactors have vertical cores, there been some interest in liquid flow in the horizontal direction. The flow of supercritical water in horizontal tubes has been studied both numerically and experimentally by past researchers. Mao et al. (2022) numerically studied the heat transfer characteristics of supercritical water in a horizontal tube and assessed the effects of heat flux, mass flux, tube diameter and buoyancy on the heat transfer performance. It was discovered that applying the Shear Stress Transport (SST) k-ω turbulence model has better agreement with the experimental data. Shang et al. (2008) investigated the effect of system pressure on the heat transfer of supercritical water in a horizontal circular tube using CFD and found that the heat transfer of supercritical water is primarily dominated by the buoyancy effect and is less influenced by the system pressure. Yu et al. (2013) experimentally analysed the

difference in heat transfer characteristics between the bottom and top of a horizontal tube and found that existing criteria could be used to predict the occurrence of buoyancy effects. Bazargan et al. (2005) experimentally measured the local heat transfer coefficients of horizontal circular tubes and found that neglecting the buoyancy effect leads to large differences between experimental data and empirical correlations. Huang et al. (2020) studied the heat transfer characteristics of supercritical water in a horizontal double tube through experiments and numerical simulations, and found that there was a drift in the heat transfer coefficient in the experiments. Hou et al. (2023) explored the heat transfer characteristics of sinusoidally heated supercritical water in an axial horizontal tube and discovered that some regions allow control of heat transfer deterioration by increasing the Reynolds number, while heat transfer could be enhanced when sidewall and bottom wall temperatures exceeded the pseudo-critical temperature. Gao and Bai (2017) examined the non-uniform heat transfer characteristics of supercritical water and its mechanism by predicting heat transfer from fluid-solid coupling through numerical simulations, and found that flow asymmetry in horizontal tubes significantly affects heat transfer. Lei et al. (2016) conducted an experimental study of heat transfer of SCW in horizontal tubes and found heat transfer deterioration with heat flux. Huang et al. (2022) conducted an experimental study on heat transfer of supercritical water in a horizontal tube and discovered the heat transfer was suppressed prior to the pseudo-critical point, and established a new correlation applicable to heat transfer of supercritical water in large diameter horizontal tubes. Shang et al. (2008) studied the effect of system pressure on heat transfer of supercritical water in a horizontal tube using CFD techniques and found that pressure changes have a significant effect on fluid heat transfer when the buoyancy effect is negligible.

In this study, we will focus on the experimental setup and test section described by Huang et al. (2022) at first, the test section found will be modelled in ANSYS FLUENT, the data achieved will be compared to the experimental data, hence providing a perspective on how modern CFD codes are accurate in predicting supercritical water behaviour. Afterwards the numerical simulation of the heat transfer behavior of supercritical water in a horizontal rod bundle containing fuel hot rods is achieved.

2.5.2 Theory

In this section, the flow and heat transfer of supercritical water in horizontal pipe can be considered as a steady-state process. The continuity equation is given by

$$\frac{\partial}{\partial x_i}(\rho u_i) = 0 \tag{57}$$

where ρ is the density of fluid and u is the velocity.

The momentum equation is given by

$$\frac{\partial}{\partial x_i}(\rho u_i u_j) = \rho g_j - \frac{\partial}{\partial x_j}\left(P + \frac{2}{3}\mu_e \frac{\partial u_i}{\partial x_i}\right) + \frac{\partial}{\partial x_i}[\mu_e(\frac{\partial u_i}{\partial x_j} + \frac{\partial x_j}{\partial u_i})] \tag{58}$$

where g is the acceleration due to gravity, P is the static pressure, and μ_e is the effective viscosity.

The energy equation is given by

$$\frac{\partial}{\partial x_i}(\rho u_i H) = \frac{\partial}{\partial x_i}[(\lambda + \frac{c_p u_i}{Pr_t})\frac{\partial T}{\partial x_i}] \tag{59}$$

where λ is the thermal conductivity, H is the enthalpy, $c_p$is the specific heat capacity, μ_e represents the effective viscosity, and Pr_t is the turbulent Prandtl number.

The Shear Stress Transport (SST) k-ω model is represented by the following equations (see Ansys Inc, 2021). The first equation is for obtaining the turbulence kinetic energy, k. The second equation is for obtaining the specific dissipation rate ω.

$$\frac{\partial}{\partial t}(\rho k) + \frac{\partial}{\partial x_i}(\rho k u_i) = \frac{\partial}{\partial x_j}\left(\alpha_k \mu_e \frac{\partial k}{\partial x_j}\right) + G_k + G_b - \rho\varepsilon - \Upsilon_M + S_k \tag{60}$$

$$\frac{\partial}{\partial t}(\rho \varepsilon) + \frac{\partial}{\partial x_i}(\rho \varepsilon u_i) = \frac{\partial}{\partial x_j}\left(\alpha_k \mu_e \frac{\partial \varepsilon}{\partial x_j}\right) + C_{1\varepsilon}\frac{\varepsilon}{k}(G_k + C_{3\varepsilon}G_b) - C_{2\varepsilon}\rho\frac{\varepsilon^2}{k} - R_\varepsilon + S_\epsilon \tag{61}$$

In the above equations, $\tilde{G}_k$ is the generation of turbulence energy due to mean velocity gradients, G_ω is the generation of ω, Γ_k is the effective diffusivity of k, Γ_ω is the effective diffusivity of ω, Y_k is the dissipation of k due to turbulence, Y_ω is the dissipation of ω due to turbulence, D_ω represents the cross-diffusion term, and S_k and S_ω are user-defined source terms.

2.5.3 Description of test rig

The experimental setup in the research conducted by Huang et al. (2022) consists of deionized water in a tank which is then filtered and pressurized using a piston pump as shown in Figure 147. The piston pump operates at a maximum pressure and mass flow rate of 40 MPa and 4700 kg/h, respectively. From there, the highly pressurized water flows into the mass flowmeter, the shell side of the heat exchanger, and preheater. Then, it flows into the test section. After the test section, it flows into the tube side of the same heat exchanger. Then, it passes via the condenser prior to returning to the water tank. A cooling tower exists to cool the secondary water from the condenser. The direct heating power on the preheater and test section are restricted to 660 KW and 250 KW, respectively.

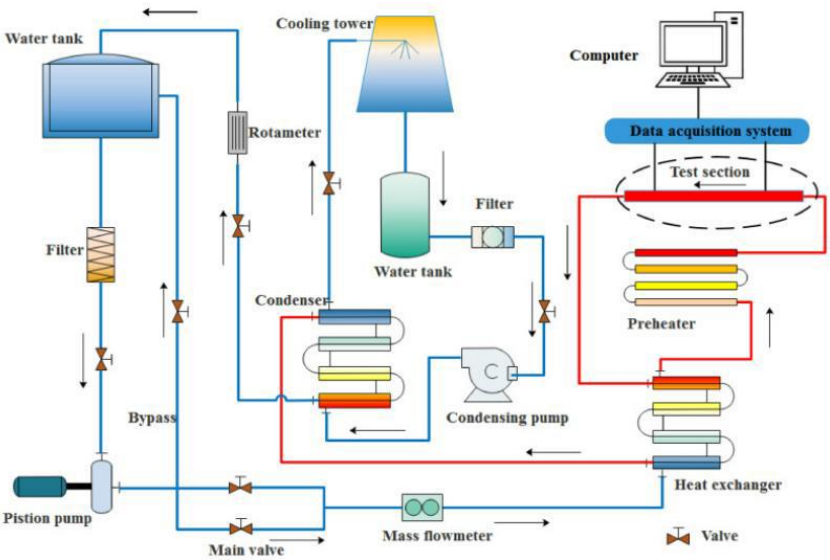

Figure 147. Full test rig schematic (Huang et al., 2022)

The test section (Figure 148) consists of a horizontal tube fabricated from 316 L stainless steel. The length of the heat transfer region was 6000 mm. Prior to the heating section, an adiabatic section of 1500 mm is there to avoid the entrance effect and ensure fully developed flow before heating. The test section has an outer diameter of 34 mm and inner diameter of 26 mm. As shown in Figure 148, the locations of electrodes, thermocouples, and differential pressure measurements are shown.

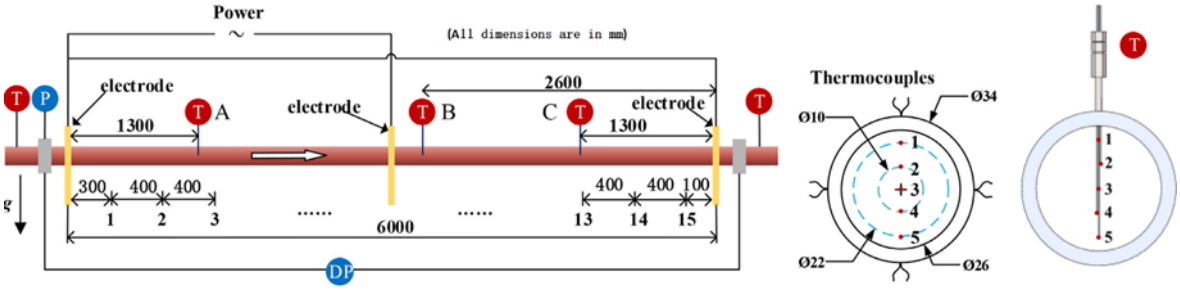

Figure 148. Horizontal test section (Huang et al., 2022)

2.5.4 Experiment and simulation settings

According to the experimental test (Huang et al., 2022), the environment settings and boundary conditions for the simulation are set as follows in Table 25.

Table 25. Boundary conditions

Parameters	Value
Pressure (reference)	25 MPa
Temperature (inlet)	523-661 K
Mass flux (inlet)	300 kg/m^{2}s
Mass flux (inlet)	50-150 kW/m^2

It is a challenge to analyse the mesh validity of the pipe because it is too long and narrow. Two mesh quantities are chosen, with the parameters shown inTable *26*.

Table 26. Mesh analysis

	Qualified value range	Mesh A average value (max, min)	Mesh B average value (max, min)
Aspect Ratio	Close to 1	0.93081 (1, 0.90032)	0.97723 (1, 0.90005)
Wrapping Factor	Close to 0	0.07001 (0.10582, 0)	0.05299 (0.08126, 0)
Mesh Metric	Close to 1	0.93040 (1, 0.85201)	0.98732 (1, 0.92500)
Skewness	Close to 0	0.06854 (0.13250, 0)	0.04424 (0.08401, 0)
Element quantity		13 million	18 million

From Table 26, it appears Mesh B is the best out of the two. Hence, it is selected for analysis and is presented in Figure *149* and Figure 150.

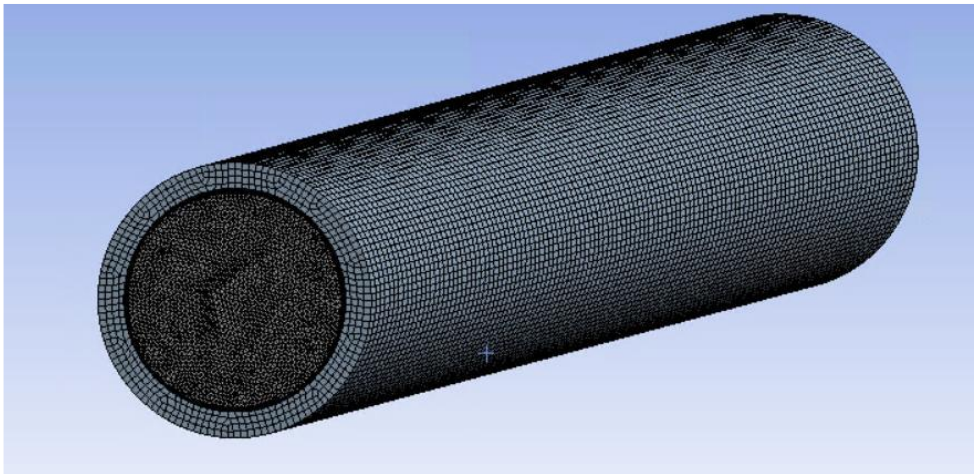

Figure 149. Full length view of geometry and mesh

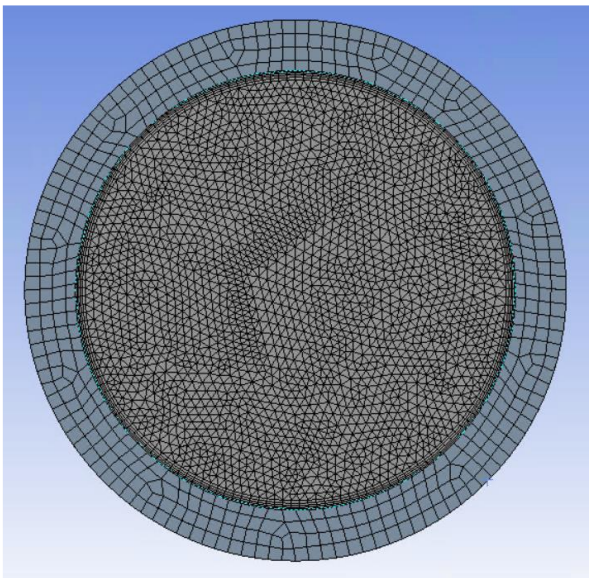

Figure 150. Meshes of pipe outlet

The mesh settings applied in ANSYS Fluent are shown inTable 27.

Table 27. Mesh settings

Settings	**Value**
Meshing method	Multizone
Defaults size	0.001m
Surface sizing of rod's wall	0.002m
Body sizing of fluid area	0.001m
Edge sizing of wall of outer surface	0.002m
Face sizing of inlet surface	0.0002m
Inflation size	0.000029m
Number of inflation layers	5

2.5.5 Results and discussion

This section gives the results of simulations using ANSYS FLUENT and compares them with the experimental data. It mainly includes the temperature distribution and the bulk enthalpy along the length of the rod.

2.5.5.1 Comparison of wall temperature

The experimental and simulation results are shown below (left and right) in Figure *151*.

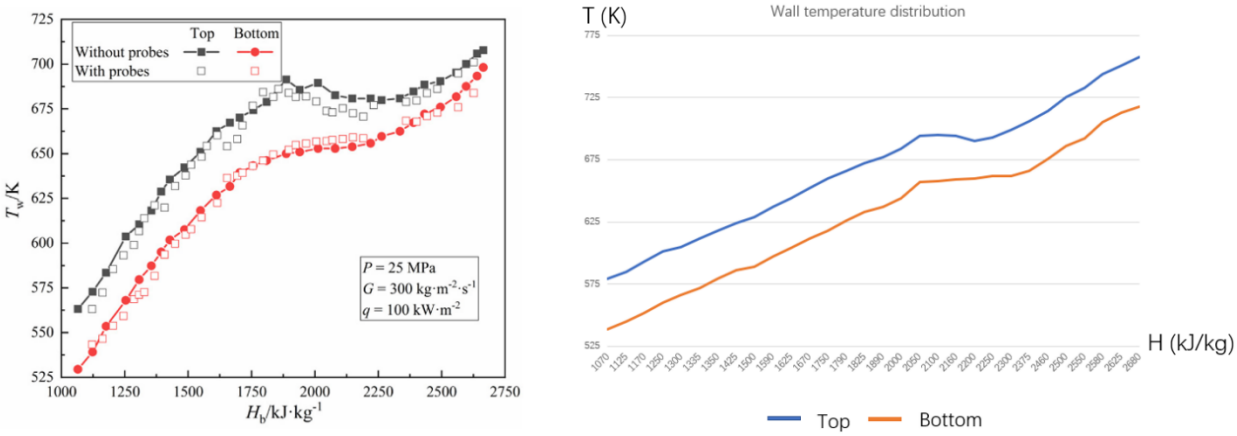

Figure 151. Wall temperature comparison

As can be seen from Figure *151*, the results are relatively similar for the two groups, but differ locally. For the top group, the trend for both is to maintain a steady rise up to 1900 kJ/kg and a steady fluctuation at 1900-2200 kJ/kg, followed by a continued steady rise. However, in terms of values, the simulated temperature data are higher than the experimental results, by about 5%. For the bottom group, the main difference between the two trends lies in the region of fluctuation from 1800 kJ/kg to 2200 kJ/kg. The experimental results maintain a slow increase in this region, while the simulated results are nearly stagnant in this region, and the smooth region lags behind the experimental results. The main reason for this difference is that the experimental and simulated materials are not exactly the same. The steel used in the experiments could not be chosen in the simulations, and the steel used in the simulations had higher thermal conductivity than the experimental materials and lower specific heat capacity than the experimental materials, resulting in higher temperature data in the simulated results.

2.5.5.2 Axial variations in the bulk enthalpy

This section will give a comparison of the change in volume enthalpy for different boundary conditions. Figure 152 shows the results for an inlet temperature of 523 K.

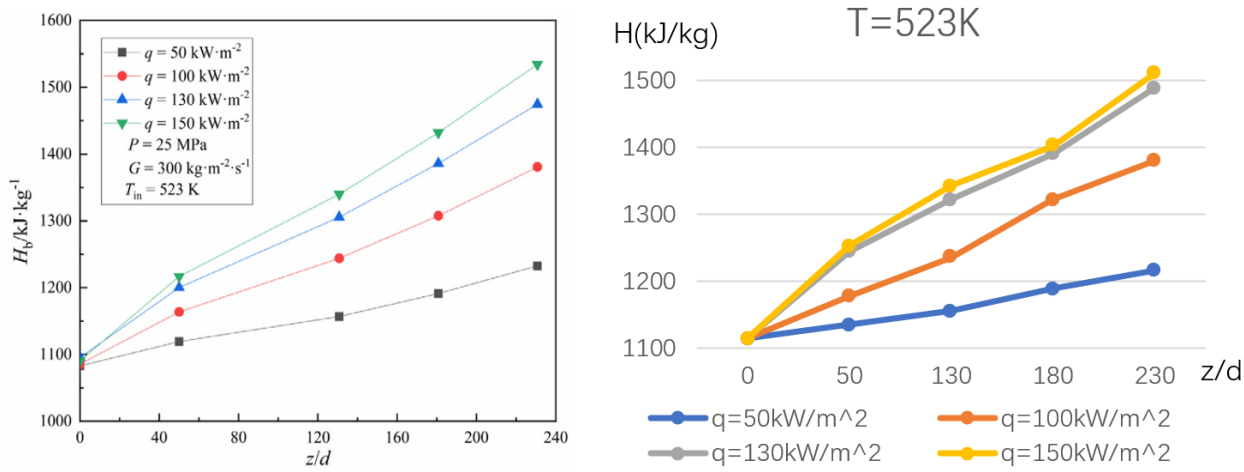

Figure 152. Results at 523 K

From the results, both show the same trend, with a smooth increase along the rod direction. In terms of the volumetric enthalpy values, the simulated results are slightly higher than the experimental results, but the difference is within acceptable limits with the maximum difference of 15%.

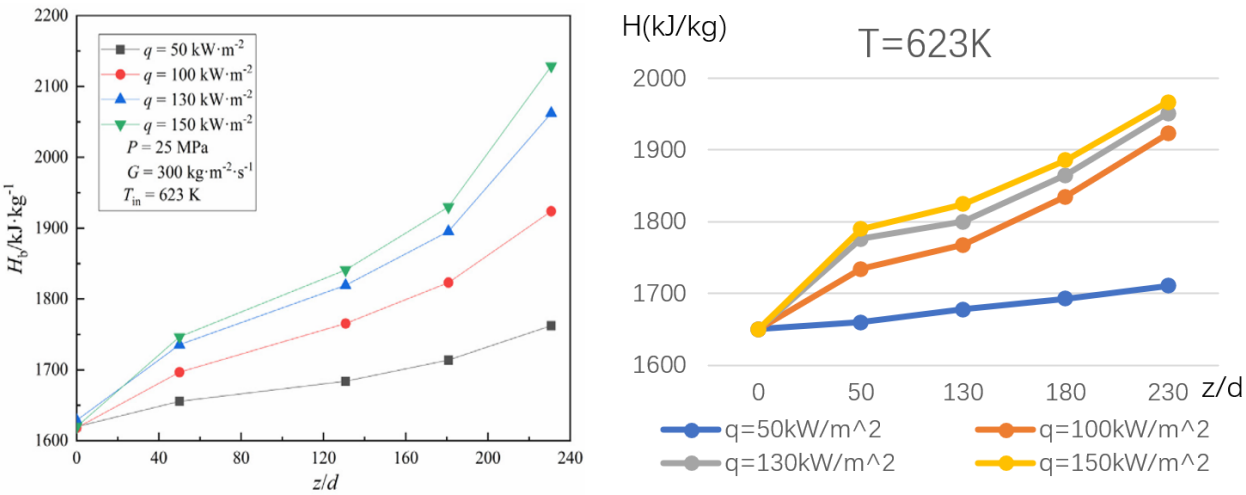

Figure 153. Results at 623 K

Figure 153 shows the results for an inlet temperature of 623 K, it can be seen that the experimental and simulated results have similar trends, but for the group with the lowest heat flux, the difference between the volumetric enthalpy and the other three groups is greater than the difference in the experiment. In terms of values, the overall volumetric enthalpy change results for the simulated results are higher than the experimental results, with an excess of approximately 3%, which is within acceptable limits.

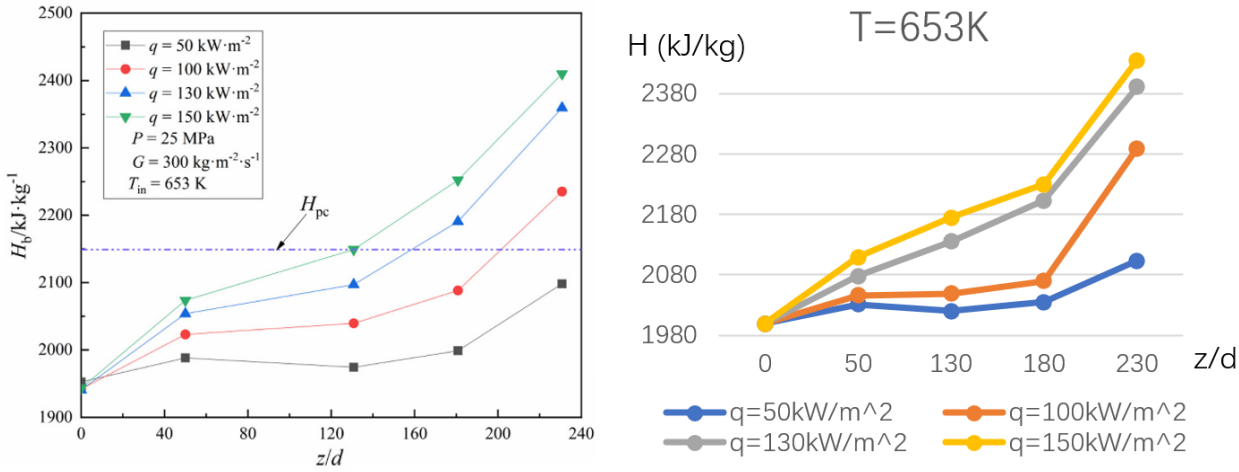

Figure 154. Results at 653 K

Figure 154 shows the results at an inlet temperature of 653 K, it is indicated that the trends are essentially the same and that the differences in volumetric enthalpy data are within acceptable limits.

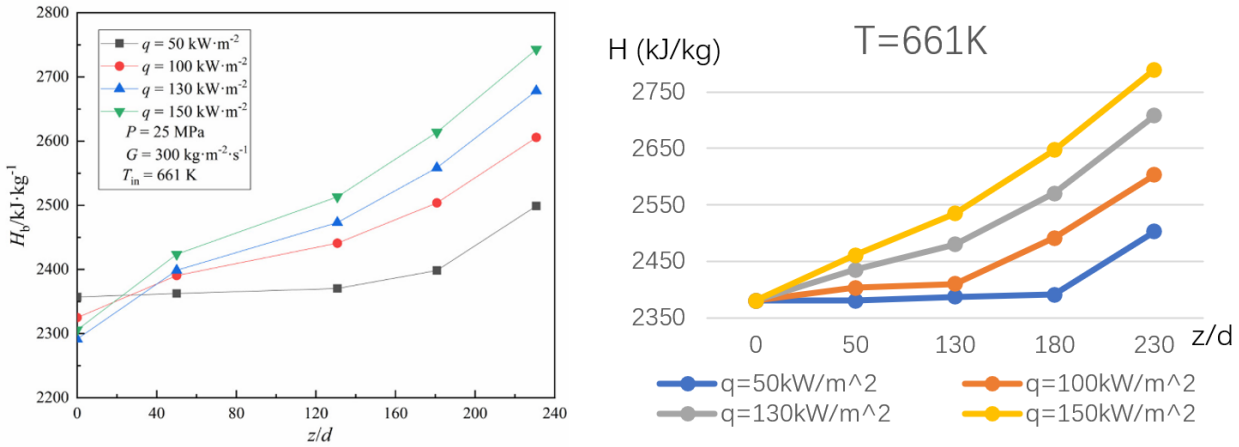

Figure 155. Results at 661 K

Figure 155 shows the results at an inlet temperature of 661K, it can be seen that the simulation results at this inlet temperature differ from the experimental results at the beginning, specifically the volumetric enthalpy for the group with a heat flux of 50 kW/m^2 is higher than the other groups in the experiment, while the difference between the simulation method and the actual results leads to the same results for all four groups at the very beginning of the simulation. For the subsequent positions of the volumetric enthalpy results, the experimental and simulated results follow the same trend, with the simulated results showing around 3% higher values than the experimental results, but within acceptable limits.

2.5.6 Rod bundle CFD simulation

The model is mainly based on the regular hexagonal rod bundle, and the simulation results will be used to compare with the results obtained by Shang et al. (2010). In the Ansys Workbench 2022R1 version, the Spaceclaim application is used to model the regular hexagonal rod bundle. The length of the rod is 3 m, the diameter of each rod in the seven-rod array is 8 mm, and the distance between the centers of every two adjacent rods is 10 mm, it is assumed that the distance is 2 mm, as shown in Figure 156.

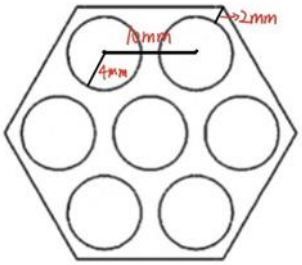

Figure 156. Rod bundle diagram

In the meshing part, the default mesh size is used. Edge sizing and face sizing are added to the outer wall of the rod bundle to reduce the number of grids. Use face sizing for fluid inlets and outlets to increase radial mesh count. The schematic diagram of mesh division is as follows. The number of meshes is investigated via mesh sensitivity analysis. Therefore, this article will use a higher mesh number. The mesh and mesh settings of each part are shown in Figure 157and Table 28.

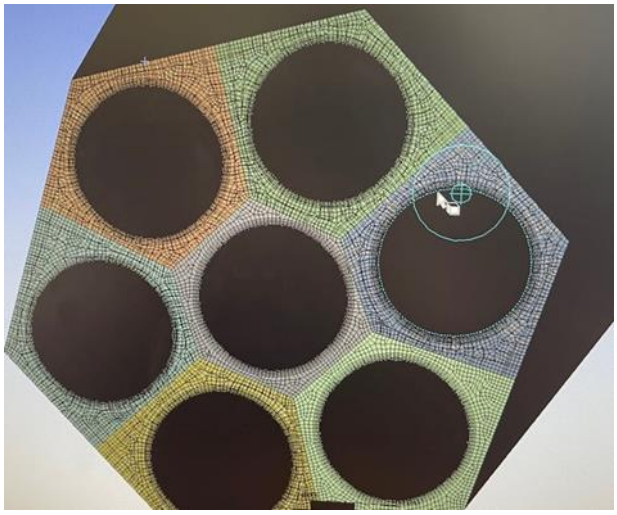

Figure 157. Mesh diagram

Table 28. Mesh settings

Settings	Value
Meshing method	MultiZone
Defaults size	0.001 m
Surface sizing of rod's wall	0.002 m
Body sizing of fluid area	0.001 m
Edge sizing of wall of outer surface	0.002 m
Face sizing of inlet surface	0.0002 m
Inflation size	0.000029 m
Number of inflation layers	8

In the Fluent setting section, the SST k-ω model is used for simulation, and all the settings of the fluid model are at the default settings. The real-gas-water is used as the fluid material in the simulation. Since there is no solid part, the material of the solid part is not set. The boundary conditions are shown in the table below. The Coupled is adopted as the simulation method, and

the Rhie-Chow: momentum-based method is accepted; the rest of the simulation methods are set in Table 29.

Table 29. Boundary conditions

Parameters (boundary conditions)	value
Pressure (reference)	25 MPa
Temperature (inlet)	623 K
Mass flux (inlet)	1050 kg/m^2s
Heat flux (wall)	600 kW/m^2

2.5.6.1 Mesh sensitivity analysis

In order to determine the appropriate range of mesh quantities to save simulation time and ensure simulation accuracy, six sets of mesh quantities are selected for preliminary simulation analysis. The characteristics of each group of meshes are shown in Table 30.

Table 30. Mesh information

Mesh number	**Element number (Approximate)**
1	1.5 million
2	4 million
3	6 million
4	8.5 million
5	10 million
6	12 million

The simulation accuracy is confirmed by performing the same setup and simulations for models with different mesh counts, using a scale of differences in the temperature simulation results, and the results are found to vary widely among 1.5 million elements, 4 million elements and 6 million elements, as shown in Table 31. However, after increasing the number of elements to 8.5 million there is almost no change. Therefore 8.5 million elements would be the appropriate number of elements for this model.

Table 31. Errors

Mesh	**Error at point 1** $\lvert T_{mesh\,new} - T_{mesh}\rvert / T_{mesh}$	**Error at point 2** $\lvert T_{mesh\,new} - T_{mesh}\rvert / T_{mesh}$	**Error at point 3** $\lvert T_{mesh\,new} - T_{mesh}\rvert / T_{mesh}$
1	0	0	0
2	0.004	0.003	0.003
3	0.013	0.012	0.013
4	0.006	0.006	0.005
5	0.001	0.001	0.001
6	0.0005	0.0006	0.0006

At the same time, the mesh quality is checked for the three groups of mesh above 8.5 million using the mesh quality check function in the mesh section. Aspect Ratio, Wrapping Factor, Mesh Metric and Skewness are used as the criteria for evaluating the quality of the meshes, as shown in Table 32.

Table 32. Mesh evaluation

	Qualified value range	Mesh 4 average value (max, min)	Mesh 5 average value (max, min)	Mesh 6 average value (max, min)
Aspect Ratio	Close to 1	0.94538 (1, 0.89506)	0.96733 (1, 0.91505)	0.99837 (1, 0.97554)
Wrapping Factor	Close to 0	0.07091 (0.10032, 0)	0.040199 (0.08236, 0)	0.02001 (0.04033, 0)
Mesh Metric	Close to 1	0.92010 (1, 0.83306)	0.96782 (1, 0.89300)	0.99002 (1, 0.97049)
Skewness	Close to 0	0.06334 (0.12040, 0)	0.04244 (0.08953, 0)	0.01453 (0.03394, 0)

2.5.6.2 Results and discussion

The results of the simulation using Ansys workbench are given and this is compared with the data produced by Shang et al. (2010). The results section mainly includes the temperature distribution along the length of the tube, the temperature distribution at specific locations on the rod surface and a comparison of the heat transfer coefficients at different locations on the rod.

2.5.6.2.1 Wall temperatures along the rod bundle in 3 detect points

This section will use the simulation results of the wall temperatures measured according to the locations of the three monitoring points (lines). A schematic diagram (cross section) of the location of the three test points in this bundle is shown in Figure 158.

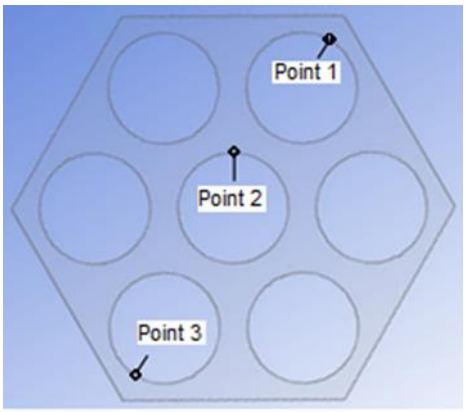

Figure 158. Section view of model

The simulation results from Shang et al. (2010) for the three monitoring points (lines) of temperature in the cylindrical rod bundle model are shown below. As the mesh sensitivity analysis has been carried out above, the results of mesh2 will be used as a comparison.

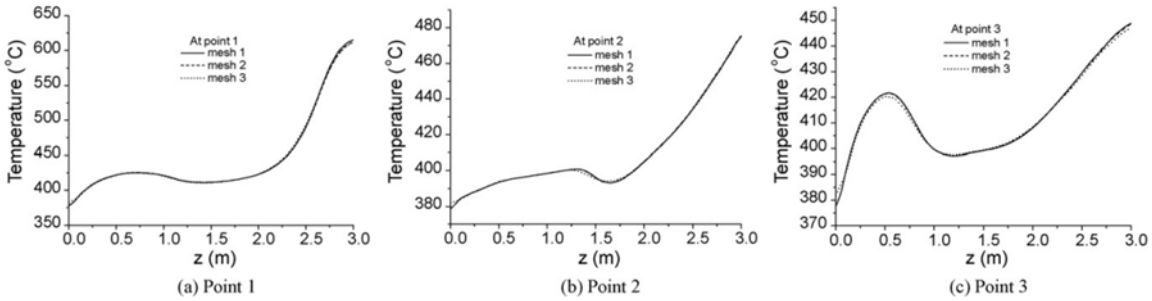

Figure 159. Results of temperature (Shang et al., 2010)

Figure 160 shows the distribution of temperature along the length of the tube at monitoring point 1. At this point, the temperature gradually increases from 350 °C at the inlet of the pipe, and a phase of temperature fluctuations of approximately 0.6 m in length occurred in the middle of the pipe wall, where the temperature of the pipe wall at this point fluctuated by approximately 30 °C. The rod wall temperature then starts to rise, eventually reaching approximately 640 °C at 3m. Compared to the simulation results in the literature, the temperature trends are relatively similar, with both showing a slow rise, a fluctuation in the middle section and then a greater rise with a similar final temperature. The difference is that the temperature fluctuation part of the literature at this monitoring site fluctuates by about 20 °C, which is less than the results of this simulation. This part of the results can initially show that in a bundle of identically arranged rods, despite the difference in the geometry of the outer wall, this difference does not significantly affect the temperature distribution in the upper outer wall of the heating tube.

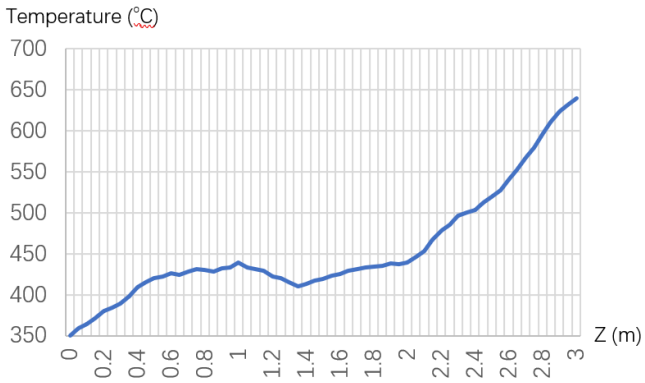

Figure 160. Temperature at point 1

Figure 161 shows the distribution of temperature along the length of the rod at monitoring point 2. At this monitoring point, the temperature distribution shows a steady increase from 350 °C at the inlet of the rod to approximately 504 °C at 3 m, with the temperature remaining stable between 1.4 m and 1.7 m in the middle section. It is worth noting that the temperature at this monitoring point increased more and at a greater rate in the second half than in the first half, while there is a tendency for the temperature to return to a stable level after 2.9 m, although the proximity to the end of the rod bundle at this point resulted in a less pronounced trend. Comparison with the results of the literature shows that the general trend in temperature distribution is similar, with both maintaining a general increase in temperature, but there is a significant drop in temperature in the middle section of the literature, rather than remaining stable as in this simulation, and the results of the original article show a significant increase in temperature in the latter section after experiencing a significant drop, and the magnitude is greater than that of the former section, which is the same as the results of this simulation. In terms of temperature data, the highest point of

temperature in this simulation is higher than the literature results, with an increase of approximately 5%, which can be regarded as a reasonable simulation error due to the different simulation settings.

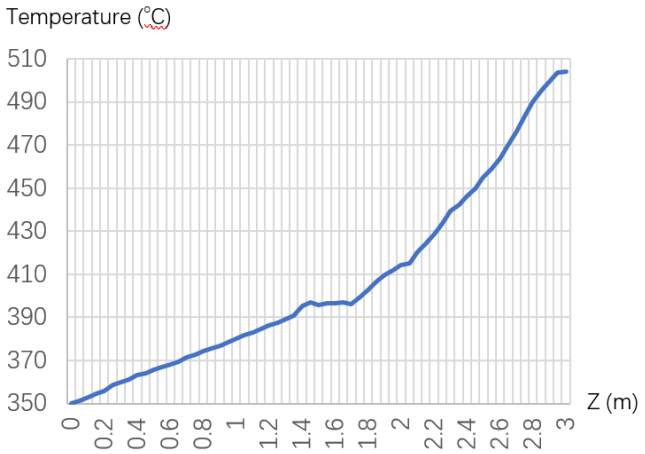

Figure 161. Temperature at point 2

Figure 162 shows the distribution of temperature along the length of the rod at monitoring point 3. At monitoring point three, the trend of temperature change was to rise then fall and finally rise again, with a significant drop in temperature of approximately 13 °C from 0.75 m to 1.2 m in the middle section, before temperatures continued to rise at a much lower rate of increase than in the previous section, eventually reaching 465 °C at 3 m. Compared to the literature, the general trend of temperature change is the same, with both rising, then falling and then continuing to rise. However, there is a significant delay in the area where the temperature drops, by a distance of approximately 0.25 m, and the magnitude of the drop in temperature is much smaller than in the literature, with a drop of 13 °C and 28 °C respectively. From the temperature data, the final temperature for this result is higher than the original result, and the increase is less than 5%, which is within a reasonable range. The reason for the large difference in the results of this simulation may be due to the difference in geometry, which makes the reaction force given to the fluid by the hexagonal fluid outer wall due to gravity more unevenly distributed in direction compared to the circular outer wall, and the shape of the bottom corner may also have an effect on the heat transfer of the fluid.

When comparing the results of the temperature simulations at the three monitoring points with the results of the literature, the overall temperature trends are essentially the same, although there are some differences in the magnitude of the changes, so it can be tentatively confirmed that the model used in this simulation, the grid settings and the feasibility of the simulation setup meet the requirements.

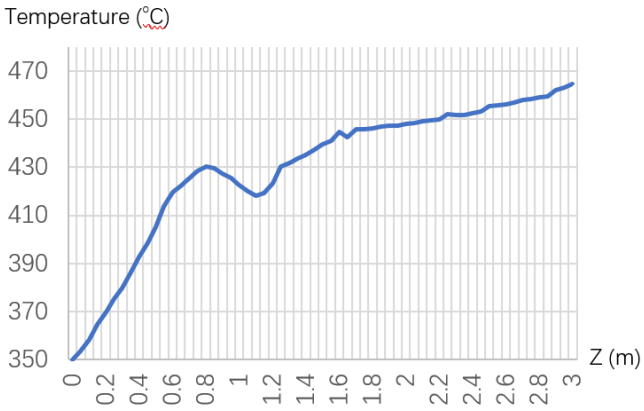

Figure 162. Temperature at point 3

2.5.6.2.2 Wall temperatures distribution at certain bulk temperature's position (360℃)

In this section the simulation results are compared with the literature results at a specific bulk temperature. The main temperature data for comparison are taken from the temperature distribution around the wall of the heating pipe at the specific bulk temperature, oriented left at 0°, with the angle of the temperature distribution calculated counter-clockwise, as shown in *Figure 163.*

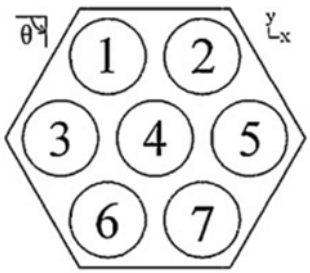

Figure 163. Orientation diagram

Since the distribution of the rods in this pipe is symmetrical from left to right, the temperature data from pipes 1, 3, 4 and 6 on the left side were used for comparison. Figure *164* shows the results of the pipe wall temperature distribution at a bulk temperature of 360 °C from Shang et al. (2010).

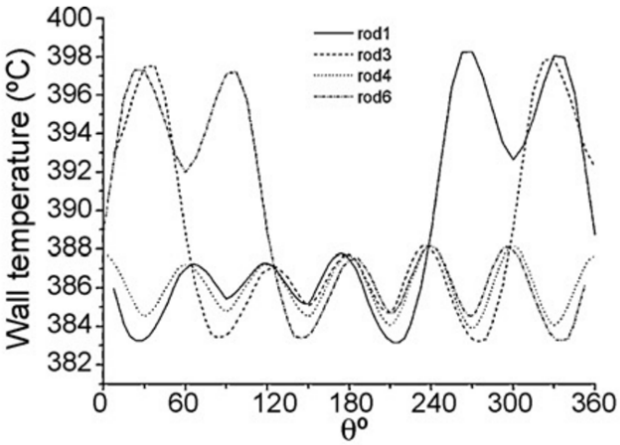

Figure 164. Results of wall temperature (Shang et al., 2010)

Figure 165 shows the temperature distribution of rod 1 at a bulk temperature of 360 °C in this simulation. As can be seen from the simulation results, in the section from 0° to 180°, the temperature fluctuates constantly between 375 °C and 395 °C, with most of the area fluctuating between 385 °C and 390 °C. After 180°, a significant drop in temperature occurs and then begins to rise sharply and reach a peak temperature of approximately 403 °C, before beginning to fluctuate and fall to 390 °C. Compared to the results of the literature, the overall trend was all for fluctuations in the front section, a more pronounced drop in the middle section and a sharp rise followed by fluctuations in the back section. However, the temperature peaks that occur at every 60° angle are not as pronounced in this simulation, but there is still a temperature peak at every 60° angle (approximately). In terms of the temperature data, the range of temperature fluctuations in the fluctuating region in the first part of the simulation results is slightly higher than the literature results, and the temperature peak is higher, with an increase of approximately 1.2%, which is within acceptable limits.

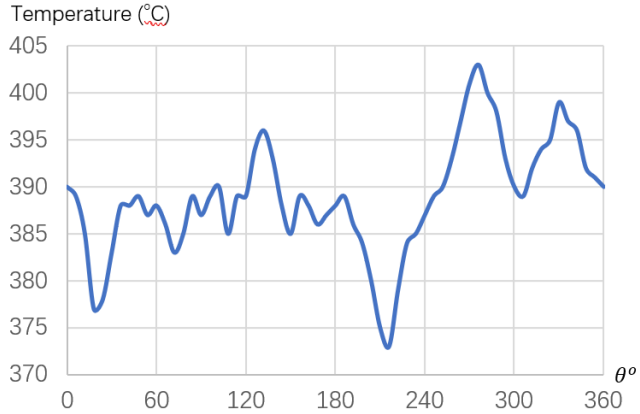

Figure 165. Results of rod 1

Figure 166 shows the temperature distribution of rod 3 at a bulk temperature of 360 °C in this simulation. As can be seen from the simulation results, the temperature change in rod 3 is in three stages, with the front section reaching a high level and then dropping, the middle section fluctuating between 387 °C and 378 °C, and the back section peaking and then dropping at the end, with the same general trend as in the literature. However, the peaks of the temperature fluctuations in the literature are around every 60°, which is not evident in the middle section of the simulation results, and the peaks in the front and back sections follow this pattern. In terms of temperature values, the temperature fluctuation range of the simulated results is slightly larger than that of the literature, but within a reasonable range.

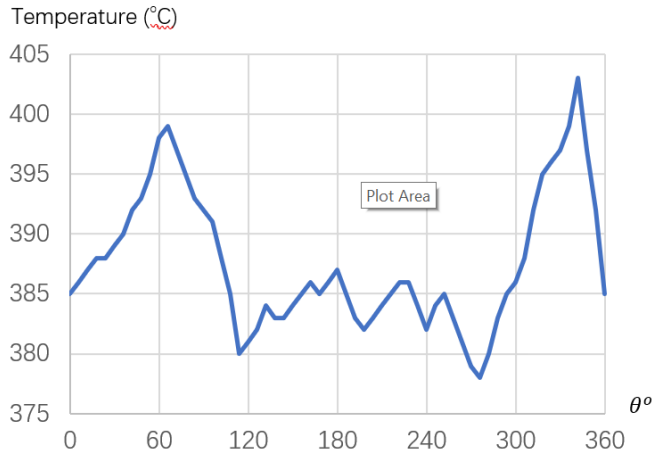

Figure 166. Results of rod 3

Figure 167 shows the temperature distribution of rod 4 at a bulk temperature of 360 °C in this simulation. From the simulation results it is easy to see that the temperature of rod4 fluctuates between 384.5 °C and 387 °C in the circumferential direction and that there is a temperature peak at approximately every 60°, which is consistent with the literature results. In terms of temperature values, the peak and minimum values of the two results are very similar. The reason for this temperature fluctuation may be that the rod is in the center and is more evenly influenced by the surrounding fluids and rod.

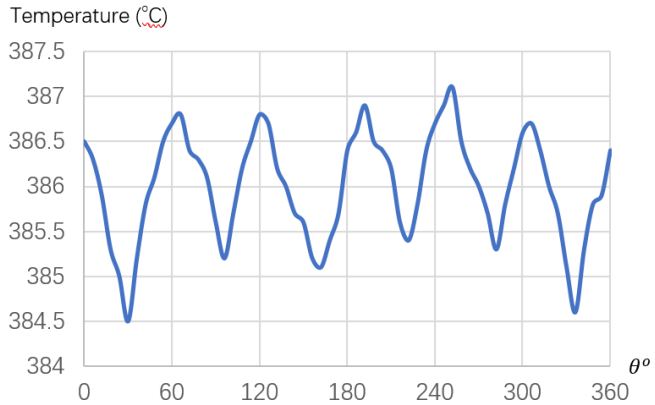

Figure 167. Results of rod 4

Figure 168 shows the temperature distribution of rod 6 at a bulk temperature of 360 °C in this simulation. The simulation results show that the temperature of rod6 rises to a peak of approximately 402 °C and then fluctuates downwards, with the temperature fluctuating in the higher temperature range in the first part and then in the lower temperature range after 150°, with a temperature peak every 60° or so. Compared to the results of the literature, the simulation results are very similar in trend and each temperature peak is generated at the same location. In terms of the temperature data, the temperature peaks are slightly higher and the temperature underestimates are slightly lower, but both are within acceptable limits.

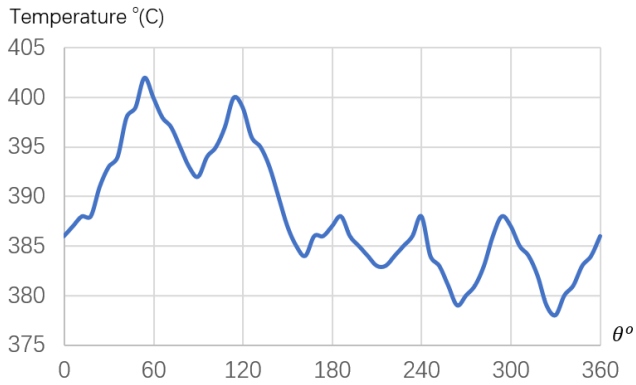

Figure 168. Results of rod 6

2.5.6.2.3 Wall temperatures distribution at certain bulk temperature's position (385℃)

In this section the simulation results are compared with the literature results at a specific bulk temperature (385 ℃). Since the distribution of the rods in this pipe is symmetrical from left to right, the temperature data from pipes 1, 3, 4 and 6 on the left side were used for comparison. The results of the pipe wall temperature distribution at a bulk temperature of 385°C from Shang et al. (2010) are shown in Figure 169.

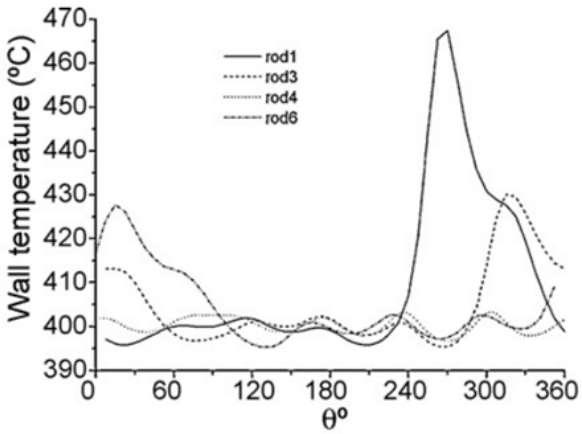

Figure 169. Rresult of wall temperature (Shang et al., 2010)

Figure 170 shows the temperature distribution of rod 1 at a bulk temperature of 385 °C in this simulation. The simulation results show that the temperature in the first half of rod1 is low and fluctuates, remaining in the range of 400 °C to 410 °C. After 180°, the temperature begins to rise sharply to a peak of approximately 485 °C, followed by a sharp drop. Compared to the literature, the overall trend is more consistent, with an initial low level fluctuation, a sharp mid-term rise and then a drop back to a low temperature level. Also, the pattern of peak temperature fluctuation occurring every 60° is consistent between the two sets of results. The difference is that the overall temperature peak for the simulation results occurs at 300°, but the overall temperature peak for the literature results occurs at around 270°. This may be due to the difference in the choice of simulation method.

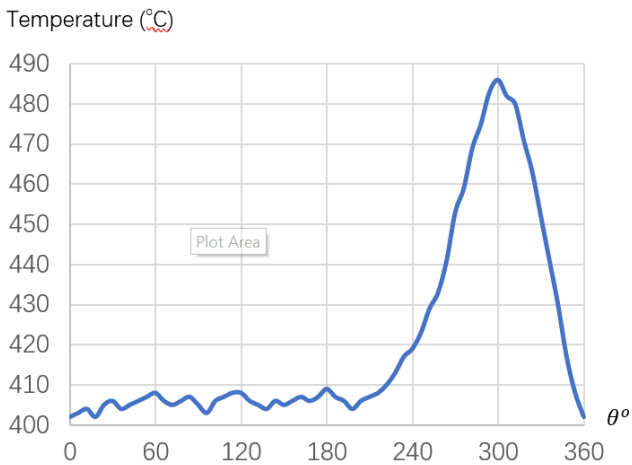

Figure 170. Results of rod 1

Figure 171 shows the temperature distribution of rod 3 at a bulk temperature of 385 °C in this simulation. The temperature trend in rod 3 shows that the temperature first stays fluctuating down and then fluctuates up until it reaches a peak temperature of about 432 °C, with the early fluctuations ranging from about 400 °C to 410 °C. Compared to the literature, the simulated results show greater temperature fluctuations, but the overall trend is one of a slow decline, a mid-term fluctuation, and a sharp rise followed by a decline at the end. The main difference between the two results is the location at which the overall temperature peak occurs, with the simulated results occurring in the 240° to 300° range, while the literature results occur between 300° and 360°. The delay in the temperature peak may be due to the different simulations chosen, resulting in this result being more influenced by buoyancy, which ultimately leads to a different peak region.

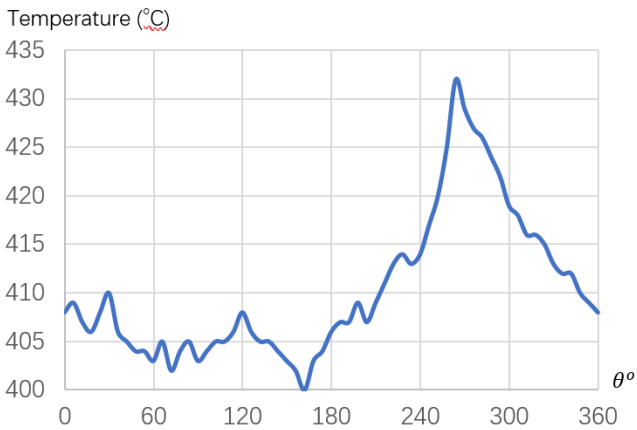

Figure 171. Results of rod 3

Figure 172 shows the temperature distribution of rod 4 at a bulk temperature of 385 °C in this simulation. As can be seen from the simulation results, the temperature of rod 4 varies less with angle, probably due to the fact that the rod is in the center of the array and receives a more uniform influence from the surrounding rods. The temperature of this rod fluctuates between 403 °C and 408 °C, with small temperature peaks at every 60° (except at 180°). Compared to the literature, the fluctuation trends are similar, but the simulation results fluctuate over a slightly higher temperature range than the article results, but within a reasonable margin of error.

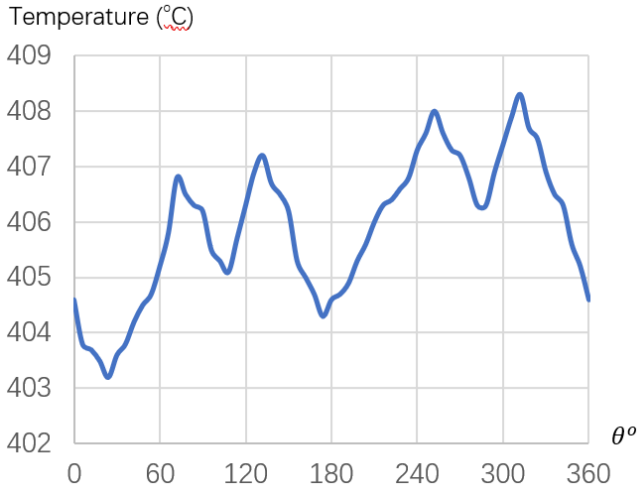

Figure 172. Results of rod 4

Figure 173 shows the temperature distribution of rod 6 at a bulk temperature of 385 °C in this simulation. The simulation results show that the temperature of rod 6 first rises to a peak of about 426 °C, then drops to a low level and begins to remain fluctuating, before starting to rise significantly towards the end. After 180°, three smaller temperature peaks appear, and the locations of their occurrence all correspond to the three adjacent rod orientations. The temperature fluctuations at the low level range from approximately 403 °C to 412 °C. Compared to the literature results, the temperature trends are generally consistent between the two, but the simulated results show a higher range of temperature fluctuations at the low end, but the difference is within a reasonable range.

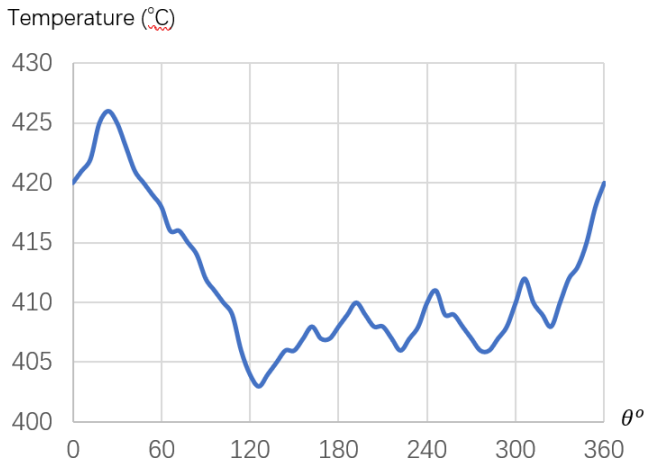

Figure 173. Results of rod 6

2.5.6.2.4 Wall temperatures distribution at certain bulk temperature's position (390℃)

In this section the simulation results are compared with the literature results at a specific bulk temperature (390 ℃). Since the distribution of the rods in this pipe is symmetrical from left to right, the temperature data from pipes 1, 3, 4 and 6 on the left side were used for comparison. The results of the pipe wall temperature distribution at a bulk temperature of 390°C from Shang et al. (2010) are shown in Figure 174.

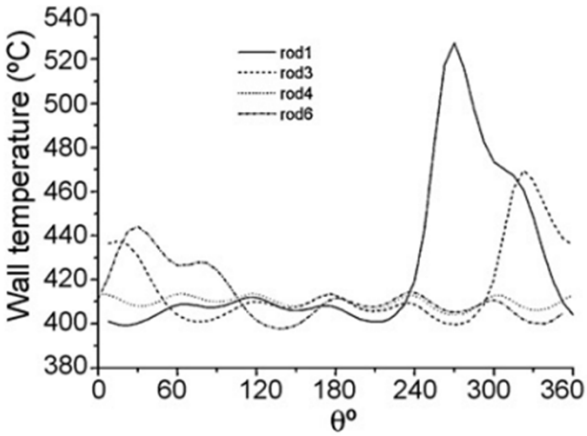

Figure 174. Results of wall temperature (Shang et al., 2010)

Figure 175 shows the temperature distribution of rod 1 at a bulk temperature of 390 °C in this simulation. As can be seen from the simulation results in the graph, the temperature of rod 1 stays at a low level of fluctuation in the early stages and then rises significantly after 180 degrees and reaches a peak temperature of approximately 550 °C. After reaching the peak temperature there is a sharp drop. Compared to the results in the literature, the trend is generally consistent, with both showing low fluctuations in the first half of the period, peaking and then decreasing in the second half. In terms of the temperature data, the two results are very similar in terms of temperature variation, with the simulated result having a ten-degree Celsius higher temperature peak than the literature result, which is within the acceptable margin of error.

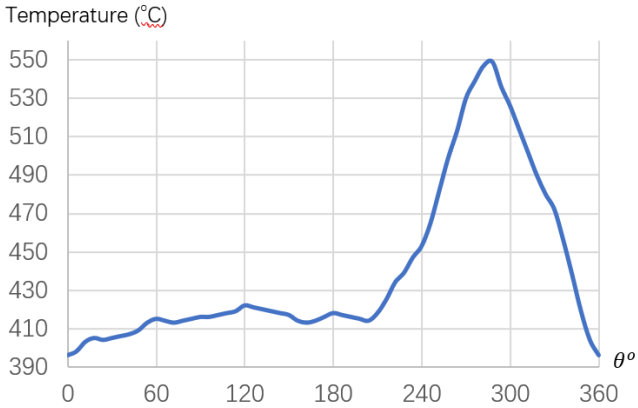

Figure 175. Results of rod 1

Figure 176 shows the temperature distribution of rod 3 at a bulk temperature of 390 °C in this simulation. As can be seen from the simulation results, the temperature of rod3 first drops to a low level and remains fluctuating, and after 270° it starts to rise sharply to a peak temperature of approximately 464°C, before dropping to its initial level. In the middle region, the temperature of this rod shows three lower peaks, which correspond to the positions of each of the three rods adjacent to it. Compared to the literature results, the trends are relatively similar and the temperature change intervals are largely consistent.

Figure 176. Results of rod 3

Figure 177 shows the temperature distribution of rod 4 at a bulk temperature of 390 °C in this simulation. For rod 4, which is in the center of this bundle and more evenly affected by each rod, the temperature fluctuates moderately between 411 °C and 417 °C throughout the wrap-around cycle and a temperature peak is generated at every 60 degrees corresponding to the adjacent pipes. Compared to the literature results, the trends are the same, but the simulated results have a slightly higher temperature fluctuation range, approximately 5 °C higher, which is within acceptable limits.

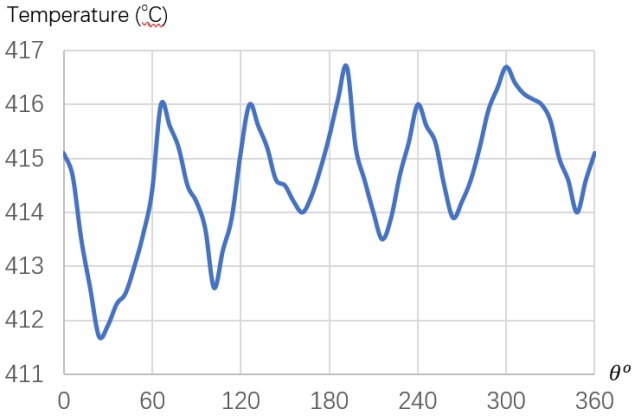

Figure 177. Results of rod 4

Figure 178 shows the temperature distribution of rod 6 at a bulk temperature of 390 °C in this simulation. For the simulation results of rod 6, it can be seen that the temperature of the tube peaks initially at approximately 443 °C and then drops and fluctuates around the 410 °C to 415 °C range, with lower temperature peaks occurring every 60° during this period. Compared to the results of the literature, both are very similar in terms of trend and temperature values.

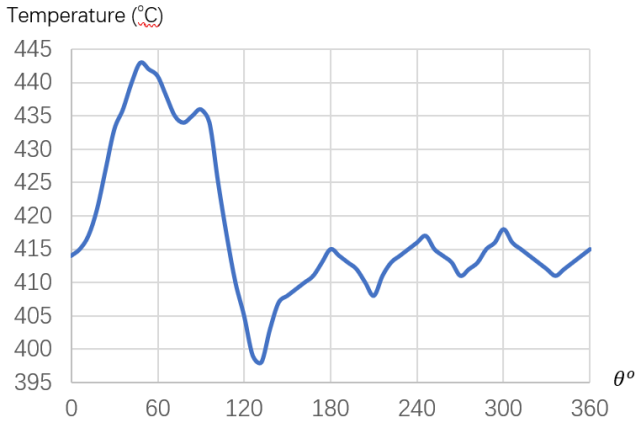

Figure 178. Reults of rod 6

2.5.6.2.5 Heat transfer coefficients of different rods under different bulk temperatures

This section will give the distribution of the heat transfer coefficients at different bulk temperatures on each rod over one week of the outer wall of the rod. The results of the heat transfer coefficients for each rod from Shang et al. (2010) are shown in Figure 179.

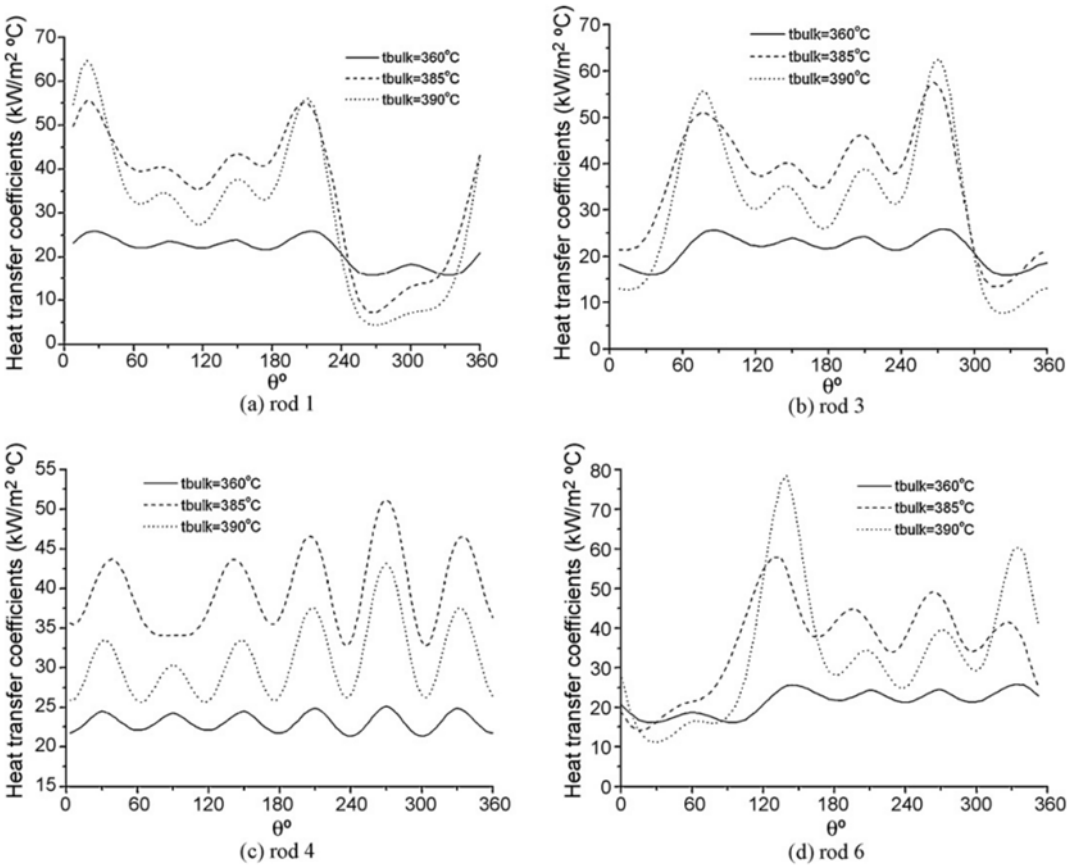

Figure 179. Heat transfer coefficients (Shang et al., 2010)

Figure 180 shows the heat transfer coefficients of rod 1 at a bulk temperature of 360 °C, 385 °C and 390 °C in this simulation. The simulation results show that the heat transfer coefficient of rod 1 at 360 °C always fluctuates smoothly, with fluctuations between approximately 20 and 24. At most locations, the heat transfer coefficient of rod 1 at 385 °C is greater than that at 390 °C, especially between 60° and 180°, i.e. where rod 1 is closer to the adjacent rod. It can also be

seen that there is a more pronounced trough in the heat transfer coefficient at the closer position to the adjacent rod. In terms of the values of the heat transfer coefficients, the simulation results are similar to the article results and both maintain the same trend.

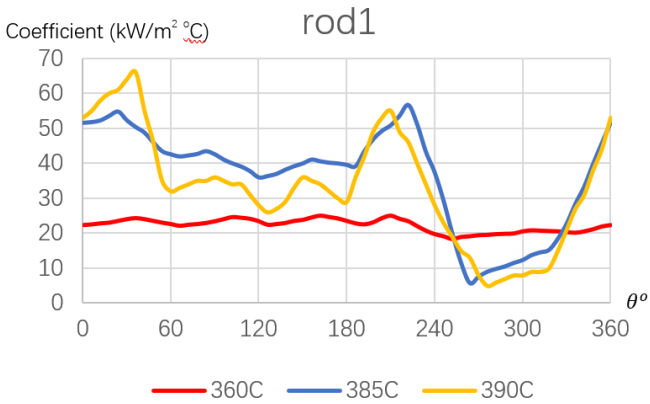

Figure 180. Heat transfer coefficients of rod 1

Figure 181 shows the heat transfer coefficient of rod 3 at a bulk temperature of 360 °C, 385 °C and 390 °C in this simulation. From the simulation results it can be seen that rod 3 and rod 1 behave similarly in terms of heat transfer coefficients, both of which fluctuate smoothly at 360 °C while the heat transfer coefficients in the other two temperature groups are higher in most cases. The heat transfer coefficients in the area close to the other rods are higher at 385 °C than at 390 °C. At the same time, the results continue to maintain the formation of a trough in the heat transfer coefficient in the adjacent region of the rod. When compared to the results of the literature, both the values of the heat transfer coefficients and the trends are relatively similar, with the heat transfer coefficients in the region between 0° and 60° being higher at 390°C than at 385 °C in the simulated results, which is contrary to the results of the literature and may be due to differences in the simulation methods leading to the differences in the simulated results.

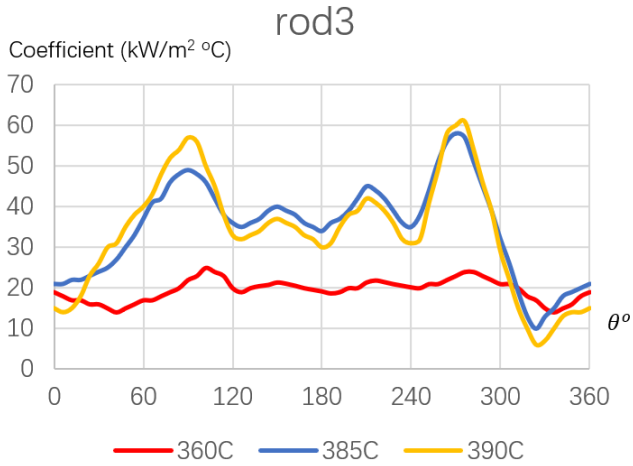

Figure 181. Heat transfer coefficients of rod 3

Figure 182 shows the heat transfer coefficient of rod 4 at a bulk temperature of 360 °C, 385 °C and 390 °C in this simulation. From the simulation results, as rod 4 is adjacent to all other rods, the results show a characteristic of producing a trough in the heat transfer coefficient every 60° in all temperature groups. Also due to the more balanced influence of the surrounding rod, the heat transfer coefficients for each temperature group are in descending order of 385 °C group,

390 °C group and 360 °C group. Compared to the results of the literature, both trends, and the magnitude of the values remain similar.

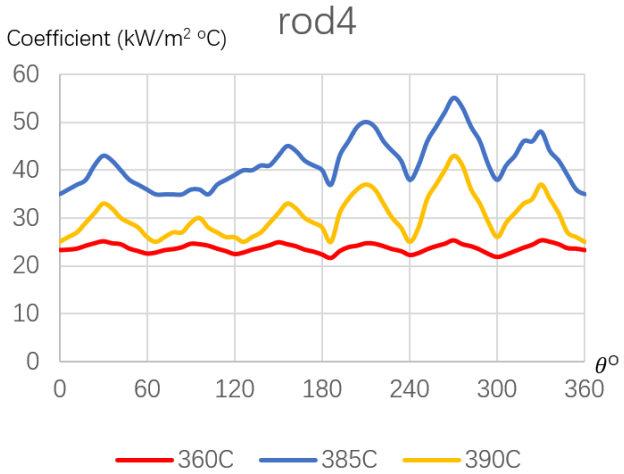

Figure 182. Heat transfer coefficients of rod 4

Figure 183 shows the heat transfer coefficient of rod 6 at a bulk temperature of 360 °C, 385 °C and 390 °C in this simulation. From the simulation results, the variation of the heat transfer coefficient of rod 6 is similar to that of rod1 and rod 3 in that both show a trough in the heat transfer coefficient in the region adjacent to the other rods and the heat transfer coefficient at 385 °C is higher than that at 390 °C. Both remain highly consistent in terms of trends and values compared to the literature results.

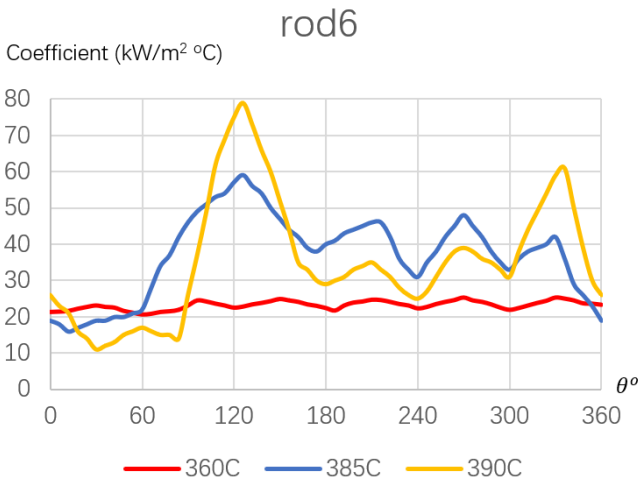

Figure 183. Heat transfer coefficients of rod 6

2.5.7 Summary

The comparisons of the simulation results with the experimental data and literature results indicate that in most cases, the CFD simulation results are very similar to the experimental data terms of temperature trends, although individual regions may be influenced by the simulation settings and inevitably differences. In terms of temperature values, most of the simulated results agree well, with some errors arising, but all within acceptable limits. The comparison of the results therefore illustrates the reliability and correctness of the simulation process.

Based on the rod bundle CFD simulation results, it is found that there is a heat transfer effect between the rods, which is demonstrated by the fact that the wall temperature in the adjacent

areas of each rod is higher than the other areas, and in most cases the wall temperature appears as a regional peak, which indicates a heat transfer attenuation effect between the adjacent rods. As 385 °C is closer to the pseudo-critical point temperature than 390°C, there is a partial inconsistency between the simulation results and the literature results when the body temperature of the fluid is 385 °C. This may be due to the fact that the properties of supercritical water vary considerably around the pseudo-critical point, and this variation may amplify the differences caused by the simulation settings. By comparing the wall temperature of each rod at different body temperatures, it is found that the heat transfer coefficients at 385 °C are higher than those at 390 °C and 360 °C, suggesting that heat transfer enhancement may occur near the pseudo-critical point.

2.6 CONTRIBUTION BY NPIC

National Power Insitute of China (NPIC) and Xian Jiao-Tong University, China organized international benchmarking activity on thermal hydraulics in supercritical water IBSCTH which was a part of the ECC-SMART project cooperation. The details on this activity are provided in the deliverable D3.2 of the WP3.

3 Subtask 3.3.3 Investigation and implementation of heat transfer correlations (CNL)

The friction correction factors have been implemented in an interim version of the subchannel code ASSERT-PV to assess their impact on pressure drop prediction. The results showed that a correction factor reduces the uncertainty of the ASSERT-PV SC predictions for pressure drop. Details on this work are presented in the subsection 2.3 of this document (pp 154 ff), for consistency. The work performed on investigation and implementation of heat transfer correlations by CNL is in additional details presented in the deliverable D3.2 of the WP3 and will be also provided within the deliverable D3.4 of ECC-SMART WP3.

4 Subtask 3.3.4 Improvement, implementation and validation of engineering models for turbulent heat transfer under supercritical conditions (IPP)

4.1 Introductory remarks

In Chapter 2, the participants of ECC-SMART project discussed the problem of predicting deteriorated heat transfer using CFD codes with engineering approaches which make it possible to rationally proceed with the analytical design activities of the promising SCW-SMR core.

This Subtask 3.3.4 summarizes the work on improvement, implementation and validation of engineering models for turbulent heat transfer under supercritical conditions, performed in IPP simultaneously in the frame of the ECC-SMART project and doctoral work of Vladislav Filonov (Filonov, 2023).

The method of wall functions is quite powerful, the capabilities of which are underestimated in the context of the calculation of non-linear heat transfer regimes at supercritical coolant parameters. Subsection 4.2 considers the existing problems of using universal wall functions in the framework of the HTD phenomena prediction and IPP's attempt to adapt UWFs to calculate, primarily, HTD zones (Filonov et al., 2021).

An attempt to modify the Eddy viscosity turbulence model to take into account non-linear effects of heat transfer became a separate direction of IPP work. For this purpose, Popov's theory for the turbulent Prandtl mixing length, as well as corrections that take into account the density pulsation field were applied (Filonov et al., 2024). Thus, it is possible to take into account the presence of gravity not only as a force factor, but also as a turbulent factor.

The constructed algebraic turbulence model is non-linear, as it is actually recursive with respect to the turbulent viscosity due to consideration of the radial tangential stresses distribution. Due to non-locality of formulations, such models cannot be easily implemented in modern CFD packages. Therefore, currently these modifications have been implemented and tested in the 2-dimensional non-linear differential procedure for predicting the intensity of heat transfer and energy dissipation at supercritical parameters (Narrow channel model), which combines the advantages of both system analysis and and CFD. A detailed description of this differential procedure is provided by IPP as part of deliverable D3.4 "Report on the improved system codes describing how they improved". In subsection 4.3 below, only the aspects related to the modification of the turbulence model are described. As a validation, the results of applying the

proposed modifications for the Eddy viscosity turbulence model are compared with the corresponding results obtained using standard RANS turbulence models – RNG, SST and EVT.

4.2 Universal wall functions adaptation for calculation the heat transfer at supercritical conditions

Universal wall functions (UWF) are a very powerful tool in the engineering practice of applying CFD methods (Allegrini et.al., 2012; Popovac and Hanjalic., 2007; Kirillov and Terent'eva, 2017). This actually makes it possible to simply "project" the values of the wall boundary conditions to the nearest node of the computational mesh (Popovac and Hanjalic., 2007). There are several types of UWF that can be conditionally divided into groups according to the transfer equation to which the wall function is applied (force - velocity; thermal - temperature/enthalpy; turbulent - turbulence kinetic energy/dissipative function). One of the main advantages of using UWF is the less strict conditions for the computational mesh discretization near the wall. Furthermore, if UWFs are applied in the parameter range for which they were actually designed and calibrated, it is usually possible to obtain agreement between the calculation and experiment in terms of heat transfer/dissipation rates (both locally and averaged). As for the disadvantages of the UWF method is that they are implicit, and thus require special implementation in calculation packages.

Modern wall functions are generalized for the entire thickness of the boundary layer and also consider the non-isothermal flow (Kader's generalization (Kader, 1981)). The concept of nonequilibrium boundary layer functions (Zhlutkov and Aksenov, 2015) makes it possible to take into account the longitudinal pressure gradient in the boundary layer.

Nevertheless, for "nonlinear" heat transfer problems, in which there is a significant change in thermophysical properties, as well as the influence of natural convection, the UWF does not actually work. That is, the predicted wall temperature profile under the second-order boundary conditions differs both quantitatively and qualitatively from the experimental data, although with the same turbulence model, there are no predictive problems with a detailed discretization of the near-wall region (see Figure 184).

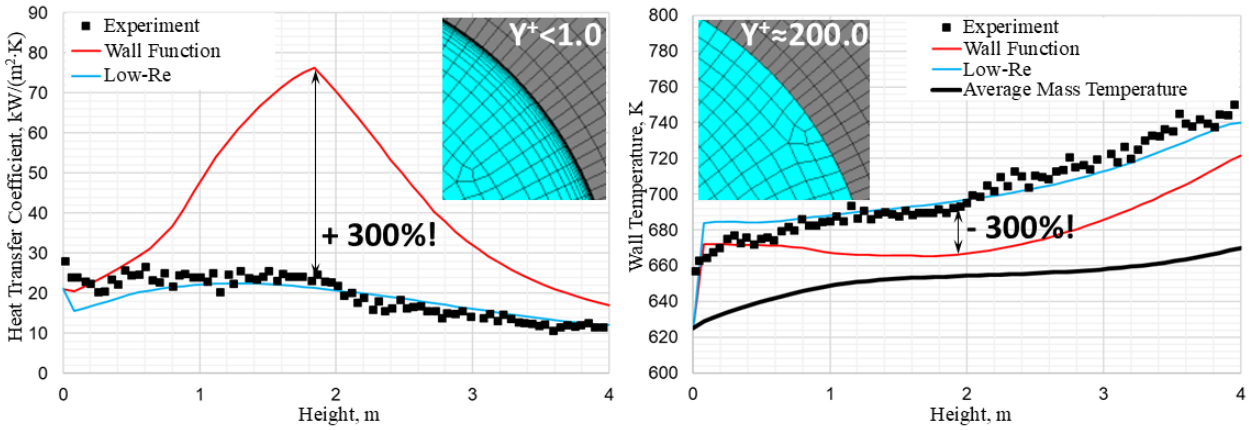

Figure 184. Demonstration of the problem of applying the UWF in the calculation of the heat transfer regime at supercritical parameters near the pseudo-phase transition point

So, the use of the UWF is not possible for the deteriorated heat transfer regimes at supercritical coolant parameters. Therefore, the main goal of this part of IPP work is an attempt to create a SWF based on the UWF, which will improve the predictive properties of CFD for heat transfer regimes with supercritical coolant parameters. Such work is important as it can preserve the applicability of wall functions that allow for the rational use of computing resources. Keeping the

discretization requirements for computational models relatively small is essential in engineering practice, as it makes it possible to go beyond the consideration of elementary channels.

4.2.1 Adaptation of "classical" temperature wall functions

The first step in the SWF development is to adapt the existing temperature UWFs based on comprehensive probe studies of the supercritical CO_2 flow, which were described in Section 2.4.2.1.

The results of the research and generalizations indicate that under the significant influence of buoyancy and changes in thermophysical properties, the velocity profiles of U+ and h+ are similar not only under normal heat transfer (NORM, Figure 185) but also under deteriorated heat transfer (DHT, Figure 185). Normal ("linear") heat transfer is characterized by a small impact of thermal acceleration, since there are no significant gradients in thermal properties and, consequently, buoyancy. In this case, i.e., when using the UWF, a satisfactory agreement between CFD results and experiment can be obtained (without taking into account low-Re effects).

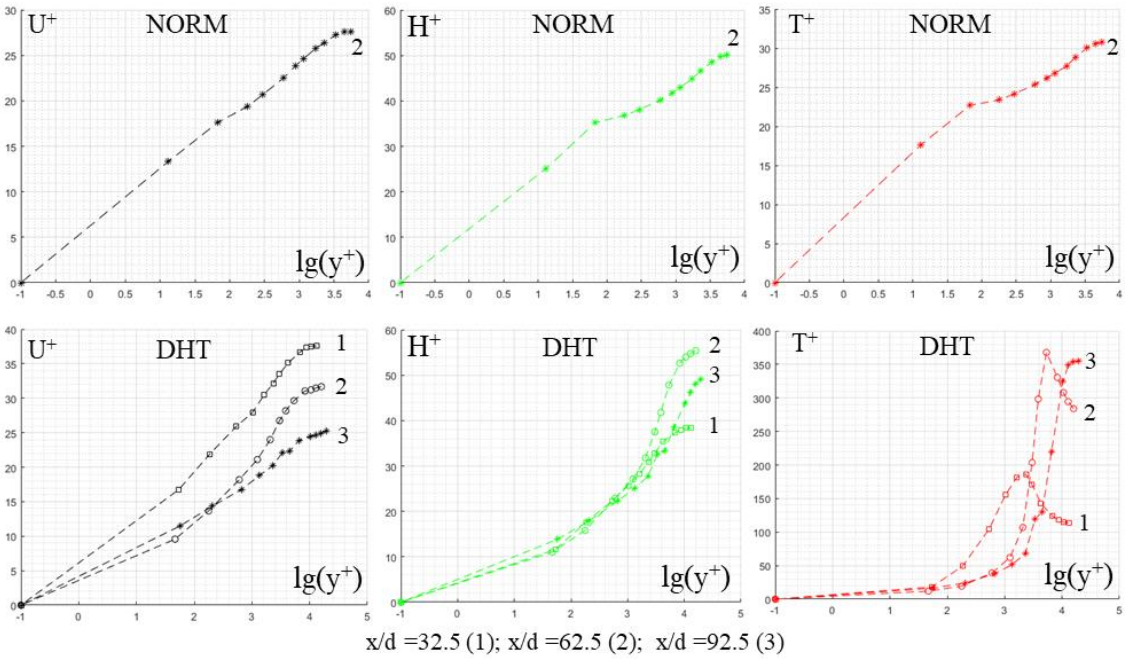

Figure 185. Experimental UWF (NORM - normal, DHT - deteriorated heat transfer)

Taking into account that the profiles of U+, h+, and T+ are similar in "linear" heat transfer, and that modern codes use U+ - T+ combinations, IPP proposed a simple modification of the wall temperature function, which can be represented as:

$$h^+ = \rho u_\tau \frac{h - h_w}{q_w} \approx \rho u_\tau \left(\frac{\partial h}{\partial T}\right)_p \frac{(T - T_w)}{q_w} = \rho u_\tau \overline{C}_p \cdot \frac{(T - T_w)}{q_w} = \frac{\overline{C}_p}{C_p} T^+ \Rightarrow T^+_{SCP} = \frac{C_p}{\overline{C}_p} T^+_{classic} \qquad (62)$$

Where $\rho u_\tau \left(\frac{\partial h}{\partial T}\right)_p \frac{(T - T_w)}{q_w}$ is a linearization of the dimensionless enthalpy h^+ relative to the wall temperature.

The pressure derivative of the enthalpy can be interpreted as the average value of the isobaric heat capacity between the wall and the point considered with coordinate y^+.

In general, the structure of a two-zone equilibrium temperature UWF can be represented as (Zhukauskas and Shlyanchyauskas, 1973):

$$T^{+} = e^{-\Gamma} f_{lam} y^{+} + e^{-\frac{1}{\Gamma}} \left[f_{turb} \ln\left(y^{+}\right) + B\left(Pr, Pr_{t}\right) \right] \tag{63}$$

The first term of Eq. (63) characterizes the laminar part of the thermal boundary layer (is usually limited to y+ ~ 11), the second term corresponds to the turbulent part. To connect the laminar and turbulent zones, exponential corrections are used as a function of Prandtl number and a dimensionless coordinate.

Function $B\left(Pr, Pr_{t}\right)$ characterizes the additional thermal resistance of the temperature boundary layer. Considering that in first approximation, the velocity profile does not change "fundamentally" when moving from normal to deteriorated heat transfer, it is possible to estimate the modification effect of $B\left(Pr, Pr_{t}\right)\frac{C_p}{\overline{C_p}}$ on the temperature UWF.

For a prior estimation (temperature and heat flux on the wall are known), we use the two-zone Kader's UWF (Kader, 1981), that can be represented as:

$$T^{+}_{classic} = e^{-\Gamma}\left(Pr\, y^{+}\right) + e^{-\frac{1}{\Gamma}}\left[2{,}39 \ln\left(9{,}79 \cdot y^{+}\right) + B\left(Pr, Pr_{t}\right)\right]; \Gamma = \frac{0{,}01\left(Pr\, y^{+}\right)^{4}}{1 + 5 \cdot Pr^{3}\, y^{+}}$$
$$B\left(Pr, Pr_{t}\right) = 9{,}28\left[\left(\frac{Pr}{Pr_{t}}\right)^{\frac{3}{4}} - 1\right]\left(1 + 0{,}28 \cdot e^{-0{,}007\frac{Pr}{Pr_{t}}}\right) \tag{64}$$

In case of applying Eq. (64) for the prior estimation (Figure 186) a fixed value of Pr_t was used, which is assumed to be equal to 0.9.

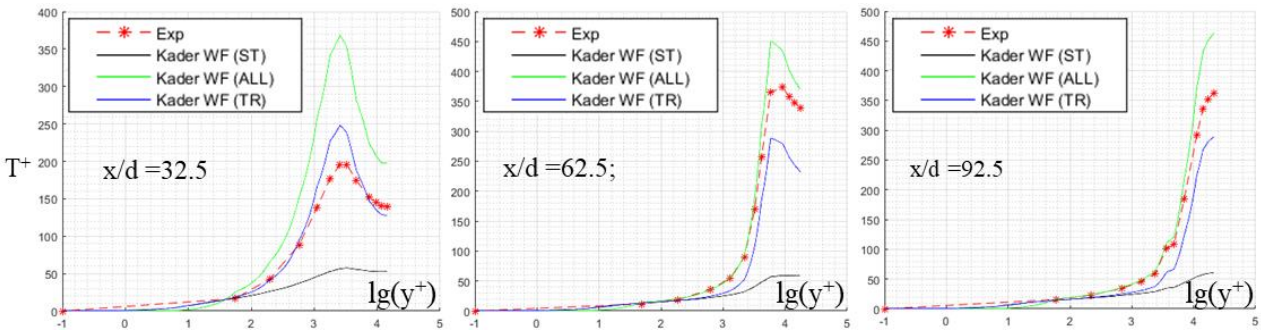

Figure 186. Adapted UWF(SWF) (ST - standard, ALL - adaptation (Eq. (62)), TR - thermal resistance adaptation $B\left(Pr, Pr_{t}\right)$)

The obtained results of the prior assessment are quite optimistic, since in the first approximation they significantly improve the predictive capabilities of the wall function, that in general, was obtained under fundamentally different temperature conditions (Kader, 1981). Even in the y^{+} region from 30 to 300 (and sometimes up to 1000 at Reynolds numbers ~10^{6}-10^{9}), which are typical for engineering calculations, the proposed modification of the UWF allows obtaining much better predictions (Figure 187).

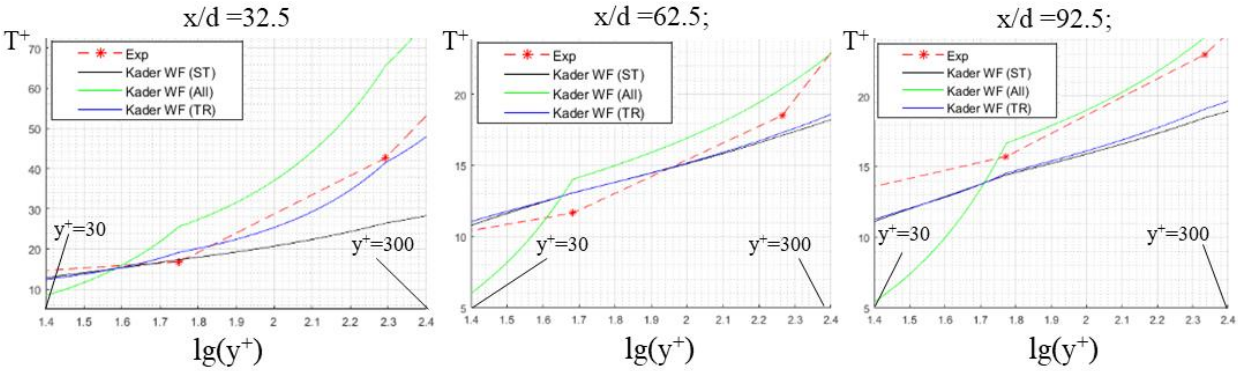

Figure 187. Adapted UWF (SWF) in the range of y+ from 30 to 300 (ST - standard, ALL - adaptation (Eq. (62)), TR - thermal resistance adaptation $B(\Pr, \Pr_t)$)

So, the proposed rather simple modification may be helpful for engineering practice. Below are the results of implementing the SWF into a CFD code.

4.2.2 Peculiarities of implementation and application of the modified wall function (SWF)

As can be seen from dependence Eq. (64), in order to determine all the coefficients, it is necessary to specify the reference value y^+ for calculating the thermal properties. If take the y^+ to be equal to the local nodal value of the first control volume, a fully explicit formulation will be obtained. If take $y^+=0$ as the defining value, a fully implicit implementation will be achived, since the required coefficients are functions of the wall temperature. It should be noted that the thermal boundary conditions of the second kind are considered, that is proper in this type of problem. According to (Berni and Fontanesi, 2020) the method of implementing the wall function is defining in many cases, and can even be realized by constructing a kind of extrapolation profile, i.e., using several wall nodes in the normal. However, from an algorithmic point of view, this method is generally very complicated and is practically not used in commercial CFD packages.

The fundamental difference from the «linear» heat transfer in the case of using the wall function is that the thermophysical properties within the characteristic height of the near-wall control volume practically do not change. In the case of heat transfer at supercritical parameters, a convergence problem may arise due to the extremely nonlinear behavior of the specific heat capacity as a function of temperature. In addition, in the case of «linear» heat transfer, the constancy of tangential stresses can be assumed, which is confirmed by many experiments (Kader, 1981; Zhukauskas and Shlyanchyauskas, 1973).

During the heat transfer at SCP, especially with HTD, the constancy of tangential stresses is not maintained not only due to changes in thermophysical properties, but also by changes in «physics», which cannot yet be considered by the UWF and SWF.

For these reasons, when applying the SPF, Eq. (62) – Eq. (64) are represented as Eq. (65), which is an implicit generalization in its form. That is, from the point of view of the calculation code, it loses some universality (a parameter that is some average function of the local temperature field will appear).

$$T^+ = c_p(T)\left(\frac{\partial h}{\partial T}\right)_p^{-1} \cdot T^+_{classic} \approx \frac{c_p(T)}{av\left[c_p(T)\right]} T^+_{classic} \tag{65}$$

Where $av[...]$ - is a certain argument averaging procedure, which is the specific isobaric heat capacity.

To use the SWF in the form of Eq. (65), it is necessary to decide which function $\mathrm{av}[\ldots]$ to select and organize an additional calculation procedure in the CFD code itself. The interface that allows to work with the user wall functions is present in commercial calculation codes, but it has some features. First, averaging can only be organized by introducing additional cyclic restarts of the setting method (CFX), which may be quite reasonable for relatively simple geometry, but for complex problems it makes no sense to use the SWF (due to the required calculation time). Secondly, ANSYS CFX uses the "Wall Adjacent Temperature" type as a reference temperature, i.e., the value of the flow temperature. As mentioned above, this is a significant disadvantage in "non-linear" heat transfer. To implement the SWF using this approach, it is necessary to create a special procedure that would synchronize the flow iterations with the wall temperature calculation subroutine.

To test the developed temperature SWF, a special subroutine was implemented, which was applied sequentially after calculating the main flow fields at supercritical parameters. This allowed, in comparison with Eq. (65), to preserve the universatility of the SWF to some extent. To determine the wall temperature, the transcendental equation Eq. (66) with respect to the wall temperature was implemented, which takes into account the above stated features that specific for the heat transfer at SCP.

$$u_\tau = \left[\begin{array}{l} \sqrt{\tau_w^{CFD} \cdot \rho\left(T_{ref}\right)^{-1}} \\ \sqrt{\rho\left(T_f\right)^{-1} \cdot \left[\mu\left(T_f\right) + \mu_f^{CFD}\right] \cdot \left.\frac{\partial U}{\partial n}\right|_f^{CFD}} \end{array}\right.; y^+ = \left[\begin{array}{l} \left(y^+\right)_{CFD} \\ y_f u_\tau\left(T_{ref}\right) \cdot \nu\left(T_{ref}\right)^{-1} \end{array}\right. \tag{66}$$

$$q_w K\left(y^+\right) T_{КЛ}^+\left(y^+; Pr\right) = \rho\left(T_{ref}\right) u_\tau \left[h\left(T_w\right) - h\left(T_f\right)\right]; Pr = Pr\left(T_{ref}\right)$$

Where T_{ref} - reference temperature, in the range from T_f to T_w . $K\left(y^+\right)$ - the proportionality factor.

The temperature T_f is determined in CFD and if it is chosen as a reference, a fully explicit approach will be obtained. It is worth noting some features of Eq. (66). The fact that the implemented SWF is a consequence of Eq. (65) is not obvious, since the transfer from dimensionless temperature to dimensionless enthalpy was managed.

To do this, in the function $\mathrm{av}[\ldots]$ of Eq. (65) should be the average enthalpy value of the heat capacity, which is defined as $\left(h_w - h_f\right)/\left(T_w - T_f\right)$. When paying attention to the difference between h^+ and T^+ (see Figure 185) at normal heat transfer (which is the limiting case for Eq. (65) in the sense of $\frac{C_p(T)}{\mathrm{av}\left[C_p(T)\right]} \to 1$), then, at a first approximation, it can be assumed that $h^+ \approx K\left(y^+\right) T^+$ for both normal and deteriorated heat transfer. For y^+<1000, $K\left(y^+\right)$ is in range from 1 to ~1,5.

4.2.3 SWF application examples

4.2.3.1 Calibration and validation of the modified temperature wall function

The calibration and validation of the proposed SWF was performed using the High-Re turbulence models EVT (one-parameter) and SST (two-parameter). Figure 188 shows the results of testing the SWF on the basis of Kurganov experimental data for CO_2 (from Section 2.4.2.1), which was used to analyze the corresponding adaptation of the UWF.

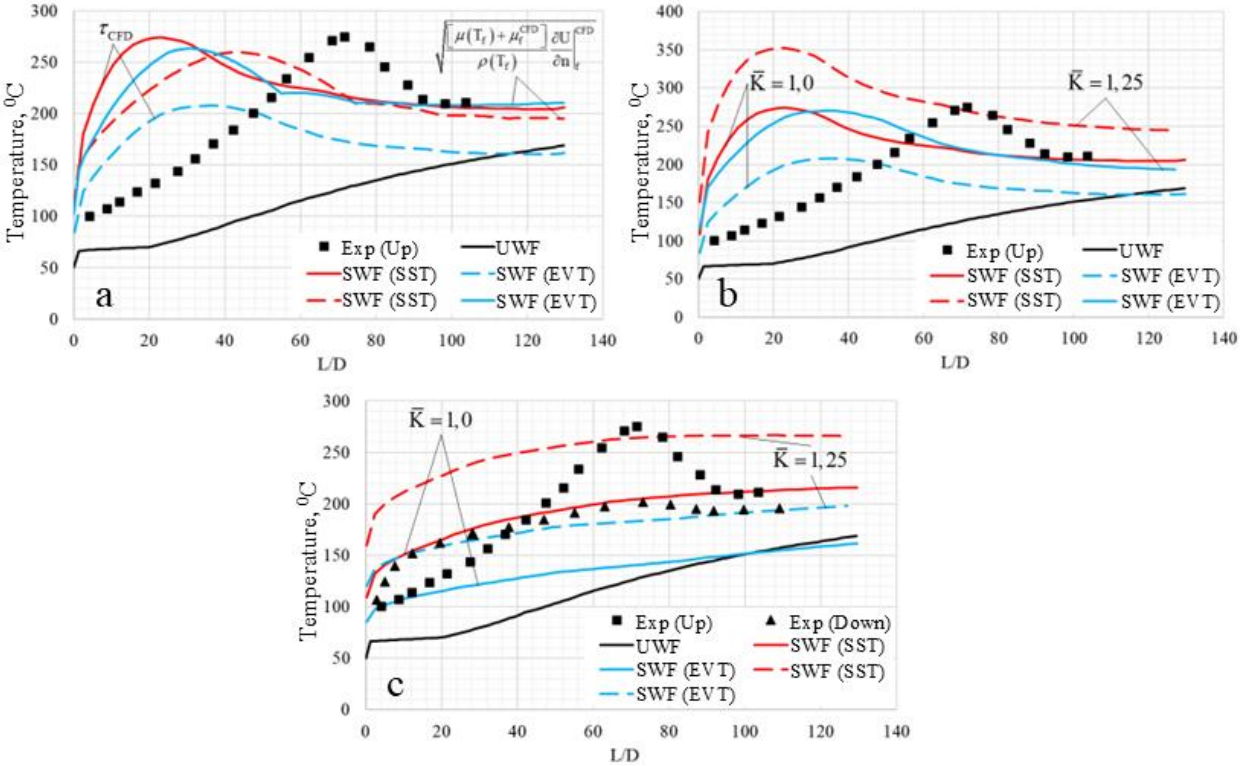

Figure 188. SWF application results (a – reference temperature at the wall for T^+ and u_τ with different methods of determining tangential stresses; б - reference temperature at the wall for T^+ and u_τ for different average values of the proportionality ratio K; в - reference wall temperature for T^+ and u_τ, implicit formulation)

The results obtained using Eq. (66) demonstrate a qualitative and quantitative change in the predicted values when using the SWF. It is worth noting that, in general, the obtained temperatures increased in absolute values, and in the case of the reference flow temperature, it is possible to predict a characteristic peak in the axial distribution (although this peak is shifted towards the heating area and may be the result of the radial temperature/velocity profile establishment). The results also demonstrate that using an alternative method of determining tangential stresses based on CFD data (by calculating the velocity gradient), it is possible to obtain a shifted peak relative to the inlet section, which is in better agreement with the experiment. The alternative method of calculating tangential stresses requires the analysis of a larger data set (it is necessary to operate with the velocity field at least a certain number of neighboring nodes normal to the heated wall). The need for an alternative definition of tangential stresses (based on the definition) is demanded by the fact that, depending on the RANS turbulence model, there may be differences in the definition of wall shear stresses in the CFD code (the formulation through the kinetic energy of turbulent pulsations is used).

In the case of using the wall temperature (unknown value) as a determinant for T^+ and u_τ the results are generally improved quantitatively, but still correspond to "linear" heat transfer qualitatively. The resulting axial profiles are similar to those that are mostly obtained when taking into account low-Re effects (Dubyk et.al., 2021), but require significantly lower computational resources (the sampling density is reduced by a factor of 4-10). The next important feature should be noted - for a fully implicit formulation, with an extremally nonlinear change in thermophysical properties, a convergence problem arises for the wall functions, which is similar to the problem with implicit correlations for SC and generally requires the use of special methods (Filonov et.al., 2022). The achieved results are expected, since, as stated above, SWF based on the UWF are not able to take into account the physical features of the processes during heat transfer deterioration.

4.2.3.2 Application of SWF for calculation test case with supercritical heat transfer conditions

The next step is a computational test that relates to heat transfer with supercritical water parameters, from that the UWF problem discussion was began (see Figure 184). Using the example of experiment that is considered a classic one for testing computational methods (Mokry et.al., 2010), the possibilities of SWF usage will be considered. The main characteristics of the selected regime are as follows: the length of the heating section – 4 m; reference pressure – 24 MPa; inlet temperature – 352 ºC; mass velocity – 1500 kg/(m^2·s); heat flux - 884 kW/m^2. According to the classification (Mokry and Maslakova, 2016), this regime corresponds to deteriorated heat transfer. Figure 189 demonstrates the results of the SWF application.

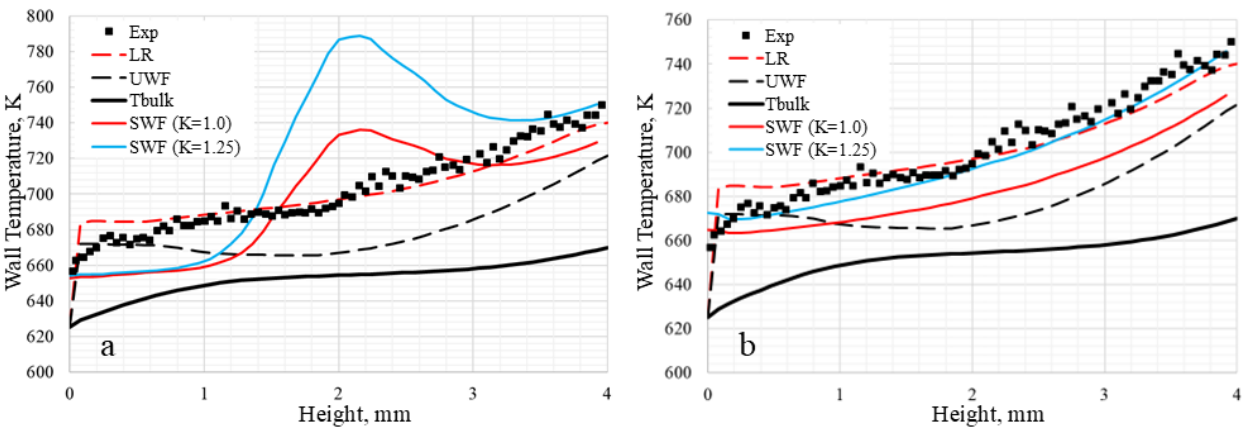

Figure 189. SWF application results (a – reference temperature at the wall for T^+ and u_τ ; б - reference wall temperature for T^+ and u_τ , implicit formulation)

The results are consistent with the declared above conclusions. The EVT model was used as the turbulence model, with a discretization corresponding to a y^+ value near the wall of ~ 400. It should be noted that in this calculation using Low-Re, the computational mesh has ~ 13 times more computational nodes only due to the additional discretization of the near-wall region.

4.2.3.3 Application of SWF for NTUU experimental data for 1- and 3-rod bundles

Below are the results of testing the SWF based on the results of NTUU experimental studies for one- and three-rod bundles at the following operating characteristics: reference pressure –

22.6/27.5 MPa; inlet temperature – 246/212ºC; mass velocity – 2500/1500 kg/(m^2·s); heat flux – 2750/2400 kW/m^2 respectively (Filonov et.al., 2018). The obtained results (see Figure 190) quite clearly demonstrate the capabilities of SWF in the context of their application for rod bundles.

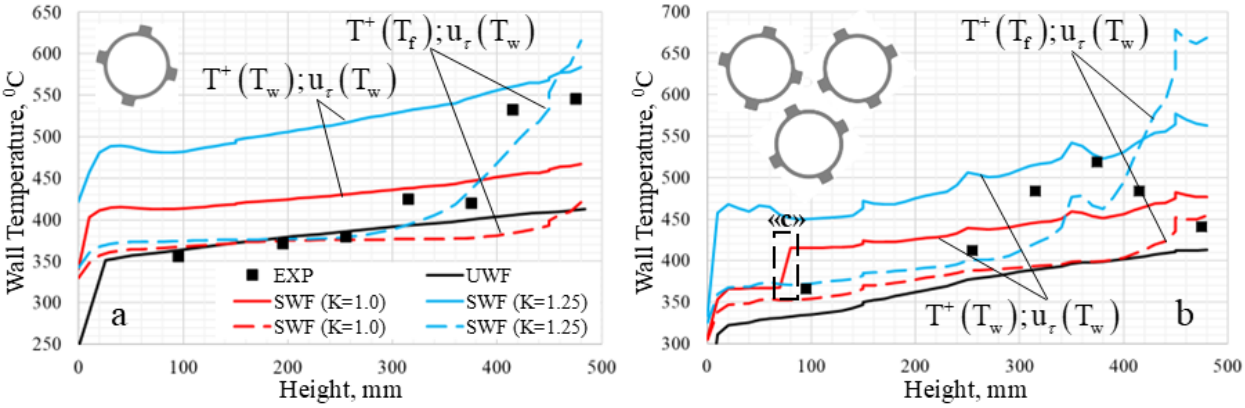

Figure 190. The results of applying the SWF for the HTD regime (a – 1-rod bundle; б – 3-rods bundle)

In general, the predictive properties of the SWF are much better compared to the UWF, but there are some peculiarities for the rod assemblies. First, it is likely that the determination of tangential stresses from the flow temperature gives a large error primarily due to the specifics of discretization caused by the presence of screws. The fact is that it is practically impossible to maintain a value of y^+>100 along the entire thermal perimeter (this applies primarily to 3- and 7-rod bundles). Second, because of the rather close rods arrangement, a situation arises when the characteristic size of the wall control volume is comparable to the characteristic size of the entire core flow. All this leads to the fact that the procedure for averaging the flow parameters along the thermal perimeter required by Eq. (66) has significant inaccuracies that apparent in the axial temperature profiles. In addition, in a completely implicit formulation, internal convergence problems in this type of calculation may arise (Filonov et.al., 2022) (see zone «c» in Figure 190). The fact that there is a problem with the determination of tangential stresses is also evidenced by the effect of the combination of reference temperatures T^+ defined by the flow temperature, and the dynamic velocity calculated implicitly (by the wall temperature).

Based on the obtained results, it can be recommended to use SWF with High-Re one- and two-parameter turbulence models within the RANS for further calculations. The characteristic size of the near-wall control volume should be chosen based on the recommended value of y^+, which is in the range from 100 to 1000. The average value of the proportionality factor is recommended to be 1,25.

4.3 Modification of Eddy viscosity turbulence model to take into account non-linear effects of heat transfer

This subsection describes an attempt made to modify the Eddy viscosity turbulence model to take into account non-linear effects of heat transfer. Subsection 4.3.1 contains a description of the proposed modifications. The validation of their application is carried out on the Kurganov experimental data for CO_2 and described in subsection 4.3.2.

4.3.1 Description of the proposed modifications for obtaining the closing turbulent characteristics

In the first approximation applying the Prandtl theory of the mixing path, and given the modern notion of non-isothermal boundary layer, the diffusion terms which define the transverse exchange functions described in Narrow channel model description (see deliverable D3.4) can be represented as follows:

$$T_p = \frac{\partial}{\partial r}\left[r\left(\nu\frac{\partial G_x}{\partial r} + \tau_t\right)\right] = \frac{\partial}{\partial r}\left[r\left(\nu\frac{\partial G_x}{\partial r} + \alpha_p\frac{\partial G_x}{\partial r} + \beta_p\frac{\partial h}{\partial r} - \overbrace{\frac{\nu G_x}{\rho}\frac{\partial \rho}{\partial r}}^{\delta\tau}\right)\right] \tag{67}$$

$$T_T = \frac{\partial}{\partial r}\left[r\left(\frac{\lambda}{c_p}\frac{\partial h}{\partial r} + q_t\right)\right] = \frac{\partial}{\partial r}\left[r\left(\chi\frac{\partial h}{\partial r} + \alpha_T\frac{\partial G_x}{\partial r} + \beta_T\frac{\partial h}{\partial r}\right)\right] \tag{68}$$

$$T_F = \frac{\partial}{\partial r}\left[\frac{r\cdot G_x}{\rho}\left(\nu\frac{\partial G_x}{\partial r} + \tau_t\right)\right] = \frac{\partial}{\partial r}\left[\frac{r\cdot G_x}{\rho}\left(\nu\frac{\partial G_x}{\partial r} + \alpha_p\frac{\partial G_x}{\partial r} + \beta_p\frac{\partial h}{\partial r} - \frac{\nu}{\rho}\frac{\partial \rho}{\partial r}\right)\right] \tag{69}$$

The coefficients α, β – are responsible for the turbulent characteristics of the flow, which are considered as functions of the coordinates.

Accepted form of Eq. (67) – Eq. (69) allows to consider "strong" nonlinear relations between the velocity and temperature field, which is especially important in the case of competition between thermal acceleration and buoyancy forces.

To simplify the formulation, it is assumed that the internal thermal energy of the flow, which can be represented through enthalpy as $h - p/\rho$ is much smaller than the kinetic energy. The governing one-dimensional equations (Filonov et.al., 2022), with added transverse mass velocity can be represented in the following form:

$$\begin{cases} \frac{\partial}{\partial r}[r\cdot G_r] + \frac{\partial}{\partial x}[r\cdot G_x] = 0 \\ \frac{\partial}{\partial r}\left[\frac{r\cdot G_r G_x}{\rho}\right] + \frac{\partial}{\partial x}\left[\frac{r\cdot G_x G_x}{\rho}\right] = -r\frac{\partial p}{\partial x} - r\cdot g(\rho - \rho_0)n_x + T_p \\ \frac{\partial}{\partial r}[r\cdot G_r h] + \frac{\partial}{\partial x}[r\cdot G_x h] = -r\cdot g\left(\rho - \frac{\rho_0}{\rho}\right)\cdot(G_x n_x + G_r n_r) + T_T + \frac{\partial}{\partial x}\left[r\cdot\chi\frac{\partial h}{\partial x}\right] + T_F \end{cases} \tag{70}$$

Where r – is the transverse coordinate x – is the longitudinal coordinate, n_x and n_r are the gravity projections on the corresponding coordinates.

It is pointed out that Eq. (70) in its form allows to take into account gravity as a force and turbulent factor through the introduced modification on the rheological laws and the form of turbulent transport functions (3). This way of describing the flow is called the "narrow channel" model and can be obtained by a more rigorous transition from the Reynolds equations by analyzing the dimensions. The peculiarity of Eq. (70) is that the equations are not closed, since there are 4 variables and the equations are still 3, as for the one-dimensional one-phase formulation.

Qualitatively analysing experimental studies (Popov, 1977, Kiss et.al., 2017), it can be stated that at the deteriorated heat transfer, the M-shaped velocity profile is observed behind the wall

temperature peak. The application of a simple formulation in the form of the Prandtl hypothesis turns out to be very productive, since at the point of maximum velocity at the M-profile the turbulent transport tends to 0, thus reducing the effective heat transfer. Considering this, Popov V.N. suggested that *the shape of the mixing path dependence under changing thermophysical properties remains the same as in isothermal conditions*. This assumption, including the expression for shear stresses, can be represented as Eq. (71).

$$\frac{\varepsilon_t}{\eta} = -\frac{1}{2} + \sqrt{\frac{1}{4} + \left(\frac{\varepsilon_t}{\eta}\right)_{T\square const}\left[\left(\frac{\varepsilon_t}{\eta}\right)_{T\square const} + 1\right]\left|\frac{\tau R_0}{\tau_w r}\right|} \tag{71}$$

For clarity, the flow in the channel is assumed to be hydrodynamically stabilized and the turbulent viscosity is determined by the Reichardt profile (Kurganov and Kaptil'ny, 1993). with quasi-constant thermophysical properties of the supercritical fluid Eq (72).

$$\left(\frac{\varepsilon_t}{\eta}\right)_{T\square const} = \begin{bmatrix} y^+ \le 50, 0.4\left[y^+ - 11th\left(y^+/11\right)\right] \\ y^+ > 50, 0.133 \cdot \left[0.5 + \left(\frac{r}{R_0}\right)^2\right]\left[1.0 + \frac{r}{R_0}\right] \end{bmatrix} \tag{72}$$

With regard to the effect of density pulsations in the gravity field, a relation to resolve the shear stresses under the influence of flow acceleration was proposed in (Kurganov and Kaptil'ny, 1992, Petukhov et.al., 1986), which, together with the adopted flow variables and the method of stress determination in Eq. (67), can be represented as:

$$\tau_t = \varepsilon_t \frac{\partial w_x}{\partial r} - \overbrace{\frac{\beta\rho}{\mathrm{Pr}_t}\underbrace{\left[w_x \frac{\partial w_x}{\partial x} + w_r \frac{\partial w_x}{\partial r} + g \cdot n_x\right]}_{-g_\Sigma} l^2 \frac{\partial T}{\partial r}}^{\Delta\tau} \tag{73}$$

After some transformations, on the basis of the balance of turbulence kinetic energy, a transcendental relation for the determination of turbulent viscosity is:

$$\left(\varepsilon_t\right)^4 + \left(\varepsilon_t\right)^2\left(\varepsilon_0\right)^2 \pm 1.15\varepsilon_t\varepsilon_0\varepsilon_\infty + \left(\varepsilon_\infty\right)^4 = 0 \tag{74}$$

Where ε_t – is desired turbulent viscosity, ε_0 and ε_∞ - asymptotic states: «0» - without density pulsations and is defined by the Prandtl relation, «∞» - is the dominant influence of density pulsations. The sign is chosen based on the sign of the product of the total acceleration by the radial temperature gradient. The mixing path length, which is included in Eq. (73) and indirectly in Eq. (74), is examined from Popov's assumption Eq. (72) and is represented as:

$$\left(\frac{l}{R_0}\right)^2 = \left(\frac{\varepsilon_t}{\eta}\right)_{T\square const}\left[1 + \left(\frac{\varepsilon_t}{\eta}\right)_{T\square const}\right]\left[\frac{\nu R_0}{|\tau_w| r}\right] \tag{75}$$

The asymptotic case of turbulent viscosity dominated by density pulsations is calculated based on the total flow acceleration:

$$\varepsilon_\infty = l^2 \sqrt{\frac{2.22\beta\rho}{\mathrm{Pr}_t c_p} g_\Sigma \left|\frac{\partial h}{\partial r}\right|} \tag{76}$$

The dimensionless boundary layer coordinate Eq. (77) is scaled in the laminar part using a correction in the form of the mean value of the dimensionless shear stress profile along the radius.

$$y^+ = \frac{R_0 - r}{\eta}\sqrt{\left|\frac{\tau_w}{\rho}\right|} \cdot \begin{bmatrix} \delta_l^+ \le y^+ \le R_0^+, 1.0 \\ y^+ < \delta_l^+, 2.5 R_0^{-2} \int_0^{R_0} \sqrt{\tau / \tau_w} r dr \end{bmatrix} \tag{77}$$

Where $R_0^+ = R_0/\nu\sqrt{|\tau_w/\rho|}$ – dimensionless radius, $\delta_l^+ = 11.1 + [396/(R_0^+ + 100)]^{3.3}$ – thickness of the laminar part of the boundary layer.

To calculate the turbulent addition to the thermal conductivity, the Reynolds analogy is used for which 7 different correlations Eq. (78) – Eq. (84) are implemented to determine the turbulent Prandtl number (Valueva, 2015).

«Myong» (1989):

$$\mathrm{Pr}_t = 0.75 + 1.63\left[\lg\left(1 + \frac{\mathrm{Pr}}{0.0015}\right)\right]^{-1} \tag{78}$$

«Hollingsworth» (1989)

$$\mathrm{Pr}_t = 1.855 - th\left[0.2\left(y^+ - 7.5\right)\right] \tag{79}$$

«Kays&Crawford» (1993)

$$\mathrm{Pr}_t = \frac{0.5882}{\left(0.5882 + 0.228\left(\frac{\varepsilon_t}{\eta}\right) - 0.0441\left(\frac{\varepsilon_t}{\eta}\right)^2\left(1 - \exp\left[\frac{-5.165\eta}{\varepsilon_t}\right]\right)\right)} \tag{80}$$

«Kays» (1994)

$$\frac{\varepsilon_t}{\eta} < 0.2, \mathrm{Pr}_t = 1.07; \frac{\varepsilon_t}{\eta} \ge 0.2, \mathrm{Pr}_t = 0.85 + \frac{2}{\mathrm{Pr}}\frac{\eta}{\varepsilon_t} \tag{81}$$

«Tang» (2016)

$$\frac{\varepsilon_t}{\eta} < 0.2, \mathrm{Pr}_t = 1.0; 0.2 \le \frac{\varepsilon_t}{\eta} \le 10, \mathrm{Pr}_t = 0.85 + \frac{\mathrm{Pr}}{15}; \frac{\varepsilon_t}{\eta} > 10, \mathrm{Pr}_t = 0.85 \tag{82}$$

«Ran»» (2018)

$$y^+ < 5, \Pr_t = 1.0; 5 \le y^+ \le 100, \Pr_t = 0.5 + 0.1\frac{\Pr\eta}{\varepsilon_t}; y^+ > 100, \Pr_t = 0.85 \quad (83)$$

« Kong» (2019)

$$\frac{\varepsilon_t}{\eta} < 0.4, \Pr_t = 1.0; 0.2 \le \frac{\varepsilon_t}{\eta} \le 10, \Pr_t = 0.3 + 0.03\frac{p}{p_{кр}}; \frac{\varepsilon_t}{\eta} > 10, \Pr_t = 0.85 \quad (84)$$

Relationships Eq. (78) – Eq. (80) were obtained theoretically, and Eq. (81) – Eq. (84) were selected based on numerical. Each of these functional dependencies is not always supported by modern commercial codes primarily because they include components of thermophysical properties or turbulent transport, which algorithmically leads to recursion.

Thereby, the formalism introduced and applied in the Narrow-channel model made it possible to remove a number of restrictions without complicating the algorithm for obtaining a solution.

The turbulent transport coefficients that are the components of Eq. (67) – Eq. (69) are as follows:

- In the equation of motion, the coefficient α_p in the case of using the Popov model is determined by dependence Eq. (71), for the Reichardt model – Eq. (72) and for Valuyeva – Eq. (74). Regarding the coefficient β_p, if the tangent stress correction option is activated (by default only for the Valuyeva model), then dependence Eq. (73) is applied.
- In the equation of thermal energy transfer, α_T is taken equal to zero. Coefficient β_T is always calculated using Eq. (71), where the turbulent viscosity is used in accordance with the equation of motion, and $\Pr_t$ – according to one of the functions Eq. (78) – Eq. (84).

4.3.2 Validation

The main aim of this subsection is to compare the possibilities of heat transfer deterioration phenomenon prediction by the proposed modified eddy viscosity turbulence model implemented in Narrow channel model (deliverable D3.4) with the corresponding capabilities of a commercial CFD package. For this purpose the computational model of experimental facility (Kurganov et.al., 2018; Kurganov and Kaptil'ny, 1993; Kurganov and Kaptil'ny 1992) described in section 2.4.2.1 is prepared in ANSYS CFX. As it was pointed out above, the uniqueness of the selected experimental studies is that the HTD regimes were obtained together with the radial profiles of velocity and temperature in the axial peak zone, both for upward and downward flow (Figure 136). Pitot microtubes (characteristic size of the inlet nozzle is 0.12 mm) together with microthermocouples were used to measure the local velocity.

General view of the equivalent hydraulic scheme adopted in (r-z) formulation is shown in Figure 191.

Two representative regimes are considered. One with the upward and other with downward flow. The following corresponding regime parameters are: G_x=2100 kg/(m^2·s), q_w = 428.4 kW/m^2, T_{in} = 34.8 ^{o}C. The reference pressure is 9.0 MPa, supercritical fluid is CO_2 (Kurganov et.al., 2018; Kurganov and Kaptil'ny, 1993; Kurganov and Kaptil'ny 1992).

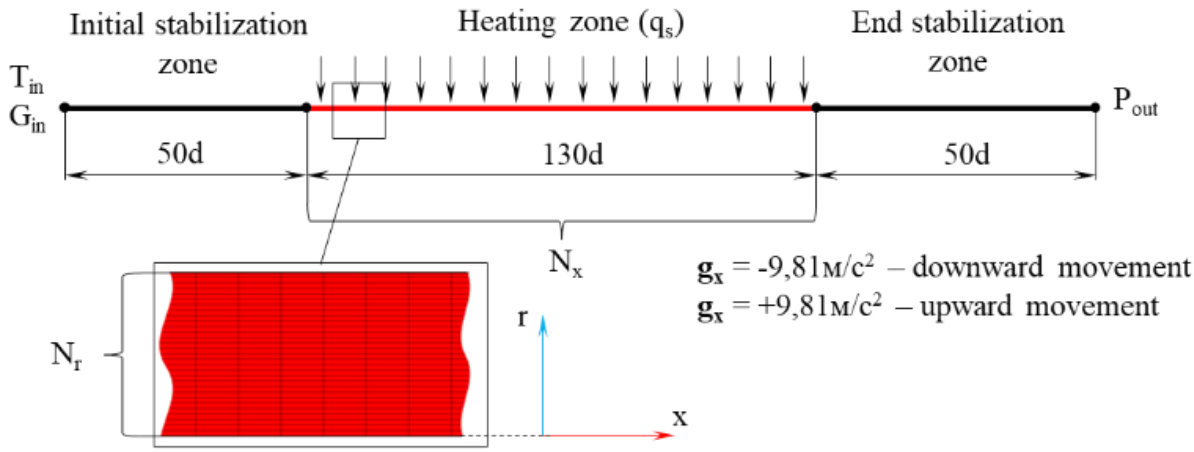

Figure 191. Schematization of the test section (calculation region)

The Narrow channel calculation model has an initial stabilization section and a heating zone. The velocity profile recovery zone (final stabilization section) is not modeled. The calculation mesh has the following discretization parameters: the number of nodes along the radius - 65, and in the axial direction - 110. The height of the first element near the wall corresponds to the value of y^+~0.1, i.e. therefore the so-called Low-Re effects are considered. In the axial and radial directions, the first order of approximation is chosen. The mesh inflation is applied near the wall. In order to neutralize the oscillation at the conditional boundary between the initial stabilization section and the heating zone caused by the stepwise growth of the heat flux, automatic adaptation was performed at a distance of 50 diameters from the inlet (Figure 190). The velocity profile at the inlet is uniform in both cases.

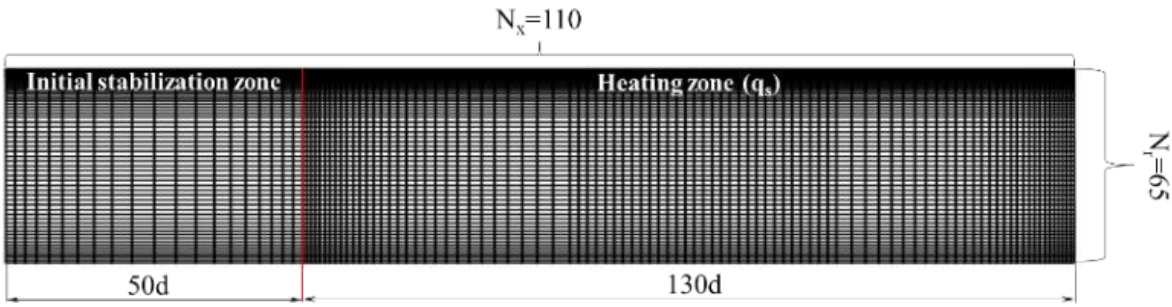

Figure 192. General view of the applied computational mesh

The calculation model in ANSYS CFX was considered in a quasi-two-dimensional formulation. Discretization of the computational domain for ANSYS CFX was performed in a way to that the dimensionless coordinate normal to the wall was within the range of the wall law (y^+>200). This option allows to evaluate the selected turbulence model in terms of sensitivity to HTD as a phenomenon of flow configuration (structure), and not only specific features of the force balance and thermophysical properties distribution in the boundary layer. In addition, preliminary tests (y^+<1.0) indicated that the predicted axial temperature peak is not physical and requires the introduction of special temperature limiters during ANSYS CFX iterations. The discretization of the computational domain in ANSYS CFX has 50 divisions in radius and 1000 in length.
Figure 193 demonstrates the comparison of calculated turbulent viscosity values obtained when applying different turbulence models (R,P,V – proposed modified Reichardt, Popov and Valueva models; and RNG, SST, EVT – standart RANS turbulence models).

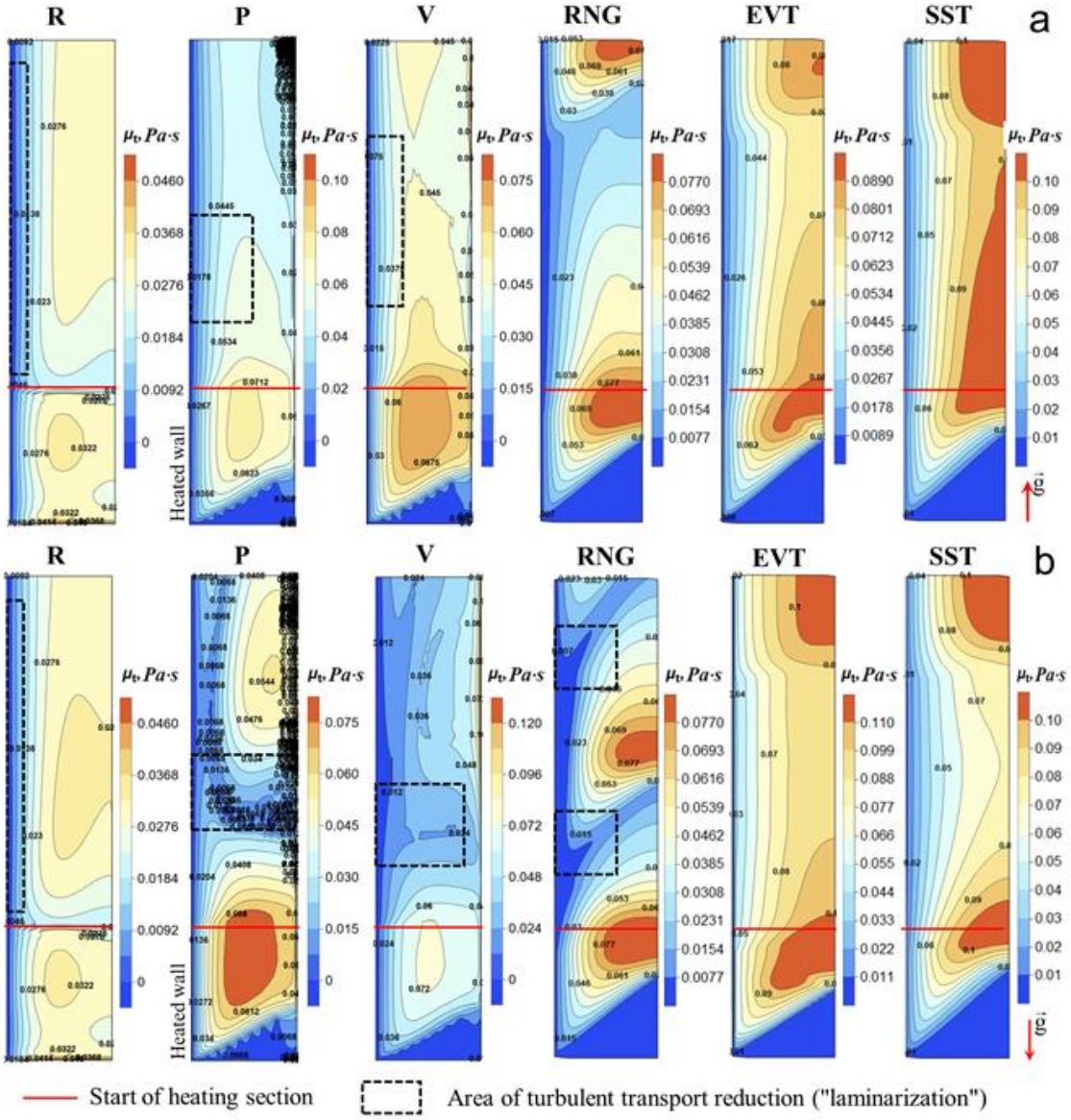

Figure 193. Calculated values of turbulent viscosity obtained by different models for upward (a) and downward (b) flows

The implemented algebraic turbulence models (named as R, P and V), in general, predict a lower value of turbulent viscosity near the wall and even in the core of the flow (Figure 193), which in some sense is a laminarization that leads to HTD.

The axial wall temperature profiles during upward and downward flow for different applied models and depending on the chosen correlation for Pr_t (see Eq. (78) – Eq. (84)) are represented in Figure 194. Radial velocity and temperature profiles in the cross section close to the axial temperature peak (see Figure 136, x/D=62.5) are shown in Figure 195.

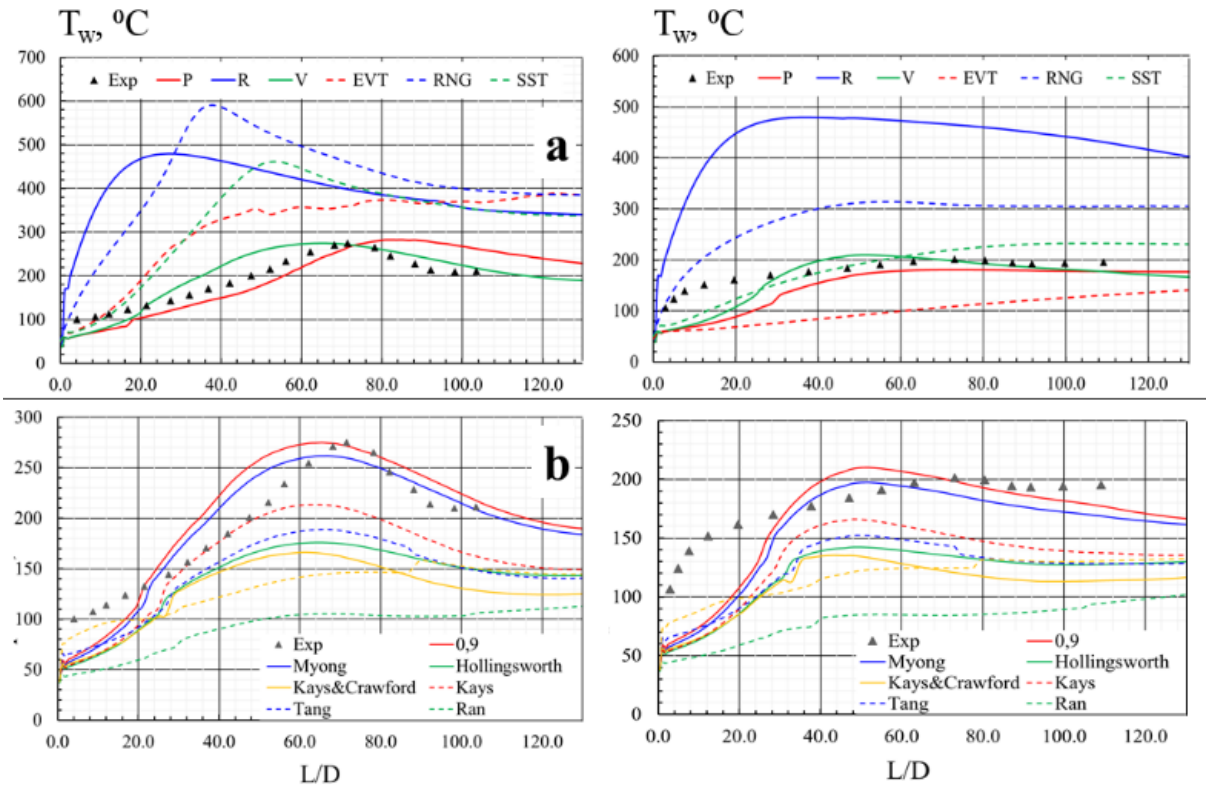

Figure 194. Comparison of axial wall temperature distribution with experimental values for upward and downward flow (a – for different applied turbulence models, b - for different correlations of Pr_t, applying them in the "V" model)

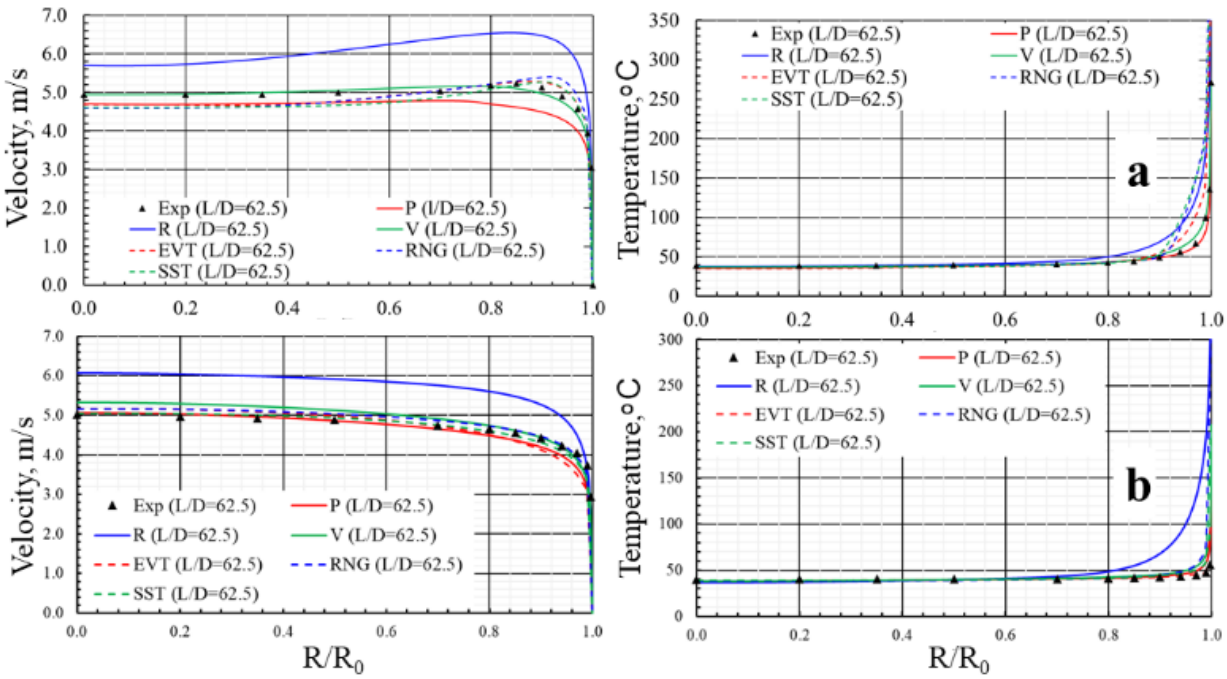

Figure 195. Comparison of the velocity and temperature radial profiles in cross section x/d = 62.5 (see subsection 2.4.2.1) (a - upward, b - downward)

To understand the "depth" of the sensitivity with respect to the HTD prediction (in the context of the distance from the wall to the flow core), the comparison of enthalpy growth fields (Figure 196) with the corresponding experimental data is performed.

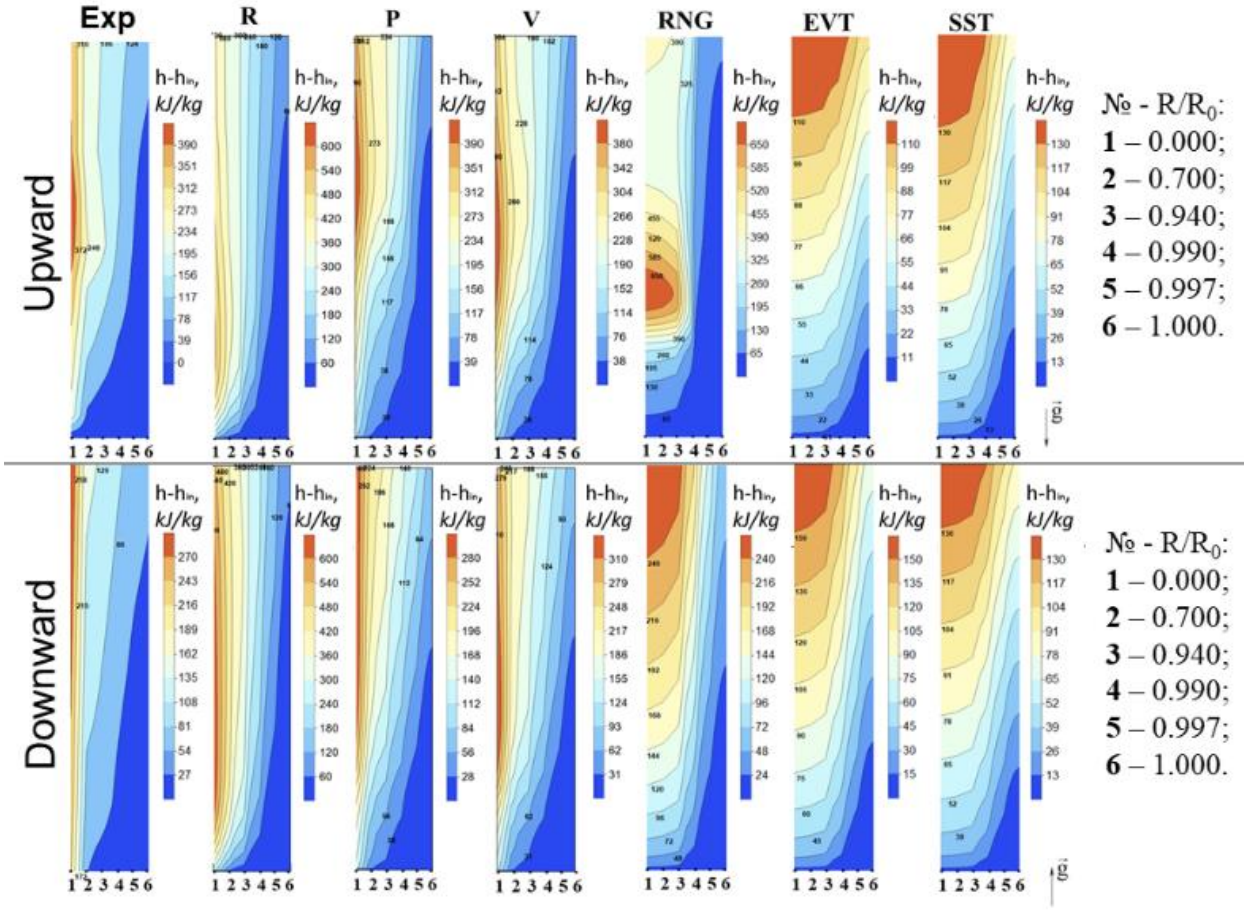

Figure 196. Enthalpy flow growth fields comparison

The obtained results demonstrate that the proposed approach with the application of nonlinear closure relations for turbulent transport allows estimating the HTD characteristics when gravity is considered. The proposed form of determining shear stresses due to mass velocity proved to be quite reliable in the calculations, i.e., no convergence problems were encountered.

The amplitude values of the wall temperature in both cases are close to the experimental ones. In upward flow case, the maximum wall temperature in the experiment is 275 ºC, while the predicted one is 283 ºC (Popov) and 274 ºC (Valueva). The peak position in the first case is overestimated by ~20 caliber higher, and in the second case, by 10 caliber lower.

During the downward flow, the maximum wall temperature in the experiment is ~202 ºC, while the predicted temperatures are 181 ºC (Popov) and 209 ºC (Valueva). The shape of the axial profiles remains similar.

The validation results demonstrate that the HTD characteristics predicted by applying proposed modifications for Eddy viscosity turbulence model are much better than those obtained using standard RNG, SST and EVT models.

The nonlinear algebraic model of Valueva proved to be quite reliable in predicting the heat transfer deterioration under the action of gravitational forces. The only difficulty is the initial section where the high heat transfer is prognosed, which is most likely due to the lack of stabilization of the velocity profile.

4.4 Concluding remarks

In the context of discussing the problem of HTD prediction by CFD codes, IPP attempted to adapt universal wall functions (UWF), which are generally quite a powerful engineering tool. The main purpose of the adaptation was the modification of UWF to calculate, first of all, the zone with heat transfer deterioration (see section 4.2). The obtained results are convincing in the perspective of this approach, because:

- Using the proposed special wall function (SWF), it is possible to significantly improve the HTD prediction capabilities not only in the bare tubes, but also in channels of complex cross-sectional geometry.
- Even with the worst predictive properties of the SPF, the results do not fundamentally differ from those obtained when low-Re effects are accounted. However, a significant increase in the calculations speed is achieved due to a mesh discretization reduction.
- The discretization of the calculation model when applying the SPF can be more than 10 times smaller only due to the near-wall area, which is significant from the point of view of analyzing the fragments of a promising SCW SMR core.
- The implementation of such functions does not fundamentally change the calculation algorithm of the CFD code and in fact can be applied consistently (at the post-processing stage).

The main drawback of the SPF, which needs to be minimized in the future, is the integrated form of the UPF. That is, UPFs are obtained under such hypotheses (for example, constancy of tangential stresses), which are generally not valid for "non-linear" heat transfer. Also, UPFs do not take into account the peculiarities of the forces balance near the non-adiabatic wall, which does not allow taking into account the physics associated with the structure of the supercritical medium flow.

Thereby, SPF allows considering only the change in thermophysical properties, which is the one of the HTD reasons. The proposed adaptation concerns just the temperature wall function, although it is more correct to consider the adaptation of the UWFs system - U^+ and T^+.

The last section 4.3 reported the proposed by IPP modification of Eddy viscosity turbulence model in order to consider the non-linear effects of heat transfer. To determine the "closing" turbulent characteristics, Popov's theory for Prandtl's turbulent mixing length, as well as Valueva's corrections considering the density pulsation field, were applied. Thus, it was possible to take into account the presence of gravity not only as a force factor, but also as a turbulent factor.

The constructed algebraic model of turbulence is nonlinear in a special way, since it is actually recursive with respect to turbulent viscosity due to considering the radial distribution of shear stresses. Such models cannot be simply implemented in modern CFD packages due to the non-local nature of the formulations, thus it’s implementation in the Narrow channel model (deliverable D3.4; Filonov et al., 2024; Filonov et al., 2025) was performed.

Validation tests were performed based on experimental probe studies for CO_2. When applying the proposed modifications, the location and amplitude of the wall temperature peak was predicted with sufficient accuracy.

5 Subtask 3.3.5 CFD modelling and validation of supercritical water heat transfer along corroded rough surfaces (KTH, UNIPI)

5.1 CONTRIBUTION BY UNIPI

This subtask summarises the work done in the past years to develop a model to account for heat transfer along corroded or rough surfaces validated against two different data sets; the first using CO_2 flowing in a vertically heated tube (see Kassem et al., 2023) the second one uses Freon R134a flowing in a verticlly heated tube (see Kassem et al., 2025). The next subsections decribe the details of the model used.

5.1.1 Model description

The model developed by Ambrosini et al. (2015), based on low-Reynolds number turbulence equations (Lien, 1996), was adopted to simulate roughness effects in terms of a source of turbulence assigned close to the wall. The development of this model was based on a simple-minded description of the effect of wall protrusions through the boundary layer on turbulence production and it was found able to repoduce the typical trends of friction factors from classical data reported by Nikuradse and summarised in the Moody diagram (see Ambrosini et al., 2015).

Insights gained from two parallel research efforts at the University of Pisa over recent years, focusing on the thermal-hydraulic behavior of supercritical fluids were leveraged to obtain the final form of the model adopted for the first time in the frame of the ECC-SMART project. The heat transfer treatment for supercritical fluids also utilizes the Lien et al. (1996) k-ε model that has been adapted to include an Algebraic Heat Flux Model (AHFM) for assessing turbulent heat flux contributions (see Pucciarelli et al., 2017, 2018). The effectiveness of this model has been evaluated in various studies (see Pucciarelli et al., 2017, 2018; Buzzi et al., 2019). These analyses have addressed both normal and deteriorated heat transfer scenarios across different supercritical fluids. Often, this model has demonstrated significant enhancements in predictive accuracy when compared to the experimental data sets analyzed and this is the reason why this was used in the frame of the studies conducted for ECC-SMART making use of the STAR-CCM+ code (Simcenter STAR-CCM+®, 2018).

The successful replication of the Moody diagram and of the Nikuradse curves with considerable accuracy for constant property fluids, as depicted in Figure *197*(left) provided the confidence necessary to adopt the roughness treatment in conjucntion with the supercritical fluid heat transfer one. In Ambrosini et al. (2015), the model was also applied to heat transfer involving supercritical fluids, which helped illustrate potential impacts of roughness on the observed phenomena, with examples shown in Figure *197*(right). At the time, without experimental data to substantiate the effects of roughness on heat transfer to supercritical fluids and before the developments that led to set up the AHFM, these results were merely indicative of a theoretical exercise, suggesting possible influences of wall roughness on the phenomena observed; they anyway showed the potential suppression of deterioratio at sufficiently large value of roughness.

Consequently, when experimental data on heat transfer to supercritical fluids for both smooth and rough walls became accessible in the literature (see Chen et al., 2022), the combination of the aforementioned models was promptly utilized in the frame of the ECC-SMART Project to evaluate their performance under these intriguing operating conditions.

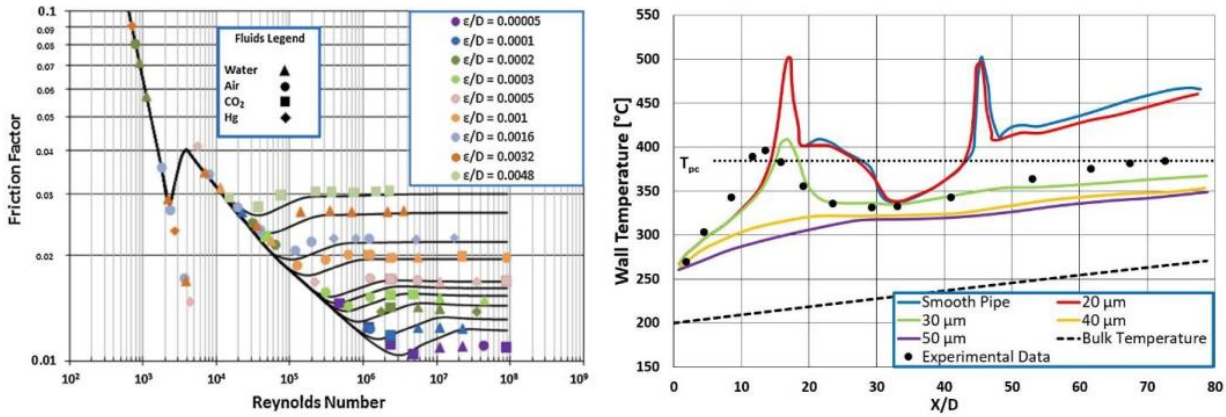

Figure 197. Nikuradse curves and the wall friction factor prediction provided by the model by Ambrosini et al. (2015) (left); and preliminary predictions of wall-roughness impact on heat transfer phenomena (right).

The adapted Lien et al. (1996) k-ε model, as detailed by Pucciarelli et al. (2018), is designed for predicting heat transfer to supercritical fluids and utilizes the Algebraic Heat Flux Model (AHFM) originally developed by Launder in 1988. This model estimates turbulent heat flux contributions, and the version implemented here includes minor modifications to Launder's original AHFM formulation, which is outlined below:

$$\overline{u_i't'} = -C_t \frac{k}{\varepsilon}\left(C_{t1}\overline{u_i'u_j'}\frac{\partial T}{\partial x_j} + C_{t2}\overline{u_j't'}\frac{\partial u_i}{\partial x_j} + C_{t3}\beta g_i\overline{t'^2}\right) \tag{85}$$

$$C_t = 1; \quad C_{t1} = 0.113; \quad C_{t2} = 0.113; \quad C_{t3} = \max\left(0, \quad e^{\frac{h_w^*}{2.5}} - 0.4\right) \tag{86}$$

In this model, a notable feature is the implicit relationship that depends on the calculation of $\overline{t'^2}$, the temperature variance. This parameter is not typically computed by two-equation turbulence models; consequently, to accommodate this, a dedicated transport equation for $\overline{t'^2}$ was incorporated into the model using the passive scalar equation tool available in STAR-CCM+ code. This addition ensures that the system is self-sufficient and complete.

Moreover, the model is complemented by assuming an algebraic relationship for the dissipation of $\overline{t'^2}$. This approach allows the model to function autonomously without relying on external inputs for this variable. A key aspect of this formulation is the C_{t3} parameter, which is dependent on wall dimensionless enthalpy a crucial parameter in the fluid-to-fluid scaling methodology showed in Chapter 3. The turbulent heat flux contributions determined using the AHFM are subsequently utilized for computing the production term of turbulence and dissipation due to buoyancy, as outlined in Equation (87). Additionally, these contributions are instrumental in enhancing the estimation of the turbulent Prandtl number distribution, particularly in the radial direction, which is crucial for applications involving 2D plane channels in pipe systems, as indicated in Equation (88).

$$G_k = g_i\overline{\rho't'} = -\rho\beta g_i\overline{u_i't'}; \qquad G_\varepsilon = -\frac{\varepsilon}{k}\rho\beta g_i\overline{u_i't'} \tag{87}$$

$$Pr_{tur} = -\frac{\upsilon_t}{\overline{u_r't'}}\frac{\partial T}{\partial x_r} \tag{88}$$

The model that accounts for wall-roughness effects, developed by Ambrosini et al. (2015), is based on physical considerations that draw parallels between the wakes generated by obstacles in a flow and those produced by roughness crests. This model was formulated through dimensional analysis, leading to the following expressions for turbulence production and dissipation terms influenced by roughness:

$$S_{k,rough} = f_{smooth}\, C_{rough} \frac{1}{2\varepsilon_{rough}} \rho u_i^3; \qquad S_{\varepsilon,rough} = \frac{\varepsilon}{k} S_{k,rough} \tag{89}$$

Where

$$f_{smooth} = \frac{1}{2}\left[1 - tanh\left(\frac{y - \varepsilon_{rough}}{0.3\, \varepsilon_{rough}}\right)\right];$$
$$C_{rough} = 6.041 \cdot 10^{-4} \left(\frac{\varepsilon_{rough}\, u_i}{\upsilon}\right)^{0.64} \tag{90}$$

In these equations, f_{smooth} acts as a smoothing factor that confines the influence of roughness to the area directly affected by the roughness crests. Here, y is the distance from the wall and ε_{rough} is the average roughness height. C_{rough} is a coefficient that has been crucial in accurately predicting friction factor values across a wide range of Reynolds numbers, fluids, and different roughness heights or more specifically, their relative heights ε_{rough}/D.

By integrating these two key components, the model aims to provide a comprehensive and accurate representation of the heat transfer processes in supercritical fluids, accommodating both smooth and rough wall conditions. The integration of these models was straightforwardly achieved by creating two additional global production contributions for the turbulent kinetic energy and its dissipation. The final production terms are thus:

$$S_{k,total} = G_k + S_{k,rough}; \qquad S_{\varepsilon,total} = G_\varepsilon + S_{\varepsilon,rough} \tag{91}$$

5.1.2 Assessing Heat Transfer Dynamics Through Parametric Analysis of Various Fluids

The model was initially used to study heat transfer in supercritical fluids with rough walls, in the absence of specific experimental data (see the first sections in Kassem et al. 2023). These early simulations aimed to assess the model ability to qualitatively capture the expected enhancement in heat transfer due to the additional source term in the turbulence production. For these simulations, the reference conditions were taken from Kline's (2017) dataset, related to carbon dioxide at 8.35 MPa flowing upward in bare tubes of various diameters. Two-dimensional CFD simulations were conducted. Specifically, Figure 198 displays wall temperature trends for one of Kline's cases with an inlet temperature of 24 °C, mass flux of 300 kg/(m^{2}s), an inner diameter of 4.6 mm and a heat flux of 20 kW/m^2. The smooth tube CFD simulation showed good quantitative agreement with the experimental data: while the onset of heat transfer deterioration was slightly early, though the overall pattern of deterioration, recovery, and a second temperature peak matched well with the experimental data. The impact of increasing roughness heights is notable; as the roughness height increases, the calculated wall temperature trend significantly decreases. For roughness values beyond 25 µm, the model does not predict the occurrence of the second peak and with further increases, even the initial deterioration is not anticipated. If supported by experimental data, these findings could offer an intriguing engineering approach to mitigate heat transfer deterioration, particularly relevant for the design of supercritical water-cooled nuclear reactors.

To broaden the scope of this analysis by including other fluids, the similarity theory based CFD results, with comparable boundary conditions, was utilized. So, the study also considers the impact of roughness in the case of these fluids and in particular Figure 199a presents the CFD-calculated wall temperature results for water at 25 MPa in similar conditions. These results closely mirror the phenomena observed for CO_2, demonstrating the effect of increasing roughness height. Notably, heat transfer deterioration in water is predicted to cease at a roughness height of about 36 µm.

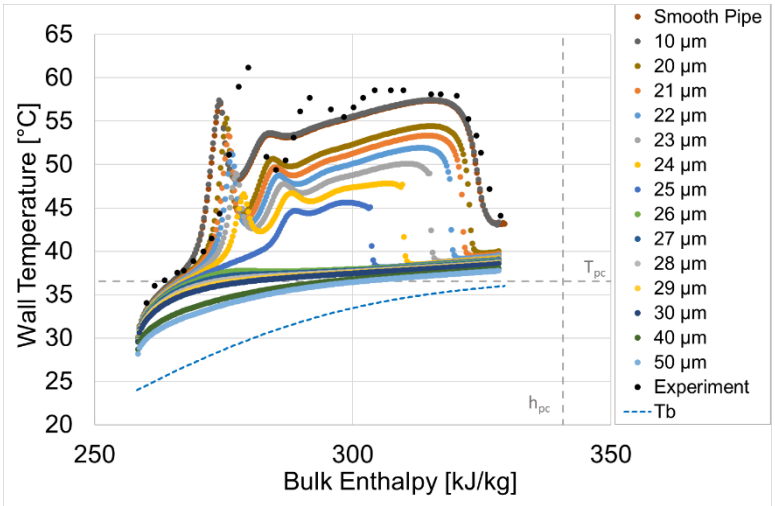

Figure 198. Wall temperature trends for Kline's CO_2 case at inlet temperature of 24 °C, mass flux of 300 kg/(m^{2}s), and heat flux of 20 kW/m^2. Adapted from Kassem et al., 2023

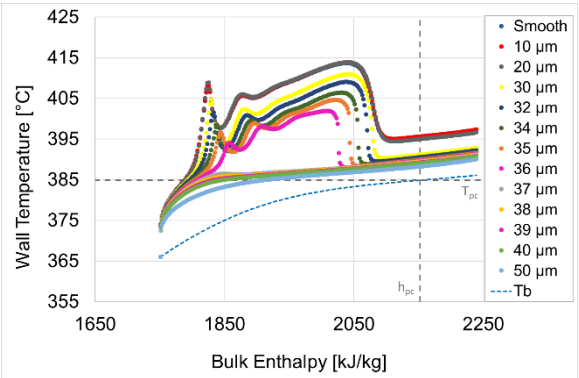

a) Water at 25 MPa

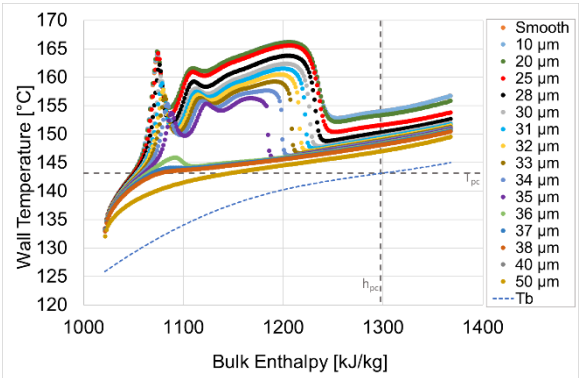

b) Ammonia at 13.6 MPa

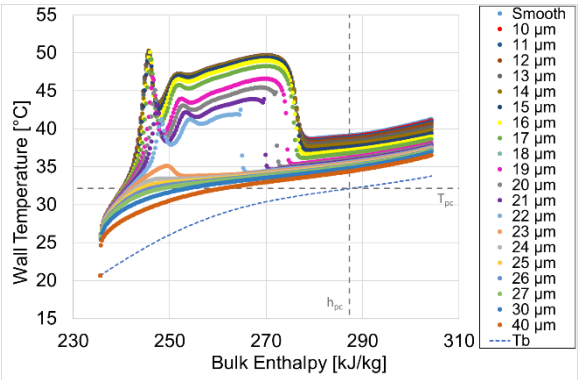

c) R23 at 5.56 MPa

Figure 199 Wall temperature trends at different roughness heights adopting the results from the similarity theory for Kline's CO_2 case at Tin of 24 °C, mass flux of 300 kg/(m^{2}s), and heat flux of 20 kW/m^2. Adapted from Kassem et al., 2023

Similar patterns are observed for ammonia and R23, as illustrated in Figure 199b and Figure 199c. In these cases, roughness significantly influences the predicted wall temperature trends; for ammonia and R23; at roughness heights of 36 µm and 23 µm, respectively, the model shifts from predicting strong heat transfer deterioration to almost normal heat transfer conditions. The fact that the roughness heights at which deterioration ceases are similar for CO_2 and R23 on one hand, and for water and ammonia on the other, suggests a possible link to the similarities in

the properties of these pairs of fluids. This connection warrants further investigation, particularly in light of experimental validation, to better understand the role of fluid properties and roughness in influencing heat transfer behaviour in supercritical conditions.

In addition, the impact of wall roughness on the velocity profile trends was examined in terms of universal turbulence definitions, under supercritical pressure conditions where thermophysical properties significantly vary across the boundary layer, often because of heat transfer deterioration. This phenomenon leads to deviations from the classical velocity profile trends observed for constant propery fluids. A dimensionless form of the velocity profile for a smooth wall is first presented, using data from Kline's experiment at an inlet temperature of 24 °C. Subsequently, the influence of roughness on this profile is explored.

Figure 200 displays the dimensionless velocity profile along the length of a smooth pipe (i.e., with only 1 mm in roughness). Notably, in the viscous sub-layer region, the velocity profile remains relatively consistent throughout the channel. However, differences emerge in the fully turbulent region due to the onset of various thermal-hydraulic phenomena. At approximately 0.3 meters from the inlet, marking the start of the heated section, the velocity in the turbulent region begins to decrease, eventually forming a plateau. Progressing further along the pipe, the flow experiences laminarization, reaching its flattest and minimum velocity profile at around 0.5 m, coinciding with the area of deteriorated heat transfer. Past this point, the velocity gradually increases again.

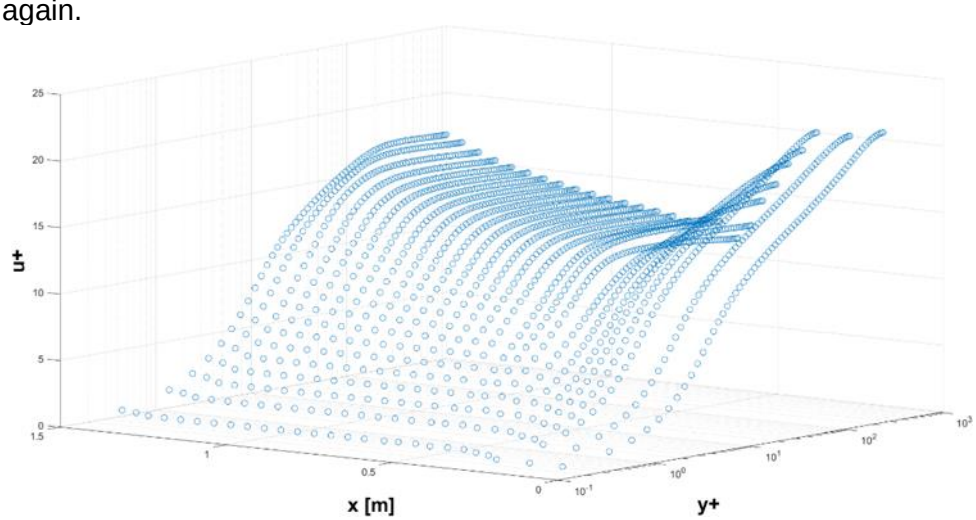

Figure 200. Universal velocity trends for CO_2 at 8.35 MPa, inlet temperature 24°C, mass flux of 300 kg/(m^{2}s), and heat flux of 20 kW/m^2 and with roughness 1 μm. Adapted from Kassem et al., 2023

Figure 201 further illustrates the velocity distribution along the channel, highlighting that heat transfer deterioration is linked to an increase in flow velocity near the wall. The emergence of a flattened velocity profile, due to the lower-density fluid adjacent to the heated wall thus inhibiting turbulence production, confirms that laminarization of this low-density fluid layer is a key mechanism driving heat transfer deterioration.

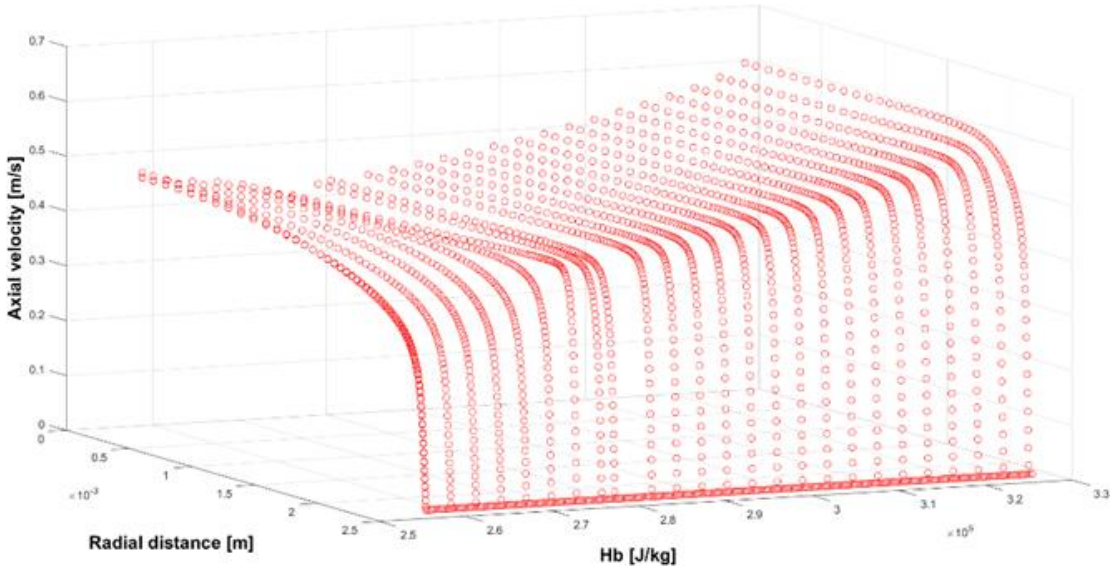

Figure 201. Axial velocity distribution across the pipe diameter for CO_2 at 8.35 MPa, inlet temperature 24°C, mass flux of 300 kg/(m^{2}s), and heat flux of 20 kW/m^2 and with roughness 1 µm. Adapted from Kassem et al., 2023

Conversely, Figure 202 illustrates the influence of wall roughness on the enhancement of the dimensionless velocity profile for Kline's case at 8.35 MPa, inlet temperature 24°C, mass flux of 300 kg/(m^{2}s), and heat flux of 20 kW/m^2. At the start of the heated section, around 0.3 meters, an increase in roughness height results in the anticipated decrease in the dimensionless velocity distribution. However, as one moves further along the pipe, turbulence production is intensified by the increased roughness, causing the dimensionless velocity profile to gradually shift upwards. Similarly, Figure 203 demonstrates that for water at 25 MPa, the dimensionless velocity profile is enhanced as the roughness height increases. This enhancement is evident in the velocity profile, highlighting the impact of roughness on the fluid dynamics.

Collectively, these results display qualitatively expected trends in velocity profile changes due to wall roughness. However, the correlation of these trends with actual physical phenomena requires empirical validation. This necessity underlines the significance of the more recent study that provided an opportunity for such comparison, lending greater weight and relevance to the ongoing research, as discussed below in the rest of this section.

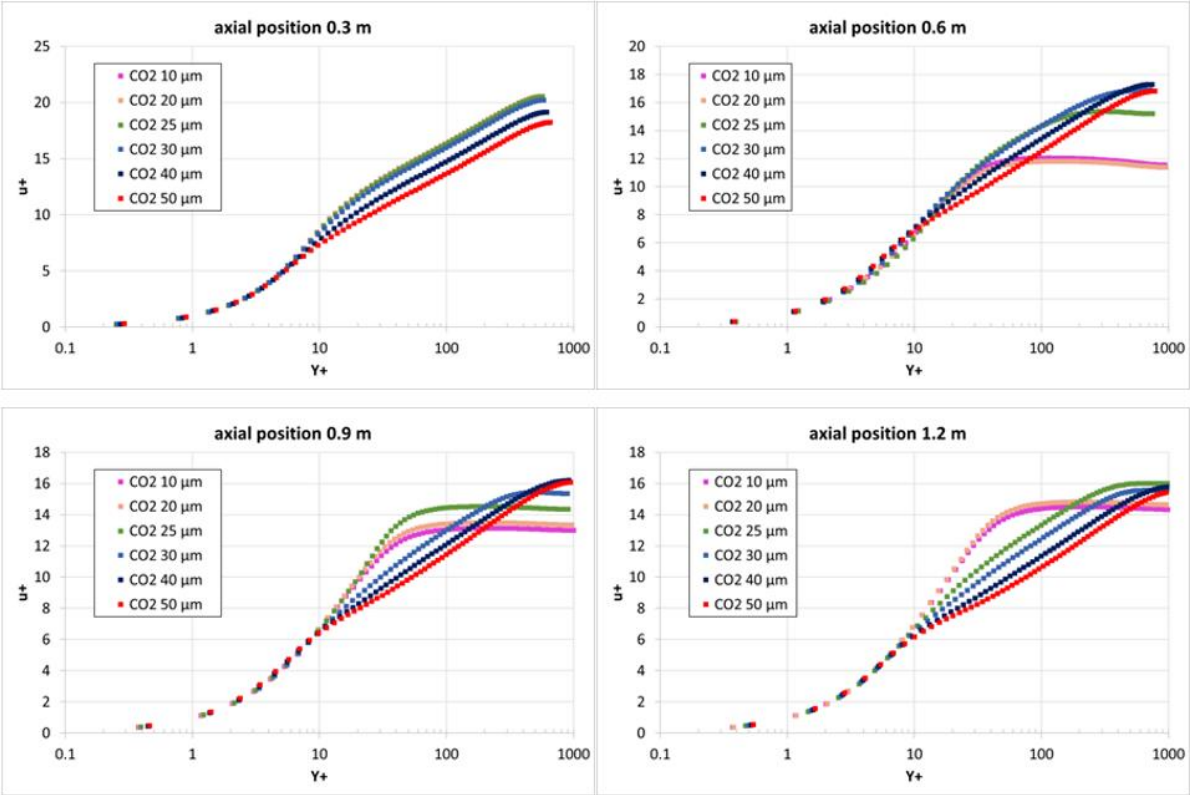

Figure 202. Dimensionless velocity trends for CO_2 at different axial positions. Adapted from Kassem et al., 2023

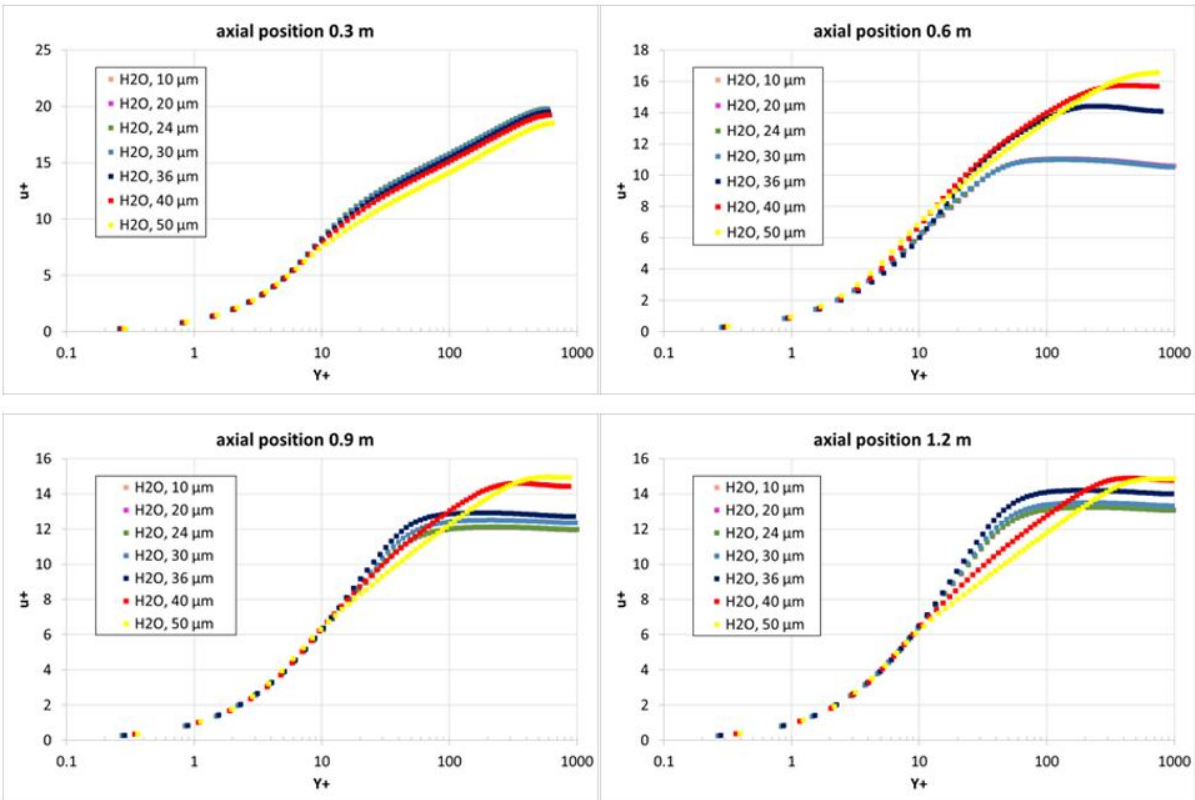

Figure 203. Dimensionless velocity trends for water at different axial positions. Adapted from Kassem et al., (2023)

5.1.3 Assessing Wall Roughness Effects on Carbon Dioxide: Data Comparison

The mentioned recent study by Chen et al. (2022) presented experimental findings on the impact of roughness on heat transfer to supercritical carbon dioxide flowing upward in vertical tubes with an inner diameter of approximately 4.57 mm. The experiments covered a Reynolds number range from 16207 to 91735 and explored various equivalent sand roughness heights from 1.5 µm to 40 µm. The authors discovered that a rough wall could mitigate heat transfer deterioration, presenting a valuable opportunity to quantitatively evaluate the developed CFD model and its qualitative predictions against experimental observations.

For the present analysis, five different inlet boundary conditions are considered, varying mass flux values while maintaining a constant heat flux. Figure 204 compares the calculated and experimental temperature profiles at various roughness and mass flux levels. The model generally succeeds in replicating the experimentally observed phenomena and illustrates the influence of increased roughness. Specifically, at a relatively low mass flux, about 300 kg/m^{2}s, the model captures the deteriorated heat transfer characterized by a local temperature peak near the inlet. High wall temperature values persist until heat transfer restoration, facilitated by the reduced buoyancy from the diminished density difference between the bulk fluid and the wall. While the model accurately predicts the peak in wall temperature, it slightly underestimates the temperature values for roughness heights of 1.5, 10, 20, and 40 µm. Conversely, for a roughness value of 30 µm, the model overestimates the wall temperature trend, see Figure 204a.

When the mass flux was increased to higher values, specifically 350 and 400 kg/m^{2}s, the wall temperature trends display a peak followed by a recovery and then maintains high temperatures. In these scenarios, the model effectively predicts the trends for lower roughness levels. However, for a mass flux of 350 kg/m^{2}s, as shown in Figure 204b and Figure 204c, the model overestimates the experimental values at a roughness of 20 µm.

The model sensitivity to roughness values is evident in Figure 204d While the experiments indicated normal heat transfer at a mass flux of 450 kg/m^{2}s and a roughness of 20 µm, the model depicted deteriorated heat transfer. A slight increase in roughness to 21 µm shifted the model's prediction to a normal heat transfer trend, highlighting the significant impact of even small changes in roughness on the heat transfer behaviour. While in the scenario with a relatively lower heat load, shown in Figure 204e, the wall temperature trend is observed to steadily increase along the pipe without exhibiting any local peak, indicating normal heat transfer. In this case, the CFD model displays a slight deviation at lower roughness values. However, as the roughness value increases, the model predictions become more accurate, closely aligning with the observed steady rise in wall temperature. This demonstrates that the model accuracy in predicting heat transfer behaviour improves with higher roughness values in scenarios of lower heat load.

Analysing the overall results, the model demonstrates a reasonable capability in predicting the effects of roughness on reducing wall temperature. The key observations are as follows.

1. Lower Sensitivity at Small Roughness Values: The model shows low sensitivity to roughness at smaller values (between 1.5 and 10 µm), predicting almost identical trends across these values. This contrasts with experimental observations, where an increase in roughness correlates with a decrease in wall temperature.
2. Anticipation of Heat Transfer Restoration: The model and experiments both indicate that heat transfer restoration following deterioration happens at similar roughness values. However, experimental data provide limited points of comparison due to the restricted range of roughness values tested.
3. Suppression of Deterioration at Higher Roughness: Both the model predictions and experimental results consistently show that deterioration is suppressed at sufficiently high roughness values. This phenomenon occurs at comparable roughness heights in both the experimental and modelled scenarios.

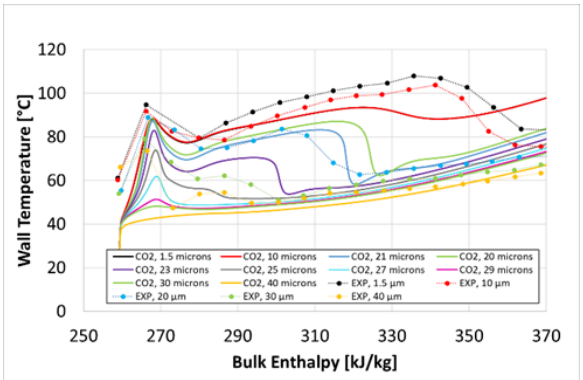

a) 300 kg/m^{2}s

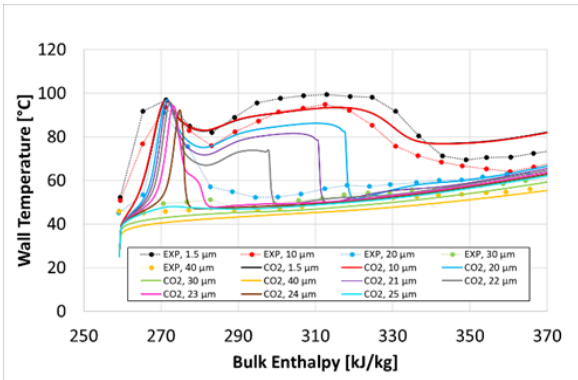

b) 350 kg/m^{2}s

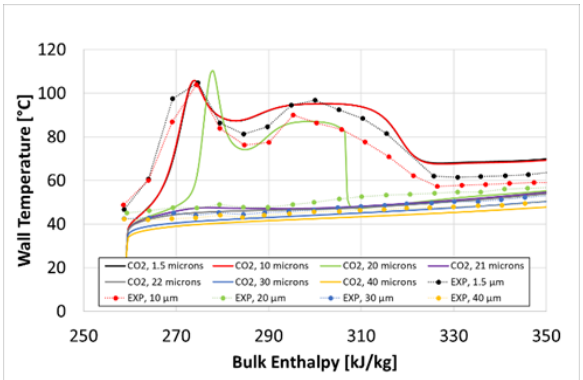

c) 400 kg/m^{2}s

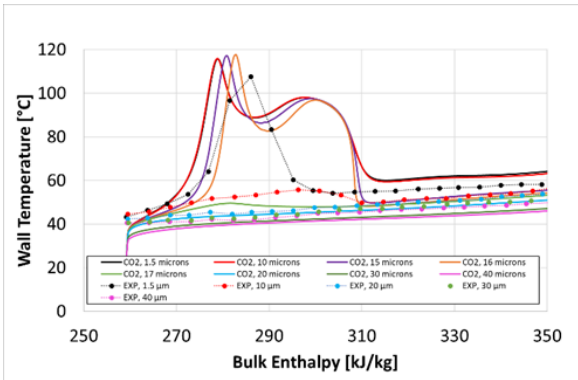

d) 450 kg/m^{2}s

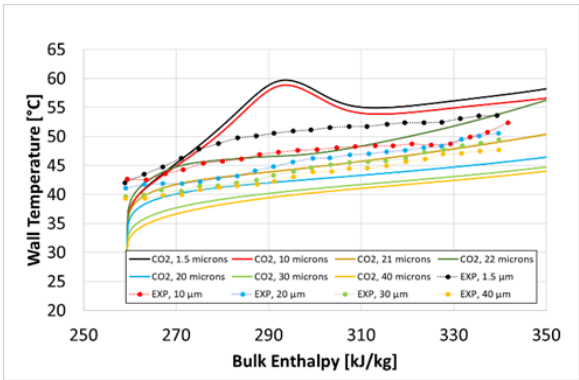

e) 500 kg/m^{2}s

Figure 204. Wall temperature trends with different roughness heights for CO_2 at 9 MPa, inlet temperature 25°C, heat flux of 50 kW/m^2. Adapted from Kassem et al., 2023

Overall, these observations highlight the model effectiveness in capturing the impact of wall roughness on heat transfer, particularly at higher roughness values, despite some discrepancies at lower roughness levels that could be fixed by a finer calibration whenever a sufficiently extended range of conditions would be available for justifying a more reliable assessment.

5.1.4 Assessing Wall Roughness Effects on R134a: A Recent Data Comparison

Recently, in the frame of the ECC-SMART project, the model developed at University of Pisa to deal with wall roughness and heat transfer at supercritical pressures was applied to the data collected by KIT making use of R134a as coolant at supercritical pressure. The KIMOF experimental apparatus adopted by KIT for collecting the experimental data addressed in this

work consists of a closed loop circulating R134a fluid at supercritical conditions (see Wiltschko 2023 and Wiltschko et al., 2024). The circulation of the coolant is obtained by a pump, while the flow rate is measured by a Coriolis flow meter, providing directly the mass flow rate. The apparatus can host up to three test sections, being pipes, annuli or rod bundles. A pressurizer is available to control the pressure of the system, which may range up to 5 MPa with a maximum fluid temperature of 250 °C. A system of pre-heaters is included to help establishing the inlet temperature of the fluid, while the power supplied to the test section is finally rejected to the external environment by cooling towers. For more information about the test section and the experimental setup the reader is refered to the detailed report by KIT (see Wiltschko 2023)

Two main values of pressure of R134a were used, being 4.6 and 4.35 MPa. The former corresponds to 25 MPa in water through the fluid-to-fluid similarity theory by Cheng et al. (2011), while the second is closer to the critical pressure of R134a, so that the fluid exhibits sharper trends of fluid properties across the pseudocritical threshold. The experimental data have been made available to ECC-SMART participants through the accessible sharepoint.

In line with previous experience in the use of the STAR-CCM+ CFD code at the University of Pisa, the experimental data were addressed by a 2D axial-symmetric model in steady-state analyses, making use of the Lien low-Re turbulence model modified for accounting surface roughness and with the Algebraic Heat Flux Model, as discussed in the above Section 5.1.1. Fluid properties were assigned in the form of cubic spline interpolation polynomials, generated by an in-house code in a form suitable for STAR-CCM+, on the basis of data from the NIST property package. Heat flux was applied directly to the outer surface of the pipe, with no account for the presence of the pipe walls that have been proven to be substantially immaterial in similar previous analyses. The length of the pipe was subdivided into 1750 equally spaced axial nodes and the radial discretisation, including 60 nodes, was refined close to the wall as needed for the application of a low-Re model, thus obtaining a values of wall y+ much lower than unity. A mass flux boundary condition was used at the inlet of the pipe and a pressure outlet was adopted at the outlet. Convergence checks were routinely made in order to assure that the segregated solution algorithm generally chosen in the analysis provided stable results. In order to compare the results of the calculations in terms of inner wall temperature with experimental measurements obtained on the outer tube surface, the heat conduction equation was used to infer inner temperature values coherent with the experiments.

Figure 205 to Figure 212 report the results obtained at different flow rates, heat fluxes and inlet temperatures for the experimental data at 4.35 MPa. The figures provide an overall meaningful picture of successes and drawbacks observed at this challenging value of pressure, close to the critical one. As it can be noted, the model succeeds in identifying deterioration in a number of cases, reasonably predicting the effect roughness in progressively improving heat transfer. While in the experiment a single value of roughness was available for the rough tube, calculations explored several values of this parameter, in order to highlight its effect.

Similar trends and series of successes and drawbacks are observed for the cases at 4.6 MPa, reported in Figure 213 to Figure 221. As it can be noted, sometimes deteriorated heat transfer is correctly predicted, anyway with variable accuracy in the evaluation of its consequences on inner wall temperatures. The decrease in its severity with increasing wall roughness is also a clear effect predicted by the model.

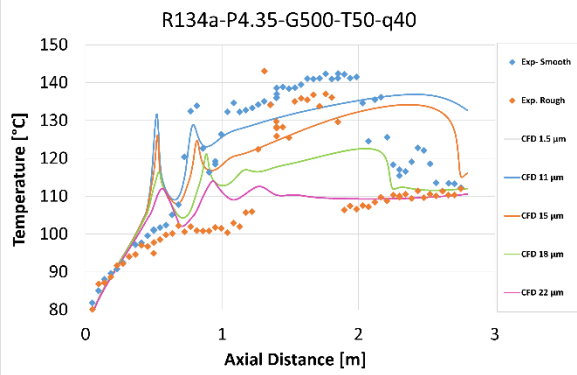

Figure 205. Inner wall temperature trends for the heated tube section at 4.35 MPa operating pressure, mass flux of 500 kg/m^{2}s, heat flux at 40 kW/m^2 and inlet temperature of 50°C

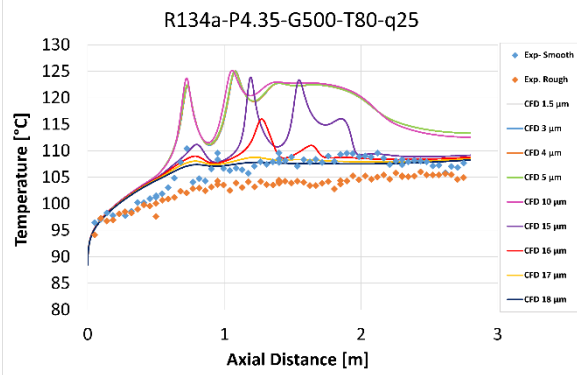

Figure 206. Inner wall temperature trends for the heated tube section at 4.35 MPa operating pressure, mass flux of 500 kg/m^{2}s, heat flux at 25 kW/m^2 and inlet temperature of 80°C

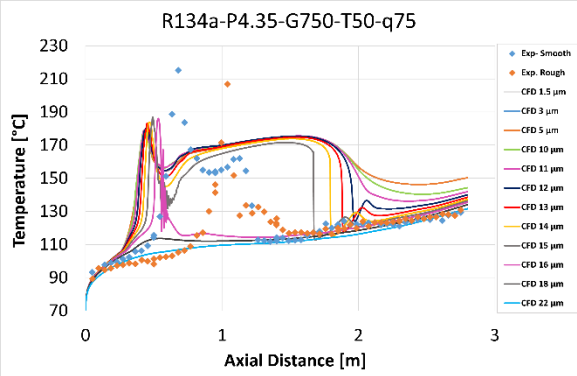

Figure 207. Inner wall temperature trends for the heated tube section at 4.35 MPa operating pressure, mass flux of 750 kg/m^{2}s, heat flux at 75 kW/m^2 and inlet temperature of 50°C

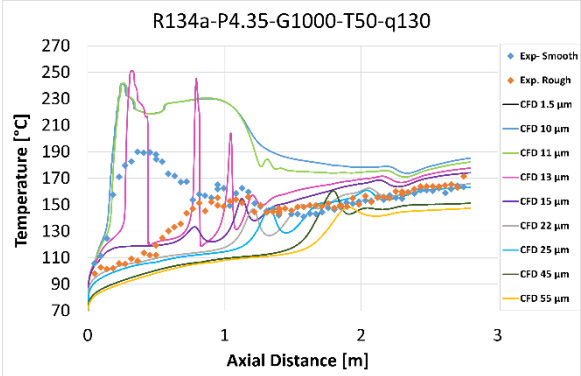

Figure 208. Inner wall temperature trends for the heated tube section at 4.35 MPa operating pressure, mass flux of 1000 kg/m^{2}s, heat flux at 130 kW/m^2 and inlet temperature of 50°C

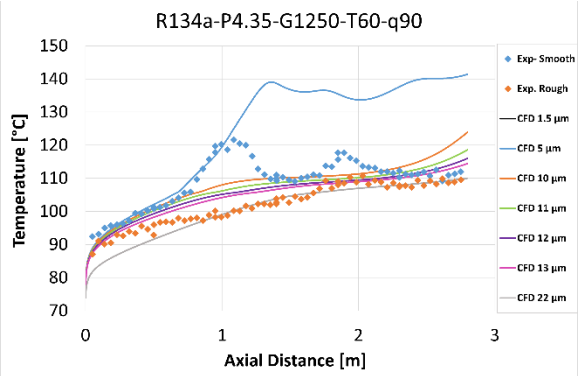

Figure 209. Inner wall temperature trends for the heated tube section at 4.35 MPa operating pressure, mass flux of 1250 kg/m^{2}s, heat flux at 90 kW/m^2 and inlet temperature of 60°C

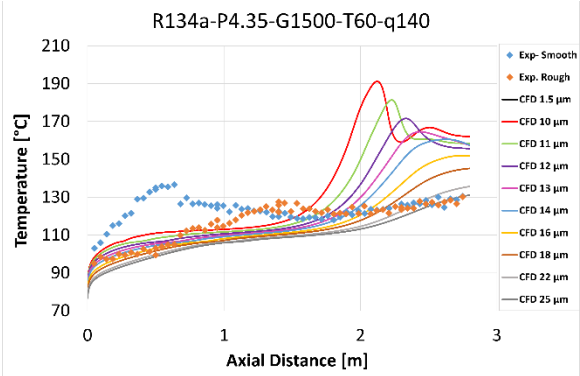

Figure 210. Inner wall temperature trends for the heated tube section at 4.35 MPa operating pressure, mass flux of 1500 kg/m^{2}s, heat flux at 140 kW/m^2 and inlet temperature of 60°C

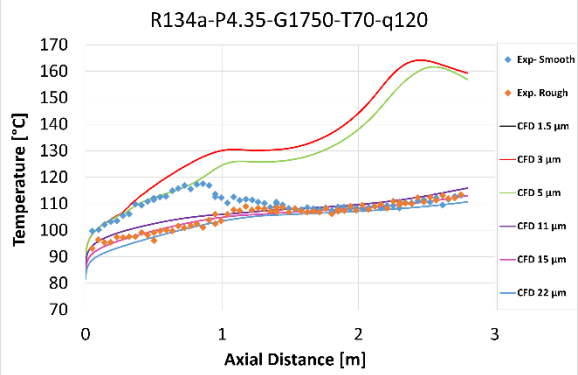

Figure 211. Inner wall temperature trends for the heated tube section at 4.35 Mpa operating pressure, mass flux of 1750 kg/m^{2}s, heat flux at 120 kW/m^2 and inlet temperature of 70°C

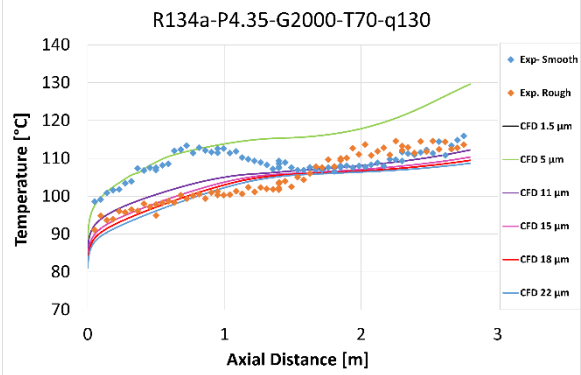

Figure 212. Inner wall temperature trends for the heated tube section at 4.35 Mpa operating pressure, mass flux of 2000 kg/m^{2}s, heat flux at 130 kW/m^2 and inlet temperature of 70°C

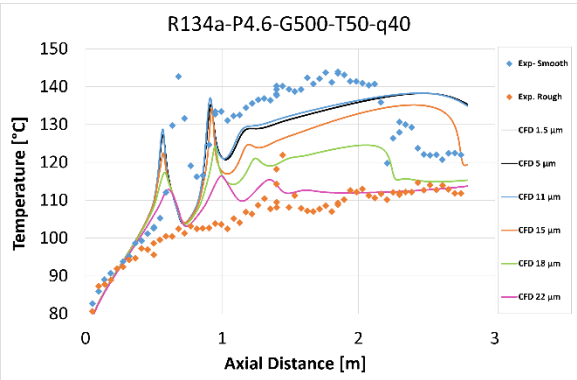

Figure 213. Inner wall temperature trends for the heated tube section at 4.6 MPa operating pressure, mass flux of 500 kg/m^{2}s, heat flux at 40 kW/m^2 and inlet temperature of 50°C

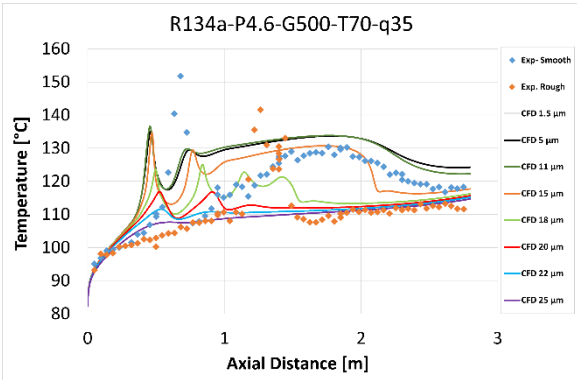

Figure 214. Inner wall temperature trends for the heated tube section at 4.6 MPa operating pressure, mass flux of 500 kg/m^{2}s, heat flux at 35 kW/m^2 and inlet temperature of 70°C

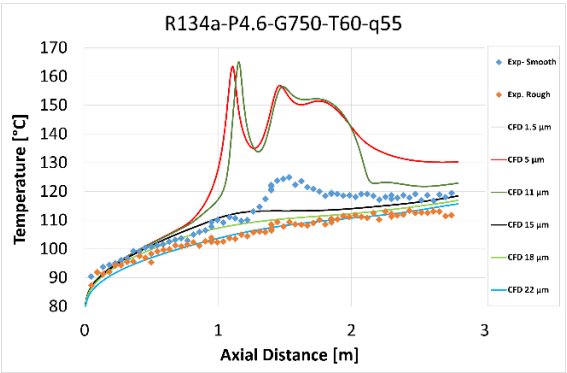

Figure 215. Inner wall temperature trends for the heated tube section at 4.6 MPa operating pressure, mass flux of 750 kg/m^{2}s, heat flux at 55 kW/m^2 and inlet temperature of 60°C

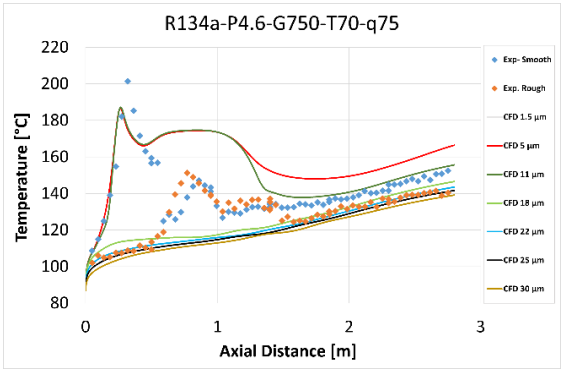

Figure 216. Inner wall temperature trends for the heated tube section at 4.6 MPa operating pressure, mass flux of 750 kg/m^{2}s, heat flux at 75 kW/m^2 and inlet temperature of 70°C

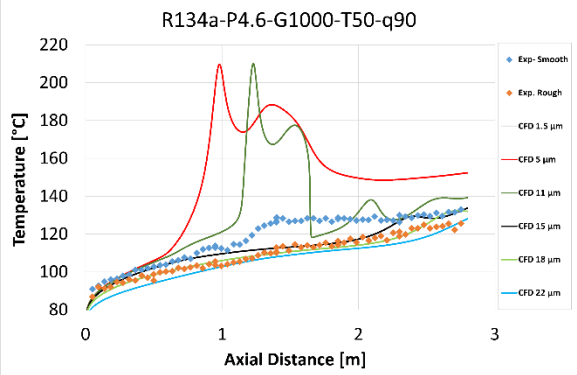

Figure 217.Inner wall temperature trends for the heated tube section at 4.6 MPa operating pressure, mass flux of 1000 kg/m^{2}s, heat flux at 90 kW/m^2 and inlet temperature of 50°C

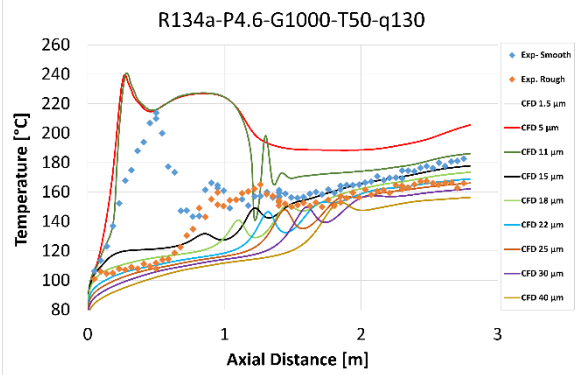

Figure 218. Inner wall temperature trends for the heated tube section at 4.6 MPa operating pressure, mass flux of 1000 kg/m^{2}s, heat flux at 130 kW/m^2 and inlet temperature of 50°C

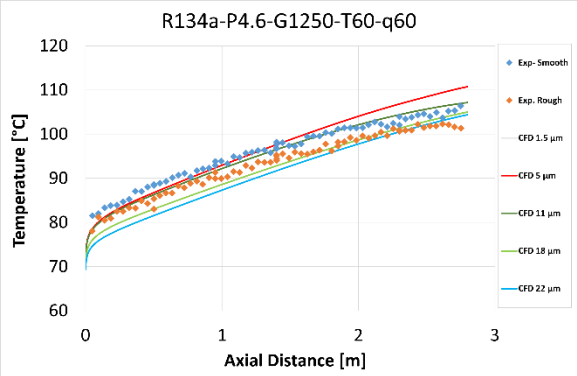

Figure 219. Inner wall temperature trends for the heated tube section at 4.6 MPa operating pressure, mass flux of 1250 kg/m^{2}s, heat flux at 60 kW/m^2 and inlet temperature of 60°C

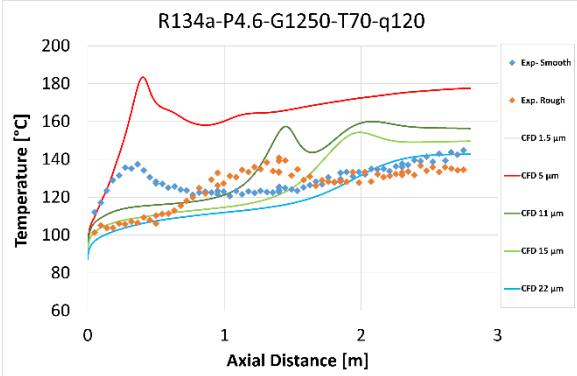

Figure 220. Inner wall temperature trends for the heated tube section at 4.6 MPa operating pressure, mass flux of 1250 kg/m^{2}s, heat flux at 120 kW/m^2 and inlet temperature of 70°C

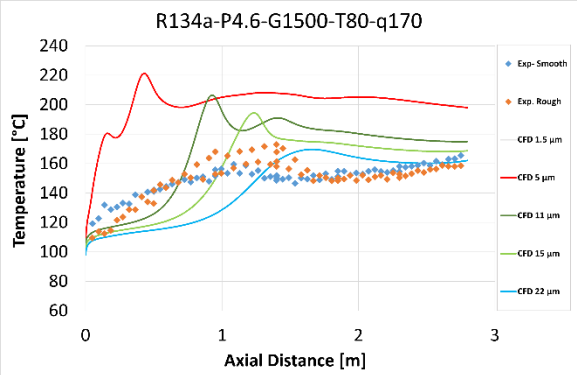

Figure 221. Inner wall temperature trends for the heated tube section at 4.6 MPa operating pressure, mass flux of 1500 kg/m^{2}s, heat flux at 170 kW/m^2 and inlet temperature of 80°C

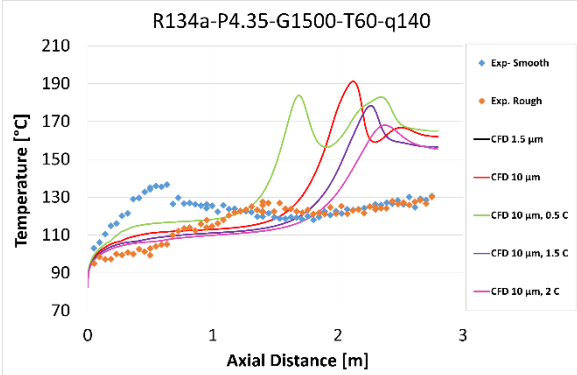

Figure 222. Inner wall temperature trends for the heated tube section at 4.35 MPa operating pressure, mass flux of 1500 kg/m^{2}s, heat flux at 140 kW/m^2 and inlet temperature of 60°C using different values of C_{rough}

Figure 222 finally shows the results of one of the attempts performed to consider the effect of a model parameter on the results obtained by the CFD analysis. Basing on the above results the following detailed observations can be made,

- Figure 205 and Figure 213 show similar experimental and computed trends for equal boundary conditions (500 kg/m^{2}s, heat flux at 40 kW/m^2 and inlet temperature of 50°C) except for the two different considered pressures. From a phenomenological point of view, deterioration is observed to start close to the inlet of the heated section; both the experiment and the computations for smooth tube then show a classical shift to a higher temperature level, being kept up to the point in which turbulence is restored when the buoyancy difference between bulk and wall is not sufficient to maintain laminarization. This phenomenon has been observed and predicted in previous works (see Buzzi et al., 2019) related to the valuable carbon dioxide data by Kline and is predicted also in this occasion in a qualitative way. The main differences between the experiment and the numerical result for the smooth tube is due to the fact that deterioration is a bit anticipated in the analyses and the level of temperature increase is predicted to be lower than observed in the experiment; moreover, heat transfer restoration at the transition to gas-like fluid appears delayed in the calculation. The effect of roughness is represented by the CFD model as expected, i.e., with decreasing values of wall temperature and earlier restoration of heat transfer, up to the point in which deterioration is limited to wall temperature oscillations; such a progressive trend cannot be appreciated in the experiment, run with only a single value of roughness. The experimental data suggest a similar behaviour for a rough tube, but the quantitative match with the computed trends is limited. Slight differences are noted for the case at 4.6 MPa with respect to one at 4.35 MPa, though the trends are very similar.
- Figure 206 to Figure 212 and Figure 214 to Figure 221 present sequences of comparisons between experimental data and computed results for cases with increasing mass flux, with different heat fluxes and inlet temperatures. Increasing the flow has the known potential to improve heat transfer, so that in cases like the one in Figure 219 deterioration is not occurring even for smooth tubes. Of course, this depends on the power-to-flow ratio and also on the inlet temperature in a way that is not simple to condense in simplistic rules of thumb. Overall, the comparisons show the role of roughness in improving heat transfer, up to the point that deterioration may be ruled out. Experiments and calculated results agree in confirming this effect in a range of roughness parameter coherent with the previous discussion, though close accuracy seems to be not easy to achieve for both smooth and rough tubes.
- Attempts were made in changing the parameters determining the effect of roughness in predictions. The results of such an attempt are shown in Figure 222, where the effect of the C_{rough} parameter on the predicted trend is checked for a particular case in which predictions were not very satisfactory in both the smooth and the rough tube cases. Indeed, increasing C_{rough} results in improving heat transfer, delaying to further downstream sections the onset of deterioration. This constant, together with the width assumed for the region of influence of the smoothing function, can be considered as one of the parameters to be calibrated in front of experimental data to achieve better agreement. Actually, at the moment the limited accuracy obtained on even smooth tube wall temperature predictions does not suggest changing the values of these parameters previously devised by the consideration of data of such general validity as the ones by Nikuradse and the Moody diagram, deferring this possible improvement to further reflections, better if based on the availability of more general data.

5.2 CONTRIBUTION BY KTH

The aim of the task is to develop numerical models for prediction of the supercritical heat transfer along rough corroded surfaces. RANS CFD models with appropriate wall treatment for rough wall

surfaces are employed. Specifically, two rough wall treatment methods valid for low-Re turbulence models are formulated, with special source terms or boundary conditions for equations of turbulent kinetic energy and dissipation, to account for the rough wall effect. The rough wall models are combined with the low-Re k-ω SST model as the reference models for the current work. The models are validated against the recent experimental data on smooth and rough wall surfaces with supercritical CO2 and supercritical R134a, where heat transfer deterioration and the enhanced heat transfer due to rough walls were observed during the experiments. The wall temperature predictions with the current rough wall models show reasonably good agreement with the experimental measurements. Nevertheless, further development of the current models is needed to improve the rough wall model prediction capabilities.

5.2.1 Introduction

The current ECC-SMART project is oriented towards assessing the feasibility and identification of safety features of an intrinsically and passively safe small modular reactor cooled by supercritical water (SCW-SMR) (Schulenberg and Starflinger, 2012). Although it is appreciated that there is no occurrence of boiling crisis as in light water reactors, there is possible phenomenon of heat transfer deterioration (HTD), which results from many factors including significantly varying physical properties and other flow specific conditions (Cheng and Schulenberg, 2001). The SCWR with small modular reactor design concept (SCW-SMR) has been the recent focus of research and development (Schulenberg and Otic, 2021). One of the main challenges identified is the corrosion of fuel cladding under supercritical water flow conditions and its impact on heat transfer, which is important to the safety assessment of the nuclear reactor. One main result of the corrosion is the increased cladding wall roughness, which typically affects the flow and heat transfer. To accurately predict the thermal behavior of the fuel rods, especially the undesired heat transfer deterioration, accurate models to account for the rough wall surfaces under supercritical water conditions need to be developed.
Computational fluid dynamics (CFD) has emerged as a powerful tool for simulating and analyzing the heat transfer behavior of supercritical water under various flow conditions, providing insights into the underlying physics and enabling the development of more accurate and efficient design models. Various CFD models have been proposed for modeling flow and heat transfer, including Direct Numerical Simulation (DNS), Large Eddy Simulation (LES), and Reynolds-Averaged Navier-Stokes (RANS) approaches. These models typically involve solving the governing equations for mass, momentum, and energy transport, as well as accounting for the effects of turbulence, compressibility, and chemical reactions. Although the recent DNS results on flow and heat transfer for supercritical fluid flow provide valuable insights and database for RANS model development and validation (Bae and Yoo, 2005; Wang and He, 2015), it is still prohibitive to apply DNS in high Re flow conditions, which are typical in SCWRs. It is well acknowledged that the main difficulties in the numerical analysis of supercritical fluid flow and heat transfer are related to turbulence modelling. There is a large variation of thermo-physical properties, especially near the pseudocritical point, which leads to strong buoyancy and acceleration near the heated wall. Previous research has shown that RANS method with low-Re turbulence models can well predict typical flow and heat transfer in prototypical SCWR conditions (Koshizuka et al., 1995; He et al., 2008; Jaromin and Anglart, 2013). As shown by recent attempts on DNS to explicitly simulate the wall roughness, it is still prohibitive to apply DNS for thermal-hydraulic design and analysis in SCWR conditions (Mann et al., 2023).

Wall roughness typically leads to an increase in turbulence production, which in turn can result in increase of wall shear stress and heat transfer coefficients. The usual way for rough wall modelling is to accordingly downward shift the logarithmic velocity profile in the wall function (Flack and Schultz, 2014). It is, however, not useful in the current work, where low-Re turbulence models are applied. To account for the wall roughness effects in low-Re turbulence models, researchers from University of Pisa (UniPi) introduced wall roughness related source terms to the turbulence equations, and encouraging results for supercritical fluid flow and heat transfer have been obtained (Ambrosini et al., 2015; Kassem et al., 2023). On the other hand, for the popular low-Re k-ω SST model, Wilcox has proposed special boundary conditions for rough walls (Wilcox, 2006). To adapt the rough wall boundary conditions, the original k-ω SST model has been extended and improved for rough wall modelling by other researchers (Menter et al., 2003; Hellsten and Laine, 1997; Hellsten 1998).
Overall, CFD modeling of supercritical fluid flow and heat transfer has made significant progress in recent years, with many studies reporting good agreement between simulation results and experimental data. In the current work, the well-developed low-Re turbulence RANS models with special treatment of rough surface walls are used to simulate supercritical fluid flow and heat transfer on rough walls.

5.2.2 Model description

The current RANS model includes the governing equations of mass, momentum and energy, and also the two-equation low-Re turbulence model.
The mass, momentum, and energy equations are

$$\frac{\partial \rho}{\partial t} + \nabla \cdot \left(\rho \vec{V} \right) = 0 \tag{92}$$

$$\frac{\partial \left(\rho \vec{V} \right)}{\partial t} + \nabla \cdot \left(\rho \vec{V} \vec{V} \right) = -\nabla p + \nabla \cdot \overline{\overline{\tau}} + \rho \vec{g} \tag{93}$$

$$\frac{\partial}{\partial t}\left(\rho \left(h + \frac{V^2}{2} \right) \right) + \nabla \cdot \left(\rho \left(h + \frac{V^2}{2} \right) \vec{V} \right) = \frac{\partial p}{\partial t} - \nabla \cdot \vec{q} + \nabla \cdot \left(\overline{\overline{\tau}} \cdot \vec{V} \right) + \rho \vec{g} \cdot \vec{V} + \rho \dot{q} \tag{94}$$

where ρ is mass density, $\vec{V}$ is velocity, p is pressure, $\overline{\overline{\tau}}$ is effective shear stress, $\vec{g}$ is gravity constant, h is specific enthalpy, $\vec{q}$ is effective heat flux, and $\dot{q}$ is internal heat source. According to the Boussinesq assumption, in which a turbulent Reynolds stress is assumed to be equal to the product between the turbulent viscosity and the velocity gradients, the effective shear stress is described as

$$\overline{\overline{\tau}} = \left(\mu + \mu_t \right) \left[\left(\nabla \vec{V} + \nabla \vec{V}^T \right) - \frac{2}{3} \left(\nabla \cdot \vec{V} \right) I \right] - \frac{2}{3} \rho k I \tag{95}$$

where μ is molecular dynamic viscosity, μ_t is turbulent dynamic viscosity, k is turbulent kinetic energy, and I is unity tensor. Similarly the effect shear stress is expressed as

$$\vec{q} = -\left(\frac{\mu}{\mathrm{Pr}} + \frac{\mu_t}{\mathrm{Pr}_t}\right)\nabla h \tag{96}$$

where Pr is Prandtl number and Pr_t is turbulent Prandtl number.

The reference low-Re number two-equation model used in the current work is the modified k-ω SST model. The transport equations are

$$\frac{\partial}{\partial t}(\rho k) + \nabla\cdot\left(\rho k\vec{V}\right) = P_k + \nabla\cdot\left[\left(\mu + \frac{\mu_t}{\sigma_k}\right)\nabla k\right] - \beta^*\rho k\omega - \frac{\mu_t}{\rho\,\mathrm{Pr}_t}\vec{g}\cdot\nabla\rho \tag{97}$$

$$\frac{\partial}{\partial t}(\rho\omega) + \nabla\cdot\left(\rho\omega\vec{V}\right) = \frac{\gamma\rho}{\mu_t}P_k + \nabla\cdot\left[\left(\mu + \frac{\mu_t}{\sigma_\omega}\right)\nabla\omega\right] - \beta\rho\omega^2 + (1-F_1)2\rho\frac{\sigma_{\omega 2}}{\omega}(\nabla k)\cdot(\nabla\omega) - \frac{\gamma}{\mathrm{Pr}_t}\vec{g}\cdot\nabla\rho \tag{98}$$

where P_k is turbulence generation rate, ω is specific dissipation rate, σ_k, β^*, γ, σ_ω, β, and $\sigma_{\omega 2}$ are model constants, and F_1 is blending function related to wall distance. The turbulent viscosity is calculated as

$$\mu_t = \frac{a_1\rho k}{\max\left(a_1\omega, |\Omega| F_2 F_3\right)} \tag{99}$$

where a_1 is model constant, $|\Omega|$ is absolute vorticity, and F_2 and F_3 are functions related to wall distance. The functions F_2 and F_3 make sure that the model follows Bradshaw's assumption, in which the turbulent shear stress in boundary layer flows depends on the turbulent kinetic energy, and also lift the model limitation in viscous sublayer and roughness layer (Menter et al., 2003; Hellsten and Laine, 1997; Hellsten 1998).

The first rough wall model considered in the current work is based on the work by Ambrosini et al. at University of Pisa, where dimensional analysis on turbulence production due to roughness is conducted (Ambrosini et al., 2015). The resultant source term for turbulent kinetic energy equation is defined as

$$S_{kr} = \frac{f_s C_r \rho V^3}{2k_s} \tag{100}$$

where f_s is smooth function to make the model valid only near the wall, C_r is model constant, and k_s is wall roughness and typically the sand grain equivalent roughness is used. The source term for turbulence dissipation rate equation is similarly defined as

$$S_{\varepsilon r} = \frac{\varepsilon}{k} S_{kr} \tag{101}$$

where ε is turbulence dissipation rate. Accordingly, the source term can be transformed to be used in the specific dissipation rate ω equation for k-ω turbulence models.

Another rough wall model considered in the current work is based on Wilcox's wall boundary condition for turbulence specific dissipation rate (Wilcox, 2006), which is prescribed on the wall as

$$\omega_w = \frac{\rho u_\tau^2}{\mu} S_R \tag{102}$$

where u_τ is friction velocity and S_R is expressed as

$$S_R = \left(\frac{200}{k_s^+}\right)^2, \quad k_s^+ \le 5$$
$$S_R = \frac{60}{k_s^+} + \left[\left(\frac{200}{k_s^+}\right)^2 - \frac{60}{k_s^+}\right] e^{5-k_s^+}, \quad k_s^+ > 5 \tag{103}$$

where k_s^+ is dimensionless roughness defined as

$$k_s^+ = \frac{\rho u_\tau k_s}{\mu} \tag{104}$$

The two rough wall models are implemented in the open source CFD code OpenFOAM based on the modified k-ω SST model. All the thermo-physical properties used for the simulations are based on NIST property library (Lemmon et al., 2013). In the current work, the default model coefficients reported have been applied (Ambrosini et al., 2015; Wilcox, 2006).

5.2.3 Results and discussion

The current rough wall models have been validated on hydrodynamics and also with heat transfer.

5.2.3.1 Results on hydrodynamics

To test the hydrodynamic prediction capability, the current rough wall model is used to calculate the friction factors and velocity profiles under various flow conditions. Usually the Moody diagram and the Nikuradse curves provide friction database for flows with smooth and rough walls. The Moody diagram can be well represented by the Colebrook correlation, or more explicitly by the Haaland correlation (Haaland, 1983), and the Nikuradse curves has been well estimated by the correlation from Yang and Joseph (Yang and Joseph, 2009). For the velocity profile under rough wall conditions, Durbin has developed a log-law region correlation based on the Nikuradse database (Durbin et al., 2001). For the current model validation, water flow in a pipe with various typical wall roughnesses for engineering pipe flow applications has been simulated to obtain friction factors and velocity profiles.

Figure *223* shows the friction factors calculated from the two rough wall models and the comparison to the Moody diagram (Haaland correlation) and Nikuradse curves. Both models (UniPi and Wilcox) show good qualitative agreement with the correlation data (Ambrosini et al., 2015; Wilcox, 2006). The two models show good agreement with each other, and the Wilcox model performs slightly better in high Re and relatively higher roughness conditions (Wilcox, 2006).

Velocity profiles from both models have good agreement with the rough wall log law profiles, as shown in Figure *224*. For high roughness, the Wilcox model is in better agreement with the log-law profile (Wilcox, 2006). The velocity profiles in the UniPi model results are more effective close

to the location of the wall roughness, which may indicate that the smooth function in the UniPi model could be improved with a higher factor near the wall (Ambrosini et al., 2015).

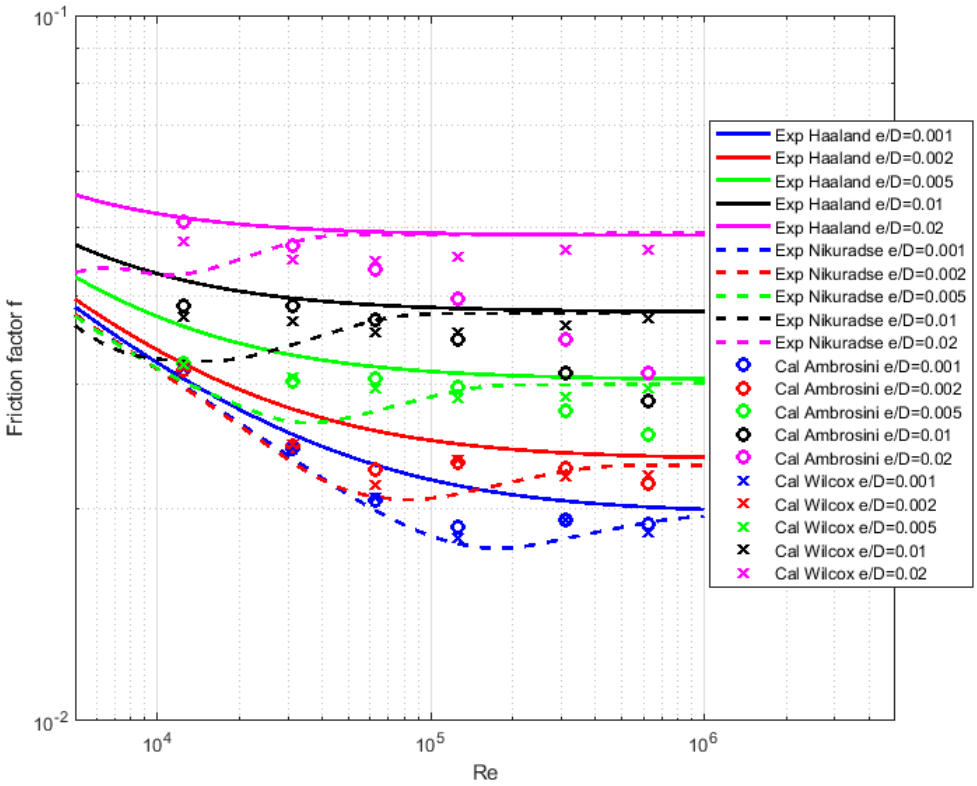

Figure 223. Friction factors calculated and the comparison to Moody diagram (Haaland correlation) and Nikuradse curves.

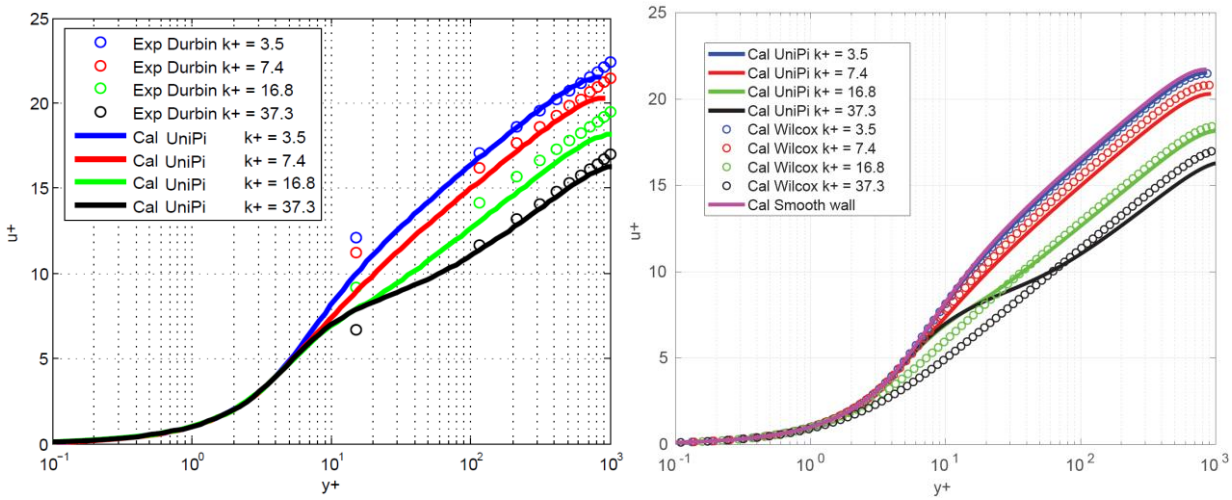

(a) (b)

Figure 224. Velocity profiles calculated from the rough wall model compared to experimental data.

5.2.3.2 Results on heat transfer

There has been some recent experimental work on supercritical fluid heat transfer with supercritical CO_2 and R134a (Chen et al., 2022; Wiltschko, 2023). The current rough wall models have been validated based on these data.

5.2.3.2.1 Results for supercritical CO_2

Recently Chen et al. from University of Science and Technology of China (USTC) reported the experimental data on heat transfer measurements for supercritical CO_2 at various wall roughness conditions (Chen et al., 2022). The test section is a heated pipe with inner diameter of 4.57 mm and heated length of 1 m. The vertical upward flow is heated with fixed inner wall heat flux of 50 kW/m^2 with inlet fluid temperature at 25 °C under pressure of 9 MPa. The inlet flow is controlled between 300 and 500 kg/m^{2}s, meaning 16207 <Re< 91735. Various wall roughnesses between 1.5 and 40 micrometers are obtained by electrical discharge machining. It should be noted that it is not clear how the reported wall roughness is calculated, although the reported wall roughness is assumed as the sand grain equivalent roughness used for the current simulations.

Figure *225* shows the wall temperature results for smooth walls at various mass flow conditions. It is noted that the current model can qualitatively predict the HTD at low flow conditions and the progression to deterioration suppression when the flow is increased. Multiple peak type HTD is obtained in both experimental data and the current simulations. This kind of HTD at low flow conditions is mainly due to buoyancy effect near the wall. The buoyancy force near the wall will flatten the velocity profile, which leads to the suppression of turbulence and therefore the reduction of the heat transfer coefficient. The simulation results show that the current model can capture the trend of the HTD occurrence.

Wall temperature results for low flow conditions at various wall roughnesses is shown in Figure *226*. Both the UniPi and the Wilcox rough wall models can predict the suppression of the HTD. The UniPi model gives higher heat transfer coefficient at lower wall roughness. The two models show very similar results for high wall roughness. Figure *227* shows the wall temperature results for elevated flow conditions. Enhanced heat transfer and reduced wall temperatures can be observed.

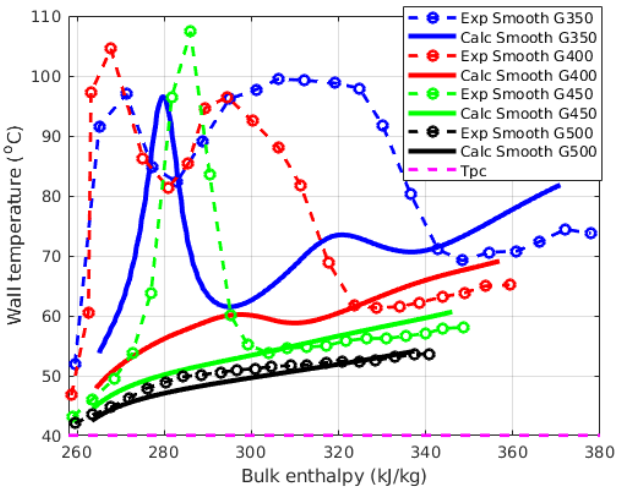

Figure 225. Wall temperature results for smooth walls.

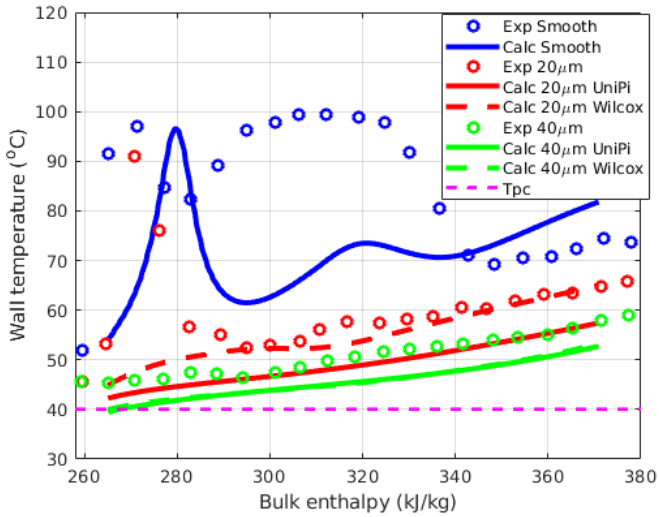

Figure 226. Wall temperature results for G=350 kg/m^{2}s at various wall roughnesses.

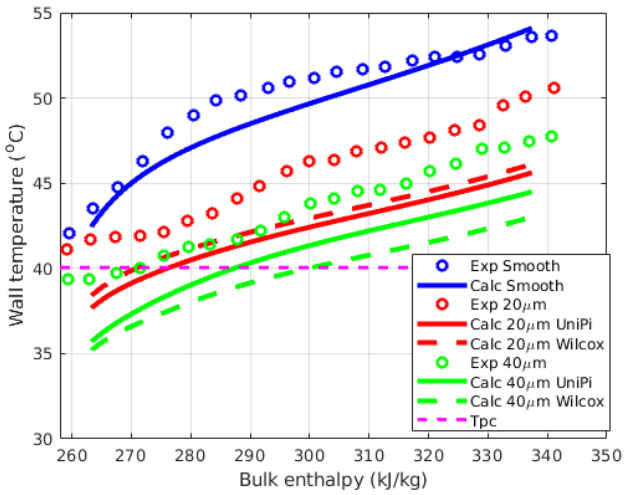

Figure 227. Wall temperature results for G=500 kg/m^{2}s at various wall roughnesses.

5.2.3.2.2 Results for supercritical R134a

A more recent experimental study on rough wall heat transfer at supercritical flow conditions is by Karlsruhe Institute of Technology (KIT) with fluid R134a (Wiltschko, 2023). The test section is a vertical heated pipe with inner diameter of 9 mm and heated length of 2.8 m. The fluid flows upward at various inlet temperature and mass flow rates under various pressures. The experiment matrix includes pressures of 46 and 43.5 bar, inlet mass flux ranging from 500 to 2000 kg/m^{2}s, inlet temperatures ranging from 50 to 80 °C, and inner wall heat flux between 20 and 200 kW/m^2. The reported sand grain equivalent wall roughness for the rough walls is 10.7 μm. In the current paper, only the representative results for pressure of 46 bar and inlet temperature of 60 °C are presented.

Figure *228* shows the wall temperature results for smooth walls at low flow conditions. Multiple peak type HTD is also obtained similar to the results from previous section. The HTD occurs when the wall heat flux is increased till certain value. The trend for HTD occurrence with increased wall heat flux is well captured. For high flow conditions, as shown in Figure *229*, the HTD trend is also captured by the current model. However, the initial heat transfer recovery starting from 0.5 m is

not fully captured, although the further wall temperature increase from 1.5 m can be qualitatively predicted. It is argued by many researchers that the high flow HTD is mainly due to the local drastic change of the physical properties near the heated wall. Figure *229* shows that HTD occurs when the wall temperatures are above the pseudocritical temperature. Similar to Figure *228*, the current model can well predict the enhanced heat transfer conditions and capture qualitatively the HTD conditions.

Wall temperature results for rough walls at low and high flow conditions are shown in Figure *230*, Figure *231*, Figure *232* and Figure *233*. When the wall heat flux is low, wall temperatures and the heat transfer enhancement due to the rough walls can be well predicted by both rough wall models. For rough walls, both models predicted heat transfer enhancement with decreased wall temperatures. Although the two rough wall models reported slightly different results, the predicted wall temperatures by both models have reasonable agreement with the experimental data.

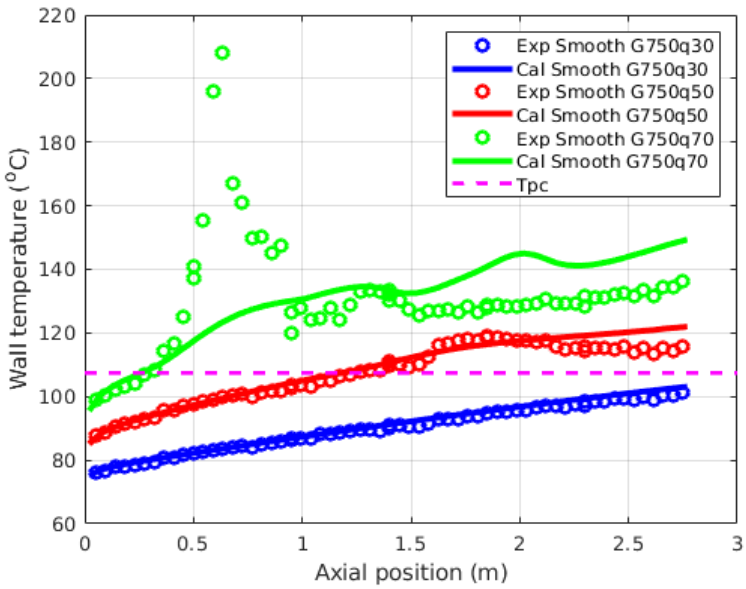

Figure 228. Wall temperature results for smooth walls, G=750 kg/m^{2}s, and at various wall heat fluxes.

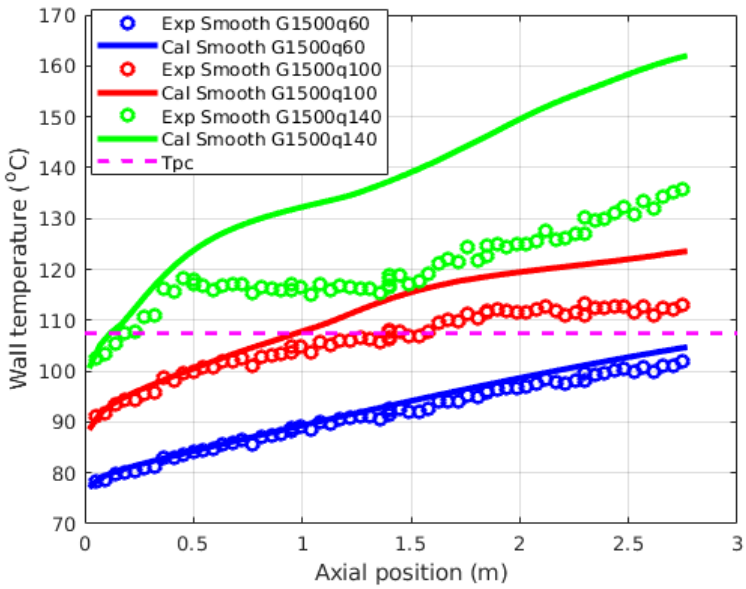

Figure 229. Wall temperature results for smooth walls, G=1500 kg/m^{2}s, and at various wall heat fluxes.

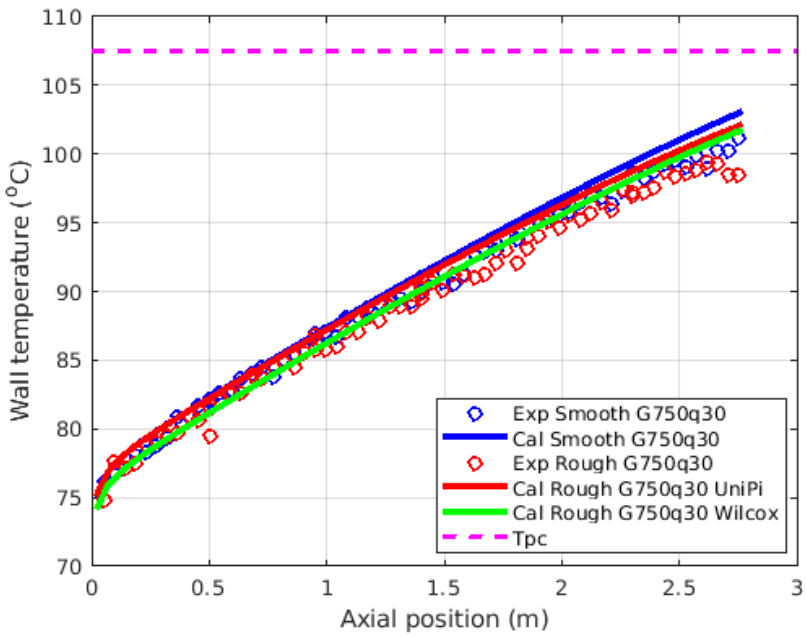

Figure 230. Wall temperature results for rough walls, G=750 kg/m^{2}s, and at low wall heat flux.

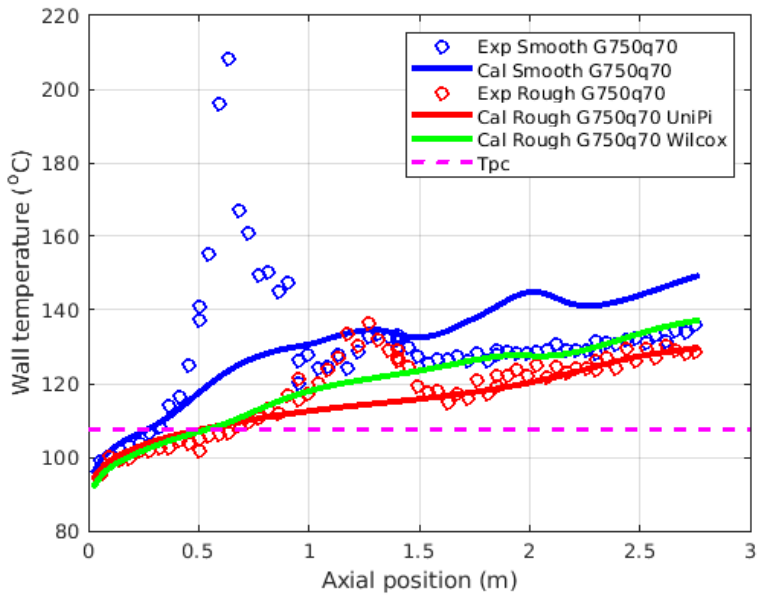

Figure 231. Wall temperature results for rough walls, G=750 kg/m^{2}s, and at high wall heat flux.

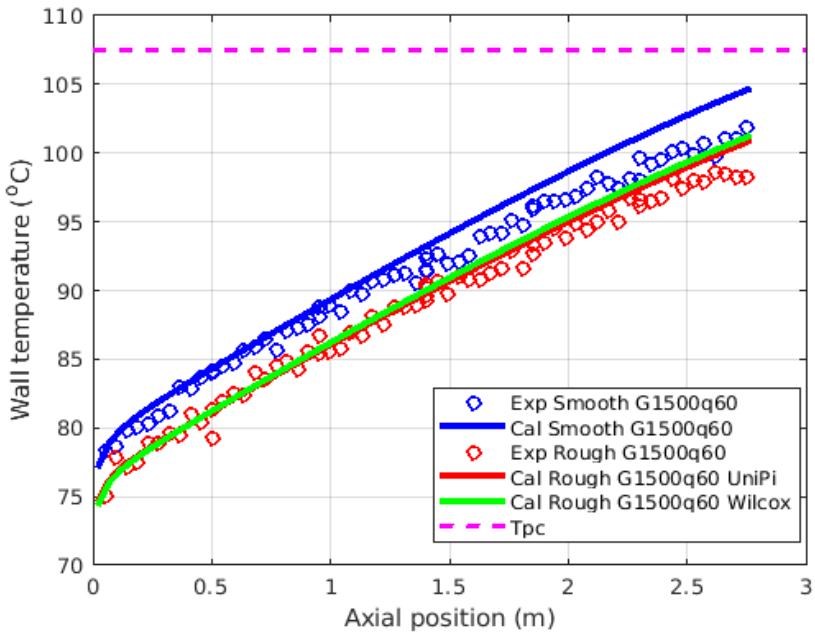

Figure 232. Wall temperature results for rough walls, G=1500 kg/m^{2}s, and at low wall heat flux.

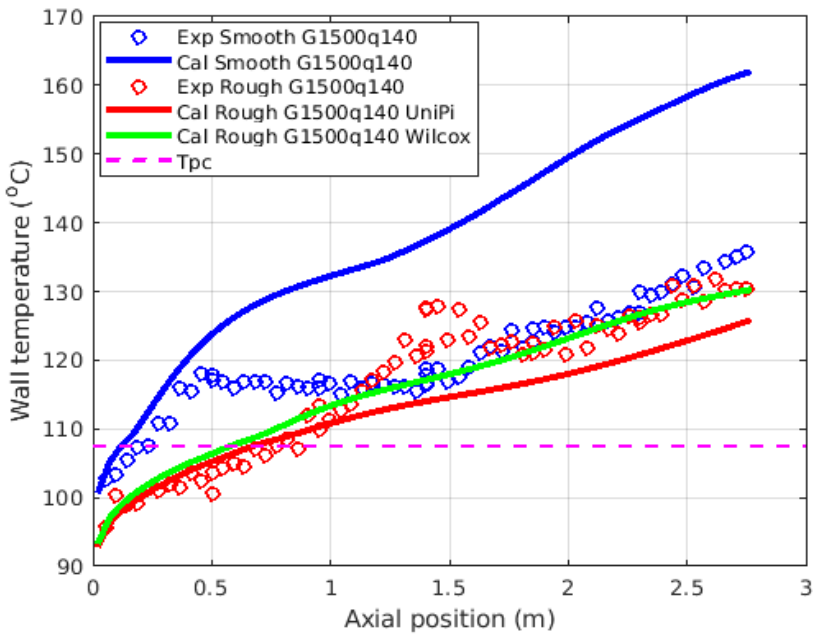

Figure 233. Wall temperature results for rough walls, G=1500 kg/m^{2}s, and at high wall heat flux.

5.2.3.2.3 Summary of the results

It is desirable to have more accurate modelling approaches like DNS to predict heat transfer of supercritical fluid flow, including rough wall simulations. However, nowadays the more realistic model approach for thermal-hydraulic design and analysis in SCWR applications is the low-Re RANS models. The prediction capabilities and drawbacks of the low-Re RANS models have been well understood from previous research work, and also demonstrated in the current work. The proposed two rough wall models combined with the low-Re RANS models can well extend the prediction capabilities for rough wall surface conditions.

5.2.4 Conclusions

The model simulation results from the current work show that the low-Re RANS CFD models can provide reasonable prediction accuracy for supercritical fluid flow and heat transfer, including the prediction of heat transfer deterioration. The modified low-Re k-ω SST turbulence model together with the proposed two rough wall treatment approaches is very promising to be used for thermal-hydraulic design and analysis of SCW-SMRs under prototypical conditions. The two rough wall models used in the current work can reasonably predict the heat transfer deterioration and its suppression and/or delay. Nevertheless, further development of the current models is needed to improve the rough wall model prediction capabilities.

6 Subtask 3.3.6 Two and more equation RANS modelling of turbulent heat and mass transfer along corroded surfaces (UoN, UNIPI)

6.1 CONTRIBUTION BY UoN

6.1.1 Introduction

With the development of computer simulation techniques, computational fluid dynamics (CFD) has been more widely used in the study of the heat transfer characteristics of supercritical fluids. There are many turbulence models in CFD simulation, such as the standard k-ε, buoyant k-ε and Shear Stress Transport (SST) k-ω turbulence models.
Several studies have been done to explore heat transfer characteristics of supercritical water in vertical and horizontal flow modes. In the vertical flow aspect, Su and Li (2022) presented that the use of a k-ω formulation in the inner parts of the boundary layer makes the model directly usable in all the way down to the wall through the viscous sub-layer, hence the SST k-ω model can be used as a Low-Re turbulence model without any extra damping functions. The SST formulation also switches to a k-ε behaviour in the free-stream and thereby avoids the common k-ω problem that the model is too sensitive to the inlet free-stream turbulence properties. The SST k-ω model often merits for its good behaviour in adverse pressure gradients and separating flow. Wang et al. (2021) claimed that the SST k-ω model does produce a bit too large turbulence levels in regions with large normal strain, like stagnation regions and regions with strong acceleration. This tendency is much less pronounced than with a normal k-ε model. The SST k-ω model uses the omega formulation whereas the realizable k-ε uses the epsilon formulation. The two models differ in their approaches both near walls and away from walls. The SST k-ω model is generally thought to be better near walls, but because it reduces to the standard k- ε model away from walls and not the realizable k-ε model.
In horizontal flow aspect, Wang et al. (2022) validated the Reynolds-Averaged Navier–Stokes (RANS) models to predict heat transfer and turbulent flow of supercritical fluid in horizontal tube by direct numerical simulation, and claimed that Abe-Kondoh-Nagano(AKN) model could provide the best results for the turbulent velocity profile and bulk parameters, such as wall temperature and Nusselt number. Podila and Rao (2015) simulated the supercritical flow heat transfer under operating pressures of 23.5, 25, and 28 MPa through SST k-ω model and compared with the normal heat transfer. Zhang et al. (2010)0 numerically investigated heat transfer of supercritical water in a horizontal circular tube with three epsilon-type models, and recommend the standard

k-ε model with enhanced wall treatment which gives a more reasonable prediction capability in a horizontal flow. Shang and Chen (2011) reported supercritical water flow heat transfer in horizontal round tubes with CFD simulation, and concluded that the discretization scheme does not affect the numerical simulations' accuracy and large diameter may cause a high risk of strong heat transfer deterioration. Mao et al. (2022) validated the k-ε and SST k-ω models in a horizontal tube, and found that the results provided by the SST k-ω model are closer to the experimental data. They also suggested that $Ri=Gr/Re^2$ predicts the buoyancy effect on heat transfer effectively.
Even though many investigations are conducted based on the SST k-ω and k-ε models to study heat transfer characteristics of supercritical water, but most of them are targeted on the smooth pipe cases, there are a few of research focusing on the surface roughness influence on heat transfer. Kassem et al. (2023) studied the supercritical fluid heat transfer on a rough surface by a low-Reynolds number turbulence model, and conducted a sensitivity analysis to characterise the obtained results with different roughness parameters. Wang et al. (2022) designed a tube with the half rough surface, adopted the SST k-ω turbulent model for the simulation and found that the tube with rough surface could provide more uniform heat transfer distribution compared with the tube with smooth surface. This study presents simulation results regarding wall temperature and pressure drop of supercritical water in a tube with rough surface by different turbulence models. The ANSYS FLUENT V2021R1 program is used for the vertical flow in a pipe with rough surface, and the Standard k-ε and SST k-ω models are adopted in this case. The OpenFOAM version 11 program is adopted for the horizontal flow in a tube with rough surface, two cases are investigated, one case is to study roughness constant effects, the other one is to explore roughness height influences, the turbulence models Standard k-ε, Buoyant k-ε and SST k-ω are applied.

6.1.2 Governing equations and turbulent models

The conservation equations of the supercritical water mass, momentum, and energy are described (see Han and Zhang, 2022):
Conservation of mass:

$$\frac{\partial \rho \overline{u_i}}{\partial x_i} = 0 \tag{105}$$

Conservation of momentum for the vertical flow:

$$\frac{\partial\left(\rho \overline{u_i}\,\overline{u_j}\right)}{\partial x_j} = -\frac{\partial \bar{p}}{\partial x_i} + \frac{\partial}{\partial x_j}\left(\mu \frac{\partial \rho \overline{u_i}}{\partial x_j} - \rho \overline{u_i}\,\overline{u_j}\right) \tag{106}$$

Conservation of momentum for the horizontal flow:

$$\frac{\partial}{\partial x_j}(\rho u_i u_j) = \rho g - \frac{\partial P}{\partial x_i} + \frac{\partial}{\partial x_j}\left[\mu\left(\frac{\partial u_i}{\partial x_j} + \frac{\partial u_j}{\partial x_i}\right) - \overline{u_i' u_j'}\right] \tag{107}$$

Conservation of energy:

$$\frac{\partial}{\partial x_i}\left(\overline{u_i}\rho c_p T\right) = \frac{\partial}{\partial x_i}\left[\left(\lambda + \frac{c_p \mu_t}{Pr_t}\right)\frac{\partial T}{\partial x_i}\right] \tag{108}$$

where x_i and x_j represent the Cartesian coordinate system components, respectively; u_i,and u_j, denote, respectively, the velocities along the x_i and $x_j$directions; *T* and *P* represent the temperature and the pressure, respectively. ρ, μ, λ stand for, respectively, the density, dynamic

viscosity, and conductivity of the fluid; μ_t represents the turbulent viscosity; $\overline{u_i' u_j'}$ represents the turbulent stress tensor; *g* is the gravitational acceleration; Pr_t is respectively the Prandtl number and the turbulent Prandtl number.
The turbulent models standard k-ε, buoyant k-ε and SST k-ω are used in this study. The CFD code uses the unstructured finite volume method to solve the Reynolds Averaged Navier-Stokes (RANS) equations and can handle a wide variety of unstructured meshes.

Standard k-ε model (see Ansys, 2011):

$$\frac{\partial}{\partial t}(\rho k) + \frac{\partial}{\partial x_i}(\rho k u_i) = \frac{\partial}{\partial x_j}\left[(\mu + \frac{\mu_t}{\sigma_k})\frac{\partial k}{\partial x_j}\right] + G_k - G_b - \rho\epsilon - Y_M + S_k \tag{109}$$

$$\frac{\partial}{\partial t}(\rho \epsilon) + \frac{\partial}{\partial x_i}(\rho \epsilon u_i) = \frac{\partial}{\partial x_j}\left[(\mu + \frac{\mu_t}{\sigma_\epsilon})\frac{\partial \epsilon}{\partial x_j}\right] + C_{1\epsilon}\frac{\epsilon}{k}(G_k + C_{3\epsilon}G_b) - C_{2\epsilon}\rho\frac{\epsilon^2}{k} + S_\epsilon \tag{110}$$

where G_k represents the generation of turbulence kinetic energy due to the mean velocity gradients. G_b is the generation of turbulence kinetic energy due to buoyancy. Y_M represents the contribution of the fluctuating dilatation in compressible turbulence to the overall dissipation rate. $C_{1\epsilon}$ and $C_{2\epsilon}$ are the constants. σ_k and $\sigma_\epsilon$are the turbulent Prandtl numbers for k and ε. S_k and S_ϵ are the user-defined source terms.

Buoyant k-ε model (see Henkes et al., 1991):
Buoyant k-ε turbulent model applies additional buoyancy generation and dissipation terms to the k and ε equations of the standard k-ε model. This implementation is based on the density rather than temperature gradient extending the applicability to systems in which the density gradient is generated by variation of composition rather than temperature. Further, the 1/Prt coefficient is replaced by Cg to provide more general control of model as proposed by Weller (2021). The k and ε equations of buoyant k- ε model are as follows:

$$\frac{\partial k}{\partial t} + u\frac{\partial k}{\partial x} + v\frac{\partial k}{\partial y} = \frac{\partial}{\partial x}\left(\nu + \frac{\nu_t}{\sigma_k}\right)\frac{\partial k}{\partial x} + \frac{\partial}{\partial y}\left(\nu + \frac{\nu_t}{\sigma_k}\right)\frac{\partial k}{\partial y} + P_k + G_k - \epsilon + D \tag{111}$$

$$\frac{\partial \epsilon}{\partial t} + u\frac{\partial \epsilon}{\partial x} + v\frac{\partial \epsilon}{\partial y} = \\ = \frac{\partial}{\partial x}\left(\nu + \frac{\nu_t}{\sigma_\epsilon}\right)\frac{\partial \epsilon}{\partial x} + \frac{\partial}{\partial y}\left(\nu + \frac{\nu_t}{\sigma_\epsilon}\right)\frac{\partial \epsilon}{\partial y} + (c_{1\epsilon}f_1(P_k + c_{3\varepsilon}G_k) - c_{2\epsilon}f_2\epsilon)\frac{\epsilon}{k} + E \tag{112}$$

With

$$P_k = v_t(2\left(\frac{\partial u}{\partial x}\right)^2 + 2\left(\frac{\partial u}{\partial y}\right)^2 + \left(\frac{\partial u}{\partial y} + \frac{\partial u}{\partial v}\right)^2) \tag{113}$$

$$G_k = -\frac{v_t}{\sigma_T} g\beta \frac{\partial T}{\partial y} \tag{114}$$

$$v_t = c_\mu f_\mu \frac{k^2}{\epsilon} \tag{115}$$

where k represents the turbulent kinetic energy, v represents the molecular kinematic viscosity, v_t represents the turbulent kinematic viscosity. P_k represents the shear production of turbulent kinetic energy, G_k represents the buoyancy production of turbulent kinetic energy. ε represents the rate of dissipation of turbulent kinetic energy, D represents the low-Reynolds-number source term in k-equation, E represents the low-Reynolds-number source term in ϵ-equation. $c_{1\epsilon}$, $c_{2\epsilon}$ and $c_{3\epsilon}$ are the coefficients in ϵ-equation, c_μ is the coefficient in v_t-equation. f_1 represents the low-Reynolds-number correction for $c_{1\epsilon}$, f_2 represents the low-Reynolds-number correction for $c_{2\epsilon}$, f_μ represents the low-Reynolds-number correction for c_μ.
SST k-ω model (see Ansys, 2011):

$$\frac{\partial}{\partial t}(\rho k) + \frac{\partial}{\partial x_i}(\rho k u_i) = \frac{\partial}{\partial x_j}\left(\Gamma_k \frac{\partial k}{\partial x_j}\right) + \tilde{G}_k - Y_k + S_k \tag{116}$$

$$\frac{\partial}{\partial t}(\rho \omega) + \frac{\partial}{\partial x_i}(\rho \omega u_i) = \frac{\partial}{\partial x_j}\left(\Gamma_\omega \frac{\partial \omega}{\partial x_j}\right) + G_\omega - Y_\omega + D_\omega + S_\omega \tag{117}$$

where G_ω represents the generation of ω, Γ_k and Γ_ω represent the effective diffusivities of k. Y_k and Y_ω represent the dissipation of k and ω due to turbulence. D_ω represents the cross-diffusion term. $S_k$and S_ω are the user-defined source terms.

6.1.3 Vertical flow in a pipe with rough surface

6.1.3.1 Geometry and mesh design

To simplify the geometry and mesh, the pipe model is designed as one pipe with a rod inside. The pipe geometry is shown in Figure 234, it is a straight pipeline without any attached part. The pipe length is 3719 mm, the pipe diameter is 20 mm and rod diameter is 10 mm as shown in Figure 235. The pipe external wall thickness is 1.5 mm, the pipe volume is 0.11684 m^3 and its effective volume is 0.055205 m^3, the rod surface area is 1.1841 m^2.

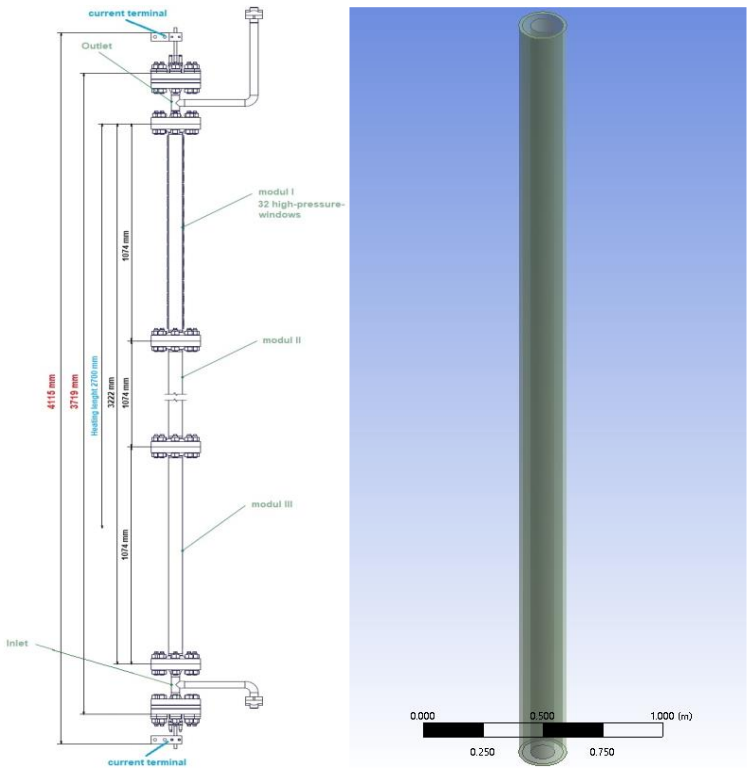

Figure 234. Pipe and its geometric model

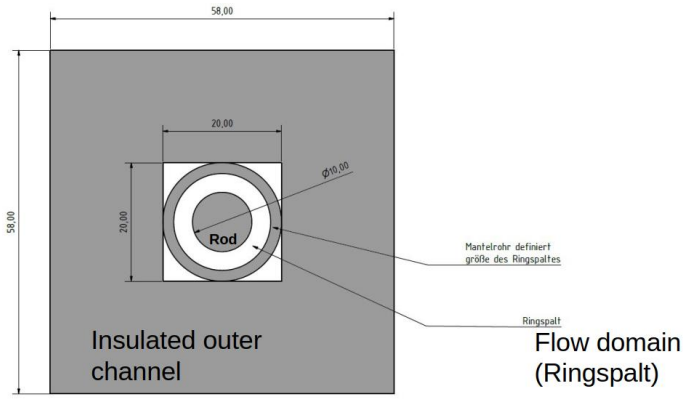

Figure 235. Pipe cross section

The generated mesh model is shown in Figure 236, the mesh element size of whole model is 0.005 m as displayed by Figure 237. The element sizes of internal pipe wall and rod wall are the same, that is 0.002 m as shown in Figure 238.

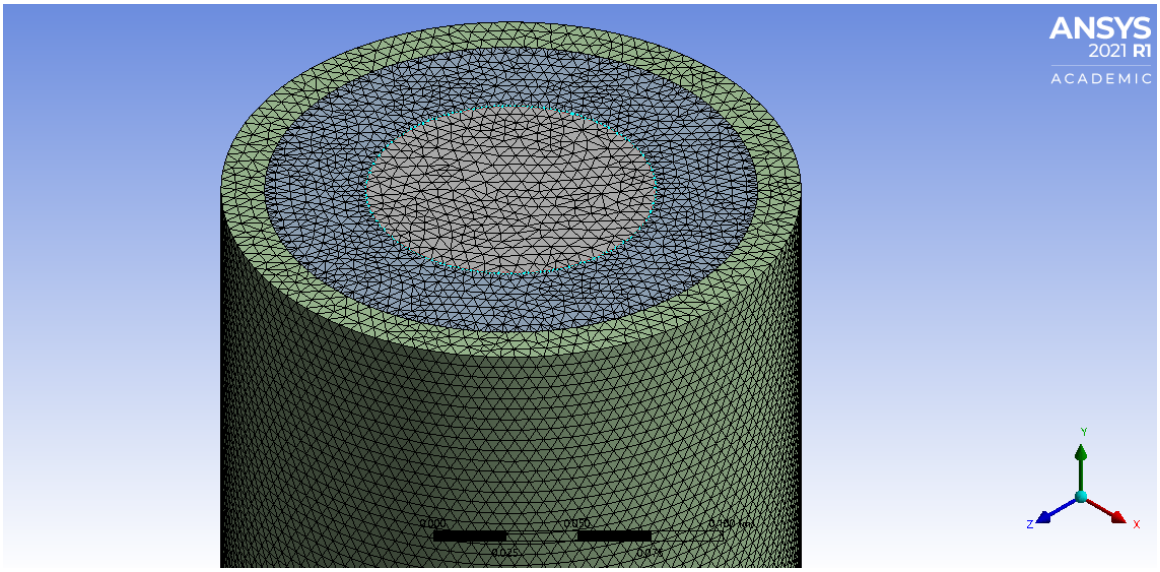

Figure 236. Mesh model

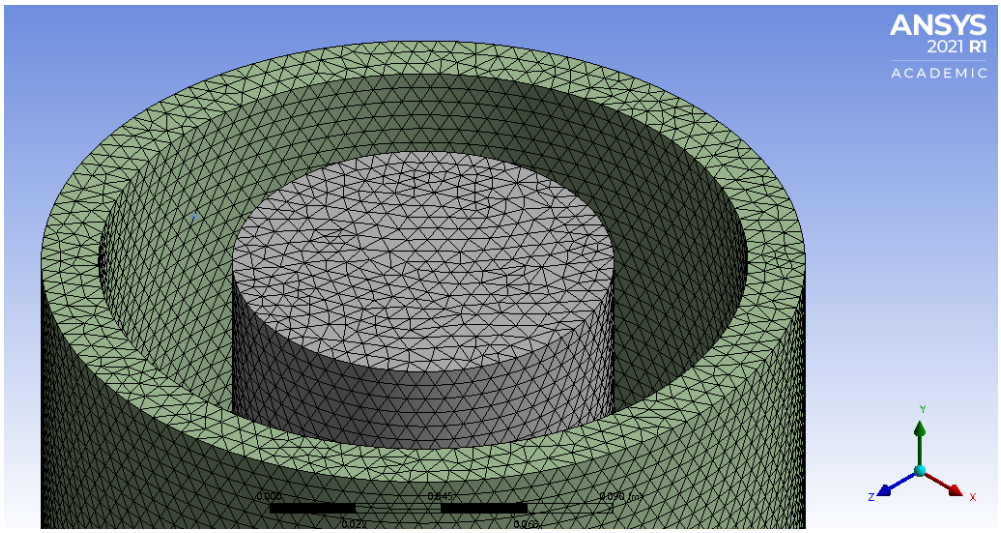

Type	Element Size
Element Size	5.e-003 m

Figure 237. Element sizes of solid bodies

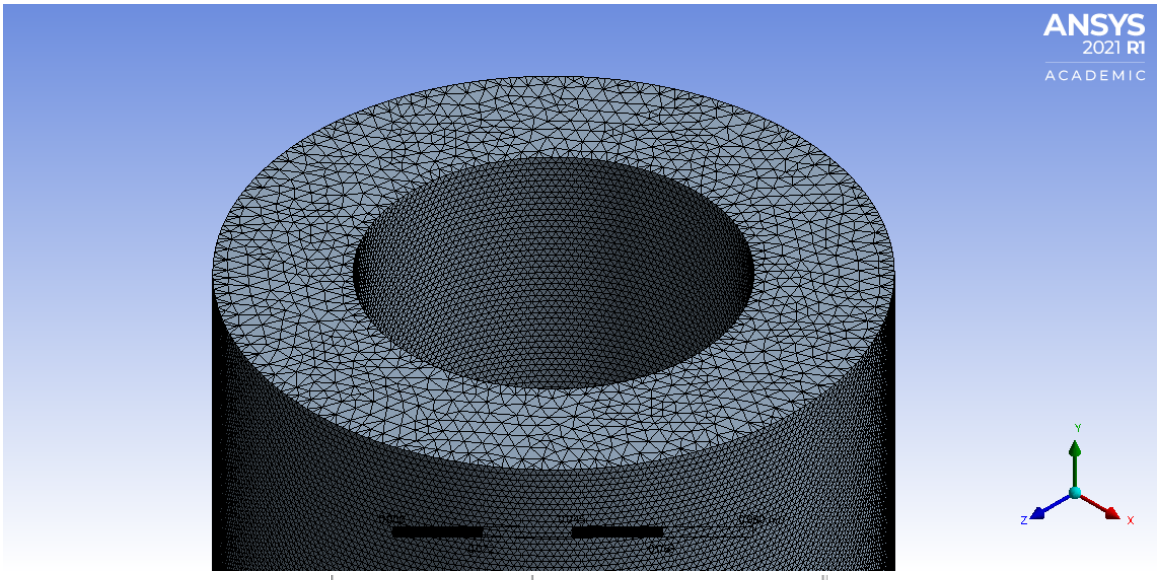

Type	Element Size
Element Size	2.e-003 m

Figure 238. Pipe element size

6.1.3.2 Boundary condition

As indicated in Figure 239, different materials have different roughness data, the considered material in this study is stainless steel, but it has only one value of 0.0015 mm which is difficult to make the comparison, so the data of PVC are used in the CFD simulation. The roughness height range is set from 0.001 mm to 0.007 mm with 0.0005 mm change step.

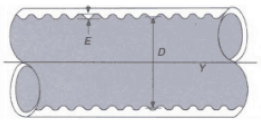

Material	Absolute Roughness (mm)
Copper, Lead, Brass, Aluminum (new)	0.001 - 0.002
PVC and Plastic Pipes	0.0015 - 0.007
Flexible Rubber Tubing - Smooth	0.006-0.07
Stainless Steel	0.0015
Steel Commercial Pipe	0.045 - 0.09
Weld Steel	0.045
Carbon Steel (New)	0.02-0.05
Carbon Steel (Slightly Corroded)	0.05-0.15
Carbon Steel (Moderately Corroded)	0.15-1
Carbon Steel (Badly Corroded)	1-3
Asphalted Cast Iron	0.1-1
New Cast Iron	0.25 - 0.8
Worn Cast Iron	0.8 - 1.5
Rusty Cast Iron	1.5 - 2.5
Galvanized Iron	0.025-0.15
Wood Stave	0.18-0.91
Wood Stave, used	0.25-1
Smoothed Cement	0.3
Ordinary Concrete	0.3 - 1
Concrete – Rough, Form Marks	0.8-3

Figure 239. Roughness property (Belyadi et al., 2017)

The pipe material properties are inputted in the Create/Edit Materials window in the program as presented in Figure 240. The densities of pipe wall and rod are 7850 kg/m^3, their Cp are 500 J/kg-k, and their thermal conductivities are 26 w/m-k.

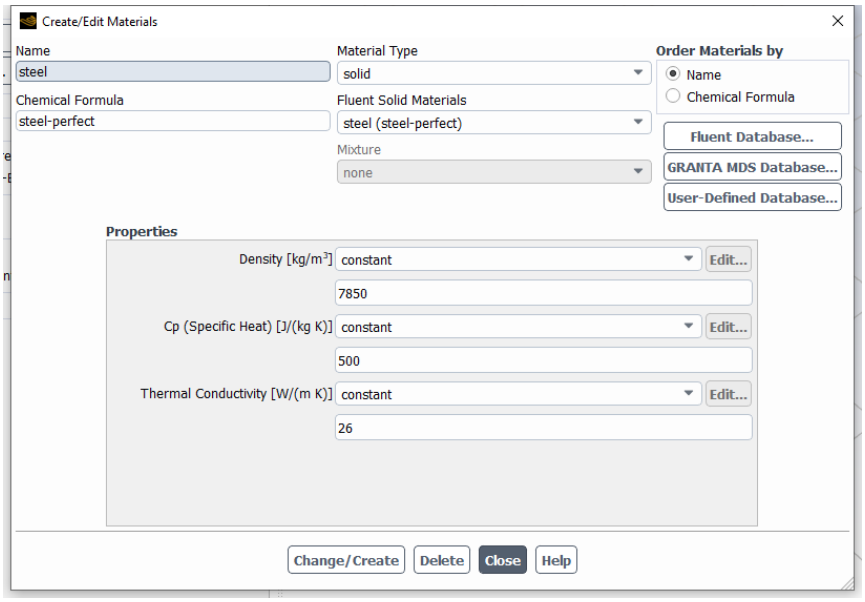

Figure 240. Pipe material

The rod wall condition is shown in Figure 241. The roughness height will be changes from 0.001mm to 0.007mm. Roughness constant is set as 0.5. The heat flux is set as 504 kw/m^2 and the wall thickness is 0.05m.

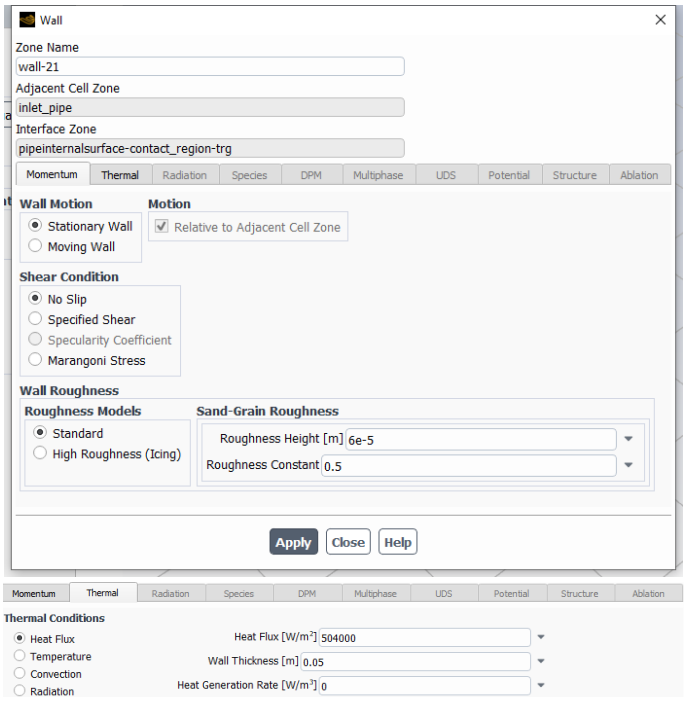

Figure 241. Rod wall condition

6.1.3.3 Test condition

The vertical flow mode is investigated. The inlet temperature of the pipe is 626.15 K, the turbulent intensity is 5 % and hydraulic diameter is 0.07 m. The mass flow rate of water is 0.004384 kg/s, the inlet of pipe set with mass-flow inlet property. The outlet pressure of pipe is 23.37 MPa with

the same turbulent intensity 5 and hydraulic diameter 0.07 m, the outlet of pipe set with pressure outlet property.
The model is solved from the pipe inlet. The gauge pressure is 25 MPa. The X and Z velocities are zero, and Y velocity is 0.000472 m/s. The turbulent kinetic energy is 0.00000375 m^2/s^2 and specific dissipation is 0.2281703 s^{-1}.

6.1.3.4 Simulation procedure

The main solution steps are shown in Figure 242.

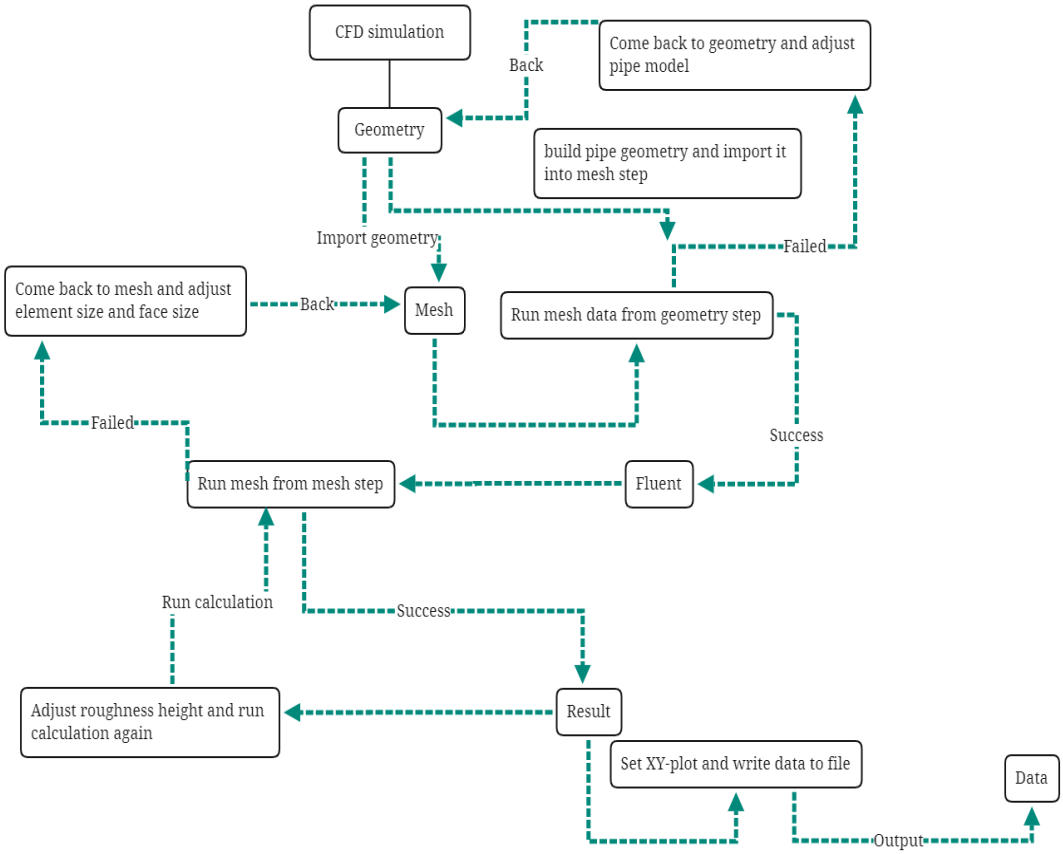

Figure 242. Main steps

At first the geometry model is generated, the model is exported to mesh step and calculation. Then the mesh result is sent to fluent step, the roughness height will be set in this step. After calculating temperature and pressure, the roughness height will be set as different values and the process is repeated.
The main variable CFD simulation parameter is the roughness. The roughness height range of 0.001 mm to 0.007 mm is adopted with step change of 0.0005 mm, the pipe with no roughness height is also considered for comparison purpose.

6.1.3.5 Results and discussion

The iso-surface plane is the middle plane of the pipe to get the largest area for reflecting the changes of temperature and pressure drop. After calculating is completed, the data of temperature and pressure at the chosen points in pipe will be obtained. The only difference of the pipe is the surface roughness height. The temperature variation and pressure drop are shown below. There results are based on two models, one is standard k- ε model and the other is SST k- ω model. It can be seen from Figure 243 and Figure 244 that the pipe wall temperature

variations are similar for the smooth and rough surface cases, the wall temperature decreases with the roughness height. But the pressure drop increases with the roughness as indicated in Figure 245.

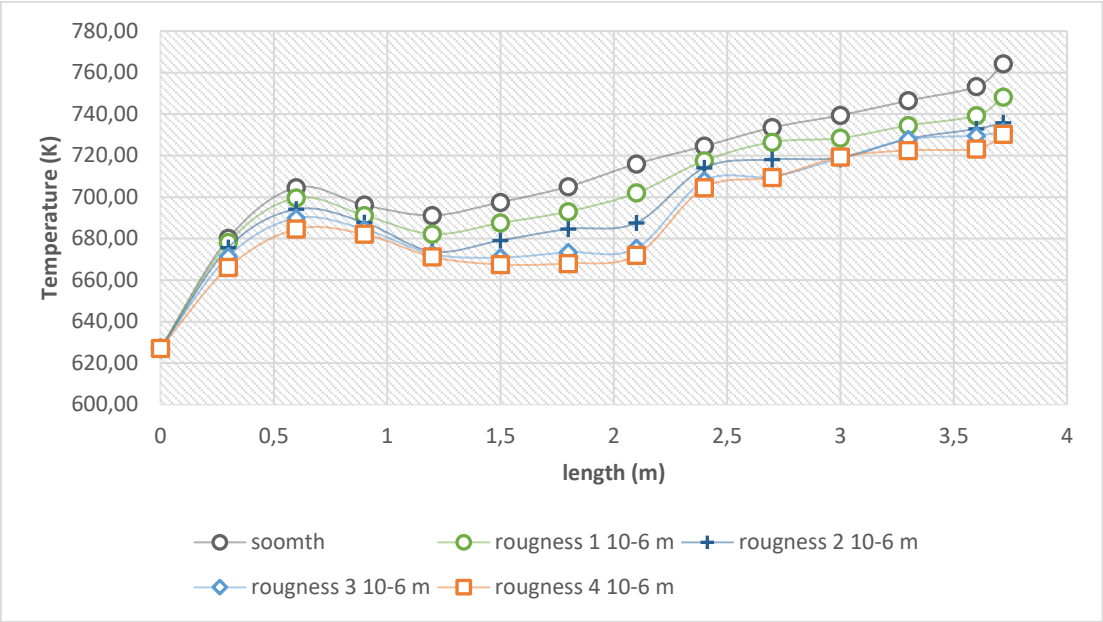

Figure 243. Temperature variations with pipe length (k-ε model)

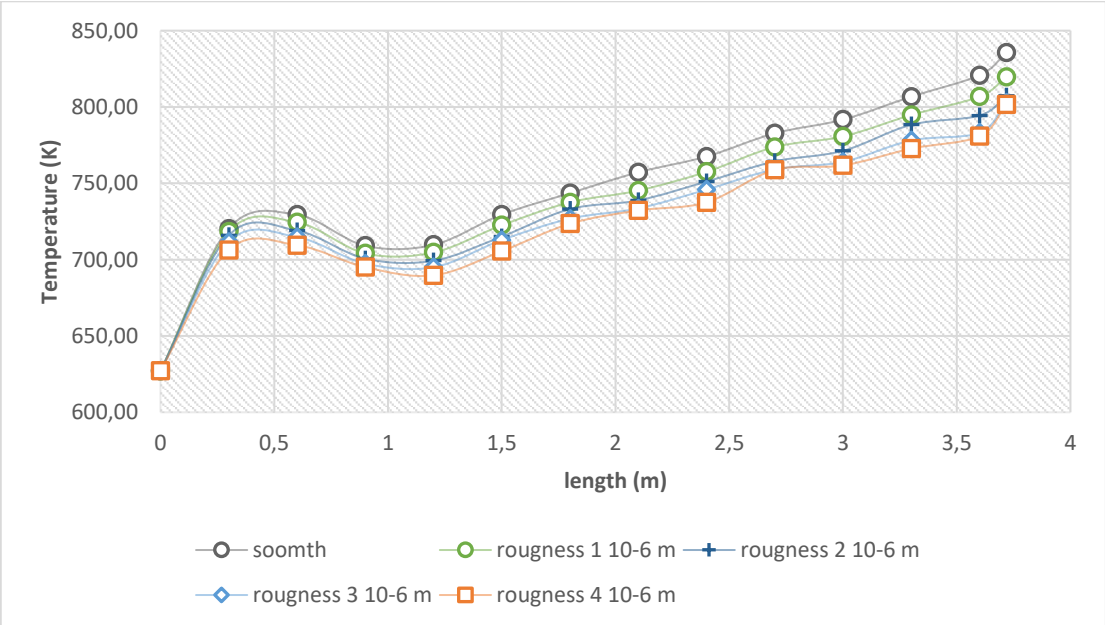

Figure 244. Temperature variations with pipe length (SST k-ω model)

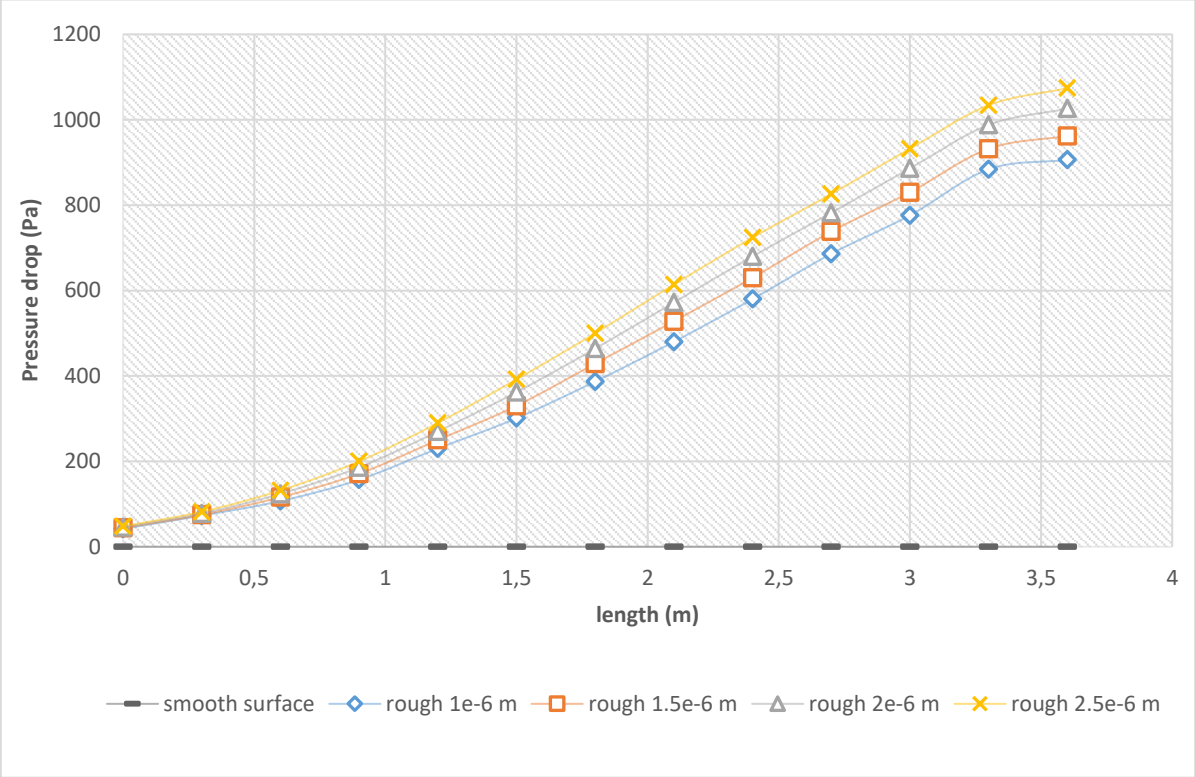

Figure 245. Pressure drop variations with pipe length (SST k-ω model)

6.1.3.6 Summary

The rough surface effects on wall temperature and pressure drop are explored by CFD simulation under supercritical operating condition, the turbulent heat and mass transfer models k-ε and SST k-ω are adopted for calculation under smooth and rough surface states. The following conclusions are drawn based on the simulation results:

- Pipe roughness has the influence on the wall temperature distribution, wall temperature decreases with the pipe roughness.
- Different models reach the similar results in simulation.
- Pressure drop in the pipe increases with the pipe roughness height.

6.1.4 Horizontal flow in a rough tube with different roughness constants

6.1.4.1 Geometry, mesh and roughness

The experimental results with the smooth tube are adopted to verify the developed model, afterwards the rough surface tube is used to investigate the effects of roughness constant. The schematic diagram shown in Figure 246 presents the layout of the test section tube, the tube Φ32×3 mm is used in the experiment conducted by Yu et al. (2011), the tube length is 2000 mm.

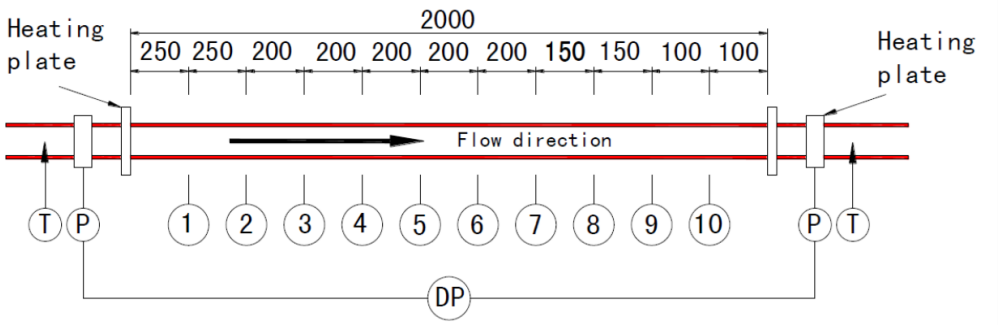

Figure 246. Structure of the test section (Yu et al., 2011)

The meshes of this study include the tube wall in order to get a more rigorous examination on the heat transfer. The tube mesh design is shown in Figure 247, the meshes near the wall are refined in the fluid and solid regions to catch the changes of temperature and flow, where the non-dimensional length y+ is lower than 0.5. The maximum, minimum, and average non-dimensional length y+ are shown in Figure 248. The cell number of the model is over 3,000,000 for the good simulation precision, the maximum non-orthogonality is 29.50 and the average non-orthogonality is 4.50.

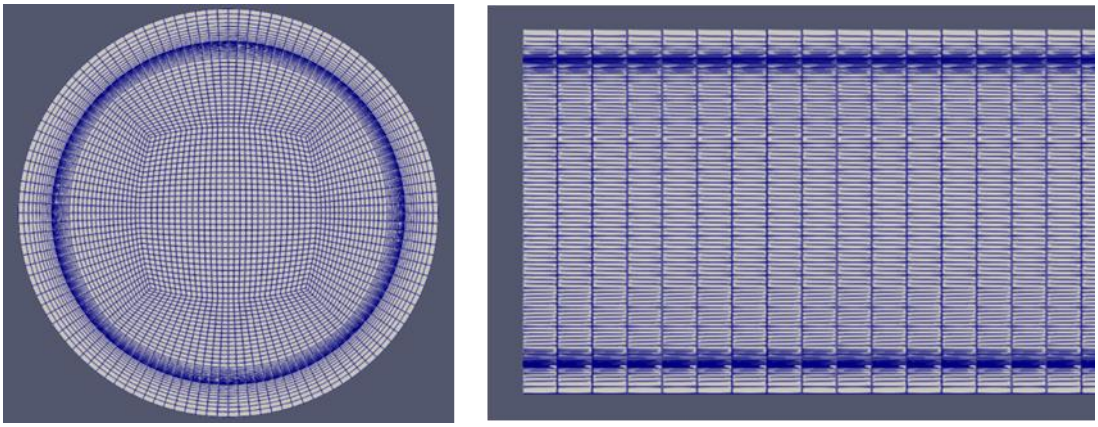

Figure 247. Tube mesh design

In the model, the rough surface is set by the boundary condition, which depends on the roughness height (Ks) and the roughness constant (Cs). According to the research conducted by Nikuradse (1950), a moderate value of the relative roughness ($\bar{\Delta} = {}^{d}/_{\Delta} = 120$) is selected, which leads to an absolute roughness height Ks=0.266 mm. The roughness constants are set as 0.5, 0.7 and 0.9 to gain uniform and non-uniform rough surfaces for comparison purpose.

```
# y+ ()
# Time          patch           min             max             average
0               fluid_to_tube   2.483340e-01    2.485300e-01    2.484181e-01
1e+03           fluid_to_tube   8.775273e-02    1.754697e-01    1.716775e-01
2e+03           fluid_to_tube   8.776253e-02    2.111229e-01    2.025354e-01
3e+03           fluid_to_tube   8.776254e-02    2.493176e-01    2.331468e-01
4e+03           fluid_to_tube   8.776254e-02    2.893875e-01    2.623861e-01
5e+03           fluid_to_tube   8.776254e-02    3.319889e-01    2.903519e-01
6e+03           fluid_to_tube   8.776253e-02    3.785547e-01    3.174297e-01
7e+03           fluid_to_tube   8.776252e-02    4.314429e-01    3.441142e-01
8e+03           fluid_to_tube   8.776251e-02    4.942660e-01    3.708234e-01
9e+03           fluid_to_tube   8.776250e-02    5.709394e-01    3.971200e-01
1e+04           fluid_to_tube   8.776249e-02    6.461290e-01    4.169636e-01
1.1e+04         fluid_to_tube   8.776245e-02    6.602918e-01    3.942096e-01
1.2e+04         fluid_to_tube   8.776243e-02    7.951341e-01    4.132974e-01
1.3e+04         fluid_to_tube   8.776245e-02    9.654688e-01    4.244749e-01
1.4e+04         fluid_to_tube   8.776246e-02    1.022004e+00    4.260569e-01
1.5e+04         fluid_to_tube   8.776246e-02    1.038089e+00    4.261110e-01
```

Figure 248. Non-dimensional length y+

6.1.4.2 Methodology

The numerical simulation is conducted by using OpenFOAM software. A finite-volume numerical solution technique is used to solve the model equations based on conjugate heat transfer mode, the fluid and solid regions are calculated respectively by fluid and solid solvers.

For the solid region, the gradient terms in the governing equations are modelled with the secondary-order linear scheme, and the diffusion terms are developed by the central-differenced and second-order accurate scheme. For the fluid region, the physical properties of supercritical water are extracted from the table based on pressure and temperature to gain accurate physical properties data. This is because that the physical properties are sharply changing in the region around the supercritical point. The convection terms in the governing equations are modelled with the secondary-order upwind scheme which uses the upstream value and gradient to compute the value at the control volume face, the diffusion terms are central-differenced and second-order accurate scheme. The velocity and pressure terms are coupled by using pressure-implicit method for pressure-linked equations (PIMPLE) algorithm. Finaly, the SST k-ω turbulent model is used in the simulation of fluid region.

The boundary conditions in the simulation is the same as the experiment, the inlet mass flow and outlet pressure boundaries are applied to obtain the pressure drop in the test section. Furthermore, in order to gain the better heat transfer simulation on the internal wall, the conjugate heat transfer mode is used in the simulation as mentioned before. The outer wall boundary condition of the tube is modelled as adiabatic, and a constant heat flux is imposed to the tube to gain a 300 kJ/m^2 average heat flux on the internal tube wall. The rough wall, as previous mentioned, is set by the boundary conditions with Ks=0.266 mm and Cs=0.5, 0.7, 0.9.

6.1.4.3 Modelling verification

The numerical models are verified by comparing simulation results with the experimental data obtained by Yu et al. (2011) under smooth surface condition. The inlet temperature is increased in the bulk enthalpy range of 1200 to 3000 kJ/kg in a 2m tube, then the bulk enthalpy range is divided into several parts in order to compare with the experimental results. The inlet pressures are 23 MPa and 25 MPa, the inlet mass flux is 600 kg/(m^2·s) and internal wall heat flux is 300 kW/m^2. The roughness sectors Ks and Cs are set as 0 and 0.5 respectively to get the smooth internal wall surface.

The variations of internal top and bottom wall temperatures at 23 MPa are shown in Figure *249*, it can be found the simulation results and the experimental data have the similar variation trends. For the top internal wall, its temperature increases in the bulk enthalpy range of 1300 to 1700 kJ/kg at first, afterwards the temperature reaches the first peak around the supercritical point of bulk temperature where the bulk enthalpy is approximately 1880 kJ/kg. The top wall temperature slightly reduces after the first peak and stays at 730 K until the bulk enthalpy reaches 2600 kJ/kg. Then the top internal wall temperature increases sharply after the bulk enthalpy is over 2600 kJ/kg. For the bottom internal wall, its temperature continually increases in the enthalpy range between 1300 kJ/kg and 1800 kJ/kg, which is similar to the top wall temperature change. After that, the bottom temperature keeps at 665 K in the bulk enthalpy range from 1800 kJ/kg to 2600 kJ/kg. The bottom internal wall temperature rises again over the enthalpy 2600 kJ/kg and shows a rapid growth in the supercritical region. Comparing with the experimental data, the top wall temperature displays the differences in the enthalpy range of 1300 kJ/kg to 1800 kJ/kg, while the bottom wall temperature shows good agreements in all regions. The maximum deviation on top wall temperature between the simulation and experimental results is 11.2% (84.34 K), and the maximum deviation of the bottom wall temperature is only 4.89% (32.15 K).

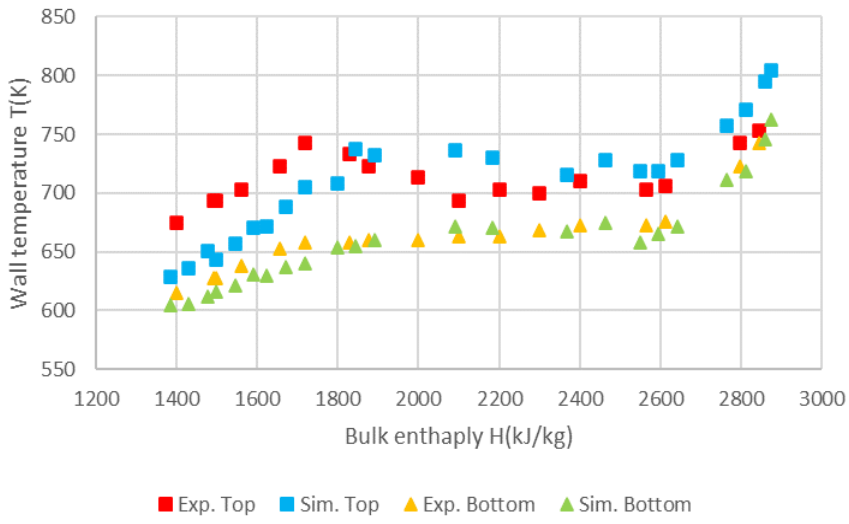

Figure 249. Wall temperature distributions at 23 MPa under smooth surface condition

The experimental and simulation results of top and bottom internal wall temperatures at 25 MPa are shown in Figure 250. For the top internal wall, the temperature increases in the bulk enthalpy range between 1300 kJ/kg and 2100 kJ/kg. After that, the increase slows down around 2100 kJ/kg and the temperature keeps at approximately 750 K in the bulk enthalpy range from 2100 kJ/kg to 2600 kJ/kg. At last, the top internal wall temperature increases rapidly when the bulk enthalpy is higher than 2600 kJ/kg. For the bottom internal wall, the temperature rises continually in the enthalpy range of 1300 to 2100 kJ/kg. Afterwards, the temperature keeps at 680 K in the bulk enthalpy range from 2100 kJ/kg to 2400 kJ/kg. Finaly, the bottom wall temperature increases slowly as the bulk enthalpy is lower than 2600 kJ/kg, but it shows a rapid growth in the supercritical region when the bulk enthalpy is higher than 2600 kJ/kg. Comparing the simulation results with the experimental data at 25 MPa case, the maximum deviation of the top wall temperature is 11.9% (89.60 K), and the maximum deviation of the bottom wall temperature is 10.8% (79.16 K).

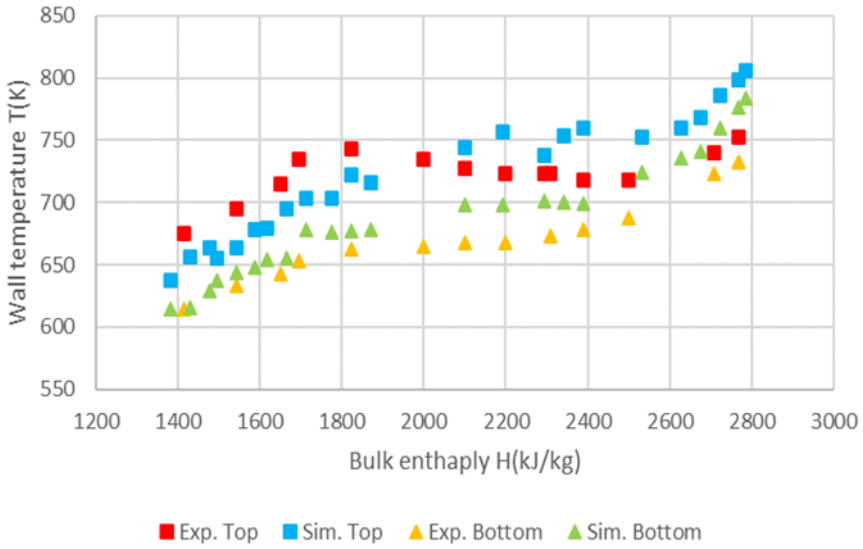

Figure 250. Wall temperature distributions at 25 MPa under smooth surface condition

To summarize, the simulation results are compared with the experimental data, it is found the simulation results of the top and bottom wall temperatures at both 23 MPa and 25 MPa states are in good agreement with the test data. Therefore, the developed modelling can be used to explore supercritical water flow characteristics in horizontal flow mode.

6.1.4.4 Roughness effect on wall temperature

The supercritical water turbulent flow and heat transfer in the horizontal tube with different roughness designs are investigated. The variations of top and bottom internal wall temperatures of supercritical water flow at 23 MPa through a tube with uniform and non-uniform rough walls are shown in Figure 251. The rough walls are set as Ks=0.266 mm and Cs=0.5, 0.7, 0.9. The variation tendencies of these rough wall results are similar with those of the smooth tube case. But the top internal wall temperatures of rough tube with Cs = 0.5 and 0.7 are approximately 4 K lower than those of the smooth case, and the maximum reduction is about 1.2%. The influence of heat transfer in the tube with Cs = 0.9 is higher than others, this leads to approximately 6 K reduction of top internal wall temperature, correspondingly the maximum reduction is 1.9%. Compared with the smooth tube case, the bottom internal wall temperatures of both the uniform and non-uniform roughness cases have approximately 2 K reduction. Compared with the uniform roughness cases, the bottom internal wall temperatures in non-uniform roughness cases have approximately 0.5 K decrease.

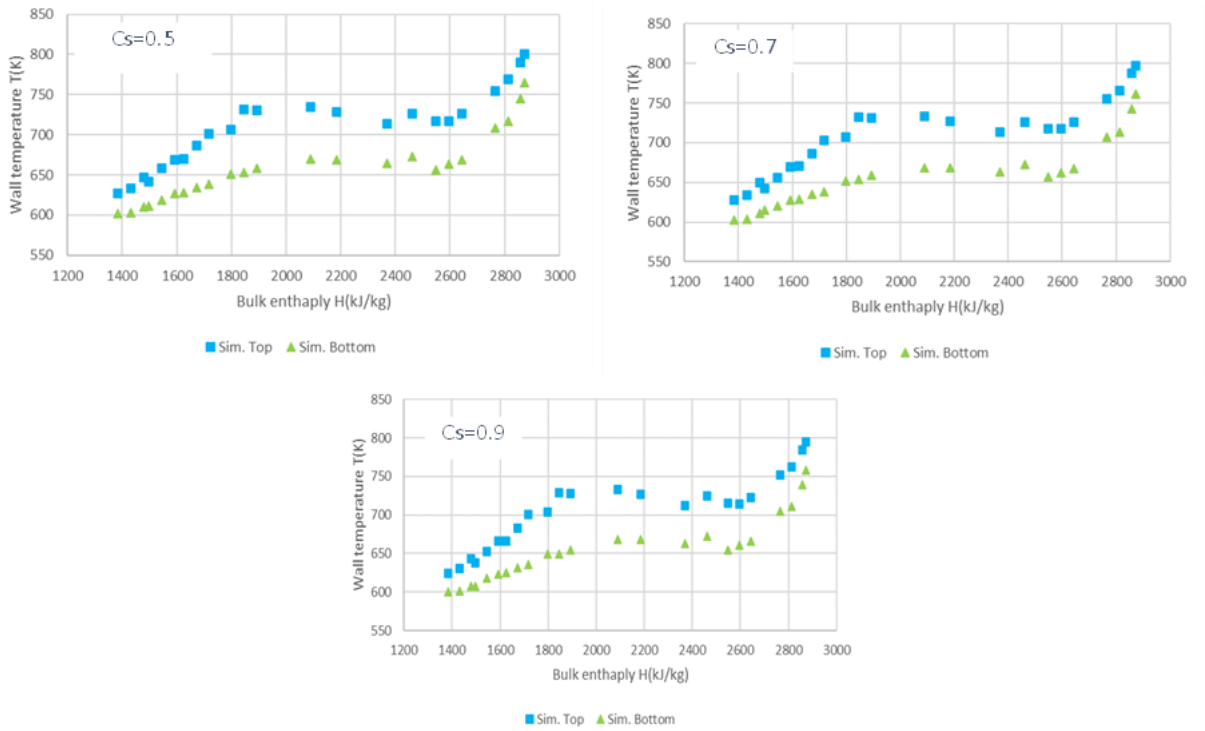

Figure 251. Wall temperatures in rough tube with P=23MPa

The changes of top and bottom internal wall temperatures of supercritical water flow at 25 MPa through the tube with uniform and non-uniform roughness walls are displayed in Figure 252. The roughness design is the same as the case at 23 MPa. The temperature variation trends of these cases are also similar to those of the smooth tube wall. The top internal wall temperatures of rough tube with Cs = 0.5 and 0.7 are approximately 4 K lower than those of the smooth tube, and the maximum reduction is 1.3%. The influence of heat transfer in rough tube with Cs = 0.9 is higher than others, this leads to approximately 6 K decrease of top internal wall temperature compared with the smooth case, and the maximum reduction is 2.1%. On the other hand, both the uniform and non-uniform rough tubes display approximately 2 K reduction of bottom internal wall temperature. Comparing with the uniform roughness cases, the bottom internal wall temperatures in non-uniform roughness cases have approximately 0.5 K decrease.

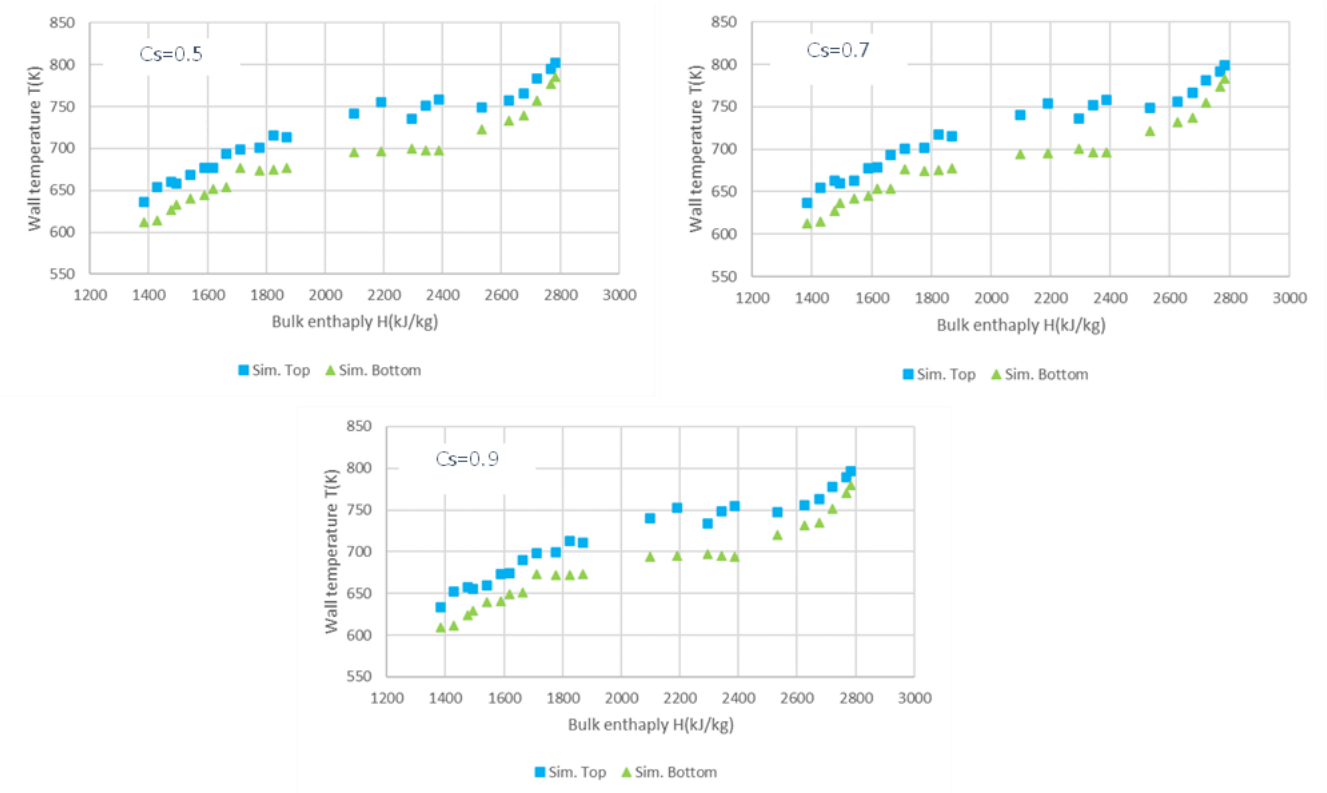

Figure 252. Wall temperatures in rough tube with P=25MPa

To summarize, the rough wall surface with Ks = 0.266 mm increases the thermal conductivity at both 23 and 25 MPa states, this is because that the rough surface improves the near wall turbulent flow. On the other hand, by comparing uniform and non-uniform rough surface cases, it is found that the difference between the maximum and minimum roughness heights could improve the turbulent flow and corresponding the heat transfer, which lead to the reduce of internal wall temperature.

6.1.4.5 Roughness effect on pressure drop

The frictional pressure drop is discussed in this section. The variations of friction factor with inlet Reynolds number under different roughness constants are shown in Figure *253*. The friction factor is calculated as:

$$f = \frac{-2(\Delta P/_{\Delta x})d}{\rho_m U_m^2} \tag{118}$$

$$T_m = \frac{T_{in} + T_{out}}{2} \tag{119}$$

where $\Delta P/_{\Delta x}$ is the pressure drop per unit length, ρ_m and U_m are the thermos-physical properties and evaluated at the mean temperature T_m, which is based on the inlet and outlet temperatures.

It can be found that the friction factor decreases with Reynolds number when the Reynolds number is less than 550,000. But the factor increases when the Reynolds number is over 550,000. Furthermore, the friction factors with non-uniform roughness's Cs=0.7 and 0.9 are higher than those of the uniform roughness Cs=0.5.

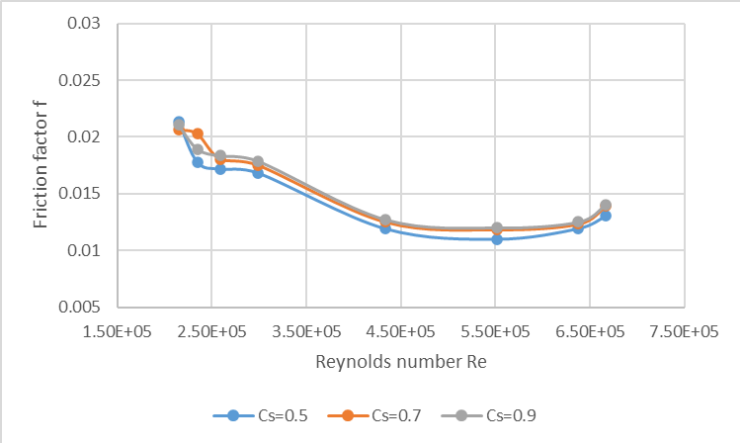

Figure 253. Friction factor variations with inlet Reynolds number

6.1.4.6 Summary

In order to achieve a better understanding of supercritical water heat transfer in a horizontal tube with rough surface, this study explores the influences of the roughness on the wall temperature and pressure drop. The CFD simulations based on the RAS model SST k-ω are performed and the following conclusions are drawn:

- The simulation model is verified by comparing the simulation results with experimental data in a smooth tube. The simulation results are in good agreement with the test data both at 23 MPa and 25 MPa states.
- The simulation results show that rough wall temperature is lower than the smooth's under the same operating condition, this means rough surface could improve heat transfer for supercritical water flow in the tube.
- The simulation results with different roughness constants are compared, it can be found that the roughness constant Cs has the positive effect on the tube heat transfer improvement.
- The friction factor is influenced by Reynolds number, the friction factor of the non-uniform rough tube is higher than that of the uniform rough tube.

6.1.5 Horizontal flow in a rough tube with different roughness heights

6.1.5.1 Geometry, mesh and roughness

As for the horizontal flow, the effect of buoyancy is a big issue which leads to a nonuniform local temperature distribution around the tube periphery. In order to clarify the tube roughness height influences, the CFD modelling is developed, at first the modelling is verified by comparing with the available experimental data achieved by Bazargan et al. (2005) under the smooth surface state, then the rough tube is investigated with supercritical water. So the tube geometry in the modelling is the same as the experiment case as shown in Figure 254. The overall tube test section length is 3 m, the inner diameter of the tube is 6.3 mm and the outer diameter is 9.4 mm.

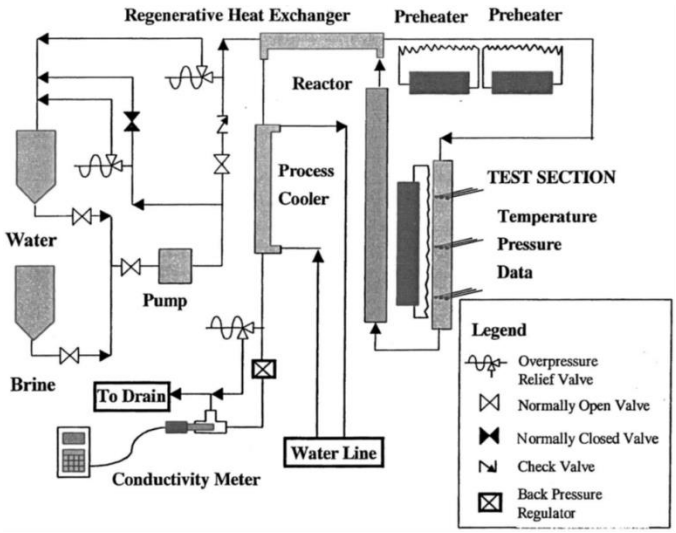

Figure 254. Schematic of test facility (Bazargan et al., 2005)

A structured non-uniform three-dimensional grid system is used to solve the discretized equations. To obtain more accurate internal wall heat transfer, the mesh adjacent to the wall has the minimum thickness, where the non-dimensional length y+ is lower than 0.5. The total number of meshes is 2,130,000, the average non-orthogonal is 5.79, the maximum non-orthogonal is 42.62, and the maximum skewness is 0.56. The tube mesh is shown in Figure 255.

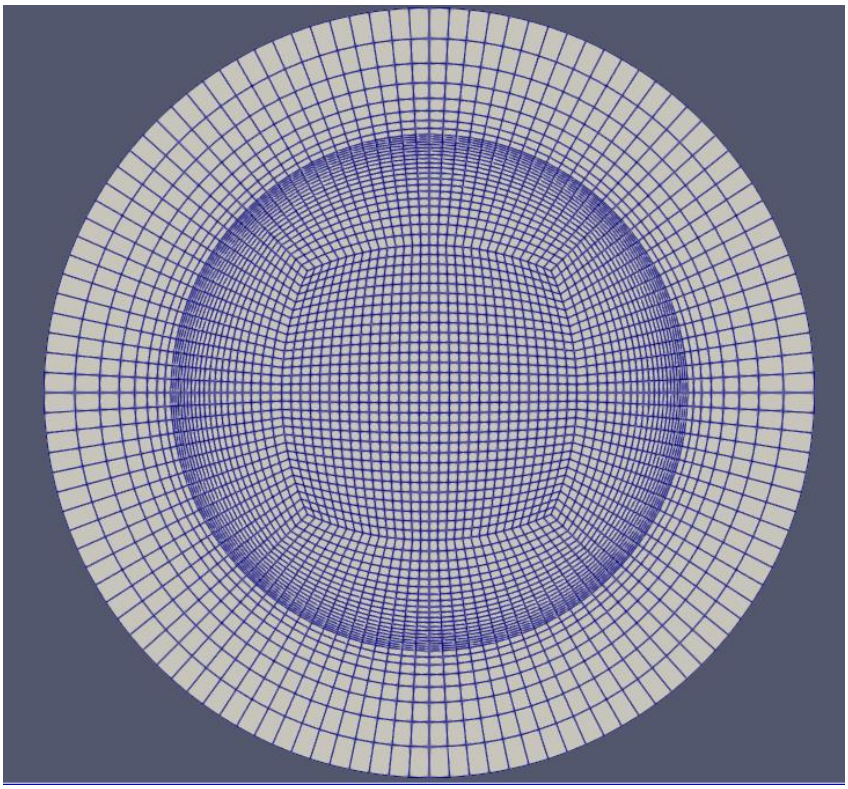

Figure 255. Meshes of tube inlet

The roughness surface is realized by the boundary condition in the research. This boundary condition provides a turbulent kinematic viscosity condition when using wall functions for rough surfaces, based on turbulence kinetic energy (see Weller 2021). Two parameters Hs and Cs are set in the boundary condition, where Hs is the sand-grain roughness height, and Cs is the roughness constant. In this study, Cs is set as 0.5 to get a uniform rough surface, Hs is set as 0 to achieve the smooth surface for the verification purpose, and 0.008d, 0.002d, and 0.0001d to simulate the heat transfer under roughness condition with different roughness height.

6.1.5.2 Methodology

Three turbulence models, standard k-ε, buoyant k-ε and SST k-ω, are used in this study. The finite volume scheme is employed to do the spatial discretization, the central differential scheme for the diffusive fluxes is adopted. For the convective fluxes, the second-order upwind scheme is used in this simulation. The solution algorithm is based on Simple solver to resolve the coupling between velocity and pressure.

To validate the developed models by comparing the simulation results with the experimental data, the boundary condition in the simulation is the same as that of the experimental study, which includes the pressure, temperature, and heat flux. The diameter of the test tube is 6.3 mm, the thickness of the tube is 1.55 mm, and the length of the test section is 3 m. The system pressure is 24.4 MPa, and the mass flux is 340 kg/m^{2}s. The coupling solver is used in the simulation to gain the better simulation results on heat transfer. Therefore, a fixed heat source is added to the tube to obtain a 300 kJ/kg average heat flux on the internal wall. For the roughness boundary condition, the roughness constant is set as Cs=0.5, and the roughness height is set as Hs=0.008d, 0.002d, and 0.0001d.

6.1.5.3 Modelling verification

In order to verify the developed modelling, the simulation results are compared with the experimental data achieved by Bazargan et al. (2005). Based on the test condition in the literature, the tube inlet water pressure is 24.4 MPa, its inlet temperature is 412 K, inlet fluid speed is 0.362 m/s and inlet Reynolds number is 10500, the mass flux is 340 kg/m^2, the tube is electrically heated with AC current to provide a uniform heat flux of 300 kW/m^2.

The simulation results under smooth surface condition and the experimental data are shown in Figure 256. As for the SST k-ω turbulent model results, it can be found that when the bulk enthalpy is lower than 1500 kJ/kg, the simulation results are in good agreement with the experimental data compared to the results in higher bulk enthalpy area, the maximum deviations of internal wall temperatures between the simulation results and the tested data are 8.28% (60.0 K) and 6.92% (46.2 K) for top and bottom surfaces respectively. For the standard k-ε turbulent model, a good agreement between the calculated results and experimental data is achieved for the bottom surface, but the simulated temperatures of top surface are much lower than the tested data, the maximum differences of internal wall temperatures between the modelling results and the experimental data are 11.47% (87.5 K) and 6.05% (31.6 K) for top and bottom surfaces respectively. As for the buoyant k-ε turbulent model, the simulation results are quite similar to those of the standard k-ε model, the maximum deviations of internal wall temperatures between the simulation results and the experimental data are 11.31% (63.7 K) and 6.08% (31.8 K) for top and bottom surfaces respectively. In summary, the overall performance of the SST k-ω turbulent model at smooth surface state is better than standard and buoyant k-ε models, but the simulated bottom surface temperatures of the SST k-ω model in supercritical region are worse than those of the two k-ε models.

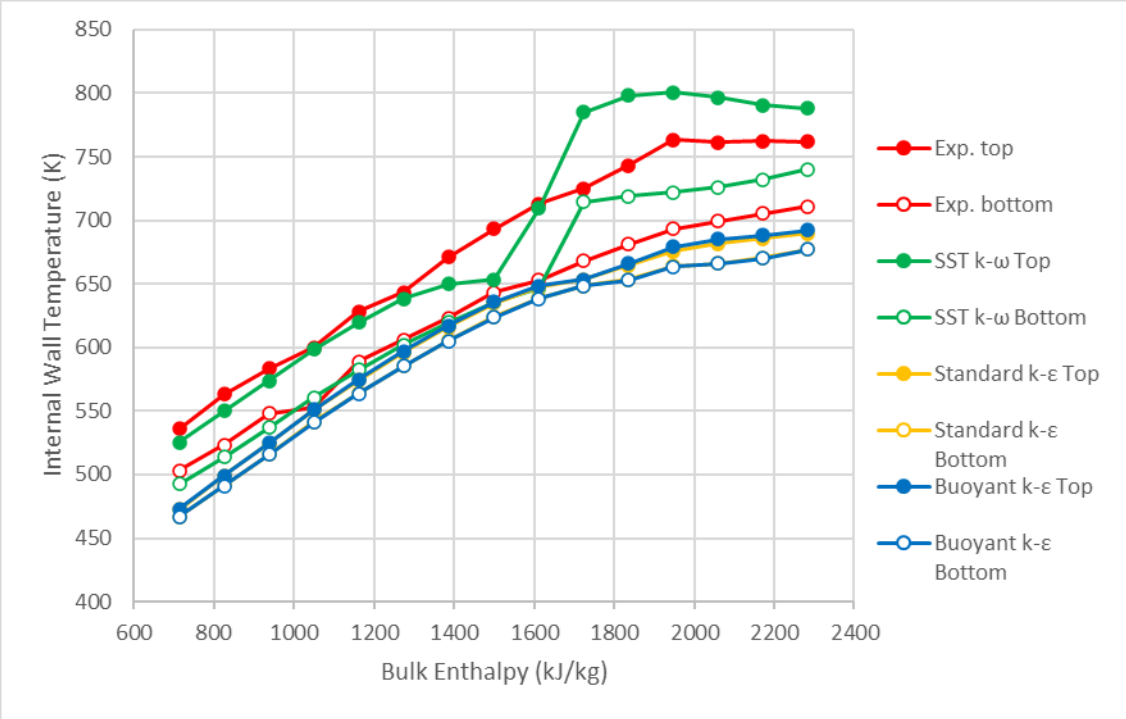

Figure 256. Model verification under smooth condition: P=24.4 MPa, G=340 kg/m^{2}s, q=300 kW/m^2

6.1.5.4 Roughness effect on wall temperature

The simulation based on standard k-ε turbulent model does not obtain satisfactory results, the top and bottom internal wall temperatures are shown in Figure 257. It can be found that the obviously influence of rough surface is in the area of bulk enthalpy over 1800 kJ/kg. Furthermore, the increase of roughness height does not provide obvious differences on internal wall temperature. The maximum temperature drop of the top wall is 28 K, and the maximum temperature reduction of the bottom wall is around 18 K in this case.

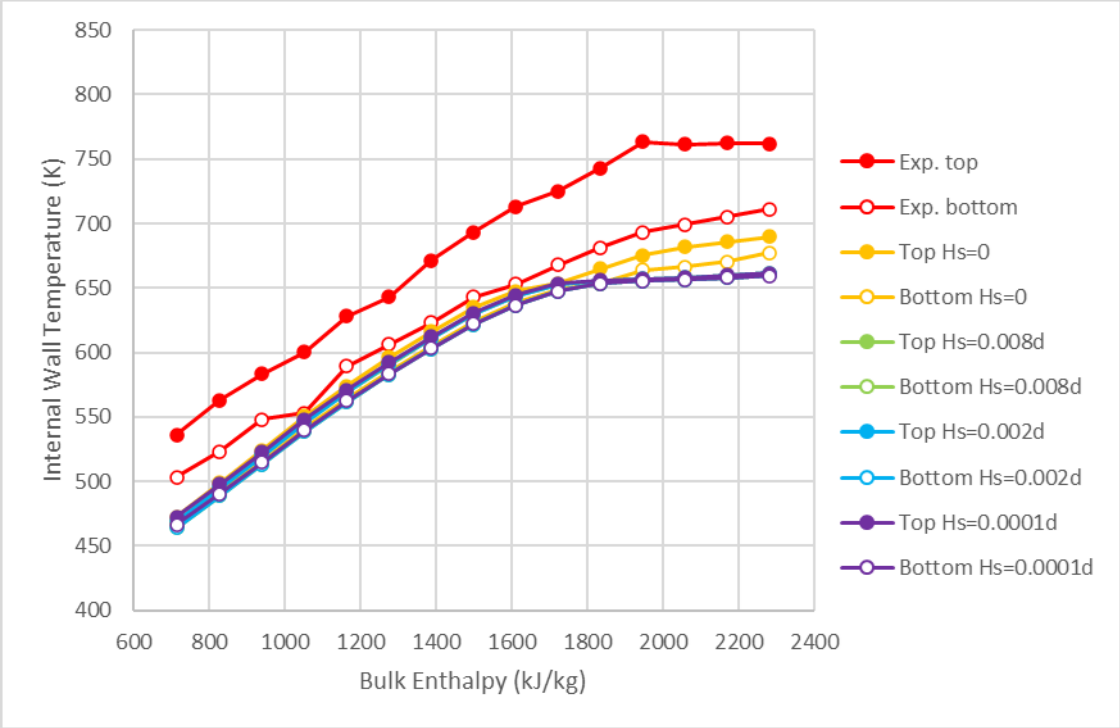

Figure 257. Wall temperature variations with bulk enthalpy by standard k-ε turbulent model: P=24.4 MPa, G=340 kg/m^{2}s, q=300 kW/m^2

The buoyant k-ε turbulent model does not obtain any better results with rough surface compared to standard k-ε model. Figure 258 shows the simulation results with different roughness heights based on the buoyant k-ε model. It can be found that even the simulation results under smooth condition are better than those of standard k-ε model because of the additional buoyancy generation and dissipation terms, but these additional buoyancy terms do not have obviously improvement for the rough surface case. The obvious influence of rough surface can be found in the bulk enthalpy range over 1800 kJ/kg and the increase of roughness height does not provide obvious differences on internal wall temperatures, which are similar with the results obtained by standard k-ε model. The maximum decrease on top wall temperature is approximately 31 K, and the maximum reduction on bottom wall temperature is around 18 K for all roughness heights. These results show that buoyant k-ε turbulent model cannot obtain satisfactory results with the change of roughness height.

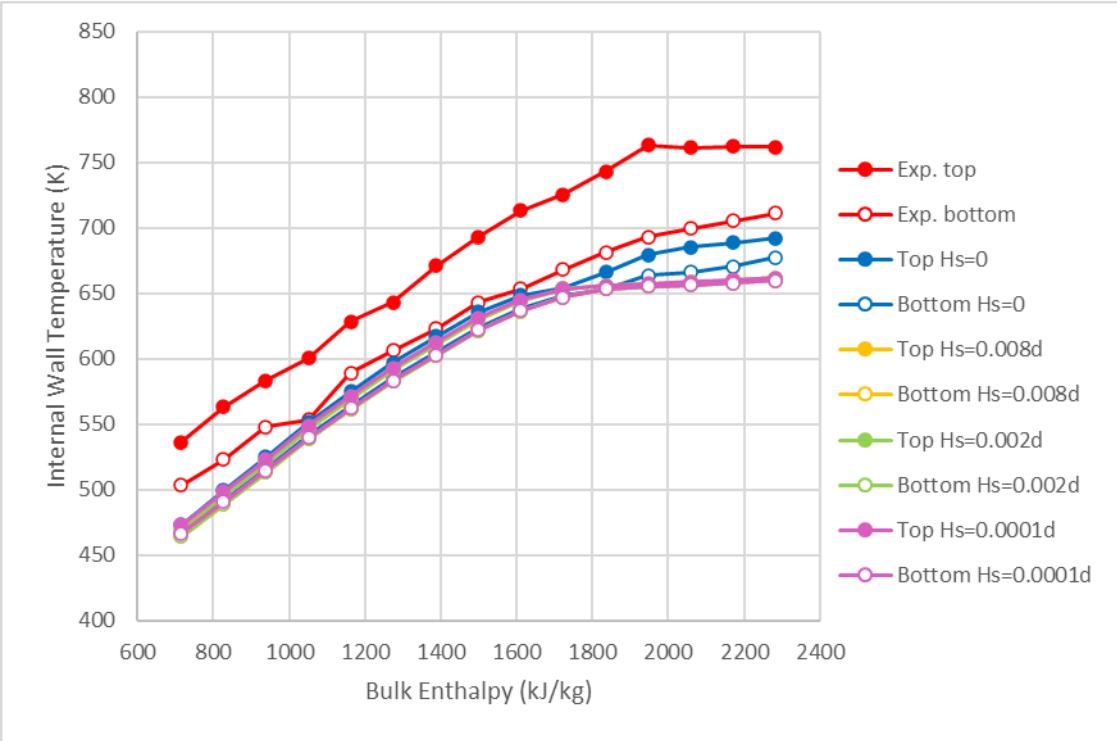

Figure 258. Wall temperature variations with bulk enthalpy by buoyant k-ε turbulent model: P=24.4 MPa, G=340 kg/m^{2}s, q=300 kW/m^2

Figure 259 shows the SST k-ω model's simulation results in rough surface condition. Compared with the smooth simulation results (Hs=0), the top wall temperature is prominently lower, and the bottom wall temperature is slightly reduced. The maximum reductions on top wall temperature are approximately 143 K when Hs=0.008d, 140 K when Hs=0.002d, and 115 K when Hs=0.0001d respectively. The maximum reductions on bottom wall temperature are around 83 K when Hs=0.008d, 81 K when Hs=0.002d, and 76 K when Hs=0.001d respectively. These mean that rough surface could increase the heat transfer on top surface. Furthermore, the influence of rough surface increases with roughness height. Compared with the results of Hs=0.002d, the simulation data of Hs=0.0001d only show prominent reduction on wall temperature when the bulk enthalpy is higher than 2000 kJ/kg. In summary, the SST k-ω model could predict the increase of heat transfer under rough surface condition, it also could reflect the change of heat transfer with roughness height.

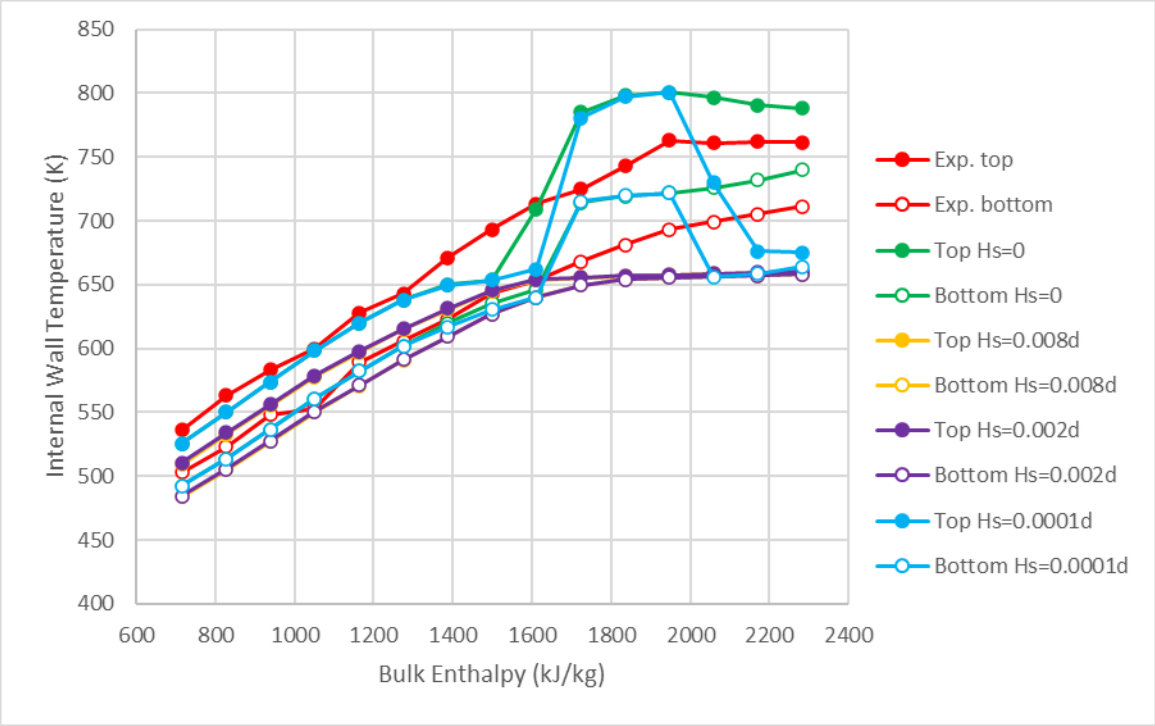

Figure 259. Wall temperature variations with bulk enthalpy by SST k-ω turbulent model: P=24.4 MPa, G=340 kg/m^{2}s, q=300 kW/m^2

6.1.5.5 Summary

This study explores the influences of the roughness height on the wall temperature with three turbulent models. The following conclusions are drawn:

- For the smooth surface state, the overall performance of the SST k-ω model is better than standard and buoyant k-ε models, except the bottom surface temperatures in supercritical region.
- Compared with standard k-ε model, buoyant k-ε model presents better simulation results under smooth surface state. This is because the additional buoyancy term in buoyant k-ε model.
- In the three tested turbulent models, the SST k-ω model is most suitable to reflect the effect of roughness height. Standard and buoyant k-ε models could not catch the influence of roughness height.

6.2 CONTRIBUTION BY UNIPI

A suitable simulation and modelling of mass transfer in supercritical water requires a deep understanding of the involved phenomena, which encompass thermal-hydraulics, chemistry and materials aspects. It is thus clear that developing a sound model for turbulent heat and mass transfer along corroded surfaces needs a widespread set of experimental data for its validation and assessment.

The present contribution reports on the activities performed at the University of Pisa in the frame of the ECC-SMART project in the frame of Subtask 3.3.6, proposing a proof of concept of the approach that could be adopted for the analysis of transported oxygen, hydrogen and corroded materials both in bulk and in the vicinity of the wall by CFD. The proposed model strongly reckons on the past experiences and lessons learned at the University of Pisa in the frame of

heat transfer to supercritical fluids. In particular, the use of the so called “passive scalars” in the STAR-CCM+ environment is again proposed in order to model transport of material in the supercritical water flow.

6.2.1 Modelling of turbulent mass transfer

The simulation of mass transfer of transported species in supercritical water can be implemented via dedicated equations, each one addressing the balance of a transported scalar identified as the concentrations of the involved species. The additional quantities could either have a “passive” status, thus just working as tracers, or an active role, affecting the results of the turbulence, thermal and flow fields.

The present proposal investigates the chance to consider the transported species as not affecting the global prediction of the mass and heat transfer in supercritical water, as an additional information regarding the possible corrosion rate at the wall and oxygen or hydrogen transport in the fluid flow. As a consequence, the concentration of each additional species may depend on the main flow parameters, as well as it is linked to other species concentrations, without affecting the global results of the calculation. As an example, the production rate of corroded materials could be dependent on the oxygen concentration near the wall, wall temperature and near wall shear stresses; on the other hand, the transport of corroded material will not have any impact on heat and mass transfer with the supercritical water.

Passive scalars transport equations are among the features that users may include in any STAR-CCM+ environment (Simcenter STAR-CCM+®, 2018) in order to increase the amount of information and phenomena to be investigated in the performed calculations. As an example, a passive scalar for the temperature variance was introduced by University of Pisa in the frame of past studies in order to allow the code adopting the AHFM relation for the prediction of the turbulent heat flux contribution (see, e.g., Pucciarelli et al., 2016). This relation indeed requires the knowledge of the temperature variance distribution, something that is not provided by 2-equation model implemented in STAR-CCM+.

A similar approach can be adopted for the mass transfer analysis addressed in the present section. Passive Scalars could be included in any fluid flow directly from the Physics node (see e.g. Figure 260 for reference).

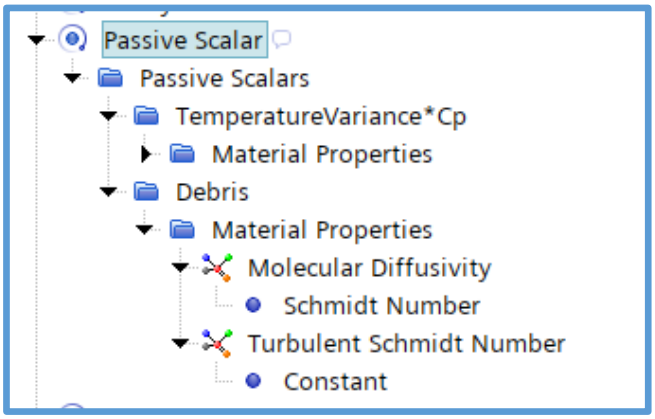

Figure 260. An example of the use of passive scalars in STAR-CCM+

The user is allowed to add as many passive scalars as needed, while a fixed structure of the passive scalar transport equation (reported below) in which transient, convective, diffusive and source terms can be included, must be adopted.

$$\frac{\partial}{\partial t}\int_V \rho\phi_i dV + \oint_A \rho\phi_i \mathbf{v}\cdot d\mathbf{a} = \oint_A \mathbf{j}_i \cdot d\mathbf{a} + \int_V S_{\phi_i} dV$$

Figure 261. Passive scalar balance equations afopted in the STAR-CCM+ code (Simcenter STAR-CCM+®, 2018)

In particular, in the above equation:

- i is the index of the i-th component (passive scalar);
- V is the control volume;
- $\mathbf{j}_i$ is the diffusion flux;
- **a** is the area vector;
- $S_{\Phi i}$ is the source term related to the i-th scalar component
- ϕ_i is the i-th transported scalar component.

The diffusion flux contribution accounts for both molecular and turbulent transport phenomena. The code indeed requires the user to provide an estimation of both the molecular and the turbulent Schmidt numbers. These quantities can be included as constant parameters as well as field functions defined on the basis of local values of other relevant properties. The source term distribution can be defined via field functions as well, thus allowing for a detailed representation of the addressed phenomena.

As it can be observed from Figure 262 (from Penttilä, 2020), the production rate of the oxide layer is strongly affected both by the selected material for the pipe wall and the wall temperature. Any developed model thus should be tuned depending on the selected operating conditions.

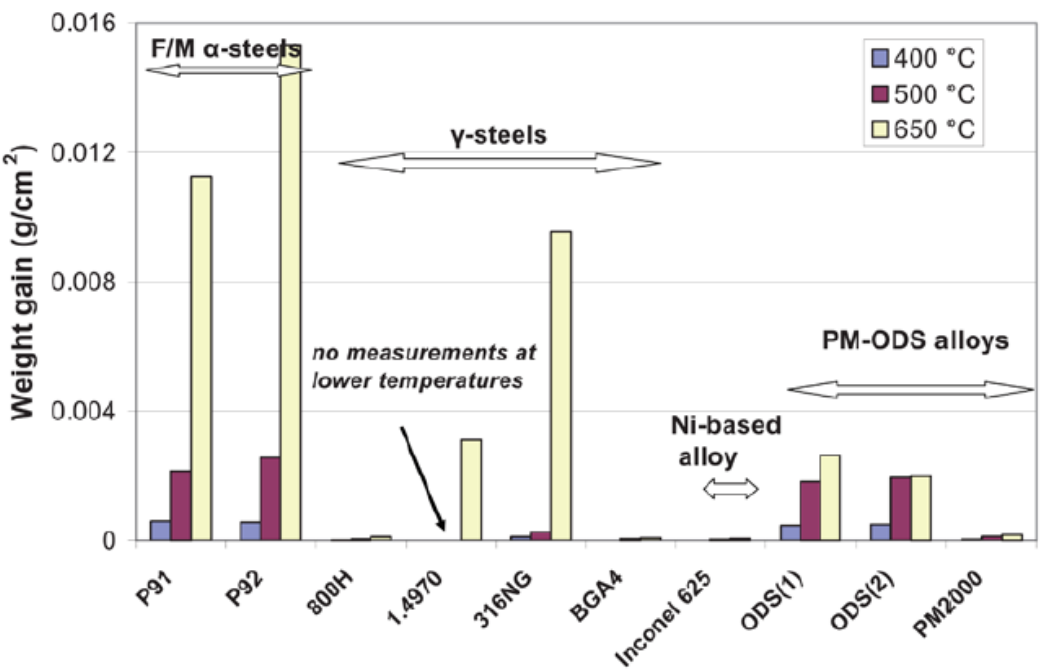

Figure 262. Weight gain due to corrosion for differet materials (from Penttilä, 2020)

As mentioned above, the present work focuses on the proof of concept of the proposed approach. It must also be noted that no reference scenario to be simulated is available at the present time; consequently, rather than achieving peculiar representations of selected experimental data and the related validation, it is instead devoted to report about its potential capabilities in reproducing the addressed phenomena. In the following, a sample of Oxygen and corroded material distributions for a selected case are reported. The obtained results are to be considered just a purely numerical demnostration of the capabilities of the model, not to provide any specific quantitative estimation of the addressed phenomenon.

6.2.2 Selected calculation case

A reference case considering heat transfer to supercritical water at 23.5 MPa is selected from the experimental data case by Pis'menny (Pis'menny et al., 2005a) already shown in Figure 13. As it can be observed in Figure 263 the wall temperature experiences values both above and below the supercritical temperature of water, also reporting a strong deterioration phenomenon. In the parametrical analysis, two surface roughness values of 15 and 30 μm were assumed. As it can be observed, for small enough roughness, heat transfer deterioration is predicted, while when roughness becomes sufficiently large, normal heat transfer is predicted as a consequence of the improved turbulence and heat transfer conditions.

Considering the above mentioned transport equation for passive scalars, two additional transported scalars are included in the model developed for ECC-SMART, combining the AHFM model and the rough wall treatment developed at the University of Pisa and described in previous sections: they are the Oxygen and corroded material concentration. The assumed inlet conditions for the Oxygen and the corroded material concentrations are set parametrically at 0.001 and 0, respectively, in arbitrary units. Concerning the molecular and turbulent Schmidt numbers, the default value of 0.9 is selected for both the parameters for the two transported scalars.

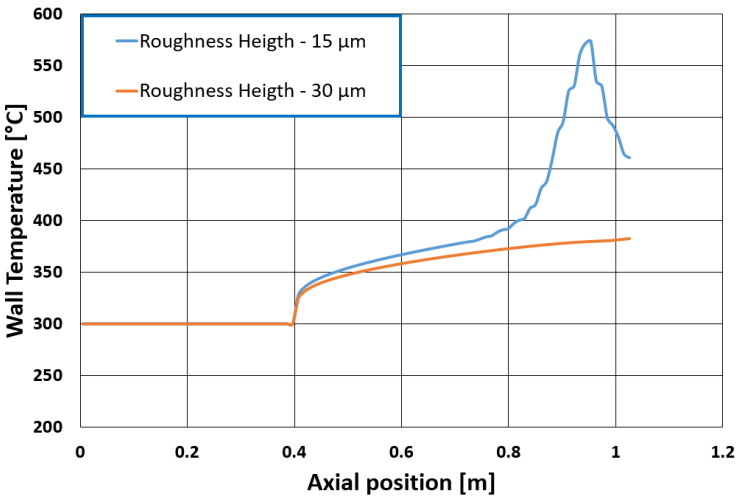

Figure 263. Predictions obtained of the data by Pis'menny et al. (2005, 2005a) with water at 23.5 MPa, 6.28 mm ID, Tin = 300 °C, G = 508 kg/(m^{2}s), q" = 390 kW/m^2 for the selected roughness heigths

For the source terms, it is assumed that they are mainly located in the near wall region; the same f_{smooth} relation described in Section 5.1.2 is here again considered:

$$f_{smooth} = \frac{1}{2}\left[1 - tanh\left(\frac{y - \varepsilon_{rough}}{0.3\ \varepsilon_{rough}}\right)\right] \tag{120}$$

The considered form of the Oxygen source is thus:

$$S_{\mathrm{O}} = -C_1 * f_{smooth} * f(T) * O \tag{121}$$

where C_1 is a model constant and O is the local Oxygen concentration. A dependence on temperature could also be assumed; in the present application, a linear dependence is considered for the sake of simplicity. Consequently, the rationale of the adopted source term is that Oxygen is assumed to be captured (thus disappearing) in the vicinty of the wall by structural materials contributing to the creation of oxyde layers. The capture rates are larger the higher the temperature and the Oxygen concentration.

Similarly, a source term for the corroded materials could be considered as well. The form

$$S_{\mathrm{CM}} = C_2 * f_{smooth} * f(T) * O \tag{122}$$

adopts similar assumptions as considered for the Oxygen source. A different model constant, C_2, can be assumed to treat the phenomenon, providing a positive value of the source term and leading to the assumption that corroded material is produced in the vicinity of the wall.

In the following, the obtained normalized distributions for the Oxygen concentration source term and actual Oxygen concentration are reported in Figure 264 - Figure 267, obtained assuming that production corrosive products and Oxygen occurs along the considered pipe according to the local value of temperature. The considered normalization factors are the maximum value of the Oxygen Source in the two calculations and the Oxigen concentration inlet value, respectively. As it can be observed, a negative value of the Oxigen source term is obtained in the vicinity of the rough wall for distances smaller than the selected ε_{rough} value. Consequently, the Oxygen concentration turns out to be smaller in the near wall region with respect to the bulk area owing to the larger capture at the wall. Additionally, as the axial coordinate increases, a general decrease in the Oxygen concentration is experienced as no Oxygen generation is assumed inside the pipe. Eventually, it must be observed that source terms are larger and near-wall concentrations are smaller for the case assuming a roughness height of 15 μm. This in accordance with the assumed source term definitions: higher wall temperatures are indeed experienced in this case and higher source terms are thus to be expected. Concerning the bulk concentrations, smaller values are instead experienced for the 30 μm case, owing to the larger region affected by the assumed source term.

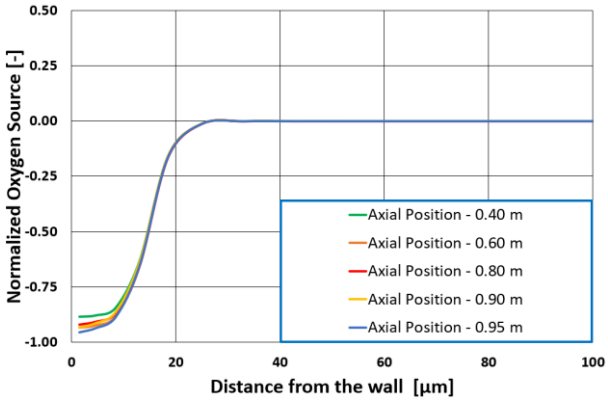

Figure 264. Values of the normalised Oxygen source along the radial direction of the pipe close to the surface (in the region of the roughness crests) at different axial locations in the pipe assumed for the selected calculation case for ε_{rough} = 15 µm

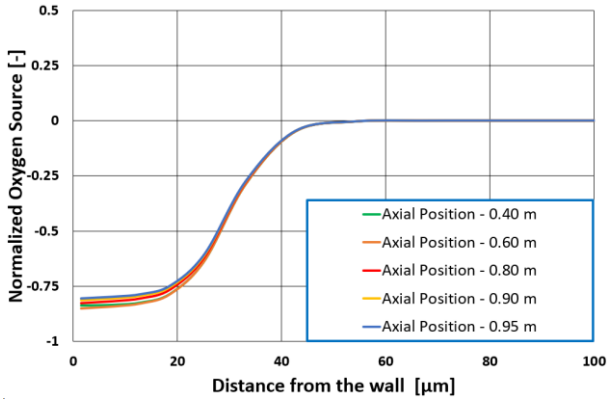

Figure 265 Values of the normalised Oxygen source along the radial direction of the pipe close to the surface (in the region of the roughness crests) at different axial locations in the pipe assumed for the selected calculation case for ε_{rough} = 30 µm

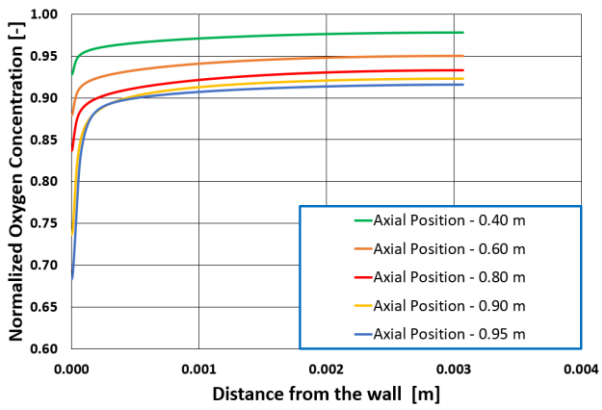

Figure 266. Normalised Oxygen concentration along the radial direction the pipe at different axial locations for εrough = 15 µm

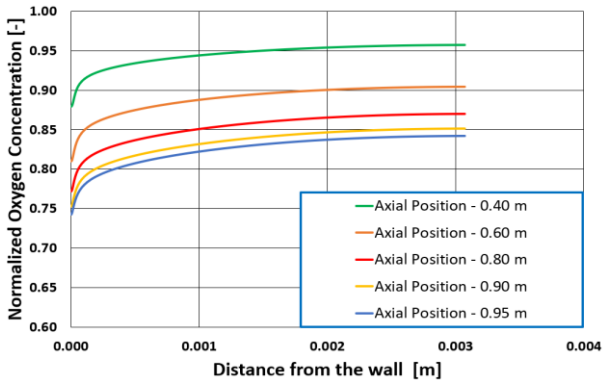

Figure 267 Normalised Oxygen concentration along the radial direction the pipe at different axial locations for εrough = 30 µm

Figure 268 and Figure 269 report about the normalized corroded material sources for the two considered cases; Figure 270, Figure 271 and Figure 272 show instead the trends obtained for the normalized corroded material source along the pipe and of the related concentrations in the radial direction. In both cases with different roughness, the normalization factor is assumed to be the maximum value calculated along the simulated domain.

It must be remarked again that, contrary to Oxygen, no corroded material is assumed to be introduced in the pipe at the inlet section in this sample case. Corroded material is instead produced in the near wall region and thus its concentration increases along the axial direction, especially near the wall; higher values are experienced in correspondece of the higher wall temperature regions coherently with the considered source terms. Eventually, it can be observed that, moving downstream along the pipe, corroded materials are also transported towards the bulk region of the pipe as consequence of both molecular and turbulent diffusion. Again, the 15 µm case reports larger values in the bulk region, owing to the larger portion of the pipe affected by the assumed source term.

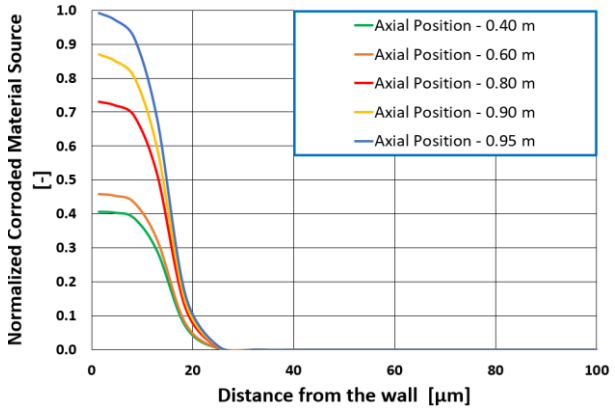

Figure 268. Values of the normalised corroded material source along the radial direction of the pipe close to the surface (in the region of the roughness crests) at different axial locations in the pipe assumed for the selected calculation case for ε_{rough} = 15 µm

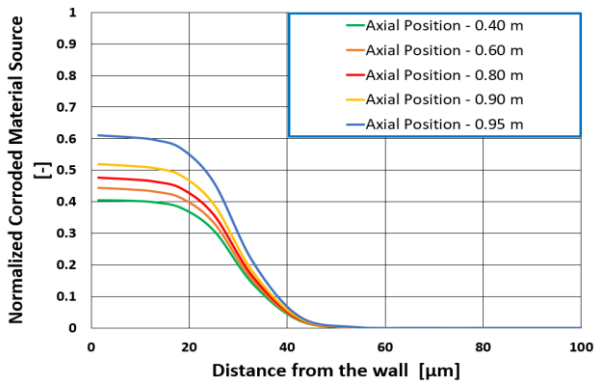

Figure 269 Values of the normalised corroded material source along the radial direction of the pipe close to the surface (in the region of the roughness crests) at different axial locations in the pipe assumed for the selected calculation case for ε_{rough} = 30 µm

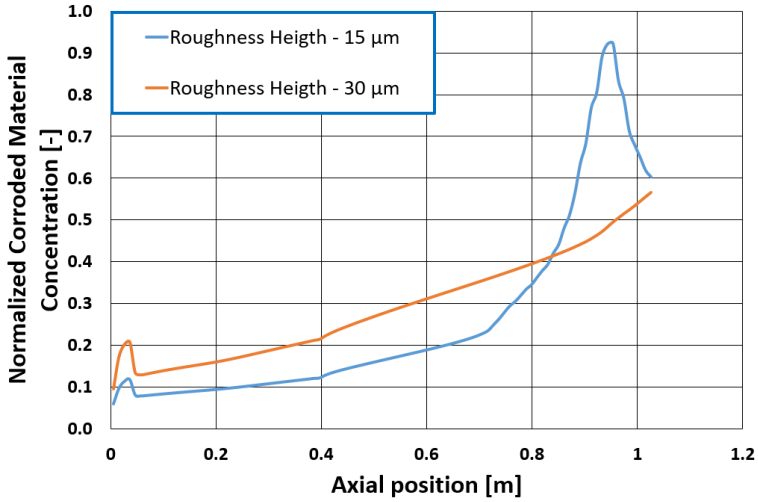

Figure 270. Normalised corroded matarial source along the pipe, as affected by the temperature distribution

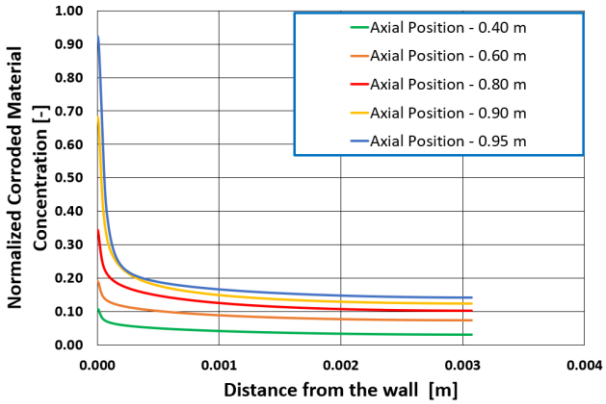

Figure 271. Normalised corroded material concentration along the radial direction of the pipe at different axial locations for ε_{rough} = 15 μm

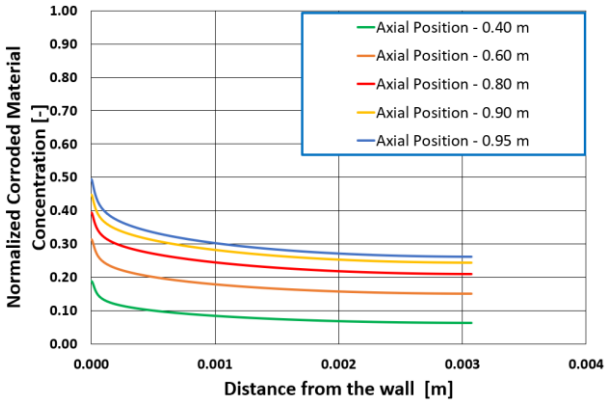

Figure 272 Normalised corroded material concentration along the radial direction of the pipe at different axial locations for ε_{rough} = 30 μm

6.2.3 Concluding Remarks

The previous sections reported the preliminary model developed in the frame of the ECC-SMART project for the analysis of mass transfer near corroded surfaces of Oxygen and corroded materials. While this contribution does not aim to achieve any level of accuracy both qualitatively and quantitatively with respect to the addressed phenomena, it serves as a proof of concept of the feasibility of the selected approach, within the capabilities of existing CFD codes. Data were thus reported in a normalized way, also trying to reinforce this concept.

Further understanding of the involved phenomena and improvement in the modelling will be thus needed in order to achieve a better representation of the transport of the selected quantities in supercritical water. For instance, instead of the assumption of a linear increase with the temperature of the sources related to the oxidation reaction, better reliable treatments could be included, e.g., an Arrhenius-type relationship with appropriate constants for each material. Anyway, though in the lack of specific data and a well-defined geometry for model comparison, the approach showed interesting capabilities and may represent the first step in the development of a more accurate methodology of analysis that may result promising enough for the treatment of specific corroded surface scenarios.

It is remarked that in this development, the availability of relatively accurate models for wall roughness treatment under heat transfer conditions at supercritical pressure, as the ones developed by the University of Pisa and combined for the first time in the frame of the ECC-SMART project, as reported in previous sections, represent the key features enabling the conception of models for the transport of reactants that, except for the validation of the physical laws to be adopted for the source terms, represent a fully possible extension in the capabilities of usual commercial CFD codes. Without the development of those models and the related coupling, the further step sketched herein could not have been achieved.

This latest effort and the first results obtained herein pave the way for further refinements. Such refinements may result in a useful tool to try predicting the more complex conditions experienced in SCWR cores. The possible presence of different structural materials and the appendages creating specific turbulence make these conditions more complicated. These may affect both Oxygen, and structural materials´ corrosion (including corrosion products´ transport), requesting detailed 3D analyses of the considered scenarios.

7 REFERENCES

A Finite Element-Based Nuclear Fuel Performance Code, BISON, Cladding corrosion model. Accessed October 25th, 2024. https://mooseframework.inl.gov/bison/theory/cladding_corrosion_model.html

Ackerman J.W., 1970, Pseudo-boiling heat transfer to supercritical pressure water in smooth and ribbed tubes. Journal of Heat Transfer. 1970, S.490-498.

Adorján, L., 2022, CFD investigation on the thermal hydraulics of SCW-SMR fuel assembly concept. MSc Thesis in the specialization of Nuclear Energy of Energy Engineering course, supervisor: A. Kiss (BME, Faculty of Natural Sciences, NTI).

Allegrini J., Dorer V., Defraeye T., Carmeliet J., 2012, An adaptive temperature wall function for mixed convective flows at exterior surfaces of buildings in street canyons. Building and Environment, 2012, Vol. 49, pp. 55–66.

Ambrosini, W., 2007, On the analogies in the dynamic behaviour of heated channels with boiling and supercritical fluids, Nuclear Engineering and Design, Volume 237, Issue 11, Pages 1164 – 1174, June 2007, DOI: 10.1016/j.nucengdes.2007.01.006.

Ambrosini, W., Sharabi, M., 2006, Dimensionless parameters in stability analysis of heated channels with fluids at supercritical pressures. Nucl. Eng. Des. 2008, 238, 1917–1929. Earlier published at the Fourteenth International Conference on Nuclear Engineering (ICONE 14), July 2006.

Ambrosini, W., 2011, Discussion of similarity principles for fluid-to-fluid scaling of heat transfer behaviour at supercritical pressures. Nucl. Eng. Des. 2011, 241, 5149–5173.

Ambrosini, W., Pucciarelli, A., Borroni I., 2015, A methodology for including wall roughness effects in k-ε low-Reynolds turbulence models.Nuclear Engineering and Design, Vol. 286, p. 175-194, ISSN: 0029-5493, doi: 10.1016 / j.nucengdes.2015.01.008

Ansys Inc, 2011, 14.0 ANSYS FLUENT Theory Guide, 2011.

Ansys Inc, 2021, 12.0 Theory Guide - 4.5.2 Shear-Stress Transport (SST) - Model, Enea.it, 2021.

ANSYS CFX-Solver Theory Guide. ANSYS, Inc. Release 18.0, Southpointe, 2016

Azih, C., Yaras, M.I., 2017, Similarity Criteria for Modeling Mixed-Convection Heat Transfer in Ducted Flows of Supercritical Fluids. J. Heat Transf. 2017, 139, 122501.

Bae, J.H., Yoo, J.Y., 2005. Direct numerical simulation of turbulent supercritical flows with heat transfer. Physics of Fluids 17, 105104.

Bazargan, M., Fraser, D. and Chatoorgan, V., 2005, Effect of Buoyancy on Heat Transfer in Supercritical Water Flow in a Horizontal Round Tube. ASME. J. Heat Transfer. August 2005; 127(8): 897–902. https://doi.org/10.1115/1.1929787.

Belyadi, H., Fathi, E. and Belyadi, F., 2017, Hydraulic Fracturing in Unconventional Reservoirs: Theories, Operations, and Economic Analysis. ISBN 978-0-12-849871-2, Gulf Professional Publishing, 107-120.

Berni F., Fontanesi S., 2020, A 3D-CFD methodology to investigate boundary layers and assess the applicability of wall functions in actual industrial problems: A focus on in cylinder simulations," Applied Thermal Engineering, 2020, Vol. 174, pp. 4–15.

Bishop A.A., Sandberg R.O., Tong L.S., 1965, Forced convection heat transfer to water near critical temperatures and super-critical pressures. A.I.Ch.E.-I.Chem.E. Symposium Series. 1965, Vol. 2, S.77- 85.

Bourke P. J., Puiling D. J., 1971, Experimental explanation of deterioration in heat transfer to supercritical carbon dioxide ASME. 1971. №71. pp. 1- 7.

Bourke P. J., Puiling D. J., Gill D. J., Denton W. H., 1968, Measurement of turbulent velocity and temperature fluctuation in the supercritical region. Symposium on heat transfer and fluid dynamics of near critical fluids. 1968. №182. pp. 58–67.

Brogna C., Pucciarelli A., Ambrosini W., 2018, Capabilities of high y+ wall approaches in predicting heat transfer to supercritical fluids in rod bundle geometries. Annals of Nuclear Energy. 2018. №120. pp. 272–278.

Buzzi, F., Pucciarelli, A., Ambrosini, W., 2019, On the mechanism of final heat transfer restoration at the transition to gas-like fluid at supercritical pressure: A description by CFD analyses, Nuclear Engineering and Design 355 (2019) 110345.

Chen W. and Fang X., 2014, A new heat transfer correlation for supercritical water flowing in vertical tubes, Int. J. Heat Mass Transf., vol. 78, pp. 156–160, 2014.

Chen, J., Yang, S., Zhao, R., Cheng, W., 2022. Experimental study on the effect of wall roughness on heat transfer characteristics of supercritical carbon dioxide in vertical tubes. International Journal of Heat and Mass Transfer 196, 123258.

Cheng, X., Schulenberg, T., 2001, Heat Transfer at Supercritical Pressures–Literature Review and Application to an HPLWR; FZKA: Karlsruhe,Germany, 2001; Volume 6609

Cheng X., Y. H. Yang, and S. F. Huang, 2009, A simplified method for heat transfer prediction of supercritical fluids in circular tubes, Annals of Nuclear Energy, vol. 36, no. 8, pp. 1120–1128, Aug. 2009, doi: 10.1016/j.anucene.2009.04.016.

Cheng, X. und Liu, X.J., Gu, H.Y. Fluid-to-fluid scaling of heat transfer in circular tubes cooled with supercritical fluids. Nuclear Engineering and Design. 2011, 241.

Collier, J. G. and Thome, J.R., 1999, Convective Boiling and Condensation, Oxford Science Publications, 3rd Edition, Clarendon Press, Oxford, 1999.

De Angelis, A., 2021, Discussion and further assessment of a fluid-to-fluid similarity theory for heat transfer at supercritical pressures, Tesi di Laurea Magistrale in Ingegneria Energetica, Università di Pisa, Anno Accademico 2019/2020.

De Angelis, A., Pucciarelli, A., Kassem, S., Ambrosini, W., 2021. Advances in the development of a fluid-to-fluid similarity theory for fluids at supercritical pressure: results from sensitivity analyses, Proceedings of the 2021 28th International Conference on Nuclear Engineering, ICONE28, August 4–6, 2021, Virtual, Online. Paper No. ICONE28-64713.

Dittus, F., 1930, Heat transfer in automobile radiators of the tubular type. Berkeley California, University of California Press, 1930.

Dubyk Y., Filonov V., Filonova Y., Kovalenko O., 2021, Deteriorated Heat Transfer Influence on the Stress-Strain State of SMR SCWR Fuel Bundles. ASME J of Nuclear Rad Sci, 2021 pp. 1–14.

Dubyk Y., Filonov V. et al, 2021, Deteriorated heat transfer influence on the stress-strain state of SMR SCWR fuel bundles, 10th International Symposium on SCWRs (ISSCWR-10), Prague, the Czech Republic, March 15-19, 2021

Durbin, P.A., Medic, G., Seo, J.-M., Eaton, J.K., Song, S., 2001. Rough wall modification of two-layer k-e. Journal of Fluids Engineering 123, 16-21.

ECC-SMART (The Consortium of ECC-SMART project), 2020, Joint European Canadian Chinese Development of Small Modular Reactor Technology (webpage). https://ecc-smart.eu/

Eter A., Groeneveld D., Tavoularis S, 2016, An Experimental Investigation of Supercritical Heat Transfer in A three-rod bundle equipped with wire wrap and grid spacers and cooled by carbon dioxide. J. Nuclear Engineering and Design. 2016. №303. pp. 173-191.

Filonov V., Filonova Y., Razumovskiy V., Pis'mennyi E., 2018, On experimental and computational investigation of heat transfer deterioration and hydraulic resistance in annular channel and SCWR 3-rod bundle. Proceedings of the ICONE-26, 2018.

Filonov V., Filonova Y. et al., 2018, On experimental and computational investigation of heat transfer deterioration and hydraulic resistance in annular channel and SCWR 3- and 7- rod bundle. In Proceedings of the 2018 26th International Conference on Nuclear Engineering, ICONE26, Volume 9. London, England, 22–26 July 2018. ICONE26-81289

Filonov V., Pis'mennyi E., Razumovskiy V., 2021, Adaptation of Temperature Wall Function for Calculation the Heat Transfer at Supercritical Coolant Parameters, POWER ENGINEERING: economics, technique, ecology, № 4 (2021):66. pp. 44–53. (In Ukrainian)

Filonov V., Filonova Y., Dubyk Y., Pis'mennyi E., 2022, Transfer matrix method for analysis of flow thermohydraulic characteristics with extremely nonlinear behavior of thermophysical

properties using channel approach. International Journal of Heat and Mass Transfer, 2022, Vol. 15, pp. 1–18.

Filonov, V., 2023, Prediction of the regimes with deteriorated heat transfer in perspective IV generation reactors with supercritical coolant parameters, National Technical University of Ukraine “Igor Sikorsky Kyiv Polytechnic Institute”, PhD Thesis.

Filonov V., Filonova Y. et al, 2024, Differential Method for Predicting Heat Transfer Deterioration Regimes in Supercritical Channels and Rod Assemblies, In Proceedings of the 2024 31th International Conference on Nuclear Engineering, ICONE31. Prague, Czech Republic, 4-8 August. ICONE31-136180

Filonov V., Dubyk Y. et al, 2024, Evaluation of Three-Dimensional Initial Dynamics of the Decompression Wave at LB LOCA in the Advanced Supercritical Reactor ECC-SMART, In Proceedings of the 2024 31th International Conference on Nuclear Engineering, ICONE31. Prague, Czech Republic, 4-8 August. ICONE31-136271

Filonov V., Kovalenko O. et al, 2024, Effect of the Heat Transfer Correlation choice on the Coupled Assessment of Energy Release and Stress-Strain State of an Elementary Supercritical Fuel Rod under Nuclear Heating Conditions, In Proceedings of the 2024 31th International Conference on Nuclear Engineering, ICONE31. Prague, Czech Republic, 4-8 August. ICONE31-136275

Filonov V., Kovalenko O. et al, 2025, Multiphysics Assessment of the SCW SMR Heat Generating Channel Condition Using Differential Method of the Heat Transfer Intensity and Resistance Calculation, Submitted at 11th International Symposium on SCWRs (ISSCWR-11), ISSCWR-11-P064, Pisa, Italy, February 3-5, 2025

Filonov V., Fedorov D. et al, 2025, Assessment of the Failure Time of the ECC-SMART Supercritical Reactor Vessel in the Late Phase of a Severe Accident, Submitted at 11th International Symposium on SCWRs (ISSCWR-11), ISSCWR-11-P065, Pisa, Italy, February 3-5, 2025

Flack, K.A., Schultz, M.P., 2014. Roughness effects on wall-bounded turbulent flows. Physics of Fluids 26, 101305.

Gao, Z. and Bai, J., 2017, Numerical analysis on nonuniform heat transfer of supercritical pressure water in horizontal circular tube. vol. 120, pp. 10–18, Jun. 2017, doi: https://doi.org/10.1016/j.applthermaleng.2017.03.109.

GIF (The Community of the Generation IV International forum), 2024, Supercritical-Water-Cooled Reactor (SCWR). The webpage of GIF. https://www.gen-4.org/gif/jcms/c_9360/scwr

Goldmann K., 1961, Heat transfer to supercritical water at 5000 psi flowing at high mass flow rates through round tubes. International developments in heat transfer, Proceedings o Heat Transfer Conference, Colorado/USA. 1961, Part II, Paper 66, S.561-568.

Grass G., Herkenrath H., Hufschmidt W., 1971, Anwendung des Prandtlschen Grenzschichtmodells auf den Wärmeübergang an Flüssigkeiten mit stark temperaturabhängigen Stoffeigenschaften bei erzwungener Strömung. WärmeundStoffübertragung. 1971, Bd. 4, S.113-119.

Griem H., 1996, A new procedure for the prediction of forced heat transfer at near- and supercritical pressure. Heat and Mass Transfer. 1996, Vol. 31, S.301-305.

Gupta S., Farah A., King K., Mokry S., and Pioro I., 2010, Developing new heat-transfer correlation for supercritical-water flow in vertical bare tubes, International Conference on Nuclear Engineering, Proceedings, ICONE, 2010, vol. 2. doi: 10.1115/ICONE18-30024.

David Guzonas, Radek Novotny, Sami Penttilä, Aki Toivonen, Wenyue Zheng, 5 - Corrosion, Editor(s): David Guzonas, Radek Novotny, Sami Penttilä, Aki Toivonen, Wenyue Zheng, Materials and Water Chemistry for Supercritical Water-cooled Reactors, Woodhead Publishing, 2018, Pages 139-218, ISBN 9780081020494, https://doi.org/10.1016/B978-0-08-102049-4.00005-2.

(https://www.sciencedirect.com/science/article/pii/B9780081020494000052)Haaland, S.E., 1983. Simple and Explicit Formulas for the Friction Factor in Turbulent Pipe Flow. Journal of Fluids Engineering 105 (1), 89-90.

Han, H. and Zhang, C., 2022, A modified turbulent model for the supercritical water flows in the vertical upward channels. The Journal of Supercritical Fluids 187 (2022) 105632.

Hasan B., 2007, Turbulent Prandtl Number and its Use in Prediction of Heat Transfer Coefficient for Liquids. College of Engineering Journal (NUCEJ). 2007. №1. pp. 53–64.

He, S., Kim, W.S., Bae, J.H., 2008. Assessment of performance of turbulence models in predicting supercritical pressure heat transfer in a vertical tube. Int. J. Heat Mass Transf. 51 (19-20), 4659–4675.

He, J., Yan, J., Wang, W., He, 2018, Direct numerical simulation study for fluid–to-fluid scaling for fluids at supercritical pressure, in: Proceedings of the 16th International Heat Transfer Conference, IHTC-16, August 10–15, 2018, Beijing, China, 2018 IHTC16-23265

Hellsten, A., Laine, S., 1997. Extension of the k-ω-SST turbulence model for flows over rough surfaces. AIAA-97-3577.

Hellsten, A., 1998. Some improvements in Menter's k-ω SST turbulence model. AIAA-98-2554.

Henkes, R., Van Der Vlugt, F. and Hoogendoorn, C., 1991, Natural Convection Flow in a Square Cavity Calculated with Low-Reynolds-Number Turbulence Models. Int. J. Heat Mass Transfer, 34 (1991), 1543-1557.

H. Zahlan, S. Tavoularis, and D. C. Groeneveld, "A look-up table for trans-critical heat transfer in water-cooled tubes," Nucl. Eng. Des., vol. 285, pp. 109–125, 2015.

Hou, Z., Huang, X., Gao, Y., Zhang, S. and Wang, H., 2023, Experimental investigation on heat transfer of supercritical water flowing in a horizontal tube with axially non-uniform heating. International Journal of Heat and Mass Transfer, vol. 211, no. 124219, pp. 1–11, Apr. 2023, doi: https://doi.org/10.1016/j.ijheatmasstransfer.2023.124219.

Hsu, Y.-Y., Graham, R.W., 1976, Transport processes in boiling and two-phase systems – Including near critical fluids, Hemisphere Publishing Corporation, McGrawHill Book Company, USA, 1976.

Huang, X., Wang, Q., Song, Z., Yin, Y. and Wang, H., 2020, Heat transfer characteristics of supercritical water in horizontal double-pipe. Applied Thermal Engineering, vol. 173, 115191–115191, Jun. 2020, doi: https://doi.org/10.1016/j.applthermaleng.2020.115191.

Huang, X., Qin, J., Hou, Z., Gao, Y., Zhang, S. and Wang, H., 2022, Heat transfer characteristics of supercritical water in a horizontal tube considering local temperature fields: An experimental study. International Journal of Heat and Mass Transfer, vol. 198, 123404, Dec. 2022, doi: https://doi.org/10.1016/j.ijheatmasstransfer.2022.123404.

IAEA, 2014, Heat Transfer Behaviour and Thermohydraulics Code Testing for Supercritical Water Cooled Reactors (SCWRs); IAEA-TECDOC-1746; IAEA: Vienna, Austria, 2014.

IAEA, 2019, Status of Research and Technology Development for Supercritical Water-Cooled Reactors; IAEA-TECDOC-1869; IAEA: Vienna, Austria, 2019.

IAEA, 2020, Understanding and Prediction of Thermohydraulic Phenomena Relevant to Supercritical Water Cooled Reactors (SCWRs); IAEA-TECDOC-1900; IAEA: Vienna, Austria, 2020.

Ikryannikov N. P., Petukhov B. S., Protopopov V. S., 1973, Calculation of heat transfer in the single-phase, near-critical region in the case of a frictional-inertial-gravitational flow, High Temperatures, 11 (5), 1973, pp. 949-955.

Jackson, J.; Hall, W., 1979, Influences of buoyancy on heat transfer to fluids flowing in vertical tubes under turbulent conditions. Turbul. Forced Convect. Channels Bundles 1979, 2, 613–640.

J.D. Jackson, 2013, Fluid flow and convective heat transfer to fluids at supercritical pressure, Nucl. Eng. Des. 264 (11) (2013) 24–40.

Jaromin, M., Anglart, H., 2013. A numerical study of heat transfer to supercritical water flowing upward in vertical tubes under normal and deteriorated conditions. Nuclear Engineering and Design 264, 61-70.

Kader B., 1981, Temperature and concentration profiles in fully turbulent boundary layers. International Journal of Heat and Mass Transfer, 1981, Vol. 9, pp. 1541–1544.

Kassem, S., Pucciarelli, A., Ambrosini, W., 2021, Insight into a fluid-to-fluid similarity theory for heat transfer at supercritical pressure: Results and perspectives. Int. J. Heat Mass Transf. 2021, 168, 120813.

Kassem, S., Pucciarelli, A., Ambrosini, W., 2021, Outcomes of a Successful Fluid-To-Fluid Similarity Theory for Heat Transfer at Supercritical Pressures. In Proceedings of the 10th International Symposium on Supercritical Water-Cooled Reactors, ISSCWR-10, Prague, Czech Republic, 15–19 March 2021. ISSCWR-10-014.

Kassem, S., Pucciarelli, A., Ambrosini, W., 2021a, Extending a Fluid-To-Fluid Similarity Rationale for Heat Transfer at Supercritical Pressure to R134a. In Proceedings of the 2021 28th International Conference on Nuclear Engineering, ICONE28, online. 4–6 August 2021. ICONE28-64822.

Kassem, S., Pucciarelli, A., and Ambrosini, W., 2022, Analysis of existing correlations for heat transfer to supercritical pressure fluids in support to the ECC-SMART Project, Università di Pisa, Dipartimento di Ingegneria Civile e Industriale, Pisa, February 11th, 2022, RL 282(2021).

Kassem. S., Pucciarelli. A., Ambrosini W. 2022a, Considerations about correlations for heat transfer to supercritical pressure fluids spanning all regimes, The 19th International Topical Meeting on Nuclear Reactor Thermal Hydraulics (NURETH-19), Log nr. 19001, Brussels, Belgium, March 6 - 11, 2022

Kassem, S., Pucciarelli, A. and Ambrosini W., 2022b, Extrapolation of Heat Transfer Data for Carbon Dioxide to the Operating Conditions of SCWR, Accepted for publication at the 19th International Topical Meeting on Nuclear Reactor Thermal Hydraulics (NURETH-19), Brussels, Belgium, March 6 - 11, 2022

Kassem, S., Pucciarelli A. and Ambrosini W., 2022c, Considerations about Correlations for Heat Transfer to Supercritical Pressure Fluids Spanning All Regimes, Accepted at the 19th International Topical Meeting on Nuclear Reactor Thermal Hydraulics (NURETH-19), Brussels, Belgium, March 6 - 11, 2022.

Kassem, S., Pucciarelli, A., Ambrosini, 2023, CFD prediction of heat transfer at supercritical pressure with rough walls: Parametric analyses and comparison with experimental data, Annals of Nuclear Energy 188 (2023) 109815

Kassem, S., Pucciarelli, A., Ambrosini, W., 2025, Modelling the influence of surface roughness on heat transfer at supercritical pressure, Submitted at 11th International Symposium on SCWRs (ISSCWR-11), ISSCWR11-P060, Pisa, Italy, February 3-5, 2025

Kassem, S., 2024, Analysis of heat transfer phenomena at supercritical pressure supported by a fluid-to-fluid similarity theory, Dipartimento di Ingegneria Civile e Industriale, Corso di Dottorato in Ingegneria Industriale, PhD Thesis. Academic Year 2022-2023.

Kirillov P., Terent'eva M., 2017, Turbulent Prandtl number (History and present),” (In Russian), Obninsk: IPE, 3271, ISBN 978-5-906512-89-5, 2017

Kiss, A., 2018, Thermal hydraulic investigations of the coolant flow in Supercritical Water-cooled Reactor relevant geometries (PhD Dissertation). December 2018. DOI: 10.13140/RG.2.2.17769.24163

Kiss, A., Laurien, E., Aszódi, A., Zhu, Y., 2011, Numerical Simulations on the Rotating Flow of Wrapped Wired HPLWR Fuel Assembly; Vancouver, Canada: 5th International Symposium SCWRs, link

Kiss, A., Mervai, B., 2016, Numerical Analysis on the Effect of Wrapped Wire Spacers on Thermal Hydraulics in a Four Rod Fuel Bundle; Helsinki, Finnland: 26th Symposium of AER on VVER Reactor Physics and Reactor Safety, link

Kiss A., Churkin A., et al., 2017, Summary on the results of two CFD benchmarks of tube and different channel geometries. Journal of Nuclear Engineering and Radiation Science. 2017. Vol. 4, №. 1. pp. 1–15.

Kitoh, K., Koshizuka, S., and Oka, Yo., 1999. Refi nement of transient criteria and safety analysis for a high temperature reactor cooled by supercritical water, Proceedings of the 7th International Conference on Nuclear Engineering (ICONE-7), Tokyo, Japan, April 19–23, Paper No. 7234.

Kline, N., 2017, An Experimental Study on Heat Transfer Deterioration at Supercritical Pressures. Master's Thesis, Ottawa-Carleton Institute for Mechanical and Aerospace Engineering, University of Ottawa, Ottawa, ON, Canada, 2017.

Kong X., Sun D., Gou L., 2020, Numerical Investigation on Heat Transfer of Supercritical Water with a Variable Turbulent Prandtl Number Model. Journal of Nuclear Engineering and Radiation Science. 2020. №6. pp. 1–10.

Koshizuka, S., Takano, N., Oka, Y., 1995. Numerical analysis of deterioration phenomena in heat transfer to supercritical water. Int. J. Heat Mass Transfer 38 (16), 3077-3084.

Kurganov V. A., Kaptil'ny A. G., 1992, Velocity and enthalpy Fields and eddy diffusivities in a heated supercritical fluid flow. Experimental Thermal and Fluid Science. 1992. №5. pp. 465–478.

Kurganov V. A., Kaptil'ny A. G., 1993, Flow structure and turbulent transport of a supercritical pressure fluid in a vertical tube under the conditions of mixed convection. Experimental data. Int. J. Heat Mass Transfer. Vol 36. 1993. pp. 3383-3392.

Kurganov V., Maslakova I., 2016, Normal and deteriorated heat transfer upon heating of turbulent flows of heat carriers with variable physical properties in tubes. High Temperature, 2016, Vol. 54, pp. 577–598.

Kurganov V., Zejgarnik Y., Yankov G., Maslakova I., 2018, Heat transfer and resistance in pipes at supercritical coolant pressures: results of scientific research and practical recommendations. Moscow: LLC "Pechatny salon shans", 2018. (ISBN 978-5-9500112-7-6).

Lei, X., Li, H., Guo, Y., Zhang, Q., Zhang, W. and Zhang, Q., 2016, Experimental study on the minimum drag coefficient of supercritical pressure water in horizontal tubes. Nuclear Engineering and Design, vol. 301, 164–174, May 2016, doi: https://doi.org/10.1016/j.nucengdes.2016.02.039.

Lemmon, E., Huber, M., McLinden, M., 2013. NIST Standard Reference Database 23: Reference Fluid Thermodynamic and Transport Properties-REFPROP, Version 9.1, Natl Std. Ref. Data Series (NIST NSRDS), National Institute of Standards and Technology, Gaithersburg, MD.

Li, H., Kong, X., Lei, X., Zhang, Q., Liao, C., Gou L., and Sun, D., 2019, Heat Transfer Correlations for Supercritical Water in Vertically Upward Tubes, Open access peer-reviewed chapter, IntechOpen Book Series, https://www.intechopen.com/chapters/69637 , October 19th 2019, DOI: 10.5772/intechopen.89580.

Liao C., 2014, Investigation on heat transfer correlations and the criterion for the onset of heat transfer deterioration of supercritical pressure water in vertical upward pipes, Master's Thesis. Xi'an: Xi'an Jiaotong University, 2014.

Lien, F.S., Chen, W.L., Leschziner, M.A., 1996, Low-Reynolds number eddy viscosity modelling based on non-linear stress-strain/vorticity relations, in: Proceedings of the 3rd Symposium on Engineering Turbulence Modelling and Measurements, 27–29 May, Crete, Greece, 1996.

Mann, A., Copping, A.W., Yaras, M.I., 2023. DNS Study of Thermohydraulic Effects of Surface Roughness in Boundary Layer and Channel Flows with Application to Heated Channel Flow of Water near Pseudocritical Temperature. Carleton University, Canada.

Mao, S., Zhou, T., Wei, D., Lu, H. and Liu, W., 2022, Numerical modeling on heat transfer of supercritical water in cooled horizontal circular tube. The Journal of Supercritical Fluids, 191 (2022), 105769, https://doi.org/10.1016/j.supflu.2022.105769.

Menter, F., Kuntz, M., Langtry, R., 2003. Ten years of industrial experience with the SST turbulence model. Turbulence, Heat Mass Transfer, vol. 4.

Mészáros, P., Babcsány, B., Varju, T., 2023, Reactor physics and thermal hydraulics analysis of the SCW-SMR conceptual design with the Serpent 2 and Apros codes, MSc thesis, BME, Budapest.

Mészáros, P., Kiss, A., Babcsány, B., 2022, Coupled thermal hydraulics and reactor physics analysis of different SCW-SMR fuel assembly concepts, MSc thesis, BME, Budapest

Mokry S., Gospodinov Y., Pioro I., Kirillov P., 2009, Supercritical water heat-transfer correlation for vertical bare tubes. In International Conference on Nuclear Engineering (Vol. 43543, pp. 747-754).

Mokry S., Pioro I., Kirillov P., Gospodinov Y., 2010, Supercritical-water heat transfer in a vertical bare tube, Nuclear Engineering and Design, vol. 240, no. 3, pp. 568–576, Mar. 2010.

Mouslim, A., Tavoularis, S., 2020, Direct tests of fluid-to-fluid scaling expressions for supercritical heat transfer in tubes. Int. J. Heat Mass Transf. 2020, 147, 118862.

Nava-Dominguez, A. 2020, Evaluation of friction-factor correlations at supercritical water conditions in support of the Canadian SCWR, J. Nucl. Eng. Radiat. Sci., vol. 6, no. 3, 2020.

Near Wall Modeling – Turbulence Modeling Using ANSYS CFX

Nikuradse, J., 1950, Laws of flow in rough pipes. J. Appl. Phys. 3.

Norris. R.H. 1970. Some simple approximative heat-transfer correlations for turbulent flows in ducts with rough surfaces. General Electric. Reprint 6770. Available on line: https://nyheritage.contentdm.oclc.org/digital/collection/p16694coll20/id/17445/

NIST REFPROP Vers. 10 Website, https://www.nist.gov/srd/refprop

NPIC, 2021, Benchmark study on SCWR thermal-hydraulic and safety Characteristics, Experimental description issued in 2021, project document

Oka, Y., Koshizuka, S., Ishiwatari, Y., Yamaji, A., 2010, Super Light Water Reactors and Super Fast Reactors: Supercritical-Pressure Light Water Cooled Reactors; Springer: New York, NY, USA, 2010.

Ornatsky A.P., Glushchenko L.F., Kalachev S.I., 1971, Heat Transfer with rising and falling flows of water in tubes of small diameter at supercritical pressures. Thermal Engineering. 1971, Vol. 18 (5), S.137-141.

Penttilä, S., 2020, Structural Materials Corrosion Testing and Modelling Assessment in Supercritical water, Aalto University Publication Series, Doctoral Dissertations, 70/2020, Helsinki 2020

Petukhov B.S., Krasnoschekov E.A., Protopopov V.S., 1961, An Investigation of Heat transfer to fluids flowing in pipes under supercritical conditions. Proceedings of 2nd International Heat Transfer Conference, Boulder. 1961, S.569-578.

Petukhov B. S., Genin L. G., Kovalyov S. A., 1986, Heat-Exchange Processes in Nuclear Power Plants (in Russian), Moscow, Energoatomizdat, 1986.

Pengcheng Guo, S. Liu, J. Yan, J. Wang, and Q. Zhang, 2020, Experimental study on heat transfer of supercritical CO_2 flowing in a mini tube under heating conditions, International Journal of Heat and Mass Transfer, vol. 153, Jun. 2020, doi: 10.1016/j.ijheatmasstransfer.2020.119623.

Pioro, I. L., Khartabil, H. F., and Duffey, R. B., 2004, Heat transfer to supercritical fluids flowing in channels - Empirical correlations (survey), Nucl. Eng. Des., vol. 230, no. 1–3, pp. 69–91, 2004.

Pioro, I.L., Duffey, R.B., 2007, Heat Transfer and Hydraulic Resistance at Supercritical Pressure in Power Engineering Applications; ASME Press: New York, NY, USA, 2007.

Pis'menny, E.N., Razumovskiy, V.G., Maevskiy, E.M., Kotoskov A.G., Pioro I.L., 2005. Heat transfer to supercritical water in gaseous state or affected by mixed convection in vertical tubes. In: Proceedings of ICONE14 ''International Conference of Nuclear Engineering". Miami, Florida, USA.

Pis'menny, E.N., Razumovskiy, V.G., Maevskiy, E.M., 2005a. Experimental study on temperature regimes to supercritical water flowing in vertical tubes at low mass fluxes. In: Proceedings of the International Conference GLOBAL-2005, Nuclear Energy Systems for Future Generation and Global Sustainability, Tsukuba, Japan, October 9–13, paper no. 519.

Podila, K. and Rao, Y., 2015, CFD analysis of flow and heat transfer in Canadian supercritical water reactor bundle. Annals of Nuclear Energy, 75, 1-10, https://doi.org/10.1016/j.anucene.2014.07.039.

Popovac M., Hanjalic K., 2007, Compound Wall Treatment for RANS Computation of Complex Turbulent Flows and Heat Transfer. Flow Turbulence Combust, 2007, Vol. 78, pp. 177–202.

Popov V. N., 1977, Calculation of heat exchange and turbulent flow of compressible fluid in a circular tube. (in Russian) High temperature thermophysics, 1977, Vol. 15, No. 4, pp. 795–801.

Pucciarelli A., Borroni I., Sharabi M., Ambrosini W., 2015, Results of 4-equation turbulence models in the prediction of heat transfer to supercritical pressure fluids. Nuclear Engineering and Design. 2015, №281. pp. 5–14.

Pucciarelli, A., Sharabi, M., Ambrosini, W., 2016, Prediction of heat transfer to supercritical fluids by the use of Algebraic Heat Flux Models. Nucl. Eng. Design 2016, 297, 257–266.

Pucciarelli, A., Ambrosini, W., 2016, Fluid-to-fluid scaling of heat transfer phenomena with supercritical pressure fluids: Results from RANS analyses. Ann. Nucl. Energy 2016, 92, 21–35.

Pucciarelli, A., 2017, Analysis of Fluiddynamic and Heat Transfer Phenomena with Supercritical Fluids; Università di Pisa, Dipartimento di Ingegneria Civile e Industriale, Corso di Dottorato in Ingegneria Industriale: Pisa, Italy, 2017.

Pucciarelli, A., Ambrosini, W., 2017, Improvements in the prediction of heat transfer to supercritical pressure fluids by the use of algebraic heat flux models, Annals of Nuclear Energy 99 (2017) 58–67.

Pucciarelli, A., Ambrosini, W., 2018. Use of AHFM for simulating heat transfer to supercritical fluids: application to carbon dioxide data. International Journal of Heat and Mass Transfer, Vol. 127, Part B (2018), 1138-1146.

Pucciarelli, A., He, S., Ambrosini, W., 2020, A successful local fluid-to-fluid similarity theory for heat transfer to supercritical pressure fluids: Merits and limitations. Int. J. Heat Mass Transf. 2020, 157, 119754.

Pucciarelli, A., Ambrosini, W., 2020, A successful general fluid-to-fluid similarity theory for heat transfer at supercritical pressure. Int. J. Heat Mass Transf. 2020, 159, 120152.

Pucciarelli, A., Kassem, S., and Ambrosini, W., 2021. Considerations on a fluid to fluid scaling theory for heat transfer to supercritical fluids: recommendations for non-uniform heat flux conditions, The 10th International Symposium on Supercritical Water-Cooled Reactors, ISSCWR-10, March 15-19, 2021, Prague, Czech Republic. Paper No. ISSCWR-10-012.

Pucciarelli, A., Kassem, S., Ambrosini, W., 2021a, Overview of a Theory for Planning Similar Experiments with Different Fluids at Supercritical Pressure. Energies 2021, 14, 3695. https://doi.org/10.3390/en14123695.

Pucciarelli, A., Kassem, S., Ambrosini, W., 2021b, On the Choice of Corresponding Pressures in a Novel Fluid-to-Fluid Similarity Theory for Heat Transfer at Supercritical Pressure, NENE2021, September 6-9, 2021, Bled Slovenia.

Pucciarelli, A., Ambrosini, W., 2022, A shape function approach for predicting deteriorated heat transfer to supercritical pressure fluids on account of a thermal entry length phenomenon, Nuclear Engineering and Design 397 (2022) 111923.

Pucciarelli, A., Kassem, S., Ambrosini, W., 2022, Characterisation of observed heat transfer deterioration modes at supercritical pressure with the aid of a CFD model, Annals of Nuclear Energy 178 (2022) 109376.

Rahman, M. M., Dongxu, J., Beni, M. S., Hei, H. C., He, W. and Zhao, J., 2016, Supercritical water heat transfer for nuclear reactor applications: A review, Ann. Nucl. Energy, vol. 97, pp. 53–65, 2016.

Razumovskiy V. G., 1984, Heat transfer and hydraulic resistance of smooth channels in turbulent flow of supercritical pressure water. Ph. D. Thesis. 01.04.14 «Thermophysics», Kiev. 1984. 220 p.

Razumovskiy V. G., Pis'mennyi E. N., Sidawi K., 2016, Experimental heat transfer in an annular channel and 3-rod bundle Cooled with upward flow of supercritical water. JNERS. 2016. №2. pp. 1–8.

Rohde, M., Peeters, J. W. R., Pucciarelli, A., Kiss, A., Rao, Y. F., Onder, E. N., Muehlbauer, P., Batta, A., Hartig, M., Chatoorgoon, V., Thiele, R., Chang, D., Tavoularis, S., Novog, D., McClure, D., Gradecka, M., and Takase, K., 2016, A Blind, Numerical Benchmark Study on Supercritical Water Heat Transfer Experiments in a 7-Rod Bundle. ASME. ASME J of Nuclear Rad Sci. April 2016; 2(2): 021012. https://doi.org/10.1115/1.4031949

Schulenberg, T., Otic, I., 2021. SUGGESTION FOR DESIGN OF A SMALL MODULAR SCWR. 10th International Symposium on SCWRs (ISSCWR-10), Prague, the Czech Republic.

Schulenberg, T., Otic, I., 2022, Concept of a Small Modular SCWR With Horizontal Fuel Assemblies, ASME Journal of Nuclear Engineering and Radiation Science, Vol. 8, Issue 3, 2022

Schulenberg, T., Starflinger, J., 2012, High Performance Light Water Reactor: Design and Analyses; KIT Scientific Publishing: Karlsruhe, Germany, 2012.

Shang, Z. and Chen, S., 2011, Numerical investigation of diameter effect on heat transfer of supercritical water flows in horizontal round tubes. Applied Thermal Engineering, 31(4) (2011), 573-581, https://doi.org/10.1016/j.applthermaleng.2010.10.020.

Shang, Z. and Lo, S., 2010, Numerical investigation of supercritical water-cooled nuclear reactor in horizontal rod bundles. Nuclear engineering and design, 240(4) 776–782. doi:10.1016/j.nucengdes.2009.10.029.

Shang, Z., Yao, Y. and Chen, S., 2008, Numerical investigation of system pressure effect on heat transfer of supercritical water flows in a horizontal round tube. Chemical Engineering Science, vol. 63, no. 16, 4150–4158, Aug. 2008, doi: https://doi.org/10.1016/j.ces.2008.05.036.

Sharabi, M., Ambrosini, W., 2009. Discussion of heat transfer phenomena in fluids at supercritical pressure with the aid of CFD models. Ann. Nucl. Energy 36 (2009), 60 – 71.

Shitsman M.E., 1963, Impairment of the transmission at supercritical pressures, high Temperature, Teplofizika Vysokih. 1963, Vol.1 (2), S.237-244.

Shitsman M.E.,1968, Temperature conditions in tubes at supercritical pressures. Thermal Engineering. 1968, Vol. 15 (5), S.72-77.

Simcenter STAR-CCM+®, version 13.06; Documentation; Siemens PLM Software: Plano, TX, USA, 2018.

Sommer T. P., So R. M., Znang H. S., 1993, Near-Wall Variable-Prandtl-Number Turbulence Model for Compressible Flows. AIAA Journal. 1993. №31. pp. 27–35.

Strykovich M., Shitzman M., Miropolsky Z., 1955, Some data on the temperature behavior of a vertical boiling tube at near-critical pressures. Teploenergetika. 1955. №12. pp. 32-36.

Swenson, H.S., Carver, J.R., Kakarala, C.R., 1965, Heat Transfer to Supercritical Water in Smooth-Bore Tubes, Journal of Heat Transfer, vol. 87, no. 4, pp. 477-483, 1965

Su, X. and Li, X., 2022, Thermal-hydraulic study in a wire-wrapped 19-rod bundle based on an isotropic four-equation model. Annals of Nuclear Energy 178 109343.

Tang G., Shi H., Wu Y., 2016, A variable turbulent Prandtl number model for simulating supercritical pressure CO2 heat transfer. International Journal of Heat and Mass Transfer. 2016. №102. pp. 1082–1092.

Todreas, N.E., Kazimi, M.S., 1900, Nuclear Systems, Volume I, Thermal-Hydraulic Fundamentals, Second Edition, 212 Taylor and Francis Group, LLC.

University of Wisconsin, 2017, Publication of the University of Wisconsin Supercritical Fluid Experiments, Experimental facility overview: PPT Presentation, 27 June 2017.

Valueva E. P., 2012, Numerical modeling of heat transfer processes and turbulent fluid flow in pipes at supercritical pressure. High temperature thermophysics. 2012, №2. pp. 298–306.

Valueva E. P., 2014, Numerical modeling of heat transfer and turbulent flow in a liquid tube at supercritical pressure considering the combined influence of density pulsations and

thermal acceleration on turbulent transfer. High temperature thermophysics. 2014, №6. pp. 899–906.

Valueva E. P., 2015, Effect of density pulsations in the buoyancy force field on heat transfer and turbulent fluid flow in a vertical tube at supercritical pressures. High temperature thermophysics. 2015, №3. pp. 403–411.

Varju, T., Csige, A., Kiss, A., Filonov, V., Filonova, Y., Fedorov, D., Pucciarelli, A., Kassem, S., Ambrosini, W., 2024, Discussion and perspectives for improvements of heat transfer correlation capabilities for fluids at supercritical pressures, Nuclear Engineering and Design, Volume 421, May 2024, 113085

Vikhrev Yu.V., Barulin Yu.D., Konkov A.S., 1967, A Study of heat transfer in vertical tubes at supercritical pressures. Thermal Engineering. 1967, Vol. 14 (9), S.116-119.

Wahl A., Mertz R., Laurien E., and J. Starflinger, 2021, “Heat transfer correlation for sCO_2 cooling in a 2 mm tube,” Journal of Supercritical Fluids, vol. 173, Jul. 2021, doi: 10.1016/j.supflu.2021.105221.

Wang, W., He, S., 2015. DIRECT NUMERICAL SIMULATION OF FLUID FLOW AT SUPERCRITICAL PRESSURE IN A VERTICAL CHANNEL. NURETH-16.

Wang C. and Li H., 2014. Evaluation of the heat transfer correlations for supercritical pressure water in vertical tubes, Heat Transf. Eng., vol. 35, no. 6–8, pp. 685–692, 2014.

Wang H., Bi Q., Leung L., 2016, Heat Transfer from a 2×2 Wire wrapped Rod Bundle to Supercritical Pressure Water. Int. J. of Heat and Mass Transfer, 2016. №97. pp. 486–501.

Wang J., Guan Z., Gurgenci H., Veeraragavan A., Kang X., and Hooman K., 2019, “A computationally derived heat transfer correlation for in-tube cooling turbulent supercritical CO 2,” International Journal of Thermal Sciences, vol. 138, pp. 190–205, Apr. 2019, doi: 10.1016/j.ijthermalsci.2018.12.045.

Wang, J., Gong, J., Kang, X., Zhao, C. and Hooman, K., 2022, Assessment of RANS turbulence models on predicting supercritical heat transfer in highly buoyant horizontal flows. Case Studies in Thermal Engineering, Volume 34, 102057, ISSN 2214-157X, https://doi.org/10.1016/j.csite.2022.102057.

Wang, J., Yang, J., Gong, J., Zhao, C. and Hooman, K., 2022, A designed wall roughness approach to improve turbulent heat transfer to supercritical CO2 flowing in horizontal tubes. The Journal of Supercritical Fluids, 190 (2022), 105738, https://doi.org/10.1016/j.supflu.2022.105738.

Wang, S. and Wang H., 2021, Numerical simulation of the thermal-hydraulic characteristics of supercritical carbon dioxide in a wire-wrapped rod bundle. Applied Thermal Engineering 198 117443.

Watts, M.J., 1980, Heat Transfer to Supercritical Pressure Water–Mixed Convection with Upflow and Downflow in a Vertical Tube. Ph.D. Thesis, University of Manchester, Manchester, UK, 1980.

Website of the Generation IV International Forum, https://www.gen-4.org/gif/

Weller, H., 2021, OpenFOAM 11 C++ Source Code Guid, The OpenFOAM Foundation, 2021, Available at: https://cpp.openfoam.org/v11/classFoam_1_1RASModels_1_1buoyantKE.html

Wilcox, D.C., 2006. Turbulence Modeling for CFD. Third Edition, DCW Industries, Inc.

Wiltschko, F., D3.1 Report summarizing the newly generated reference data for natural convection, forced and mixed convection and decay heat removal, 2023 ECC-SMART, Joint European Canadian Chinese development of Small Modular Reactor Technology, GA No. 945234.

Wiltschko F., Sipova M., Vit, J. and Cheng, X., 2024, Experimental investigation of heat transfer to supercritical pressure R134a in artificially roughened tubes, 31st International Conference on Nuclear Engineering (ICONE31), August 4-8, Prague, Czech Republic.

Wood R. D., Smith J. M., 1964, Heat transfer in the critical region-temperature and velocity profiles in turbulent flow. AIChE Journal. 1964. №10. №2 – pp. 180–186.

Yamagata, K., Nishikawa, K., Hasegawa, S., et al., 1972. Forced convective heat transfer to supercritical water flowing in tubes, International Journal of Heat & Mass Transfer, 15 (12), pp. 2575–2593.

Yang, B.H., Joseph D.D., 2009. Virtual Nikuradse. Journal of Turbulence 10, N11, 1-28.

Yaras M. I., 2015, Steady and Unsteady Forced-Convection Heat Transfer Measurements in Upward Flow of R134a at Supercritical Thermodynamic States in a Heated Bundle Test Section with a Wire wrap Spacer. Carleton University Report submitted to Canadian Nuclear Laboratories. Report CU-M&A-2014-03. 2015.

Yoon-Yeong Bae, Hwan-Yeol Kim, 2009, Convective heat transfer to CO_2 at a supercritical pressure flowing vertically upward in tubes and an annular channel, Experimental Thermal and Fluid Science, vol. 33, no 2, 2009, pp. 329-339.

Yu, S., Li, H., Lei, X., Zhang, Y. and Chen, T., 2011, Study of the effect of buoyancy on flow and heat transfer of supercritical pressure water in horizontal pipes. American Society of Mechanical Engineers, Power Division (Publication) POWER. 2. 10.1115/POWER2011-55435.

Yu, S., Li, H., Lei, X., Feng, Y., Zhang, Y., He, H. and Wang, T., 2013, Influence of buoyancy on heat transfer to water flowing in horizontal tubes under supercritical pressure. Applied Thermal Engineering, vol. 59, no. 1–2, pp. 380–388, Sep. 2013, doi: https://doi.org/10.1016/j.applthermaleng.2013.05.034.

Yu Zhu., 2010, Numerical Investigation of the Flow and Heat Transfer within the Core Cooling Channel of a Supercritical Water Reactor, Universität Stuttgart, Dr-Ing. Thesis. ISSN - 0173 - 6892. November 2010, 122 p.

Zahlan, H., Leung, L., Huang Y., and Liu, G., 2018, Convection heat transfer correlations for multiple geometries and fluids at supercritical pressure, CNL Nuclear Review, Vol 7, Number 1, June 2018.

Zhang, B., Shan, J. and Jiang, J., 2010, Numerical analysis of supercritical water heat transfer in horizontal circular tube. Progress in Nuclear Energy, 52 (2010), 678-684.

Zhao M., H. Y. Gu, and X. Cheng, 2014, Experimental study on heat transfer of supercritical water flowing downward in circular tubes, Ann. Nucl. Energy, vol. 63, pp. 339–349, 2014.

Zhu, B., Xu, J., Yan, C., & Xie, J., 2020, The general supercritical heat transfer correlation for vertical up-flow tubes: K number correlation. International Journal of Heat and Mass Transfer, 148, 119080.

Zhukauskas A., Shlyanchyauskas A., 1973, Heat transfer in a turbulent fluid flow. (In Russian), Vilnius: Mintis, 1973.

Zhlutkov S., Aksenov A., 2015, Near-wall functions for high-Reynolds calculations in the FlowVision software package. (In Russian). Computer research and modeling, 2015, Vol. 6, pp. 1221–1239.

APPENDIX – Table of correlations from the survey by UNIPI

#	Author	Correlation	Range of Applicability	Remarks
1	Dittus Boelter 1930	$Nu = 0.023 Re_{\mathrm{b}}^{0.8} \mathrm{Pr}_{\mathrm{b}}^{0.4}$	Subcritical pressures	
2	McAdams et al. 1950	$Nu_{\mathrm{f}} = 0.0214 \mathrm{Re}_{\mathrm{f}}^{0.8}\ Pr_{\mathrm{f}}^{0.33} \left(1 + \frac{2.3}{L/D_{\mathrm{hy}}}\right)$	D_{hy} = 3.32 mm L/D_{hy} = 14.7 – 80.0 P: 0.8 – 24 [MPa] G: 75 - 224 [kg m^{-2} s^{-1}]	annulus
3	Shitsman et al. 1957	$\mathrm{Nu} = 0.023 \mathrm{Re}_{\mathrm{b}}^{0.8} \mathrm{Pr}_{min}^{0.8}$ $\mathrm{Pr}_{min} = \mathrm{Pr}_{\mathrm{b}}$ for $\mathrm{Pr}_{\mathrm{b}} < \mathrm{Pr}_{\mathrm{w}}, \mathrm{Pr}_{min} = \mathrm{Pr}_{\mathrm{w}}$ for $\mathrm{Pr}_{\mathrm{w}} < \mathrm{Pr}_{\mathrm{b}}$	P: 0.4 – 27.4 [MPa], G: 170 - 3000 [kg m^{-2} s^{-1}], q: 0.42 – 8.4 [MWm^{-2}], d: 7.8/8.2 [mm]	H_2O vertical tubes, upward flow
4	Bringer and Smith 1957	$Nu_x = C Re_x^{0.77} Pr_{\mathrm{w}}^{0.55}$ C = 0.0266 for water, C = 0.0375 for carbon dioxide Nu_x and Re_x are evaluated at t_x $t_x = \begin{cases} t_{\mathrm{b}} \text{ if } \left((t_{\mathrm{pc}} - t_{\mathrm{b}})/(t_{\mathrm{w}} - t_{\mathrm{b}})\right) < 0 \\ t_{\mathrm{pc}} \text{ if } 0 \leq \left(t_{\mathrm{pc}} - t_{\mathrm{b}}/t_{\mathrm{w}} - t_{\mathrm{b}}\right) \leq 1.0 \\ t_w \text{ if } \left(t_{\mathrm{pc}} - t_{\mathrm{b}}\right)/(t_{\mathrm{w}} - t_{\mathrm{b}}) > 1.0 \end{cases}$	P: up to 34.5 [MPa]	H_2O, CO_2

5	Krasnoshchekov and Protopopov 1960	$Nu = Nu_0 \left(\frac{\mu_b}{\mu_w}\right)^{0.11} \left(\frac{k_b}{k_w}\right)^{-0.33} \left(\frac{\bar{c}_p}{c_{pb}}\right)^{0.35}$ $Nu_0 = \frac{(\xi/8)\mathrm{Re_b}\ \overline{Pr}}{12.7\sqrt{\xi/8}(\overline{Pr}^{2/3}-1)+1.07}$ $\xi = \frac{1}{(1.82\log_{10}\ \mathrm{Re_b} - 1.64)^2}$	$8\times10^4 < \mathrm{Re_b} < 5\times10^5$ $0.85 < \overline{Pr_b} < 65$ $0.02 < \frac{\bar{c}_p}{c_{pb}} < 4$ $1.00 < \frac{\rho_w}{\rho_b} < 6.00$ $0.9 < \frac{T_w}{T_{pc}} < 2.5$ $4.6\times10^4 < q < 2.6\times10^6$ (q is in W/m^2)	H_2O, CO_2
6	Petukhov et al. 1961	$\mathrm{Nu} = \frac{\left[f\mathrm{Re_b}\ \mathrm{Pr_b}\left(\frac{\mu}{\mu_w}\right)^{0.11}\left(\frac{\lambda_w}{\lambda_b}\right)^{0.33}\left(\frac{\bar{C}_p}{c_{p,b}}\right)^{0.35}/8\right]}{\left[12.7\sqrt{\frac{f}{8}}\left(\mathrm{Pr_b}^{2/3}-1\right)+1.07\right]}$ $f = [1.82\log_{10}(\mathrm{Re}_b) - 1.64]^{-2}$	$2\times10^4 < \mathrm{Re_b} < 8.6\times10^5$ $0.85 < \overline{Pr_b} < 65$ $0.90 < \frac{\mu_b}{\mu_w} < 3.60$ $1.00 < \frac{\lambda_b}{\lambda_w} < 6.00$ $0.07 < \frac{\bar{c}_p}{c_{pb}} < 4.50$	H_2O, CO_2
7	Domin et al. 1963	$\mathrm{Nu} = \begin{cases} 0.1\mathrm{Re_b}^{0.66}\ \overline{Pr}_b^{1.2}, T_w \geq 623.15\mathrm{K} \\ 0.036\mathrm{Re_b}^{0.8}\ \overline{\mathrm{Pr}}_b^{0.4}\left(\frac{\mu_w}{\mu_b}\right), 523.15\mathrm{K} < T_w < 623.15\mathrm{K} \end{cases}$	P: 23.3/26.3 [MPa], q: 0.58–4.65 [MW/m^2], d: 2/4 [mm]	H_2O horizontal tubes

8	Bishop et al. 1964	$Nu = 0.0069\mathrm{Re}_b^{0.9}\,\overline{Pr}_b^{0.66}\left(\frac{\rho_w}{\rho_b}\right)^{0.43}\left(1+2.4\frac{d}{z}\right)$	P: 22.8 – 27.6 [MPa], G: 651 - 3662 [kg m^{-2} s^{-1}], q: 310 - 3460 [kWm^{-2}]	H_2O vertical tubes, upward flow
9	Swenson et al. 1965	$Nu_w = 0.00459\mathrm{Re}_\mathrm{w}^{0.923}\,\overline{Pr}_\mathrm{w}^{0.613}(\rho_w/\rho_b)^{0.231}$	P: 22.7 - 41.3 [MPa], G: 542 - 2149 [kg m^{-2} s^{-1}], q: 204–1820 [kWm^{-2}], d: 9.4 [mm]	H_2O
10	Krasnoschekov et al. 1967	$Nu = Nu_0\left(\frac{\rho_\mathrm{w}}{\rho_\mathrm{b}}\right)^{0.3}\left(\frac{\bar{c}_\mathrm{p}}{c_\mathrm{pb}}\right)^n, Nu_0 = \frac{\left(\frac{\xi}{8}\right)\mathrm{Re}_b\,\overline{Pr}}{12.7\sqrt{\frac{\xi}{8}}\left(\overline{\mathrm{Pr}}^{\frac{2}{3}}-1\right)+1.07}$ $\xi = (1.82\log Re_\mathrm{b} - 1.64)^{-2}$ $n = 0.4$, for $T_\mathrm{w} \le T_\mathrm{pc}$ or $T_\mathrm{b} > 1.2T_\mathrm{pc}$ $n = n_1 = 0.22 + 0.18(T_\mathrm{w}/T_\mathrm{pc})$, for $T_\mathrm{pc} \le T_\mathrm{w} \le 2.5T_\mathrm{pc}$ $n = n_1 + (5n_1 - 2)(1 - T_\mathrm{b}/T_\mathrm{pc})$, for $T_\mathrm{pc} < T_\mathrm{b} < 1.2T_\mathrm{pc}$	$8\times10^4 < \mathrm{Re}_\mathrm{b} < 5\times10^5$ $0.85 < \overline{Pr_b} < 65$ $0.02 < \frac{\bar{c}_\mathrm{p}}{c_\mathrm{pb}} < 4$ $0.9 < \frac{\rho_w}{\rho_b} < 1$ $0.9 < \frac{T_w}{T_{pc}} < 2.5$ $4.6\times10^4 < q < 2.6\times10^6$ (q is in W/m^2) $x/D \ge 15$	H_2O, CO_2
11	Kondratev et al. 1969	$Nu = 0.02Re_\mathrm{b}^{0.8}$	Based on the experimental database see Pioro and Duffey (2007)	H_2O, the database includes

				vertical, vertical annular and horizontal channels
12	Ornatsky et al. 1970	$\mathrm{Nu} = 0.023\mathrm{Re_b^{0.8}}\ \mathrm{Pr}_{min}^{0.8}\left(\frac{\rho_w}{\rho_b}\right)^{0.3}$ $\mathrm{Pr}_{min} = \mathrm{Pr_b}$ for $\mathrm{Pr_b} < \mathrm{Pr_w}, \mathrm{Pr}_{min} = \mathrm{Pr_w}$ for $\mathrm{Pr_w} < \mathrm{Pr_b}$	P: 22.6/29.4 [MPa], G: 450–3000 [kg m^{-2} s^{-1}], d: 3 [mm]	H_2O
13	Grass et al. 1971	$\mathrm{Nu} = \frac{(f/8)\mathrm{Re_b}\ \mathrm{Pr_b}}{1.07 + 12.7\sqrt{f/8}\left(\mathrm{Pr_G^{2/3}}\ C_{p,b}/C_{p,w} - 1\right)}$ $f = [1.82\log_{10}(\mathrm{Re_b}) - 1.64]^{-2}$ $\mathrm{Pr_G} = \mathrm{Pr_b}$ for $\mathrm{Pr_b} < 0.5\mathrm{Pr_w}, \mathrm{Pr_G} = \mathrm{Pr_w}$ for $\mathrm{Pr_b} > 0.5\mathrm{Pr_w}$	P: 14/25 [MPa], G: 700–3500 [kg m^{-2} s^{-1}], q: 400–2000 [kWm^{-2}], d: 10/20 [mm]	H_2O
14	Yamagata et al. 1972	$\mathrm{Nu} = 0.0135\mathrm{Re_b^{0.85}}\ \mathrm{Pr_b^{0.8}}\ F_C$ $F_C = \begin{cases} 1.0 & (T_{pc} - T_b)/(T_w - T_b) > 1 \\ 0.67\mathrm{Pr_{pc}^{-0.05}}\left(\bar{C}_p/C_{p,b}\right)^{n_1} & 0 \le (T_{pc} - T_b)/(T_w - T_b) \le 1 \\ \left(\bar{C}_p/C_{p,b}\right)^{n_2} & (T_{pc} - T_b)/(T_w - T_b) < 0 \end{cases}$ $n_1 = -0.77\left(1 + \frac{1}{\mathrm{Pr_{pc}}}\right) + 1.49, n_2 = 1.44\left(1 + \frac{1}{\mathrm{Pr_{pc}}}\right) - 0.53$	P: 22.6/29.4 [MPa], G: 310–1830 [kg m^{-2} s^{-1}], q: 116–930 [kWm^{-2}], d: 7.5/10 [mm]	H_2O
15	Jackson and Fewster 1975	$Nu = 0.0183\mathrm{Re_b^{0.82}}\ \overline{Pr}^{0.5}\left(\frac{\rho_w}{\rho_b}\right)^{0.3}$	Based on the experimental database see Pioro and Duffey (2007)	

16	Yaskin et al. 1977	$\frac{Nu}{Nu_0} = \left[1 - 0.2\frac{Nu}{Nu_0}\beta(T_\mathrm{w} - T_\mathrm{b})\right]^2$ where Nu_0 is calculated according to the Dittus–Boelter	Based on the experimental database see Pioro and Duffey (2007)	He
17	Dyadyakin and Popov 1977	$Nu_x = 0.021\mathrm{Re}_x^{0.8}\ \overline{\mathrm{Pr}}_x^{0.7}\left(\frac{\rho_\mathrm{w}}{\rho_\mathrm{b}}\right)_x^{0.45}\left(\frac{\mu_\mathrm{b}}{\mu_\mathrm{in}}\right)_x^{0.2} \times\left(\frac{\rho_\mathrm{b}}{\rho_\mathrm{in}}\right)_x^{0.1}\left(1 + 2.5\frac{D_\mathrm{hy}}{x}\right)$	P: 24.5 [MPa], G: 500–4000 [kg m^{-2} s^{-1}], q <4700 [kWm^{-2}], d: 5.2 [mm]	H_2O, seven-rod bundle with helical fins
18	Yeroshenko et al. 1981	$\mathrm{Nu} = 0.023\mathrm{Re}_\mathrm{b}^{0.8}\ \mathrm{Pr}_\mathrm{b}^{0.4}\left[\frac{2}{(0.8\psi + 0.2)^{0.5} + 1}\right]^2 F$ $\psi = 1 + \beta(T_w - T_b)$ $F = \begin{cases}\left(\frac{\overline{C_p}}{C_{p,b}}\right)^{0.28} & \text{for } \overline{C_p} > C_{p,b} \\ 1 & \text{for } \overline{C_p} \le C_{p,b}\end{cases}$	Based on the experimental database see Pioro and Duffey (2007)	He
19	Watts-Chou et al. 1982	$\mathrm{Nu} = 0.021\mathrm{Re}_\mathrm{b}^{0.8}\mathrm{Pr}_\mathrm{b}^{0.55}\left(\frac{\rho_w}{\rho_b}\right)^{0.35}\phi$ $\phi = \begin{cases}1 & \text{for } \mathrm{Bu} \le 10^{-5} \\ (1 - 3000\mathrm{Bu})^{0.295} & \text{for } 10^{-5} < \mathrm{Bu} \le 10^{-4} \\ (7000\mathrm{Bu})^{0.295} & \text{for } \mathrm{Bu} \ge 10^{-4}\end{cases}$ $\mathrm{Bu} = \frac{\overline{Gr}}{\mathrm{Re}^{2.7}\,\overline{\mathrm{Pr}}^{0.5}}$	P: 25 [MPa], G: 132–1060 [kg m^{-2} s^{-1}], q: 175–440 [kWm^{-2}], d: 25.4/32.2 [mm]	H_2O
20	Petukhov et al. 1983	$\mathrm{Nu} = \mathrm{Re}_\mathrm{b}\ \overline{Pr_b}(f/8)/\left[1 + 900/\mathrm{Re}_b + 12.7(f/8)^{0.5}\left(\mathrm{Pr}^{2/3} - 1\right)\right]$ $f = f_0(\rho_w/\rho_b)^{0.4}(\mu_w/\mu_b)^{0.2}$ $f_0 = [1.82\log_{10}(\mathrm{Re}_b/8)]^{-2}(\rho_w/\rho_b)^{0.4}$	P: 7.7; 8.9 [MPa], G: 1000–4100 [kg m^{-2} s^{-1}], q: 384–1053 [kWm^{-2}], d: 8 [mm]	CO_2, Horizontal and

				vertical tubes upward, downward and horizontal flows
21	Bogachev et al. 1983	$\frac{Nu}{Nu_0} = \left(\frac{\bar{c}_\mathrm{p}}{c_\mathrm{pb}}\right)^{0.35}$ $Nu_0 = \frac{(\xi/8)\mathrm{Re_b}\ \overline{Pr}}{12.7\sqrt{\xi/8}(\overline{Pr}^{2/3} - 1) + 1.07}$ $\xi = \frac{1}{(1.82\log_{10}\ \mathrm{Re_b} - 1.64)^2}$	P: 0.23 – 0.3 [MPa], m: (0.19–0.26) ×10^{-3} [kg s^{-1}], q: 0.1 – 1.85 [kWm^{-2}], d: 1.8 [mm]	He, vertical tube.

22	Kirillov et al. 1990	$\mathrm{Nu} = \mathrm{Nu}_0 \left(\frac{\rho_w}{\rho_b}\right)^{0.4} \left(\frac{\overline{C_p}}{C_{p,b}}\right)^n \varphi(k^*)$ $\mathrm{Nu}_0 = \mathrm{Re_b}\ \mathrm{Pr_b}\ (f/8) / \left(1 + 900/\mathrm{Re_b} + 12.7(f/8)^{0.5}\left(\mathrm{Pr_b}^{\frac{2}{3}} - 1\right)\right)$ $f = (1.82 \log_{10} \mathrm{Re_b})^{-2}, k^* = \left(1 - \frac{\rho_w}{\rho_b}\right)\frac{\mathrm{Gr_b}}{\mathrm{Re_b}^2}, \mathrm{Gr_b} = \frac{g\left(1 - \frac{\rho_w}{\rho_b}\right)D^3}{\nu_b^2}$ $n = \begin{cases} 0.4 \text{ for } \frac{T_w}{T_{pc}} < 1.0 \text{ and } \frac{T_b}{T_{pc}} > 1.2 \\ 0.22 + 0.18\frac{T_w}{T_{pc}} \text{ for } \frac{T_w}{T_{pc}} < 1.0 \text{ and } \frac{T_b}{T_{pc}} < 1.0 \\ 0.9\frac{T_b}{T_{pc}}\left(1 - \frac{T_w}{T_{pc}}\right) + 1.08\frac{T_w}{T_{pc}} - 0.68 \text{ for } \frac{T_w}{T_{pc}} < 1.0 \text{ and } \frac{T_b}{T_{pc}} < 1.2 \\ 0.7 \text{ for } \bar{C}_p/C_{p,b} \geq 1.0 \text{ other conditions} \end{cases}$ $\varphi(k^*) = \begin{cases} 0.8 - 1.65\ln k^* - 2.75(\ln k^*)^2 - 1.74(\ln k^*)^3 \\ -0.55(\ln k^*)^4 - 0.09(\ln k^*)^5 - 0.0056(\ln k^*)^6 \quad \text{for } k^* \leq 0.4 \\ 1.4(k^*)^{0.37} \text{ for } k^* > 0.4 \end{cases}$	See Pioro and Duffey (2007)	CO_2
23	Gorban' et al. 1990	$Nu = 0.0059 Re_b^{0.90} Pr_b^{-0.12}$; for H_2O $Nu = 0.0094 Re_b^{0.86} Pr_b^{-0.15}$; for R-12	Based on the experimental database see Pioro and Duffey (2007)	H_2O, R-12
24	Razumovskiy et al. 1990	$\mathrm{Nu} = \mathrm{Re_b}\ \mathrm{Pr_b}\ (f/8)\left(\frac{\overline{C_p}}{C_{p,b}}\right)^{0.65} / \left[1.07 + 12.7\left(\frac{f}{8}\right)^{0.5}\left(\mathrm{Pr}_b^{2/3} - 1\right)\right]$ $f = [1.82\log_{10}(\mathrm{Re}_b/8)]^{-2}\left((\rho_w/\rho_b)(\mu_w/\mu_b)\right)^{0.18}$	P: 23.5 [MPa], G: 2190 [$kgm^{-2}s^{-1}$], q: 0.657–3.385, 1600,1800[MWm^{-2}], d: 6.28 [mm]	H_2O, downward flow

25	Griem et al. 1996	$\mathrm{Nu} = 0.0169\mathrm{Re}_\mathrm{b}^{0.84}\ \mathrm{Pr}_{sel}^{0.432}\ \omega$ $\mathrm{Pr}_{sel} = \mu_b C_{p,\mathrm{sel}}/\lambda_m, \lambda_m = 0.5(\lambda_w + \lambda_b)$ $\omega = \begin{cases} 0.82 & \text{for } h_b < 1540\mathrm{kJ/kg} \\ 1 & \text{for } h_b > 1740\mathrm{kJ/kg} \\ 0.82 + 9 \times 10^{-4} & \text{for } 1540\mathrm{kJ/kg} \le h_\mathrm{b} \le 1740\mathrm{kJ/kg} \end{cases}$ $c_{p,sel} = \frac{1}{3}\left\{\sum_{i=1}^{5} c_p(T_i) - c_{p,max} - c_{p,2max}\right\}$ $T_i = \left\{T_w, \frac{1{,}5T_w + T_b}{2}, \frac{T_w + T_b}{2}, \frac{T_w + 1{,}5T_b}{2}, T_b\right\}$	P: 22/27 [MPa], G: 300–2500 [kgm^{-2}s^{-1}], q: 200–700 [kWm^{-2}], d: 10/20 [mm]	H_2O
26	Kitoh et al. 1999	$\mathrm{Nu} = 0.015\mathrm{Re}_\mathrm{b}^{0.85}\ \mathrm{Pr}_\mathrm{b}^{m}, m = 0.69 - 81000/200G^{1.2} + f_c q$ $f_c = 2.9 \times 10^{-8} + 0.11/200G^{1.2}$ for $0 \le h_b \le 1.5 \times 10^6\mathrm{J/kg}$ $f_c = -8.7 \times 10^{-8} - 0.65/200G^{1.2}$ for $1.5 \times 10^6\mathrm{J/kg} \le h_b \le 3.3 \times 10^6\mathrm{J/kg}$ $f_c = -9.7 \times 10^{-7} - 1.3/200G^{1.2}$ for $3.3 \times 10^6\mathrm{J/kg} \le h_b \le 4 \times 10^6\mathrm{J/kg}$	G: 100 – 1750 [kgm^{-2} s^{-1}], q: up to 1800 [kWm^{-2}]	H_2O
27	Fang 1999	$Nu_w = Nu_{o,w}\left(1 - 0.001\frac{q}{G}\right)\left(\frac{\bar{c}_p}{c_{p,w}}\right)^n$ $Nu_{o,w} = \frac{(f/8)(\mathrm{Re}_b - 1000)\mathrm{Pr}_b}{A + 12.7\sqrt{f/8}\left(\mathrm{Pr}_b^{2/3} - 1\right)}$ $f = 8\left\{\left(\frac{8}{\mathrm{Re}}\right)^{12} + \left[\left(2.457\ln\frac{1}{(7/\mathrm{Re})^{0.9} + 0.27\varepsilon/D}\right)^{16} + \left(\frac{37530}{\mathrm{Re}}\right)^{16}\right]^{-1.5}\right\}^{1/2}$	Based on the experimental database see Pioro and Duffey (2007)	CO_2

		$A = \begin{cases} 1 + 7 \cdot 10^{-8}\mathrm{Re}_w, & \mathrm{Re}_w < 10^6 \\ 1.07, & \mathrm{Re}_w \geq 10^6 \end{cases}$ $n = \begin{cases} 0.66 - 4 \times 10^{-4}(q_w/G) & \bar{c}_p/c_{p_w} \leq 1 \\ 0.9 - 4 \times 10^{-4}(q_w/G) & \bar{c}_p/c_{p_w} > 1 \end{cases}$		
28	Hu et al. 2001	$\mathrm{Nu} = 0.0068\mathrm{Re}_\mathrm{b}^{0.9}\overline{Pr_b}^{0.63}(\rho_w/\rho_b)^{0.17}(\lambda_w/\lambda_b)^{0.29}$	P: 23/26/30 [MPa], G: 600/900/1200 [kgm^{-2}s^{-1}], q: 200–500 [kWm^{-2}], d: 26 [mm]	H_2O
29	Jackson 2002	$\mathrm{Nu} = 0.0183\mathrm{Re}_\mathrm{b}^{0.82}\ \mathrm{Pr}_\mathrm{b}^{0.5}\left(\frac{\rho_w}{\rho_b}\right)^{0.3}\left(\frac{\overline{C_p}}{C_{\mathrm{p},b}}\right)^{\mathrm{n}}$ $n = 0.4$ for $T_b < T_w < T_{pc}, 1.2T_{pc} < T_b < T_w$ $n = 0.4 + 0.2(T_w/T_{pc} - 1)$ for $T_b < T_{pc} < T_w$ $n = 0.4 + 0.2(T_w/T_{pc} - 1)[1 - 5(T_b/T_{pc} - 1)]$ for $T_{pc} < T_b < 1.2T_{pc}$ and $T_b < T_w$	Based on the correlation by Krasnoschekov et al. see Pioro and Duffey (2007)	H_2O, CO_2
30	Liao S et al. 2002	$Nu_w = 0.128\mathrm{Re}_w^{0.8}\ \mathrm{Pr}_w^{0.3}\left(\frac{Gr}{\mathrm{Re}_b^2}\right)\left(\frac{\rho_b}{\rho_w}\right)^{0.437}\left(\frac{\bar{c}_p}{c_{p,w}}\right)^{0.411}$	P: 7.4 - 12 [MPa], q: 10 - 200 [kWm^{-2}], d: 0.5 – 2.16 [mm]	CO_2, horizontal channel
31	Seok Ho Yoon et al. 2003	for $T_\mathrm{b} > T_\mathrm{pc}$, $Nu = 0.14Re_b^{0.69}\ Pr_b^{0.66}\left(\frac{\rho_{pc}}{\rho_b}\right)^0$ for $T_\mathrm{b} \leqslant T_\mathrm{pc}$, $Nu = 0.013Re_b^{1.0}\ Pr_b^{-0.05}\left(\frac{\rho_{pc}}{\rho_b}\right)^{1.6}$	P: 7.5 - 8.8 [MPa], G: 255 – 450 [kg m^{-2}s^{-1}], d: 7.73 [mm]	CO_2, horizontal channel

32	Dang C et al. 2004	$HTC = Nu k_f/d$ $Nu = \frac{(f_f/8)(\mathrm{Re_b} - 1000)\mathrm{Pr}}{1.07 + 12.7\sqrt{f_f/8}(\mathrm{Pr}^{2/3} - 1)}$ $f_f = [1.82\log_{10}(\mathrm{Re_f}) - 1.64]^{-2}$ $\mathrm{Pr} = \begin{cases} c_{p_b}\mu_b/k_b, & \text{for } c_{p_b} \geq \bar{c}_p \\ \bar{c}_p\mu_b/k_b, & \text{for } c_{Pb} < \bar{c}_p \text{ and } \mu_b/k_b \geq \mu_f/k_f \\ \bar{c}_p\mu_f/k_f, & \text{for } c_{p_b} < \bar{c}_p \text{ and } \mu_b/k_b < \mu_f/k_f \end{cases}$	P: 8 - 10 [MPa], G: 200 - 1200 [kg m^{-2} s^{-1}], q: 6 - 33 [kWm^{-2}], d: 1 - 6 [mm]	CO_2, horizontal channel
33	Son et al. 2005	$Nu = \mathrm{Re}_b^{0.55}\ \mathrm{Pr}_b^{0.23}\left(\frac{c_{p,b}}{c_{p,w}}\right)^{0.15}, \quad T_b/T_{pc} > 1$ $Nu = \mathrm{Re}_b^{0.35}\ \mathrm{Pr}_b^{1.9}\left(\frac{\rho_b}{\rho_w}\right)^{-1.6}\left(\frac{c_{p,b}}{c_{p,w}}\right)^{-3.4}, \quad T_b/T_{pc} \leq 1$	P: 7.5/10 [MPa], G: 200–400 [kg m^{-2} s^{-1}], d: 7.75 [mm]	CO_2, horizontal channel
34	Huai et al. 2007	$\mathrm{Nu} = 2.22 \times 10^{-2}\mathrm{Re}^{0.8}\mathrm{Pr}^{0.3}\left(\frac{\rho_r}{\rho_w}\right)^{-1.47}\left(\frac{\bar{C}_p}{C_{pw}}\right)^{0.083}$	P: 8 [MPa], G: 127.1–411.2 [kg m^{-2} s^{-1}], d: 2 [mm]	CO_2, horizontal channel

$$Nu = Nu_{\text{var}} \cdot f(B), \quad B = \frac{\overline{\text{Gr}}}{\text{Re}_b^{2.7}\,\overline{Pr}^{0.5}}$$

$$Nu_{\text{var}} = 0.0183\text{Re}_b^{0.82}\ \text{Pr}_b^{0.5}\left(\frac{\rho_w}{\rho_b}\right)^{0.3}\left(\frac{\bar{c}_p}{c_{pb}}\right)^{n}$$

35	Kim et al. 2008	$n = \begin{cases} 0.4 \text{ for } \frac{T_b}{T_{pc}} < \frac{T_{w'}}{T_{pc}} \le 1 \text{ or } 1.2 \le \frac{T_b}{T_{pc}} < \frac{T_w}{T_{pc}} \\ 0.4 + 0.2\left(\frac{T_w}{T_{pc}} - 1\right) \text{ for } \frac{T_b}{T_{pc}} \le 1 < \frac{T_{w'}}{T_{pc}} \\ 0.4 + 0.2\left(\frac{T_{wc}}{T_{pc}} - 1\right)\left[1 - 5\left(\frac{T_b}{T_{pc}} - 1\right)\right] \text{ for } 1 < \frac{T_b}{T_{pc}} < 1.2 \text{ and } \frac{T_b}{T_{pc}} < \frac{T_w}{T_{pc}} \end{cases}$ $f(B) = \begin{cases} (0.8 + 6.0 \times 10^6 B)^{-0.8} & \text{for } B \le 7.0 \times 10^{-8} \\ 0.261 + 3.068 \times B^{0.1} & \text{for } 7.0 \times 10^{-8} < B \le 7.0 \times 10^{-7} \\ 1.47 - 6.7 \times 10^5 B & \text{for } 7.0 \times 10^{-7} < B \le 1.0 \times 10^{-6} \\ 0.8 & \text{for } 1.0 \times 10^{-6} < B \le 1.0 \times 10^{-5} \\ 0.1423 \times B^{-0.15} & \text{for } 1.0 \times 10^{-5} < B \end{cases}$	P: 7.75/8.12 [MPa] G: 400 – 1200 [kg m^{-2} s^{-1}] q: up to 150 [kWm^{-2}] d: 10 [mm]	CO_2, vertical channel
36	Simoes et al. 2008	$Nu = 0.558\text{Re}_\text{b}^{0.8}\ \text{Pr}_\text{b}^{0.4}\left(\frac{\bar{c}_p}{c_{p,\text{b}}}\right)^{0.362}\left(\frac{\rho_\text{w}}{\rho_\text{b}}\right)^{0.224}\left(\frac{Gr_\text{b}}{Re_\text{b}^2}\right)^{0.07}$	P: 8/21 [MPa] q: 10 - 500 [kWm^{-2}]	CO_2, static mixers
37	Kuang et al. 2008	$Nu = 0.001546{Re_b}^{1.054}\ {\text{Pr}_b}^{0.653}\left(\frac{\rho_w}{\rho_b}\right)^{0.367}\left(\frac{\bar{c}_p}{c_p}\right)^{0.4}$	P: 8 - 10 [MPa] G: 300 – 1200 [kg m^{-2} s^{-1}] d: 0.79 [mm]	CO_2, horizontal channel

38	Kuang et al. 2008	$\mathrm{Nu} = 0.0239\mathrm{Re_b}^{0.759}\mathrm{Pr_b}^{0.833}\left(\frac{\lambda_w}{\lambda_b}\right)^{0.0863}\left(\frac{\rho_w}{\rho_b}\right)^{0.31}\left(\frac{\mu_w}{\mu_b}\right)^{0.1} \cdot (\mathrm{Gr}^*)^{0.014}(q^*)^{-0.021}$ $\mathrm{Gr}^* = g\beta d^4 q/\lambda\nu^2, q^* = \frac{q\beta}{G\bar{C}_p}$	P: 22.75/31 [MPa] G: 380–2600 [kg m^{-2} s^{-1}] q: 233–3474 [kWm^{-2}] d: 7.5/26 [mm]	H_2O
39	Cheng et al. 2009	$\mathrm{Nu} = 0.023\mathrm{Re_b}^{0.8}\ \mathrm{Pr_b}^{1/3}\mathrm{F}$ $\mathrm{F} = \min(\mathrm{F_1}, \mathrm{F_2})$ $\mathrm{F_1} = 0.85 + 0.776(10^3\pi_\mathrm{A})^{2.4}$ $\mathrm{F_2} = \frac{0.48}{(10^3\pi_{\mathrm{A,pc}})}\Big)^{1.55} + 1.21\left(1 - \frac{\pi_\mathrm{A}}{\pi_{\mathrm{A,pc}}}\right)$ $\pi_\mathrm{A} = \frac{\beta}{c_p}\frac{q}{G}$	P: 22.5/25 [MPa] G: < 3500 [kg m^{-2} s^{-1}] q: < 2000 [kWm^{-2}] d: 10.2 [mm]	H_2O
40	Yu et al. 2009	$\mathrm{Nu} = 0.01378\mathrm{Re_b}^{0.9078}\overline{Pr_b}^{0.6171}\left(\frac{\rho_w}{\rho_\mathrm{b}}\right)^{0.4356}(\mathrm{Gr}^*)^{-0.012}(q^*)^{0.0605}$ $\mathrm{Gr}^* = g\beta d^4 q/\lambda\nu^2, q^* = \frac{q\beta}{G\bar{C}_p}$	Based on the experimental database see Pioro and Duffey (2007)	H_2O
41	Bruch et al. 2009	$\frac{Nu}{Nu_{FC}} = 15\left(\frac{Gr}{\mathrm{Re}^{2.7}}\right)^{0.4}$ $Nu_{FC} = 0.0183\mathrm{Re}_b^{0.82}\ \mathrm{Pr}_b^{0.5}\left(\frac{\rho_b}{\rho_w}\right)^{-0.3}$	P: 7.4/12 [MPa] G: 50 – 590 [kg m^{-2} s^{-1}] q: up to 150 [kWm^{-2}] d: 0.5 – 2.16 [mm]	CO_2, vertical channel

42	Bae et al. 2009	$Nu = Nu_0 * f(Bu)$ $f(Bu) = (1 + 1.0 \times 10^8 Bu)^{-0.032}$, for $5.0 \times 10^{-8} < Bu < 7.0 \times 10^{-7}$ $f(Bu) = 0.00185 \times Bu^{-0.43465}$, for $7.0 \times 10^{-7} < Bu < 1.0 \times 10^{-6}$ $f(Bu) = 0.75$, for $1.0 \times 10^{-6} < Bu < 1.0 \times 10^{-5}$ $f(Bu) = 0.0119 \times Bu^{-0.36}$, for $1.0 \times 10^{-5} < Bu < 3.0 \times 10^{-5}$ $f(Bu) = 32.4 \times Bu^{0.40}$, for $3.0 \times 10^{-5} < Bu < 1.0 \times 10^{-4}$ $\mathrm{Nu_0} = 0.021\mathrm{Re_b}^{0.82}\ \mathrm{Pr_b}^{0.5} \left(\frac{\rho_w}{\rho_b}\right)^{0.3} \left(\frac{\overline{C_p}}{C_{p,b}}\right)^{n}$ $n = 0.4$ for $T_b < T_w < T_{pc}, 1.2T_{pc} < T_b < T_w$ $n = 0.4 + 0.2(T_w/T_{pc} - 1)$ for $T_b < T_{pc} < T_w$ $n = 0.4 + 0.2(T_w/T_{pc} - 1)[1 - 5(T_b/T_{pc} - 1)]$ for $T_{pc} < T_b < 1.2T_{pc}$ and $T_b < T_w$	P: 7.75, 8.12, 8.85 [MPa] G: 400, 500, 750, 1000, 1200 [kg m^{-2} s^{-1}] q: up to 150 [kWm^{-2}] d: 0.5 – 2.16 [mm]	CO_2, vertical channel
43	Oh et al. 2010	$\mathrm{Nu} = 0.023\mathrm{Re}_b^{0.7} \cdot \mathrm{Pr}_b^{2.5} \cdot \left(\frac{c_{p,b}}{c_{p,w}}\right)^{-3.5}$ for $T_b/T_{pc} > 1$ $\mathrm{Nu} = 0.023\mathrm{Re}_b^{0.6} \cdot \mathrm{Pr}_b^{3.2} \cdot \left(\frac{\rho_b}{\rho_w}\right)^{3.7} \cdot \left(\frac{c_{p,b}}{c_{p,w}}\right)^{-4.6}$ for $T_b/T_{pc} \leqslant 1$	P: 7.5/10 [MPa] G: 200–600 [kg m^{-2} s^{-1}] d: 4.55/7.75 [mm]	CO_2, horizontal channel
44	Gupta et al. 2010	$\mathrm{Nu}_w = 0.004\mathrm{Re}_w^{0.923}\ \overline{Pr}_w^{0.773} \left(\frac{\rho_w}{\rho_b}\right)^{0.186} \left(\frac{\mu_w}{\mu_b}\right)^{0.366}$	P: 22.8/29.4 [MPa], G: 200–1500 [kg m^{-2} s^{-1}], q: 70–1250 [kWm^{-2}], d: 10 [mm]	H_2O
45	Mokry et al. 2010	$\mathrm{Nu} = 0.0061\mathrm{Re}_\mathrm{b}^{0.904}\overline{Pr}_\mathrm{b}^{0.684} \left(\frac{\rho_w}{\rho_b}\right)^{0.564}$	P: 22.8/29.4 [MPa], G: 200–1500 [kg m^{-2} s^{-1}] q: 70–1250 [kWm^{-2}],d: 10 [mm]	H_2O

46	Preda et al. 2012	$Nu_w = 0.0015\mathrm{Re}_w^{1.03}\ \mathrm{Pr}_w^{0.76}\left(\frac{\mu_w}{\mu_b}\right)^{0.53}\left(\frac{\rho_w}{\rho_b}\right)^{0.46}\left(\frac{k_w}{k_b}\right)^{-0.43}$	Based on the experimental database see Pioro and Duffey (2007)	CO_2
47	Gupta et al. 2012	$Nu_w = 0.0038\mathrm{Re}_w^{0.957}\ \mathrm{Pr}_w^{0.139}\left(\frac{\mu_w}{\mu_b}\right)^{-0.222}\left(\frac{\rho_w}{\rho_b}\right)^{0.836}\left(\frac{k_w}{k_b}\right)^{-0.754}$	P: 7.4/8.8 [MPa] G: 900 – 3000 [kg m^{-2} s^{-1}] q: 15 – 615 [kWm^{-2}] d: 8 [mm]	CO_2, vertical channel
48	Wang et al. 2012	$\mathrm{Nu} = 0.0122\mathrm{Re}_\mathrm{b}^{0.752}\ \overline{Pr}_\mathrm{b}^{0.8775}\left(\frac{\lambda_w}{\lambda_b}\right)^{0.0746}\left(\frac{\rho_w}{\rho_b}\right)^{0.0402}$ $(\mathrm{Gr}^*)^{0.0157}K_V^{-0.031}$ $\mathrm{Gr}^* = g\beta d^4 q/\lambda\nu^2, K_V = 4q_w D\beta/(\mathrm{Re}^2\ \mu C_p)$	Based on the experimental database see Pioro and Duffey (2007)	H_2O, vertical tubes
49	Liu et al. 2012	$\mathrm{Nu} = 0.01\mathrm{Re}_\mathrm{b}^{0.889}\ \overline{Pr}_\mathrm{b}^{0.73}\left(\frac{\lambda_\mathrm{w}}{\lambda_\mathrm{b}}\right)^{0.24}\left(\frac{\mu_\mathrm{w}}{\mu_\mathrm{b}}\right)^{0.153}\left(\frac{\rho_\mathrm{w}}{\rho_\mathrm{b}}\right)^{0.401}\left(\frac{\overline{C_p}}{C_{\mathrm{p,b}}}\right)^{0.014}$ $\cdot(\mathrm{Gr}^*)^{0.007}(q^*)^{0.041}$ $\mathrm{Gr}^* = g\beta d^4 q/\lambda\nu^2, q^* = \frac{q\beta}{G\overline{C_p}}$	Based on the experimental database see Pioro and Duffey (2007)	H_2O, vertical tubes
50	F Wang et al. 2013	$\mathrm{Nu} = 0.0182\mathrm{Re}_\mathrm{b}^{0.8}\ \mathrm{Pr}_\mathrm{b}^{0.38}\left(\frac{\lambda_w}{\lambda_b}\right)^{0.39}\left(\frac{\mu_w}{\mu_b}\right)^{1.47}\left(\frac{\rho_w}{\rho_b}\right)^{0.54}$	P: 23-26 [MPa] G: 450 – 1500 [kg m^{-2} s^{-1}] q: 450 – 1250 [kWm^{-2}] d: 10 [mm]	H_2O, vertical tubes

51	Lee et al. 2013	$Nu = \mathrm{Re}_b^{0.56}\ \mathrm{Pr}_b^{0.27}\left(\frac{c_{p.b}}{c_{p,w}}\right)^{0.2}$ for $\mathrm{T_b/T_{pc}} > 1$ $Nu = \mathrm{Re}_b^{0.35}\ \mathrm{Pr}_b^{2.0}\left(\frac{c_{p,b}}{c_{p,w}}\right)^{-3}$ for $\mathrm{T_b/T_{pc}} \leq 1$	P: 8/10 [MPa] G: 1200–2000 [kg m^{-2} s^{-1}] d: 4.6 [mm]	CO_2, horizontal channel
52	Chen and Fang, 2014	$\mathrm{Nu} = 0.46\mathrm{Re}_b^{0.16}\left(\frac{Pr_w}{Pr_b}\right)^{0.1}\left(\frac{v_w}{v_b}\right)^{-0.55}\left(\frac{\overline{C_p}}{C_{p,b}}\right)^{0.88}\left(\frac{Gr_b^*}{Gr_b}\right)^{0.81}$	Based on the experimental database see Pioro and Duffey (2007)	H_2O, vertical tubes
53	Liao et al. 2014	$\mathrm{Nu} = 0.032089\mathrm{Re}_\mathrm{b}^{0.88832}\overline{\mathrm{Pr}}_\mathrm{b}^{0.71399}\left(\frac{\lambda_\mathrm{w}}{\lambda_\mathrm{b}}\right)^{0.03339}\left(\frac{\rho_\mathrm{w}}{\rho_\mathrm{b}}\right)^{0.68707}$ $\cdot\,(\mathrm{Gr}^*)^{0.00417}(q^*)^{0.18212}$ $\mathrm{Gr}^* = g\beta d^4 q/\lambda v^2, q^* = \frac{q\beta}{G\overline{C_p}}$	Based on the experimental database see Pioro and Duffey (2007)	H_2O, vertical tubes
54	Wang and Li et al. 2014	$\mathrm{Nu} = 0.00684\mathrm{Re}_\mathrm{b}^{0.9}\ \overline{\mathrm{Pr}}_\mathrm{b}^{0.69}\left(\frac{\lambda_w}{\lambda_b}\right)^{0.26}\left(\frac{\rho_w}{\rho_b}\right)^{0.31}$	P: 24/24.5 [MPa] G: 500–1500 [kg m^{-2} s^{-1}] q: 240–883 [kWm^{-2}] d: 7.5/10 [mm]	H_2O vertical tubes
55	Zhao et al. 2014	$\mathrm{Nu} = 0.023\mathrm{Re}_\mathrm{b}^{0.8}\ \mathrm{Pr}_\mathrm{b}^{1/3}\ F, F = min(F_1, F_2)$ $F_1 = 0.62 + 0.06\ln(\pi_B)$ $F_2 = 11.46\ln(\pi_B)^{-1.04}$ $\pi_B = \frac{\beta_\mathrm{b} q_w D}{\lambda_b}$	P: 23 - 26 [MPa] G: 450 -1500 [kg m^{-2} s^{-1}] q: 170 - 1400 [kWm^{-2}] d: 7.6 [mm]	H_2O vertical tubes, downward flow

56	Zhan-Bin Liu et al. 2014	$Nu_{\mathrm{w}} = 0.01\mathrm{Re}_{\mathrm{w}}^{0.9}\ \mathrm{Pr}_{\mathrm{w}}^{0.5}\left(\frac{\rho_{\mathrm{w}}}{\rho_{\mathrm{b}}}\right)^{0.906}\left(\frac{c_{p,\mathrm{w}}}{c_{p,\mathrm{b}}}\right)^{-0.585}$	P: 7.5/8.0/8.5 [MPa] d: 4/6/10.7 [mm]	CO_2, horizontal channel
57	Saltanov et al. 2015	$\mathrm{Nu} = 0.0331\mathrm{Re}_b^{0.784}\overline{Pr}_b^{0.444}\left(\frac{\rho_w}{\rho_b}\right)^{0.640}$	P: 7.57 – 8.85 [MPa], G: 694 - 2987 [kg m^{-2} s^{-1}], q: 180 - 616 [kWm^{-2}], d: 8.1 [mm]	CO_2
58	J Wang et al. 2019	$\mathrm{Nu}_f = 1.2838\mathrm{Nu}_{iso}\left(\frac{\rho_w}{\rho_b}\right)^{-0.1458}$ $\mathrm{Nu}_{iso} = \frac{(f_f/8)(\mathrm{Re}_b - 1000)\mathrm{Pr}_f}{1.07 + 12.7\sqrt{f_f/8}\left(\mathrm{Pr}_f^{2/3} - 1.0\right)}$ $f_f = \left(0.79\ln\ \mathrm{Re}_f - 1.64\right)^{-2}$	P: 8 - 10 [MPa] G: 200 - 800 [kg m^{-2} s^{-1}] q: 5 - 36 [kWm^{-2}] d: 15.75/20/24.36 [mm]	CO_2, horizontal channel
59	Zhu et al. 2020	$Nu = 0.0012Re_{\mathrm{b}}^{0.9484}Pr_{\mathrm{b,ave}}^{0.718}K^{-0.0313}$ $K = \left(\frac{q_{\mathrm{w}}}{G \cdot h_{\mathrm{w}}}\right)^2\frac{\rho_{\mathrm{b}}}{\rho_{\mathrm{w}}}$	Based on the experimental database see Li et al. (2019)	H_2O, CO_2, R134a
60	Li et al. 2020]	$\mathrm{Nu} = 0.83\mathrm{Re}_{\mathrm{b}}^{0.062}\ \mathrm{Pr}_{\mathrm{b}}^{-0.2}\left(\frac{\rho_w}{\rho_b}\right)^{-0.26}\left(\frac{\nu_w}{\nu_b}\right)^{-0.97}\left(\frac{\overline{C_p}}{C_{p,b}}\right)^{0.86}\left(\frac{\mathrm{Gr}^*}{\mathrm{Gr}_{\mathrm{b}}}\right)^{0.92}$	Based on the experimental database see Li et al. (2019)	H_2O vertical tubes
61	Guo et al. 2020	$Nu = 0.114Re_{\mathrm{b}}^{0.589}\ \overline{Pr}_b^{0.465}\left(\frac{Gr}{Re_{\mathrm{b}}^2}\right)^{-0.125}\left(\frac{\rho_{\mathrm{w}}}{\rho_{\mathrm{b}}}\right)^{0.240}\left(\frac{\bar{c}_p}{c_{p,\mathrm{b}}}\right)^{0.096}$	P: 7.6 – 8.4 [MPa] G: 400 -700 [kg m^{-2} s^{-1}] q: 100 - 200 [kWm^{-2}] d: 2 [mm]	CO_2, horizontal channel

62	Andreas Wahl et al. 2021]	for $T_w \geq T_{pc}$ $Nu_w = 0.0495\, Re_w^{0.771} Pr_w^{0.455} \left(\frac{\rho_b}{\rho_w}\right)^{1.450} \left(\frac{\overline{C_p}}{C_{p,b}}\right)^{-0.026} \left(\frac{\lambda_b}{\lambda_w}\right)^{1.604} \left(\frac{\eta_b}{\eta_w}\right)^{-2.623}$ for $T_w < T_{pc}$ $\mathrm{Nu}_w = 0.0052\, \mathrm{Re}_w^{0.971}\ \mathrm{Pr}_w^{0.388} \left(\frac{\rho_\mathrm{b}}{\rho_\mathrm{w}}\right)^{1.279} \left(\frac{\overline{C_p}}{C_{p,b}}\right)^{0.450} \left(\frac{\lambda_\mathrm{b}}{\lambda_\mathrm{w}}\right)^{2.158} \left(\frac{\eta_\mathrm{b}}{\eta_\mathrm{w}}\right)^{-2.923}$	P: 77 - 85 [bar] G: 400 -1300 [kg m^{-2} s^{-1}] d: 2 [mm]	CO_2, horizontal channel

i